

NASA CR-176691

NASA-CR-176691
19860013313

The Telecommunications and Data Acquisition Progress Report 42-84

October—December 1985

E. C. Posner
Editor

LIBRARY COPY

February 15, 1986

MAR 7 1986

LANGLEY RESEARCH CENTER
LIBRARY, NASA
HAMPTON, VIRGINIA



National Aeronautics and
Space Administration

Jet Propulsion Laboratory
California Institute of Technology
Pasadena, California



NF00450

The Telecommunications and Data Acquisition Progress Report 42-84

October – December 1985

E. C. Posner
Editor

February 15, 1986



National Aeronautics and
Space Administration

Jet Propulsion Laboratory
California Institute of Technology
Pasadena, California

N86-22784#

The research described in this publication was carried out by the Jet Propulsion Laboratory, California Institute of Technology, under a contract with the National Aeronautics and Space Administration.

Reference herein to any specific commercial product, process, or service by trade name, trademark, manufacturer, or otherwise, does not constitute or imply its endorsement by the United States Government or the Jet Propulsion Laboratory, California Institute of Technology.

Preface

This quarterly publication provides archival reports on developments in programs managed by JPL's Office of Telecommunications and Data Acquisition (TDA). In space communications, radio navigation, radio science, and ground-based radio astronomy, it reports on activities of the Deep Space Network (DSN) and its associated Ground Communications Facility (GCF) in planning, in supporting research and technology, in implementation, and in operations. Also included is TDA-funded activity at JPL on data and information systems and reimbursable DSN work performed for other space agencies through NASA. The preceding work is all performed for NASA's Office of Space Tracking and Data Systems (OSTDS).

In geodynamics, the publication reports on the application of radio interferometry at microwave frequencies for geodynamic measurements. In the search for extraterrestrial intelligence (SETI), it reports on implementation and operations for searching the microwave spectrum. The latter two programs are performed for NASA's Office of Space Science and Applications (OSSA).

Finally, tasks funded under the JPL Director's Discretionary Fund and the Caltech President's Fund which involve the TDA Office are included.

This and each succeeding issue of the TDA Progress Report will present material in some, but not necessarily all, of the following categories:

OSTDS Tasks:

- DSN Advanced Systems
 - Tracking and Ground-Based Navigation
 - Communications, Spacecraft-Ground
 - Station Control and System Technology
 - Network Data Processing and Productivity
- DSN Systems Implementation
 - Capabilities for New Projects
 - Networks Consolidation Program
 - New Initiatives
 - Network Sustaining
- DSN Operations
 - Network Operations and Operations Support
 - Mission Interface and Support
 - TDA Program Management and Analysis
- GCF Implementation and Operations
- Data and Information Systems

OSSA Tasks:

- Search for Extraterrestrial Intelligence
- Geodynamics
 - Geodetic Instrument Development
 - Geodynamic Science

Discretionary Funded Tasks

This Page Intentionally Left Blank

Contents

OSTDS TASKS DSN Advanced Systems TRACKING AND GROUND-BASED NAVIGATION

The Effect of the Dynamic Wet Troposphere on VLBI Measurements	1
R. N. Treuhaft and G. E. Lanyi	
NASA Code 310-10-60-60-00	

COMMUNICATIONS, SPACECRAFT-GROUND

New Reflective Symmetry Design Capability in the JPL-IDEAS Structure Optimization Program	18
D. Strain and R. Levy	
NASA Code 310-20-65-04-10	
Preliminary Results Toward Injection Locking of an Incoherent Laser Array	26
J. Daher	
NASA Code 310-20-67-55-00	
Low-Loss Off-Axis Feeds for Symmetric Dual-Reflector Antennas	35
T. Veruttipong, V. Galindo-Israeli, and W. Imbriale	
NASA Code 310-20-65-04-00	
A Note on the Wideband Gaussian Broadcast Channel	60
R. J. McEliece, E. C. Posner, and L. Swanson	
NASA Code 310-30-71-83-04	
On the Decoder Error Probability for Reed-Solomon Codes	66
R. J. McEliece and L. Swanson	
NASA Code 310-30-71-83-02	
A Single Chip VLSI Reed-Solomon Decoder	73
H. M. Shao, T. K. Truong, I. S. Hsu, L. J. Deutsch, and I. S. Reed	
NASA Code 310-30-70-84-08	
Effects of Quantization on Symbol Stream Combining in a Convolutionally Coded System	82
F. Pollara and L. Swanson	
NASA Code 310-30-71-84-04	
Acquisition Times of Carrier Tracking Sampled Data Phase-Locked Loops	88
S. Aguirre	
NASA Code 310-30-70-84-02	

DSN Systems Implementation CAPABILITIES FOR NEW PROJECTS

Physical Optics Analysis of a Four-Reflector Antenna: Part 1	94
A. G. Cha	
NASA Code 314-30-56-04-01	
Performance Characteristics for an Array of Two Receiving Systems With Unequal Predetection Signal-to-Noise Ratios and Enhanced Radio Frequency Carrier Margin Improvement	101
M. H. Brockman	
NASA Code 311-03-41-82-11	

Performance Characteristics for an Array of Two Receiving Systems With Equal Apertures and Enhanced Radio Frequency Carrier Margin Improvement	112
M. H. Brockman	
NASA Code 311-03-41-82-11	

A Conceptual 34-Meter Antenna Feed Configuration for Joint DSN/SETI Use From 1 to 10 GHz	127
S. D. Slobin	
NASA Code 314-30-69-01-11	

NETWORK SUSTAINING

DSN Command System Mark IV-85	135
H. C. Thorman	
NASA Code 314-40-41-81-12	

Deep Space Network Radio Science System for Voyager Uranus and Galileo Missions	143
T. K. Peng and F. F. Donovan	
NASA Code 314-40-41-82-10	

The Search for Reference Sources for ΔVLBI Navigation of the Galileo Spacecraft	152
J. S. Ulvestad and R. P. Linfield	
NASA Code 314-30-51-38-45	

Gain, Phase, and Frequency Stability of DSS-42 and DSS-43 for Voyager Uranus Encounter	164
A. G. Cha and R. Levy	
NASA Code 314-30-56-04-01	

ICE ENCOUNTER OPERATIONS

ICE Encounter Operations	176
N. Fanelli and D. Morris	
NASA Code 314-40-22-34-01	

Usuda Deep Space Center Support for ICE	186
J. P. Goodwin	
NASA Code 314-40-22-51-01	

Arecibo Observatory Support of the U.S. International Cometary Explorer Mission Encounter at Comet Giacobini-Zinner	197
D. D. Gordon and M. T. Ward	
NASA Code 314-40-32-10-13	

ICE Telemetry Performance	203
J. W. Layland	
NASA Code 314-40-31-30-03	

Periodic Variations in the Signal-to-Noise Ratios of Signals Received From the ICE Spacecraft	214
T. Nadeau	
NASA Code 310-30-70-84-06	

Intercontinental Antenna Arraying by Symbol Stream Combining at ICE Giacobini-Zinner Encounter	220
W. J. Hurd, F. Pollara, M. D. Russell, B. Siev, and P. U. Winter	
NASA Code 310-30-70-84-06	

OSSA TASKS

Search for Extraterrestrial Intelligence

Time and Space Integrating Acousto-Optic Folded Spectrum Processing for SETI	229
K. Wagner and D. Psaltis	
NASA Code 119-50-62-09-06	

DISCRETIONARY TASKS

Viterbi Algorithm on a Hypercube: Concurrent Formulation	249
F. Pollara	
NASA Code 404-00-73-02-96	
Author Index, 1985	256

The Effect of the Dynamic Wet Troposphere on VLBI Measurements

R. N. Treuhaft and G. E. Lanyi
Tracking Systems and Applications Section

Calculations using a statistical model of water vapor fluctuations yield the effect of the dynamic wet troposphere on Very Long Baseline Interferometry (VLBI) measurements. The statistical model arises from two primary assumptions: (1) the spatial structure of refractivity fluctuations can be closely approximated by elementary (Kolmogorov) turbulence theory, and (2) temporal fluctuations are caused by spatial patterns which are moved over a site by the wind. The consequences of these assumptions are outlined for the VLBI delay and delay rate observables. For example, wet troposphere induced rms delays for Deep Space Network (DSN) VLBI at 20-deg elevation are about 3 cm of delay per observation, which is smaller, on the average, than other known error sources in the current DSN VLBI data set. At 20-deg elevation for 200-s time intervals, water vapor induces approximately 1.5×10^{-13} s/s in the Allan standard deviation of interferometric delay, which is a measure of the delay rate observable error. In contrast to the delay error, the delay rate measurement error is dominated by water vapor fluctuations. Water vapor-induced VLBI parameter errors and correlations are calculated. For the DSN, baseline length parameter errors due to water vapor fluctuations are in the range of 3–5 cm. The above physical assumptions also lead to a method for including the water vapor fluctuations in the parameter estimation procedure, which is used to extract baseline and source information from the VLBI observables.

I. Introduction

Very Long Baseline Interferometry (VLBI) measures the differential phase of an electromagnetic wave between two antennas on the Earth's surface. Typically the waves originate from compact extragalactic radio sources, such as quasars. The inferred group delay, which is the primary VLBI observable, reflects the distance between the two antennas as well as the angle between the vector connecting the antennas and the vector pointing to the radio source (Refs. 1, 2, and 3). In

establishing a radio reference frame of radio source and baseline coordinates for navigation, delays other than the geometric delay are regarded as errors in the VLBI measurement. The presence of atmospheric water vapor along the lines of sight from each antenna to the source will affect the index of refraction of the traversed medium, and will therefore corrupt the geometric delay measurement (Ref. 4). The rate of change of the phase delay over few-minute time scales, which is the other principal observable of VLBI, will also be affected by water vapor (Ref. 5).

Parameters estimated from the group delay and phase delay rate observables will in turn suffer errors due to the fluctuating water vapor, or wet troposphere. Typical estimated parameters include baseline length, baseline orientation radio source positions, clock offsets, and zenith troposphere delays (Refs. 6 and 7). In most intercontinental VLBI data reduction, zenith troposphere delay parameters are statistically estimated. This technique essentially accounts for a spatially and temporally average troposphere, for each station, for the time over which the zenith parameter is estimated. The wet troposphere fluctuations around these averages are the dominant tropospheric errors, which map to errors in VLBI astrometric and geodetic parameters.

When centimeter-level VLBI observable accuracies are required, the deviations from a temporally and spatially constant wet troposphere must be considered. This article therefore concentrates on the fluctuations in the wet troposphere delay, which cannot be removed as an error source by the VLBI zenith parameter estimation. While the external calibration technique of using water vapor radiometers (WVRs) (Ref. 8) can largely remove the water vapor-induced radiometric error, understanding the character and effect of the fluctuating wet delay is important. Such an understanding will help to evaluate errors in data which are not accompanied by WVR measurements, which constitute almost all of the DSN VLBI data set as well as most VLBI data taken at other institutions. Due to the low elevation limit of 20 deg for current WVRs, direct, external calibration of the low elevation angle observations necessary in intercontinental VLBI will remain impossible. The analysis of such observations will benefit from a statistical description of tropospheric fluctuations at low elevations. This report is also motivated by the need to assess how WVRs can be used to the best advantage when they are available.

We quantify the effect of the wet troposphere by first describing a statistical model of spatial and temporal tropospheric fluctuations in Section II. In Section III the magnitude of the effect indicated by the statistical model on the VLBI delay and delay rate observables is explored. Evidence of the effects of tropospheric fluctuation from the DSN VLBI data set is also shown. Section IV describes a general procedure for calculating the average VLBI parameter errors induced by the wet troposphere. Errors induced in the baseline length parameter are derived as an example of the general error calculation. Section IV also outlines a method for including the statistical description of the troposphere in the VLBI estimation procedure to obtain improved parameter estimates and parameter covariances. Comparisons of model results with data and other calculations are shown in Section V on model validation. In Section VI, we present conclusions and plans for future experimental and analytical approaches to the problem of wet delay fluctuations.

II. A Statistical Model of Water Vapor Fluctuations

There are two principal assumptions in the statistical model developed below: (1) the spatial structure of index of refraction fluctuations can be closely approximated by elementary (Kolmogorov) turbulence theory, and (2) temporal fluctuations are caused by spatial patterns which are moved over a site by the wind. To simplify model calculations, we will further assume that the water vapor spatial structure as well as the wind vector is independent of height up to an effective height to be discussed at the end of this section. Unless otherwise noted, we will also assume that this finite slab of atmospheric water vapor moves across a flat Earth. The model will be described below, and the results of the calculations will be compared to some of the existing data in Section V.

In describing the spatial statistics of the wet troposphere, we will frequently use a quantity called the structure function. For a random function $f(\vec{r})$, where \vec{r} is a vector in space, the structure function for a displacement vector \vec{R} is defined as (Ref. 9):

$$D_f(\vec{r}, \vec{R}) = \langle (f(\vec{r} + \vec{R}) - f(\vec{r}))^2 \rangle \quad (1)$$

where the $\langle \rangle$ brackets mean ensemble average. The fundamental randomly varying function to be considered will be the refractivity $n(\vec{r})$ as a function of the spatial coordinate \vec{r} .¹ Following Ref. 9, we will assume that its structure function is homogeneous and isotropic, that is, that $D_n(\vec{r}, \vec{R})$ is a function of $|\vec{R}| = R$ only, and that it has the form

$$D_n(R) = \langle (n(\vec{r} + \vec{R}) - n(\vec{r}))^2 \rangle = C^2 R^{2/3} \quad (2)$$

where C in Eq. (2) characterizes the ensemble or the "rockiness" of the spatial inhomogeneity. In most of our applications, we assume that C does not vary with \vec{r} or \vec{R} . The consequences of this assumption will be discussed in Section V. It will be shown in the next section that an average C can be determined from WVR data or from the VLBI data itself. Equation (2) is the principal assumption of Kolmogorov turbulence, which is generally derived from dimensional considerations (Refs. 9 and 10). For the refractivity function $n(\vec{r})$, ensemble averaging means considering the behavior of this function for a set of possible tropospheric spatial patterns.

An important random function in calculations which follow is the delay experienced by an electromagnetic wave as it passes through the turbulent atmosphere,

¹Throughout this article, refractivity is represented by n (refractivity = index of refraction - 1). Note that n in the literature is more commonly used for the index of refraction.

$$\tau_{\theta,\phi}(\vec{x}) = (1/\sin \theta) \int_0^h dz n(\vec{x} + \vec{r}(\theta, \phi, z))$$

The vector \vec{r} is along the direction described by the elevation and azimuth θ and ϕ with vertical projection z . The coordinate \vec{x} represents an observation site on the surface of Earth, and h is the effective height of the wet troposphere. The ensemble averaged, squared difference between the delay for two antennas separated by a vector $\vec{\rho}$ on the Earth's surface is the structure function of the delay

$$D_{\tau,\theta,\phi}(\rho) = \langle (\tau_{\theta,\phi}(\vec{x} + \vec{\rho}) - \tau_{\theta,\phi}(\vec{x}))^2 \rangle \quad (3)$$

where each antenna is looking along a ray with elevation θ and azimuth ϕ . The expression for $D_{\tau,\theta,\phi}(\rho)$ in terms of $D_n(R)$ can be calculated by integrating through the finite atmosphere the time delay of a signal as it approaches Earth. Extending the derivation of Ref. 9 yields

$$\begin{aligned} D_{\tau,\theta,\phi}(\rho) = & (1/\sin \theta)^2 \int_0^h \int_0^h D_n \left(\left[\rho^2 + 2(z - z')\rho \cot \theta \cos \phi \right. \right. \\ & \left. \left. + \frac{(z - z')^2}{\sin^2 \theta} \right]^{1/2} \right) dz dz' \\ & - (1/\sin \theta)^2 \int_0^h \int_0^h D_n(|z - z'|/\sin \theta) dz dz' \end{aligned} \quad (4)$$

In Eq. (4), h is taken to be the effective height of the wet troposphere. Equation (4) is the general expression for the structure function of signals arriving at antennas separated by a distance ρ . The azimuth ϕ is relative to the line connecting the two antennas. Equation (4) is derived in Appendix A.

We have numerically integrated Eq. (4) as a function of ρ for two geometrical cases: $\theta = 90^\circ$ and $(\theta, \phi) = (20^\circ, 45^\circ)$, and the result is shown in Fig. 1 versus $\alpha = \rho/h$. $D_{\tau,\theta,\phi}(\rho)$ was normalized to $C^2 h^{8/3}$, since only the shape of the curve in Fig. 1 is important for now. The novel result of Fig. 1 is that $D_{\tau,\theta,\phi}(\rho)$ is not a strict power law. It is often assumed (e.g., Ref. 9) that $\rho \ll h$, which yields the result that $D_{\tau,\theta,\phi}(\rho) \propto \rho^{5/3}$ and power functions are frequently used to describe the spatial structure function. In most of the applications that follow, $\rho \geq h$. The result of integrating Eq. (4) without restrictions on the size of ρ relative to h demonstrates that the structure function behaves as $\rho^{5/3}$ at small ρ and as $\rho^{2/3}$ at large ρ , and changes continuously between those two limits. This important result will surface repeatedly in calculations of rms scatters and Allan variances, both of which are usually con-

sidered to be power functions of time, but in this picture deviate from power law in a fashion analogous to the deviation in Fig. 1.

Another feature of Fig. 1, which will be common to many of the calculations which follow, is the elevation dependence of the structure function. At small antenna separations, the structure function is roughly proportional to the tropospheric path length. We use the phrase "path length" to mean the effective distance traveled by a wave from the top of the wet troposphere to an antenna; it is approximately proportional to $(\sin(\text{elevation angle}))^{-1}$. As the distance ρ becomes many times the wet troposphere height, the structure function becomes proportional to the path length squared. Since the structure function is an average squared delay difference, the rms delay difference between the two antennas will be approximately proportional to $(\text{path length})^{0.5}$ for distances less than the troposphere height and to $(\text{path length})^{1.0}$ for distances greater than the troposphere height. This result is consistent with the intuitive picture that many small irregularities contribute to the short distance structure while a small number of larger irregularities dominate the large distance structure.

The second assumption of the fluctuation model outlined here is that temporal fluctuations are caused by spatial fluctuations which are moved past a site by the wind. The persistence of this "frozen" spatial structure (Ref. 11) allows the calculation of temporal structure functions by replacing $\rho = \nu T$ in Eq. (4), where ν is the wind speed and T is the time at which the structure function is to be evaluated. In other words, the temporal structure function

$$\bar{D}_{\tau,\theta,\phi}(T) = \langle (\tau_{\theta,\phi}(\vec{x}, t + T) - \tau_{\theta,\phi}(\vec{x}, t))^2 \rangle$$

for a time interval T at a single station is equivalent to the spatial structure function $D_{\tau,\theta,\phi}(\rho)$ between two antennas separated by a distance $\rho = \nu T$. That is,

$$\bar{D}_{\tau,\theta,\phi}(T) = D_{\tau,\theta,\phi}(\rho)|_{\rho=\nu T} \quad (5)$$

Thus, an interesting feature of Eq. (4) is that it describes not only the differential fluctuations between two antennas but the temporal fluctuations observed at a single antenna as well. Temporal structure functions therefore have the same curved shape as Fig. 1, and can be described by fitting a polynomial to Fig. 1, as detailed in Appendix A. In Eqs. (4) and (5), ϕ is the angle between the direction of the wind and the antenna line of sight projected on the surface of Earth.

Before discussing the effect of the above model assumptions and derivations on VLBI observables, it will be useful to assign values to the three free parameters implicit in Eqs. (4)

and (5): The effective wet troposphere height h , the wind speed v , and the structure function constant C . Except as noted, subsequent calculations assume h to be 2 km, which is the approximate scale height of the wet troposphere. The wind speed v is taken to be 8 m/s, representative of typical winds at 1-km altitude at Goldstone, California. It will be shown below that once h and v are specified, C can be calculated knowing the standard deviation of the zenith wet delay over any given time interval. The standard deviation can be determined either from VLBI estimates of the zenith parameter for individual experiments or from WVR data. To arrive at a value of C which represents average Goldstone water vapor conditions, we will use WVR data taken at the Mojave station over a period of years. As noted below, C derived in this way is $1.99 \times 10^{-7} \text{ m}^{1/3}$.

III. The Effect of Water Vapor Fluctuations on VLBI Observables

The fluctuating water vapor refractivity will cause errors in the delay and delay rate VLBI observables. In order to assess the average magnitude of the delay error, the variance of the water vapor delay fluctuation for arbitrary antenna orientation will be written as a function of observation time interval. We use the variance at zenith to calculate the structure function normalization constant C . The Allan standard deviation of the fluctuations is then presented to indicate the effect of the fluctuations on the delay rate observable. At the end of this section, the observable elevation dependence for selected time scales will be presented and compared to elevation signatures in the DSN VLBI data set.

The variance of the delay at a single station along the ray-path with elevation θ and a projected angle ϕ with respect to the wind is given by

$$\sigma_{\tau,\theta,\phi}^2(T) = (1/T)^2 \int_0^T (T-t) \bar{D}_{\tau,\theta,\phi}(t) dt \quad (6)$$

Equation (6) is derived in Appendix B. The constant C enters in Eq. (6) through $\bar{D}_{\tau,\theta,\phi}(T)$ as in Eq. (5). Standard deviations of WVR data taken at Goldstone over a several year period show that $\sigma_{\tau,0,0}(T)|_{T=24 \text{ hours}}$ is $1.67 \pm 0.73 \text{ cm}$ of delay (Ref. 12). The Goldstone result applied to Eq. (6) yields a value of $C = 1.99 \times 10^{-7} \text{ m}^{-1/3}$. The standard deviation of the zenith delay is shown versus time interval in Fig. 2 along with the standard deviation for $\theta = 90^\circ$ and $(\theta, \phi) = (20^\circ, 45^\circ)$. Again, the model describes a curved rather than power law shape. Over very small time intervals, the standard deviation is proportional to $T^{5/6}$; over very large intervals, it is proportional to $T^{1/3}$. The elevation dependence also exhibits

the same qualitative feature as it did for the square root of the structure function calculated above.

The Allan variance is a relatively good approximation to the delay rate variance and is therefore calculated in terms of the structure function in Appendix B. The result is the simple formula

$$A_{\tau,\theta,\phi}(T) = (4\bar{D}_{\tau,\theta,\phi}(T) - \bar{D}_{\tau,\theta,\phi}(2T))/(2T^2) \quad (7)$$

The Allan standard deviation, which is the square root of Eq. (7), is shown in Fig. 3 for the same angle combinations as in Figs. 1 and 2. The curved spectrum which maps more strongly with elevation at large time scales than at small is evident again in the Allan standard deviation. The Allan standard deviation is proportional to $T^{-1/6}$ at short time intervals and $T^{-2/3}$ at large time intervals. For reference, the hydrogen maser Allan standard deviation is also shown in Fig. 3.

To compare observable model predictions to VLBI data, delay and delay rate elevation dependences for specified time intervals are presented below. VLBI analysts are typically concerned with delay fluctuations on the order of a few hours if zenith delays are statistically estimated. In that case, fluctuations on longer time scales are largely absorbed by troposphere parameters in the least squares solution. Plotted in Fig. 4(a) is the calculated standard deviation of tropospheric delay for a 3-h time period. The standard deviation is plotted versus the path length in zenith units. The dashed line in Fig. 4(a) shows the contribution of the mean thermal noise, called system noise (Ref. 3), for the DSN VLBI data set. According to this figure, system noise on the average is a more severe error source than that due to water vapor fluctuation. The main conclusion from Fig. 4(a) is that if the parameterization of the troposphere presented here is realistic, the delays of the DSN data set are not currently dominated by the dynamic wet troposphere.

Figure 4(b) shows the Allan standard deviation as calculated from the model for a typical DSN scan length time of 200 s, versus the path length in zenith units. Because the delay rate observable is the average rate of change of delay over a 200-s scan length, the Allan standard deviation at that time interval is close to the delay rate scatter. The dashed line on Fig. 4(b) shows the estimated Allan standard deviation due to instrumental phase instability as measured at DSS 13.² Instrumental phase instability due to amplification and heterodyning is believed to be the largest non-atmospheric error in

²Edwards, C. D., IOM 335.4-473 to Tracking Systems and Applications Section, Jet Propulsion Laboratory, February 1985.

the delay rate measurement; for example, it is approximately an order of magnitude larger than the error due to the hydrogen maser clock. According to the model, with the atmospheric parameters of Section II, the delay rate observable error, unlike the delay error, is dominated by the dynamic wet troposphere.

To test the above conclusions, Figs. 5(a) and 5(b) show the rss delay and delay rate residuals from the DSN VLBI data set as a function of the sum of the path lengths for the raypaths of an observation. The figures are based on 1978–1985 VLBI data taken on the California–Spain and California–Australia baselines. In agreement with the above model considerations, the delay residuals of Fig. 5(a) show no trend with path length. For the delay rates in Fig. 5(b), however, there is a significant increase in rss residuals as the path length increases, much like the model result of Fig. 4(b). The solid line represents the curve in Fig. 4(b), increased 30% with an overall scaling factor. The shape of the model curve is in agreement with the VLBI data. The underestimation of the normalization of the model curve by 30% is in part due to uncertainties in normalization parameters and in part to the tendency of the Allan standard deviation to underestimate the delay rate scatter. In the future, we plan to calculate the delay rate temporal standard deviation, which could be directly compared with the data and perhaps alleviate the need for most of the 30% scaling factor. Comparing Figs. 4 and 5 shows that the calculated levels of wet tropospheric disturbance are in approximate agreement with the levels observed in the DSN VLBI data set. In the case of the delay rate observable, the calculated path length dependence is also consistent with the data.

It should also be noted from Fig. 5(a) that if the DSN noise levels can be reduced below 1–2 cm per observation, the VLBI errors will be dominated in both delay and delay rate by the fluctuating wet troposphere. Dry tropospheric inhomogeneities may also become important. When, for example, DSS 13 is instrumented with a Mark III data acquisition system in the next year, 1–2 cm noise levels should be attainable on most sources. Because of the magnitude of the delay and delay rate tropospheric effects indicated by Figs. 4 and 5, the delay rate observable is usually down-weighted relative to the delay in VLBI analysis. Since the delay observable is therefore much more important in the parameter estimation procedure than the delay rate, the lower noise levels available with improved instrumentation will allow a more thorough empirical study of tropospheric effects on the entire VLBI solution.

In the model calculations in this section, the wet troposphere effective height h , wind speed v , and normalization constant C were assigned the values given at the end of Sec-

tion II. Below we give the dependence of the delay and Allan standard deviations (Eqs. 6 and 7) on h , v , and C . Numerical analyses of Eqs. (4), (6), and (7) imply that the delay standard deviation is proportional to $Chv^{1/3}$ for $T \gg 250$ s. The Allan standard deviation at 200-s time intervals is proportional to $Ch^{0.7} v^{0.6}$. These approximate relations can be used to coarsely gauge the dependence of the statistical quantities on the properties of the frozen-in wet troposphere.

IV. The Effect of Water Vapor Fluctuations on VLBI Parameter Estimates

The effect of the dynamic wet troposphere on the delay and delay rate observables ultimately corrupts the determination of geometric parameters in the VLBI estimation procedure. As mentioned in the introduction, the geometric parameters of baseline and source position define the radio reference frame relative to which spacecraft are navigated. The model presented in previous sections leads to a calculation of the covariance of any two parameters due to the dynamic wet troposphere. Along with the aforementioned model parameters, such as wind speed and the overall normalizing constant, the particular VLBI observing schedule is needed.

In VLBI, parameters are usually estimated by a linear least squares procedure. The parameter estimates to be discussed are actually corrections to *a priori* values. These estimates can be expressed as linear functions of the delay and delay rate observables. They will be expressed below as a function of the delay observable only, because the delay observable dominates the VLBI solution. In the least squares analysis, the i th parameter P_i is calculated as a linear combination of the observables. It is given by

$$P_i = \sum_k F_{i,k} (\tau_{2k} - \tau_{1k}) \quad (8)$$

where $F_{i,k}$ are the observing schedule dependent coefficients generated by the least squares process which multiply the k th observable in the summation for the i th parameter. The $\tau_{m,k}$'s are the delays experienced by the wave arriving at the m th station for the k th observation. In this treatment, the statistical variation of the $\tau_{m,k}$'s are assumed to be due only to the dynamic wet troposphere. From Eq. (8) follows the expression for the parameter covariance between the i th and the j th parameters.

$$\begin{aligned} \langle (P_i - \langle P_i \rangle) (P_j - \langle P_j \rangle) \rangle &= \sum_k \sum_l F_{ik} F_{jl} \\ &[\text{cov}(\tau_{2k}, \tau_{2l}) + \text{cov}(\tau_{1k}, \tau_{1l})] \end{aligned} \quad (9)$$

where

$$\text{cov}(\tau_{mk}, \tau_{ml}) = \langle (\tau_{mk} - \langle \tau_{mk} \rangle) (\tau_{ml} - \langle \tau_{ml} \rangle) \rangle \quad (10)$$

It has been assumed in Eq. (9) that the stations are far enough apart that their tropospheres are uncorrelated. The brackets refer to the same ensemble average as in Eq. (1), where each ensemble member consists of a value of the randomly varying refractivity for each point in space.

The frozen-in statistical model described above allows for the calculation of the covariance of Eq. (10). Substituting the expression in Appendix A, Eq. (A-1), into Eq. (10) and using the relation Eq. (A-3), yields the result

$$\begin{aligned} \text{cov}(\tau_k, \tau_l) = & (1/\sin \theta_k) (1/\sin \theta_l) \left[h^2 \sigma_n^2 \right. \\ & \left. - \frac{1}{2} \int_0^h \int_0^h D_n(|\vec{r}_k(z) - \vec{r}_l(z')|) \right. \\ & \left. - (\vec{r}_l(z') - \vec{v}t_l) \cdot (\vec{r}_k(z) - \vec{v}t_k) \right] \quad (11) \end{aligned}$$

where the station index has been suppressed and σ_n^2 is the variance of wet refractivity fluctuations. It is given by

$$\sigma_n^2 = \langle n(\vec{r})^2 \rangle - \langle n(\vec{r}) \rangle^2 \quad (12)$$

where the $n(\vec{r})$ and $D_n(r)$ functions are as in Eq. (2), and θ_k and θ_l are the elevation angles for the k th and l th observations. $\langle n(\vec{r}) \rangle$ and $\langle n(\vec{r})^2 \rangle$ are independent of \vec{r} in the homogeneous picture of the atmosphere. The times t_k and t_l correspond to the k th and l th observations, and $\vec{r}_k(z)$ and $\vec{r}_l(z')$ describe the point in space associated with the k th and l th lines of sight at heights z and z' , respectively. The wind velocity in Eq. (11) is assumed to be independent of scan number. Within the framework of this model, Eq. (11) is the covariance of the wet tropospheric delay for observations along any two rays separated by arbitrary times.

Substituting Eq. (11) into Eq. (10) and Eq. (10) into Eq. (9) yields the complete expression for the VLBI parameter covariances. We write it below with the modification that the actual curvature of Earth be considered in describing the mapping of a zenith path length to arbitrary elevation angles (Ref. 13):

$$\begin{aligned} \text{cov}(P_i, P_j) = & \sum_k \sum_l F_{ik} F_{jl} \left[m_k m_l h^2 \sigma_n^2 \right. \\ & \left. - (2 \sin \theta_k \sin \theta_l)^{-1} \int_0^{h'_k} \int_0^{h'_l} dz dz' D_n(s) \right] \quad (13) \end{aligned}$$

where

$$\begin{aligned} s^2 = & (z \cot \theta_k \cos \phi_k - z' \cot \theta_l \cos \phi_l - v(t_k - t_l))^2 \\ & + (z \cot \theta_k \sin \phi_k - z' \cot \theta_l \sin \phi_l)^2 + (z - z')^2 \end{aligned}$$

where m_k and m_l are the actual mapping from zenith to the lines of sight at θ_k and θ_l , respectively. h'_k is $h m_k \sin \theta_k$ and h'_l is $h m_l \sin \theta_l$. The wind vector is along the x axis and ϕ_k and ϕ_l are the azimuths of the k th and l th scan relative to the wind vector direction.

Before giving a sample parameter covariance result, it is important to clarify the meaning of the σ_n^2 term in Eqs. (11), (12), and (13). To get a finite ensemble averaged value for σ_n^2 , the troposphere must be completely uncorrelated at points infinitely distant from each other. Then

$$\sigma_n^2 = (1/2) D_n(\infty) \quad (14)$$

from the definition of the structure function in Eq. (1) and the assumption of homogeneity. The structure function of Eq. (2) does not converge at infinity, and this unphysical feature of the Kolmogorov structure function must be altered. A phenomenological function must be used which takes the form of Eq. (2) for small distances and converges to a constant at $r = \infty$. We choose the modified structure function to be

$$D'_n(R) = C^2 R^{2/3} / [(1 + (R/L)^{2/3})] \quad (15)$$

where L is a saturation scale length. L is chosen to be 2000 km to be in approximate agreement with Ref. 11. This value of L also produces reasonable very long term rms tropospheric variations of about 3.5 cm, consistent with the total tropospheric fluctuation over many months at mid-latitudes. In actual calculations, $D'_n(R)$ must be substituted into Eq. (13) in place of $D_n(R)$ to calculate parameter covariances. It will be demonstrated below that the actual covariances calculated for geometric parameters are very insensitive to the choice of L , provided L is in a physically reasonable range.

Figure 6 shows the baseline length error as calculated by Eqs. (13), (14), and (15) as a function of time over which troposphere zenith parameters are estimated in the VLBI analysis. The experiment was conducted in May 1983 on the

California–Australia baseline. Two different sets of constants were used in the plot with the constraint that the daily zenith delay standard deviation be 1.67 cm. As noted, the wind speed was assumed to be 8 and 2 m/s. In each case the daily zenith constraint was met by adjusting C to the value of 1.99×10^{-7} and 3.19×10^{-7} , respectively. Figure 6 shows by the similarity of the two curves that the baseline length covariances calculated are sensitive mainly to the zenith standard deviation. The covariances shown in Fig. 6 are insensitive to changing the more uncertain parameters of troposphere height, refractivity structure function normalization, or the wind speed. A similar statement can be made about the choice of the scale distance L . To test the length error sensitivity to h , h was changed from 2 km to 1 km and L varied between 3000 km to 1000 km; no appreciable change in the length error calculation resulted in either case.

Figure 6 also allows the determination of the optimal number of troposphere parameters for a given VLBI schedule. The figure shows that baseline length errors for the experiment considered can be reduced from the 5-cm to the 3-cm range if the length of time for the zenith solution is less than approximately 4 h. Estimating the zenith more frequently than every 2 h, however, does not reduce the length error much below the 3.5-cm level. Figure 6 is only an example of how the model presented here can be used to calculate VLBI parameter errors. The estimate of baseline length errors varies with observing schedule as well as with the troposphere fluctuation normalization, which can be approximated from the fluctuation of the VLBI estimated troposphere parameters.

Equations (11) through (15) also suggest a possible refinement to the VLBI parameter estimation procedure. Most VLBI estimation schemes currently in use do not allow for a correlation between observations, because system noise is in principle uncorrelated from time to time. But the troposphere noise is correlated, as is evidenced, for example, by the shape of the delay standard deviation calculated in Section III. If the model outlined provides a sufficiently accurate description of the troposphere-induced delays, then Eq. (11) evaluated with D'_n as given in Eq. (15) can be used in the least squares analysis. This expression for the observable covariance could be used in the observable covariance matrix in the VLBI parameter estimation routines. Work is in progress at JPL to modify the MASTERFIT parameter estimation software to include these off-diagonal elements in the covariance matrix. At present, it is not known whether the inclusion of the troposphere covariance will be adopted as a standard procedure because of the large computer resources needed to compute the covariance of Eq. (11). We will either include the results of calculations based on Eq. (11) or simply calculate the parameter errors caused by the troposphere in the current estimation scheme using Eq. (13) with D'_n .

V. Model Validation

The above model description rests on the two aforementioned physically appealing but simplified assumptions about frozen-in turbulence. Here we compare the salient results of the model to published results. Comparisons between model calculations and spatial structure function results are followed by comparisons with Allan standard deviations and power spectra. At the end of this section, the question of the altitude independence of C and the wind vector is discussed.

Spatial structure functions $D_{\tau,\theta,\phi}(\rho)$ were measured by Armstrong and Sramek (Ref. 14) at the Very Large Array. For each ρ , θ and ϕ were averaged over many observations. Armstrong and Sramek fit their structure functions to power laws and found powers between 0.84 and 1.95 with an average of 1.4. Plotted in Fig. 7 are the exponents from local power law fits to the calculated structure functions of Fig. 1, as a function of α . Assuming a troposphere height of 2 km and taking the average ρ of Ref. 14 to be about 3 km yields an expected average exponent between 0.95 and 1.35 corresponding to the zenith and 20-deg elevation prediction from the model. The exact model value depends on the elevation angle spread of the actual experiment. Thus, the model qualitatively agrees with the data, slightly underestimating the measured slope. There is some indication in the figures of Ref. 14 that the structure function does curve at large ρ , but the evidence is not conclusive.

In Ref. 11, Dravskikh and Finkelstein describe a structure function which conforms to the atmospheric data they have studied. They state that the data are consistent with a structure function made up of two power laws. The function is proportional to $\rho^{5/3}$ for spatial scales less than 5.6 km, and proportional to $\rho^{2/3}$ for scales larger than 5.6 km. The asymptotic power law exponents agree with our model calculation. For a troposphere height of 2 km, the point where the power laws change would be at $\alpha = 2.8$. Such a change could easily be imagined to take place at this value of α in Fig. 1, if one were trying to fit the model result of Fig. 1 to a two-component power law. Although the agreement with our model is very good, it should be noted that Dravskikh and Finkelstein do not clearly describe the origin of either their data or their model assumptions.

The Allan standard deviation of VLBI phase fluctuations, presumably due to the wet troposphere, $A_{\tau,\theta,\phi}(T)$, was measured by Rogers et al. in Ref. 15. It is of the same order of magnitude as that shown in Fig. 3, but, more importantly, it is clearly curved. The curvature is not as extreme as the model predicts. This could be in part due to system noise contributions to the Allan standard deviation at very short time scales as well as to inadequacies in the above model.

Tropospheric temporal power spectra measured with a WVR by Hogg et al. (Ref. 16) exhibit nearly power law behavior with an exponent of roughly 1.75, corresponding to an Allan standard deviation slope of -0.625 (see Ref. 9 and Eq. 7). This is close to the model prediction behavior for long time scales, but there is no evidence of the curved shape predicted by the model at short time scales. Again, either instrumental noise or inadequacies in the above model could be responsible for the discrepancies between the model and the published data.

Power spectra measured by Thompson et al. (Ref. 17) show more of a curved shape as expected from the above discussion. At high frequencies near 0.1 Hz, the power law exponent for the power spectrum shown is near -2.86 . Near the low frequency of 0.01 Hz, the exponent is approximately -1.92 . These two slopes correspond to short- and long-term Allan standard deviation slopes of -0.07 and -0.54 , respectively, in qualitative agreement with model predictions.

A summary of the power law exponents from model predictions and data is presented for the discussed statistical quantities in Table 1. The table shows a list of statistical quantities in the first column and the mathematical expression used in the text in the second. The third column shows the exponent of the independent variable describing local power law fits for small and large scales of the variable, connected by an arrow. For distance, small means much less than the water vapor scale height (~ 2 km). Large scales mean distances much greater than the scale height. Small and large time scales correspond to the small and large distance scales divided by the average wind speed. The fourth column shows the power laws determined from measurements, with small and large scales noted as before, if available from the data. The fifth column shows the reference for the data quoted in the fourth column.

Investigations of the range of validity of the above calculations will have to address the validity of the homogeneity ascribed to the constant C and the wind vector. Measurements of C (Ref. 18) show varying altitude dependencies. The insensitivity to the effective height h discussed in Section IV and calculations with an exponentially decreasing C suggest the adequacy of the slab model used in this article for most applications. Data on the wind vector (Ref. 19) also show a variety of altitude dependences. Again, some average wind speed present over an average height may suffice, but this must be investigated. In the worst case, the equations for the wet tropospheric effects on observables and parameters could be modified to include altitude dependences for C and the wind speed, at the cost of calculational complexity.

The model qualitatively agrees with the references cited; however, more experiments are needed to really test the limitations of the model. To that end, we have conducted a set of WVR experiments with simultaneous wind vector monitoring at Goldstone. The data are currently being analyzed and will be reported in the near future.

VI. Conclusions and Discussion

The description of water vapor fluctuations based on frozen-in Kolmogorov turbulence leads to estimates of the effect of the dynamic wet troposphere on VLBI observables and parameters. Based on this description, one finds that the current DSN VLBI data set errors are troposphere-dominated for delay rates only. Since parameters are largely determined by the delay observables, formal errors in the 1978-1985 DSN VLBI data set do not have to be substantially modified to account for the dynamic wet troposphere.

Estimated parameter covariances were derived within the framework of the statistical model. A sample calculation of baseline length errors for one of the DSN California-Australia experiments showed the capability of repeated zenith parameter estimation to reduce baseline length error. The example showed that, under typical observing conditions, troposphere-induced baseline length error could be reduced from 5 cm to 3 cm as the estimation time for zenith delay was decreased.

All estimates of observable and parameter effects in this article are dependent upon normalization to the Goldstone WVR data, as mentioned in Section III. The spread of the measured daily zenith standard deviations mentioned in Section III is about 40% of the nominal 1.67 cm used throughout the article. This is a good indication of how much quoted numbers can vary over time at a particular site. As has been mentioned, it may be possible to use VLBI or WVR data to obtain zenith standard deviations and normalize the statistics for individual experiments. The reliability of that procedure is being checked with the recent WVR data taken at Goldstone.

Our future efforts include the analysis of several WVR experiments performed in the last few months, which should help to resolve the limitations of the model. These experiments should also prove useful in assessing the character of the noise contribution of the WVR instruments. The practical benefits of putting the calculated troposphere covariance into the JPL VLBI parameter estimation scheme will be studied with a test version of MASTERFIT. VLBI data will then be processed with the troposphere covariance and the results compared to processing with WVR measurements.

Acknowledgment

We would like to acknowledge O. J. Sovers for analyses of the DSN VLBI data set used in this article.

References

1. Gold, T., "Radio Method for the Precise Measurement of the Rotation Period of the Earth," *Science*, Vol. 157, pp. 302–304, July 1967.
2. Rogers, A. E. E., "Very Long Baseline Interferometry with Large Effective Bandwidth for Phase-Delay Measurements," *Radio Science*, Vol. 5, pp. 1239–1247, October 1970.
3. Thomas, J. B., *An Analysis of Long Baseline Radio Interferometry*, Technical Report 32–1526, Vol. VII, Jet Propulsion Laboratory, Pasadena, Calif., pp 37–50, 1972.
4. Hinder, R. A., "Observations of Atmospheric Turbulence with a Radio Telescope at 5 GHz," *Nature*, Vol. 225, pp. 614–617, February 1970.
5. Treuhaft, R. N., Lanyi, G. E., and Sovers, O. J., "The Dynamic Wet Troposphere Error Budget for Intercontinental VLBI," *Transactions, American Geophysical Union (EOS)*, Vol. 66, p. 858, November 1985.
6. Sovers, O. J., Thomas, J. B., Fanselow, J. L., Cohen, E. J., Purcell Jr., G. H., Rogstad, D. H., Skjerve, L. J., and Spitzmesser, D. J., "Radio Interferometric Determination of Intercontinental Baselines and Earth Orientation Utilizing Deep Space Network Antennas: 1971 to 1980," *Journal of Geophysical Research*, Vol. 89, pp. 7597–7607, September 1984.
7. Shapiro, I. I., "Estimation of Astrometric and Geodetic Parameters from VLBI Observations," in *Methods of Experimental Physics*, M. L. Meeks, Ed., New York: Academic Press, pp. 261–276, 1976.
8. Resch, G. M., Hogg, D. E., and Napier, P. J., "Radiometric Correction of Atmospheric Path Length Fluctuations in Interferometric Experiments," *Radio Science*, Vol. 19, pp. 411–422, January 1984.
9. Tatarskii, V. I., *Wave Propagation in a Turbulent Medium*, New York: Dover, 1961.
10. Ishimaru, A., *Wave Propagation and Scattering in Random Media*, Vol. 2, New York: Academic Press, 1978.
11. Dravskikh, A. F., and Finkelstein, A. M., "Tropospheric Limitations in Phase and Frequency Coordinate Measurements in Astronomy," *Astrophysics and Space Science*, Vol. 60, pp. 251–265, 1979.
12. NASA Crustal Dynamics Data Information System, Goldstone Water Vapor Radiometer Data, 1981–1983.
13. Lanyi, G. E., "Tropospheric Delay Effects in Radio Interferometry," *TDA Progress Report 42–78*, pp. 152–159, Jet Propulsion Laboratory, Pasadena, Calif., 1984.
14. Armstrong, J. W., Sramek, R. A., "Observations of Tropospheric Phase Scintillations at 5 GHz on Vertical Paths," *Radio Science*, Vol. 17, pp. 1579–1586, November 1982.

15. Rogers, A. E. E., Moffet, A. T., Backer, D. C., and Moran, J. M., "Coherence Limits in VLBI Observations at 3-Millimeter Wavelength," *Radio Science*, Vol. 19, pp. 1552-1560, November 1984.
16. Hogg, D. C., Guiraud, F. O., and Sweezy, W. B., "The Short-Term Temporal Spectrum of Precipitable Water Vapor," *Science*, Vol. 213, p. 1112, September 1981.
17. Thompson, M. C., Wood, L. E., Janes, H. B., and Smith, D., "Phase and Amplitude Scintillations in the 10 to 40 GHz Band," *IEEE Transactions on Antennas and Propagation*, AP-23, pp. 792-797, November 1975.
18. Thompson, Jr., M. C., Marler, F. E., and Allen, K. C., "Measurement of the Microwave Structure Constant Profile," *IEEE Transactions on Antennas and Propagation*, AP-28, pp. 278-280, March 1980.
19. Chadwick, R. B., Moran, K. P., Strauch, R. G., Morrison, G. E., and Campbell, W. C., "Microwave Radar Wind Measurements in the Clear Air," *Radio Science*, Vol. 11, pp. 795-802, October 1976.

Table 1. Comparison of behavior of calculated and measured tropospheric statistics

Statistic	Expression from text	Power law exponent		
		This model	Data	Reference for data
Spatial structure function	$D_{\tau,\theta,\phi}(\rho)$ Eq. (4)	$5/3 \rightarrow 2/3$	1.4 $5/3 \rightarrow 2/3$	Ref. 14 Ref. 11
Temporal structure function	$\bar{D}_{\tau,\theta,\phi}(T)$ Eq. (5)	$5/3 \rightarrow 2/3$	— — —	— — —
Standard deviation of zenith display	$\sigma_{\tau,\theta,\phi}(T)$ Eq. (6)	$5/6 \rightarrow 1/3$	— — —	— — —
Allan standard deviation	$\sqrt{A_{\tau,\theta,\phi}(T)}$ Eq. (7)	$-1/6 \rightarrow -2/3$	$-0.25 \rightarrow -0.50$ - 0.63 $-0.07 \rightarrow -0.54$	Ref. 15 Ref. 16 Ref. 17

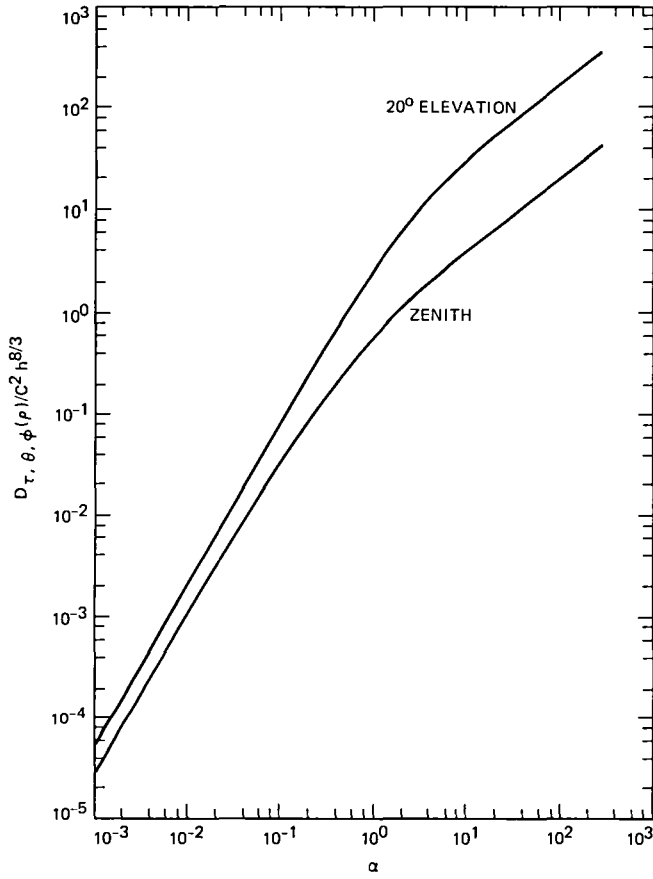


Fig. 1. The spatial structure function, calculated from Eq. (4) normalized to $C^2 h^{8/3}$, as a function of $\alpha = \rho/h$, where ρ is the distance between two points on Earth at which the wave is received, and h is the effective height of the wet troposphere. Curves are shown for $(\theta, \phi) = (90^\circ, 0^\circ)$ and $(\theta, \phi) = (20^\circ, 45^\circ)$.

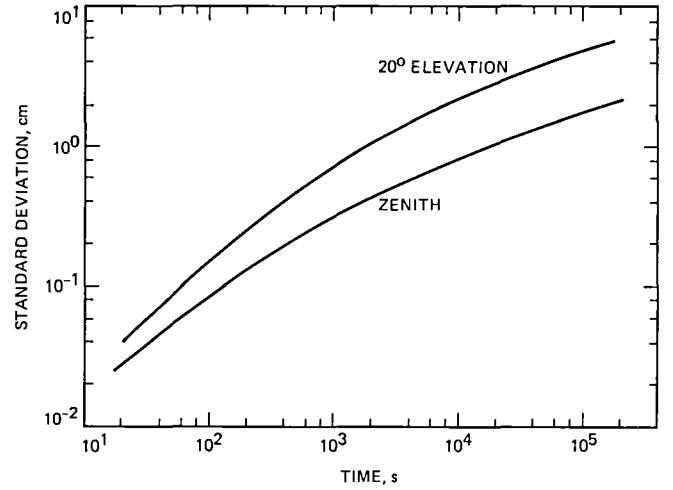


Fig. 2. The single-site, calculated standard deviation of the delay fluctuation as a function of time interval. The standard deviation is shown for zenith and 20-deg elevation. Refractivity structure function normalization, wet troposphere height, and wind speed are as noted at the end of Section II.

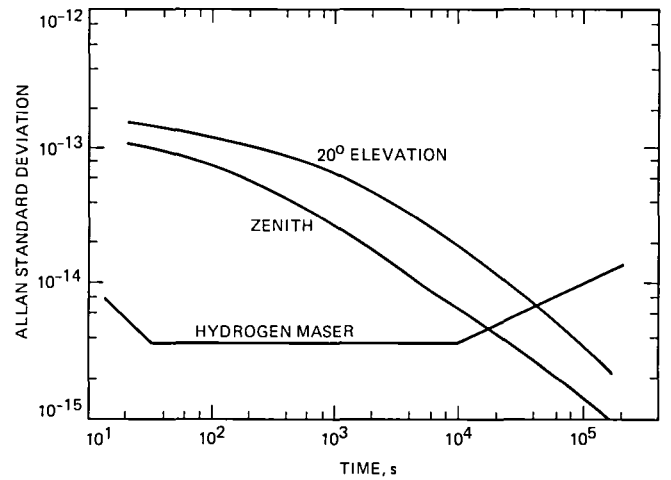


Fig. 3. The single-site, calculated Allan standard deviation of the delay fluctuation as a function of time interval. The Allan standard deviation is shown for zenith and 20-deg elevation.

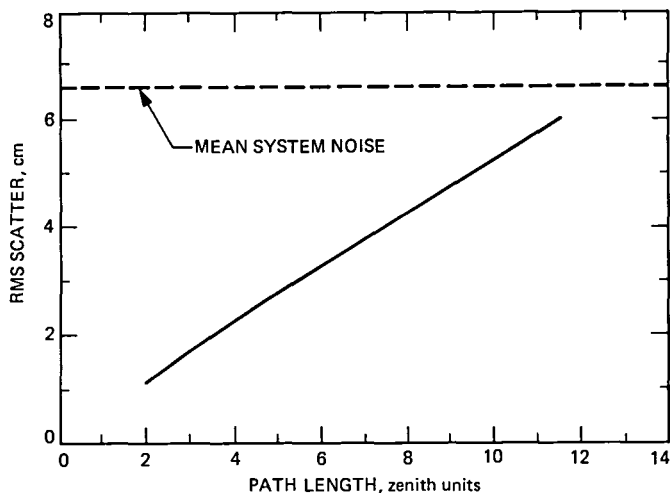


Fig. 4(a). The calculated delay standard deviation at a 3-h time interval as a function of total path length for two raypaths through the atmosphere for a VLBI observation. The dashed line is the mean system noise for the 1978–1985 DSN VLBI data set.

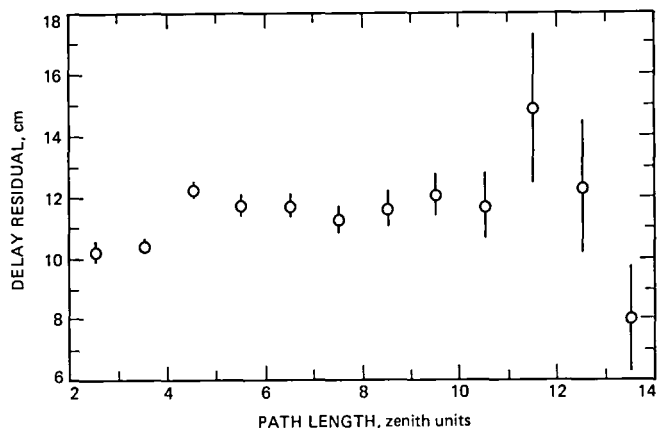


Fig. 5(a). The rms delay residual from the 1978–1985 DSN VLBI data set, for intercontinental observations only, versus path length through the atmosphere.

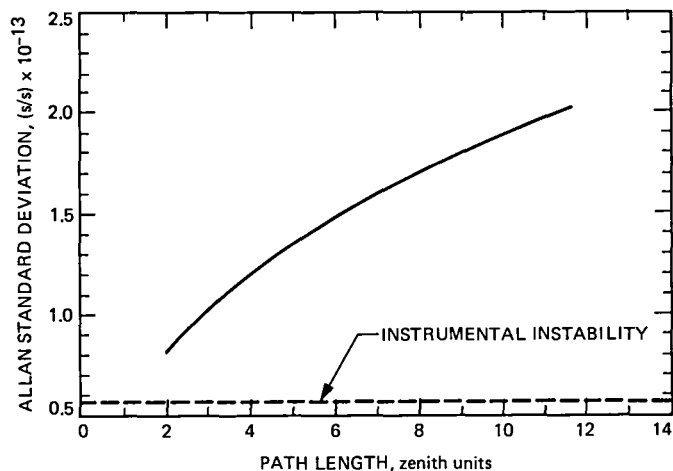


Fig. 4(b). The calculated delay Allan standard deviation at a 200-s time interval as a function of path length for two raypaths for a VLBI observation. The dashed line is an estimate of the current instrumental instability as measured at DSS 13.

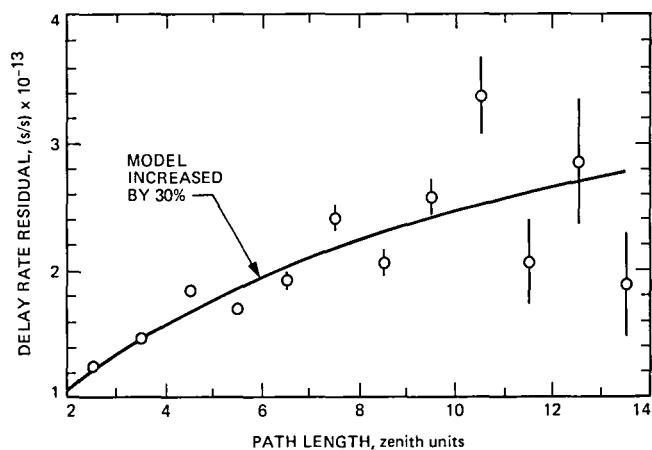


Fig. 5(b). The rms delay rate residual from the 1978–1985 DSN VLBI data set, for intercontinental observations only, versus path length through the atmosphere. The solid curve is the model prediction of Fig. 4(b) increased by 30%.

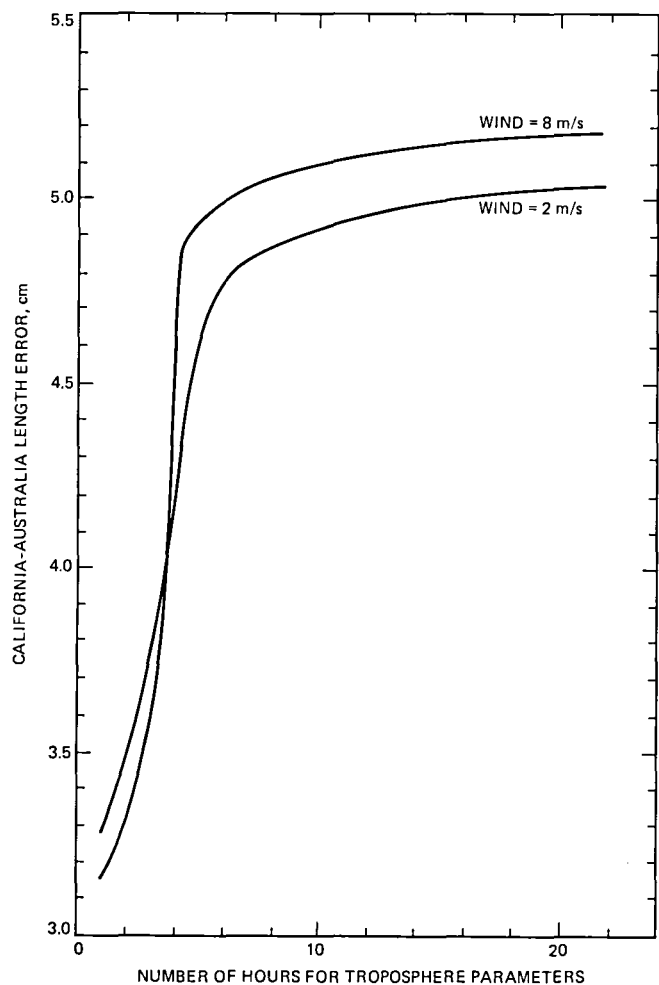


Fig. 6. The calculated California–Australia baseline length error as a function of the time over which zenith troposphere parameters are solved. Two curves are shown, one in which the wind speed was assumed to be the standard 8 m/s, and one in which the wind speed was assumed to be 2 m/s. For both curves the daily zenith standard deviation was taken to be 1.67 cm.

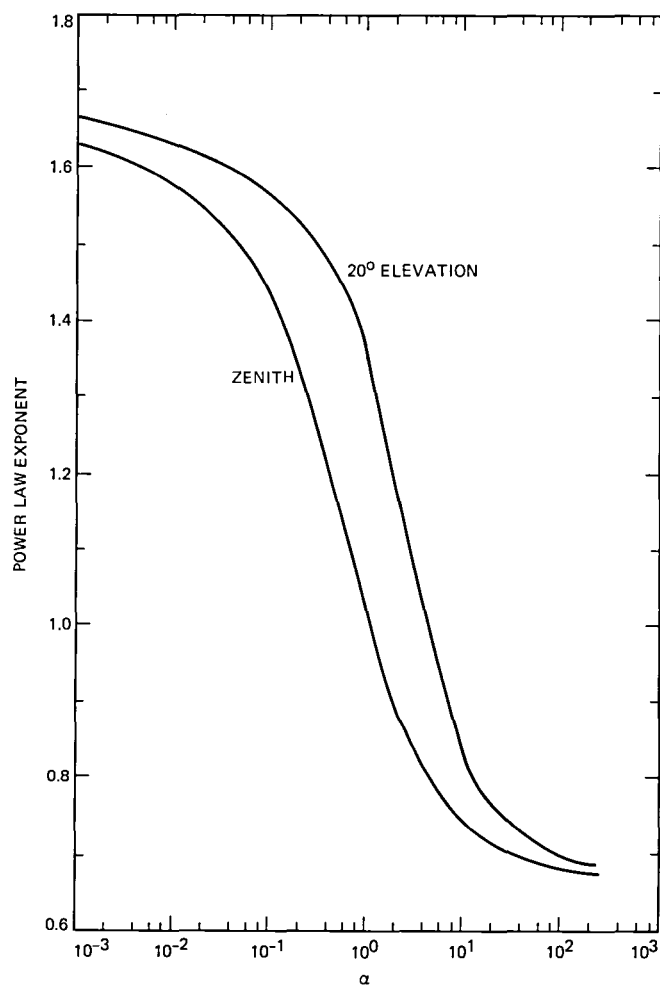


Fig. 7. Exponents from local power law fits to the curves in Fig. 1 versus α , where $\alpha = \rho/h$.

Appendix A

The Spatial Structure Function

The spatial structure function for the delay of waves propagating through the atmosphere to Earth is defined by Eq. (3). In order to derive the result of Eq. (4) for arbitrary lines of sight separated by a distance ρ , Earth will be considered flat. This will result in less than a 5% error at 6-deg elevation. Let $\tau_{\theta,\phi}(\vec{x})$ be the tropospheric delay experienced by a wave incident at a point on the Earth's surface \vec{x} . The wave arrives along the line of sight with elevation θ and azimuth ϕ .

Assuming geometric optics holds, $\tau_{\theta,\phi}(\vec{x})$ can be expressed as an integral of the refractivity along the raypath, as in Section II,

$$\tau_{\theta,\phi}(\vec{x}) = (1/\sin \theta) \int_0^h n(\vec{x} + \vec{r}(\theta, \phi, z)) dz \quad (\text{A-1})$$

where $n(\vec{x} + \vec{r}(\theta, \phi, z))$ is the refractivity evaluated at height z along the raypath originating at \vec{x} and extending along the vector \vec{r} with elevation and azimuth of θ and ϕ . The spatial structure function is

$$D_{\tau,\theta,\phi}(\rho) = \langle (\tau_{\theta,\phi}(\vec{x} + \vec{\rho}) - \tau_{\theta,\phi}(\vec{x}))^2 \rangle \quad (\text{A-2})$$

To calculate the structure function of Eq. (4), the following relation is used: For any two arbitrary vectors \vec{x}_1 and \vec{x}_2 , where $r = |\vec{x}_1 - \vec{x}_2|$,

$$D_n(r) = D_n(\vec{x}_1, \vec{x}_2) = 2 \langle n^2 \rangle - 2 \langle n(\vec{x}_1) n(\vec{x}_2) \rangle \quad (\text{A-3})$$

Equation (A-3) follows from the definition of the structure function and the assumption mentioned in the text that the structure function of n depends only on the magnitude of the vector difference of its arguments. This assumption also implies that $\langle n^2 \rangle$ is independent of spatial coordinates. Substituting Eq. (A-1) into Eq. (A-2) and using Eq. (A-3) yields Eq. (4) in the text.

Since most of the quantities calculated in this article depend on the form of the spatial structure function of Fig. 1, parameters describing a polynomial fit to the curve of Fig. 1 are shown in Table A-1. The parameterization is as follows:

$$\log D_{\tau,\theta,\phi}(\alpha) = \sum_i a_i (\log \alpha)^i \quad (\text{A-4})$$

where $\alpha = \rho/h$ and $D_{\tau,\theta,\phi}(\alpha)$ has been normalized to $C^2 h^{8/3}$. The a_i parameters are given in Table A-1.

Table A-1. Parameters from fit to numerical integration of spatial structure function

Parameter	Theta = 90	Theta = 20
0	-0.22318D+00	0.43292D+00
1	0.10108D+01	0.13450D+01
2	-0.22470D+00	-0.23695D+00
3	0.25715D-01	-0.85416D-01
4	0.32032D-01	0.30830D-01
5	-0.44802D-02	0.26228D-01
6	-0.47644D-02	-0.35145D-02
7	0.43030D-03	-0.39578D-02
8	0.40255D-03	0.11101D-03
9	-0.16176D-04	0.22698D-03
10	-0.13693D-04	0.95718D-04

Appendix B

Calculating Standard Deviations and Allan Variances From Structure Functions

Consider a random function of time $f(t)$. The variance of $f(t)$ over a time T is

$$\sigma_f^2(T) = (1/T^2) \int_0^T (T-t) D_f(t) dt \quad (\text{B-3})$$

$$\sigma_f^2(T) = \langle (1/T) \int_0^T dt' [f(t') - (1/T) \int_0^T dt'' f(t'')]^2 \rangle \quad (\text{B-1})$$

as in Eq. (6).

By squaring the indicated bracketed quantity in Eq. (B-1) and using the relation in Eq. (A-3), one arrives at the following expression:

$$\sigma_f^2(T) = (1/T^2) \int_0^T \int_0^T D_f(t, t')/2 dt dt' \quad (\text{B-2})$$

Assuming, as always, that $D_f(t, t') = D_f(|t - t'|)$ allows the simplification of Eq. (B-2) as follows:

To calculate the Allan variance, start from the following form of the definition of the Allan variance for the random delay function $f(t)$:

$$A(T) = \langle [(f(t+T) - f(t)) - (f(t) - f(t-T))]^2 \rangle / 2T^2 \quad (\text{B-4})$$

where t is an arbitrary time. Squaring the indicated quantity in Eq. (B-4) and applying the relation in Eq. (A-3) to the random function f yields a result analogous to Eq. (7) in the text.

New Reflective Symmetry Design Capability in the JPL-IDEAS Structure Optimization Program

D. Strain and R. Levy

Ground Antennas and Facilities Engineering Section

The JPL-IDEAS antenna structure analysis and design optimization computer program was modified to process half-structure models of symmetric structures subjected to arbitrary external static loads, synthesize the performance, and optimize the design of the full structure. Significant savings in computation time and cost (more than 50%) were achieved compared to the cost of full-model computer runs.

I. Introduction

The present X-band upgrade of NASA's Deep Space Network (DSN) 64-m diameter antennas to 70 m requires stripping the existing support structure trusswork back to a 34-m diameter, reinforcing the remaining interior structure, and adding new trusswork to provide the 70-m aperture. To achieve these extensive structural modifications while maintaining very close tolerances on structural deformation, it was decided to use the IDEAS program (Ref. 1, 2, 3) to size the truss members used in the new construction and to determine the amount of reinforcement needed for the existing structure. The IDEAS program is a special purpose finite element structural analysis computer program with unique features for the analysis and optimal design of microwave antenna structures. Unique features include the ability to automatically analyze and optimize the antenna reflector structure for surface accuracy and/or boresight errors due to various gravity, wind, thermal, and other environmental loads. An optimality criteria algorithm is used for the iterative optimization (redesign) of structural elements to achieve the

displacement constraints. Stress and buckling limits are automatically included side constraints for all optimization design constraints.

At the beginning of the project it was realized that the IDEAS program, operating on a UNIVAC 1100/81 computer, could not accommodate the large number of degrees of freedom (over 12,000) needed to represent the mathematical model of the entire 70-m diameter structure. The structure has, though, one plane of structural symmetry, and the capacity of the program was adequate to analyze a half-structure model.

It is known that an arbitrary loading condition for a geometrically symmetrical structure can be decomposed into symmetric and anti-symmetric components. After separate load-displacement solutions, the responses (displacements, stress resultants, etc.) of the two half-structure models can be combined to recover the responses for the full structure. While the IDEAS program was organized to accomplish analysis and redesign of a geometrically symmetrical structure based on

the modeling of one half, only symmetrical loading conditions (e.g., gravity or zero-azimuth wind load) would have physical significance. Independent optimization of half-structure models could not consider effects of general wind or thermal loading conditions. This would have been inconsistent with a comprehensive design.

The large size of the new 70-m antenna structure model prevented automated optimization of the full-structure. It was necessary to reorganize the IDEAS program to automate multiple half-structure analyses and full structure response synthesis. In this way, the IDEAS multiple-constraint design optimization scheme could be applied for any general loading condition with the additional benefit of reduced time and cost. The automation of the optimal design of symmetrical structures based on half-structure model analyses is, we believe, unique to the IDEAS program.

II. Discussion

The 2-axis steerable microwave antennas which are treated by the IDEAS program are represented in a particular right-handed Cartesian coordinate system fixed to the tilting reflector. The Z -axis is the boresight axis, the X -axis is parallel to the elevation axis and the Y -axis is positive upwards when the antenna points to the horizon (Figs. 1 and 2). The Y - Z plane is assumed to be the plane of geometrical symmetry. The right (positive X coordinate) half of symmetric structures is that represented by our half-structure models. This convention was incorporated into the program to facilitate program design and input data preparation. The remaining discussions are based on this convention.

An arbitrary load on a structure is modeled as discrete loads applied to discrete points of a finite element model. A geometrically symmetric structure has pairs of symmetric discrete points, one point on each side of the plane of symmetry. The discussion of discrete loads applied to one of these pairs of points can be generalized to the remaining pairs. The general load applied to the pair of points can be represented by their discrete components applied to the right side point (R) and left side point (L). These R and L components must be further broken down into their components parallel to and normal to the plane of symmetry (subscripts p and n). The symmetric and anti-symmetric components (S and A) of the original loading case can be calculated as follows: For loads normal to the plane of symmetry,

$$S_n = \frac{R_n - L_n}{2}$$

$$A_n = \frac{R_n + L_n}{2}$$

and for loads parallel to the plane of symmetry,

$$S_p = \frac{R_p + L_p}{2}$$

$$A_p = \frac{R_p - L_p}{2}$$

Figures 3 and 4 illustrate the decomposition of a general load and the method of recovery of the general displacement condition. For clarity, only loads parallel to the structures plane of symmetry are shown.

When applied to a half-structure model, these loads produce decomposed components of the response of the full structure. Appropriate boundary constraints (supports) must be imposed on the half-structure model to insure compatible deflections at the plane of symmetry (Fig. 3). For symmetrical loads (thus symmetrical deformations) the plane of symmetry cannot translate normal to the plane of symmetry or rotate about an axis in the plane of symmetry. Thus for anti-symmetric deformations, the plane of symmetry cannot translate parallel to the plane of symmetry or rotate about an axis normal to the plane of symmetry.

The application of these decomposed components of the loads permits the calculation of decomposed response components which are then superimposed to obtain the response of the full structure. Since the models are linear elastic, response components (deflections, stress resultants, etc.) are proportional to load components. Hence, for simplicity, components of load and the responses to that load will be expressed using the same notation. Thus, symmetric (S) and antisymmetric (A) components of load will cause symmetric (S) and anti-symmetric (A) components of deflection. The right (R) and left (L) side components of load or deflection can then be recovered from the symmetric (S) and antisymmetric (A) components of the right side model according to the formulas:

$$R_p = S_p + A_p$$

$$L_p = S_p - A_p$$

for deflections normal to the plane of symmetry, and

$$R_n = S_n + A_n$$

$$L_n = A_n - S_n$$

for deflections parallel to the plane of symmetry.

III. Program Organization

Data input to IDEAS to describe the structure and loading conditions is similar to that used by the NASTRAN structure analysis program. With minor modifications, the same bulk data deck can be used to make a NASTRAN analysis run. Other input is accomplished via FORTRAN V NAMELIST for parameter input and NASTRAN-like cards for bulk data input.

The modifications to implement reflective symmetry, which are described below, were made in view of the organization of the existing IDEAS program. The program performs the following steps:

- (1) Construct data base
 - (a) Input data
 - (b) Collate data
- (2) Determine external and inertial loading vectors,
- (3) Decompose stiffness matrix,
- (4) Analyze natural frequency and, as an option for the frequency design constraints, calculate (equivalent) real and virtual stress resultants,
- (5) Compute displacement and solve for reactions and elemental stress resultants,
- (6) Calculate antenna performance (path length and bore-sight error analysis) and calculate virtual loads and virtual stress resultants,
- (7) Calculate virtual work from real and virtual stress resultants,
- (8) Apply the re-design algorithm for resizing rod areas and plate thicknesses.

Note: If displacement performance is not acceptable and/or structure weight change from the preceding cycle is not within convergence criteria, analysis design iterations resume starting at step (2).

IV. Program Modifications for Reflective Symmetry Design

Much of the effort of program reorganization for reflective symmetry was within step (1b). Additional input data is required for reflective symmetry analysis and design to identify:

- (1) Which boundary constraint sets and loading cases are symmetric and which are antisymmetric,
- (2) How these loads are to be synthesized to obtain full-structure response,

- (3) Which loads are to be considered as the design loads.

Extensive data checks were implemented to ensure that input data errors and inconsistencies were identified during the data input and collation phases of the program.

The program was reorganized to repeat the sequence of step (2) through step (5) first for the symmetric and then for antisymmetric configurations. The reactions and displacements from each sequence are saved. After completion of both the symmetric and anti-symmetric sequences, the responses are combined to form the response of the full structure.

The antenna performance algorithms in step (6) were rewritten to process both half- and/or full-structure displacement data. Generating the virtual stress resultants for virtual work coefficient calculations was rather involved. Virtual displacements for the full structure were recovered from the symmetric and antisymmetric components of the response to decomposed full-structure virtual loads.

For the redesign algorithm, steps (7) and (8), individual finite elements were combined into user-specified design variable linking groups. For a structure assumed symmetrical, the full- and half-structure models will have the same number of design variable linking groups — an element on the right and its opposite on the left will be in the same group. Virtual work sums for design variables include contributions from pairs of modeled (right side) and inferred (left side) elements. As an illustration using one right-left pair of 1-dimensional rods,

$$C_{ij} = (F_{ij} + F_{ji}) \frac{1_i}{a_i E_i}$$

in which the product of the real and virtual stress resultants (F) for the left side is as follows where P is the internal bar force:

$$\begin{aligned} F_{ij} &= P_{ir} P_{id} \\ &= (P_{ir} - P_{ir}) (P_{id} - P_{id}) \end{aligned}$$

and for the right side is

$$\begin{aligned} F_{ji} &= P_{ir} P_{id} \\ &= (P_{ir} - P_{ir}) (P_{id} - P_{id}) \end{aligned}$$

This simplifies to

$$C_{ij} = 2 (P_{ir} P_{id} + P_{ir} P_{id}) \frac{1_i}{a_i E_i}$$

Once the virtual work for the half and/or full structures is calculated, the redesign algorithm is invoked. The redesign algorithm only operates on design variable groups so that it does not have to be changed for reflective symmetry.

V. New Program Testing and Verification

Test models verified the new program. Several half-structure computer runs produced iterative design results identical to those of full-structure models. All natural frequency modes present in the full structure were found in either the symmetric or the anti-symmetric modes of the half-structure.

Some of the verifications were done on full- and half-structure models of a medium sized antenna backup structure (2,048 nodes in the full model, 1,058 in the half), as seen in Table 1. The computer costs of the two executions showed them to be in the ratio of about 2.5:1. Actual run times were about 1/2 hour for the half and 2 hours for the full model.

The projected cost for one full-structure 70-m antenna model containing about 4020 nodes would be about \$520. The projected cost for the two-half-structure model cycle containing 2,050 nodes is \$200. On the other hand, very small models suffered slightly in cost comparisons because of the overhead associated with two solution sequences; this difference might be outweighed by the fact that half models are considerably easier to generate and verify.

VI. Summary

The addition of the new reflective symmetry analysis-design capabilities to the IDEAS program allows processing of structure models whose size would otherwise prevent automated design optimization. The new program produced synthesized full-model iterative design results identical to those of actual full-model program executions at substantially reduced cost, time, and computer storage.

Nomenclature for Variables and Subscripts

- R, L Right and left components of a generalized load, displacement, etc., condition
- S, A Symmetric or antisymmetric components of a generalized load, displacement, etc., condition
- a Group rod area (design variable)
- l Sum of group rod lengths
- E Elastic modulus
- F Sensitivity coefficient
- P Load
- u Displacement
- p, n Indicates load or displacement components parallel or normal, respectively, to the structure's plane of symmetry
- i Design variable index
- j Design constraint index
- r Real load index
- d Virtual load index

References

1. Levy, R., and Strain, D., "Design Optimization of 70-m Antenna with Reflective Symmetry," Proc. 21st Annual Meeting, Society of Engineering Science, Virginia Polytechnic Institute and State University, Blacksburg, Va., Oct. 15-17, 1985, pp. 453-454.
2. Levy, R., and Melosh, R. J., "Computer Design of Antenna Reflectors," *Journal of the Structural Division*, Proc. ASCE 99(ST-11), Proc. Paper 10178, pp. 2269-2285, Nov. 1973.
3. Levy, R., "Computer-Aided Design of Antenna Structures and Components," *Computers and Structures*, Vol. 6, pp. 419-428, 1976.

Table 1. Comparison of 40-m verification model characteristics*

Full Structure	Half Structure	Characteristics
2048	1056	Nodes
6132	3098 3034	Unconstrained D.O.F.
201	102	Matrix wavefront, D.O.F.
9.8 min	1.4 min	Matrix decomposition CPU time
\$50 (for 1)	\$12 (for 2)	Decomposition cost
\$475	\$150	Cost of analysis/design sequence
2 hr	0.5 hr	Design sequence through-put time
104 K	54 K	Core size, words

*The half-structure column represents two half-structure finite element models equivalent to the full-structure model represented in the other column. The design sequence was five iterations of static analysis/optimum redesign. The intermediate and final results of both runs were identical.

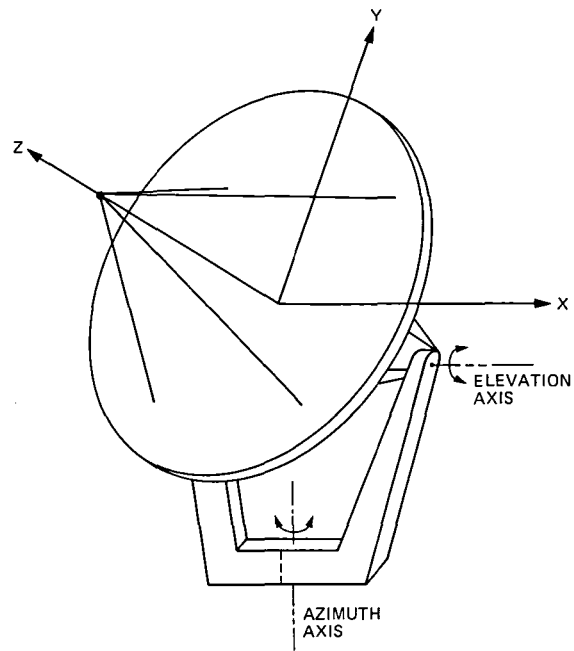


Fig. 1. The IDEAS program antenna coordinate system

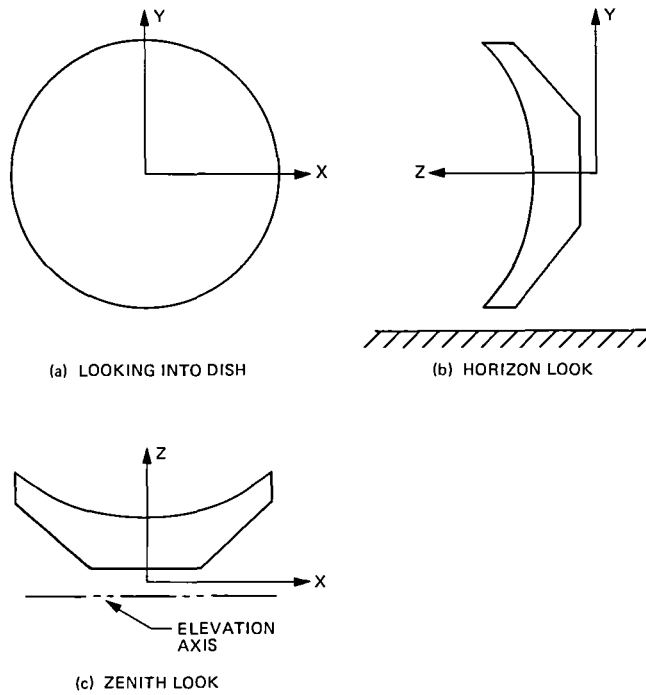
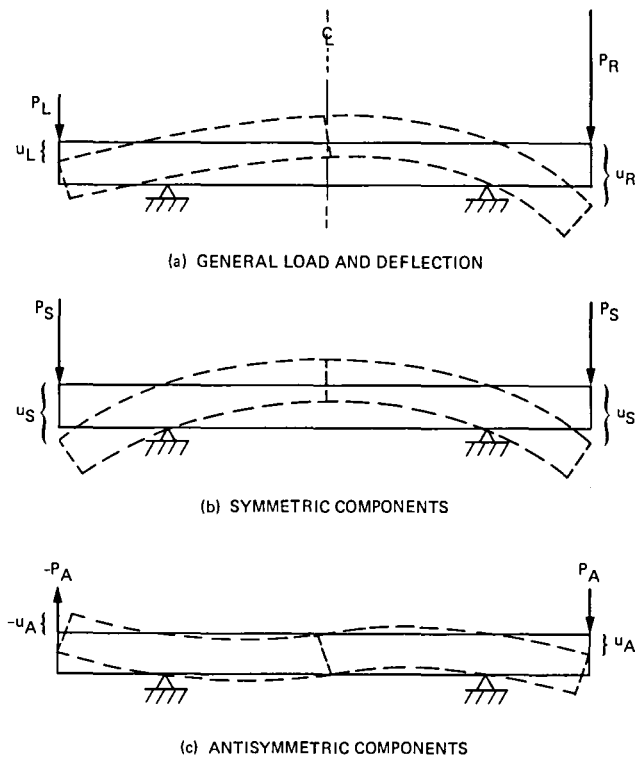
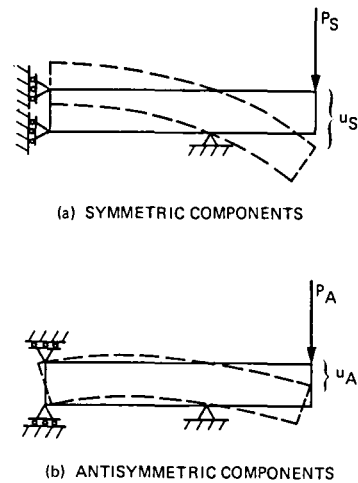


Fig. 2. Details of the IDEAS program antenna coordinate system



LOADS	SYMMETRIC COMPONENTS	ANTISYMMETRIC COMPONENTS	
		RIGHT SIDE	LEFT SIDE
$P_L = 1$	$P_S = \frac{P_L + P_R}{2}$	$P_A = \frac{P_R - P_L}{2}$	$P_A = \frac{P_L - P_R}{2}$
$P_R = 3$	$= \frac{1 + 3}{2}$	$= \frac{3 - 1}{2}$	$= \frac{1 - 3}{2}$
	$= 2$	$= 1$	$= -1$
		($= -P_A$ RIGHT SIDE)	

Fig. 3. Decomposition of general load into symmetric and anti-symmetric components (load components parallel to plane of symmetry only)



SINCE $P_R = P_S + P_A$ THEN $u_R = u_S + u_A$
 AND
 SINCE $P_L = P_S - P_A$ THEN $u_L = u_S - u_A$

Fig. 4. Recovery of full-structure response from the application of half-structure symmetric and anti-symmetric load components

Preliminary Results Toward Injection Locking of an Incoherent Laser Array

James Daher¹

Communications Systems Research Section

The preliminary results of phase-locking an incoherent laser array to a master source in an attempt to achieve coherent operation are presented. The techniques necessary to demonstrate phase-locking are described along with some topics for future consideration. As expected, the results obtained suggest that injection locking of an array, where the spacing between adjacent longitudinal modes of its elements is significantly larger than the locking bandwidth, may not be feasible.

I. Introduction

Recently, a project was initiated to determine the ease and feasibility of injection locking an incoherent laser diode array. Previous experimental work directly related to this task consisted of the injection locking of a coherent phase-coupled array (Ref. 1) and the locking of single and multiple slave laser diodes to a master oscillator. In the former case, one is interested in transforming the stable 180° out-of-phase operation of adjacent lasers, which results in a two-lobed far field pattern, to that of in-phase operation leading to a single lobed far field. In the cases of single (Refs. 2,3) and multiple (Ref. 4) slaves, locking of both frequency and relative phase was accomplished. Each of these activities is a natural precursor to the current aim, though none have been as demanding in the nature of the interaction between the master and slave lasers. Before discussing the goals of the present experiment, it will be helpful to briefly review the accomplishments of previous work done in this area.

The work undertaken by Kobayaski and Kimura was to demonstrate the applicability of the theoretical injection locking model of Adler (Ref. 5) to semiconductor injection lasers. Earlier, experimental results supporting Adler's theory had been obtained using He-Ne lasers by Stover and Steier (Ref. 6), but no such results had been obtained for semiconductor lasers. Adler's model was developed for the case of a general oscillator and has been extended by Lang (Ref. 7) to the specific problems of injection lasers whose index of refraction is carrier-density dependent. Kobayaski and Kimura found that the locking bandwidth is 3 GHz (0.1 Å) when the injection locking gain is 23 dB and 500 MHz at 40 dB gain. These values agree well with those predicted by Adler's theory.

The first multi-slave laser locking results were obtained by Goldberg, et al. (Ref. 1), on the locking of four single diode lasers to a master laser. They measured a locking bandwidth of 3 GHz using an injected input of 100 μ W and a slave output of 5 mW (17 dB gain). They also reported that they could force the laser to oscillate 22 modes away from its free running mode with a single laser output of 3 mW and an injected power of 40 μ W (19 dB gain). Goldberg, et al., was also the

¹ Formerly a JPL Summer Student, the author is now a graduate student at MIT.

first group to use injection locking techniques on a laser array. Their phase coupled array was successfully converted to single lobe operation and the spectral width was slightly narrowed.

Laboratory set-ups for all of the prior experiments have been of a design (Fig. 1) similar to that used for the present measurements. A few of the differences are as follows:

- (1) Prior experiments have utilized Fabry-Perot interferometers to achieve a finer resolution often needed to determine the locking bandwidth (typically 0.1 Å). The present experiment did not seek a quantitative measure of the bandwidth but only a demonstration that locking could be achieved.
- (2) An optical isolator was used in previous experiments to shield the master laser from influences of the slave laser. Optical feedback can manifest itself in two ways (Ref. 8):
 - (a) Radiation from the slave may enter the master causing a frequency push/pull battle, or
 - (b) Reflected radiation from the injected facet of the slave may induce instability and mode break up in the master. These problems were minimized by injecting off axis although coupling efficiency was sacrificed.

II. Description of Apparatus

The master laser, a Mitsubishi ML 3101, was focused onto the back facet of the slave array using a 10X, numerical aperture 0.30 microscope objective. The object distance was 3 mm with an image distance of 495 mm resulting in an image size at the back facet of the array of 1,500 μm^2 . The output of the array was then imaged onto the screen of a vidicon placed 21 cm away using another 10X objective to obtain the near field pattern. This leg of the beam path was sent through a beam splitter and a portion of the beam was focused into a monochromator placed 76 cm away using a 1-in. diameter, $f = 100$ mm lens. Placed before the monochromator was a dove prism to rotate the horizontally separate spatial modes of the array into the vertical plane, allowing the imaging of the spatial and temporal modes simultaneously.

The slave laser array used was an index-guided, 10 element incoherent laser array obtained from Ortel Corporation with a threshold current of 175 milliamps (Fig. 2) and which emits equal power levels from both front and rear facets. The maximum current limit was presumed to be around 450 milliamps and care was taken not to exceed this limit. The intensities of the individual elements were quite uneven (Fig. 3) as were the center frequencies and the number of lasing modes (Fig. 4). Throughout the experiment the laser

was normally operated at 275 milliamps peak current with a 5 kHz repetition rate and 0.22 μsec pulse width. The power emitted in each mode under these conditions is listed in the matrix of Table 1. The spectrum of the array is centered around 8518 Å. The master laser used in this experiment had a wavelength of 8529 Å at 25 milliamps and 8550 Å at 50 milliamps. No locking was seen (as was expected) at these wavelengths and power levels. A thermo-electric heater/cooler was attached to the array's heatsink to raise the operating temperature, and resulted in a shift of the resonances to longer wavelengths. GaAlAs lasers typically display a shift of 3 Å/K. Coarse tuning of the master and slave laser frequencies was usually accomplished by controlling the temperature of the heatsinks on which the lasers were mounted and fine control was achieved by varying the current injected into the lasers. Unfortunately, at these higher temperatures the array exhibited a spreading of the gain profile, giving rise to many more lasing modes (Fig. 5).

III. Theory

Locking (Ref. 9) is predicted to occur when the power injected into a laser cavity and the cavity gain at that injected frequency exceed the gain of the free running natural frequency (Fig. 6). From Adler's theory, the approximate locking bandwidth is described by:

$$\Delta f = \left(\frac{f_o}{2Q} \right) \sqrt{\frac{P_{in}}{P_{osc}}} \quad (1)$$

where P_{in} and P_{osc} are the powers of the injected laser and locked laser power, respectively, inside the oscillator, f_o is the center frequency and Q is the cavity Q of the slave given by:

$$Q = \omega_0 T_P \quad (2)$$

$T_P = \text{photon lifetime}$

The measured average spacing of the cavity modes of the laser array was 2.7 Å. From this a cavity length of 400 μm was determined assuming a reflection coefficient of 0.32 and refractive index of 3.6. The resulting cavity Q was 6176. This is only an approximate analysis. A more precise formulation done by Lang has determined that the locking curve has a very asymmetric shape. Lang has found that locking is easier to a mode which is below the resonant frequency rather than above because of the carrier-density dependence of the index of refraction. More recent results indicate a more complicated behavior than predicted by Eq. (1) or Lang's calculations.

IV. Procedure and Results

The initial laser locking trials were carried out with the master driven at the same pulse repetition rate as the array but with a slightly longer pulse width of $0.5\ \mu\text{sec}$. The master and slave both support horizontally polarized light and were positioned to emit this polarization to optimize coupling. The array was heated to emit wavelengths in the region of the master. About 8% of the energy radiated by the master was actually incident on the facet of the array. This gives rise to approximately $8.2\ \mu\text{W}$ of power actually coupled into each element of the slave array. A typical element of the array (No. 3, for example) emits $1.3\ \text{mW}$. This yields a locking bandwidth of $3.9\ \text{GHz}$ with a $22\ \text{dB}$ gain. As the two lasers were brought into synchronization, some of the lower power elements were noticeably shifted by as many as four modes (Fig. 7). The master could be tuned, using the current, to a point where a maximum of four (numbers 2, 3, 4, and 6) out of the ten elements showed signs of locking simultaneously. The energy in the wings of the beam footprint may have been too low to exert influence on elements 1 and 10 together with 2, 3, 4, and 6. Elements 1-4, 6, and 10 all showed some measure of locking at one time or another during the demonstration. No discernible change could be seen in the stronger elements 5, 7, 8, and 9. This may have been a result of the narrow gain profiles of these elements and low power injected from the master. As the power of the master laser was increased, its nearly single mode operation became predominately multimode, making the detection of frequency locking difficult.

Often when a laser is locked to a particular mode determined by the master, it does not necessarily operate in a single longitudinal mode. Injecting may create an unusual two-lobed gain profile. This problem seems to be more common in lasers with a narrow free-running gain profile than those with broad gain. Possibly, with higher injected power levels, the gain in the injected mode may be large enough to dominate the available population inversion initiating single mode operation. Figure 7 does show that for a low power element, the frequency spectrum can be dominated by the master effecting single mode operation.

Considering the nominal locking bandwidth (typically $0.1\ \text{\AA}$), it is possible in an incoherent array with mode spacings on the order of $3\ \text{\AA}$ that if the elements have cavity resonances which are further apart than $\sim 0.3\ \text{\AA}$ from each other, it may not be possible to lock an array. Careful measurements of the longitudinal modes should be made with a Fabry-Perot interferometer to determine if a problem along this line actually exists.

V. Future Considerations

One of the most serious drawbacks of the present attempt has been the low powers actually injected into the slave laser. The bulk of the problem should be correctable by using a different set of optics and using a cylindrical lens to achieve a footprint commensurate with the shape of the array. Another approach may be to use a higher power laser diode. A combination of both of these may be appropriate.

The critical need for an isolator was not readily apparent during these trials. The multimode behavior of the master laser was attributed to high injection current levels instead of optical feedback. Perhaps with the use of a Fabry-Perot interferometer and with more exact measurements, the presence of small frequency instabilities ($\sim 500\ \text{MHz}$) will be found to be much more bothersome.

VI. Conclusion

We have shown that the injection locking of an incoherent laser array is feasible provided the cavity modes of all elements of the slave device are within the locking bandwidth of each other. It was also shown that the lower power elements are more easily influenced and locked by the master laser than the higher power ones. Both of these results are in agreement with theoretical models of injection locking of semiconductor lasers. Further work should determine the characteristics of the far field profile and its usefulness for communication purposes.

Acknowledgment

The author wishes to thank Ortel Corp. for supplying the laser diode array used in this work.

References

1. Goldberg, L., Taylor, H. F., Weller, J. F., and Scifres, D. R. "Optical Injection Locking of a GaAlAs Phase Coupled Laser Array." Post deadline papers to IQEC '84, pp. PD-B4-1, PD-BA-2, June 18-22, 1984.
2. Kobayashi, S. and Kimura, T., Coherence of Injection Phase-Locked AlGaAs Semiconductor Laser, *Electronic Letters* 16, pp. 668-670, 1980.
3. Kobayashi, S., and Kimura, T., Injection Locking Characteristics of an AlGaAs Semiconductor Laser, *IEEE J. Quantum Electron.* E-16, No. 9, pp. 915-917, 1980.
4. Goldberg, L., Taylor, H. F. and Wheeler, J. F., Coherent Operation of Four GaAlAs Laser by Injection Locking, *CLEO '84 Technical Digest*, p. 212, June 19-22, 1984.
5. Adler, R., A Study of Locking Phenomena in Oscillators, *Proc. IRE* 34, pp. 351-357 1946.
6. Stover, H. L. and Steier, W. H., Locking of Laser Oscillators by Light Injection, *Appl. Phys. Lett.* 8, No. 4, pp. 92-93, 1966.
7. Lang, R., Injection Locking Properties of a Semiconductor Laser, *IEEE J. of Quantum Electron.* QE-18, No. 6, pp. 976-983, 1982.
8. Kanada, T. and Nawata, K., Injection Laser Characteristics Due to Reflected Optical Power, *IEEE J. of Quantum Electron.* QE-15, No. 7, pp. 559-565, 1979.
9. Buczek, C. J., Freiberg, R. J. and Skolnick, M. L., Laser Injection Locking, *Proc. of the IEEE* 61, No. 10, pp. 1411-1431, 1973.

Table 1. Power vs mode matrix

Element	Mode Power, 10^{-3} W							
1					0.02		0.05	
2	0.02	0.07	0.07	0.07	0.14	0.07	0.05	0.02
3			0.05	0.19	0.56	0.38	0.05	
4		0.05	0.19	0.56	0.75	0.09*		
5	0.09	0.19	0.28	0.38	0.75	0.38	0.05	
6		0.19	0.70	0.75	0.09			
7			0.05	0.19	0.75	0.84	0.75	0.09
8		0.05	0.28	0.75	0.84	0.75	0.33	0.05
9	0.05	0.19	0.70	0.75	0.14	0.05		
10				0.09	0.14			

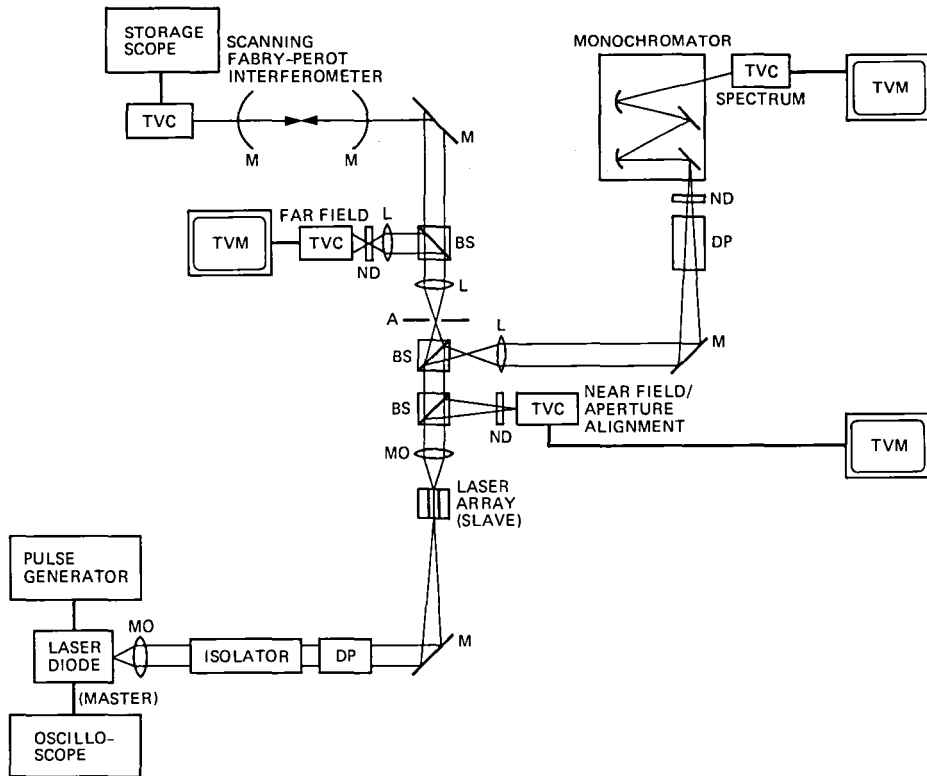


Fig. 1. Optical set-up used for injection locking

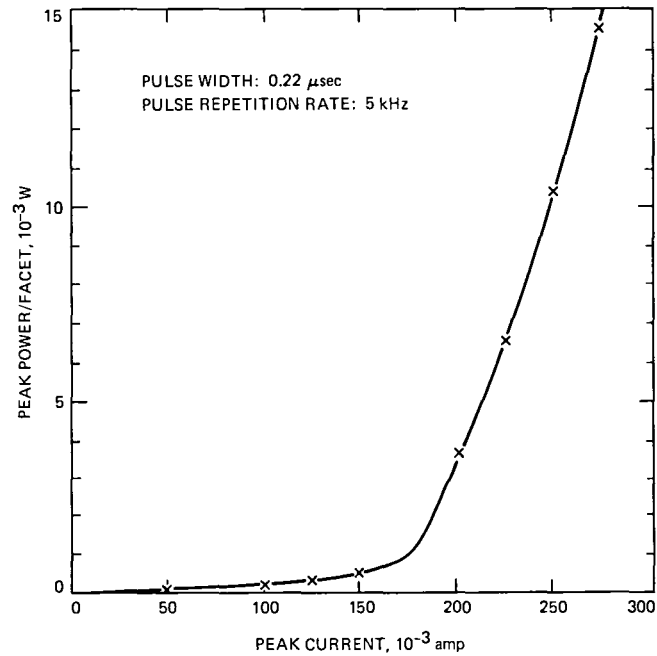


Fig. 2. Power vs injected current for array

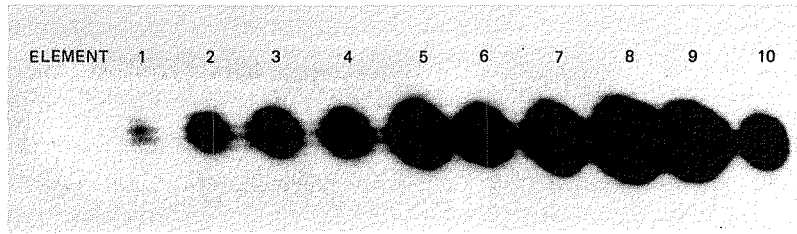


Fig. 3. Amplitude profile of array

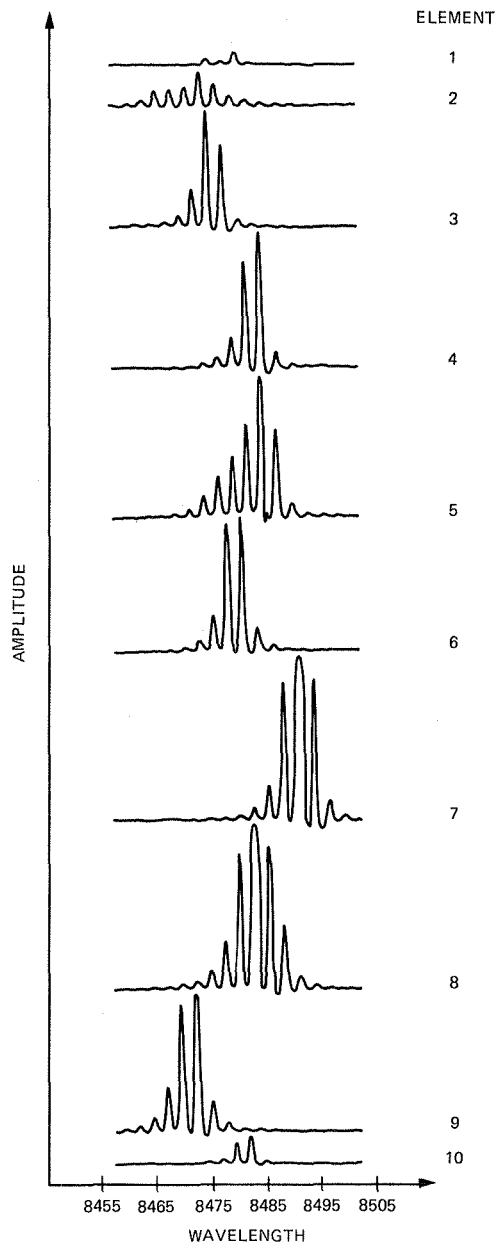


Fig. 4. Frequency spectrum of array

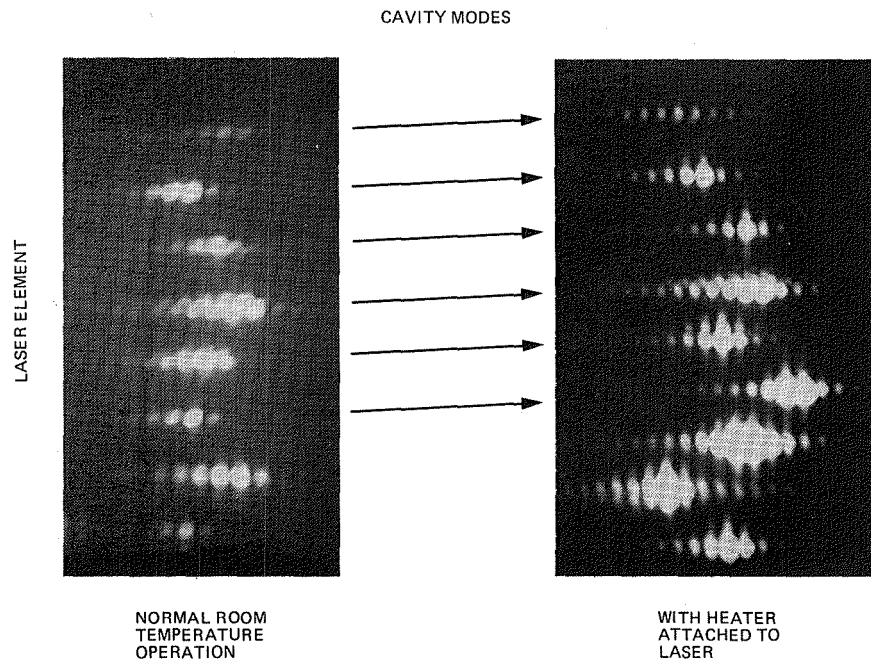


Fig. 5. Spectral profile of the slave array before and after heating

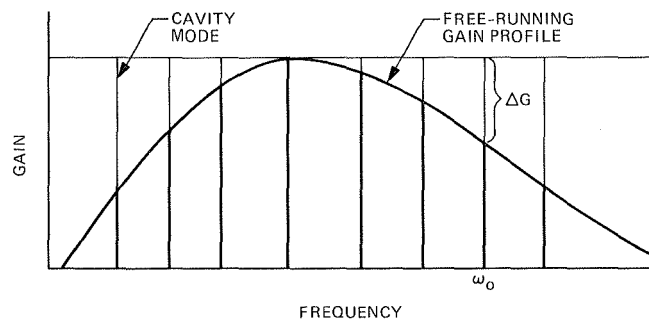


Fig. 6. Condition for injection locking

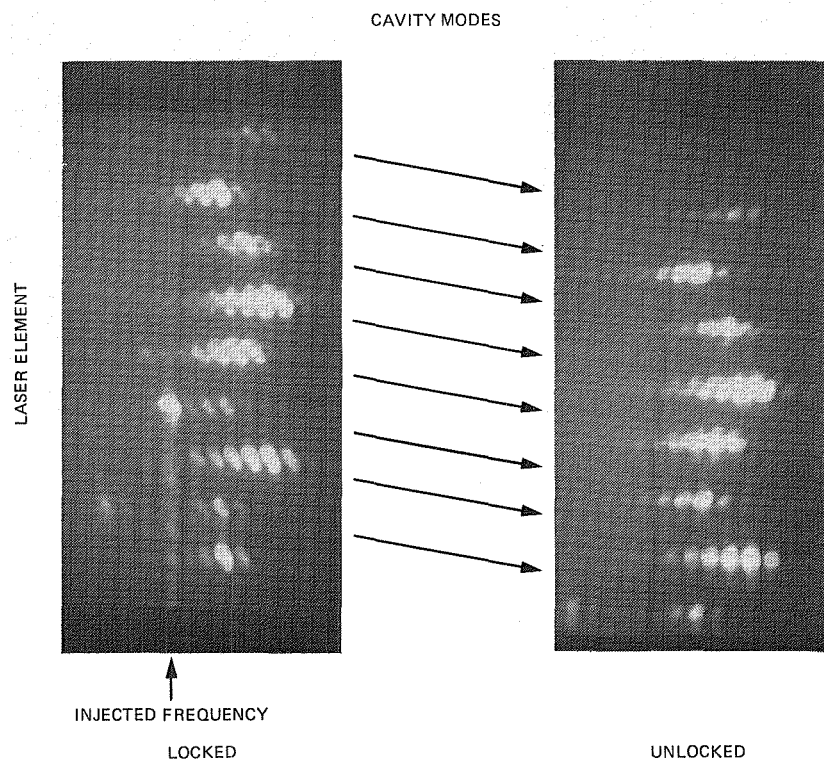


Fig. 7. Locked and unlocked spectra

Low-Loss Off-Axis Feeds for Symmetric Dual-Reflector Antennas

T. Veruttipong, V. Galindo-Israel, and W. Imbriale
Radio Frequency and Microwave Subsystem Section

Circularly symmetric, dual-reflector, high-gain antenna systems often require feeds placed off the system's axis because of the need for multiple feeds to use the reflector antenna. Also, the constraint requiring the hyperboloid or shaped subreflector to remain circularly symmetric is sometimes added. In a Cassegrainian system, the subreflector and feed may be rotated off-axis around the paraboloid focus and retain main reflector focusing. However, substantial spillover results in considerable noise with a high-gain/low-noise temperature system. In a shaped system, the tilt of the shaped subreflector and feed together results in substantial defocusing as well as spillover noise. If the subreflector is tilted approximately one-half the angle of the feed tilt in either the Cassegrainian or the dual-shaped reflector antenna, it is found that spillover and noise are substantially reduced with tolerable defocusing. An extensive numerical analysis of these effects was conducted to determine the characteristics of a planned 70-meter, dual-shaped reflector versus Cassegrainian antenna and to gain some understanding of the cause of the observed effects.

I. Introduction

In large ground antenna systems, it is often necessary to use multiple feeds for the same main reflector. Thus, a number of feeds can be tilted off the axis of the symmetric main reflector, each illuminating a tilted subreflector, often the same subreflector that is rotated into position for a given feed. This type of antenna system is shown in Fig. 1.

In some systems, such as the JPL 70-meter upgrade of the 64-meter antenna, the subreflector diameter can be more than 200 wavelengths at 8.45 GHz. A considerable cost savings is

possible if a circularly symmetric subreflector is used in place of an asymmetric offset subreflector. This is especially true for shaped reflectors (Refs. 1, 2, 3) that have no larger "parent" circularly symmetric reflector from which they could be cut. A circularly symmetric subreflector, if tilted, can also be useful for a feed located on the axis of the symmetric main reflector. This would result in "best" or "reference" performance, given the ability to "retilt" the otherwise tilted subreflector.

In the study of the off-axis-fed antenna system, the tilt angle of the feed relative to the tilt angle of the subreflector

was varied. The absolute angle of the tilt was also varied. These tilt angles for the feed (α) and for the subreflector (β) are shown in Fig. 2.

The actual point of rotation of the feed and subreflector depends upon the type of reflector design used. For a Cassegrainian (parabola/hyperbola) system, the obvious choice for a rotation point is the paraboloid focus. For a dual-shaped reflector system, the choice is not obvious. The "optimum" choice for the shaped reflectors is discussed later.

In either case, when large (in wavelengths) reflectors are used, the off-axis displacements of the feeds may be many tens of wavelengths. Consideration will be given to the characteristics of a 70-meter dual-shaped reflector antenna that is an upgrade of a National Aeronautics and Space Administration/Deep Space Network (NASA/DSN) 64-meter design with off-axis feeds (see Fig. 2).

II. Gain vs Off-Axis Rotation

There are two types of off-axis rotations of the feed and subreflector. In one case, $\beta = \alpha$: that is, the subreflector and feed are rotated by the same angle. For the Cassegrainian system, note that, in this case, the phase on the main reflector remains correct except where the main reflector becomes under-illuminated.

In a second case, $\beta = \alpha/2$. For this choice of β , we find that the main reflector remains neither under- nor over-illuminated. However, it is clear that a phase error is introduced for the Cassegrainian system. The significance of the proper amplitude illumination of the main reflector is that spillover past the main reflector results in a large receiving noise caused by the relatively hot earth surface beyond the main reflector. In the case when $\beta = \alpha/2$, the feed is always pointed toward the center of the subreflector.

The geometry and dimensions for the Cassegrainian system under study are shown in Fig. 3. An experimental corrugated feed horn was used for the dual-shaped reflector antenna geometry, shown in Fig. 4. The overall dimensions of the two antenna systems were kept approximately the same. The Cassegrainian subreflector was illuminated with a -10 dB taper at the edge of the subreflector.

The dual-shaped subreflector was illuminated with a -16 dB taper at the edge of the subreflector. The dual shaping was chosen for maximum gain. There was a small taper allowed near the edge of the main reflector. A slight extension of the main reflector beyond the geometric optics edge was introduced to reduce the noise temperature increase that normally comes from the tapering edge of the subreflector scattered

pattern. The subreflector was synthesized with a vertex plate blended into the synthesis (Ref. 1).

As a function of α , the Cassegrainian system maintains a better gain curve than the shaped reflector antenna for $\beta = \alpha$ (except for noise considerations). The dual-shaped reflector system maintains a significantly better gain curve than the Cassegrainian for $\beta = \alpha/2$ provided that an optimum rotation point is chosen).

The gain versus α -angle curves for the 70-meter designs are shown in Fig. 5 for the Cassegrainian and in Fig. 6 for the dual-shaped reflector systems.

The gain versus α curve for $\beta = \alpha$ in Fig. 5 is relatively flat, although the noise temperature increases with α . The principal cause of a loss in gain is reduced illumination on one side of the main reflector (discussed in detail later). This reduction could be eliminated by choosing an offset asymmetric hyperboloid. However, the offset asymmetric subreflector can be used for only one α angle and is more costly. The $\beta = \alpha/2$ gain curve for the Cassegrainian antenna drops off rapidly with increasing α because of an increasing aperture phase error. In this case, however, the illumination amplitude across the main reflector aperture has considerably less spillover and, therefore, considerably less noise is collected. Note also that for the $\beta = \alpha$ case, there is no beam-pointing shift. The beam points in the $\theta = 0$ direction for all α . For the case with $\beta = \alpha/2$, there is an approximately linear shift of beam-pointing direction, as indicated in Fig. 5.

The gain versus α results for the dual-shaped reflector are shown in Fig. 6. For $\alpha = 0$, the gain of the dual-shaped reflector is about 0.75 dB higher than for the Cassegrainian system. The relative aperture efficiencies (spillover and depolarization accounted for) are 80.5% for the Cassegrain and 96.5% for the dual-shaped system (in both cases for $\alpha = 0^\circ$).

The gain versus α angle results for the dual-shaped antenna show that the performance for the case $\beta = \alpha$ degrades rapidly and badly because of the introduction of both a phase and an amplitude error in the main reflector aperture distribution by the rotation of the feed and subreflector as a unit. The degradation in gain caused by the under-illumination of amplitude but is greater here than for the Cassegrainian antenna because the object illumination function resulting from dual shaping is nearly uniform.

When the shaped subreflector is rotated by the angle $\beta = \alpha/2$ around the appropriate point of rotation, the results in gain versus α angle are comparable to the Cassegrainian gain versus α angle results for the $\beta = \alpha$ case. Note that the shaped reflector system has the advantage over the Cassegrainian of a

lower noise amplitude distribution. Further explanation for this result will follow in the next section.

The actual frequency for these computations was 8.45 GHz. The radius of the main reflector was taken as 986.3 wavelengths. The computations were greatly facilitated by the use of a GTD analysis of the subreflector scattered field and a Jacobi-Bessel analysis (Refs. 4, 5, 6) of the main reflector scattered field. Various global and local interpolation methods (Ref. 7) were employed to analyze the shaped subreflector and main reflector.

A relevant question at this point is: Why is $\beta = \alpha/2$ an "optimum" value of β as opposed to some other fractional portion of α ? It does turn out that at $\beta \cong \alpha/2$, the amplitude distribution on the main reflector has minimum under-illumination. Figures 7 through 9 show the gain of Cassegrainian and dual-shaped reflector antennas as a function of the β -angle (tilt angle of the subreflector) with the α -angle (tilt angle of the feed) fixed.

For the Cassegrain antenna (with α fixed at 10.52°), note that the gain peaks when $\beta = \alpha$. This is expected because the aperture phase is correct at $\beta = \alpha$, and the phase is more critical than the amplitude. For the dual-shaped reflectors, the result is quite different. In this case, the gain peaks at approximately $\beta = \alpha/2$ for both $\alpha = 10.52^\circ$ and $\alpha = 4.482^\circ$ (see Figs. 8 and 9). Again, the phase, as well as the amplitude, is optimum. As noted later (for the shaped reflectors), the phase function is optimum at approximately $\beta = \alpha/2$ when the "best" rotation point is chosen. This is related to the fact that the field scattered from the subreflector has an extended set of two caustic surfaces as opposed to the single caustic point for the Cassegrainian antenna. These caustic surfaces are discussed later.

All the preceding results were for circularly symmetric subreflectors, shaped and conic (Table 1). For the case $\beta = \alpha/2$, the Cassegrainian system suffers a phase error in the main reflector aperture. For the case $\beta = \alpha$, the Cassegrainian system suffers an amplitude distortion with subsequent increased receiver noise. Both of these deficiencies can be removed with an asymmetric hyperboloid (in the plane of rotation of the feed and subreflector). For comparison, results with an asymmetric hyperboloid subreflector are shown in Table 1. For α less than about 6° , there is only about 0.1 dB difference between the various cases (see Fig. 5). Although the asymmetric reflector gives marginally better performance, the $\beta = \alpha/2$ case gives equivalent results with a less expensive symmetric hyperboloid. Note that when diffraction from the subreflector is ignored, the gain is increased by 0.1 dB, a direct measure of spillover loss for the Cassegrain (usually much higher for electrically smaller antennas).

A final point for consideration in this section is the determination of the point of rotation of the subreflector and feed for the dual-shaped reflector system. Because an incoming plane wave reflected from the shaped main reflector will not come to a virtual point focus, the precise optimum point of rotation is not immediately clear. In Fig. 10, all rays do intersect along a caustic line behind the subreflector (in the non-rotated position). For a Cassegrain antenna, this line degenerates into a point. Actually, this caustic arises from the curvature out of the plane of the paper. It would seem that an "optimum" point of rotation for the shaped system would lie within the limits of this caustic line.

The position may be weighted along the caustic by plotting the caustic intersection point versus position (ρ) along a radius of the main reflector (also shown in Fig. 10). For the Cassegrain, all rays intersect at a fixed z position, which is the focus. For the shaped system, different radial positions along the main reflector correspond to different positions of intersection along the z -axis. Because the main reflector aperture distribution is nearly uniform, an accordingly weighted mean z position may be chosen as an optimum point of rotation.

A more direct method of choosing the optimum point is observed in Fig. 11. The feed lateral displacement is fixed at ΔX ; then the subreflector is rotated to the position $\beta = \alpha/2$ with different points, F' , of rotation. It is known that $\beta = \alpha/2$ is an approximately optimum ratio between α and β for the shaped reflectors. The optimum position, F' , of rotation is in the vicinity of the weighted curve of Fig. 10.

Figure 10 shows that the main reflector line caustic z -position doubles back on itself near $\rho = 9.75 \lambda$. Thus, there is an additional intersection of rays off the z -axis. This intersection is the caustic from curvature of the field in the plane.

III. Far-Field Patterns and Reflector Currents

In this section, the far-field patterns of both the Cassegrainian and the dual-shaped 70-meter antennas are presented as a function of the α and β angles ($\beta = \alpha$ and $\beta = \alpha/2$ cases). The main reflector current distributions are also reviewed to obtain some insight into the characteristics of these antennas with α and β angles of feed and subreflector rotation.

Figure 12 shows the far-field patterns of the 70-meter shaped and Cassegrain systems with $\alpha = \beta = 0$, the concentric case. In addition to the vertex plate on the subreflector of the shaped reflectors, the shaped main reflector also has an extension that serves as a noise shield; i.e., it shields the feed from the average 240 K ground noise in that critical area of sharp energy drop-off near the main reflector edge. The shaped sys-

tem attains about 96.6% efficiency, whereas the Cassegrainian system attains about 70.2% efficiency (with a -10 dB feed taper and blockage not accounted for). Spillover and cross-polarization losses are accounted for in these computations.

The pattern degradation of the Cassegrainian system with an increasing α angle is not great because the main reflector currents remain properly in phase over most of the reflector, except the under-illuminated portion. The degradation is, however, more apparent for the $\beta = \alpha/2$ case. This is illustrated in the patterns of Fig. 13. Note that the vertical gain scale is shifted for each pattern; the change in gain between patterns is noted next to each pattern. Of special interest is the actual beam-pointing direction for each pattern, noted next to the pattern by θ_B . With a 3-dB beamwidth of less than 0.05° , the beam shift from the concentric $\alpha = \beta = 0^\circ$ case is many beamwidths.

The pattern degradation is very great for the shaped reflector antenna when $\alpha = \beta$. This is clear because even when the subreflector and feed are rotated about an optimum point on the caustic (see Fig. 10), there is substantial phase defocusing for the $\alpha = \beta$ case. However, for the $\beta = \alpha/2$ case, the defocusing is substantially reduced, and the beam is shifted with considerably less loss in gain and degradation in pattern structure. This is shown in Fig. 14.

Of special interest in the far field is what occurs to the phase and the amplitude monopulse patterns when the feed and subreflector are rotated so that $\beta = \alpha/2$. To observe this effect with the Cassegrainian antenna, a "synthetic" feed monopulse pattern was used. This pattern, as well as the sum pattern for the Cassegrainian feed, is shown in Fig. 15. The effect of the asymmetry for the case with $\alpha = 4.52^\circ$ is shown in Fig. 16. Although the "null" of the amplitude pattern is not as deep as for the $\alpha = 0^\circ$ case and the phase shift of 180° at the sum pattern maxima is not as sharp, the monopulse pattern might be usable.

Before investigating the currents on the main reflector, it is of interest to look at the $\alpha = 0^\circ$ concentric scattered fields from the shaped subreflector and the hyperboloid subreflector. These are shown in Fig. 17. The patterns are for the near fields in the vicinity of the main reflectors. It is apparent for such large subreflectors (approximately 200λ) that the vertex plate is extremely effective. Furthermore, the optical projection approximation accounting for subreflector blockage is also accurate. Also apparent is the relatively precise secant squared behavior (for high gain) achieved by the shaped reflector system.

The current distributions on the main reflectors in the plane of feed and subreflector rotation are shown in Figs. 18

through 21. Both amplitude and phase are shown for the Cassegrainian and shaped systems at $\beta = \alpha$ and $\beta = \alpha/2$. The object is to gain some further insight into what is occurring within the reflector systems that causes the result in gains and the far-field patterns that has already been observed.

Figure 18 shows the paraboloid currents as a function of parameter α when $\beta = \alpha$. (The curves are displaced vertically so that their relative functional characteristics are easily compared.) Note that the phase curves remain flat except where under-illumination of the paraboloid occurs (to the left). The under-illumination is evident in the amplitude curves. The under-illumination to the left is matched by an over-illumination to the right. This over-illumination increases the noise of the antenna substantially for a ground system antenna looking toward zenith. The over-illumination receives an average of approximately 240 K ground radiation, as compared to an over-illuminated space antenna which would receive approximately 2.7 K galactic noise. This is one of the principal motivations for using rotation angles $\beta = \alpha/2$ for the feed and subreflector of a ground Cassegrainian antenna.

When $\beta = \alpha/2$, the over- and under-illumination of the paraboloid are reduced substantially. This is observed in Fig. 19 over a wide range of α from $\alpha = 0^\circ$ to $\alpha = 14.52^\circ$. The penalty for this well-illuminated paraboloid in amplitude is a phase error illumination, which is also observed in Fig. 19. A linear beam-shift phase term has been subtracted from the phase curves so that what is depicted as displaced from a flat curve is a phase error. As observed in Fig. 3, the phase error is not significant (relative to the $\alpha = \beta$ case) until α is greater than 6° .

For the dual-shaped reflectors, the situation is very different. When $\alpha = \beta$ is maintained and α is increased, not only does a poorly illuminated main reflector suffer in amplitude, but it also displays substantial phase error. This is shown in Fig. 20. Also, the amplitude over- and under-illumination effects are more severe here than for the Cassegrainian antenna because the illumination amplitude is nearly uniform or flat. This is a result of the secant-squared subreflector scattered pattern (see Fig. 17).

As a result, it is fortuitous that rotating the subreflector with $\beta = \alpha/2$ gives such excellent results for the dual-shaped reflector antenna. The current distributions for this situation as a function of the parameter α are shown in Fig. 21. The phase curves are relatively flat for a large range of α (after subtraction of the appropriate linear beam-shift phase). The resulting gain curve as a function of α (see Fig. 4) is comparable to that obtained for the Cassegrainian curve, although higher in value as a result of the shaping.

The main reflector current curves clarify what is occurring to the amplitude distribution on the main reflectors when $\alpha = \beta$ and when $\beta = \alpha/2$. It is clear that when $\alpha = \beta$, a large noise temperature can occur for ground system antennas looking upward, and that setting β equal to $\alpha/2$ will largely alleviate this problem for both the Cassegrainian and the dual-shaped reflector systems.

It is also evident why the main reflector current phase is excellent (nearly flat) for the Cassegrainian antenna when $\beta = \alpha$. However, an understanding of why the main reflector current phase curves are as flat as they are for $\beta = \alpha/2$ requires further investigation.

IV. Caustic Characteristics of the Subreflector Scattered Fields

Further insight into why the shaped main reflector phase current distributions are as flat as observed for $\beta = \alpha/2$ (see Fig. 21) can be obtained by studying the caustic surfaces of the geometrical optics fields scattered from the subreflector.

In the plane of rotation of the feed and subreflector, the Gaussian curvature matrix is diagonal (by symmetry), and a line caustic for the radius of curvature out of the plane $-R_o$ can be observed; another line caustic for the radius of curvature is parallel to the plane $-R_p$.

A set of the above line caustics (for different α) can be plotted relative to the subreflector and relative to the main reflector. When the caustic lines relative to the main reflector for $\alpha = 0^\circ$ and for $\alpha > 0^\circ$ are plotted, a relative comparison can be made of how much the $\alpha > 0^\circ$ caustic lines deviate from the ideal $\alpha = 0^\circ$ caustic line. This deviation is a visual measure of the phase distortion that is observed on the main reflector for $\alpha > 0^\circ$.

For the Cassegrainian antenna and $\alpha = \beta$, both caustic lines degenerate into a point for all α . This point is the focal point of the hyperboloid and paraboloid. When $\beta = \alpha/2$, caustic lines are obtained as shown in Fig. 22. In Fig. 22, the caustic lines are plotted relative to the subreflector for all α . To observe the caustics relative to the main reflector, each caustic must be rotated about the rotation point (focal point) by the value of α .

In Fig. 23, the same caustic lines are observed in an enlarged diagram. The rays emanating from the caustics are tangent to the caustic surfaces. For the R_o curves, the rays are tangent to a cusp of the surface in the plane of the paper. The rays depicted in the top diagram are all directed toward one end of the main reflector. However, because of the rotation of the feed and subreflector assembly, the main reflector is rotated

for each caustic line by α ; i.e., the curves are plotted relative to the subreflector. (The rays appear parallel, but they are not.) The lower diagram of Fig. 23 shows rays distributed to all parts (in the plane) of the main reflector.

The computation and plotting of the caustics were performed during a geometrical optics analysis of the field scattered by the subreflector. In this analysis, two radii of curvature were computed by the equations shown in Fig. 24. These radii of curvature, R_1 and R_2 , relate directly to R_o and R_p , but not uniquely or consistently (a branch choice must be made). In order to relate R_1 and R_2 to R_o and R_p through the scattered field (α fixed), the expedient of making the subreflector cylindrical is used as indicated in the lower diagram of Fig. 24. This immediately makes R_o extremely large (less than infinity because of the spherical wave incident upon the subreflector from the feed). The curvature R_p is not changed by this artifice. An appropriate match of R_1 to R_o or R_p and of R_2 to R_p or R_o is made accordingly.

The principal motive for examining the caustic lines is to further understand the phase characteristics of the dual-shaped reflectors. The caustic lines for the shaped subreflector scattered fields are very different from those encountered for the field scattered by the hyperboloid. This is apparently true for offset as well as circularly symmetric-shaped reflectors.

Figure 25 shows the caustic lines for the field scattered by a focused feed from an offset shaped subreflector (Refs. 8, 9). Note that the vertical scale for the inset diagram is many times greater than the scale for the full diagram; thus, the R_p caustic is extremely large. The wavefront scattered from the subreflector is nearly planar in the plane of the diagram and near the extremities. It is also now clear that the caustic line discussed earlier and displayed in Fig. 10 is an R_o caustic or is due to curvature orthogonal to the plane of the diagram.

The R_p caustic lines for different α , with $\beta = \alpha/2$, are displayed in Fig. 26 for the 70-meter shaped reflectors. They are similar in character to the offset-shaped case of Fig. 25, though this case is distinct from that of the Cassegrainian system. In Fig. 26, the R_p caustics are shown with respect to the subreflector. In Fig. 27, the same R_p caustic lines are plotted with respect to the main shaped reflector. The subreflector is appropriately located only for the $\alpha = 0^\circ$ case. The main reflector is to the left, fixed for all α values. Note that the caustic lines for various α all lie nearly parallel, especially for $\alpha < 6^\circ$. Thus, the phase of the geometrical optic field incident upon the main reflector will be relatively unchanged for $\beta = \alpha/2$. This phase compensation occurs in addition to very little over- and under-illumination of the main reflector. Therefore, the shaped reflector performance with $\beta = \alpha/2$ is very good.

In Fig. 28, observe the R_o (curvature orthogonal to the diagram) caustic characteristics for various α for the same 70-meter shaped reflector system. Note again that with respect to the main reflector (right-hand diagram), the caustic lines become much closer. The enlarged diagrams of Fig. 29 show this more clearly.

V. Conclusion

In a circularly symmetric, high-gain, dual-reflector antenna system, a very substantial off-axis feed displacement can be accommodated while retaining a circularly symmetric sub-reflector. This can be done with little gain or gain/noise temperature (G/T) loss for both Cassegrainian and dual-shaped reflectors. In both cases (the Cassegrainian and the dual-shaped antennas), performance is substantially improved if the subreflector is rotated off-axis by an angle β that is one-half the angle of rotation of the feed, α . This is imperative for the shaped reflectors because there is no unique phase center about which to rotate the subreflector and feed. However, to obtain an optimum G/T for the Cassegrain reflectors (as well as the shaped reflectors), maintaining $\beta = \alpha/2$ is important. Although the main reflector phase distortion is kept fairly small, the relationship $\beta = \alpha/2$ ensures very little spillover of energy past the main reflector into a hot (240 K) ground.

In the hypothetical Cassegrain system discussed in this article, no noise shield was used. Thus, the noise temperatures

shown as a function of α (feed rotation angle about the Cassegrainian focal point), with $\beta = \alpha/2$ or $\beta = \alpha$, are higher than can be obtained with a noise shield.

A typical good system (a DSN 64-meter antenna) may have a noise temperature distribution as shown in Table 2. If the dichroic and rear spillover noises are removed from the zenith elevation values of Table 2, about 14.6 K remains. The noise temperatures displayed in Fig. 30 can be added to this value as a function of α , and G/T values can be obtained as a function of α for the Cassegrainian system used herein for $\beta = \alpha$ and for $\beta = \alpha/2$. This result is displayed in Fig. 31(a). Note in Fig. 31(a) that the G/T performance is superior for the $\beta = \alpha/2$ case despite the phase error introduced by the $\beta = \alpha/2$ value of the feed location. This is a direct result of the substantially flat and low noise temperature found for the $\beta = \alpha/2$ case (see Fig. 30). The difference in the G/T curves in Fig. 31(a) would be even greater if a noise shield were built into the Cassegrainian design. The difference is slightly less if a less optimistic noise temperature for the system is assumed: i.e.,

$$T_{\text{system}} - T_{\text{antenna}} = 20 \text{ K}$$

The result, shown in Fig. 31(b), would apply for an antenna elevation angle below zenith.

Acknowledgment

The concept of rotating a symmetric subreflector by one-half the feed offset angle to minimize the scan loss was originally proposed by Gerry Levy (Ref. 10) for a nonshaped Cassegrainian system. The authors wish to thank R. C. Clauss for providing both the funding, through the Advanced Systems Program, and the impetus to study the problem by insisting that it would also work for a shaped system.

References

1. Galindo-Israel, V., and Mittra, R., Synthesis of Offset Dual-Shaped Reflectors with Arbitrary Control of Phase and Amplitude, *1977 URSI Symp. on Electromagnetic Theory, 20-24 June 1977*, pp. 7-10, International Scientific Radio Union, 1977.
2. Galindo-Israel, V., Mittra, R., and Cha, A., Aperture Amplitude and Phase Control of Offset Dual Reflectors, *IEEE Trans. Antennas Propagat.*, AP-27: 154-164, 1979.
3. Galindo, V., Design of Dual Reflector Antennas and Arbitrary Phase and Amplitude Distribution, *IEEE Proc. Int. Symp. Antennas and Propagat.*, Boulder, Colorado; also in *IEEE Trans. Antennas Propagat.*, AP-12: 403-408, 1963-1964.
4. Galindo-Israel, V., and Mittra, R., A New Series Representation for the Radiation Integral with Application to Reflector Antennas, *IEEE Trans. Antennas Propagat.*, 25:631-641, 1977.
5. Mittra, R., Rahmat-Samii, Y., Galindo-Israel, V., and Norman, R., An Efficient Technique for the Computation of Vector Secondary Patterns of Offset Paraboloid Reflectors, *IEEE Trans. Antennas Propagat.*, 27:294-304, 1979.
6. Rahmat-Samii, Y., and Galindo-Israel, V., Shaped Reflector Antenna Analysis Using the Jacobi-Bessel Series, *IEEE Trans. Antennas Propagat.*, 28:425-435, 1979.
7. Galindo-Israel, V., Imbriale, W., Rahmat-Samii, Y., and Veruttipong, T., Interpolation Methods for GTD Analysis of Shaped Reflectors, *TDA Progress Report 42-80*, pp. 62-67, Jet Propulsion Laboratory, Pasadena, Calif., 1984-1985.
8. Cha, A., Wideband Diffraction Improved Dual-Shaped Reflectors, *IEEE Trans. Antennas Propagat.*, AP-30: 173-176 (theoretical predictions herein subsequently totally verified experimentally).
9. Cha, A., Galindo-Israel, V., and Mittra, R., Efficient Design of Offset Dual-Shaped Reflectors for Antenna and Beam Waveguide Applications, *1979 Int. Symp. Digest, Antennas and Propagat., Vol. 1*, pp. 84-87, 79-CH1456-3 AP, IEEE, New York, 1979.
10. Levy, G. S., and Katow, M. S., Multi-feed Cone System for the Advanced Antenna Systems, *Space Prog. Summary 37-45 Vol. III*, pp. 48-50, Jet Propulsion Laboratory, Pasadena, Calif., 1967.

Table 1. Cassegrain gains

Configuration	Angle Case, deg	Gain, dBi
Concentric Cassegrain	$\beta = \alpha = 0$	74.90
Asymmetric Hyperboloid	$\beta = \alpha = 4.5165$	74.86
Asymmetric Hyperboloid (No Diffraction from Subreflector)	$\beta = \alpha = 4.5165$	74.96
Symmetric Hyperboloid	$\beta = \alpha = 4.5165$	74.71
Symmetric Hyperboloid	$\alpha = 4.5165 \left(\beta = \frac{\alpha}{2} \right)$	74.82

Table 2. Noise for very good Cassegrainian system

Noise Source	Zenith, K	30° Elevation
Amplifier	4.0	4.0
Waveguide at 300 K	4.7	4.7
Dichroic Surface	2.0	2.0
Galactic Noise	2.7	2.7
Atmosphere	2.6	5.2
Antenna		
Quadrapod	2.6	5.2
Rear Spillover	~0.4	~0.2
Total Noise	~17.0 K	~22.0 K

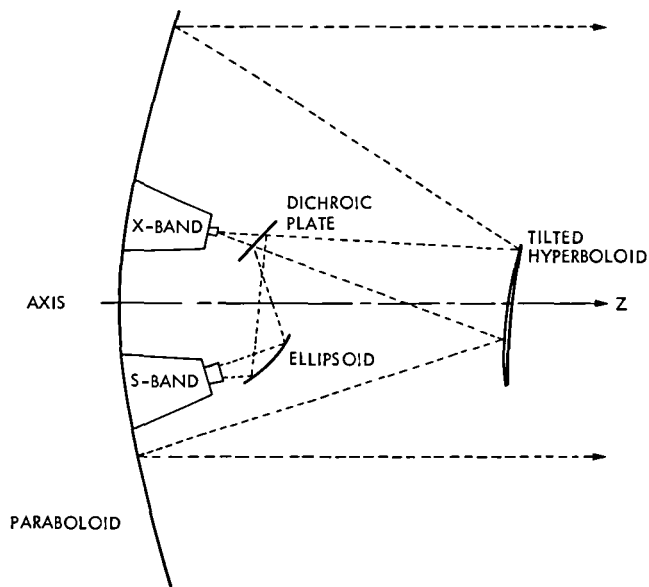


Fig. 1. Multiple feed, off-axis antenna system

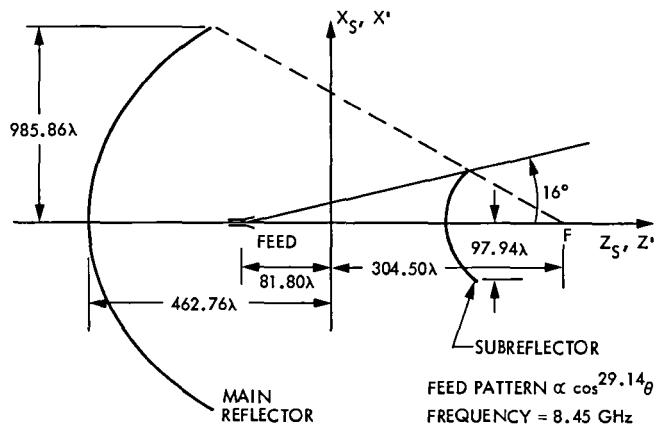


Fig. 3. Cassegrainian antenna geometry

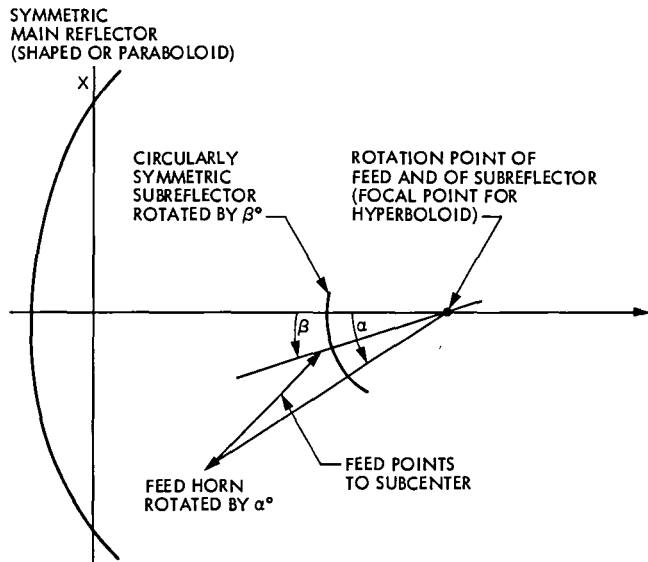


Fig. 2. Geometry for feed and subreflector rotation

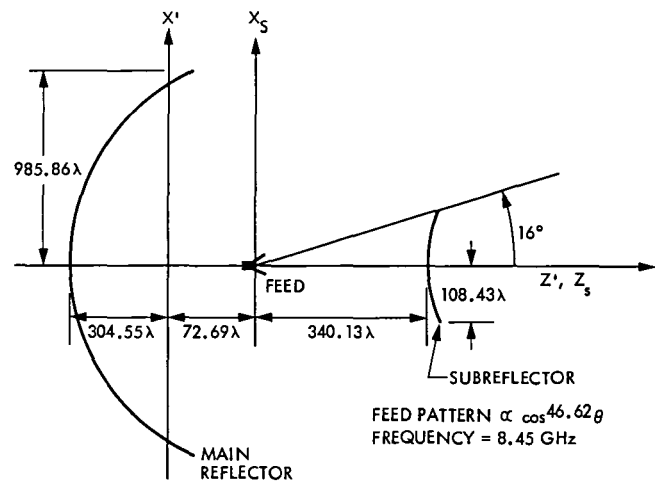


Fig. 4. Dual symmetric-shaped reflector antenna geometry

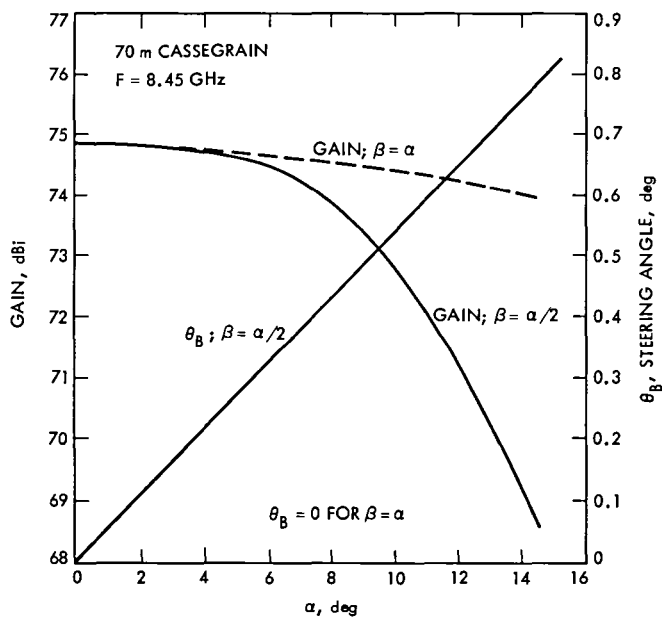
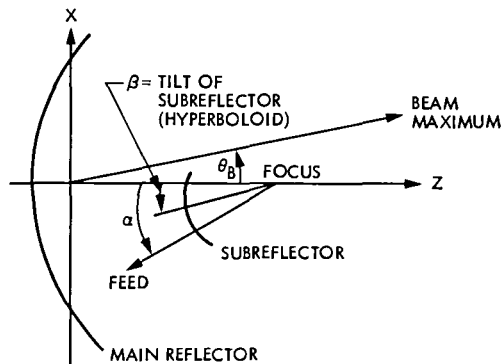


Fig. 5. Gain and steering angle vs feed horn rotated angle (α) for 70-m Cassegrainian antenna

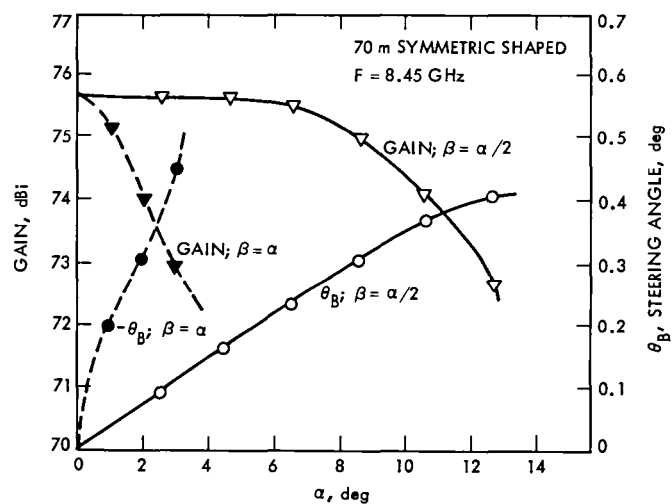
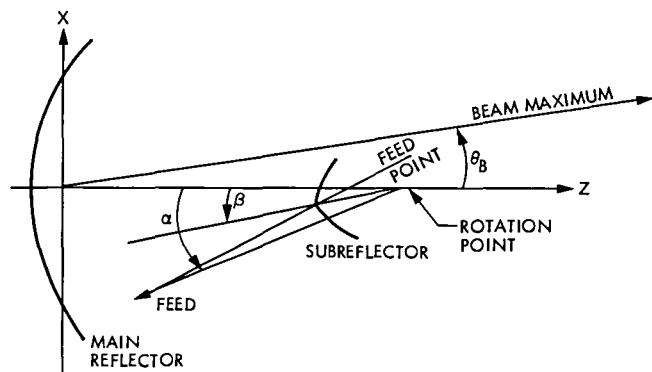


Fig. 6. Gain and steering angle vs feed horn rotated angle (α) for 70-m dual symmetric-shaped reflector antenna

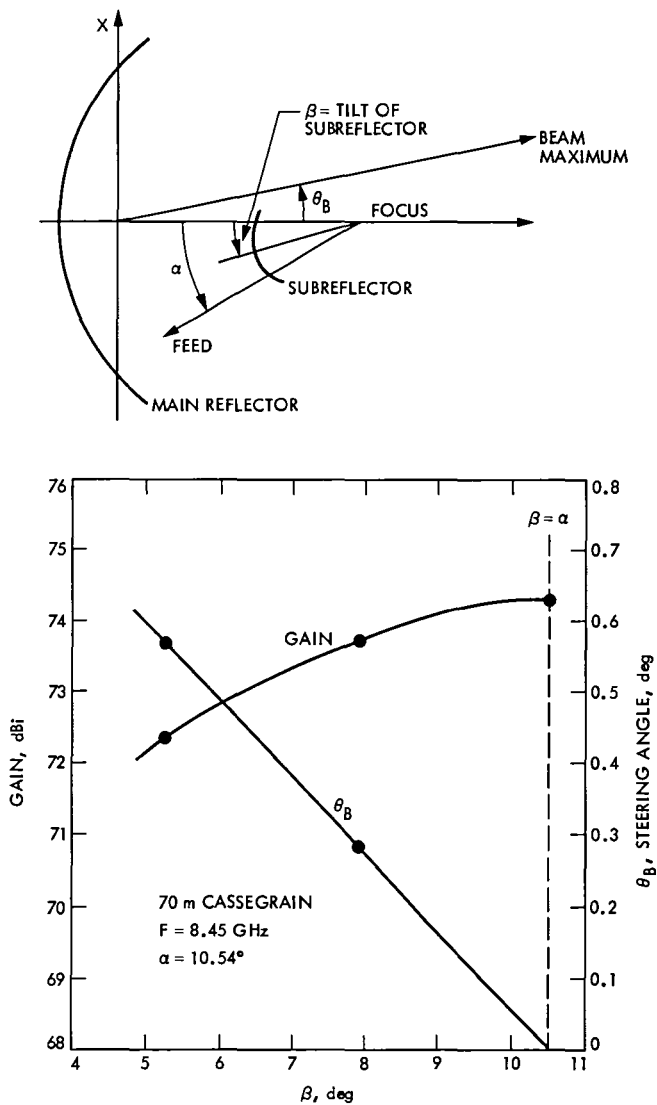


Fig. 7. Gain and steering angle vs tilt angle of subreflector (β) for 70-m Cassegrainian antenna

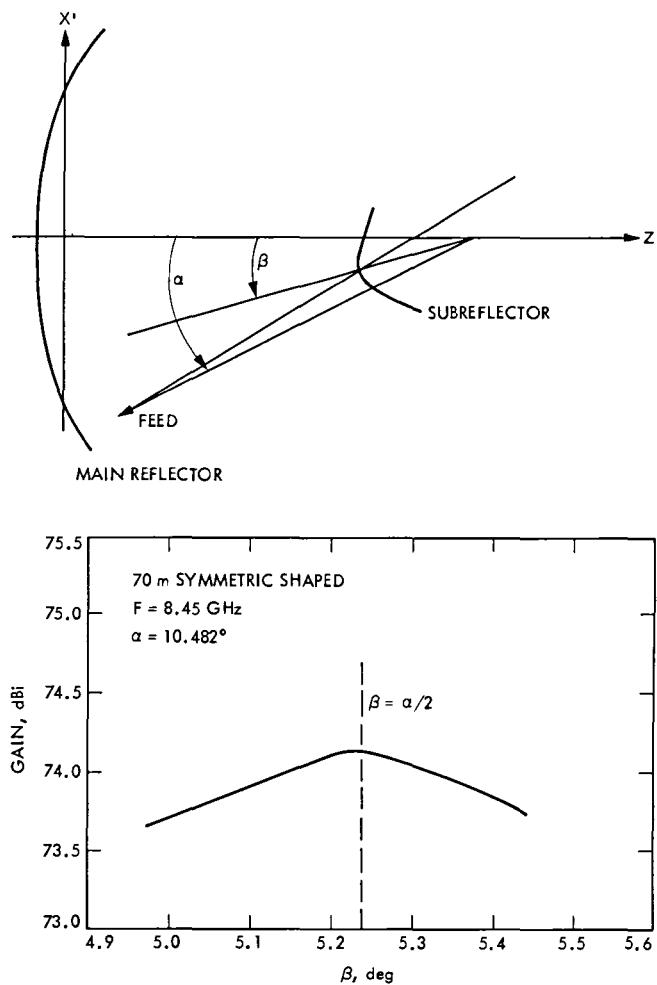


Fig. 8. Gain vs tilt angle of subreflector (β) for 70-m dual symmetric-shaped reflector antenna with $\alpha = 10.482^\circ$

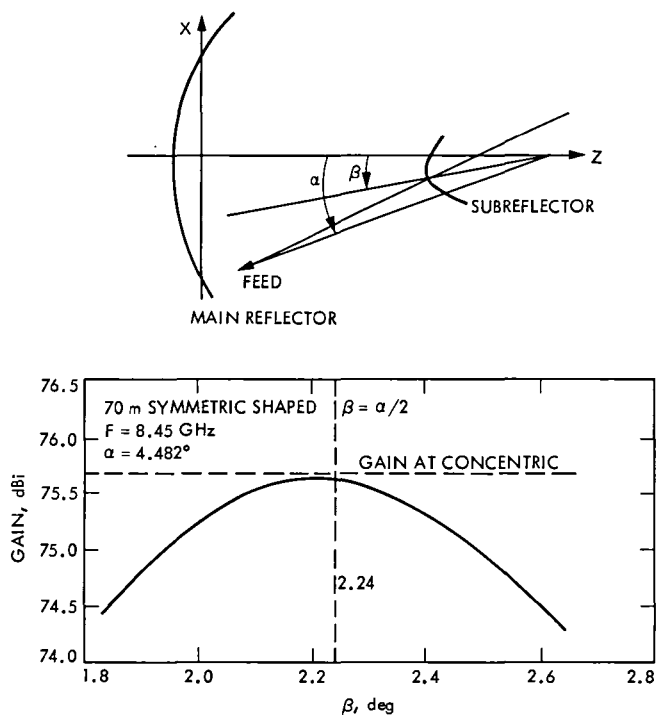


Fig. 9. Gain vs tilt angle of subreflector (β) for 70-m dual symmetric-shaped reflector antenna with $\alpha = 4.482^\circ$

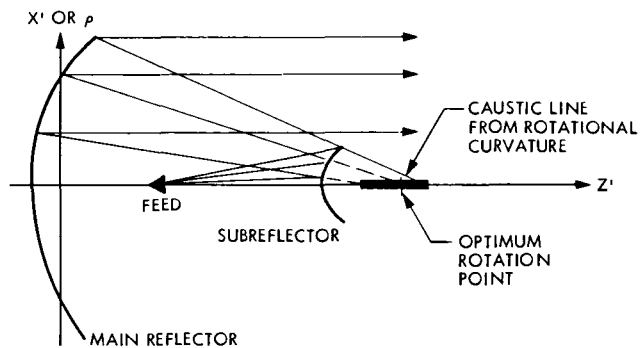
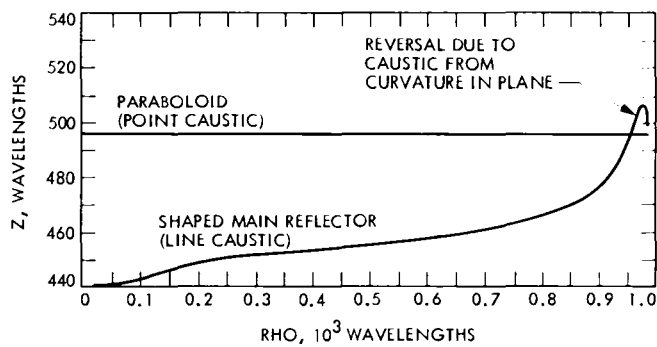
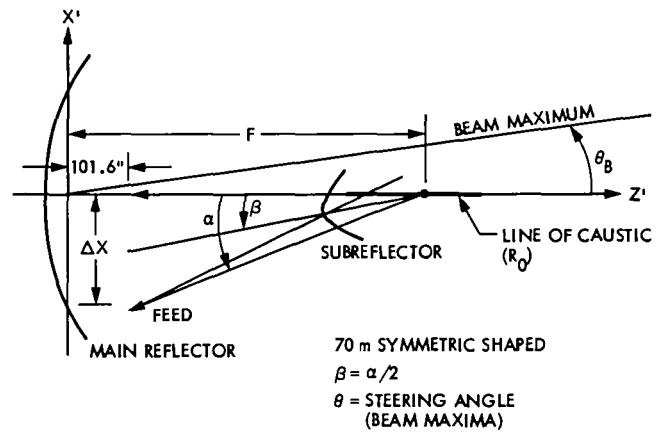


Fig. 10. The z-caustic position due to rotational curvature (curvature out of plane)



NO.	ΔX , in.	F, in.	α , deg	GAIN, dBi	θ_B , deg	
1	0.000	645.76	0.000	75.65	0.00	CONCENTRIC CASE
2	42.523	615.01	4.751	75.48	0.10	
3	42.523	645.76	4.482	75.58	0.16	
4	42.523	710.06	4.007	75.20	0.26	
5	42.523	641.60	4.517	75.59	0.15	BEST CASE

Fig. 11. The determination of the optimum point of rotation

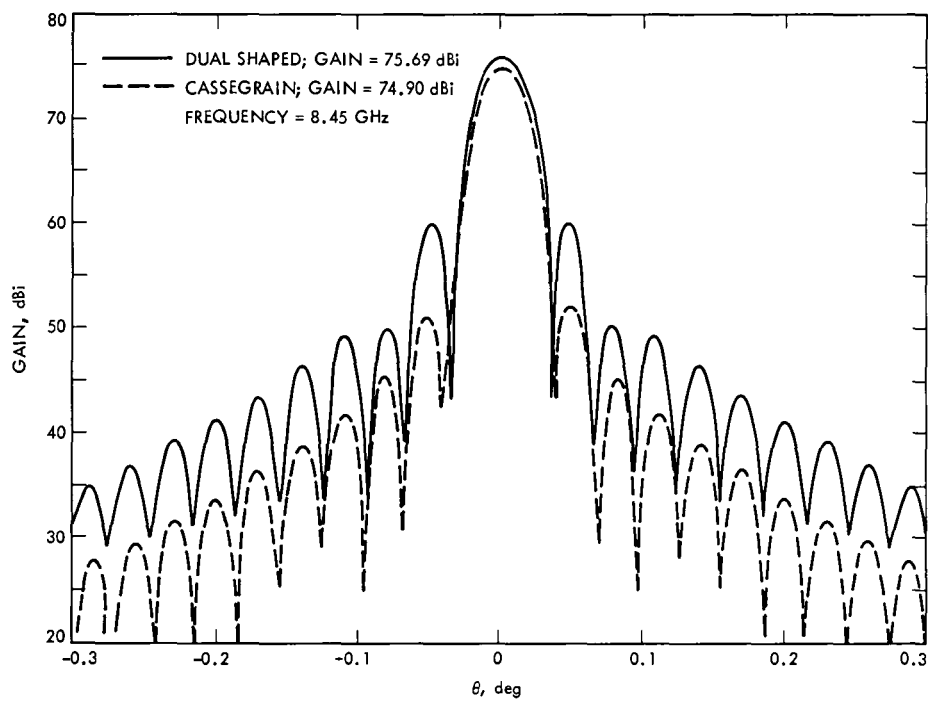


Fig. 12. Far-field gain patterns of the dual-shaped (with vertex plate) and Cassegrainian antennas with $\alpha = \beta = 0^\circ$

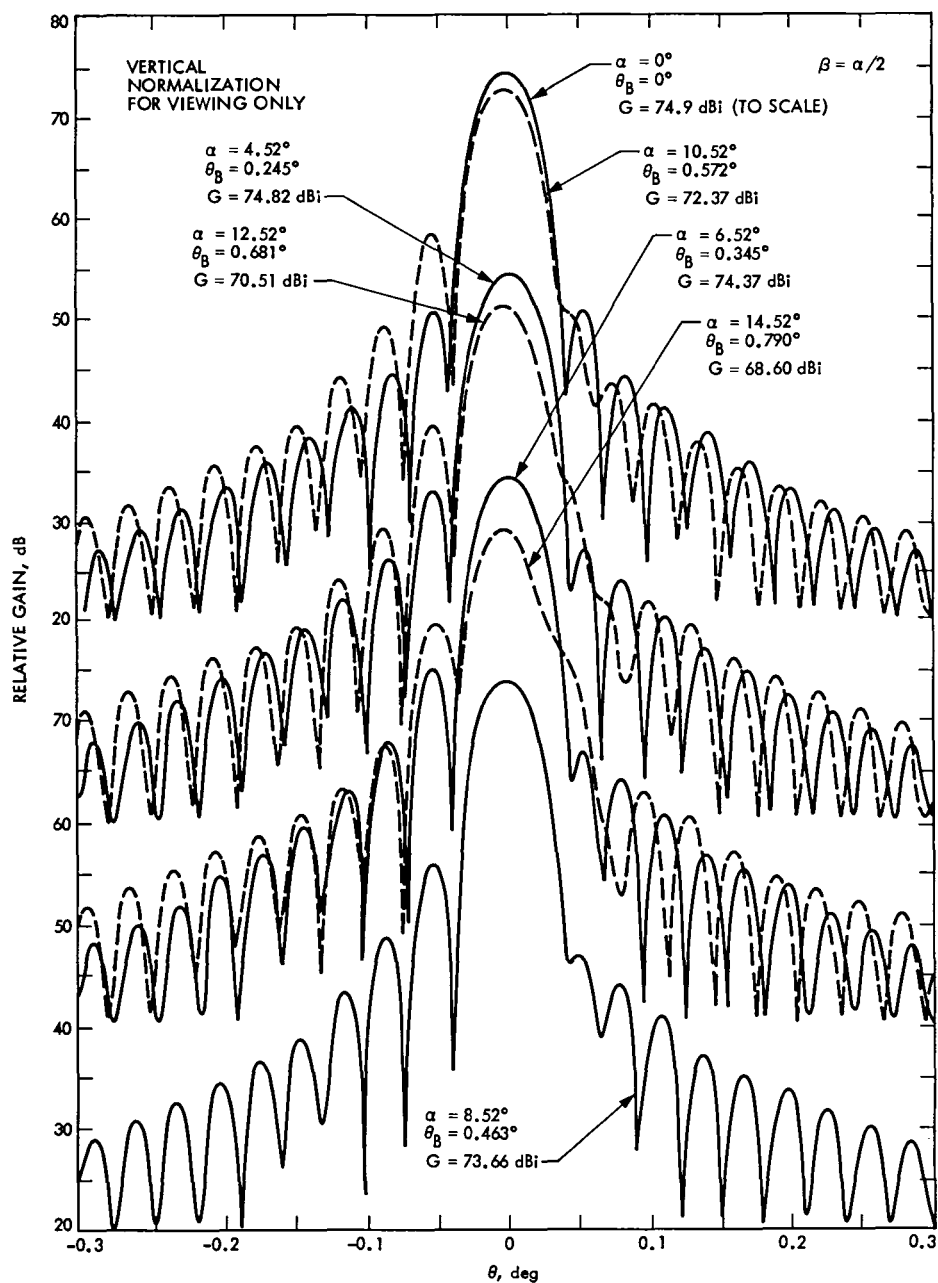


Fig. 13. Far-field gain patterns of the Cassegrainian antenna with $\beta = \alpha/2$

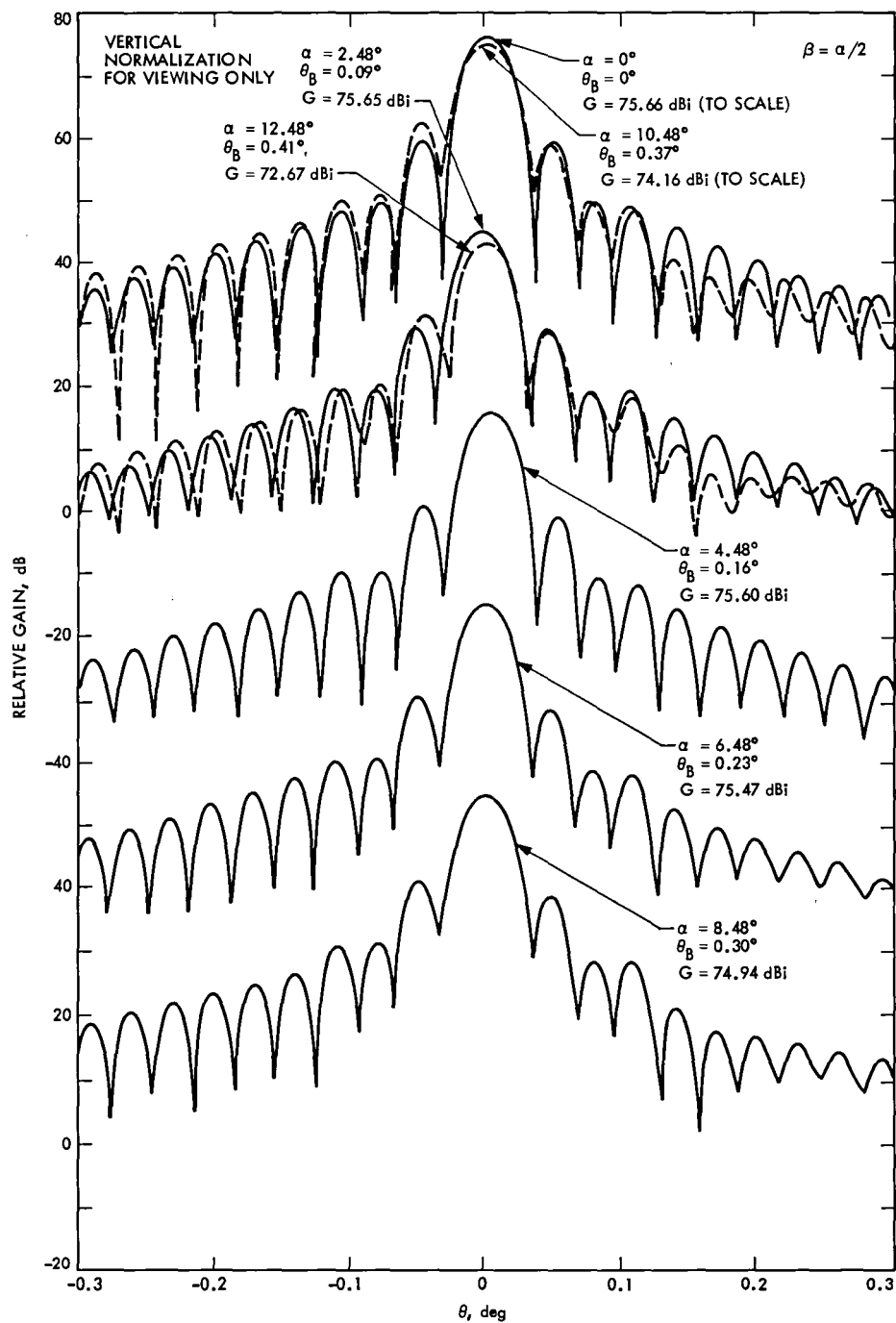


Fig. 14. Far-field gain patterns of the dual-shaped (with vertex plate) antenna with $\beta = \alpha/2$

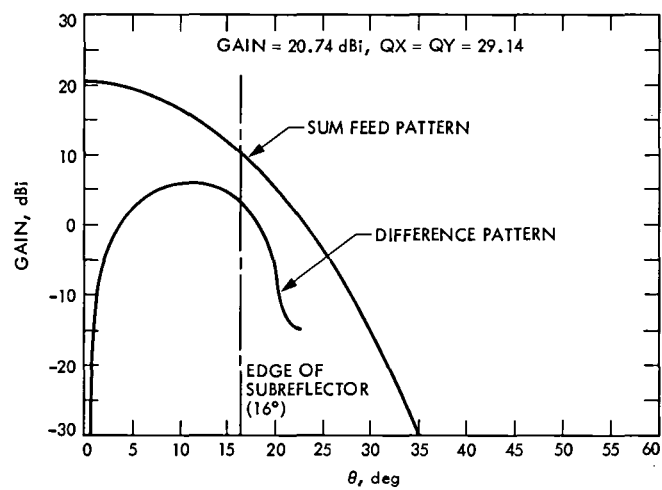


Fig. 15. Feed horn radiation patterns

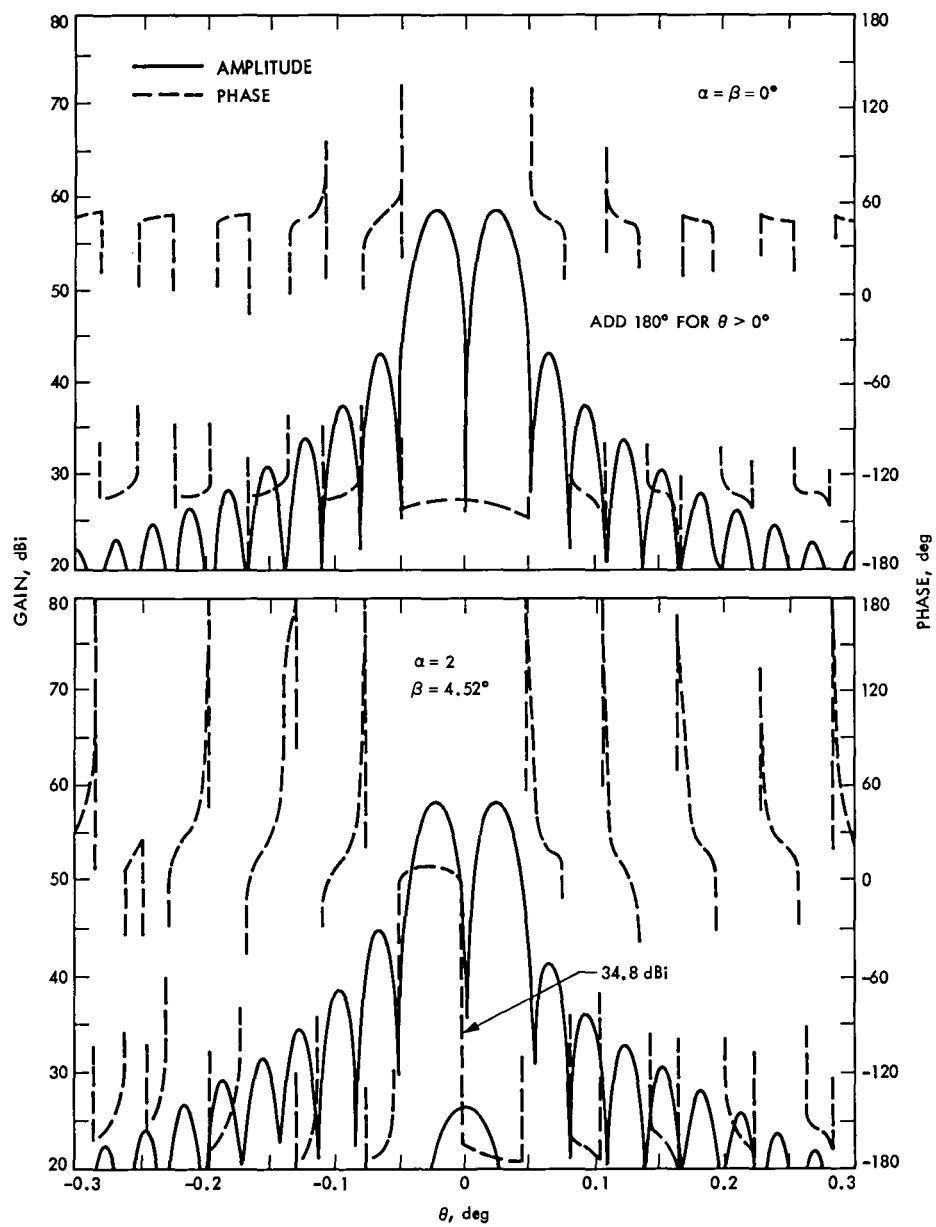


Fig. 16. Difference pattern of the Cassegrainian antenna

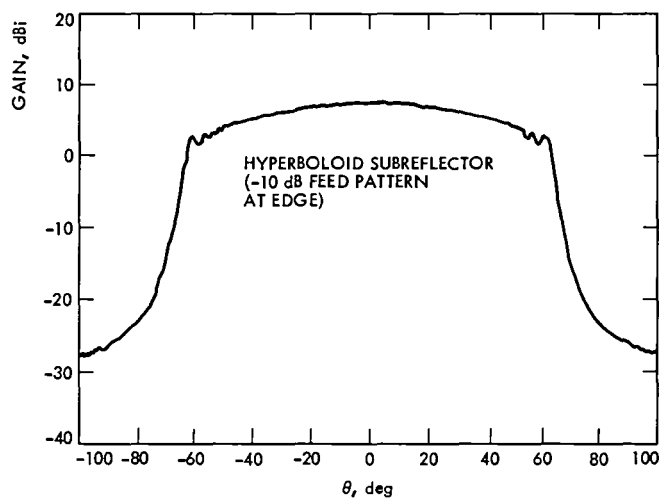
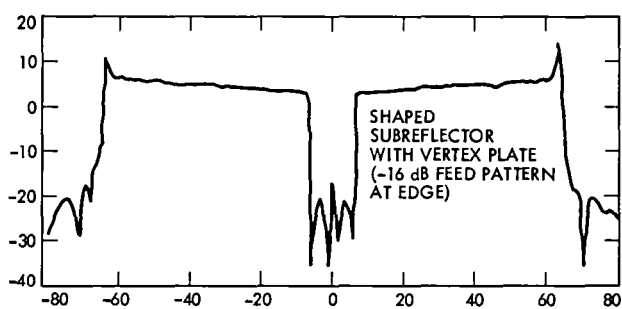
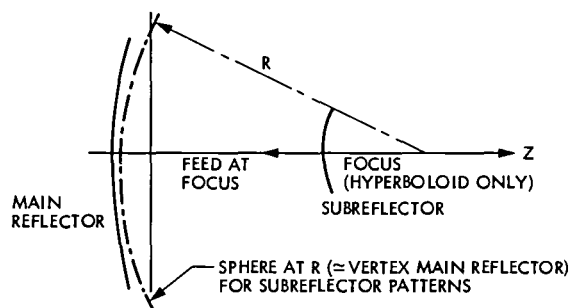


Fig. 17. Subreflector scatter patterns

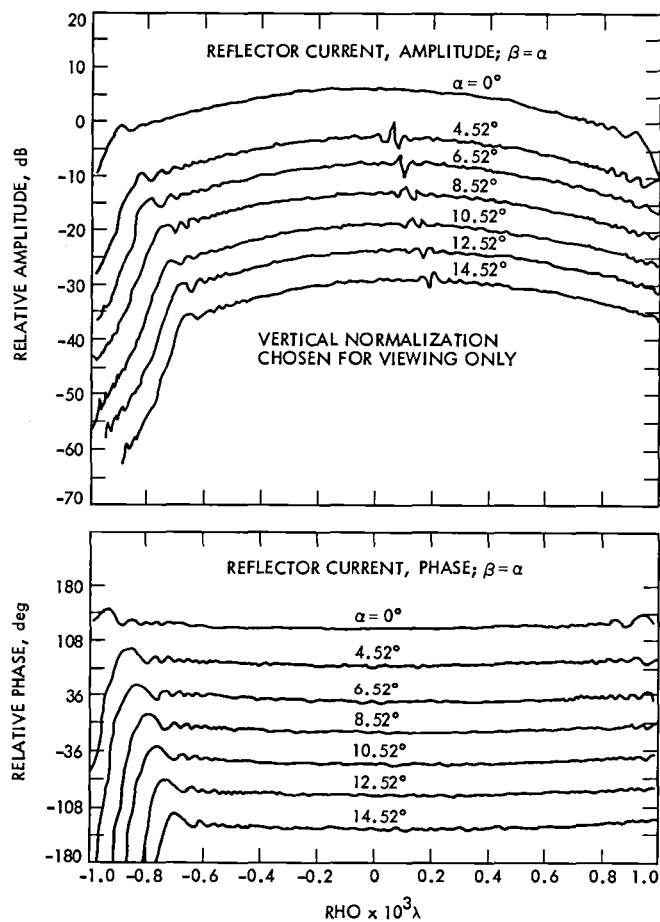


Fig. 18. Aperture current distributions of the Cassegrainian antenna for $\beta = \alpha$

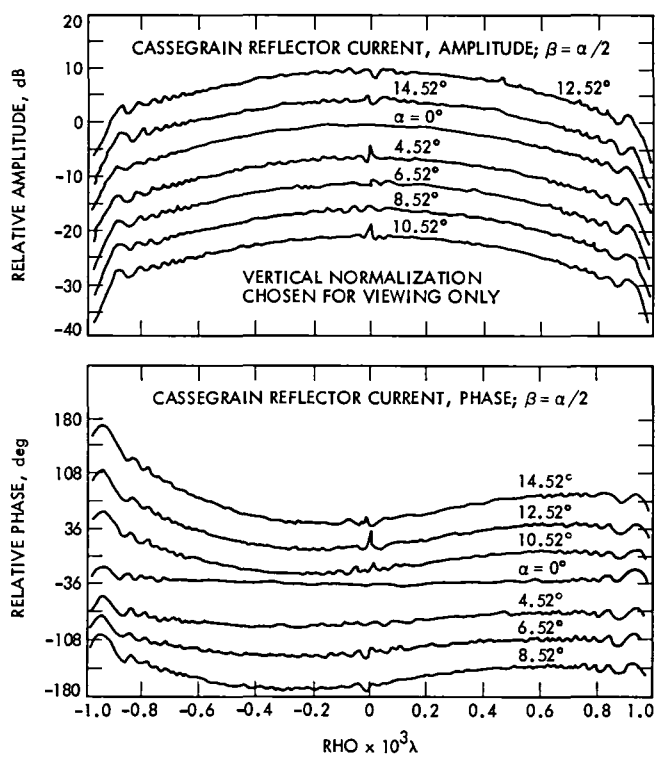


Fig. 19. Aperture current distributions of the Cassegrainian antenna for $\beta = \alpha/2$

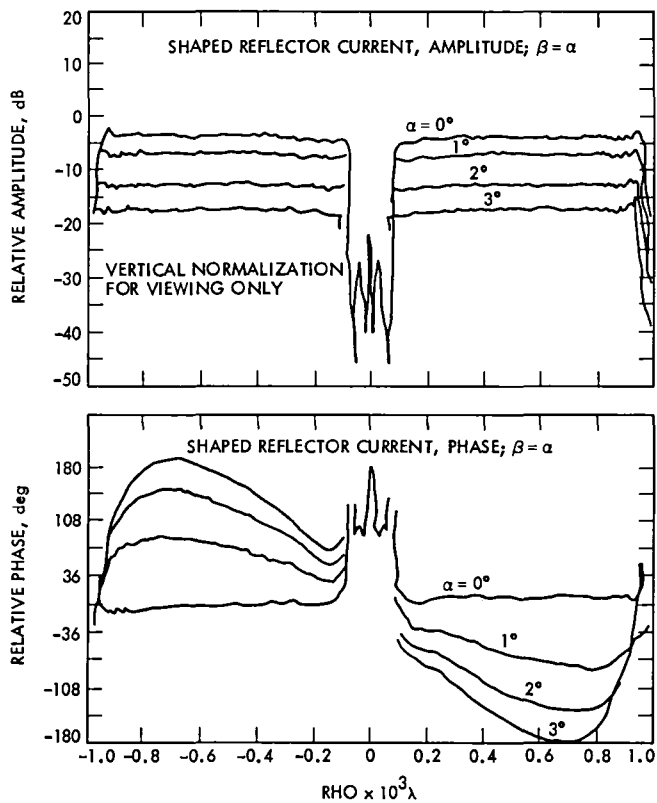


Fig. 20. Aperture current distribution of the shaped antenna for $\beta = \alpha$

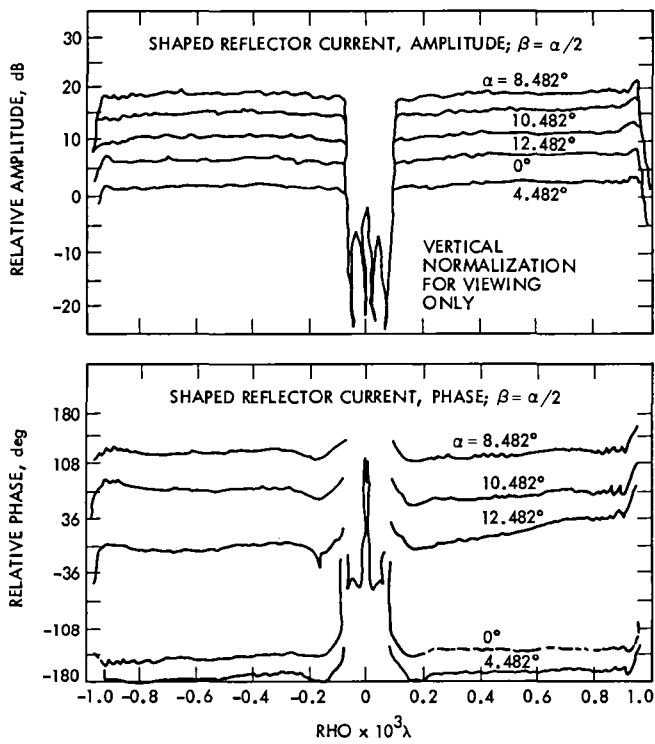


Fig. 21. Aperture current distribution of the shaped antenna for $\beta = \alpha/2$

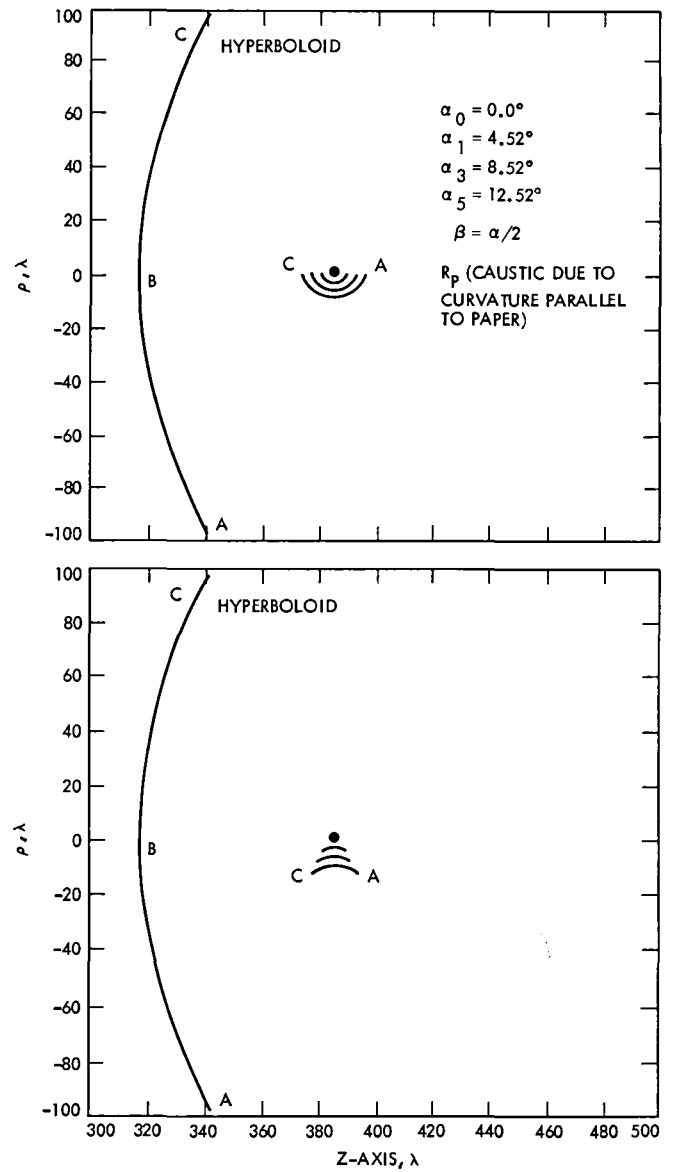


Fig. 22. Caustic surfaces of field scatter from the subreflector of the Cassegrainian antenna

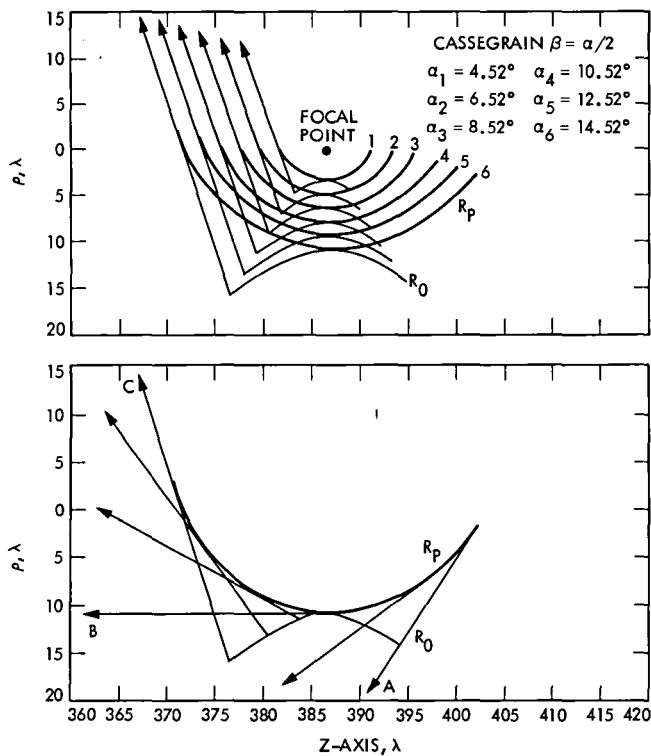


Fig. 23. Caustic surfaces of field scatter from the subreflector of the Cassegrainian antenna, expanded scale

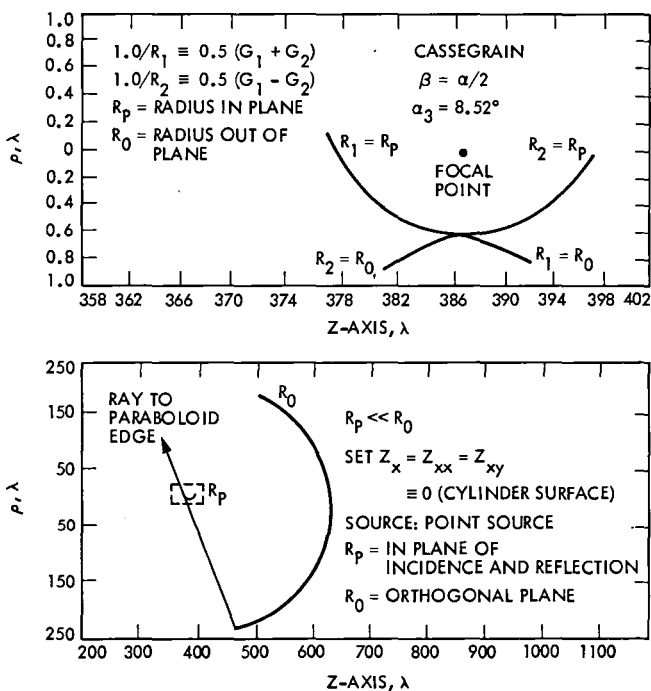


Fig. 24. Caustic surfaces of field scatter from the subreflector of the Cassegrainian antenna where set $Z_x = 0$

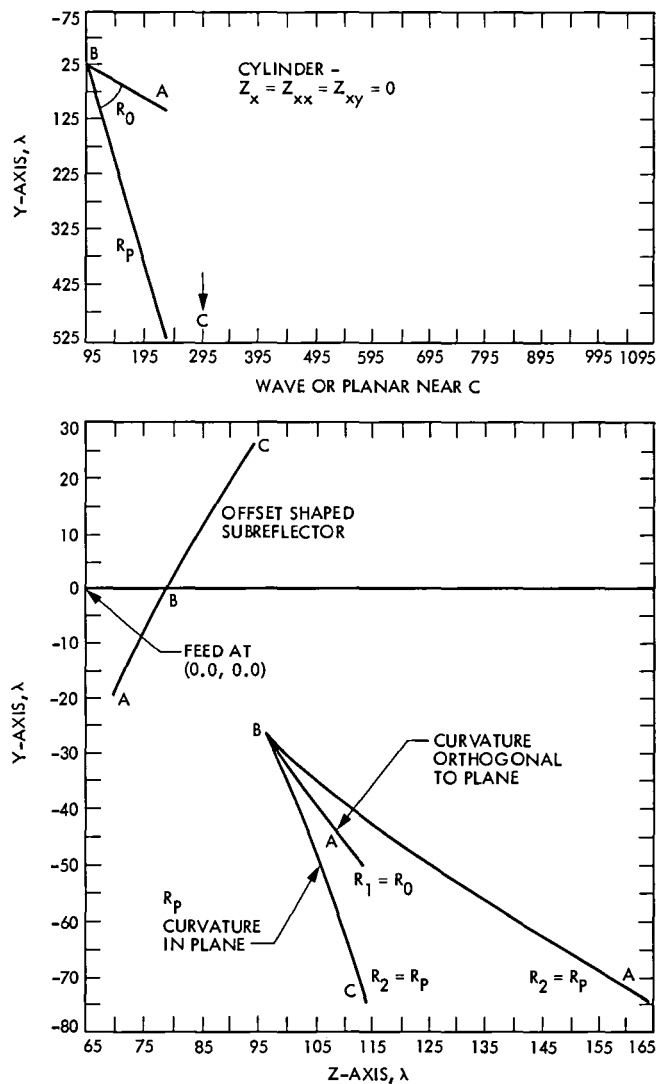


Fig. 25. Caustic surfaces of field scatter from the subreflector of the dual-offset shaped reflectors

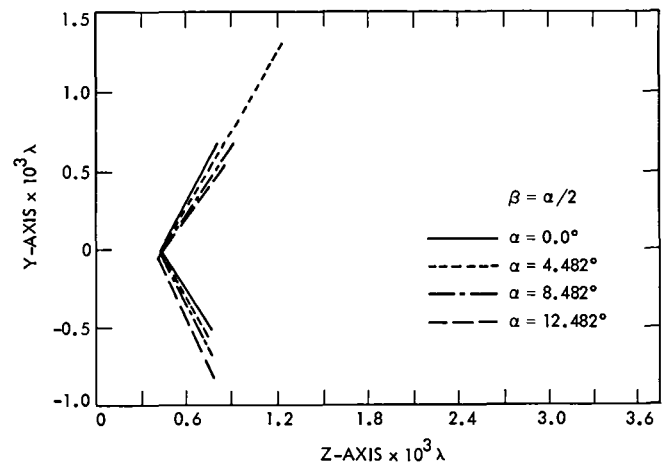
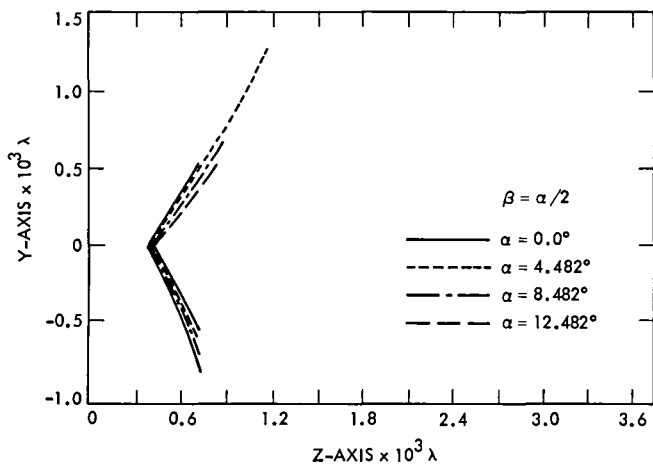
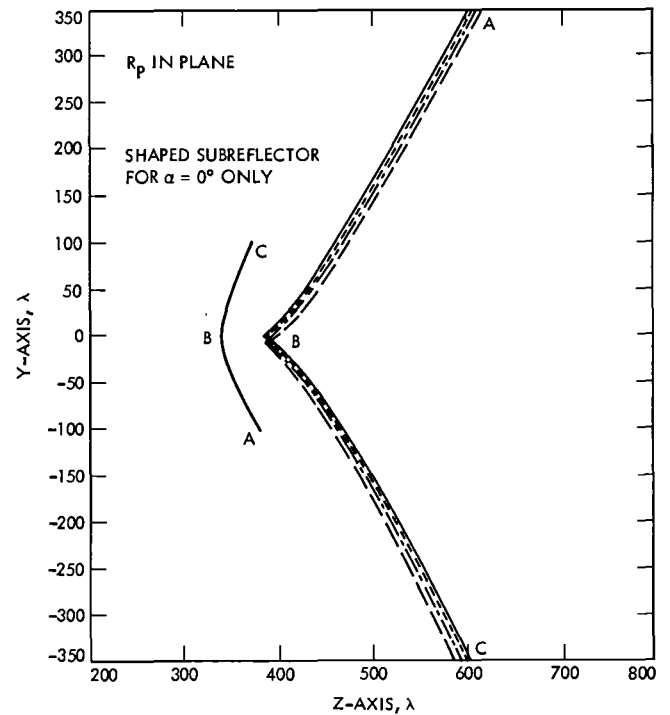
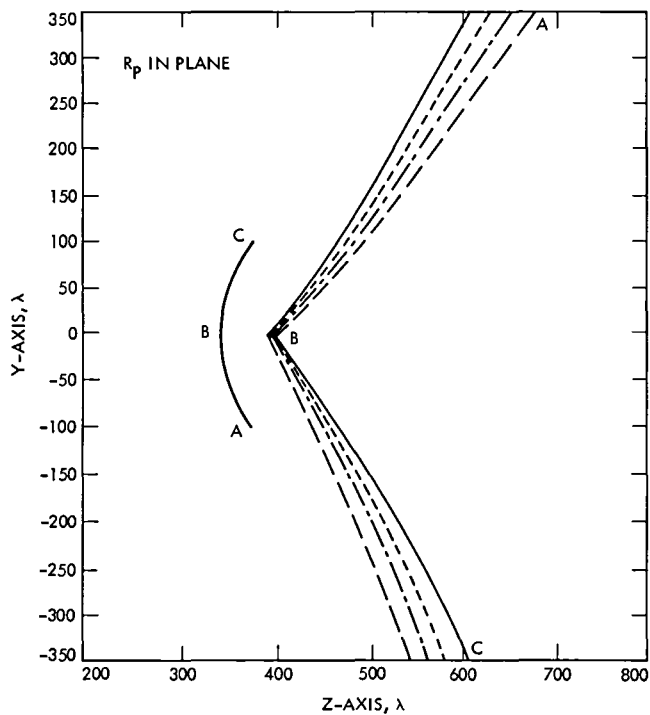


Fig. 26. The R_p caustics (parallel to plane) with respect to shaped subreflector (70-m)

Fig. 27. The R_p caustics (parallel to plane) with respect to shaped main reflector (70-m)

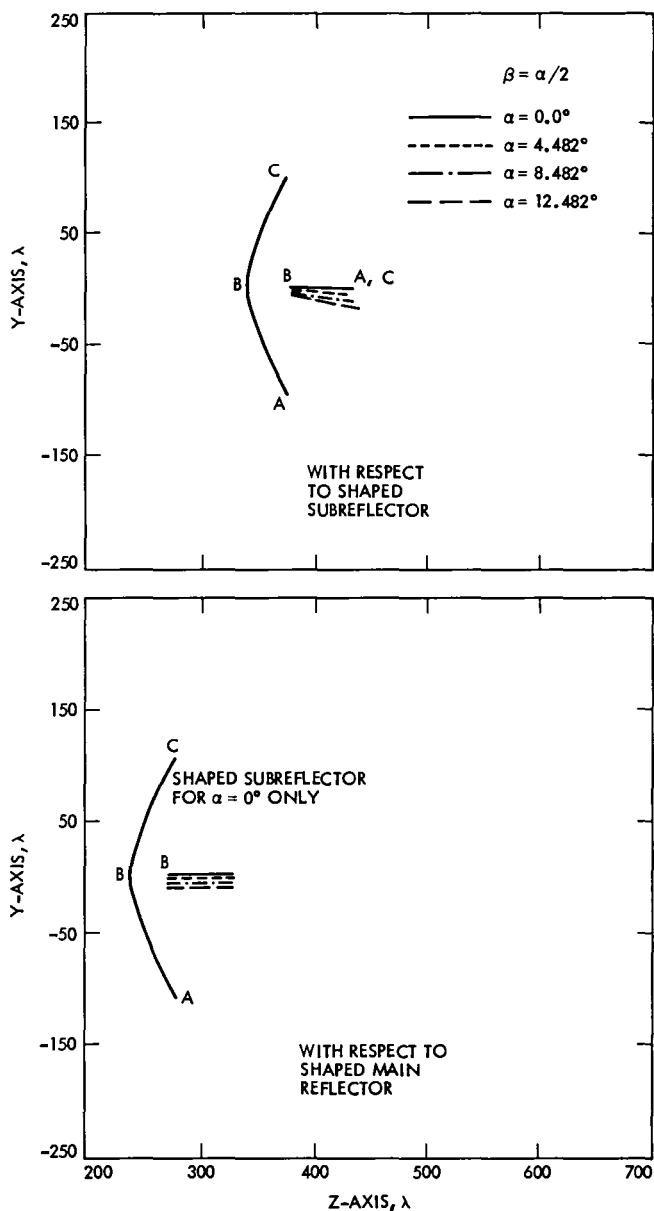


Fig. 28. The R_0 caustics (orthogonal to plane) with respect to shaped subreflector and shaped main reflector (70-m)

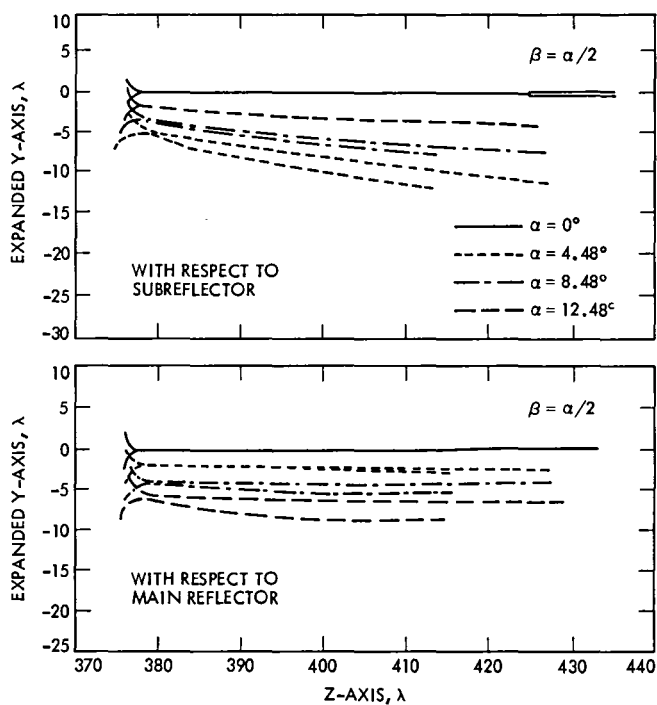


Fig. 29. The R_0 caustics (orthogonal to plane) with respect to shaped subreflector and shaped main reflector (70-m), expanded scale

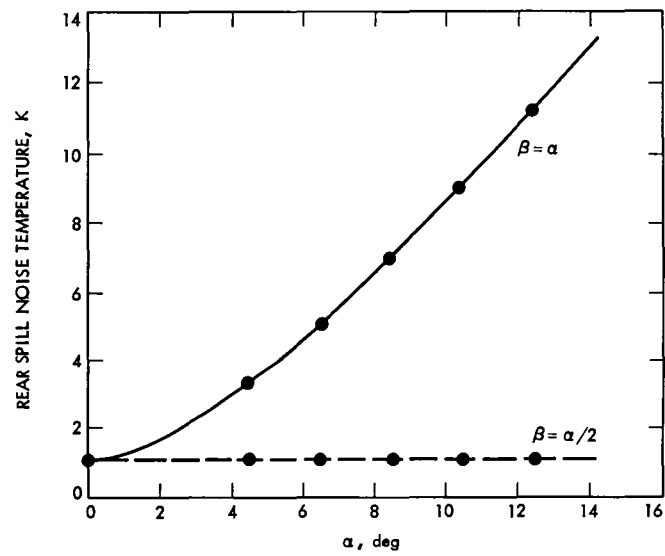
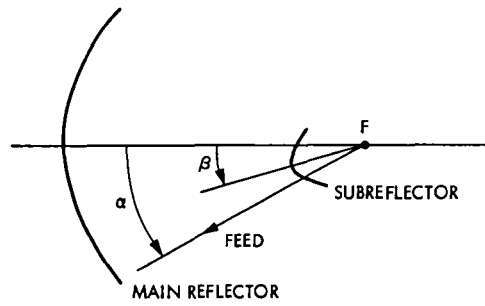


Fig. 30. The 70-m Cassegrainian near spillover noise temperature

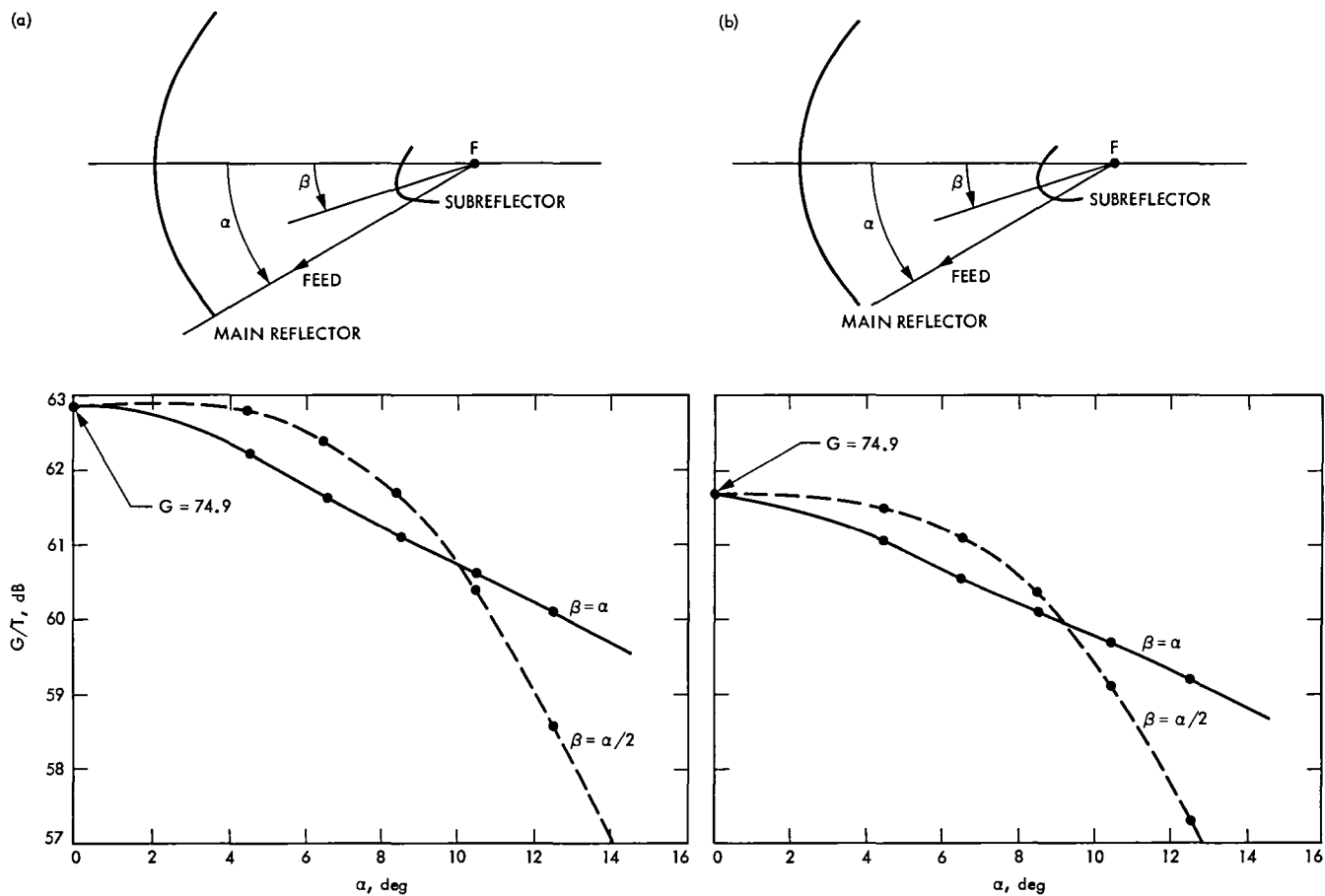


Fig. 31. The 70-m Cassegrainian G/T where $T_{\text{system}} - T_{\text{antenna noise}}$ equals (a) 14.6 K and (b) 20 K

A Note on the Wideband Gaussian Broadcast Channel

R. J. McEliece

California Institute of Technology

E. C. Posner

Office of Telecommunications and Data Acquisition

L. Swanson

Communications Systems Research Section

It is well known that for the Gaussian broadcast channel, timeshared coding is not as efficient as more sophisticated "broadcast" coding strategies. However, in this article we will show that the relative advantage of broadcast coding over timeshared coding is small if the signal-to-noise ratios of both receivers are small. One surprising consequence of this is that for the wideband Gaussian broadcast channel, which we shall define, broadcast coding offers no advantage over timeshared coding at all, and so timeshared coding is optimal.

I. Introduction

T. M. Cover (Ref. 1) introduced the "broadcast channel" with one transmitter and two (or more) different receivers. Following Ref. 4, we ask the following question about a broadcast channel: certain common information is to be communicated simultaneously to both receivers. How much additional information can be communicated to the better receiver at the same time?

For channels like Gaussian channels, where one receiver is just a degraded version of the other, one obvious approach is timeshared coding: devote a fixed fraction of the total transmission time to sending the common information, coded for the weaker channel. This information will be comprehensible to both receivers. During the remaining time, transmit addi-

tional information coded for the stronger receiver. This information will not be comprehensible to the weaker receiver.

But in Ref. 1, Cover introduced a technique called broadcast coding, and showed that, in general, broadcast coding achieves greater, often much greater, data rates than time sharing. Later El Gamal and Cover (Ref. 2) found that broadcast coding cannot be further improved upon.

In this article we will discuss the Gaussian broadcast channel. For this channel, we will show that the relative advantage of broadcast coding over timeshared coding is small if the signal-to-noise ratios of both receivers are small. One surprising consequence of this is that for the wideband Gaussian broadcast channel, which we shall define, broadcast coding offers no

advantage over timeshared coding at all, and so timeshared coding is optimal.

II. The Gaussian Channel: A Review

A Gaussian channel is a discrete-time memoryless channel model whose input X and output Y are related by $Y = X + Z$, where Z is a mean zero Gaussian random variable independent from X . If the input is constrained by $E(X^2) \leq S$, and if the variance of Z is denoted by σ^2 , it is well known that the channel capacity depends only on the ratio $x = S/\sigma^2$, which is called the signal-to-noise ratio, and is given by the formula

$$C(x) = \frac{1}{2} \log(1 + x) \quad (1)$$

In Eq. (1), $C(x)$ represents the maximum possible amount of information (measured in bits, nats, etc., depending on the base of the logarithm) which can be reliably transmitted per channel use; in the usual physical sense, $C(x)$ is dimensionless.

Equation (1) can be used to derive the following formula for the capacity of a continuous-time, band- and power-limited Gaussian channel model:

$$C = B \log \left(1 + \frac{P}{N_0 B} \right) \quad (2)$$

where B is the channel bandwidth in Hertz, P is the average transmitter power in Watts, and N_0 is the noise spectral density in Watts per Hertz. The transition from Eq. (1) to Eq. (2) is explained in Ref. 3 (Chapter 4), for example. In Eq. (2), C represents the maximum possible information which can be reliably transmitted per unit of time; the physical dimensions of C are sec^{-1} .

If in Eq. (2) we assume natural logarithms and pass to the limit as the bandwidth B approaches infinity, we obtain

$$C = \frac{P}{N_0} \quad (3)$$

which is the well-known formula for the capacity of the infinite bandwidth white Gaussian channel. The units in Eq. (3) are nats per second.

III. The Gaussian Broadcast Channel

In Ref. 1, Cover introduced a discrete-time memoryless channel model with one transmitter and two receivers, which he called a Gaussian broadcast channel. This channel has one input X , and two outputs Y_1 and Y_2 , related by

$$Y_1 = X + Z_1$$

$$Y_2 = X + Z_2$$

where now Z_1 and Z_2 are mean zero Gaussian random variables, and X , Z_1 , and Z_2 , are independent. Let us denote by σ_1^2 and σ_2^2 the variances of Z_1 and Z_2 , respectively, and assume that $\sigma_1^2 \leq \sigma_2^2$, so that Y_1 is received more reliably than Y_2 . If the channel input X is constrained as in Section I by $E(X^2) \leq S$, then separately channels 1 and 2 have capacity $C(x_1)$ and $C(x_2)$, respectively, where $x_1 = S/\sigma_1^2$ and $x_2 = S/\sigma_2^2$.

In Ref. 4 a Gaussian broadcast channel was used to model deep-space communications in the presence of weather uncertainties; the high signal-to-noise ratio corresponds to good weather, and the low signal-to-noise ratio, to bad weather. The problem posed there was the following. Suppose the weather on earth is unknown to a distant spacecraft, and that data must be sent to earth so that even in bad weather, certain minimal but critical information will get through; but if the weather is good, additional information will be received.

Motivated by this point of view, we state the fundamental question about broadcast channels in the following somewhat unusual way. Suppose we wish to send certain information, called the common information, simultaneously to both receivers. If we do this, how much extra information, called bonus information, can we send to the better receiver at the same time?

One approach to this problem is the timesharing approach, in which the transmitter devotes a fixed fraction $1 - \rho$ (where $0 < \rho < 1$) of the total transmission time to sending the common information. During this time the information is coded for the weaker receiver. This information will also be comprehensible to the stronger receiver. By Eq. (1), during this common time, information can be transmitted at a maximum rate of $C(x_2)$. During the remaining fraction ρ of the transmission time, the transmitter sends bonus information to the stronger channel, at the rate $C(x_1)$. This will not be comprehensible to the weaker receiver.

It follows that for the timesharing strategy, the data rates will be

$$\text{Common Rate} = (1 - \rho) C(x_2) \quad (4)$$

$$\text{Bonus Rate} = \rho C(x_1)$$

and the parameter ρ can be selected arbitrarily by the transmitter.

Cover showed, however, that it is possible to do better than timesharing. Using a technique called broadcast coding,

he showed that for any choice of the parameter α , $0 < \alpha < 1$, the following rates are achievable:

$$\begin{aligned} \text{Common Rate} &= C(x_2) - C(\alpha x_2) \\ \text{Bonus Rate} &= C(\alpha x_1) \end{aligned} \quad (5)$$

(Actually Cover gave the common rate in the form

$$C\{[(1 - \alpha)x_2]/(1 + \alpha x_2)\},$$

but it is an easy exercise to show that this is the same as we have given in Eq. [5].) Later El Gamal and Cover (Ref. 2) showed that in fact no improvement over Eq. (5) is possible, so that the region of the first quadrant bounded by the curve given parametrically by Eq. (5) is now called the capacity region of the Gaussian Broadcast Channel (see Fig. 1).

Motivated by the discussion in Section I, let us pass from the discrete-time Gaussian broadcast channel to the continuous-time band- and power-limited Gaussian broadcast channel. The resulting expressions are for timesharing:

$$\begin{aligned} \text{Common Rate} &= (1 - \rho) B \log \left(1 + \frac{P}{N_2 B} \right) \\ \text{Bonus Rate} &= \rho B \log \left(1 + \frac{P}{N_1 B} \right) \end{aligned} \quad (6)$$

and for broadcast coding:

$$\begin{aligned} \text{Common Rate} &= B \log \left(1 + \frac{P}{N_2 B} \right) - B \log \left(1 + \alpha \frac{P}{N_2 B} \right) \\ \text{Bonus Rate} &= B \log \left(1 + \alpha \frac{P}{N_1 B} \right) \end{aligned} \quad (7)$$

where P is the transmitter power, B is the transmission bandwidth, and N_1, N_2 , are the noise spectral densities for the two receivers. In Eqs. (6) and (7) the units are nats per second.

To investigate wideband Gaussian broadcast channels, we pass as before to the limit as $B \rightarrow \infty$. The results follow easily from Eqs. (6) and (7) for wideband timesharing:

$$\begin{aligned} \text{Common Rate} &= (1 - \rho) \frac{P}{N_2} \\ \text{Bonus Rate} &= \rho \frac{P}{N_1} \end{aligned} \quad (8)$$

and for wideband broadcast coding:

$$\begin{aligned} \text{Common Rate} &= (1 - \alpha) \frac{P}{N_2} \\ \text{Bonus Rate} &= \alpha \frac{P}{N_1} \end{aligned} \quad (9)$$

We thus reach the surprising conclusion that for wideband Gaussian broadcast channels, broadcast coding offers no advantage over timesharing. (Actually, this was mentioned but not further investigated in Ref. 4.) We investigate this interesting phenomenon more closely in the next section.

IV. A More Detailed Analysis

In this section we will see that the reason wideband broadcast coding offers no advantage over wideband timesharing is that, for a given common rate, the bonus rates in Eqs. (4) and (5) are nearly equal, when the "good" SNR x_1 is small. More precisely, we have the following:

Theorem: If α and ρ are chosen so that the common rates in Eqs. (4) and (5) are equal, then

$$\begin{aligned} \frac{\text{Broadcast bonus rate (BBR)}}{\text{Timesharing bonus rate (TBR)}} &= \frac{C(\alpha x_1)}{\rho C(x_1)} \\ &\leq \frac{x_1}{C(x_1)} \cdot \frac{C(x_2)}{x_2} \\ &= \frac{x_1}{x_2} \cdot \frac{\log(1 + x_2)}{\log(1 + x_1)} \end{aligned}$$

Corollary 1: Since $\log(1 + x_2) \leq x_2$, we also have

$$\frac{\text{BBR}}{\text{TBR}} \leq \frac{x_1}{\log(1 + x_1)}$$

independent of x_2 . Thus also

$$\lim_{x_1 \rightarrow 0} \frac{\text{BBR}}{\text{TBR}} = 1$$

again independent of x_2 .

Corollary 2: For the continuous time channel, the corresponding result is

$$\begin{aligned} \frac{\text{BBR}}{\text{TBR}} &\leq \frac{N_2}{N_1} \cdot \frac{\log(1 + P/N_2 B)}{\log(1 + P/N_1 B)} \\ &< \frac{P/N_1 B}{\log(1 + P/N_1 B)} \\ &\rightarrow 1 \text{ as } B \rightarrow \infty \end{aligned}$$

Proof of Theorem: For the two common rates to be equal, we have, from Eqs. (4) and (5), that

$$C(\alpha x_2) = \rho C(x_2) \quad (10)$$

On the other hand, the ratio of the bonus rates is

$$\frac{C(\alpha x_1)}{\rho C(x_1)} \quad (11)$$

Combining Eqs. (10) and (11), we see that, for a fixed common rate, the ratio of the bonus rates is

$$\frac{C(\alpha x_1)}{C(\alpha x_2)} \cdot \frac{C(x_2)}{C(x_1)}$$

The desired result now follows from the fact that the function $C(\alpha x_1)/C(\alpha x_2)$ is a decreasing function of α , and approaches x_1/x_2 as $\alpha \rightarrow 0$. ■

We conclude with a brief discussion of the shape of the broadcast capacity regions as a function of x_1 and x_2 . It is useful to normalize the parametric curves described by Eq. (5)

by dividing the common rate by its maximum value $C(x_2)$, and the bonus rate by its maximum value $C(x_1)$:

$$\begin{aligned} \text{Normalized Common Rate (NCR)} &= 1 - \frac{C(\alpha x_2)}{C(x_2)} \\ \text{Normalized Bonus Rate (NBR)} &= \frac{C(\alpha x_1)}{C(x_1)} \end{aligned} \quad (12)$$

For a given value of x_1 , the parametric curves described by Eq. (12) vary monotonically outward from $x_2 = x_1$, in which case they reduce to

$$\text{NCR} = 1 - \frac{C(\alpha x_2)}{C(x_2)}$$

$$\text{NBR} = \frac{C(\alpha x_1)}{C(x_1)}$$

which is just the timesharing straight line, to $x_2 = 0^+$, in which case they reduce to

$$\text{NCR} = 1 - \alpha$$

$$\text{NBR} = \frac{C(\alpha x_1)}{C(x_1)}$$

Thus for a given good SNR x_1 , broadcast coding offers the largest relative advantage over timesharing when $x_2 \rightarrow 0$, and the smallest relative advantage (none at all) when $x_2 = x_1$. Of course, as we have seen, when x_1 is small, even the largest relative advantage is quite small. In Fig. 2, we have graphed the outer ($x_2 = 0$) and inner ($x_2 = x_1$) envelopes for several values of x_1 .

References

1. Cover, T. M., "Broadcast Channels," *IEEE Trans. Inform Theory* IT-11, pp. 2-14, 1972.
2. El Gamal, A., and Cover, T. M., "Multiple User Information Theory," *Proc. IEEE* 68, pp. 1466-1483, 1980.
3. McEliece, R. J., *The Theory of Information and Coding*, Reading, Mass.: Addison-Wesley, 1977.
4. Posner, E. C., "Strategies for Weather-Dependent Data Acquisition," *IEEE Trans. Communications*, COM-31, pp. 509-417, 1983.

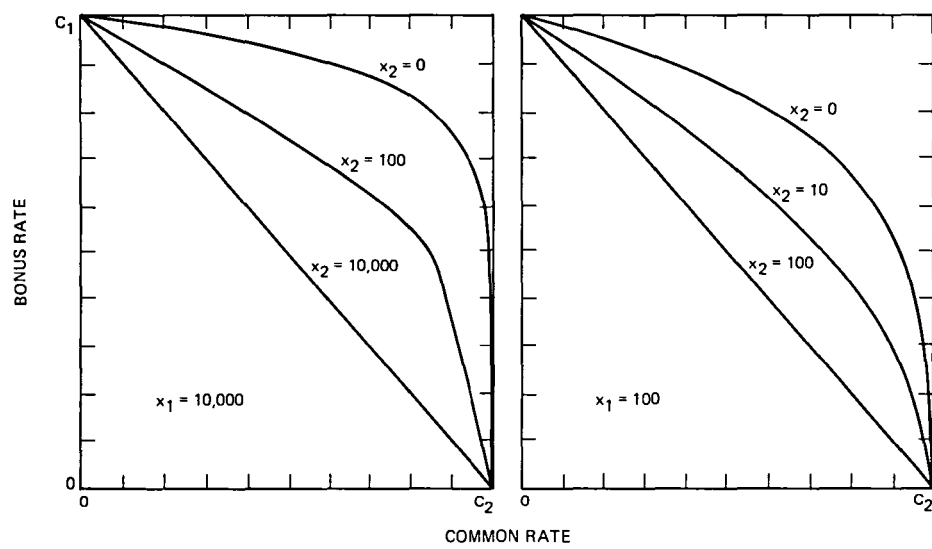


Fig. 1. The capacity region of some Gaussian broadcast channels

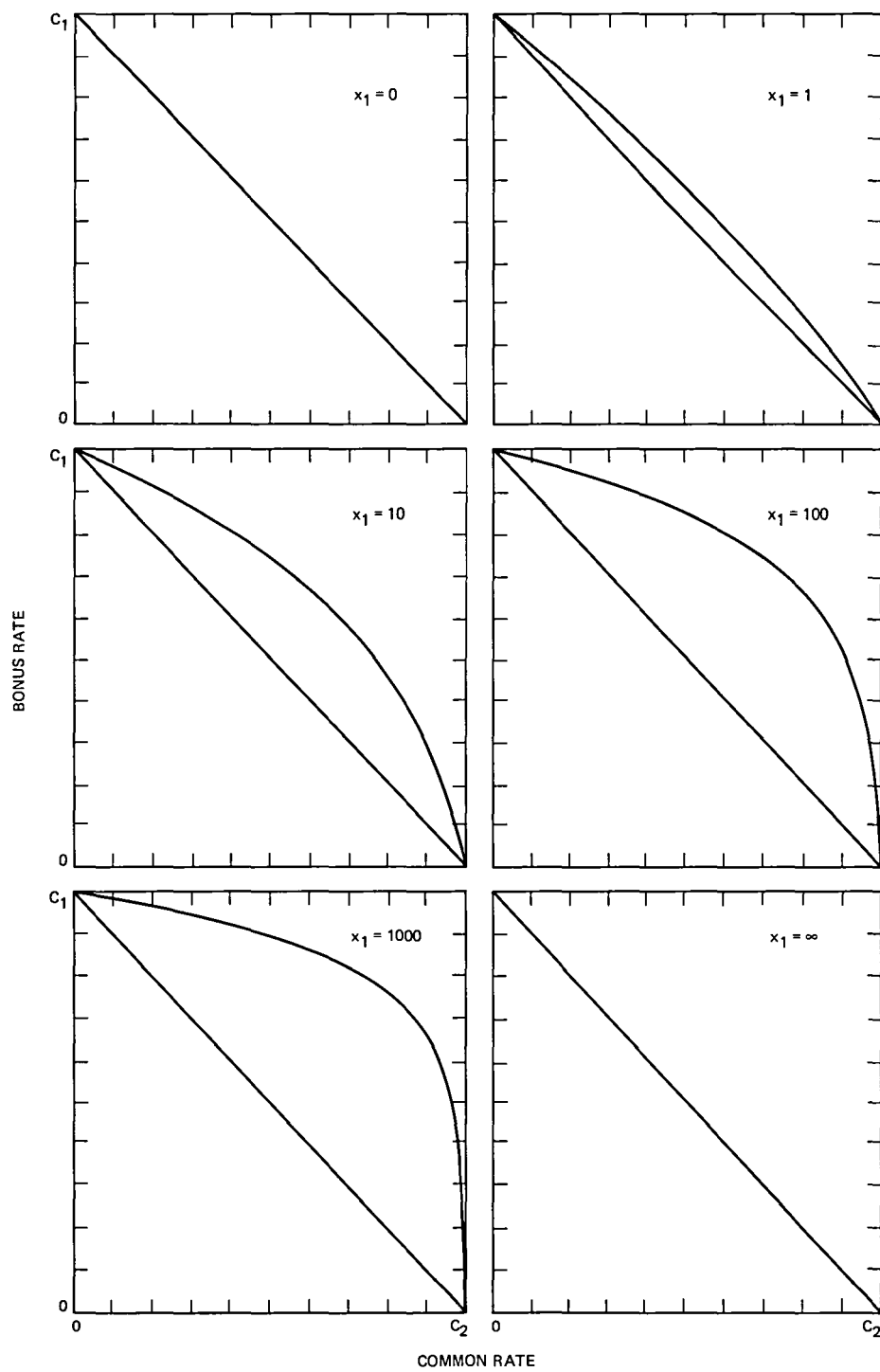


Fig. 2. The extreme capacity regions ($x_2 = 0$ and $x_2 = x_1$) for several values of x_1

On the Decoder Error Probability for Reed-Solomon Codes

R. J. McEliece

California Institute of Technology

L. Swanson

Communications Systems Research Section

In this article we derive upper bounds on the decoder error probability for Reed-Solomon codes. By definition, "decoder error" occurs when the decoder finds a codeword other than the transmitted codeword; this is in contrast to "decoder failure," which occurs when the decoder fails to find any codeword at all. Our results imply, for example, that for a t error-correcting Reed-Solomon code of length $q - 1$ over $GF(q)$, if more than t errors occur, the probability of decoder error is less than $1/t!$. In particular, for the Voyager Reed-Solomon code, the probability of decoder error given a word error is smaller than 3×10^{-14} . Thus, in a typical operating region with probability 10^{-5} of word error, the probability of undetected word error is about 10^{-19} .

I. Introduction

Deep Space missions, including Voyager, use error-correcting codes to allow very low probability of error in messages from the spacecraft to earth, even though signal-to-noise ratios are very low. One of the digital coding schemes used by Voyager is shown in Fig. 1. This scheme allows a bit-error rate as low as 10^{-6} with a bit signal-to-noise ratio E_b/N_0 as low as 2.3 dB.

Besides low decoder bit-error rate, we would like a system with very low probability of undetected error. That means that, in case there are bit errors in a certain region, we would like to know that. (Of course, knowing exactly where the bit errors are is equivalent to having no bit errors, which is impossible. But we would like to know that a certain string of bits

contains errors or, preferably, that it is very unlikely to contain errors.)

Our Reed-Solomon code is a (255,223) 8-bit code. This means that bits are arranged in symbols of 8 bits each, which are in turn arranged in words of 255 symbols, of which 223 symbols are information and the other 32 are parity. Whenever our decoders detect 16 or fewer symbol errors, they correct these errors. But if the string going into the decoder differs from *every* codeword in at least 17 symbols, we are able to detect this, and we know that many symbols (and therefore many bits) in the word are in error. We would like to know the probability that, in the fairly rare instance that 17 or more symbol errors are made, the decoder makes further correction and therefore incorrectly reports successful decoding. This article shows that this probability is less than 3×10^{-14} .

Let \mathbf{C} be an (n, k) code over $GF(q)$, with minimum distance d . We assume \mathbf{C} is being used to correct t errors, where t is a fixed integer satisfying $2t \leq d - 1$. We further assume the decoder is a *bounded distance* decoder, i.e., it looks for a codeword within distance t of the received word; if there is such a codeword, the decoder finds it, and if not, the decoder reports "failure."

If the transmitted codeword suffers t or fewer errors, it will be decoded correctly. If, on the other hand, it suffers more than t errors, one of two things can happen. Either the decoder will fail to find a codeword (*decoder failure*), or it will find a codeword other than the transmitted codeword (*decoder error*). We denote by P_F and P_E the probabilities of decoder failure and error, respectively. Of course if the number of errors is t or less, $P_F = P_E = 0$. If the number of errors exceeds t , but is less than $d - t$, then $P_F = 1$ and $P_E = 0$, since fewer than $d - t$ errors occurring cannot move the transmitted codeword to within distance t of another codeword.

If $d - t$ or more errors occur, it is in general quite difficult to calculate, or even estimate, P_F and P_E , although if the code is being used in a practical communications system, it is important to do so. A useful heuristic estimate can be based on the assumption that if at least $d - t$ errors occur, the error pattern can be treated as if it were *completely random*. The probability that a completely random error pattern will cause decoder error (i.e., lie within distance t of a nonzero codeword) is given by

$$Q = \frac{(q^k - 1) \cdot V_n(t)}{q^n} = (q^{-r} - q^{-n}) V_n(t) \quad (1)$$

where $r = n - k$ is the code's redundancy and

$$V_n(t) = \sum_{s=0}^t \binom{n}{s} (q-1)^s \quad (2)$$

is the volume of a Hamming sphere of radius t . This argument leads to the following estimate for P_E :

$$P_E \approx Q \cdot \Pr\{\geq d - t \text{ errors}\} \quad (3)$$

It is difficult to justify this estimate in general, but in this article we will see that if we increase Q slightly by defining Q' as

$$Q' = (q-1)^{-r} V_n(t) \quad (4)$$

then for Reed-Solomon codes,

$$P_E \leq Q' \cdot \Pr\{\geq d - t \text{ errors}\} \quad (5)$$

In fact Eq. (5) will follow from more detailed results, which we now describe.

If q_u denotes the probability that the error pattern has weight u , then plainly

$$P_E = \sum_{u=0}^n P_E(u) q_u \quad (6a)$$

$$P_F = \sum_{u=0}^n P_F(u) q_u \quad (6b)$$

where $P_E(u)$ and $P_F(u)$ denote the *conditional* probabilities of decoder error and failure, respectively, given u channel errors. As mentioned above, we have $P_E(u) = P_F(u) = 0$ for $u \leq t$ and $P_E(u) = 0, P_F(u) = 1$ for $t < u < d - t$. For $u \geq d - t$ we have $P_F(u) + P_E(u) = 1$, and so if $P_E(u)$ is known, $P_F(u)$ can be calculated, and vice versa.

Here is our main result. Let \mathbf{C} be an (n, k) Reed-Solomon, or any other maximum distance separable (MDS) code, with minimum distance $d = n - k + 1$. We assume as above that the code is being used to correct t errors, for some fixed value of t with $2t \leq d - 1$. We further assume that the code is being used on a channel for which all error patterns of the same weight are equiprobable, for example, a q -ary symmetric channel. Under these assumptions, we shall prove in Section III that

$$P_E(u) = 0 \quad \text{for } u \leq d - t - 1 \quad (7a)$$

$$P_E(u) \leq (q-1)^{-r} \sum_{s=d-u}^t \binom{n}{s} (q-1)^s \quad \text{for } d-t \leq u \leq d-1 \quad (7b)$$

$$P_E(u) \leq Q' \quad \text{for } u \geq d \quad (7c)$$

Of course Eq. (7a) needs no further proof; it is included only to make the bounds in Eq. (7) apply to all values of u . The bound (7b) actually follows from a slightly sharper, but more complicated bound on $P_E(u)$ that appears in Section III as Eq. (15).

We can combine Eqs. (7b) and (7c), at the cost of weakening Eq. (7b) slightly, to obtain an upper bound on $P_E(u)$ which is uniform in u for $u \geq d - t$:

$$P_E(u) \leq Q' \quad \text{for } u \geq d - t \quad (8)$$

The ratio of this uniform bound Q' to the heuristic estimate Q in Eq. (1) is usually very close to 1, and is always less than $(q/(q-1))^n$, which for $n \leq q-1$ cannot exceed $e = 2.718 \dots$. In any event, combining Eq. (6a) with (7a) and (8), we obtain the bound (5).

Although as a practical matter it is not hard to compute the bound Q' numerically, for some applications it may be worthwhile to have a simpler, though weaker, bound. In the Appendix, we show that Eq. (8) implies that provided $n \leq q-1$, for all $u \geq d - t$,

$$P_E(u) \leq \begin{cases} \frac{1}{(q-1)^{r-2}} + \frac{1}{(q-1)^r} & \text{if } t = 1 \\ \frac{1}{(q-1)^{r-2t}} \cdot \frac{1}{t!} & \text{if } t \geq 2 \end{cases} \quad (9)$$

Since $r \geq 2t$ in all cases, Eq. (9) implies, whenever $n \leq q-1$,

$$P_E(u) \leq \frac{1}{t!} \quad \text{for all } u \geq t+1 \quad (10)$$

Kasami and Lin (Ref. 2) have also studied the problem of decoder error for Reed-Solomon codes. They showed that on a q -ary symmetric channel P_E is at most Q , i.e., that

$$\sum_{u=d-t}^n P_E(u) \binom{n}{u} \epsilon^u (1-\epsilon)^{n-u} \leq Q \quad (11)$$

where ϵ is the probability of channel symbol error. They further showed that $P_E = Q$ only when $\epsilon = (q-1)/q$, i.e., when the error pattern is completely random. This shows that Q is the tightest possible bound on the sum in Eq. (11) which is independent of ϵ . However, except when the probability of $\geq d-t$ errors is very nearly 1, our bound (5) will be smaller than Kasami and Lin's bound (11). And since most well-designed systems will have $\Pr\{u \geq d-t\} \ll 1$, we conclude that our bound is likely to be more useful in practice than Kasami and Lin's.

Finally we note that since with $\epsilon = (q-1)/q$ equality holds in Eq. (11), the *average* of the $P_E(u)$'s with respect to one particular probability distribution is Q . Since $P_E(u)$ is 0 for $u < d-t$, it follows that for some values of u , $P_E(u) > Q$. Thus the conjecture that $P_E(u) \leq Q$ for all u isn't tenable.

(It would be nice to have a uniform *lower* bound on the $P_E(u)$'s, but we have been unable to find one.)

II. Preliminaries

In this section we will review some known results about MDS codes which are needed in our proof. Our remarks will be self-contained, but proofs may also be found in Ref. 4, Chapter 11.

Let C be a code, not necessarily linear, of length n with q^k codewords over $GF(q)$. If we examine any set of $k-1$ components of the codewords, we find that there are only q^{k-1} possibilities for the q^k codewords. Thus there must be a pair of codewords which agree on these $k-1$ components, and so the minimum distance d of the code must satisfy $d \leq n - k + 1$. A code for which $d = n - k + 1$ is called a *maximum-distance separable* (MDS) code. By this definition, Reed-Solomon codes and cosets of Reed-Solomon codes are MDS codes.

Let K be a subset of k coordinate positions of an MDS code. If two codewords were equal on K , the distance between them would be at most $n - k$. But this is impossible, since $d = n - k + 1$. We conclude that all q^k codewords are different on K , and so, for any possible k -tuple of elements from $GF(q)$, say $\alpha = (\alpha_1, \alpha_2, \dots, \alpha_k)$, there is a unique codeword, which, when restricted to K , equals α . This important fact we call the *basic combinatorial property* of MDS codes.

We now wish to estimate the number of codewords of weight u , for $u \geq d$, in an MDS code. A word of weight u must vanish on a set of $v = n - u$ coordinates. Thus let V be an arbitrary subset of v coordinates. We will estimate the number of codewords that vanish on V . Since $u \geq d$, then $v \leq k-1$. Thus by the basic combinatorial property, if we specify that the codeword is zero exactly on V , we may specify $(k-v)$ other, nonzero, components arbitrarily. There are $(q-1)^{k-v} = (q-1)^{u-r}$ ways to do this, and so there are at most $(q-1)^{u-r}$ codewords that vanish exactly on V . Since there are $\binom{n}{v} = \binom{n}{u}$ possibilities for V , if A_u denotes the number of codewords of weight u , we have:

$$A_u \leq \binom{n}{u} (q-1)^{u-r} \quad \text{for } u \geq d \quad (12)$$

Next we let V be a subset of v coordinate positions, where $v \geq k$. If we project the original code onto V , the result will be a certain (v, k) code. Since the parent (n, k) code has $d = n - k + 1$, the new code must have distance $d' \geq d - (n - v) = v - k + 1$. Since it is impossible for d' to be greater than $v - k + 1$, equality must hold and it follows that the projected

code is a (v, k) MDS code. This simple fact will be referred to in the proof in the next section.

III. Proof of Results

We call a word, not necessarily a codeword, decodable if it lies within distance t of some codeword. If D_u denotes the number of decodable words of weight u , then for $u \geq t + 1$, we have, assuming that all error patterns of weight u are equiprobable,

$$P_E(u) = \frac{D_u}{\binom{n}{u} (q-1)^u} \quad (13)$$

Thus the problem of finding the $P_E(u)$'s is essentially the same as that of finding the weight enumerator for the set of decodable words. For example, Eq. (7c) is equivalent to

$$D_u \leq \binom{n}{u} (q-1)^{u-r} V_n(t) \quad \text{for } u \geq d \quad (14)$$

The plan is to obtain upper bounds on D_u which will imply our various bounds on $P_E(u)$. We need to distinguish two cases, $u \geq d$ and $u \leq d - 1$.

First we assume $u \geq d$. Each decodable word can be written uniquely as $C + E$, where C is a codeword and E is a word of weight $\leq t$. For a fixed E , as C runs through the set of codewords, $\{C + E\}$ is a coset of the RS code. Since any coset of a RS code is an MDS code, by Eq. (12) we know that the number of words of weight u is less than or equal to $\binom{n}{u} (q-1)^{u-r}$, since we are assuming $u \geq d$. Since the set of decodable words is the disjoint union of $V_n(t)$ cosets of the RS code, Eq. (14) (and therefore Eq. [7c]) follows.

Now we assume that $u \leq d - 1$. A decodable word of weight u will vanish on a set of size $v = n - u$. For each of the $\binom{n}{u}$ subsets V of v coordinates, we will obtain an upper bound on the number of decodable words of weight u that vanish on V . This upper bound will imply Eq. (7b).

As before, we will use the fact that each decodable word is of the form $C + E$, where C is a codeword and E has weight $\geq t$. If the sum $C + E$ vanishes on V , then C must have weight $\leq t$ on V , say weight w . We note that $w = 0$ isn't possible, since $u \geq t + 1$. By our remarks in Section II, we know that C restricted to V is a linear (v, k) MDS code, and so its minimum weight (distance) is $d - u$. Thus w , the weight of C on V , satisfies $d - u \leq w \leq t$. (If $d - u > t$, there are no such words; this gives another proof of Eq. [7a].) By Eq. (12), it follows

that the number of codewords with weight w on V is at most $\binom{v}{w} (q-1)^{w-r'}$, where $r' = r - u$ is the redundancy of the restricted code.

For each codeword C with weight w in V , we must count the number of E 's such that $C + E$ vanishes on V . Suppose that E has weights $s \geq w$. On V , E must match C exactly, but the $(s - w)$ other nonzero components can be arbitrarily placed outside V . Thus the total number of E 's, for a given C of weight w , is

$$\sum_{s=w}^t \binom{u}{s-w} (q-1)^{s-w}$$

Therefore the total number of decodable words vanishing on V is at most

$$\begin{aligned} & \sum_{w=d-u}^t \binom{v}{w} (q-1)^{w-r'} \sum_{s=w}^t \binom{u}{s-w} (q-1)^{s-w} \\ &= (q-1)^{-r'} \sum_{s=d-u}^t (q-1)^s \sum_{w=d-u}^s \binom{v}{w} \binom{u}{s-w} \end{aligned}$$

This is a bound on the number of decodable words of weight u vanishing on V . If we multiply it by the number of possible subsets V with v elements, viz. $\binom{n}{v} = \binom{n}{u}$ we obtain a bound on D_u , and hence by Eq. (13),

$$P_E(u) \leq (q-1)^{-r} \sum_{s=d-u}^t (q-1)^s \sum_{w=d-u}^s \binom{v}{w} \binom{u}{s-w} \quad (15)$$

This bound is a bit clumsy for everyday use, but we note in passing that for $u = d - t$ (the smallest value of u for which $P_E(u)$ isn't 0) it simplifies to

$$P_E(d-t) \leq (q-1)^{-(d-t-1)} \binom{n-d+t}{t} \quad (16)$$

which is in fact the exact value of $P_E(u)$ in this case (Ref. 1).

Finally, we simplify the bound (15) by recalling a well-known combinatorial identity (Ref. 3, Eq. [1.2.6.21]):

$$\sum_{w \geq 0} \binom{v}{w} \binom{u}{s-w} = \binom{v+u}{s}$$

Since $v + u = n$, this means that the inner sum in Eq. (15) is at most $\binom{n}{s}$, and so Eq. (7b) follows from Eq. (15).

IV. Numerical Results

Using Eq. (8) we are able to compute an upper bound to the probability of undetected error, given that a word has more than t errors. In the case of the Voyager Reed-Solomon code, this gives an upper bound of 2.97×10^{-14} . Better

bounds depend on knowing the error probability so that the expected number of errors can be taken into account. For example, the probability of undetected error, given that a word has exactly 17 errors (the smallest number that the code is unable to decode correctly) is 1.09×10^{-14} (see Eq. [16]). This means that at a low error rate, when most words which fail to decode have exactly 17 errors, the probability of undetected word error given that a word fails to decode correctly, can be as low as 1.1×10^{-14} . In any case, we have very good confidence in those words which do decode.

References

1. Berlekamp, E. R., and Ramsey, J. L., "Readable Erasures Improve the Performance of Reed-Solomon Codes," *IEEE Trans. Inform. Theory*, Vol. IT-24, pp. 632-633, Sept. 1978.
2. Kasami, T., and Lin, S., "On the Probability of Undetected Error for the Maximum Distance Separable Codes," *IEEE Trans. Comm.*, Vol. COM-32, pp. 998-1006, Sept. 1984.
3. Knuth, D. E., *The Art of Computer Programming, Vol. 1, Fundamental Algorithms*. Reading, Mass., Addison-Wesley, 1968.
4. MacWilliams, F. J., and Sloane, N. J. A., *The Theory of Error-Correcting Codes*. Amsterdam, North Holland, 1977.
5. Peterson, W. W., *Error-Correcting Codes*. New York, Wiley-M.I.T. Press, 1961.

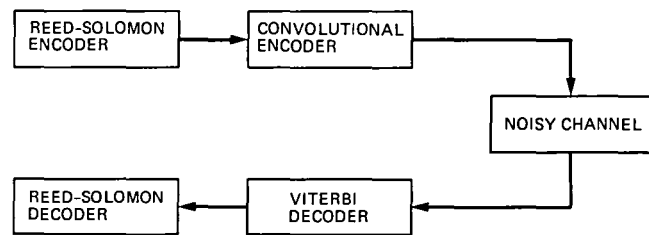


Fig. 1. A digital data coding scheme

Appendix

In this appendix we will derive several useful approximations to the bound Q' that appears in Eq. (8). In fact all of our results will follow from bounds on the binomial sum $V_n(t)$ defined in Eq. (2).

It follows from results in Ref. 5 (Appendix A, Eqs. [A-5] and [A-9]) that

$$V_n(t) \leq \left\{ \frac{(n-t)(q-1)}{(n-t)q-n} \right\} \binom{n}{t} (q-1)^t \quad (\text{A-1})$$

provided the denominator within the braces is positive. (This will certainly be the case in our application, since $2t+1 \leq n$ and $q \geq 2$.) Now if we assume that $n \leq q$ (which holds for all RS codes and all but a few exotic MDS codes described in

Chapter 11 of Ref. 4), the term within the braces will be $\leq (n+1)/n$. Thus we have

$$V_n(t) \leq \frac{n+1}{n} \binom{n}{t} (q-1)^t \quad (\text{A-2})$$

Since $(n+1)(n-1) < n^2$, it follows from Eq. (A-2) that

$$V_n(t) \leq \frac{n^t}{t!} (q-1)^t, \quad \text{for } t \geq 2 \quad (\text{A-3})$$

If $n \leq q-1$, the bound (A-3) immediately implies Eq. (9) for $t \geq 2$. The case $t=1$ in Eq. (9) must be handled separately, and follows from the fact that $V_n(1) = 1 + n(q-1)$ is less than or equal to $1 + (q-1)^2$, if $n \leq q-1$.

A Single Chip VLSI Reed-Solomon Decoder

H. M. Shao, T. K. Truong, I. S. Hsu, and L. J. Deutsch
Communications Systems Research Section

I. S. Reed
University of Southern California

A new VLSI design of a pipeline Reed-Solomon decoder is presented. The transform decoding technique used in a previous design is replaced by a time domain algorithm. A new architecture that implements such an algorithm permits efficient pipeline processing with minimum circuitry. A systolic array is also developed to perform erasure corrections in the new design. A modified form of Euclid's algorithm is implemented by a new architecture that maintains the throughput rate with less circuitry. Such improvements result in both enhanced capability and a significant reduction in silicon area, therefore making it possible to build a pipeline (31,15) RS decoder on a single VLSI chip.

I. Introduction

Recently Brent and Kung (Ref. 1) suggested a systolic array architecture to compute the greatest common divisor (gcd) of two polynomials. Based on this idea a VLSI design of a pipeline Reed-Solomon decoder was developed (Ref. 2). The syndrome computation of this decoder for a 4-bit (15,9) RS code was implemented on a chip (Ref. 3).

In the design of the chip for the above-mentioned decoder, three major problems arose:

- (1) While the architecture for syndrome computation took $(N - I)$ cells for an (N, I) RS code, it required N identical cells to implement the inverse transform in the architecture suggested in Ref. 2. As a consequence for a long code such as the (255,223) RS code, the inverse transform circuit would need 255 cells and be quite large.

- (2) The basic cell of the systolic array needed to perform a modified form of Euclid's algorithm occupied considerable silicon area, approximately 60 times the size of a syndrome computing cell. Since the decoding algorithm in Ref. 2 required $(N - I)$ of such cells, the entire systolic array needed much more silicon area than desired.

- (3) Erasure corrections became necessary and were not included in the original design. Hence the decoder required several modifications of the original architecture design in Ref. 2.

To reduce the large circuit area required by the inverse transform operation it was decided to modify the original transform decoding algorithm. Also after considering the need for erasure correction, it was found that the decoding algorithm given in Ref. 4 could accommodate both requirements.

In this algorithm the errata magnitudes are calculated in the time domain and a Chien search is used to find the error locations. The architecture of the new algorithm is designed to operate sequentially in a pipeline, thereby enabling the circuit size to grow with the error correcting capability $(N - t)$ instead of the code length N .

The systolic array designed originally for the modified form of Euclid's algorithm could process polynomials continuously (Ref. 2). However, in real-time RS decoding, there is a need to compute only one syndrome polynomial for each received codeword. If one takes advantage of this by a better utilization of multiplexing, the required pipeline throughput rate can be maintained by the use of fewer basic cells.

In this article, an improved VLSI architecture over that in Ref. 2 is developed utilizing the above observations. A systolic array is also designed for the needed polynomial expansion used in the erasure polynomial computation. These new modifications result in both an enhanced capability and a significant reduction in silicon area without any loss in the pipeline throughput rate.

II. The Decoder Architecture

Let $N = 2^m - 1$ the length of the (N, t) RS code over $GF(2^m)$ with design distance d . Suppose that t errors and s erasures occur, and $s + 2t < d - 1$. The decoding procedure in Ref. 4 is summarized as follows:

Let X_i be an error location or an erasure location and $\Lambda = \{X_i | X_i \text{ is an erasure location}\}$, $\lambda = \{X_i | X_i \text{ is an error location}\}$. Let Y_i be the corresponding errata magnitude and $r = (r_0, r_1, \dots, r_{N-1})$ be the received vector.

Step 1. Compute the syndrome polynomial

$$S(Z) = \sum_{k=1}^{\infty} S_k Z^{-k}$$

where

$$\begin{aligned} S_k &= \sum_{n=0}^{N-1} r_n \alpha^{nk} \\ &= \sum_{i=1}^{s+t} Y_i X_i^k \end{aligned} \quad (1)$$

for $1 \leq k \leq d - 1$

Step 2. Compute the erasure locator polynomial

$$\Lambda(Z) = \prod_{X_i \in \Lambda} (Z - X_i) \quad (2)$$

from Λ .

Step 3. Multiply $S(Z)$ and $\Lambda(Z)$ to obtain the Forney syndrome polynomial

$$T(Z) = S(Z) \Lambda(Z) \quad (3)$$

Step 4. Compute the errata evaluator polynomial $A(Z)$ and the error locator polynomial $\lambda(Z)$ from $T(Z) = [A(Z)] / \lambda(Z)$ by the modified Euclid's algorithm.

Step 5. Multiply $\Lambda(Z)$ and $\lambda(Z)$ to get the errata locator polynomial

$$P(Z) = \Lambda(Z) \lambda(Z) \quad (4)$$

Step 6. Perform Chien search on $\lambda(Z)$ to find the error location set λ .

Step 7. Compute the errata magnitudes

$$Y_k = \frac{A(X_k)}{X_k P'(X_k)}$$

for $1 \leq k \leq s + t$ by evaluating $A(Z)$ and $P'(Z)$. Use sets λ and Λ to direct the additions of Y_k to the received vector r .

The pipeline architecture of the RS decoder is shown in Fig. 1. The decoder computes the syndrome polynomial $S(Z)$ by the transform circuit given in Ref. 2. The erasure information Λ enters the decoder in the form of a binary sequence.

The systolic array described in the next section expands the factors of

$$\Lambda(Z) = \prod_{X_i \in \Lambda} (Z - X_i)$$

into the polynomial. Polynomial multiplications are performed with a circuit described in Ref. 5. A new architecture is developed which implements the modified Euclid's algorithm by operating on the product of $S(Z)$ and $\Lambda(Z)$. The resulting error locator polynomial $\lambda(Z)$ is then multiplied by $\Lambda(Z)$, thereby obtaining the errata locator polynomial $P(Z)$,

The derivative $P'(Z)$ of $P(Z)$ is obtained by dropping the even terms of $P(Z)$. The errata magnitudes Y_k are calculated then by a field inversion and a number of multiplications. Next the error locations are obtained in the form of a binary sequence by the use of another polynomial evaluation circuit which performs the Chien search on $\lambda(Z)$. This sequence of error locations, together with the input erasure location binary sequence, directs the addition of Y_k to the received message.

III. A VLSI Design for Expanding the Erasure Locator Polynomial

It is reasonable to assume that the erasure location information derived from outside the chip, possibly from a convolutional decoder. Let it arrive serially in the form of 1's and 0's. A simple circuit of the form shown in Fig. 2(a) first converts this erasure data into a sequence of α^k 's and 0's, where $\alpha^k \in \Lambda$.

Given $\alpha^k \in \Lambda$, the computation of the erasure polynomial demands the expansion of

$$\begin{aligned}\Lambda(Z) &= \prod_{\alpha^k \in \Lambda} (Z - \alpha^k) \\ &= (Z - \alpha^{k_1})(Z - \alpha^{k_2}) \dots (Z - \alpha^{k_s})\end{aligned}\quad (6)$$

Note that for an arbitrary polynomial $Q(Z)$ that

$$Q(Z)(Z - \alpha^k) = ZQ(Z) - \alpha^k Q(Z) \quad (7)$$

Such an operation involves polynomial shifts, scalar multiplications and additions. Thus the multiplications of $(Z - \alpha^k)$ in Eq. (6) can be implemented by the systolic array given in Fig. 2(b). Since it contains zeros as well as α^k 's, the input stream is used to control the updating of the latches in each basic cell. At the end of the arrivals of the erasure locations, the coefficients of $\Lambda(Z)$ are loaded from the latches into registers and shifted out serially.

IV. A New Architecture to Perform the Modified Euclidean Algorithm

A systolic array was designed in Ref. 2 to compute the error locator polynomial by a modified Euclidean algorithm. The array required $2t$ cells, twice the number of correctable errors. It is capable of performing the modified Euclidean algorithm continuously.

In the modified Euclidean algorithm only one syndrome polynomial is computed in the time interval of one code word. As a consequence, for the original architecture in Ref. 2, a pipeline RS decoder is not as efficient as it might be. A substantial portion of the systolic array is always idling. This fact makes possible a more efficient design with fewer cells and no loss in the throughput rate.

For the (N, I) RS code, the length of the syndrome polynomial is $N - I$. The maximum length of the resultant Forney syndrome polynomial is also $N - I$. Imagine now that a single cell is used recursively to perform the successive steps of the modified Euclidean algorithm instead of pipelining data to the next cell. Then it would take $N - I$ recursions to complete the algorithm, where each recursion requires $N - I$ symbol times. Therefore, using a single cell recursively requires only a total of $(N - I)^2$ symbol time to complete the modified form of Euclidean algorithm. Since a syndrome polynomial needs to arrive every N symbol times, only $\lfloor (N - I)^2 / N \rfloor$ cells are needed to process successive syndrome polynomials at a full pipeline throughput rate.

Figure 3 shows the new alternate architecture design. The input multiplexer directs the syndrome polynomials to different cells. Each processor cell is almost identical to the cell presented in Ref. 2, except that it is used to process data recursively.

The primary difference in the new cell structure from the architecture of the previous cell (Ref. 2) is presented as follows: Since division is avoided in the modified form of Euclid's algorithm, a scalar factor appears at the output. Although such a scale factor, call it K , is irrelevant to the problem of finding roots of the error locator polynomial $\lambda(Z)$, it must be removed from the errata evaluator polynomial $A(Z)$. In order to effectively utilize the processor cell given in Ref. 2, the factor K which appears at the output of each cell is calculated independently of the cell computation. This is accomplished by using a multiplier, operating recursively, to accumulate the product of all the nonzero leading coefficients of the divisor polynomials. An inverse computation circuit and a multiplier after the demultiplexer is used to remove the unwanted scalar K from $KA(Z)$. This computational process is illustrated in Fig. 3.

The architecture of the new basic cell is given in Fig. 4. Compared with the previous systolic array design (Ref. 2), the present scheme for multiplexing the recursive cell computations significantly reduces the number of cells and as a consequence the number of circuits. Table 1 shows that the cell reduction is greater for high rate codes.

V. A Polynomial Evaluation Pipeline

Polynomials are evaluated not only in the Chien search process, but also when the errata magnitudes are computed. In RS decoding, one needs to evaluate

$$A(Z) = \sum_{i=0}^{s+t-1} A_i Z^i \quad (8)$$

for $Z = \alpha^k$ and $0 \leq k \leq N-1$ given A_i , $0 \leq i \leq s+t-1$. Note that Eq. (8) has a form which is identical to the syndrome computation Eq. (1).

However, in Eq. (8) the polynomial is shorter than in Eq. (1). Also since $N > s+t-1$, Eq. (8) is evaluated over a wider range than Eq. (1) is computed. These two differences make it inefficient to implement Eq. (8) in a manner similar to that used for syndrome computations. A better method is to evaluate $A_i(\alpha^i)^k$ sequentially for each k at cell i . This is illustrated in Fig. 5. The polynomial coefficient A_i is multiplied by α^i at the initialization of cell i . From then on a feedback loop computes the quantities $A_i(\alpha^i)^k$ for $k = 1, 2, 3, \dots, N-1$. The summation shown at the bottom of the figure is implemented quite simply since all quantities are binary.

VI. Conclusion

An improved VLSI architecture of a pipeline Reed-Solomon decoder is presented herein. Compared with the previous design in Ref. 2, this architecture not only now corrects erasures, it is simpler, more regular, smaller in chip area and operates equally as fast. It is estimated that the polynomial expansion circuit and the polynomial multiplication circuit need approximately the same number of transistors as the syndrome computing pipeline. On the other hand, each polynomial evaluation circuit takes about half the number of transistors. Finally, each cell in the modified form of Euclid's algorithm circuit requires approximately the same chip area as the syndrome circuit.

Based on a previous nMOS chip fabrication of the syndrome pipeline (Ref. 3) and the design of the basic cell of the modified form of Euclid's algorithm (Ref. 6), it is estimated that a (15,9) RS decoder chip would require about 29 thousand transistors. A (31,15) RS decoder would require about 88 thousand transistors. Considering the presently existing VLSI technology, a high throughput 5-bit (31,15) RS decoder could be implemented readily on a single VLSI chip. Of course such a chip would have a possible immediate application to JTIDS (for Joint Tactical Information Distribution System of DoD).

References

1. Brent, R. P., and Kung, H. T., "Systolic VLSI arrays for polynomial GCD computations," Dep. Computer Science, Carnegie-Mellon Univ., Pittsburgh, PA, Rep., 1982.
2. Shao, H. M., Truong, T. K., Deutsch, L. J., Yuen, J. H., and Reed, I. S., "A VLSI Design of a Pipeline Reed-Solomon Decoder," *IEEE Trans. on Computer*, Vol. C-34, No. 5, May 1985, pp. 393-403.
3. Shao, H. M., "A VLSI Syndrome Computing chip for Reed-Solomon Decoding," to be published in *TDA Progress Report 42-85*, Jet Propulsion Laboratory, Pasadena, Calif.
4. Reed, I. S., Truong, T. K. and Miller, R. L., "Decoding of B. C. H. and R. S. codes with errors and erasures using continued fractions," *Electronic Letters*, August 1979, Vol. 15, No. 17, pp. 542-544.
5. Peterson and Weldon, *Error-Correcting Codes*, 2nd Edition, the MIT Press, Cambridge, pp. 172-173, 1972.
6. Hsu, I. S. and Shao, H. M., "A VLSI chip for the implementation of the modified Euclid's Algorithm," to be published in *TDA Progress Report 42-85*, Jet Propulsion Laboratory, Pasadena, Calif.

Table 1. The comparison of the number of cells required in the modified Euclid's algorithm computation

RS Code	Full Systolic Array	Multiplexing on Recursive Calls
(15,9)	6	3
(31,15)	16	9
(255,223)	32	5

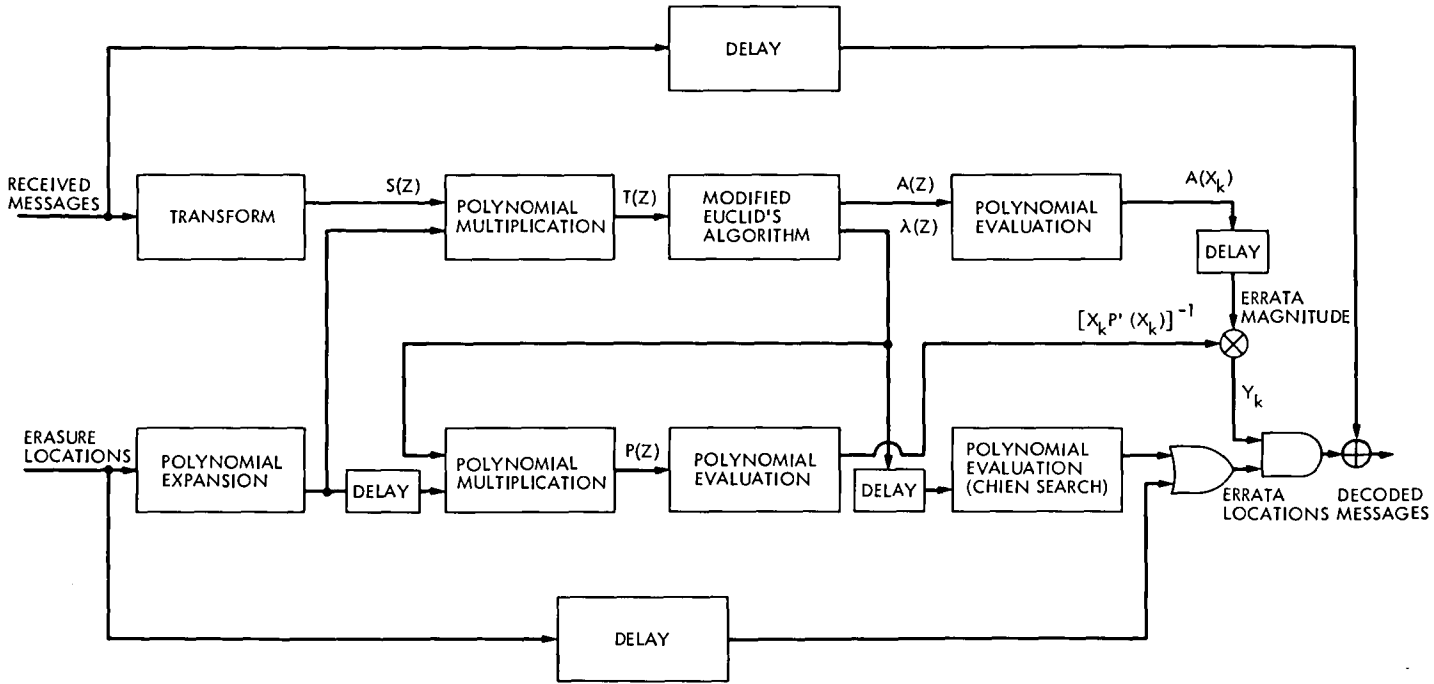


Fig. 1. VLSI architecture of a pipeline Reed-Solomon decoder for both errors and erasures correction

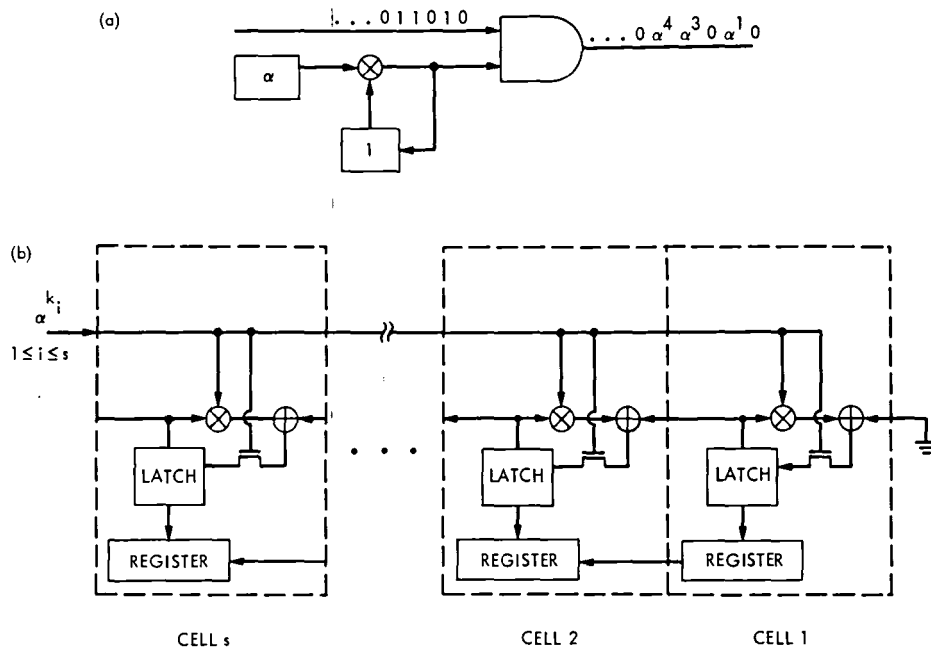


Fig. 2. A systolic array to expand a polynomial

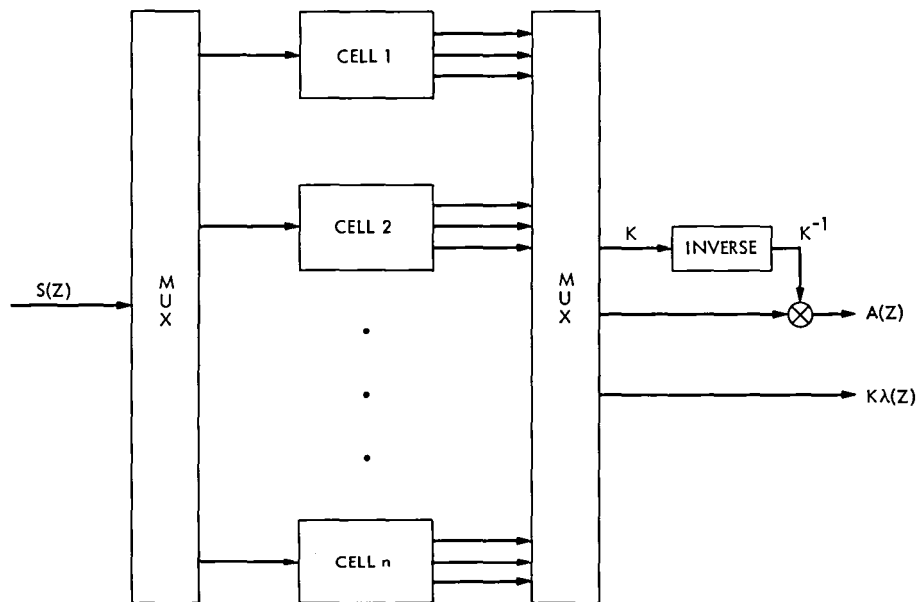


Fig. 3. The new architecture to perform the modified form of Euclid's algorithm where $n = \lfloor (N-1)^2/N \rfloor$

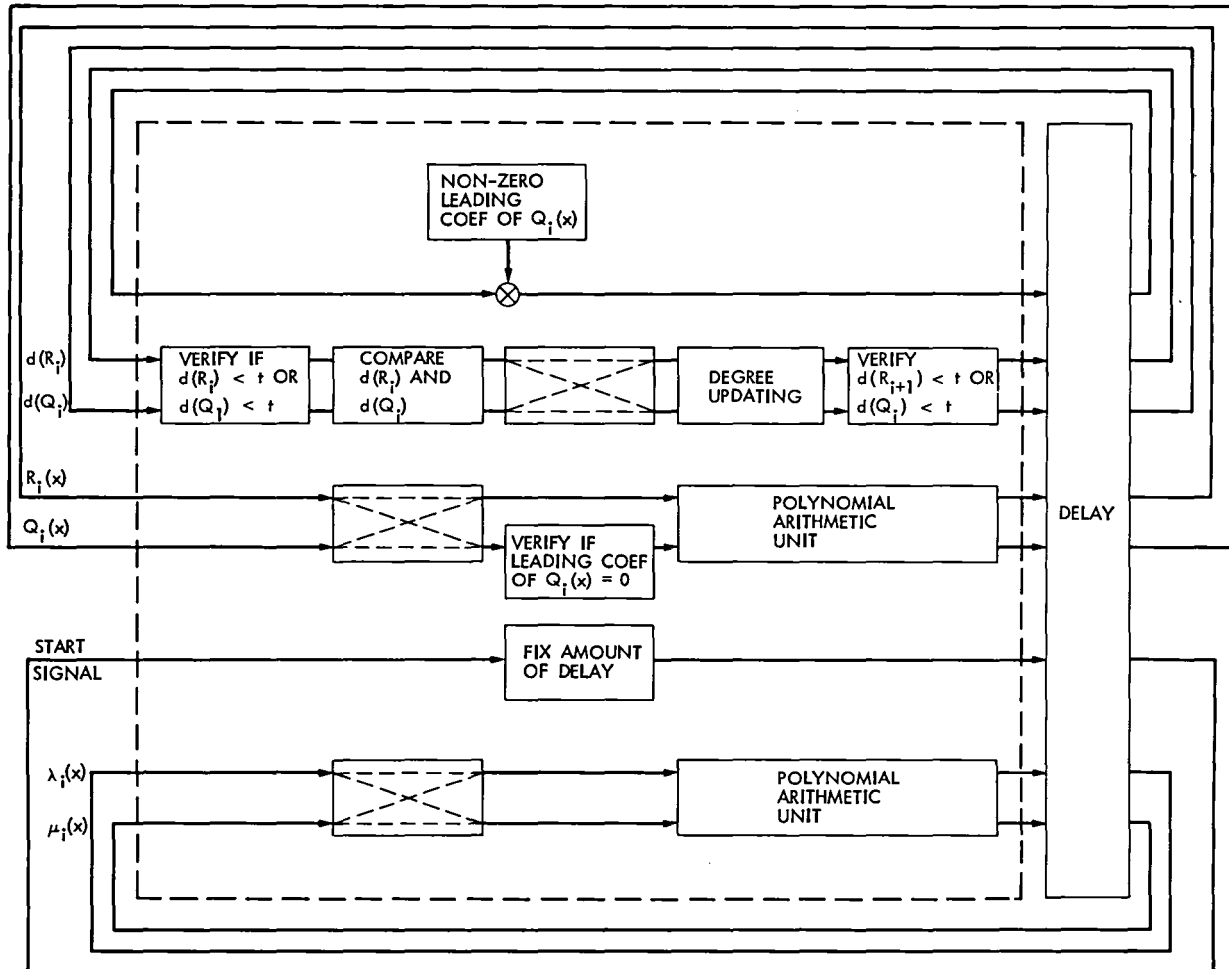


Fig. 4. The structure of a recursive cell that performs the modified Euclid's algorithm

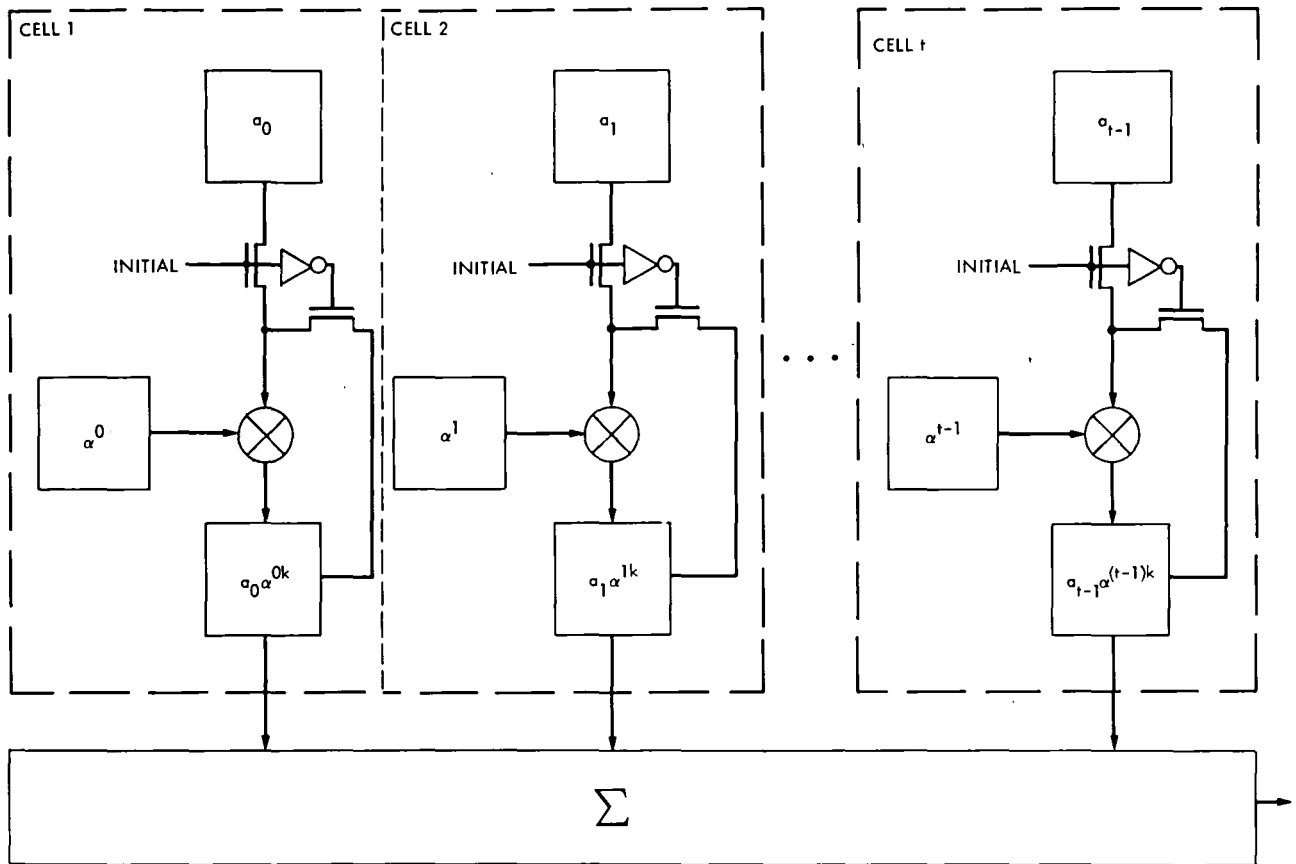


Fig. 5. A polynomial evaluation pipeline circuit

Effects of Quantization on Symbol Stream Combining in a Convolutionally Coded System

F. Pollara and L. Swanson

Communications Systems Research Section

Symbol stream combining has been proposed as a method for arraying signals at different antennas. If the received symbol streams are recorded on tape, it is desirable to limit the required storage without significantly affecting the performance. It is shown that 4-bit quantized symbols introduce an E_b/N_0 penalty of only 0.05 dB.

I. Introduction

Symbol stream combining (Ref. 1) has been shown to be an effective method to increase data return in critical missions (Ref. 2) by arraying possibly distant receiving stations. Received symbols are recorded on tape at the output of two or more Symbol Synchronizer Assemblies (SSAs) and then combined off-line by properly aligning the data on the tapes and forming a weighted sum.

While the SSA is capable of delivering 8-bit (246 levels) uniformly quantized symbols, it is desirable to reduce this information to only 3 to 5 bits per symbol in order to limit the storage required on tape.

This study considers the situation shown in Fig. 1, where two quantized symbol streams are optimally combined by using unquantized weight coefficients. The resulting combined signal is then delivered to the maximum-likelihood convolutional decoder (MCD), which uses a 3-bit quantized input. A complete simulation of the quantized combiner, MCD and additive Gaussian noise channel was developed to measure the bit error rate at the output of the MCD, with different numbers of quantization levels at the combiner

input. It is assumed that the two symbol streams have independent additive Gaussian noise components and that they are combined with optimal weights, as described in Ref. 3. It is concluded that 4-bit quantization represents a good compromise between tape storage and performance.

II. Branch Metric Quantization

The existing simulation of the MCD (Viterbi algorithm) did not take into account any branch metric quantization effect. Because the performance of this system can depend heavily on the interaction of combiner and metric quantization, it was necessary to include metric quantization in the simulation. Therefore, before considering the effects of quantization at the input of the combiner, we briefly review the quantization of branch metrics and choose one quantization scheme which we believe to be similar to that used in the DSN decoders.

It is known that optimum 3-bit quantization with uniform step size requires only 0.2 to 0.25 dB more E_b/N_0 than the unquantized case (Ref. 4). Ideally, the branch metric is proportional to the logarithm of the probability that a specific

information bit was transmitted, given a particular pair of received soft symbols from the SSA.

In practice (Ref. 5), the branch metrics are assigned according to one of the tables in Fig. 2, where a small branch metric represents a highly probable event, while larger metrics represent less probable events. Figures 2(a) and 2(b) are two different examples of *linear metric* assignments, while Fig. 2(c) is the so called *square metric*, since it is just a quantized version of the square Euclidean distance of the received symbol pair from the hypothesized correct pair, which is optimum. Note that the metrics in Figs. 2(a) and 2(b) require only a 3-bit representation, while that in Fig. 2(c) requires 4 bits due to only one entry with value 8. The tables are used by selecting the value corresponding to the two quantized symbol values, as shown in Fig. 2. The bit error rate performance of the three schemes of Fig. 2 is shown in Fig. 3. Throughout this study it is assumed that the survivor path memory in the Viterbi decoder is 32 bits long. In the study of Section III, we use the method of Fig. 2(c).

III. Combiner Input Quantization

Consider for simplicity a combiner with two inputs:

$$s_1 = a + n_1$$

$$s_2 = a + n_2$$

where $a = \pm 1$ and n_1, n_2 are two independent, zero mean, Gaussian random sequences. In this model, a is the coded message stream and n_1 and n_2 are the noise sequences due to the respective receivers. We are assuming that there is no gain control error in adjusting the amplitude of the two signals, and thus the a 's have no coefficients. Then the combiner output y is the weighted sum:

$$y = cf(s_1) + (1 - c)f(s_2)$$

where $f(\cdot)$ is a nonlinear function representing the quantization to a certain number of bits.

Defining $\lfloor x \rfloor$ as the largest integer less than x , the function $f(x)$ for 8-bit quantization is given by

$$f(x) = \begin{cases} b(\lfloor x/q \rfloor + 1/2), & 0 \leq x \leq 2^7 q \\ b(2^7 - 1/2), & x > 2^7 q \\ -f(-x), & x < 0 \end{cases}$$

where $q = 0.0465$, and b is chosen so that $f(1) = 1$. Thus, uniform N -bit quantization, $2 \leq N \leq 8$, can be of the form

$$f(x) = \begin{cases} b(\lfloor x/Lq \rfloor + 1/2), & 0 \leq x \leq 2^{N-1} Lq \\ b(2^{N-1} - 1/2), & x > 2^{N-1} Lq \\ -f(-x), & x < 0 \end{cases}$$

for $1 \leq L \leq 2^{8-N}$. The parameter L can be chosen to trade large dynamic range (large L) for fine quantization (small L), and tells how many 8-bit quantized levels are to be combined into an N -bit quantized level. In practice, a quantizer is easier to implement if L is a power of 2.

The DSN's Viterbi decoders use 3-bit quantization with $L = 2^3$. The results described below were therefore obtained for 3-bit quantization with $L = 2^3$, and for 4-bit quantization with $L = 2^3$ and $L = 2^2$. Because it proved superior, $L = 2^3$ was used for 4-bit quantization. An example of $f(x)$ for 3-bit quantization is given in Fig. 4.

The effects of quantization at the inputs of the combiner are shown in Fig. 5 in terms of probability of bit error at the output of the Viterbi decoder versus E_b/N_{01} of signal s_1 , assuming that $E_b/N_{01} = E_b/N_{02} = (1/2)(E_b/N_0)$, and that the branch metrics are computed according to Fig. 2(c).

The baseline curve is for no MCD input quantization and no combiner quantization. The remaining three curves show the performance for 3-bit, 4-bit quantization, and no quantization in the combiner, when the MCD uses a 3-bit input. All results are based on simulation and are accurate to $\pm 3\%$ with a 95% confidence interval. Figure 6 shows the 4-bit combiner performance when $E_b/N_{02} = (1/2)(E_b/N_{01})$.

These results led us to conclude that a combiner using 4-bit quantized recorded inputs may be the most reasonable compromise of storage and performance loss.

References

1. Divsalar, D., "Symbol Stream Combining Versus Baseband Combining for Telemetry Arraying," *TDA Progress Report 42-74*, Jet Propulsion Laboratory, Pasadena, Calif., pp. 13-28, Aug. 1983.
2. Hurd, W. J., Pollara, F., Russell, M. D., Siev, B., and Winter, P. U., "Intercontinental Antenna Arraying by Symbol Stream Combining at Giacobini-Zinner Encounter," *TDA Progress Report*, this issue.
3. Vo, Q. D., "Signal-to-Noise Ratio Combiner Weights Estimation for Symbol Stream Combining," *TDA Progress Report 42-76*, Jet Propulsion Laboratory, Pasadena, Calif., pp. 86-98, Feb. 1984.
4. Heller, J. A., and Jacobs, I. M., "Viterbi Decoding for Satellite and Space Communications," *IEEE Trans. Comm.*, Vol. COM-19, pp. 835-848, Oct. 1971.
5. Clark, G. C., and Cain, J. B., *Error Correction Coding for Digital Communications*, Plenum Press, 1981.

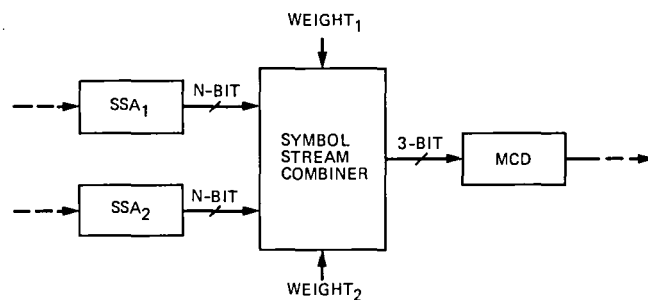


Fig. 1. Symbol stream combiner model

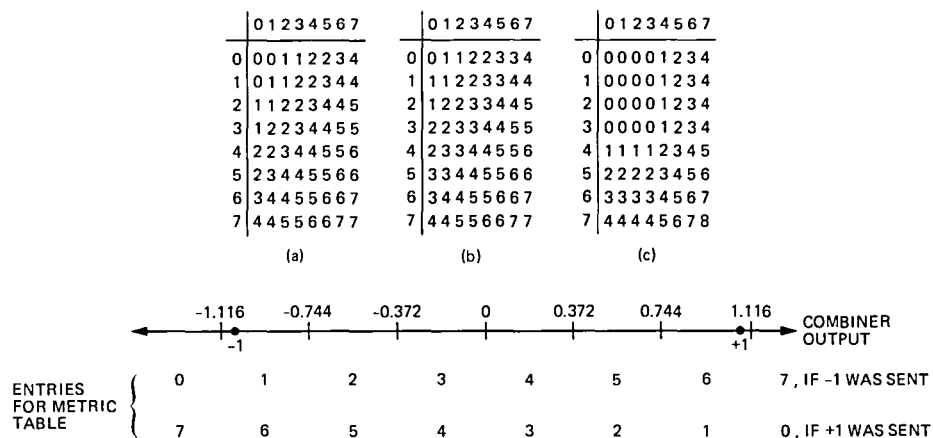


Fig. 2. Branch metric tables

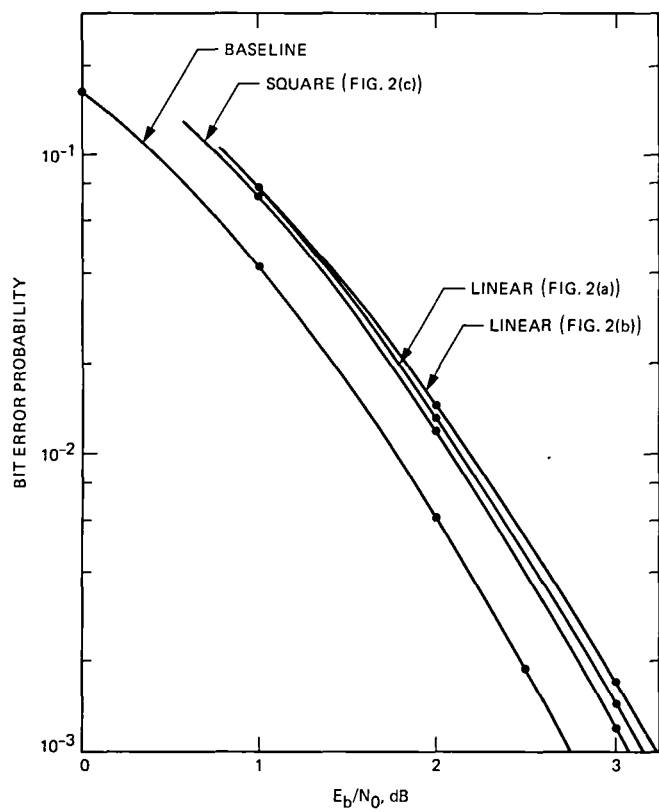


Fig. 3. Branch metric quantization effects

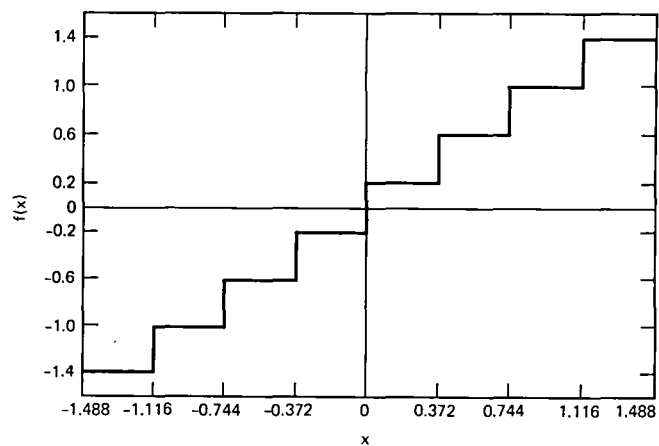


Fig. 4. Function $f(x)$ for 3-bit quantization

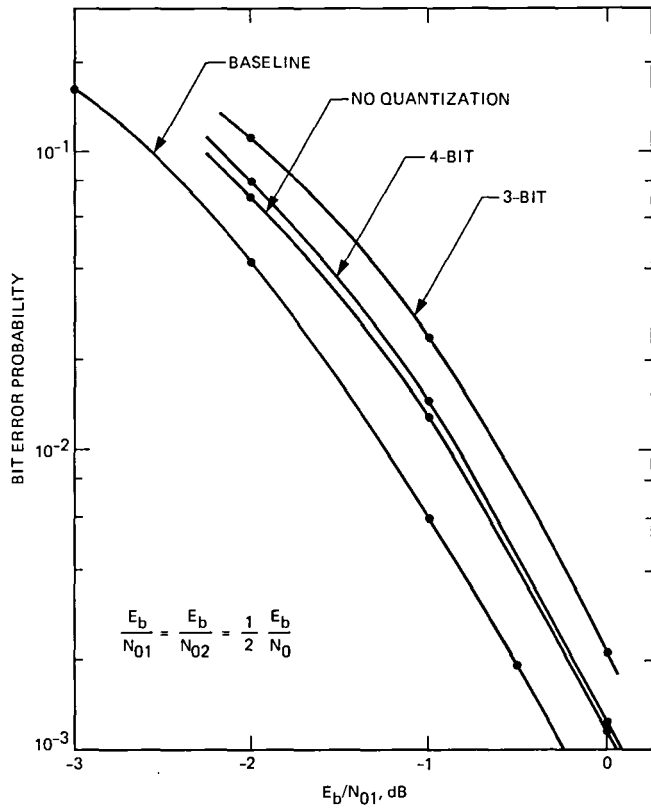


Fig. 5. Combiner quantization effect

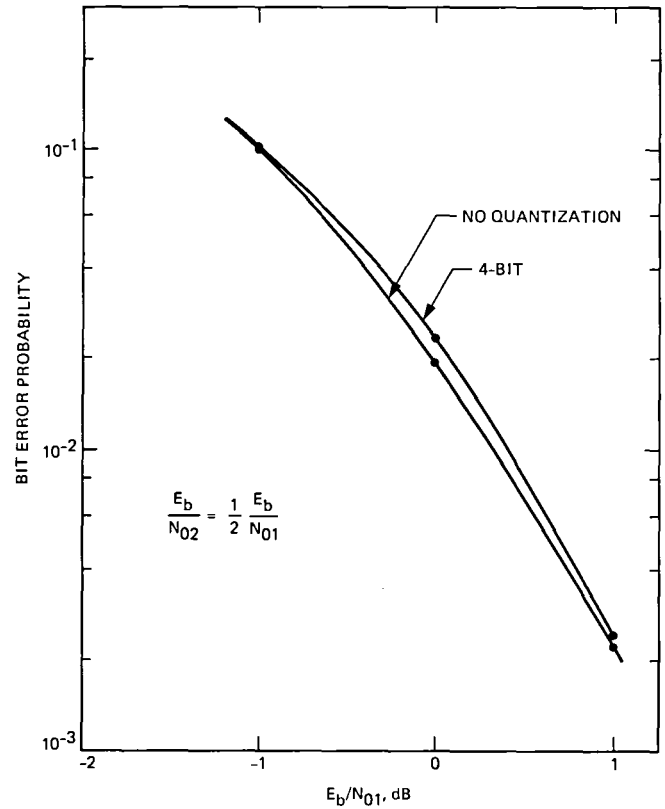


Fig. 6. Combiner with unequal strength inputs

Acquisition Times of Carrier Tracking Sampled Data Phase-Locked Loops

S. Aguirre

Communications Systems Research Section

Phase acquisition times of type II and III loops typical of the Advanced Receiver are studied by computer simulations when the loops are disturbed by gaussian noise. Reliable estimates are obtained by running 5000 trials for each combination of loop signal-to-noise ratio (SNR) and frequency offset. The probabilities of acquisition are shown versus time from start of acquisition for various loop SNRs and frequency offsets. For frequency offsets smaller than one-fourth of the loop bandwidth and for loop SNRs of 10 dB and higher, the loops acquire with probability 0.99 within $2.5/B_L$ for type II loops and within $7/B_L$ for type III loops.

I. Introduction

During the acquisition mode, the nature of the phase-locked loop is highly nonlinear. This is further complicated by the presence of noise, thus precluding a detailed analysis of the behavior of the loop during this mode of operation.

Very little analytical work has been published in the open literature on the subject of acquisition. Viterbi (Ref. 1) and Lindsey (Ref. 2), among others, developed approximate expressions for the time necessary to acquire in a noiseless environment. Their expressions are useful when the frequency offset is large compared to the bandwidth of the loop. Hurd and Anderson (Ref. 3) and Holmes (Ref. 4) present results of acquisition experiments in a noisy environment for a digital transition tracking loop (DTTL) symbol synchronizer and continuous time carrier tracking loops, respectively. Although all previous sources serve as a general guidance, more specific results are needed for the proposed carrier tracking loops of the DSN Advanced Receiver (Ref. 5).

In this article, we show results based on Monte Carlo simulations of phase acquisition for types II and III sampled data loops typical of the Advanced Receiver, where the type of loop indicates the number of perfect integrators present, including that contributed by the NCO. Plots of probability of acquisition versus normalized time are presented with initial frequency detuning (frequency offset) as a parameter, for different loop signal-to-noise ratios.

II. Description of the Sampled Data Loop Model

A block diagram of the nonlinear baseband model employed in the simulation is shown in Fig. 1. The symbols contained in the diagram are defined as follows:

A = rms value of carrier signal (V)

$\theta_n = \phi_0 + \Omega_0 t_n$

= input phase at time t_n (rad)

ϕ_0 = initial phase offset (rad)

Ω_0 = initial frequency detuning (rad/s)

ϕ_n = phase estimation error at time t_n (rad)

AK = loop gain

W_n = zero mean white gaussian noise sample with variance $N_0/2T$

T = update time (s)

$$F(z) = G_1 + \frac{G_2}{1-z^{-1}} + \frac{G_3}{(1-z^{-1})^2} \quad (1)$$

= loop filter

$$N(z) = T(z+1)/2z^2(z-1) \quad (2)$$

= NCO transfer function including the transport lag of the loop

The loop modeled in Fig. 1 is the proposed implementation for the carrier tracking loop of the Advanced Receiver (Ref. 5). Operationally, the behavior of the loop is characterized by

$$\phi_n = \theta_n - \hat{\theta}_n \quad (3)$$

$$\phi_n = \theta_n - AKF(z) \{ \sin(\phi_n) + W_n/A \} N(z) \quad (4)$$

The PLLs considered are sampled data analogies of continuous time loops. For the type II and III loops with update time T , sampled data PLLs analogous to continuous loops of one-sided bandwidth b/T Hz have parameters (see Appendix for details):

$$AKTG_1 = rd \quad (5a)$$

$$AKTG_2 = rd^2 \quad (5b)$$

$$AKTG_3 = krd^3 \quad (5c)$$

$$d = \frac{4b}{r} \left(\frac{r-k}{r-k+1} \right) \quad (6)$$

where r is the damping parameter, and k is a type III loop gain component ($k=0$ for type II loop). The actual loop noise bandwidths, B_L , of the sampled data loops are given by:

$$B_L = \frac{1}{2T} \frac{1}{H^2(1)} \frac{1}{2\pi j} \oint_{|z|=1} H(z)H(z^{-1}) \frac{dz}{z} \quad (7)$$

where $H(z)$ is the closed loop transfer function. These bandwidths are approximately b/T for $b \ll 1$, and are somewhat wider for larger b . The analogy is used so that the typical continuous loop parameters (Ref. 6 and TR 900-450¹) can be specified as inputs to perform the simulations (note that B_L and b here correspond to B_L^* and $B_L T$ of Ref. 5).

III. Description of Simulation

Introducing the state variables u_n, v_n , defined as the outputs of the first and second integrators in the loop filter $F(z)$, it can be shown (see Appendix) that the difference equations describing the behavior of the PLL are given by:

$$u_n = u_{n-1} + rd^2 d_n \quad (8)$$

$$v_n = v_{n-1} + kdu_n \quad (9)$$

$$y'_n = rdd_n + u_n + v_n \quad (10)$$

$$d_n = \sin(\phi_n) + W_n/A \quad (11)$$

$$\hat{\theta}_{n+1} = \hat{\theta}_n + (y'_{n-1} + y'_{n-2})/2 \quad (12)$$

The simulations were conducted by solving Eq. (4) with help from Eqs. (8)-(12) with zero initial conditions for the state variables.

In order to obtain accurate estimates, 5000 independent runs, produced by 5000 nonoverlapping sequences of pseudo-random noise, were employed to generate a single probability of acquisition curve for a given frequency offset and loop signal-to-noise ratio $SNR = A^2/N_0 B_L$. The phase offset for each run was randomly selected between $(-\pi, \pi)$.

To assure phase locking, each simulation was run for a maximum of $50/B_L$. The loop was declared to be in lock when the magnitude of the phase error dropped below 90 deg for at least $10/B_L$. This threshold is arbitrarily chosen so that PLLs operating with small loop SNRs (large variance of the tracking phase error) may be studied.

The simulations were performed on a VAX 11/750 computer. To generate the noise samples, a gaussian noise generator was synthesized using the direct method (Ref. 7) based on

¹Tausworthe, R. C., and Crow, R. B., *Practical Design of Third Order Phase-Locked Loops*, Technical Report 900-450, Jet Propulsion Laboratory, Pasadena, Calif., Apr. 27, 1971.

the uniform random number generator provided by the VAX 11/750. The simulations were run for $B_L T = 0.02$, which is representative of the numbers presently imposed by both hardware speed (which influences T) and bandwidth requirements to track input dynamics.

IV. Summary of Results

Figures 2–5 present the distribution functions resulting from simulations of phase acquisitions. The ordinates of these figures are the probability of phase acquisitions occurring within time t . Time t , as indicated on the abscissa, is normalized by the bandwidth of the loop. For example, consider a type II loop with bandwidth $B_L = 50$ Hz, a loop SNR of 10 dB, and a frequency offset of 25 Hz, or $B_L/2$. From Fig. 3(b), phase acquisition with probability of 0.95 is achieved at $B_L t = 3$ or $t = 3/B_L = 0.06$ s. The figures show that for the normal range of loop SNRs, greater than 10 dB, and for frequency offset values smaller than one-half the loop bandwidth, the loops attain phase lock with high probability (0.99) within $5/B_L$ or $15/B_L$, for type II and type III loops, respectively. Acquisition times are approximately reduced by one-half if the offset is reduced to $B_L/4$.

Larger frequency offsets may require an excessive time to lock. Aiding of acquisition by sweeping the local oscillator or by estimating the frequency offset by a fast Fourier transform (FFT) is indicated when the frequency offset is large.

Since type II loops lock faster than type III loops, it is often useful to acquire with a type II loop and then change to a type III. This can be done without loss of phase lock.

Our results are in close agreement with the earlier results for symbol synchronizers and for continuous time PLLs. This is not surprising for the continuous time PLL since for small values of $B_L T$ the sampled data loop behaves very similarly.

If we use equations (3.21) and (10–18) of Refs. 1 and 2, respectively, we can get an upper bound for the necessary time to phase lock a noiseless type II continuous time PLL. These equations show that when the frequency offset equals the loop bandwidth, and $r = 2$, the loop locks in $7.9/B_L$. The simulations indicate $9.2/B_L$ with probability 0.99 when the loop SNR = 16 dB.

Although the DTTL symbol synchronizer does not possess a sinusoidal characteristic for its phase detector, in Ref. 3 it was found that for low symbol SNR, acquisition is obtained in about $7/B_L$ for an optimized midphase integration window of one-quarter of the symbol time and a frequency offset of $B_L/2$. Large symbol SNRs require roughly $0.6/B_L$ for the same frequency offset. Interpolation of the data of Ref. 4 indicates that a continuous loop locks in $3.8/B_L$ when SNR = 10 dB and the frequency detuning is $B_L/2$. The close agreement in acquisition times adds confidence in the results.

References

1. Viterbi, A. J., *Principles of Coherent Communication*, McGraw-Hill, New York, 1966.
2. Lindsey, W. C., *Synchronization Systems in Communication and Control*, Prentice-Hall, Englewood Cliffs, N.J., 1972.
3. Hurd, W. J., and Anderson, T. O., "Acquisition Time for Symbol Synchronizer for Low SNR Coded Systems," *Space Programs Summary 37–61*, Vol. II, pp. 57–63, Jet Propulsion Laboratory, Pasadena, Calif., Jan. 31, 1970.
4. Holmes, J. K., *Coherent Spread Spectrum Systems*, John Wiley and Sons, Inc., New York, 1982.
5. Aguirre, S., and Hurd, W. J., "Design and Performance of Sampled Data Loops for Subcarrier and Carrier Tracking," *TDA Progress Report 42–79*, Jet Propulsion Laboratory, Pasadena, Calif., pp. 81–94, Nov. 15, 1984.
6. Tausworthe, R. C., *Theory and Practical Design of Phase-Locked Receivers*, Technical Report 32–819, Jet Propulsion Laboratory, Pasadena, Calif., Feb. 1966.
7. Abramowitz, A., and Stegun, I., *Handbook of Mathematical Functions*, Section 26.8, National Bureau of Standards, Washington, D.C., 1965.

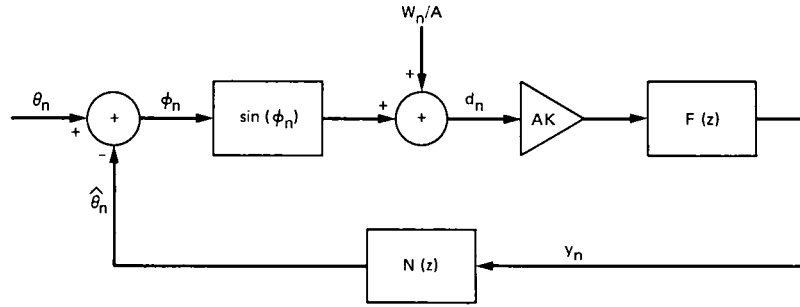


Fig. 1. Nonlinear baseband sampled data loop model

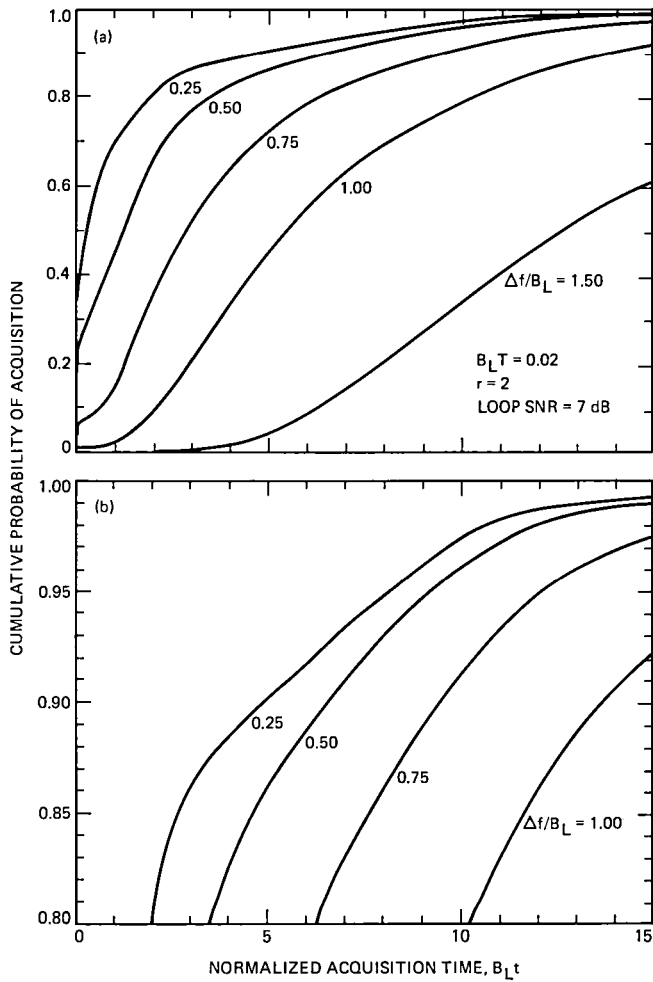


Fig. 2. Cumulative probability of phase acquisition as a function of normalized time for type II sampled data loop at 7-dB loop SNR: (a) Probability range 0 to 1, (b) Expansion of high probability region

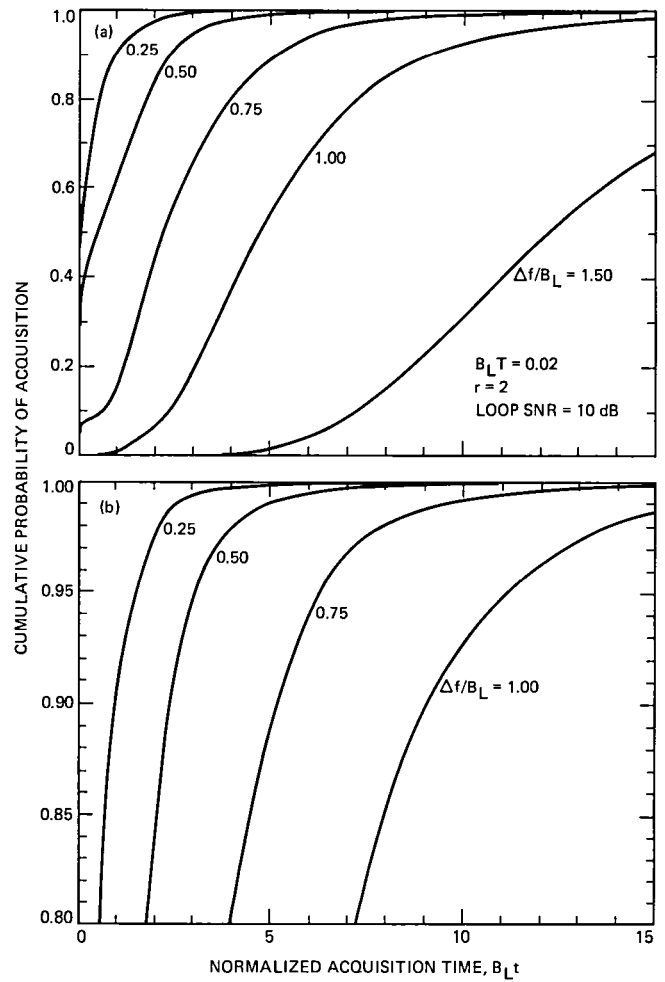


Fig. 3. Cumulative probability of phase acquisition as a function of normalized time for type II sampled data loop at 10-dB loop SNR: (a) Probability range 0 to 1, (b) Expansion of high probability region

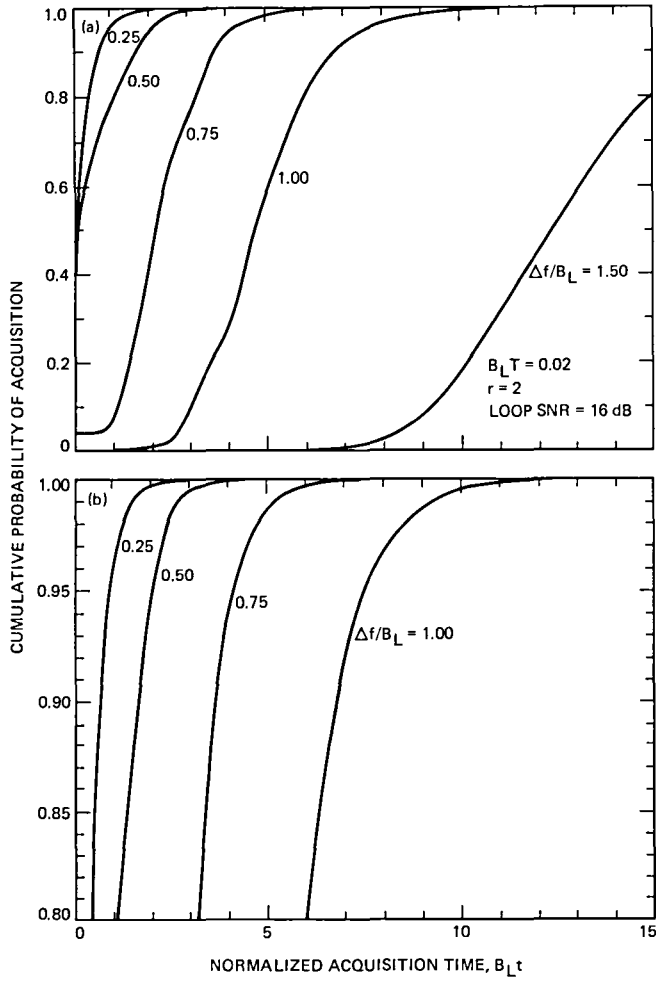


Fig. 4. Cumulative probability of phase acquisition as a function of normalized time for type II sampled data loop at 16-dB loop SNR: (a) Probability range 0 to 1, (b) Expansion of high probability region

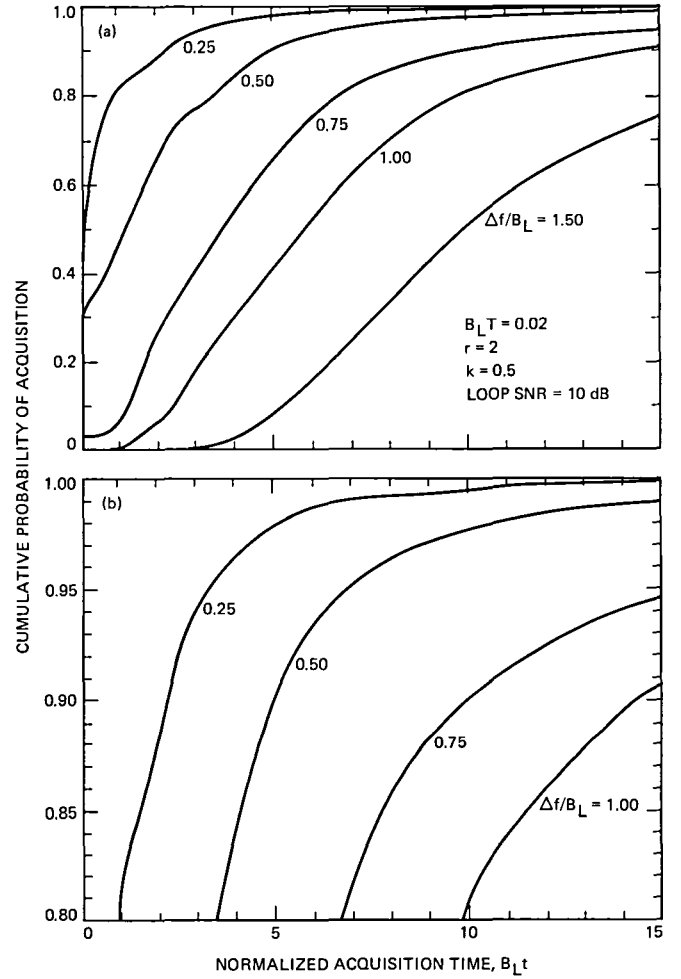


Fig. 5. Cumulative probability of phase acquisition as a function of normalized time for type III sampled data loop at 10-dB loop SNR: (a) Probability range 0 to 1, (b) Expansion of high probability region

Appendix

Setup of Equations for Simulation

From Ref. 4 and TR 900-450, a type II loop filter of a continuous time PLL can be expressed as

$$F(s) = \frac{1 + \tau_2 s}{\tau_1 s} + \frac{1}{\tau_1 \tau_3 s^2} \quad (\text{A-1})$$

which is related to the commonly used parameters

$$r = AK\tau_2^2/\tau_1 \quad (\text{A-2})$$

$$k = \tau_2/\tau_3 \quad (\text{A-3})$$

$$\frac{b}{T} = \frac{r}{4\tau_2} \left(\frac{r-k+1}{r-k} \right) \text{ one-sided loop bandwidth} \quad (\text{A-4})$$

Define

$$G_1 = \tau_2/\tau_1 \quad (\text{A-5})$$

$$G_2 = T/\tau_1 \quad (\text{A-6})$$

$$G_3 = T^2/\tau_1 \tau_3 \quad (\text{A-7})$$

Substitution of Eqs. (A-2)–(A-7) into the transfer function of the sampled data loop filter $F(z)$ produces Eq. (5). Notice that the term AKT was absorbed by the filter coefficients. With this in mind, define

$$\frac{Y'(z)}{D(z)} = AKTF(z) = rd + \frac{rd^2}{1 - z^{-1}} + \frac{krd^3}{(1 - z^{-1})^2} \quad (\text{A-8})$$

where $Y'(z) = TY(z)$ (see Fig. 1), from which Eqs. (8)–(12) follow easily. These, in conjunction with Eq. (4), are the required equations for simulation.

Physical Optics Analysis of a Four-Reflector Antenna

Part 1

A. G. Cha

Radio Frequency and Microwave Subsystems Section

Concern has been raised for the 64-m to 70-m antenna upgrade project that the 70-m system may experience greater S-band beam-pointing perturbations than the 64-m system. The S-band perturbations are due to minor (higher order) mode generation, causing subtle cross-polarization fields affecting beam pointing direction, as described herein. For the antennas in their present configuration (64 m), a slight S-band gain degradation of about 0.05 dB can be attributed to these effects. Therefore, a full physical optics analysis was performed for the present-day 64-m system, as described herein. The results were compared with past analyses and experimental observations in order to verify the algebra and computer code with the intent of deriving a valid analysis method for accurately analyzing the 70-m shaped dual-reflector Cassegrainian antenna. The results of the new analysis appear to be in excellent agreement with previous analyses and experimental data, and extension of the analysis methods to the 70-m system will follow in a second article.

I. Introduction

In support of the DSN 64-m to 70-m antenna upgrade project, several RF performance analyses were made based on a two-reflector, linearly polarized antenna system at X-band and S-band. However, the two-reflector analysis is valid only at X-band. At S-band, the antenna (64-m or 70-m) is in reality a four-reflector system. The present-day DSN 64-m antennas use conventional paraboloidal and hyperboloidal Cassegrainian reflectors, with the hyperboloidal subreflector modified in three major ways. First, the vertex is displaced from the main reflector centerline such that a line connects the main reflector focal point, the subreflector vertex, and the primary feedhorn phase center. Second, the subreflector rim is trimmed to describe a cone of $2\Theta = 120^\circ$, centered on the main reflector axis of symmetry. Lastly, a special spillover-reducing conical flange is used around the periphery of the offset and asymmetrically trimmed hyperboloid. The overall antenna system

employs two additional S-band reflectors near the primary feeds, one ellipsoidal and the other planar, to make up a four-reflector antenna at S-band. These reflectors, which enable simultaneous S- and X-band use of the overall antenna (S-band uplink and downlink and X-band downlink), complicate the analyses because of the close proximity to geometric optics focal points (see Fig. 1).

The 70-m Cassegrainian subreflector is specially shaped for uniform amplitude illumination of the primary reflector and is slightly asymmetric in order to accommodate offset primary feeds. Two additional reflectors in the primary feed region are also used in the same manner mentioned above for the 64-m antenna.

Neither reflector in the primary feed region can be analyzed using simple geometric optics or usual far-field ap-

proaches. Figure 2 shows the complex physics involved, i.e., the divergence and bunching of the RF energy beam as computed from a near-field analysis. Furthermore, the necessary physical asymmetries involved in these multi-function antenna instruments cause second-order (but important) perturbations in the final aperture beam directions when circular polarization is used. The beam-direction perturbation can be predicted only in a four-reflector antenna analysis that also takes into account near-field and circular polarization effects.

It was necessary to use some approximations in the previous analyses of the present-day system. For example, only a rough analysis of final aperture beam directions was made. Concern exists that the 70-m system, which effectively illuminates the main reflector in a uniform way, may experience greater S-band perturbations or beam squints (i.e., non-coincident right circularly polarized/left circularly polarized beams) than the 64-m system. Accordingly, it was decided to first perform a full analysis of the existing 64-m S-band system, since previous experimental results are available for comparison (Ref. 1).

If the present analysis effort is verified by comparison with previous experiments, the work will be extended to include the 70-m shaped asymmetric subreflector and shaped symmetric main reflector. For a full analysis, the S-band horn fields will be carried through all four reflectors (resulting in a transmission viewpoint of final antenna system beams) to account fully for all near-field, cross-polarization, and higher order mode generation effects caused by various intentional asymmetries. This appears to be the first time such a complete and rigorous analysis has been performed on such a complex antenna system.

II. Background

A comprehensive description of the 64-m antenna S/X-band reflex feed system was presented by Bathker in 1974 (Ref. 1). An analysis of the observed 64-m antenna S-band beam position offset from antenna boresight was performed by the author in 1977 (Ref. 2). The analysis made use of a diffraction analysis (physical optics) of the feedhorn/ellipsoid/dichroic assembly performed by Potter (Ref. 3). The analysis by Potter was combined with a geometric-optics analysis of the hyperboloid scattering, and with an aperture field integration computation of the antenna secondary field, to predict the final antenna beam direction. While this early approach worked very well in the 64-m antenna case, the algebra and computer code developed were essentially limited to the hyperboloid/paraboloid case, and could not be easily extended to the 70-m dual-shaped reflector system.

The present analysis goes far beyond previous analyses in many ways. The analysis methods can be used for both hyperbolic/parabolic and dual-shaped reflectors. It is a true four-reflector, circular-polarization, near-field physical optics analysis. Figure 1 shows the four-reflector system, consisting of the S-band feedhorn the ellipsoid, the dichroic plate, the asymmetric subreflector, and the symmetric main reflector. Figure 3 shows a simplified block diagram of the analysis approach. Near-field diffraction patterns were computed using standard JPL spherical wave expansion (SWE) techniques developed by Ludwig. The far field of each subreflector is first found by use of conventional physical optics integrations. This is followed by a numerical expansion of the far field to obtain the spherical wave mode coefficients. Finally, near-field computations result from using these coefficients (Ref. 4).

III. Results

The observed RF beam positions of the 64-m antenna are shown in Fig. 4. There are two significant beam position offsets from the antenna boresight, as explained in Ref. 1. The 0.0114° offset (Fig. 4) of the X-band beam is due to the finite thickness of the dichroic plate, which causes a refraction effect as the X-band wave propagates through the dichroic plate. When this was found, the position of the dichroic plate was shimmed by 1 in. The shimming brought the S- and X-band beams together in the direction of center-to-center line of the S- and X-band feedhorns, as seen in Fig. 4. The S-band right circularly polarized beam has another offset of 0.0086° normal to this direction. This offset is attributed to the higher order ($m \neq 1$) modes generated at the ellipsoid and is predicted to be observable only for circularly polarized waves. Alternately, this offset can be considered as a depolarization effect caused by the asymmetric ellipsoid geometry.

The new numerical results are 90% in agreement with experimental results observed in Fig. 4. Beam offset of a right circularly polarized wave from the antenna boresight was previously measured at 0.0086° and computed to be 0.0095° (0.061 beamwidth measured; 0.068 beamwidth computed). (It is expected that the left circularly polarized wave offset would be 0.0086° in the opposite direction from the antenna boresight, although this was not measured.) Beam offset due to a 1-in. shim in the position of the dichroic was measured at 0.0114° and computed to be 0.010° (0.081 BW measured; 0.071 BW computed). Table 1 shows the computed beam offset caused by the 1-in. shim of the dichroic position. Table 2 shows the right circularly polarized beam offset from antenna boresight. Together, Tables 1 and 2 indicate that the S-band beam position will be offset by 0.010° and 0.0095° in the two mutually perpendicular directions.

In addition to good correlation with observed RF beam positions, the present analysis also yields a reflector gain computation that can be compared with previous efficiency computations. A gain of 62.66 dB, corresponding to an efficiency of 77.6%, was computed, including spillover losses, non-uniform illumination and phase, higher order mode ($m \neq 1$), and polarization losses. These losses were previously computed to be (Ref. 1):

$$\begin{aligned}\eta_{FS} &= -0.133 \text{ dB} \\ \eta_{RS} &= -0.010 \text{ dB} \\ \eta_I &= -0.84 \text{ dB} \\ \eta_P &= -0.07 \text{ dB} \\ \eta_x &= -0.005 \text{ dB} \\ \eta_{m \neq 1} &= -0.089 \text{ dB}\end{aligned}$$

The total losses computed previously (Ref. 1) were -1.147 dB (76.8%), compared to present computed losses of -1.10 dB (77.6%). An item-by-item loss comparison is not possible because the present gain computation does not provide a breakdown of individual loss components.

The only small uncertainty of the analysis is that the hyperboloid flange was not included. It is not believed this would make any difference in the beam position prediction. However, efficiency (gain) computation is affected. It is likely that the difference in the two efficiency computations is mostly due to the fact that the subreflector flange was modeled in the earlier analysis. Since future DSN systems will not use such flanges, no effort was expended patching this part of the model into the new software. The difference is less likely due to numerical inaccuracies of either computation.

The new capabilities developed with this work include (1) software for analyzing the arbitrary wave polarization case (linear, circular, and elliptic) at near-field distance (see Appendix A), and (2) a physical optics program for computing symmetric main reflector diffraction when illuminated by asymmetric feed radiation patterns in the form of spherical wave harmonics. These programs enhance physical optics analysis capability and will be useful in other analysis activities. They are applicable to ongoing ground station antenna research and development efforts such as beam waveguide feed systems, holographic data reduction, and verification of GTD analysis software. As stated, this appears to be the first time such a complete and rigorous analysis has been performed on such a complex antenna system. Future work will extend the present results to the planned DSN 70-m dual-shaped reflector system with reflex-dichroic feed.

Acknowledgment

Many helpful discussions on the reflex feed with D. A. Bathker and D. Nixon are acknowledged. The author also thanks P. W. Cramer for providing the SYM-SCAT program used to analyze the main reflector in the four-reflector analysis.

References

1. Bathker, D. A., "Dual-Frequency Dichroic Feed Performance," presented at 26th Meeting of Avioincs Panel, AGARD, Munich, Germany, November 26-30, 1973, *AGARD Conference Proceedings #139*, pp. 29-1-29-9, June 1974, NATO.
2. Cha, A. G., "Beam Squint in Large Ground Station Antennas," presented at International Antennas and Propagation Symposium, Stanford, California, 1977, *1977 International Symposium Digest, Antennas and Propagation*, pp. 538-541.
3. Potter, P. D., "S- and X-band RF Feed System," *JPL Technical Report 32-1526, Vol. III*, pp. 53-60. Jet Propulsion Laboratory, Pasadena, Calif., April 1972.
4. Ludwig, A. C., "Near-Field, Far-Field Transformations Using Spherical Wave Expansions," *IEEE Transactions on Antennas and Propagation*, March 1971, Vol. AP-19, pp. 214-220.

Table 1. Beam offset caused by 1-in. shim of dichroic position*

Theta	E Theta		E Phi		Axial Ratio	Ellipse Tilt Angle	RCP Gain, dB
	Volts	Phase	Volts	Phase			
0.00000	148.981325	-98.451	148.897799	171.534	0.005	166.91661	62.600
0.00100	149.165831	-98.443	149.075554	171.540	0.006	166.89899	62.610
0.00200	149.331051	-98.435	149.234343	171.547	0.006	166.85301	62.620
0.00300	149.476992	-98.426	149.374123	171.554	0.007	166.78256	62.628
0.00400	149.603628	-98.418	149.494875	171.561	0.007	166.69550	62.635
0.00500	149.710876	-98.409	149.596622	171.569	0.007	166.57938	62.641
0.00600	149.798769	-98.400	149.679274	171.576	0.008	166.45171	62.646
0.00700	149.867254	-98.392	149.742825	171.584	0.008	166.30922	62.650
0.00800	149.916344	-98.382	149.787300	171.592	0.008	166.14984	62.653
0.00900	149.945999	-98.373	149.812653	171.600	0.009	165.97935	62.654
0.01000**	149.956234	-98.363	149.818916	171.608	0.009	165.79265	62.655**
0.01100	149.947079	-98.354	149.806078	171.617	0.009	165.59603	62.654
0.01200	149.918497	-98.344	149.774174	171.625	0.010	165.38231	62.652
0.01300	149.870565	-98.334	149.723173	171.634	0.010	165.15844	62.650
0.01400	149.803247	-98.321	149.653156	171.646	0.010	164.92001	62.646
0.01500	149.716541	-98.310	149.564074	171.655	0.010	164.66658	62.640
0.01600	149.610556	-98.300	149.456049	171.665	0.010	164.39746	62.634
0.01700	149.485386	-98.288	149.329130	171.675	0.011	164.11704	62.627
0.01800	149.340899	-98.276	149.183241	171.685	0.011	163.81953	62.618
0.01900	149.177284	-98.265	149.018515	171.695	0.011	163.50879	62.609
0.02000	148.994564	-98.253	148.835079	171.706	0.011	163.17743	62.598

*Plane $\phi = 180^\circ$ (direction of 0.0114° beam offset, see Fig. 4).

**Beam position for peak gain.

Table 2. Offset of right circularly polarized beam from antenna boresight*

Theta	E Theta		E Phi		Axial Ratio	Ellipse Tilt Angle	RCP Gain, dB
	Volts	Phase	Volts	Phase			
0.00000	148.897789	171.534	148.981325	81.549	0.005	166.91653	62.600
0.00100	149.070080	171.480	149.155140	81.495	0.005	168.19427	62.610
0.00200	149.223063	171.427	149.309898	81.440	0.005	169.51804	62.619
0.00300	149.356670	171.375	149.445599	81.386	0.005	170.87561	62.627
0.00400	149.470888	171.323	149.562214	81.332	0.006	172.24525	62.633
0.00500	149.565687	171.271	149.659662	81.279	0.006	173.60888	62.639
0.00600	149.641045	171.219	149.737972	81.225	0.006	174.95147	62.643
0.00700	149.696924	171.167	149.797089	81.172	0.006	176.25542	62.647
0.00800	149.733271	171.116	149.836979	81.120	0.006	177.50557	62.649
0.00900**	149.750128	171.065	149.857647	81.067	0.006	178.69234	62.650**
0.01000**	149.747488	171.015	149.859093	81.015	0.006	179.81087	62.650**
0.01100	149.725349	170.964	149.841316	80.963	0.007	0.85489	62.649
0.01200	149.683687	170.914	149.804310	80.911	0.007	1.82267	62.646
0.01300	149.622532	170.864	149.748096	80.860	0.007	2.71287	62.643
0.01400	149.541880	170.817	149.672674	80.811	0.008	3.52796	62.639
0.01500	149.441759	170.768	149.578032	80.760	0.008	4.26989	62.633
0.01600	149.322292	170.719	149.464272	80.709	0.008	4.94688	62.626
0.01700	149.183455	170.671	149.331474	80.660	0.009	5.55535	62.618
0.01800	149.025164	170.623	149.179470	80.610	0.009	6.10518	62.609
0.01900	148.847649	170.574	149.008514	80.560	0.010	6.59810	62.599
0.02000	148.650909	170.526	148.818573	80.510	0.010	7.04187	62.588

*Plane $\phi = 270^\circ$ (direction of 0.0086° beam offset, see Fig. 4).

**Beam position for peak gain.

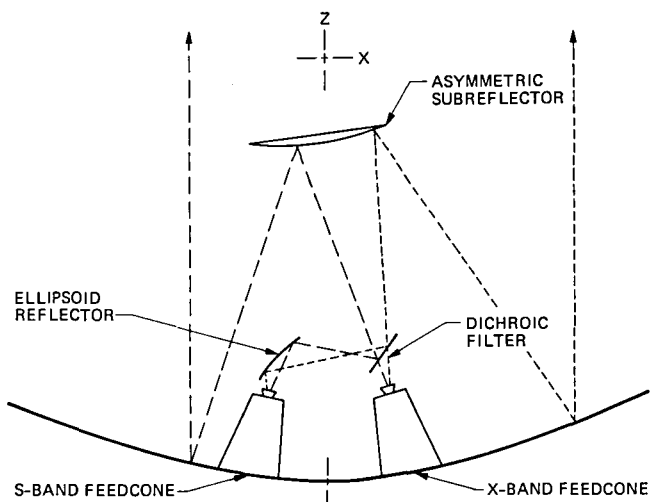


Fig. 1. The 64-m antenna four-reflector antenna system using S/X-band reflex dichroic feed

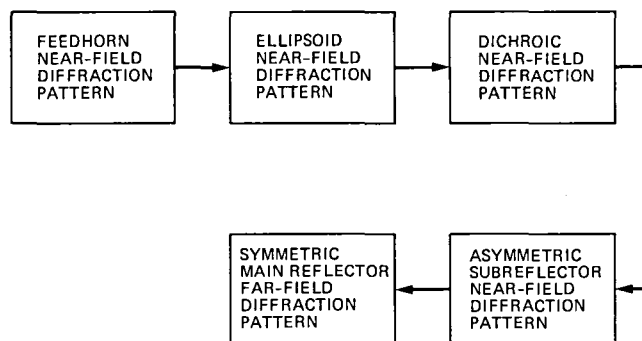


Fig. 3. Block diagram of physical optics analysis approach

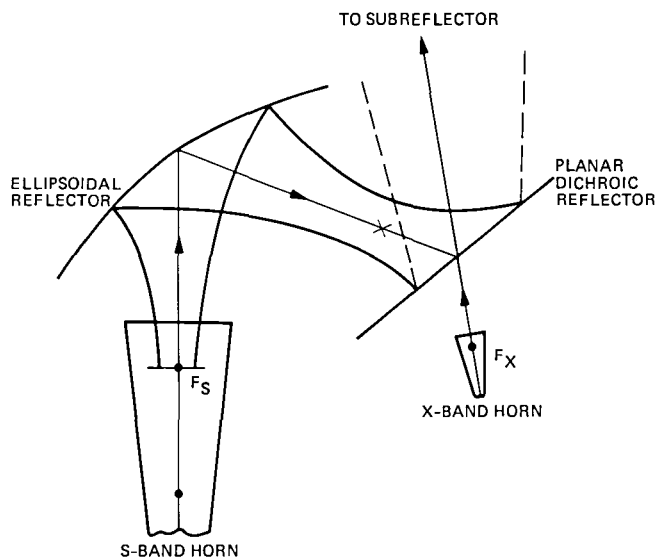


Fig. 2. Detail of reflex dichroic optics

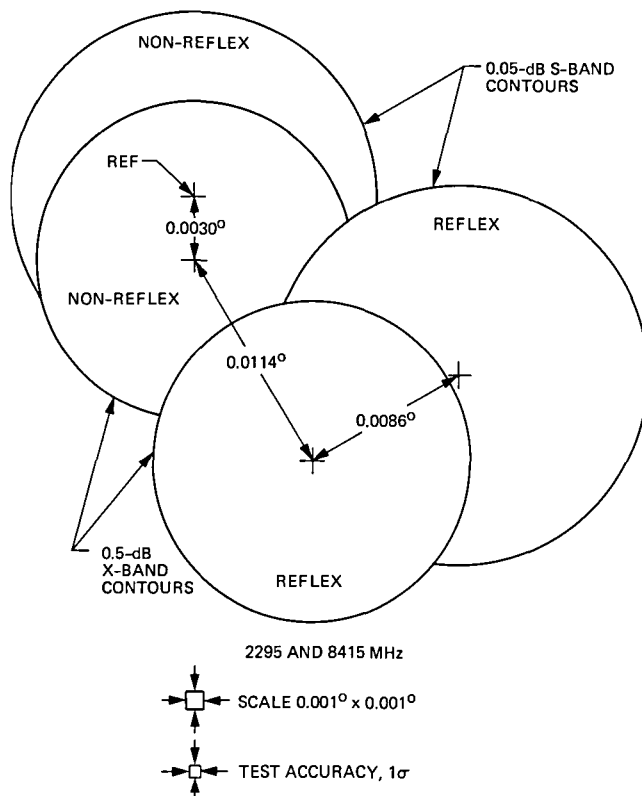


Fig. 4. Dual-frequency dichroic feed RF beam positions

Appendix A

Computer Program List

Program Name	Usage
HYBRIDHORN	Computes corrugated horn pattern and spherical wave coefficients for vertical (y) polarization.
YTXPOL/SWCOE	Obtains horn pattern spherical wave coefficient set for horizontal (x) polarization. Input is spherical wave coefficient set for y polarization.
YTORCP/SWCOE	Obtain horn pattern spherical wave coefficient set for RCP. Input is spherical coefficient wave set for y polarization.
FSCATT	Ludwig (Ref. 4) asymmetric reflector physical optics analysis program. Computes far-field diffraction patterns of ellipsoid, dichroic plate, and hyperboloid.
AZ-EXPAND-LG and SPW-ITER	Programs for computing spherical wave coefficient set of given (near- or far-field) pattern. Performed four times for ellipsoid, dichroic, and hyperboloid.
SYM-SCAT	Cramer symmetric reflector physical optics analysis program, used in computing far-field pattern of 64-m parabolic main reflector.
PHASE-CENT	Determines near-field phase center for given source (near- or far-field), pattern, and distance.
FGRID	Produces FSCATT integration grid for ellipsoid.
FSURF	Produces FSCATT surface definition for ellipsoid.
FGRIDPLT	Provides FSCATT integration grid for dichroic plate.
FSVRFPLT	Produces FSCATT surface definition for dichroic plate.

Performance Characteristics for an Array of Two Receiving Systems With Unequal Predetection Signal-to-Noise Ratios and Enhanced Radio Frequency Carrier Margin Improvement

M. H. Brockman

Telecommunications Science and Engineering Division

Enhanced radio frequency carrier margin improvement for arrayed receiving systems for coherent reception of phase modulated signals with residual carrier provides a significant reduction in carrier loop phase noise and increase in signal-to-noise ratio in the RF carrier tracking loop with an attendant reduction in telemetry radio loss. A significant increase in doppler frequency rate capability is also realized relative to operating at a narrower tracking loop bandwidth to obtain the same carrier sensitivity improvement. This report examines these performance characteristics for an array of two receiving systems with unequal apertures and statistically independent predetection noise.

I. Introduction

An earlier report (Ref. 1) presented a technique for providing enhanced radio frequency carrier margin improvement for coherent carrier reception and demodulation of phase modulated signals with residual carrier for an array of receiving systems with unequal antenna apertures. This report presents additional performance information for receiver design parameters and with array parameters representative of a 34-meter-diameter high-efficiency (listen only) antenna receiving system arrayed with a 64-meter-diameter antenna-receiving system. In this report, the various components of operating system noise temperature (T_{op}) are treated as statistically independent among the receiving systems of the array (as in Ref. 1).

The information presented in this report provides additional performance characteristics for the RF carrier phase tracking loop to illustrate the manner in which the enhanced RF carrier margin improvement performance characteristics for an array shown in Ref. 1 were obtained for a given set of design parameters. Performance characteristics are presented herein that show RF carrier tracking loop phase noise reduction and signal-to-noise ratio improvement (e.g., 3.2 db) as well as enhanced RF carrier margin improvement (e.g., 4.8 db). In addition, performance characteristics are shown to illustrate the increase in doppler rate capability realized (i.e., 2.9 times) relative to that obtained by switching to a narrower tracking loop bandwidth to obtain the same RF carrier signal level sensitivity improvement.

The performance characteristics presented in this report apply to a second order RF carrier phase tracking loop which includes a bandpass limiter and a sinusoidal phase detector. The technique presented herein is also applicable to higher order tracking loops and to digitally implemented tracking loops that incorporate a bandpass limiter or equivalent at an intermediate frequency (IF) in each of the receiving systems of the array.

II. Receiver Configuration

Figure 1 illustrates a method for achieving RF carrier arraying (Ref. 1, Fig. 1). A modification of Fig. 1 (so that much larger antenna separation for the array can be handled conveniently) was presented in Ref. 2 with a discussion of predetection noise resulting from operating equivalent system noise temperature T_{op} . Figure 2 illustrates a second configuration that provides additional filtering of receiving system 2 (through N) local oscillator phase noise which couples into receiving system 1 via the RF carrier summing junction. Consequently, Fig. 2 generally provides an increase in carrier margin relative to Fig. 1. The received signal is an RF carrier (ω_{RF}) phase modulated with a square-wave subcarrier (ω_{sc}) at a peak modulation index m_{pd} that is, in turn, biphase modulated with data $D(t)$.

$$\underbrace{2^{1/2} A \cos m_{pd} \cos \omega_{RF} t}_{\text{carrier}} + \underbrace{2^{1/2} A \sin m_{pd} \times D(t) \times \cos(\omega_{sc} t) \times \sin \omega_{RF} t + n(t)}_{\text{sidebands}} \quad (1)$$

The term $n(t)$ represents receiver noise which has a double-sided noise spectral density $N_o/2$.

III. Predetection Signal-to-Noise Ratio and RF Carrier Tracking Loop Phase Noise

The improvement in predetection carrier power-to-noise spectral density in receiving system 1 for two receiving systems arrayed (η_2) is

$$\eta_2 = \frac{\left[1 + \beta_2 \gamma_2 \left(\frac{N_{o2}}{N_{o1}} \right)^{1/2} \right]^2}{\left[1 + \frac{N_{o2}}{N_{o1}} \beta_2^2 \right]} \quad (2)$$

where β_2 is the voltage coupling of receiving system 2 relative to receiving system 1 at the summing junction. The term γ_2^2 is the ratio of the carrier power-to-noise spectral density ratio of receiving system 2 relative to the carrier power-to-noise spectral density ratio of receiving system 1. Receiving system 1 has a double-sided noise spectral density $N_{o1}/2$ related to T_{op1} and receiving system 2 has a double-sided noise spectral density $N_{o2}/2$ related to T_{op2} . Note that for N receiving systems

$$\eta_N = \frac{\left[1 + \beta_2 \gamma_2 \left(\frac{N_{o2}}{N_{o1}} \right)^{1/2} + \cdots + \beta_N \gamma_N \left(\frac{N_{oN}}{N_{o1}} \right)^{1/2} \right]^2}{\left[1 + \frac{N_{o2}}{N_{o1}} \beta_2^2 + \cdots + \frac{N_{oN}}{N_{o1}} \beta_N^2 \right]} \quad (3)$$

It should be noted that in Ref. 1, the terms $(N_{o2}/N_{o1})^{1/2}$ and $(N_{oN}/N_{o1})^{1/2}$ in the numerators of expressions (2) and (3) above should have been included in expressions (1), (2), (7), (8), (11) and (12). This omission was also made in expressions (2), (3), (4) and (5) of Ref. 3. For the system noise temperature ratios in Refs. 1 and 3 and the antenna spacings and orientation planned for the 64- and 34-m antennas at the three DSN complexes, the omission described above represents a 0.1 db error in the results presented.

Consider the RF carrier phase tracking loop in receiving system 1 for the situation where the predetection IF filters F_{A2} through F_{AN} in receiving systems 2 through N have k times the noise bandwidth of predetection filter F_{A1} in receiving system 1 (see Ref. 1). The RF carrier tracking loop is a second-order phase tracking loop which includes a bandpass limiter and a sinusoidal phase detector. With receiving system 1 only connected to the summing junction, the resultant rms phase noise (σ_{ϕ_n}) at the output of the RF carrier tracking loop (i.e., on the first local oscillator) becomes (Ref. 1, Expression [4b]):

$$\sigma_{\phi_{n1}} = \frac{\frac{N_{o1}}{2} \cdot 2B_{L1}}{P_{c1}}$$

$$\times \left[\frac{1 + \frac{P_{c1}}{NBW_{F_{A1}} \cdot N_{o1}}}{0.862 + \frac{P_{c1}}{NBW_{F_{A1}} \cdot N_{o1}}} \cdot \frac{\exp\left(\frac{N_{o1} B_{L1}}{P_{c1}}\right)}{\sinh\left(\frac{N_{o1} B_{L1}}{P_{c1}}\right)} \right]^{1/2} \quad \text{radians, rms} \quad (4)$$

where $P_{c1}/NBW_{FA1} \cdot N_{o1}$ is the RF carrier signal-to-noise power ratio at the input to the bandpass limiter in the carrier phase tracking loop. The term NBW_{FA1} represents the noise bandwidth of predetection IF filter F_{A1} in receiving system 1. The two-sided closed-loop noise bandwidth can be expressed as:

$$2B_{L1} = \frac{2B_{Lo1}}{r_o + 1} \left(1 + r_o \frac{\alpha_1}{\alpha_{o1}} \right) \quad (5)$$

where $r_o = 2$ by design at design point (0.707 damping) and $2B_{Lo1}$ is the design point (threshold) two-sided closed-loop noise bandwidth in receiving system 1. The term α_1 is the limiter suppression factor resulting from the noise-to-carrier power ratio due to NBW_{FA1} at the input to the bandpass limiter. The suppression factor α_1 has a value of α_{o1} at design point (threshold). At threshold, the predetection carrier-to-noise power ratio in a noise bandwidth equal to $2B_{Lo1}$ is unity (i.e., $P_c/(2B_{Lo} \cdot N_o) = 1$).

With receiving systems 1 and 2 connected to the summing junction, the RF carrier signal-to-noise power ratio at the input to the bandpass limiter is (Ref. 1, Expression 6)

$$\frac{P_{c1 \Sigma 1,2}}{P_{n1 \Sigma 1,2}} = \frac{(A_1 \cos m_{pd} + \beta_2 A_2 \cos m_{pd})^2}{[NBW_{FA1} \cdot N_{o1} + \beta_2^2 NBW_{FA2} \cdot N_{o2}]} \quad (6)$$

where m_{pd} is the peak phase modulation index, and $NBW_{FA2} = k_2 \cdot NBW_{FA1}$. Expression (6) can be rewritten as:

$$\frac{P_{c1 \Sigma 1,2}}{P_{n1 \Sigma 1,2}} = \frac{P_{c1}}{NBW_{FA1} \cdot N_{o1}} \cdot \frac{\left[1 + \beta_2 \gamma_2 \left(\frac{N_{o2}}{N_{o1}} \right)^{1/2} \right]^2}{\left[1 + \frac{N_{o2}}{N_{o1}} \beta_2^2 k_2 \right]} \quad (7)$$

The change in RF carrier signal-to-noise power ratio at the input to the bandpass limiter in receiving system 1 is then:

$$\Delta_2 = \frac{\left[1 + \beta_2 \gamma_2 \left(\frac{N_{o2}}{N_{o1}} \right)^{1/2} \right]^2}{\left[1 + \frac{N_{o2}}{N_{o1}} \beta_2^2 k_2 \right]} \quad (8)$$

The limiter suppression factor due to the change in noise-to-carrier power ratio becomes $\alpha_1 \Delta_2$ which provides a two-sided closed-loop noise bandwidth:

$$2B_{L1 \Delta 2} = \frac{2B_{Lo1}}{r_o + 1} \left(1 + r_o \frac{\alpha_1 \Delta_2}{\alpha_{o1}} \right) \quad (9)$$

The resultant rms phase noise at the output of the RF carrier tracking loop (i.e., on the first local oscillator) in receiving system 1 becomes:

$$\sigma_{\phi_{n1 \Sigma 1,2}} = \frac{\frac{N_{o1}}{2} \cdot 2B_{L1 \Delta 2}}{P_{c1}} \cdot \frac{1}{\eta_2} \cdot \left[\frac{1 + \frac{P_{c1} \cdot \Delta_2}{NBW_{FA1} \cdot N_{o1}}}{0.862 + \frac{P_{c1} \cdot \Delta_2}{NBW_{FA1} \cdot N_{o1}}} \cdot \frac{\exp \left(\frac{N_{o1} \cdot B_{L1 \Delta 2}}{P_{c1} \cdot \eta_2} \right)}{\sinh \left(\frac{N_{o1} \cdot B_{L1 \Delta 2}}{P_{c1} \cdot \eta_2} \right)} \right]^{1/2} \quad \text{rad, rms} \quad (10)$$

Note that the total rms phase noise at the output of the RF carrier tracking loop (i.e., on the first local oscillator) in receiving system 1 for Fig. 1 (Ref. 1) is:

$$\left[\sigma_{\phi_{n1 \Sigma 1,2}}^2 + \left(\frac{\beta_2 \sigma_{\phi_{n2}}}{1 + \beta_2} \right)^2 \right]^{1/2} \quad (11)$$

In Fig. 2, additional filtering of the output rms phase noise $\sigma_{\phi_{n2}}$ is provided by the local oscillator tracking loop in receiving system 2. Designate the additionally filtered rms phase noise as $\sigma'_{\phi_{n2}}$ which is less than $\sigma_{\phi_{n2}}$ by the square root of the ratio of local oscillator tracking loop noise bandwidth to $2B_{L2}$. Consequently for Fig. 2, $\sigma'_{\phi_{n2}}$ is substituted into expression (11) in place of $\sigma_{\phi_{n2}}$. Note that since receiving system 2 has the same first local oscillator as receiving system 1, receiving system 2 has effectively the same RF carrier characteristics and sensitivity as receiving system 1.

The rms phase noise (Expression [11]) represents a different RF carrier margin when compared to $\sigma_{\phi_{n1}}$ for receiving system 1 alone (Expression [4]). The change in RF carrier margin represents the enhanced carrier margin improvement for two receiving systems arrayed.

The RF carrier phase tracking loop in receiving system 2 is also a second-order phase tracking loop ($r_o = 2$) which utilized a bandpass limiter and sinusoidal phase detector. Since the closed loop noise bandwidth of the carrier phase tracking loop for receiving systems 2 through N is much narrower (by design) than that in receiving system 1, phase noise in receiving system 1 carrier tracking loop produces a reduction in predetection carrier signal-to-noise ratio in receiving systems 2 through N . The resultant predetection carrier signal-to-noise ratio in receiving system 2 for two systems arrayed is then

$$\frac{P_{c2\Sigma 1,2}}{P_{n2}} = \frac{P_{c2} \left(1 - \frac{\sigma_{\phi n1\Sigma 1,2}^2}{2}\right)^2}{NBW_{FA2} \cdot N_{o2}} \quad (12)$$

which produces an rms phase noise

$$\sigma_{\phi n2\Sigma 1,2} = \frac{\frac{N_{o2}}{2} \cdot 2B_{L2}}{P_{c2\Sigma 1,2}} \times \left[\frac{1 + \frac{P_{c2\Sigma 1,2}}{NBW_{FA2} \cdot N_{o2}}}{0.862 + \frac{P_{c2\Sigma 1,2}}{NBW_{FA2} \cdot N_{o2}}} \cdot \frac{\exp\left(\frac{N_{o2} \cdot B_{L2}}{P_{c2\Sigma 1,2}}\right)}{\sinh\left(\frac{N_{o2} \cdot B_{L2}}{P_{c2\Sigma 1,2}}\right)} \right]^{1/2} \quad (13)$$

rad, rms

IV. Performance

Performance characteristics are presented in this report for an array of two receiving systems with a 64-meter-diameter antenna (system 1) and a 34-meter-diameter high-efficiency (listen only) antenna (system 2) with $\gamma_2 = 0.61$ (-4.3 db), $k_2 = 9$, $N_{o2}/N_{o1} = 0.925$ and $\beta_2 = 1.0$. Design parameters for receiving system 1 are $2B_{Lo1} = 30$ Hz and $NBW_{FA1} = 2000$ Hz while design parameters for receiving system 2 are $2B_{Lo2} = 1.0$ Hz and $NBW_{FA2} = k_2 \cdot NBW_{FA1}$. The local oscillator tracking loop for receiving system 2 (Fig. 2) has a two-sided noise bandwidth of 1.0 Hz.

Figure 3 shows the rms phase noise $\sigma_{\phi n1}$ at the output of the RF carrier tracking loop (i.e., on the first local oscillator) for receiving system 1 by itself. Phase noise is shown as a function of initial 64-m receiver RF carrier margin (carrier level above design point) as calculated from Expression (4) above

using the design parameters in the preceding paragraph. Figure 3 also shows the total rms phase noise (Expression [11]) at the output of the RF carrier tracking loop in receiving system 1 for an array of two receiving systems with a 64-meter-diameter antenna (system 1) and a 34-meter-diameter high-efficiency (listen-only) antenna (system 2). Total rms phase noise is shown for array configurations that are representative of Figs. 1 and 2 with $k_2 = 9$.

Note, in Fig. 3, that with receiving system 1 by itself (prior to arraying) initially at 5.5 db above design point threshold (carrier margin), the rms phase noise for the array is 21.9 and 21.7 degrees respectively for array configurations representative of Figs. 1 and 2 ($k_2 = 9$). These rms phase noise levels (21.9 and 21.7 degrees) when compared to the phase noise characteristic of system 1 by itself represent an enhanced RF carrier margin of 10.1 and 10.3 db, respectively. The improvement in the 64-m receiver (system 1) carrier margin is then 4.6 and 4.8 db, respectively, with receiving system 1 and 2 arrayed (see Fig. 7, Ref. 1, $k = 9$). Note that the difference in carrier margin improvement for Fig. 2 relative to Fig. 1 increases for three receiving systems arrayed (see Fig. 15, Ref. 1). Figure 4 shows receiver array enhanced RF carrier margin versus initial 64-m receiver RF carrier margin for the array described above.

Consider the RF carrier tracking loop signal-to-noise ratio (SNR) for receiving system 1 by itself. Using the linear theoretical model (Refs. 4 and 5):

$$\rho_{L1} = \frac{P_{c1}}{N_{o1} B_{L1} \Gamma_1} \quad (14)$$

where ρ_{L1} is the RF carrier loop SNR for receiving system 1 (64 m) by itself and Γ_1 is the bandpass limiter performance factor:

$$\Gamma_1 = \frac{1 + \frac{P_{c1}}{NBW_{FA1} N_{o1}}}{0.862 + \frac{P_{c1}}{NBW_{FA1} N_{o1}}} \quad (15)$$

Figure 5 shows the RF carrier loop SNR for receiving system 1 by itself (ρ_{L1}) as a function of initial 64-m receiver RF carrier margin as calculated from Expression (14). Note the interrelationship provided by Figs. 3 and 5 between rms phase noise at the output of the RF carrier tracking loop and tracking loop SNR. Using this relationship, the total rms phase noise (Expression [11]) at the output of the RF carrier tracking loop in receiving system 1 for the two receiver array provides the RF carrier loop SNR in receiving system 1 also

shown in Fig. 5 for array configurations representative of Figs. 1 and 2 with $k_2 = 9$ and design parameters as discussed above. Using the linear theoretical model for the array:

$$\rho_{L1\Sigma 1,2} = \frac{P_{c1} \eta_2}{N_{o1} B_{L1\Delta 2} \Gamma_{1\Delta 2}} \quad (16)$$

where

$$\Gamma_{1\Delta 2} = \frac{1 + \frac{P_{c1} \cdot \Delta_2}{NBW_{F_{A1}} \cdot N_{o1}}}{0.862 + \frac{P_{c1} \cdot \Delta_2}{NBW_{F_{A1}} \cdot N_{o1}}} \quad (17)$$

The RF carrier loop SNR for receiving system 1 for the two receiver array calculated from Expression (16) provides essentially the same curve as the array configuration representative of Fig. 2 shown in Fig. 5. This results from the additional local oscillator filtering in receiving system 2. Note the 3.2 db improvement in the 64-m receiving system (system 1) RF carrier tracking loop signal-to-noise ratio in Fig. 5 for the two-receiver array relative to system 1 by itself initially at 10 db above design point threshold (carrier margin). Reduction in RF carrier loop rms phase noise (Fig. 3) and resultant improvement in carrier loop SNR (Fig. 5) provide an attendant reduction in telemetry radio loss (Refs. 1, and 5).

The reduction in rms phase noise on the first local oscillator (system 1) for the receiver array shown in Fig. 3 (with $2B_{Lo1} = 30$ Hz) raises the point of switching to a narrower bandwidth in the RF carrier tracking loop to accomplish essentially the same reduction in rms phase noise. Switching system 1 (64 m) by itself to a $2B_{Lo1}$ of 10 Hz improves its carrier margin by 30/10 or 4.77 db relative to operation with $2B_{Lo1} = 30$ Hz. This narrower closed-loop noise bandwidth provides very nearly the same rms phase noise as the array in Fig. 3. Consider the following discussion.

Figure 6 shows the two-sided closed-loop noise bandwidth $2B_{L1}$ (Expression [5]) of the RF carrier tracking loop for receiving system 1 (64 m) by itself as a function of initial 64-m receiver carrier margin for $2B_{Lo1} = 30$ Hz. Figure 6 also shows the two-sided closed-loop noise bandwidth $2B_{L1\Delta 2}$ (Expression [9]) for the array of two receiving systems described above with $k_2 = 9$. Note the 5.5 db offset in RF carrier level of $2B_{L1\Delta 2}$ relative to $2B_{L1}$. Doppler rate capability (for a 10 degree phase error due to doppler rate) is shown in Fig. 7 for receiving system 1 by itself as a function of initial 64-m receiver carrier margin for $2B_{Lo1} = 30$ Hz. Figure 7 also shows

the resulting doppler rate capability for the array described above for a 10 degree phase error ($k_2 = 9$). Note the 5.5 db offset in RF carrier level between the doppler rate curves. Finally, Fig. 8 shows the doppler rate capability for a 10 degree phase error as a function of RF carrier margin for $2B_{Lo1} = 10$ Hz. The information for two-sided noise bandwidth and doppler rate capability is contained in JPL Document 810-5, Rev. D, *Deep Space Network/Flight Project Interface Design Handbook*, Volume 1, TRK 20, (internal document).

Consider an initial RF carrier margin of 10 db for receiving system 1 (64 m) by itself with $2B_{Lo1} = 30$ Hz. The doppler rate capability for an array of two receiving systems ($k_2 = 9.0$) is 37.5 Hz/s for a 10 degree phase error (Fig. 7). In Fig. 8, the corresponding RF carrier margin for $2B_{Lo1} = 10$ Hz is 14.77 db. At this carrier margin, the doppler rate capability for a 10 degree phase error is 12.8 Hz/s. Consequently the array of two receiving systems with $2B_{Lo1} = 30$ Hz and $k_2 = 9$ has a doppler rate capability of 37.5/12.8 or 2.9 times the doppler rate capability of receiving system 1 by itself operating with a $2B_{Lo1}$ of 10 Hz. With an array of two receiving systems for $2B_{Lo1} = 10$ Hz with $k_2 = 1$, the above ratio becomes 2.6.

Performance characteristics for the RF carrier tracking loop in receiving system 2 (34 m) are shown in Figs. 9 and 10 for the design parameters shown above. Figure 9 shows the rms phase noise $\sigma_{\phi_{n2}}$ at the output of the RF carrier tracking loop for receiving system 2 by itself. Phase noise is shown as a function of initial 34-m receiver carrier margin (carrier level above design point for $k_2 = 1.0$) as calculated from Expression (13) above. Figure 9 also shows rms phase noise for $k_2 = 9$, as calculated from Expression (13). The corresponding two-sided closed-loop noise bandwidth $2B_{L2}$ is shown in Fig. 10 for $k_2 = 1.0$ and 9.0 as a function of initial 34-m receiver carrier margin (carrier level above design point for $k_2 = 1.0$). Taking into account the effect of Expression (12) and γ_2 , the information shown in Figs. 9 and 10 for $k_2 = 9$ permits calculation of total rms phase noise (Expression [11]) at the output of the RF carrier tracking loop in receiving system 1 for array configurations representative for Figs. 1 and 2.

V. Discussion

Enhanced RF carrier margin improvement for an array representative of a 34-meter-diameter high-efficiency (listen only) antenna receiving system and a 64-meter-diameter antenna receiving system with $k_2 = 9$ is presented in this report. With an initial RF carrier margin of 10 db for the 64-m receiving system (by itself) with $2B_{Lo1} = 30$ Hz, the enhanced RF carrier margin improvement is 4.8 db and 5.0 db (Figs. 1 and 2 configurations, respectively). This enhanced carrier margin im-

provement (4.8 and 5.0 db) is realized with an improvement in predetection signal power-to-noise spectral density in receiving system 1 of 1.2 db. The corresponding improvement in RF carrier tracking loop signal-to-noise ratio improvement is 3.15 db and 3.25 db (Fig. 5). In addition, the array has 2.9 times the doppler rate capability relative to operating the 64-m receiving system with $2B_{L_{01}} = 10$ Hz.

The additional RF carrier sensitivity realized by enhanced carrier margin improvement provides a performance capability

that should be investigated and verified by further Laboratory investigation including operation at initial carrier margins (prior to arraying) of less than 10 db. In light of the performance shown in this report, the array presented herein should acquire the RF carrier when the initial 64-m receiver carrier margin is as low as 5.5 db. After RF acquisition at this signal level, the effective RF carrier margin of the array would be 10.2 db (Fig. 4) as determined by rms phase noise at the output of the RF carrier phase tracking loop (i.e., on the first local oscillator).

References

1. Brockman, M. H., "Enhanced Radio Frequency Carrier Margin Improvement for an Array of Receiving Systems with Unequal Predetection Signal-to-Noise Ratios," *TDA Progress Report 42-76*, pp. 170-188, Jet Propulsion Laboratory, Pasadena, California, February 15, 1984.
2. Brockman, M. H., "The Effect of Partial Coherence in Receiving System Noise Temperature on Array Gain for Telemetry and Radio Frequency Carrier Reception for Similar Receiving Systems," *TDA Progress Report 42-66*, pp. 219-235, Jet Propulsion Laboratory, Pasadena, California, December 15, 1981.
3. Brockman, M. H., "The Effect of Partial Coherence in Receiving System Noise Temperature on Array Gain for Telemetry and Radio Frequency Carrier Reception for Receiving Systems with Unequal Predetection Signal-to-Noise Ratios," *TDA Progress Report 42-72*, pp. 95-117, Jet Propulsion Laboratory, Pasadena, California, February 15, 1983.
4. Tausworthe, R. C., "Limiters in Phase-Locked Loops: A Correction to Previous Theory," *Space Programs Summary No. 37-54*, Vol. III, pp. 201-203, Jet Propulsion Laboratory, Pasadena, California, 1968.
5. Divsalar, D., and Yuen, J. H., "Improved Carrier Tracking Performance with Coupled Phase-Locked Loops," *TDA Progress Report 42-66*, pp. 148-171, Jet Propulsion Laboratory, Pasadena, California, December 15, 1981.

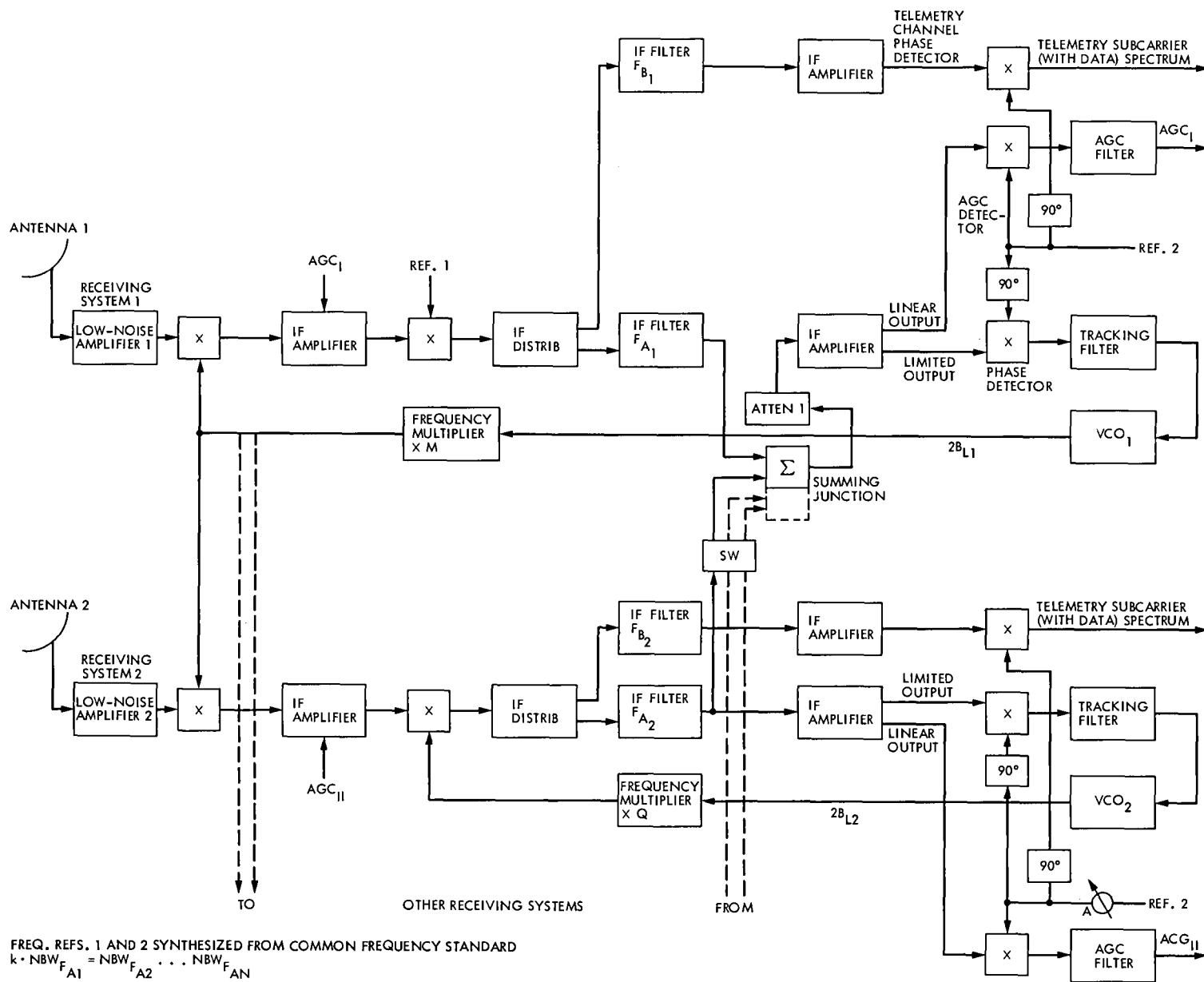


Fig. 1. Enhanced radio frequency carrier arraying

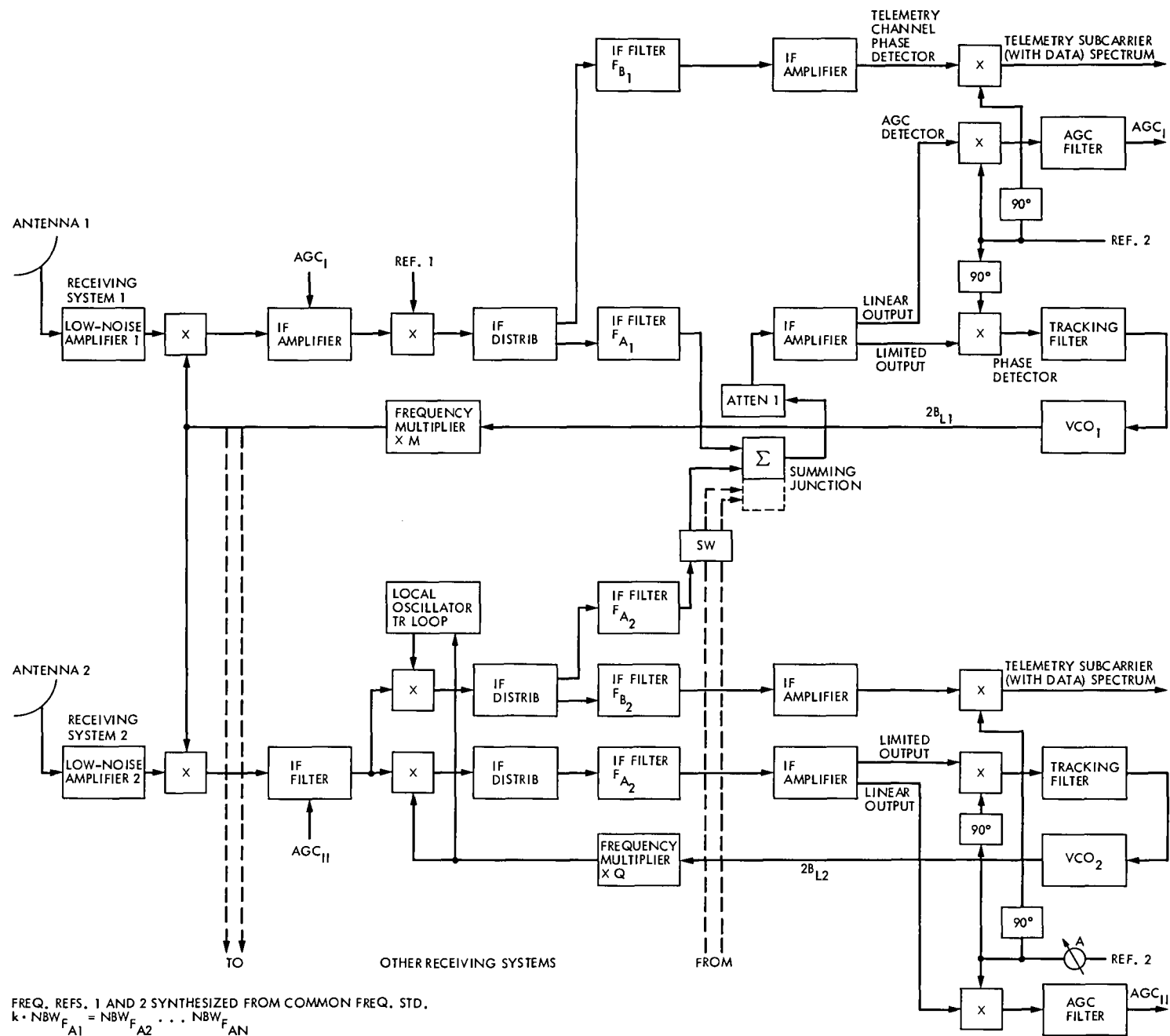


Fig. 2. Enhanced radio frequency carrier arraying with additional local oscillator filtering

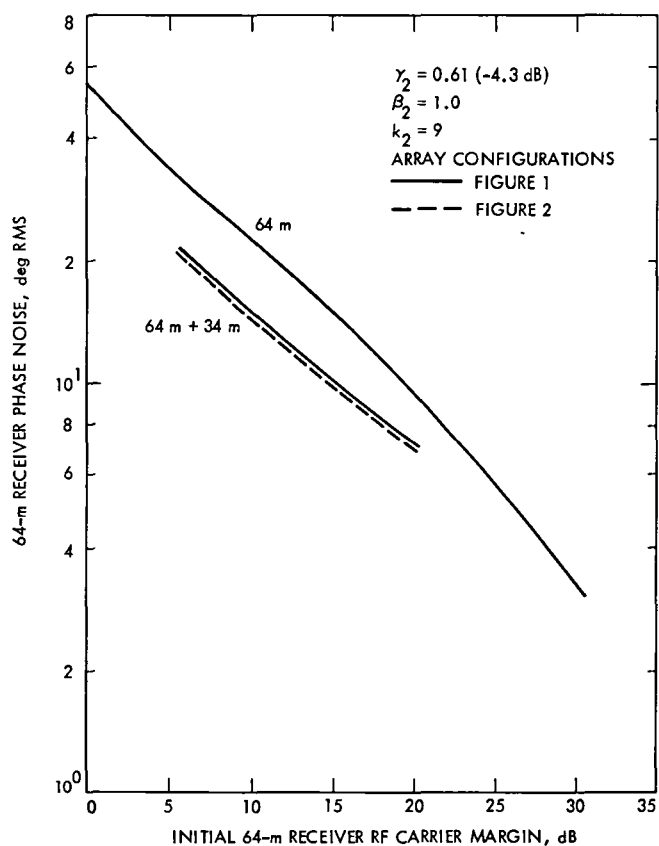


Fig. 3. 64-m receiver by itself and with enhanced RF carrier margin improvement. RF carrier tracking loop phase noise vs initial 64-m receiver carrier margin. Two receiving systems arrayed: 64-m and 34-m diameter high efficiency (listen only) ($2B_{L_{o1}} = 30$ Hz).

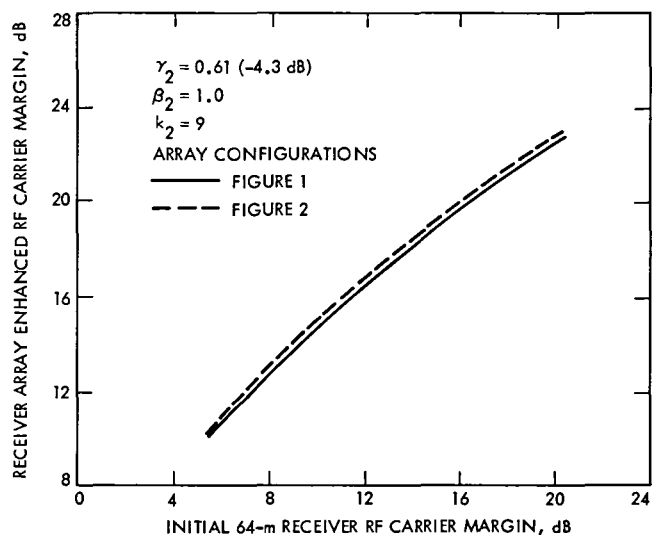


Fig. 4. Receiver array enhanced RF carrier margin vs initial 64-m receiver carrier margin. Two receiving systems arrayed: 64-m and 34-m diameter high-efficiency (listen only) ($2B_{L_{o1}} = 30$ Hz).

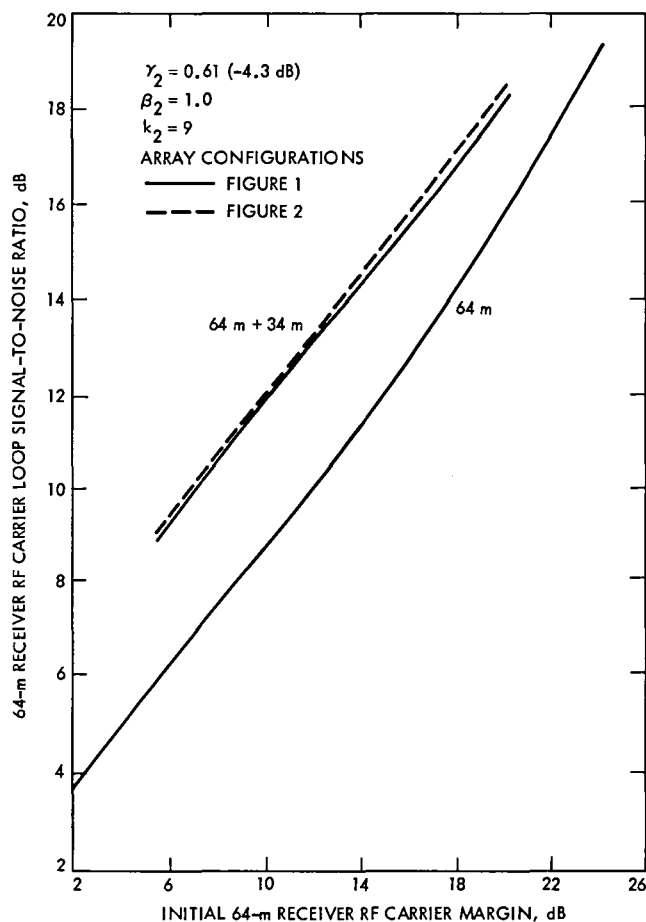


Fig. 5. 64-m receiver by itself and with enhanced RF carrier margin improvement. RF carrier tracking loop signal-to-noise ratio vs initial 64-m receiver carrier margin. Two receiving systems arrayed: 64-m and 34-m diameter high efficiency (listen only) ($2B_{L_{o1}} = 30$ Hz).

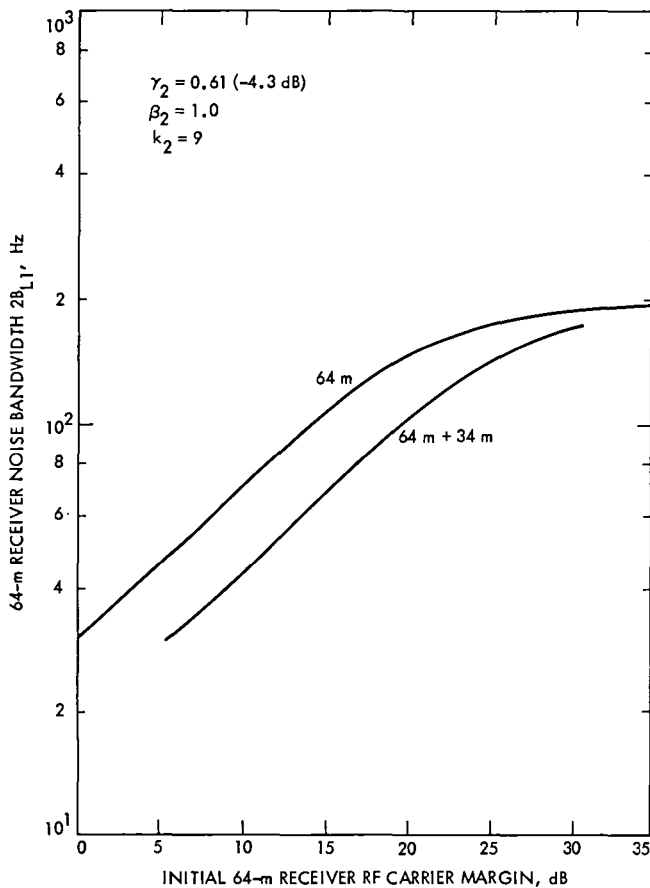


Fig. 6. 64-m receiver by itself and with enhanced RF carrier margin improvement. RF carrier tracking loop two-sided closed loop noise bandwidth vs initial 64-m receiver carrier margin. Two receiving systems arrayed: 64-m and 34-m diameter high-efficiency (listen only) ($2B_{L_{01}} = 30$ Hz).

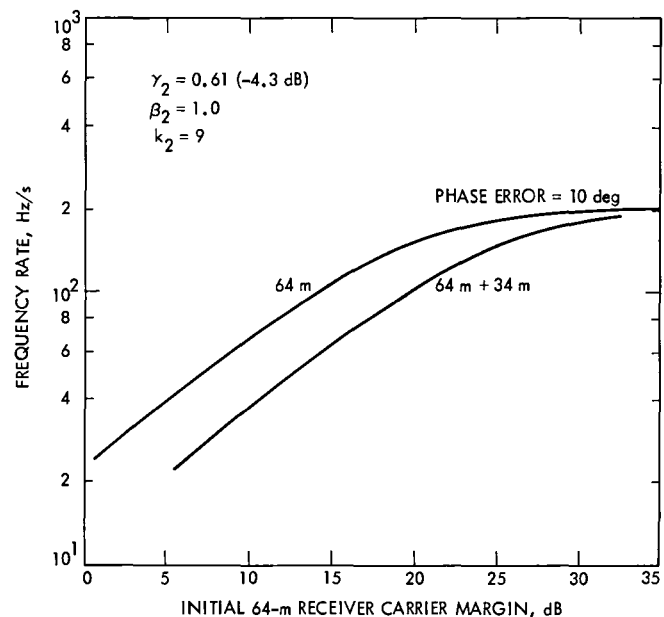


Fig. 7. 64-m receiver by itself and with enhanced RF carrier margin improvement. Frequency rate capability vs initial 64-m receiver carrier margin. Two receiving systems arrayed: 64-m and 34-m diameter high-efficiency (listen only) ($2B_{L_{01}} = 30$ Hz).

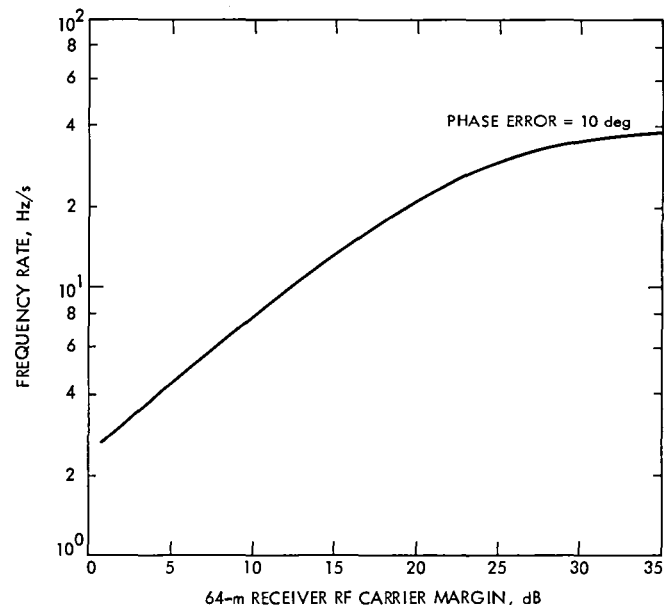


Fig. 8. 64-m receiver frequency rate capability vs RF carrier margin ($2B_{L_{01}} = 10$ Hz).

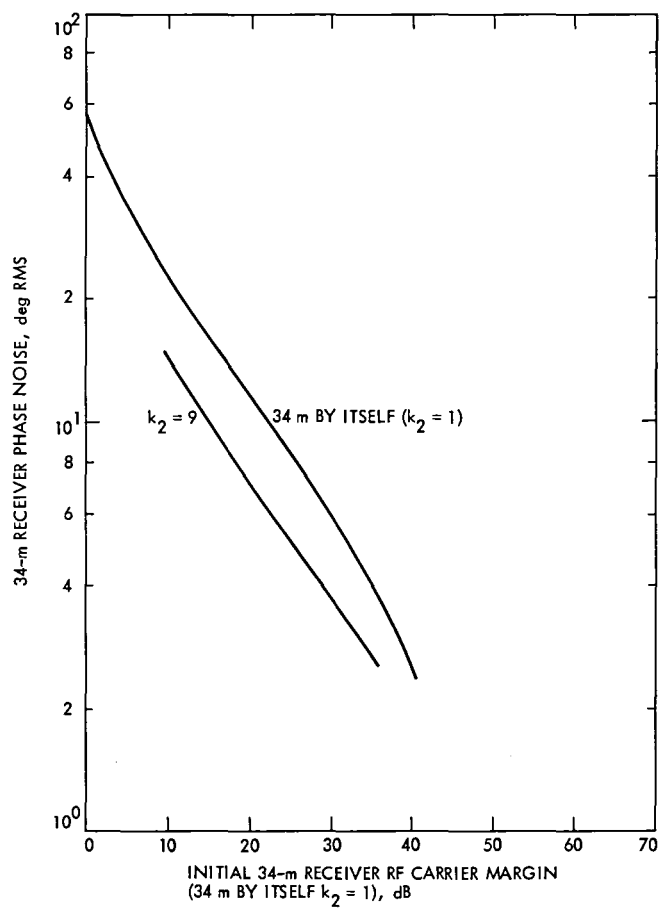


Fig. 9. 34-m receiver RF carrier tracking loop phase noise vs initial 34-m receiver carrier margin (34-m by itself $k_2 = 1$) ($2B_{L_{02}} = 1.0$ Hz).

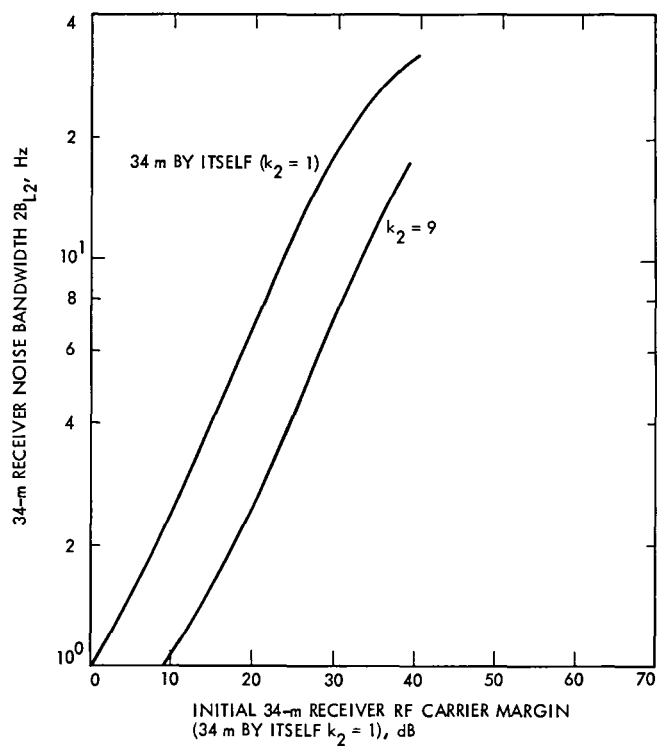


Fig. 10. 34-m receiver RF carrier tracking loop two sided closed loop noise bandwidth vs initial 34-m receiver carrier margin (34 m by itself $k_2 = 1$) ($2B_{L_{02}} = 1.0$ Hz).

Performance Characteristics for an Array of Two Receiving Systems With Equal Apertures and Enhanced Radio Frequency Carrier Margin Improvement

M. H. Brockman

Telecommunications Science and Engineering Division

Enhanced radio frequency carrier margin improvement for arrayed receiving systems for coherent reception of phase modulated signals with residual carrier provides a significant reduction in carrier loop phase noise and an increase in the signal-to-noise ratio in the RF carrier tracking loop with an attendant reduction in telemetry radio loss. A significant increase in doppler frequency rate capability is also realized relative to operating at a narrower tracking loop bandwidth to obtain the same carrier sensitivity improvement. This report examines these performance characteristics for an array of two receiving systems with equal apertures and statistically independent prediction noise.

I. Introduction

A technique for providing enhanced radio frequency carrier margin improvement at low carrier margins has been described, and expected performance has been presented for a selected array of receiving systems with unequal apertures in Refs. 1 and 2. This report provides performance information for enhanced radio frequency carrier margin improvement for coherent carrier reception and demodulation of phase modulated signals with residual carrier for an array of two receiving systems with equal antenna apertures. Performance characteristics are presented that show RF carrier tracking loop phase noise reduction and signal-to-noise ratio improvement as well as enhanced RF carrier margin improvement. The performance presented herein is representative of a 34 meter-diameter high efficiency (listen only) antenna receiving system arrayed with a 34 meter-diameter antenna receiving system with transmit and receive capability. Comparative performance is discussed for the array and also to illustrate the increase in doppler rate capability for the two-receiver array relative to switching to a narrower tracking loop bandwidth with a single 34 meter-diameter receiving system. In addition, comparative RF carrier

performance is discussed for the two receiving system arrays (with 34-meter-diameter antennas) relative to a 64-meter-diameter antenna receiving system. In this report, the various components of operating system temperature (T_{op}) are treated as statistically independent for the two receiving systems of the array. A considerable portion of the following material in Section II and III of this report was presented in Ref. 1 and is included here for continuity of discussion.

II. Receiver Configuration

Figure 1 illustrates a method for achieving RF carrier arraying. A modification of Fig. 1 (so that much larger antenna separation for the array can be handled conveniently) was presented in Ref. 3 with a discussion of predetection noise resulting from operating equivalent system noise temperature T_{op} . Figure 2 illustrates a second configuration that provides additional filtering of receiving system 2 (through N) local oscillator phase noise which couples into receiving system 1 via the RF carrier summing junction. Consequently, Fig. 2 generally provides an increase in carrier margin relative to Fig. 1.

The received signal is an RF carrier (ω_{RF}) phase modulated with a square-wave subcarrier (ω_{sc}) at a peak modulation index m_{pd} that is, in turn, biphas modulated with data $D(t)$.

$$\underbrace{2^{1/2} A \cos m_{pd} \cos \omega_{RF} t}_{\text{carrier}} + \underbrace{2^{1/2} A \sin m_{pd} \times D(t) \times \cos(\omega_{sc} t) \times \sin \omega_{RF} t + n(t)}_{\text{sidebands}} \quad (1)$$

The term $n(t)$ represents receiver noise which has a double-sided noise spectral density $N_o/2$.

III. Predetection Signal-to-Noise Ratio and RF Carrier Tracking Loop Phase Noise and Signal-to-Noise Ratio

The improvement in predetection carrier power-to-noise spectral density in receiving system 1 for two receiving systems arrayed (η_2) is

$$\eta_2 = \frac{\left[1 + \beta_2 \gamma_2 \left(\frac{N_{o2}}{N_{o1}} \right)^{1/2} \right]^2}{\left[1 + \frac{N_{o2}}{N_{o1}} \beta_2^2 \right]} \quad (2)$$

where β_2 is the voltage coupling of receiving system 2 relative to receiving system 1 at the summing junction. The term γ_2^2 is the ratio of the carrier power-to-noise spectral density ratio of receiving system 2 relative to the carrier power-to-noise spectral density ratio of receiving system 1. Receiving system 1 has a double-sided noise spectral density $N_{o1}/2$ related to T_{op1} and receiving system 2 has a double-sided noise spectral density $N_{o2}/2$ related to T_{op2} . Note that for N receiving systems

$$\eta_N = \frac{\left[1 + \beta_2 \gamma_2 \left(\frac{N_{o2}}{N_{o1}} \right)^{1/2} + \dots + \beta_N \gamma_N \left(\frac{N_{oN}}{N_{o1}} \right)^{1/2} \right]^2}{\left[1 + \frac{N_{o2}}{N_{o1}} \beta_2^2 + \dots + \frac{N_{oN}}{N_{o1}} \beta_N^2 \right]} \quad (3)$$

Consider the RF carrier phase tracking loop in receiving system 1 for the situation where the predetection IF filters F_{A2} through F_{AN} in receiving systems 2 through N have k times the noise bandwidth of predetection filter F_{A1} in receiving system 1. The RF carrier tracking loop is a second-order phase tracking loop which includes a bandpass limiter and a sinusoidal phase detector. With receiving system 1 only connected to the summing junction, the resultant rms phase noise

(σ_{ϕ_n}) at the output of the RF carrier tracking loop (i.e., on the first local oscillator) becomes (Ref. 2, Expression 4b):

$$\sigma_{\phi_n} = \frac{\frac{N_{o1}}{2} \cdot 2B_{L1}}{P_{c1}} \times \left[\frac{1 + \frac{P_{c1}}{NBW_{F_{A1}} \cdot N_{o1}}}{0.862 + \frac{P_{c1}}{NBW_{F_{A1}} \cdot N_{o1}}} \cdot \frac{\exp\left(\frac{N_{o1} B_{L1}}{P_{c1}}\right)}{\sinh\left(\frac{N_{o1} B_{L1}}{P_{c1}}\right)} \right]^{1/2} \quad (4)$$

radians, rms

where $P_{c1}/(NBW_{F_{A1}} \cdot N_{o1})$ is the RF carrier signal-to-noise power ratio at the input to the bandpass limiter in the carrier phase tracking loop. The term $NBW_{F_{A1}}$ represents the noise bandwidth of predetection IF filter F_{A1} in receiving system 1. The two-sided closed-loop noise bandwidth can be expressed as:

$$2B_{L1} = \frac{2B_{Lo1}}{r_o + 1} \left(1 + r_o \frac{\alpha_1}{\alpha_{o1}} \right) \quad (5)$$

where $r_o = 2$ by design at design point (0.707 damping) and $2B_{Lo1}$ is the design point (threshold) two-sided closed-loop noise bandwidth in receiving system 1. The term α_1 is the limiter suppression factor resulting from the noise-to-carrier power ratio due to $NBW_{F_{A1}}$ at the input to the bandpass limiter. The suppression factor α_1 has a value of α_{o1} at design point (threshold). At threshold, the predetection carrier-to-noise power ratio in a noise bandwidth equal to $2B_{Lo1}$ is unity (i.e., $P_c/(2B_{Lo} \cdot N_o) = 1$).

With receiving systems 1 and 2 connected to the summing junction, the RF carrier signal-to-noise power ratio at the input to the bandpass limiter is (Ref. 2, Expression 6)

$$\frac{P_{c1 \Sigma 1,2}}{P_{n1 \Sigma 1,2}} = \frac{(A_1 \cos m_{pd} + \beta_2 A_2 \cos m_{pd})^2}{\left[NBW_{F_{A1}} \cdot N_{o1} + \beta_2^2 NBW_{F_{A2}} \cdot N_{o2} \right]} \quad (6)$$

where m_{pd} is the peak phase modulation index, and $NBW_{F_{A2}} = k_2 \cdot NBW_{F_{A1}}$. Expression (6) can be rewritten as:

$$\frac{P_{c1 \Sigma 1,2}}{P_{n1 \Sigma 1,2}} = \frac{P_{c1}}{NBW_{F_{A1}} \cdot N_{o1}} \cdot \frac{\left[1 + \beta_2 \gamma_2 \left(\frac{N_{o2}}{N_{o1}} \right)^{1/2} \right]^2}{\left[1 + \frac{N_{o2}}{N_{o1}} \beta_2^2 k_2 \right]} \quad (7)$$

The change in RF carrier signal-to-noise power ratio at the input to the bandpass limiter in receiving system 1 is then:

$$\Delta_2 = \frac{\left[1 + \beta_2 \gamma_2 \left(\frac{N_{o2}}{N_{o1}}\right)^{1/2}\right]^2}{\left[1 + \frac{N_{o2}}{N_{o1}} \beta_2^2 k_2\right]} \quad (8)$$

The limiter suppression factor due to the change in noise-to-carrier power ratio becomes $\alpha_{1\Delta 2}$ which provides a two-sided closed-loop noise bandwidth:

$$2B_{L1\Delta 2} = \frac{2B_{L01}}{r_o + 1} \left(1 + r_o \frac{\alpha_{1\Delta 2}}{\alpha_{o1}}\right) \quad (9)$$

The resultant rms phase noise at the output of the RF carrier tracking loop (i.e., on the first local oscillator in receiving system 1) becomes:

$$\sigma_{\phi_{n1\Sigma 1,2}} = \frac{\frac{N_{o1}}{2} \cdot 2B_{L1\Delta 2}}{P_{c1}} \cdot \frac{1}{\eta_2} \times \left[\frac{1 + \frac{P_{c1} \cdot \Delta_2}{NBW_{FA1} \cdot N_{o1}}}{0.862 + \frac{P_{c1} \cdot \Delta_2}{NBW_{FA1} \cdot N_{o1}}} \cdot \frac{\exp\left(\frac{N_{o1} \cdot B_{L1\Delta 2}}{P_{c1} \cdot \eta_2}\right)}{\sinh\left(\frac{N_{o1} \cdot B_{L1\Delta 2}}{P_{c1} \cdot \eta_2}\right)} \right]^{1/2} \quad \text{rad, rms} \quad (10)$$

Note that the total rms phase noise at the output of the RF carrier tracking loop (i.e., on the first local oscillator) in receiving system 1 for Fig. 1 is:

$$\left[\sigma_{\phi_{n1\Sigma 1,2}}^2 + \left(\frac{\beta_2 \sigma_{\phi_{n2}}}{1 + \beta_2}\right)^2 \right]^{1/2} \quad (11)$$

In Fig. 2, additional filtering of the output rms phase noise $\sigma_{\phi_{n2}}$ is provided by the local oscillator tracking loop in receiving system 2. Designate the additionally filtered rms phase noise as $\sigma'_{\phi_{n2}}$ which is less than $\sigma_{\phi_{n2}}$ by the square root of the ratio of local oscillator tracking loop noise bandwidth to $2B_{L2}$. Consequently for Fig. 2, $\sigma'_{\phi_{n2}}$ is substituted into expression (11) in place of $\sigma_{\phi_{n2}}$. Note that since receiving system 2 has the same first local oscillator as receiving system 1, receiving system 2 has effectively the same RF carrier characteristics and sensitivity as receiving system 1.

The rms phase noise (Expression [11]) represents a different RF carrier margin when compared to $\sigma_{\phi_{n1}}$ for receiving system 1 alone (Expression [4]). The change in RF carrier margin represents the enhanced carrier margin improvement for two receiving systems arrayed.

The RF carrier phase tracking loop in receiving system 2 is also a second-order phase tracking loop ($r_o = 2$) which utilized a bandpass limiter and sinusoidal phase detector. Since the closed loop noise bandwidth of the carrier phase tracking loop for receiving systems 2 through N is much narrower (by design) than that in receiving system 1, phase noise in receiving system 1 carrier tracking loop produces a reduction in predetection signal-to-noise ratio for receiving systems 2 through N . The resultant predetection carrier signal-to-noise ratio in receiving system 2 for two systems arrayed is then

$$\frac{P_{c2\Sigma 1,2}}{P_{n2}} = \frac{P_{c2} \left(1 - \frac{\sigma_{\phi_{n1\Sigma 1,2}}^2}{2}\right)^2}{NBW_{FA2} \cdot N_{o2}} \quad (12)$$

which produces an rms phase noise

$$\sigma_{\phi_{n2\Sigma 1,2}} = \frac{\frac{N_{o2}}{2} \cdot 2B_{L2}}{P_{c2\Sigma 1,2}} \times \left[\frac{1 + \frac{P_{c2\Sigma 1,2}}{NBW_{FA2} \cdot N_{o2}}}{0.862 + \frac{P_{c2\Sigma 1,2}}{NBW_{FA2} \cdot N_{o2}}} \cdot \frac{\exp\left(\frac{N_{o2} \cdot B_{L2}}{P_{c2\Sigma 1,2}}\right)}{\sinh\left(\frac{N_{o2} \cdot B_{L2}}{P_{c2\Sigma 1,2}}\right)} \right]^{1/2} \quad \text{rad, rms} \quad (13)$$

Consider the signal-to-noise ratio (SNR) of the RF carrier phase tracking loop in receiving system 1. Using the linear theoretical model (Refs. 4 and 5), the RF carrier tracking loop SNR (ρ_{L1}) for receiving system 1 by itself is:

$$\rho_{L1} = \frac{P_{c1}}{N_{o1} B_{L1} \Gamma_1} \quad (14)$$

where Γ_1 is the bandpass limiter performance factor:

$$\Gamma_1 = \frac{1 + \frac{P_{c1}}{NBW_{FA1} N_{o1}}}{0.862 + \frac{P_{c1}}{NBW_{FA1} N_{o1}}} \quad (15)$$

With receiving system 1 and 2 connected to the summing junction, the RF carrier tracking loop SNR in receiving system 1 for the array is:

$$\rho_{L1\Sigma 1,2} = \frac{P_{c2} \eta_2}{N_{o1} B_{L1\Delta 2} \Gamma_{1\Delta 2}} \quad (16)$$

where

$$\Gamma_{1\Delta 2} = \frac{1 + \frac{P_{c1} \cdot \Delta_2}{NBW_{FA1} \cdot N_{o1}}}{0.862 + \frac{P_{c1} \cdot \Delta_2}{NBW_{FA1} \cdot N_{o1}}} \quad (17)$$

IV. Performance

Performance characteristics are presented in this report for an array of two receiving systems which are representative of a 34 meter-diameter high efficiency (listen only) antenna receiving system and a 34 meter-diameter antenna receiving system with transmit and receive capability. The sets of design parameters for receiving system 1 are:

Threshold Two-Sided Noise Bandwidth		
$2B_{Lo1}$	2.0	48 Hz
Predetection IF Filter Noise Bandwidth		
NBW_{FA1}	2200	2200 Hz

while the corresponding set of parameters for receiving system 2 are:

Threshold Two-Sided Noise Bandwidth		
$2B_{Lo2}$	1	1 Hz
Predetection IF Filter Noise Bandwidth		
NBW_{FA2}	$k_2 \cdot NBW_{FA1}$	$k_2 \cdot NBW_{FA1}$
Local Oscillator Tracking Loop Two-Sided Noise Bandwidth (Fig. 2)		
	1	1 Hz

Performance is presented for the case where receiving system 1 of the array represents a 34-meter-diameter high efficiency

antenna and also for the case where receiving system 1 of the array represents a 34 meter-diameter antenna with transmit and receive capability.

Consider first the case where receiving system 1 is representative of a 34 meter-diameter high efficiency (listen only) antenna and receiving system 2 is representative of a 34-meter-diameter transmit and receive antenna. For this situation, $\gamma_2 = 0.88$ (-1.11 dB) and the ratio of noise spectral densities (N_{o2}/N_{o1}) (of receiving system 2 relative to receiving system 1) is 1.16 (21.5k/18.5k). Figure 3 shows the rms phase noise $\sigma_{\phi n1}$ at the output of the RF carrier phase tracking loop (i.e., on the first local oscillator) for receiving system 1 by itself as a function of initial RF carrier margin (carrier level above design point) for $2B_{Lo1} = 12$ Hz as calculated from Eq. (4) in Section III. Figure 3 also shows the total rms phase noise (Eq. [11]) at the output of the RF carrier tracking loop in receiving system 1 for the array of receiving systems 1 and 2 for $k_2 = 3.5$ and 9 with $\beta_2 = 1.0$. Total rms phase noise is shown for array configurations that are representative of Figs. 1 and 2.

In Fig. 3, note that with receiving system 1 by itself (prior to arraying) initially at 5 dB above design point threshold (carrier margin), the rms phase noise for the array ($k_2 = 3.5$) is 23.8 and 23.3 degrees respectively for array configurations representative of Figs. 1 and 2. These rms phase noise values represent an enhanced RF carrier margin of 9.3 and 9.6 dB respectively when compared to the phase noise characteristics of system 1 by itself. This corresponds to an improvement in receiving system 1 carrier margin of 4.3 and 4.6 dB respectively for $k_2 = 3.5$ (see Fig. 4). The corresponding performance values for the array, with $k_2 = 9$ and an initial carrier margin of 5 dB for receiving system 1, are 20.2 and 19.9 degrees rms phase noise at the output of the RF carrier tracking loop for receiving system 1 which represents an enhanced RF carrier margin of 11.5 and 11.7 dB respectively for array configurations representative of Figs. 1 and 2. This corresponds to an improvement in the receiving system 1 carrier margin of 6.5 and 6.7 dB respectively for $k_2 = 9$, (see Fig. 4). Continuing as above, Fig. 4 shows enhanced RF carrier margin improvement for receiving system 1 as a function of initial RF carrier margin for $k_2 = 3.5$ and 9 with $2B_{Lo1} = 12$ Hz.

It should be noted, in Fig. 4, that at a 5 dB initial RF carrier margin for receiving system 1 (by itself) and with receiving systems 1 and 2 arrayed ($k_2 = 9$), the two-sided closed loop noise bandwidth $2B_{L1\Delta 2}$ (Eq. [9]) of the RF carrier tracking loop in receiving system 1 is 12 Hz (design point noise bandwidth). With $k_2 = 3.5$, $2B_{L1\Delta 2}$ for receiving system 1 is 12 Hz at slightly less than a 2 dB initial RF carrier margin for receiving system 1 by itself prior to arraying. At

this 2 dB initial RF carrier margin, the enhanced RF carrier margin for the array ($k_2 = 3.5$) is 6.2 dB (2 + 4.2 dB) and carrier cycle slipping will occur in the RF carrier phase tracking loop. The recommended minimum DSN RF carrier margin is 10 dB which occurs at an initial RF carrier margin for receiving system 1 (by itself) of 5.7 dB. Figure 5 shows the effect of varying the voltage coupling β_2 of receiving system 2 relative to receiving system 1 at the summing junction on enhanced RF carrier margin improvement ($2B_{L_{o1}} = 12$ Hz) for $k_2 = 3.5$ and 9 with a 10 dB initial RF carrier margin for receiving system 1 (prior to arraying).

Consider next the signal-to-noise ratio (SNR) of the RF carrier phase tracking loop in receiving system 1 for this first case. Figure 6 shows the RF carrier loop SNR for receiving system 1 by itself (ρ_{L1}) as a function of initial RF carrier margin as calculated from Eq. (14) above for $2B_{L_{o1}} = 12$ Hz. Note the interrelationship provided by Figs. 3 and 6 between rms phase noise at the output of the RF carrier tracking loop and the tracking loop SNR. Using this relationship, the total rms phase noise (Eq. [11]) at the output of the RF carrier tracking loop in receiving system 1 for the two receiving system array provides the RF carrier loop SNR in receiving system 1 also shown in Fig. 6 for array configurations representative of Figs. 1 and 2 for $k_2 = 3.5$ and 9 with the design parameters discussed above. The RF carrier loop SNR for receiving system 1 with the two receiving system array calculated from Eq. (16) above provides essentially the same characteristics as the array configuration representative of Fig. 2 due to the additional local oscillator filtering in receiving system 2. At an initial RF carrier margin of 2 dB for $k_2 = 3.5$ and 5 dB for $k_2 = 9$, the RF carrier loop SNR calculated from Eq. (16) is 0.2 dB greater than the carrier loop SNR for the array configuration representative of Fig. 2. This difference decreases to zero at about a 10 dB RF carrier margin. Note the 2.6 dB and 2.8 dB improvement in the system 1 receiver RF carrier tracking loop signal-to-noise ratio for $k_2 = 3.5$ in Fig. 6 for the two receiving system array relative to system 1 by itself initially at 5 dB above design point (carrier margin). The corresponding improvement in the system 1 receiver RF carrier tracking loop SNR is 4.1 dB and 4.3 dB for $k_2 = 9$.

Figures 7, 8 and 9 show performance characteristics (which are similar to Figs. 3, 4 and 6) for the same array as above with $2B_{L_{o1}} = 48$ Hz and $\beta_2 = 1.0$ for $k_2 = 3.5$ and 9. In this case ($2B_{L_{o1}} = 48$ Hz), the RF carrier loop SNR calculated from Eq. (16) above provides the same characteristic in Fig. 9 as the array configuration representative of Fig. 2 due to the additional local oscillator filtering in receiving system 2.

Consider the second case where receiving system 1 is representative of a 34 meter-diameter transmit and receive antenna

and receiving system 2 is representative of a 34 meter-diameter high efficiency (listen only) antenna. For this case, $\gamma_2 = 1.14$ (+1.11 dB) and the ratio of noise spectral densities (N_{o2}/N_{o1}) is 0.86. Figure 10 shows the rms phase noise for receiving system 1 by itself as a function of initial RF carrier margin and for the array of receiving systems 1 and 2 for $k_2 = 3.5$ and 9, $2B_{L_{o1}} = 12$ Hz and $\beta_2 = 1.6$ (as calculated from Eqs. [4] and [11]) with array configurations that are representative of Figs. 1 and 2. Figure 11 shows the resulting enhanced RF carrier margin improvement for receiving system 1 (similar to Fig. 4) for this array. In Fig. 11, with system 1 by itself initially at a 5 dB carrier margin, the improvement in the receiving system 1 carrier margin is 5.9 and 6.2 dB respectively with $k_2 = 3.5$ for array configurations representative of Figs. 1 and 2. The corresponding improvement in receiving system 1 carrier margin is 7.9 and 8.2 dB with $k_2 = 9$. Figure 12 shows the effect (for this array) of varying the voltage coupling β_2 of receiving system 2 relative to receiving system 1 at the summing junction on enhanced RF carrier margin improvement ($2B_{L_{o1}} = 12$ Hz) for $k_2 = 3.5$ and 9 with a 10 dB initial RF carrier margin for receiving system 1 (prior to arraying). The signal-to-noise ratio (SNR) of the RF carrier phase tracking loop in receiving system 1 for this second case is shown in Fig. 13 (see discussion relative to Fig. 6). In Fig. 13, the improvement in the system 1 receiver RF carrier tracking loop SNR for $k_2 = 3.5$ is 3.5 and 3.7 dB for the two receiving system array relative to system 1 by itself initially at 5 dB carrier margin. The corresponding improvement in the system 1 receiver RF carrier tracking loop SNR is 4.8 and 5 dB for $k_2 = 9$.

Figures 14, 15 and 16 show performance characteristics (which are similar to Figs. 10, 11 and 13) for the same (second case) array as above with $2B_{L_{o1}} = 48$ Hz and $\beta_2 = 1.6$ for $k_2 = 3.5$ and 9. The RF carrier loop SNR calculated from Eq. (16) in Section III provides the same characteristics in Fig. 16 as the array configuration representative of Fig. 2 due to the additional local oscillator filtering in receiving system 2.

Initial measurements of enhanced carrier margin improvement have been made in the laboratory with $\gamma_2 = 1$. The measurement was made with a predetection filter noise bandwidth of 2200 Hz with a $2B_{L_{o1}}$ of 152 Hz for system 1 and a $2B_{L_{o2}}$ of 1 Hz with $k_2 = 3.5$ for system 2 with $N_{o2}/N_{o1} = 1$. Measured RF carrier margin improvement was 3.2 dB at an initial RF carrier margin of 14.5 dB for receiving system 1 (prior to arraying) with $\beta_2 = 0.9$. Predicted performance is 3.35 dB. At this same 14.5 dB initial RF carrier margin, measured carrier margin improvement was 2.4 dB for $\beta_2 = 0.54$ while predicted performance is 2.7 dB. Description of the Laboratory measurement technique was presented in Ref. 6.

V. Discussion

Performance characteristics for an array of two receiving systems with equal antenna apertures for $k_2 = 3.5$ and 9 are presented in this report that show RF carrier tracking loop phase noise reduction and signal-to-noise ratio improvement as well as enhanced RF carrier margin improvement. The two receiving systems are representative of a 34 meter-diameter high efficiency (listen only) antenna receiving system and a 34 meter-diameter antenna receiving system with transmit and receive capability. The performance presented with the figures and accompanying discussion in the preceeding section of this report for $2B_{L_{o1}} = 12$ and 48 Hz show that receiving system 1 of the array can be representative of either the 34 meter-diameter high efficiency (listen only) antenna or the 34 meter-diameter antenna with transmit and receive capability.

With system 1 of the array representative of a 34 meter-diameter high efficiency antenna receiving system (first case), the array has a minimum received RF carrier level capability that is 1.1 dB more sensitive than for the second case with the 34 meter-diameter antenna receiving system with transmit and receive capability as system 1. However, comparison of Figs. 4 and 11 for $2B_{L_{o1}} = 12$ Hz and of Figs. 8 and 15 for $2B_{L_{o1}} = 48$ Hz at equal input signal levels above minimum carrier level capability show that the array for the second case has up to 0.6 dB greater RF carrier margin than for the first case. Note that reception of the same signal represents 1.1 dB less initial RF carrier margin for case 2 relative to case 1. Also, comparison of Figs. 6 and 13 for $2B_{L_{o1}} = 12$ Hz and of Figs. 9 and 16 for $2B_{L_{o1}} = 48$ Hz at equal input signal levels show that the array for the second case has up to 0.4 dB greater RF carrier tracking loop signal-to-noise ratio than for the first case.

As discussed in Refs. 1 and 2, the reduction in rms phase noise on the first local oscillator (System 1) for the two system receiver array raises the point of switching to a narrow bandwidth in the RF carrier tracking loop to accomplish reduction in rms phase noise and achieve essentially the same carrier margin improvement with a single receiving system. Consider operation of the array with $2B_{L_{o1}} = 48$ Hz compared to operation of a single 34 meter-diameter antenna receiving system by itself with $2B_{L_o} = 12$ Hz. Operation of the receiving system by itself at a $2B_{L_o} = 12$ Hz relative to operation with $2B_{L_o} = 48$ Hz improves the carrier margin by 48/12 or 6 dB. Consequently, operation of the receiving system with $2B_{L_o} = 12$ Hz at a 11 dB RF carrier margin corresponds to operation with $2B_{L_o} = 48$ Hz at a 5 dB initial carrier margin. At a 11 dB carrier margin ($2B_{L_o} = 12$ Hz), the single receiving system has a RF carrier doppler rate capability of 12.4 Hz/sec for a 10 degree phase error in the RF carrier tracking loop (Fig. 17). With the same receiving system as system 1 of a two system array (presented herein) operating with a $2B_{L_{o1}} = 48$ Hz at an initial carrier margin of 5 dB, the doppler rate

capability for a 10 degree phase error (due to doppler rate) is 85 Hz/sec for $k_2 = 3.5$ and 57 Hz/sec for $k_2 = 9$ (Fig. 18). The 85 Hz/sec for $k_2 = 3.5$ represents a 6.8 times improvement in doppler rate capability while the improvement is 4.6 times for $k_2 = 9$ relative to the single system with $2B_{L_o} = 12$ Hz.

A preliminary comparison of RF carrier performance can also be made between the two receiving system arrays with 34 meter-diameter antennas described above ($2B_{L_{o1}} = 12$ or 48 Hz) and a 64 meter-diameter antenna receiving system operating by itself with $2B_{L_{o1}} = 10$ or 30 Hz (Ref. 1). It should be noted that reception of the same signal by the 34-meter and 64-meter receivers represents the following relative RF carrier margins. An array with a 34-meter-diameter high efficiency antenna for receiving system 1 ($2B_{L_{o1}} = 12$ Hz) has 5.2 dB less initial RF carrier margin (system 1) than a 64 meter-diameter antenna receiving system ($2B_{L_o} = 10$ Hz). This difference in RF carrier margin becomes 6.5 dB for $2B_{L_{o1}} = 48$ Hz (system 1) and $2B_{L_o} = 30$ Hz (64 m). An array with a 34-meter-diameter antenna with transmit and receive capability for receiving system 1 ($2B_{L_{o1}} = 12$ Hz) has 6.3 dB less initial RF carrier margin (system 1) than a 64-meter-diameter receiving system ($2B_{L_o} = 10$ Hz). This difference in RF carrier margin becomes 7.6 dB for $2B_{L_{o1}} = 48$ Hz (system 1) and $2B_{L_o} = 30$ Hz (64 m). The following comparison applies down to a minimum RF carrier level which provides an initial 5 dB carrier margin for receiving system 1 of the array.

Consider the situation where doppler rate is small enough so that it is not a primary consideration. With receiving system 1 of the array representative of either of the 34-meter-diameter antennas, $k_2 = 9$ and $2B_{L_{o1}} = 12$ Hz, the array would provide improved (1 to 2 dB) performance (lower RF carrier loop rms phase noise and higher RF carrier tracking loop signal-to-noise ratio) relative to a 64-meter-diameter antenna receiving system ($2B_{L_{o1}} = 10$ Hz). With $2B_{L_{o1}} = 12$ Hz and $k_2 = 3.5$, the array with either 34-m antenna as system 1 would provide slightly reduced performance (fraction of a dB less) relative to a 64-meter-diameter antenna receiving system ($2B_{L_{o1}} = 10$ Hz). With $k = 9$ and $2B_{L_{o1}} = 48$ Hz, the array with either 34-m antenna as system 1 would provide equivalent performance (essentially equal RF loop rms phase noise and RF loop SNR) to a 64-meter-diameter antenna receiving system ($2B_{L_o} = 30$ Hz). With $2B_{L_{o1}} = 48$ Hz and $k_2 = 3.5$, the array would provide reduced performance (1 to 2 dB less) relative to a 64-meter-diameter antenna receiving system ($2B_{L_o} = 30$ Hz).

Next consider the situation where doppler rate is a prime consideration. With receiving system 1 of the array representative of either of the 34-meter-diameter antennas, $k_2 = 3.5$ and $2B_{L_{o1}} = 48$ Hz, the array would provide essentially the

same doppler rate capability as a 64-meter-diameter antenna receiving system ($2B_{Lo} = 30$ Hz — Ref. 1, Fig. 7). With $2B_{Lo1} = 48$ Hz and $k_2 = 9$, the array would provide about 2/3 the doppler rate capability of a 64-meter-diameter antenna

receiving system ($2B_{Lo} = 30$ Hz). With $2B_{Lo1} = 12$ Hz, the array would provide about 2/3 ($k_2 = 3.5$) and about 1/2 ($k_2 = 9$) the doppler rate capability of a 64-meter-diameter antenna receiving system ($2B_{Lo} = 10$ Hz).

References

1. Brockman, M. H., "Performance Characteristics for an Array of Two Receiving Systems with Unequal Predetection Signal-to-Noise Ratios and Enhanced Radio Frequency Carrier Margin Improvement," *TDA Progress Report 42-84*, Jet Propulsion Laboratory, Pasadena, California, February 15, 1986.
2. Brockman, M. H., "Enhanced Radio Frequency Carrier Margin Improvement for an Array of Receiving Systems with Unequal Predetection Signal-to-Noise Ratios," *TDA Progress Report 42-76*, pp. 170-188, Jet Propulsion Laboratory, Pasadena, California, February 15, 1984.
3. Brockman, M. H., "The Effect of Partial Coherence in Receiving System Noise Temperature on Array Gain for Telemetry and Radio Frequency Carrier Reception for Similar Receiving Systems," *TDA Progress Report 42-66*, pp. 219-235, Jet Propulsion Laboratory, Pasadena, California, December 15, 1981.
4. Tausworthe, R. C., "Limiters in Phase-Locked Loops: A Correction to Previous Theory," *Space Programs Summary No. 37-54*, Vol. III, pp. 201-203, Jet Propulsion Laboratory, Pasadena, California, 1968.
5. Divsalar, D., and Yuen, J. H., "Improved Carrier Tracking Performance with Coupled Phased-Locked Loops," *TDA Progress Report 42-66*, pp. 148-171, Jet Propulsion Laboratory, Pasadena, California, December 15, 1981.
6. Brockman, M. H., "The Effect of Partial Coherence in Receiving System Noise Temperature on Array Gain for Telemetry and Radio Frequency Carrier Reception for Receiving Systems with Unequal Predetection Signal-to-Noise Ratios," *TDA Progress Report 42-72*, pp. 95-117, Jet Propulsion Laboratory, Pasadena, California, February 15, 1983.

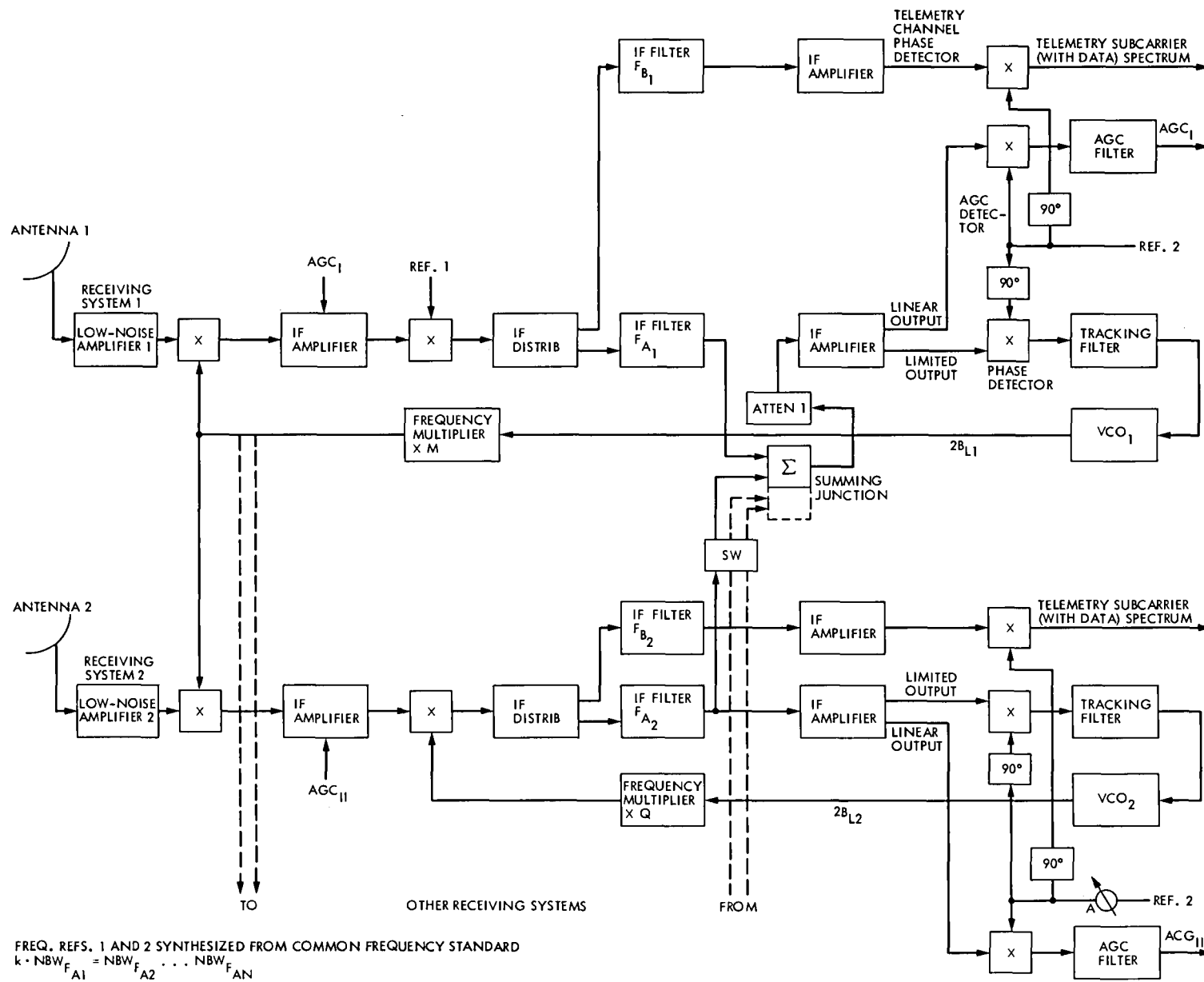


Fig. 1. Enhanced radio frequency carrier arraying

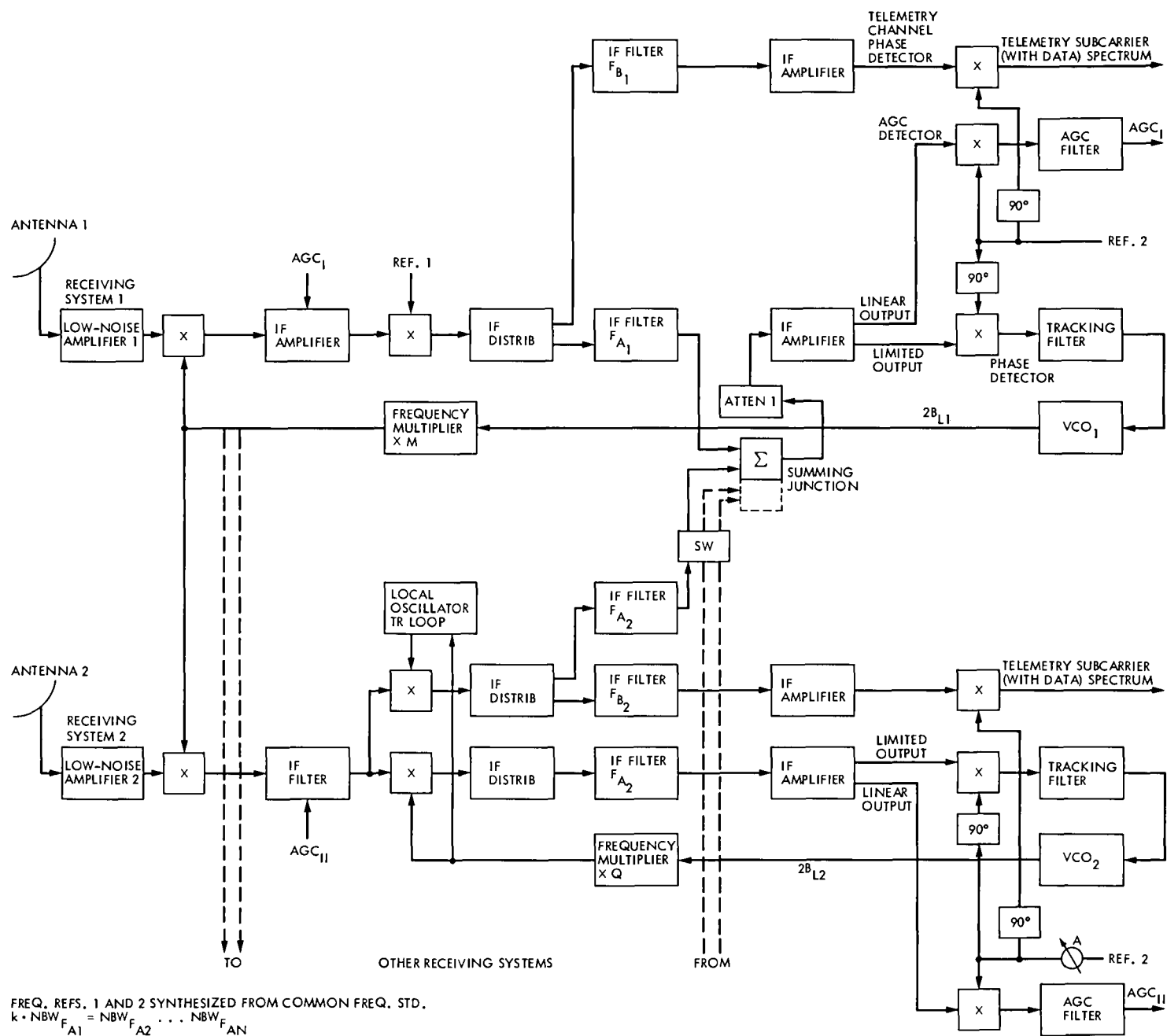


Fig. 2. Enhanced radio frequency carrier arraying with additional local oscillator filtering

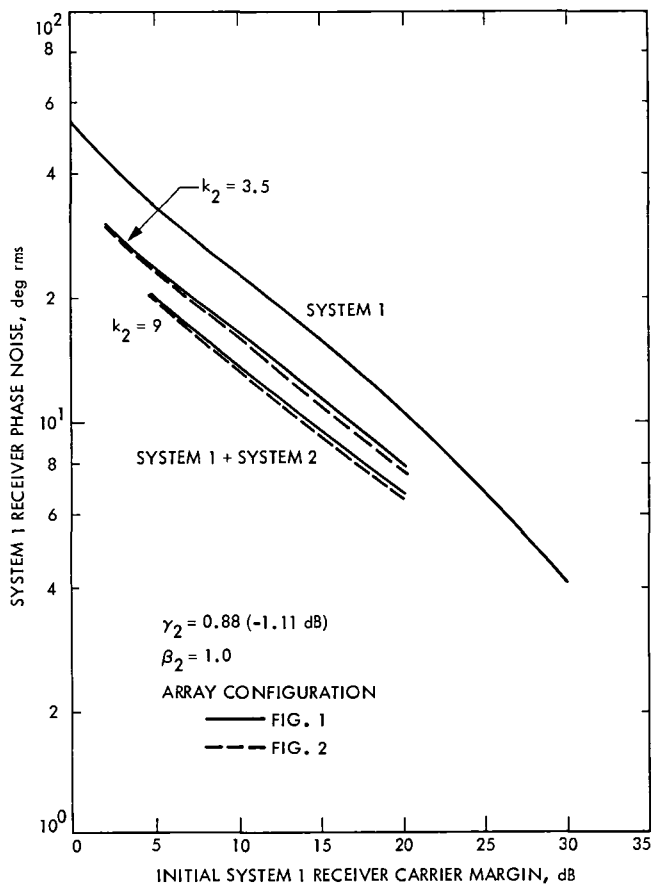


Fig. 3. The 34-m (high efficiency) receiver by itself and with enhanced RF carrier margin improvement. RF carrier tracking loop phase noise vs initial 34-m (high efficiency) receiver carrier margin. Two receiving systems arrayed: System 1 is the 34-m diameter high efficiency; System 2 is the 34-m diameter transmit/receive ($2B_{L_{o1}} = 12$ Hz).

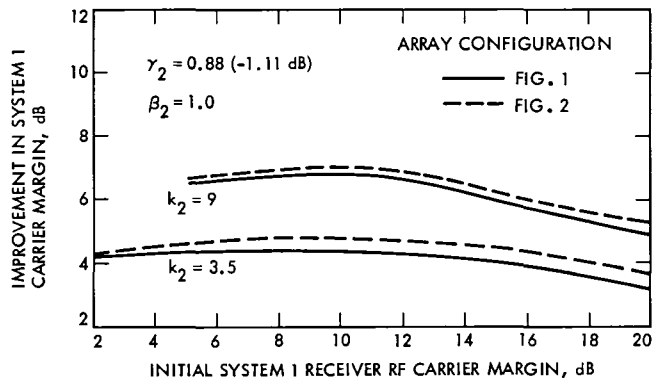


Fig. 4. Enhanced RF carrier margin improvement vs initial 34-m (high efficiency) receiver RF carrier margin. Two receiving systems arrayed: System 1 is the 34-m diameter high efficiency; System 2 is the 34-m diameter transmit/receive ($2B_{L_{o1}} = 12$ Hz).

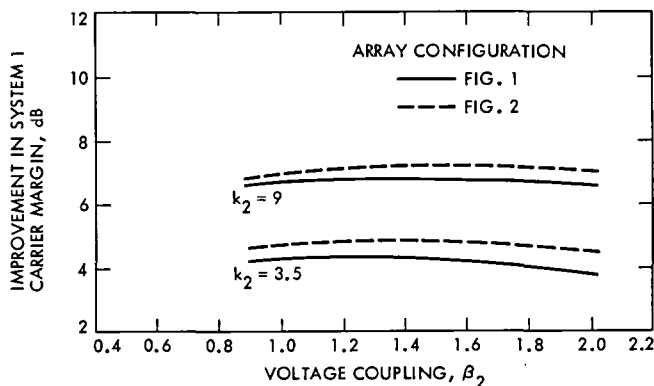


Fig. 5. The effect of summing junction voltage coupling on enhanced RF carrier margin improvement. Two receiving systems arrayed: System 1 is the 34-m diameter high efficiency; System 2 is the 34-m diameter transmit/receive ($2B_{L_{o1}} = 12$ Hz and $\gamma = 0.88$).

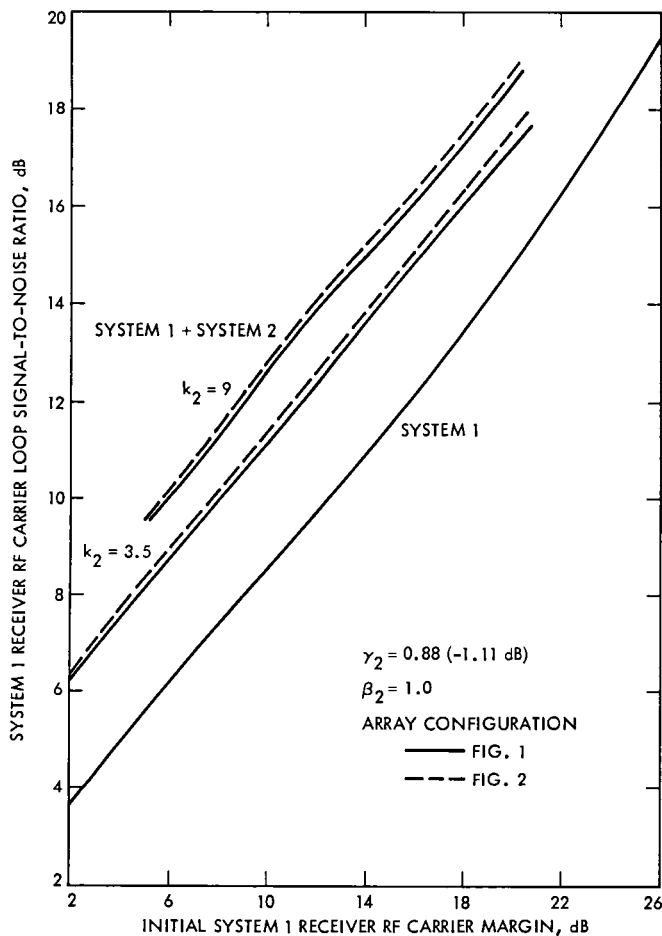


Fig. 6. The 34-m (high efficiency) receiver by itself and with enhanced RF carrier margin improvement. The RF carrier tracking loop signal-to-noise ratio vs initial 34-m (high efficiency) receiver carrier margin. Two receiving systems arrayed: System 1 is the 34-m diameter high efficiency; System 2 is the 34-m diameter transmit/receive ($2B_{L_{o1}} = 12$ Hz).

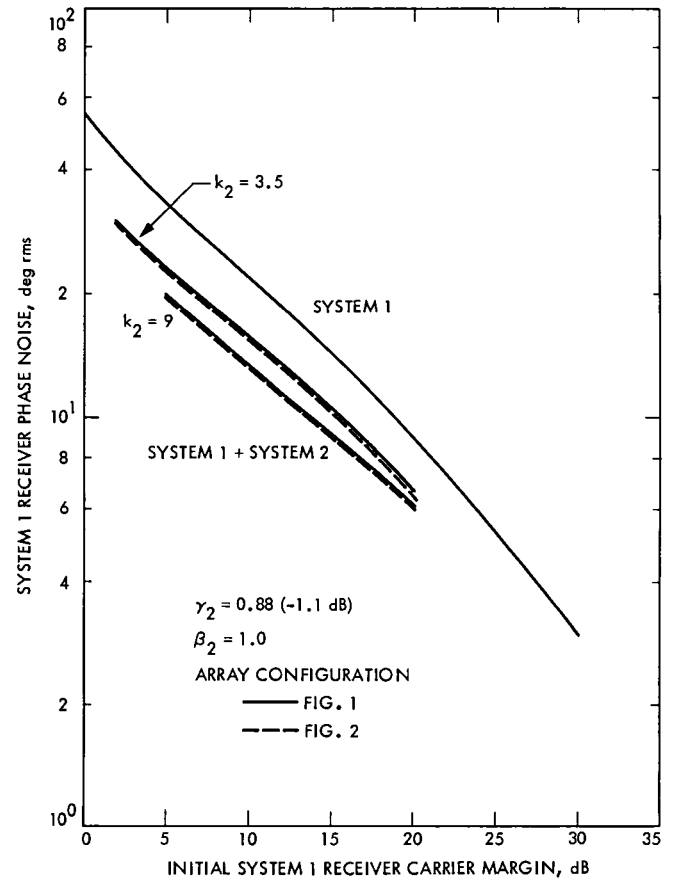


Fig. 7. The 34-m (high efficiency) receiver by itself and with enhanced RF carrier margin improvement. RF carrier tracking loop phase noise vs initial 34-m (high efficiency) receiver carrier margin. Two receiving systems arrayed: System 1 is the 34-m diameter high efficiency; System 2 is the 34-m diameter transmit/receive ($2B_{L_{o1}} = 48$ Hz).

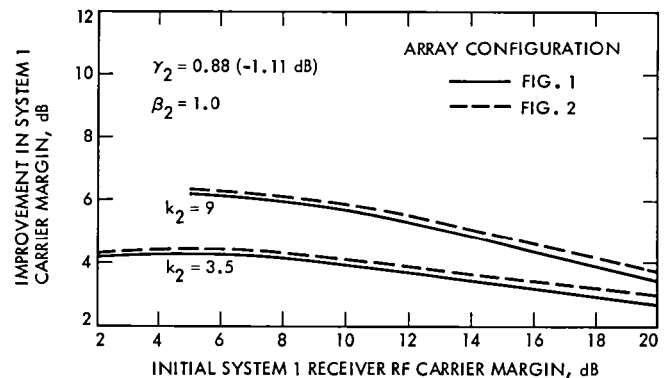


Fig. 8. Enhanced RF carrier margin improvement vs initial 34-m (high efficiency) receiver RF carrier margin. Two receiving systems arrayed: System 1 is the 34-m diameter high efficiency; System 2 is the 34-m diameter transmit/receive ($2B_{L_{o1}} = 48$ Hz).

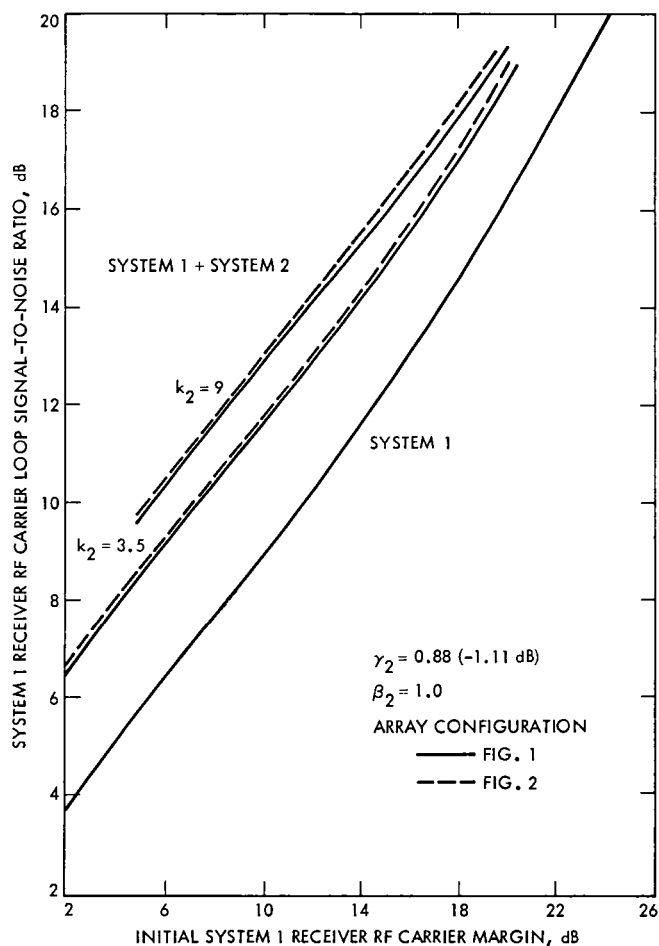


Fig. 9. The 34-m (high efficiency) receiver by itself and with enhanced RF carrier margin improvement. RF carrier tracking loop signal-to-noise ratio vs initial 34-m (high efficiency) receiver carrier margin ($2B_{L_{01}} = 48$ Hz). Two receiving systems arrayed: System 1 is the 34-m diameter transmit/receive; System 2 is the 34-m diameter high efficiency; System 2 is the 34-m diameter transmit/receive.

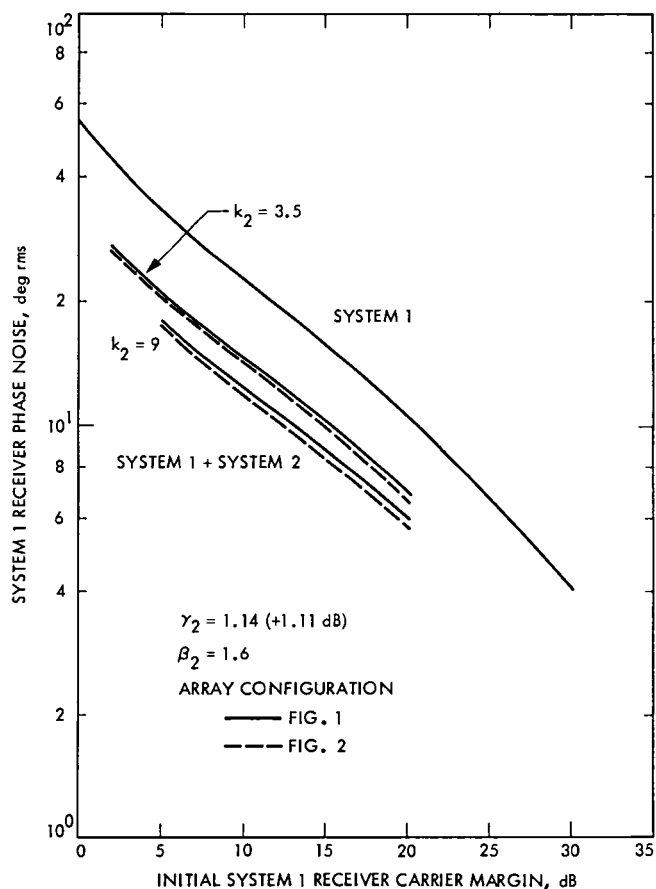


Fig. 10. The 34-m (transmit/receive) receiver by itself and with enhanced RF carrier margin improvement. RF carrier tracking loop phase noise vs initial 34-m (transmit/receive) receiver carrier margin. Two receiving systems arrayed: System 1 is the 34-m diameter transmit/receive; System 2 is the 34-m diameter high efficiency ($2B_{L_{01}} = 12$ Hz).

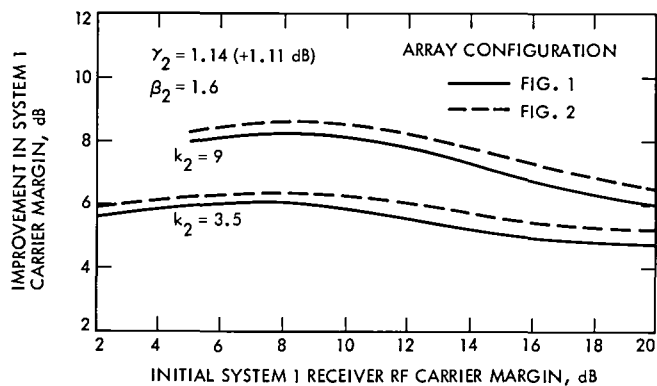


Fig. 11. Enhanced RF carrier margin improvement vs initial 34-m (transmit/receive) receiver RF carrier margin. Two receiving systems arrayed: System 1 is the 34-m diameter transmit/receive; System 2 is the 34-m diameter high efficiency ($2B_{L_{o1}} = 12$ Hz).

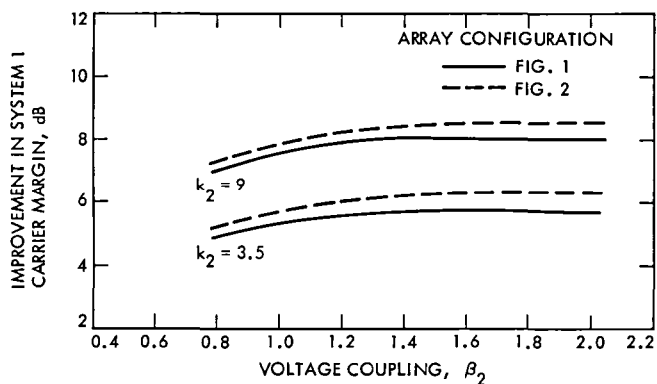


Fig. 12. The effect of summing junction voltage coupling on enhanced RF carrier margin improvement. Two receiving systems arrayed: System 1 is the 34-m diameter transmit/receive; System 2 is the 34-m diameter high efficiency ($2B_{L_{o1}} = 12$ Hz and $\gamma_2 = 1.14$).

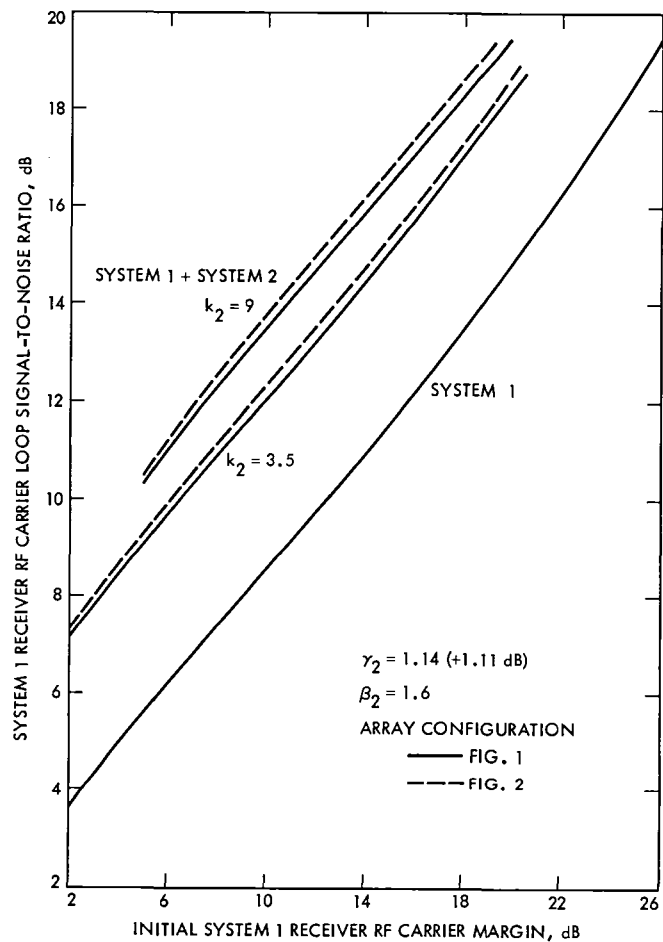


Fig. 13. The 34-m (transmit/receive) receiver by itself and with enhanced RF carrier margin improvement. RF carrier tracking loop signal-to-noise ratio vs initial 34-m (transmit/receive) receiver carrier margin ($2B_{L_{o1}} = 12$ Hz). Two receiving systems arrayed: System 1 is the 34-m transmit/receive; System 2 is the 34-m high efficiency.

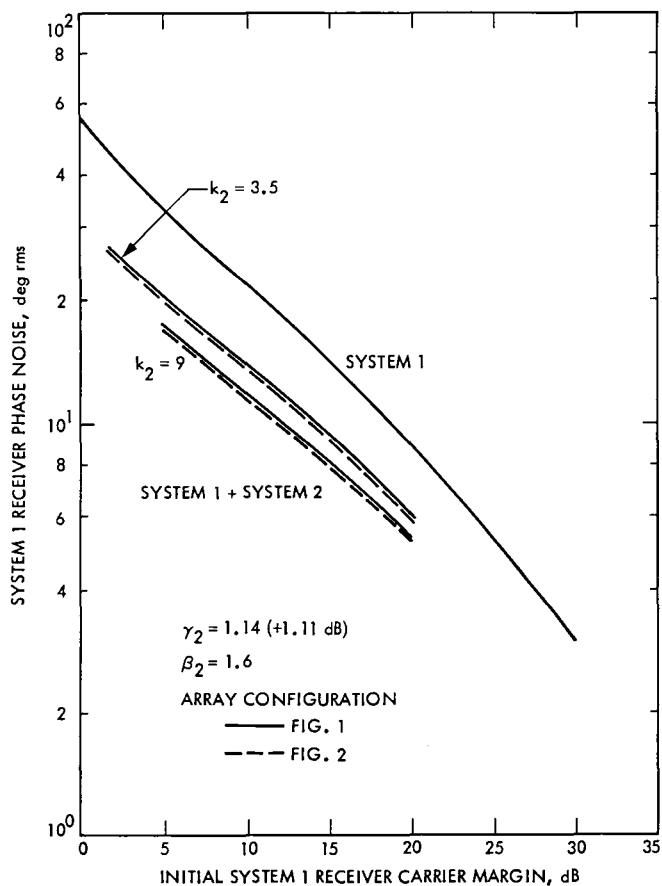


Fig. 14. The 34-m (transmit/receive) receiver by itself and with enhanced RF carrier margin improvement. RF carrier tracking loop phase noise vs initial 34-m (transmit/receive) receiver carrier margin. Two receiving systems arrayed: System 1 is the 34-m diameter transmit/receive; System 2 is the 34-m diameter high efficiency ($2B_{L_{o1}} = 48$ Hz).

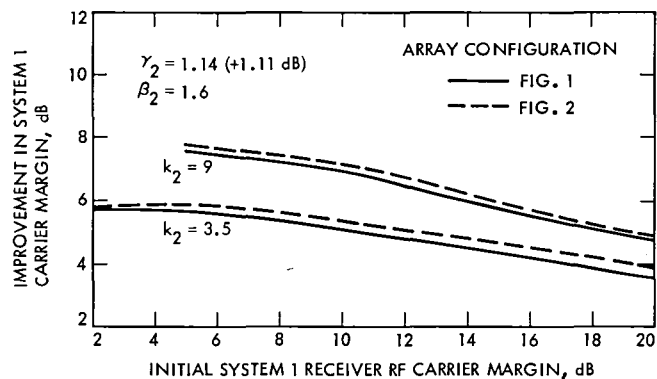


Fig. 15. Enhanced RF carrier margin improvement vs initial 34-m (transmit/receive) receiver RF carrier margin. Two receiving systems arrayed: System 1 is the 34-m diameter transmit/receive; System 2 is the 34-m diameter high efficiency ($2B_{L_{o1}} = 48$ Hz).

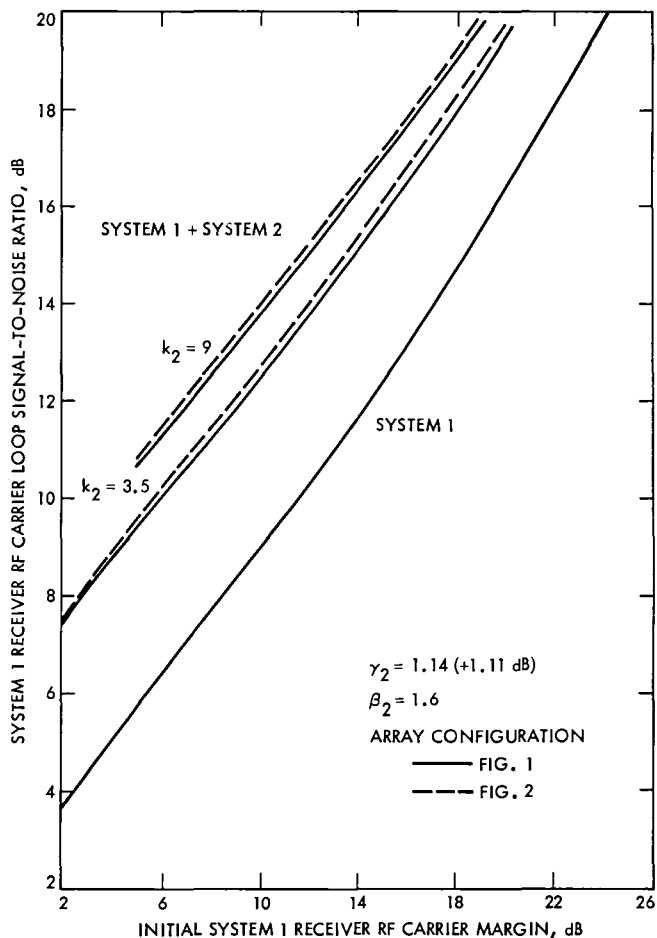


Fig. 16. The 34-m (transmit/receive) receiver by itself and with enhanced RF carrier margin improvement. RF carrier tracking loop signal-to-noise ratio vs initial 34-m (transmit/receive) carrier margin ($2B_{L_{o1}} = 48$ Hz). Two receiving systems arrayed: System 1 is the 34-m transmit/receive; System 2 is the 34-m high efficiency.

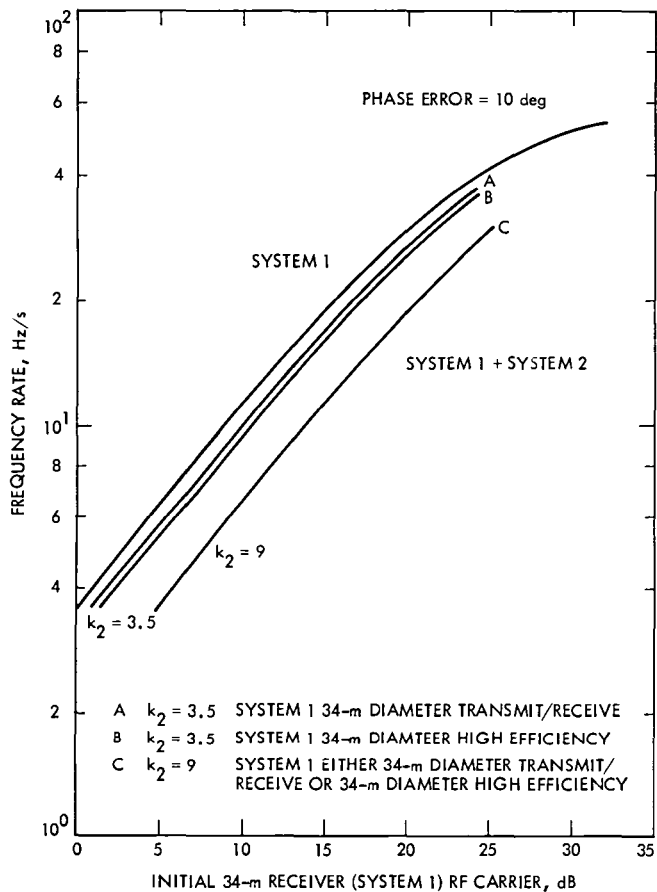


Fig. 17. The 34-m receiver by itself and with enhanced RF carrier margin improvement. Frequency rate capability vs initial 34-m receiver carrier margin. Two 34-m diameter antenna receiving systems arrayed ($2B_{L_{01}} = 12$ Hz).

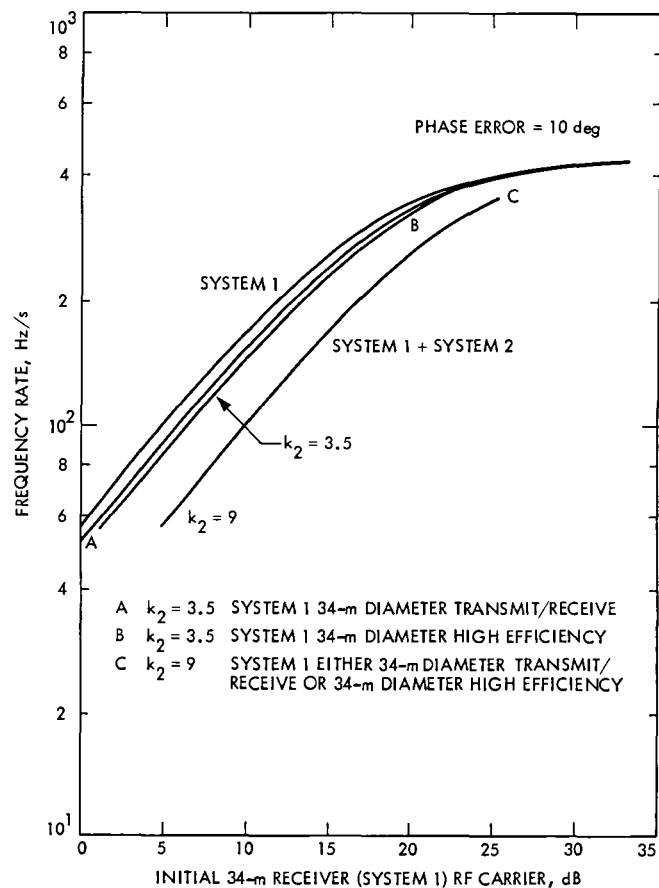


Fig. 18. The 34-m receiver by itself and with enhanced RF carrier margin improvement. Frequency rate capability vs initial 34-m receiver carrier margin. Two 34-m diameter antenna receiving systems arrayed ($2B_{L_{01}} = 48$ Hz).

A Conceptual 34-Meter Antenna Feed Configuration for Joint DSN/SETI Use From 1 to 10 GHz

S. D. Slobin

Radio Frequency and Microwave Subsystem Section

This article is a continuation and expansion of previous work and demonstrates the very satisfactory performance of a conceptual 34-m DSS-12 type HA-Dec antenna feed system over the frequency range of 1 to 10 GHz. A seven-feedhorn baseline design is developed which will allow Search for Extra-Terrestrial Intelligence (SETI) investigations using each horn over a 1.4:1 frequency range. A gain/system noise temperature (G/T) figure of merit is calculated for the frequency range of each horn; it is found that system performance down to 20° elevation is possible with a G/T degradation of less than 3 dB at every frequency. The design presented here will allow shared but independent antenna use by the Deep Space Network (DSN) and SETI with a minimum of operational impacts to DSN functions and no intrusions into the DSN microwave equipment configuration.

I. Introduction

Previous work (Ref. 1) has shown that the existing DSN 34-m HA-Dec (hour angle-declination) antenna feed system is capable of operating over the frequency ranges of 1.9 to 2.6 GHz and 7.0 to 9.4 GHz (34% of the 1–10 GHz SETI range) with no deleterious effects due to gain degradation or system noise temperature increase. Figure 1 shows the DSS-12 34-m antenna with the S/X reflex feed system. To achieve the stated bandwidth, X-band wideband operation with this antenna would require removal of the narrow band dichroic plate. In general, gain reduction comes about because of decreased aperture efficiency (a function of feedhorn illumination) and decreased surface efficiency (due to reflector roughness and deviation of shape). Increased system noise temperature results from illumination spillover, causing interference from the ground and atmosphere. Quadripod scatter noise temperature is not a significant function of frequency

(in these systems) and thus is independent of the number of horns or frequency ranges considered.

Work has begun to study DSN antenna performance over the entire 1- to 10-GHz frequency range. Initially, it was felt that the existing S/X reflex feed system could remain in place and other horns could be added externally to the existing feedcone to fill in the 1.0–1.9, 2.6–7.0, and 9.4–10.0 GHz frequency ranges. This possible design would share use of the existing DSN S- and X-band feedhorns for SETI investigations; consequently, intrusion into controlled DSN tracking configurations was a recognized concern. Further thought resulted in a decision to design a SETI feed system completely independent of the DSN S/X feed system. This will allow a minimum of impact with DSN operations, and will allow both DSN and SETI operations, maintenance, and modification tasks to proceed without interference. In particular, periodic modification (for SETI use) of controlled DSN equipment configura-

tions would be eliminated. It is anticipated that the switchover from DSN to SETI use, or back again, would take only a matter of minutes.

To cover the 1- to 10-GHz frequency range with DSN-type corrugated feedhorns, each operating over a 1.4:1 frequency range, would require seven feedhorns ($1.4^7 = 10.54$). A preliminary design requires all feedhorns to be scaled (by frequency) from the existing DSN S- and X-band feedhorns. As these horns have a narrow 6.25° flare (half-angle), the low frequency horns (long wavelength) scale to enormous size. The 1.0–1.4 GHz horn would have a length of 187 inches. Since the existing DSS-12 feedcone has a height of 131 in., it was decided to limit the horn design to a flare section length not to exceed 100 in. The overall horn length will be slightly longer than this with the addition of an orthomode polarizer. This length limitation causes the flare angle to increase because the horn diameter is held equal to its scaled size.

Table 1 shows the results of a series of horn performance calculations for the low-frequency horn operating at its nominal design frequency of 1.18 GHz (the geometric mean of 1.0 and 1.4 GHz). Horn 1 is the DSN-type scaled horn with a 6.25° flare angle and an aperture of 50.67 in. Shorter horn lengths (using the same aperture) result in increased hyperboloid edge illumination and hence more forward spillover (as evidenced by the decreased beam efficiency). Note also that the far-field phase center position changes as a function of horn length. Compared to the 187-in. horn, the 100-in. horn shows acceptable performance. Although the edge illumination increases by 2.38 dB, the beam efficiency (fraction of horn power intercepted by the subreflector) decreases from 0.965 to 0.925, a gain loss of only 0.18 dB.

Table 2 describes the seven horns selected to cover the 1- to 10-GHz range. Note that neither the S-band horn (horn 3) nor the X-band horn (horn 7) is identical to its DSN counterpart (Ref. 1). There is no reason for any correspondence, as the SETI system is being purposefully designed to be physically and operationally independent of the configuration-controlled DSN system.

II. Feedcone, Feedhorn, and Subreflector Design

The existing DSS-12 feed system operates in the reflex mode, where the S- and X-band beams appear to emanate from the same location (the X-band horn). This is accomplished by placing an ellipsoidal reflector over the S-band horn and a dichroic plate over the X-band horn. This system is described in Refs. 1, 2, and 3.

The feedcone used on DSS-12 type antennas (Fig. 1) is an asymmetrically tapered cylinder, with a base 120 in. in diameter, and an oval top 86 by 120 in. The S- and X-band horns are installed in the top of the feedcone, with their apertures elevated approximately 2 ft above the surface.

Because of the reflex design, the hyperboloidal subreflectors on DSS-12 type antennas remain fixed and do not tilt or rotate to access different horns as do those on 64-m antennas, which rotate to access the different feedcones. The X-band horn position in the S/X reflex system is the location of the subreflector "focus"; thus the addition of seven feedhorns for SETI use would result in a grossly asymmetric system if no provision for subreflector movement were made.

A first simple approach to the seven-horn design (nine, if the existing S- and X-band horns are included) might be to add on the horns in a circle or semicircle surrounding the existing cone (as in the 64-m L-band feed). This simple arrangement is shown in Fig. 2. Note that the phase centers of these horns are all displaced from the X-band horn position, so that large asymmetries due to offset feeds would result. This is a particular problem for the high-frequency (short wavelength) horns, where displacements are large in units of wavelength. Antenna efficiency is greatly reduced by even small amounts of misfocus. Also, the dichroic plate over the X-band horn might have to be tipped off, or folded away, depending on interference with the horn patterns.

To minimize the asymmetry problem, the subreflector would have to rotate *and* tip in order to access each individual horn. The tipping portion of this motion will result in varying and detrimental main reflector illumination, as the subreflector shape and angular tilt (in both the 34-m and 64-m designs) are optimized for maximum illumination, with special concern for minimum rear spillover. This "add-on" concept might save the cost of a new feedcone, but requires a rotatable and tilting subreflector assembly. Because of the numerous inherent RF performance problems in this design, including especially the detailed question of main reflector spillover and blockage, this concept has been rejected. Other versions of the add-on technique can be imagined, but one or another of the above problems will still remain.

III. Improved Conceptual Design

The improved conceptual design involves both feedcone and subreflector redesign. It is proposed that the feedcone be enlarged to a 120-in. diameter for its entire height, rather than tapered, as in the present design. In this manner, all feedhorns can be properly contained within the cone, and excessive waveguide runs can be eliminated. As any additional horn will

not be located at the X-band horn position, it becomes necessary to rotate and index the subreflector as in the proven 64-m system. The phase center of any added horn must be on a circle centered on the paraboloid center line and passing through the X-band horn. In this way, there will be no beam position shift as different horns are accessed. Figure 3 shows this concept with all seven horns in place in addition to the existing S- and X-band DSN horns. Clearly, in this design, both the dichroic plate over the X-band horn and the ellipsoidal reflector over the S-band horn must be tipped or folded away from the top of the cone area during SETI use. Precedent for this exists (the initial 64-m reflex system was foldable for precise gain and noise differencing tests) but it is an unwieldy solution at best.

IV. Suggested Conceptual Design

A suggested simpler design recognizes that SETI does not require all horns in place at a given time, and has one or two horns located in large adapter plates (or plug-in modules) as shown in Fig. 4. SETI plans to use only one frequency band (horn frequency range) at a time; thus it would not be necessary to have all seven horns in place simultaneously. Perhaps several weeks or months of observation would be carried out in each band, and then the horn and waveguide assembly would be changed (not to exceed a 1-day job) to continue operation in another band. Plug-in modules designed to accommodate all horns would facilitate this exchange. The use of two modules enables the operation of one SETI system, with a second system in an installation, maintenance, or checkout mode.

V. Performance Evaluation

Calculations have been carried out to determine G/T (gain/system noise temperature) figures of merit similar to those determined in Ref. 1. This analysis is valid for any feed system in which the various feedhorns can be precisely focused and in which the resulting antenna beam does not "squint" or move away from its normal position along the main reflector axis of symmetry (cf. Figs. 3 and 4). G/T is defined as

$$G/T \sim \frac{\eta_{\text{aperture}} \times \eta_{\text{surface}}}{T_{\text{ground}} + T_{\text{atmosphere}} + T_{\text{quadripod}} + T_{\text{base}}}$$

The aperture efficiency, η_{aperture} , represents the fraction of incident power (in the sense of illumination) actually captured by the feedhorn. The surface efficiency, η_{surface} , is a function of both surface roughness and main reflector deformation due to gravity loading; T_{ground} is the noise temperature contribution from the ground due to both forward and rear spillover;

$T_{\text{atmosphere}}$ is the atmospheric noise contribution due to the same two causes; $T_{\text{quadripod}}$ is the quadripod noise temperature contribution due primarily to scattering of ground radiation. T_{base} is the non-changing baseline noise temperature due to low-noise amplifier, cosmic background, and waveguide contributions. Since no DSN operational systems exist over the needed range of frequencies, it is necessary to estimate a plausible T_{base} value for each of the seven different horn systems. In fact, for the purposes of this study, the baseline noise temperature component is defined to be a constant 20 K at all frequencies.

Note that the *total* system noise temperature includes T_{base} plus ground, atmosphere, and quadripod contributions, the last three varying with frequency and/or elevation angle. The zenith atmospheric noise temperature is accepted to vary linearly from 2 to 4 K over the 1- to 10-GHz range. Spillover effects will result in atmospheric contributions (at zenith) somewhat higher than these values. Quadripod noise temperature varies as a function of elevation angles only, from 2.5 K at zenith to 6 K at 0 deg. Surface efficiency varies with frequency and elevation from 0.999 at 1.0 GHz and 30-deg elevation to 0.762 at 10.54 GHz and 90-deg elevation. These values result from estimates of the DSS-12 type antenna mechanical surface tolerance due to both antenna gravity distortions and surface roughness.

The highest calculated figure-of-merit value occurs at 3.24 GHz (the middle of the middle horn) and 90-deg elevation. For comparison purposes, all other figures-of-merit were referred to this value. The components of this reference figure-of-merit are

$$\eta_{\text{aperture}} = 0.783$$

$$\eta_{\text{surface}} = 0.975$$

$$T_{\text{ground}} = 1.11 \text{ K}$$

$$T_{\text{atmosphere}} = 2.74 \text{ K}$$

$$T_{\text{quadripod}} = 2.50 \text{ K}$$

$$T_{\text{base}} = 20.00 \text{ K}$$

(Note: Quadripod blockage is not considered in this figure-of-merit comparison, as it is common to all frequencies and elevation angles.) Table 3 shows the G/T figures-of-merit (dB) relative to the peak value at 3.24 GHz and 90-deg elevation. Figure 5 shows the G/T figure-of-merit values with each horn G/T separately drawn.

Table 3 shows that G/T degradation less than 3 dB is available for all elevation angles greater than 20 deg. If an observing scheme has sufficient freedom to view only portions of the sky

at elevations greater than 30 deg (e.g., Goldstone and sources with declinations greater than -25 deg), a less than 2-dB degradation will be experienced. In either event, even a single-band reflector antenna would suffer a similar G/T degradation, primarily due to atmospheric and quadripod noise contributions.

VI. Conclusions

A conceptual seven-horn feed system is considered for SETI use on a 34-m HA-Dec type antenna over the frequency range of 1 to 10 GHz. Only one or two of the seven proposed feed

systems would be mounted at a given time, and independence of DSN systems from the SETI systems is preserved, an aspect considered very important to the DSN. This system shows quite acceptable performance over the entire frequency range. Again, it should be noted that this design considers only antenna and feedhorn performance. The design of wideband low-noise preamplifiers, polarizers, and orthomode components over this frequency range has not yet been accomplished and may require a substantial development effort. Further studies will address this consideration and the use of beam waveguide in a shaped dual-reflector system for wideband SETI requirements.

References

1. Slobin, S. D., "DSN 34-Meter Antenna Optics Analysis for Wideband SETI Investigations," *TDA Progress Report 42-80*, Jet Propulsion Laboratory, Pasadena, Calif., pp. 202-219, Feb. 15, 1985.
2. Slobin, S. D., "Antennas" in *The Deep Space Network - A Radio Communications Instrument for Deep Space Exploration*, JPL Publication 82-104, Jet Propulsion Laboratory, Pasadena, Calif., pp. 3-1 through 3-23, July 15, 1983.
3. Nixon, D. L., and Bathker, D. A., "S-/X-Band Microwave Optics Design and Analysis for DSN 34-Meter-Diameter Antenna," *DSN Progress Report 42-41*, Jet Propulsion Laboratory, Pasadena, Calif., pp. 146-165, Sept. 15, 1977.

**Table 1. Low-frequency corrugated horn comparison, frequency = 1.18 GHz,
aperture diameter = 50.67 in.**

Horn	Flare Length, in.	Flare Half-Angle, deg	Hyperboloid Edge Illumination, dB	Beam Efficiency	Phase Center Position, in. ^a
1	186.572	6.250	-16.25	0.965	17.648
2	160.	7.277	-15.82	0.959	20.870
3	140.	8.304	-15.37	0.953	22.530
4	120.	9.663	-14.75	0.942	25.428
5	100.	11.548	-13.87	0.925	29.014
6	80.	14.328	-12.57	0.896	33.407
7	60.	18.806	-10.56	0.838	38.482

^aInside horn, relative to aperture. Phase center calculated from $\pm 15.79^\circ$ spread of far-field points (the edges of the DSS-12 subreflector).

Table 2. Corrugated horns to cover the 1- to 10-GHz frequency range

Horn	Frequency Range, GHz	Nominal Design Frequency GHz	Phasing Section Length, in.	Diameter of Phasing Section and Small End of Flare, in.	Flare Length, in.	Aperture Diameter, in.	Groove Depth, in.	Phase Center Position Inside Horn Aperture at Nominal Frequency, in. ^a
1	1.00-1.40	1.18	0.0	9.803	100.000	50.67	3.080	27.418
2	1.40-1.96	1.66	0.0	6.969	100.000	36.02	2.189	14.787
3	1.96-2.74	2.32	0.0	4.986	94.917	25.78	1.566	8.244
4	2.74-3.84	3.24	0.0	3.570	67.965	18.46	1.122	5.908
5	3.84-5.38	4.55	0.0	2.542	48.397	13.14	0.799	4.197
6	5.38-7.53	6.36	0.0	1.819	34.624	9.40	0.571	2.999
7	7.53-10.54	8.91	0.0	1.298	24.715	6.71	0.408	2.143

^aInside horn, relative to aperture. Phase center calculated from $\pm 16^\circ$ spread of far-field points.

Table 3. G/T figure-of-merit, dB

Horn	Frequency GHz	Elevation Angle, deg.									
		0	10	20	30	40	50	60	70	80	90
1	1.00	-5.237	-3.194	-2.143	-1.494	-1.237	-1.104	-1.036	-1.061	-1.299	-1.358
	1.18	-5.040	-2.856	-1.677	-1.072	-0.811	-0.667	-0.568	-0.545	-0.580	-0.675
	1.40	-5.266	-2.907	-1.696	-1.161	-0.894	-0.731	-0.614	-0.557	-0.602	-0.592
2	1.40	-4.821	-2.723	-1.662	-1.097	-0.845	-0.704	-0.632	-0.639	-0.851	-0.873
	1.66	-4.644	-2.364	-1.286	-0.761	-0.500	-0.346	-0.242	-0.206	-0.302	-0.285
	1.96	-5.042	-2.605	-1.481	-0.980	-0.707	-0.536	-0.406	-0.337	-0.346	-0.321
3	1.96	-4.704	-2.502	-1.401	-0.863	-0.599	-0.446	-0.363	-0.355	-0.520	-0.480
	2.32	-4.539	-2.156	-1.119	-0.611	-0.341	-0.182	-0.066	-0.025	-0.088	-0.056
	2.74	-5.052	-2.526	-1.455	-0.953	-0.677	-0.499	-0.366	-0.291	-0.278	-0.259
4	2.74	-4.871	-2.578	-1.394	-0.828	-0.556	-0.391	-0.293	-0.266	-0.370	-0.321
	3.24	-4.736	-2.244	-1.169	-0.630	-0.352	-0.179	-0.054	-0.001	-0.030	-0.000
	3.84	-5.330	-2.709	-1.604	-1.079	-0.791	-0.607	-0.476	-0.404	-0.403	-0.404
5	3.84	-5.222	-2.796	-1.492	-0.880	-0.577	-0.393	-0.280	-0.227	-0.273	-0.249
	4.55	-5.185	-2.553	-1.404	-0.830	-0.529	-0.348	-0.226	-0.165	-0.197	-0.215
	5.38	-5.784	-3.007	-1.844	-1.291	-0.991	-0.809	-0.683	-0.627	-0.652	-0.681
6	5.38	-5.758	-3.166	-1.793	-1.158	-0.837	-0.644	-0.526	-0.478	-0.529	-0.571
	6.36	-5.773	-2.966	-1.744	-1.140	-0.828	-0.647	-0.540	-0.501	-0.580	-0.634
	7.53	-6.465	-3.485	-2.222	-1.626	-1.307	-1.127	-1.026	-0.994	-1.074	-1.159
7	7.53	-6.520	-3.777	-2.318	-1.643	-1.311	-1.135	-1.051	-1.046	-1.200	-1.295
	8.91	-6.552	-3.500	-2.173	-1.520	-1.194	-1.016	-0.945	-0.953	-1.104	-1.222
	10.54	-7.362	-4.984	-2.673	-2.012	-1.678	-1.500	-1.441	-1.461	-1.627	-1.807

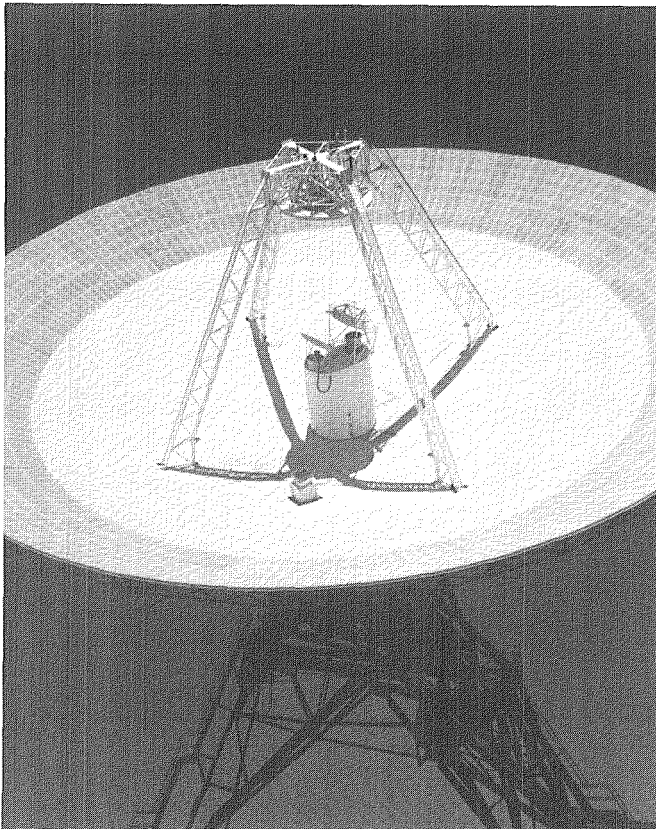


Fig. 1. DSS 12 34-m HA-Dec antenna with S/X reflex feed system

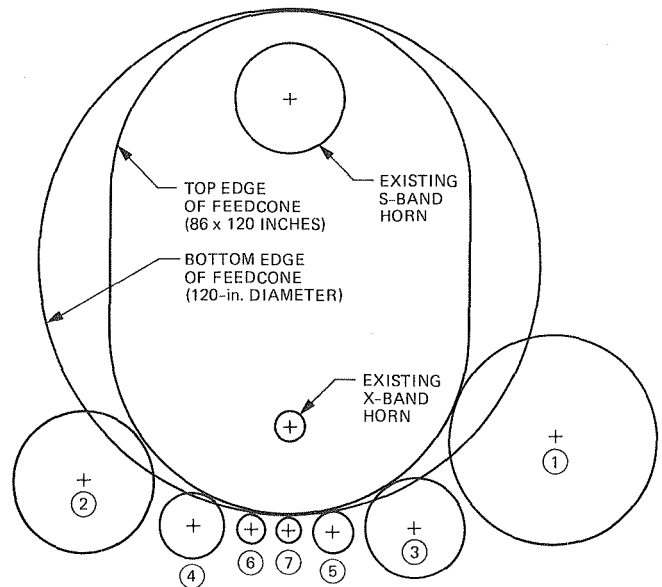


Fig. 2. Existing 34-m antenna feedcone with add-on horns

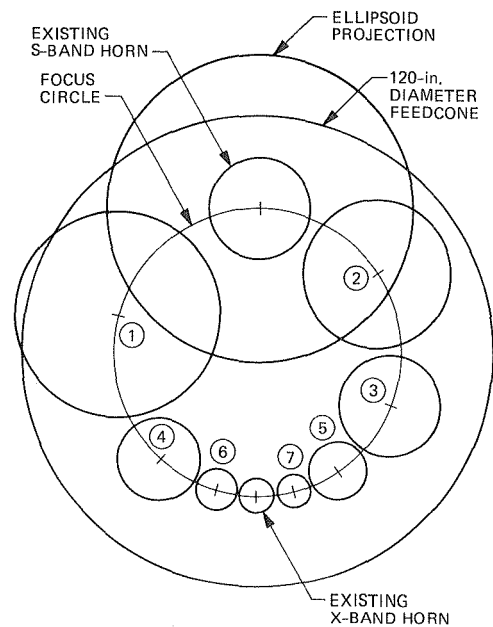


Fig. 3. New design 120-in. diameter feedcone with seven SETI horns in place

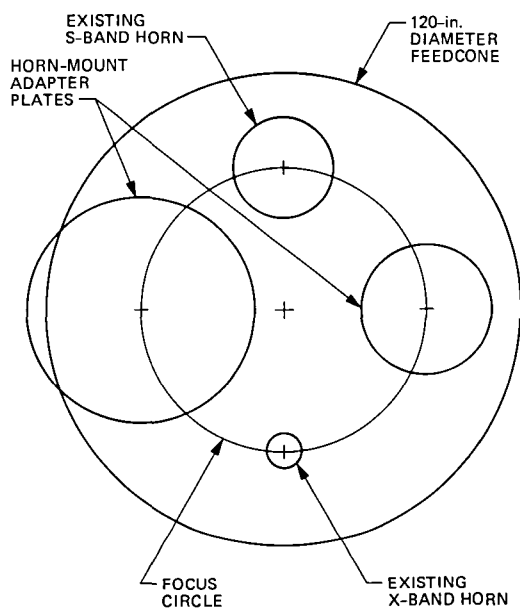


Fig. 4. New design feedcone with adapter plates for mounting SETI feedhorns

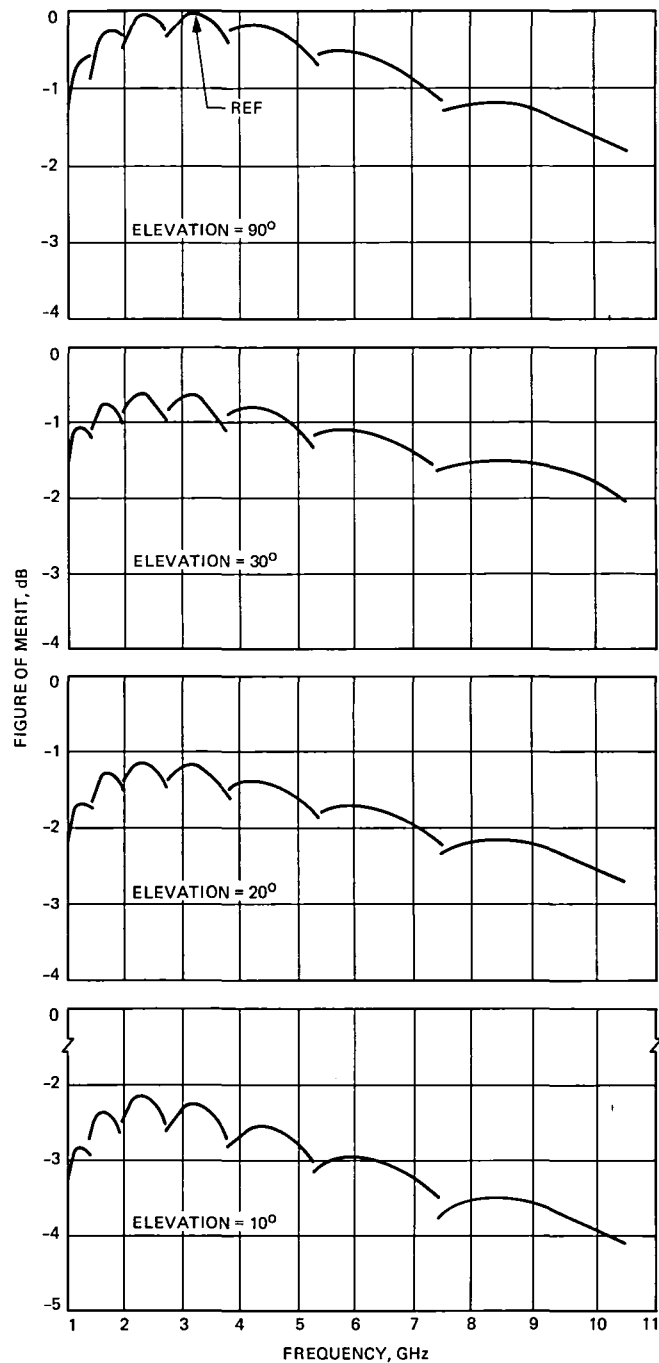


Fig. 5. Gain/system noise temperature figure-of-merit

DSN Command System Mark IV-85

H. C. Thorman
TDA Engineering Office

This article presents a functional description of the Deep Space Network Command System and its subsystems as implemented in 1985.

I. Mark IVA Network Implementation

A. General

The Mark IVA Network implementation, completed in 1985, provides a Signal Processing Center (SPC) at each of the three Deep Space Communications Complexes (Goldstone, California; Canberra, Australia; and Madrid, Spain). The Ground Communications Facility (GCF) provides communications between JPL and each SPC. The Networks Consolidation Program (Ref. 1) required the Mark IVA Network to support high-apogee Earth-orbital missions in addition to the deep space missions.

Figure 1 is a block diagram of the DSN Command System Mark IV-85. Each Deep Space Communications Complex (DSCC) has a 64-m antenna with deep space uplink, a 34-m antenna with both deep space and Earth-orbiter uplinks, and a 26-m, former Ground Spacecraft Tracking and Data Network (GSTDN) antenna with Earth-orbiter uplink. (A decision to incorporate the 26-m, instead of the 9-m, GSTDN antennas in the Networks Consolidation Program was made after the publication of Refs. 1 and 2.)

B. DSN Command System Implementation

The DSN Command System Mark IV-85 was implemented approximately in accordance with the plan described in

Ref. 2. The Mark IVA configuration at each complex includes four strings of DSCC command subsystem equipment. The DSCC Monitor and Control Subsystem, as shown in Fig. 1, provides operation of any three strings.

C. Performance Requirements

Support of the Mark IVA mission set requires Command System performance characteristics compatible with the NASA standard transponders, which are to be used on future spacecraft, and also compatible with current inflight spacecraft and certain planned spacecraft that do not use the standard transponder. Some of the required capabilities are listed below:

- (1) Data rates. Data rates from 1 to 2000 bits/s are provided.
- (2) Subcarrier frequencies. Sine-wave and square-wave subcarriers are generated at frequencies of 100 Hz to 16 kHz.
- (3) Subcarrier data modulation. Selection is provided for phase-shift-keyed (PSK) or frequency-shift-keyed (FSK) modulation of the subcarrier by a pulse-code-modulated NRZ-L command symbol stream. An option for amplitude modulation (AM) of the FSK subcarrier is also provided.

- (4) Carrier modulation. The command-modulated sub-carrier is phase-modulated on an S-band carrier for radiation to the spacecraft. Control of modulation index angle is provided over a range from 0.35 to 1.5 rad.
- (5) Carrier frequencies. Generation of the uplink carrier at S-band frequencies assigned for deep space missions is provided at the 64-m and 34-m antennas. S-band frequencies assigned for Earth orbit missions are provided at the 34-m and 26-m antennas.

II. Store-and-Forward Command Functions for Deep Space Missions

Many of the spacecraft supported by the DSN have onboard storage and sequencing capabilities that permit command sequences to be sent well in advance of the actions to be taken by the spacecraft. Thus, fewer direct action (real-time) commands are needed. Ground system capabilities providing massive storage of spacecraft commands, multimission operating functions, and standardized protocol were incorporated in the DSN Command System in 1978 (Ref. 3). These capabilities are continued in the Mark IV-85 system configuration.

A. Operational Functions

End-to-End spacecraft command operations are represented functionally in Fig. 2. Command sequences for one or more spacecraft are generated and stored at a Mission Operations Center (MOC). Commands for a particular spacecraft are selected from the command files, formatted into messages, and stored for transmittal to a specified link of a DSCC. Command data are extracted from the message received and are stored and queued until radiated. Finally, the commands arrive at the spacecraft and are either executed immediately or stored aboard for later execution.

The functions of the DSN Command System in this process include the following:

- (1) Establishing the DSCC configuration for the specified spacecraft.
- (2) Receiving and storing command data at the DSCC.
- (3) Queuing command data to be radiated to the spacecraft.
- (4) Radiating the command data to the spacecraft.
- (5) Monitoring system status and reporting events and alarms.

B. Operational Procedure

The key onsite input to the DSCC Command (DCD) Subsystem is the spacecraft number (SCN). This input causes the

Command Processor Assembly (CPA) software to transfer a specified configuration and standards and limits table from disk storage to memory, and to configure the Command Modulator Assembly (CMA) according to the table. Standards and limits changes may later be made by messages from the Network Operations Control Center (NOCC) via the GCF (or by keyboard entries at the Link Monitor and Control Console in an emergency).

Prior to the beginning of the scheduled spacecraft track, the control of DSCC command functions is transferred to NOCC. Configuration standards and alarm/abort limits can be updated by GCF transmission of messages from the NOCC Command Subsystem (NCD) real-time monitor processor. The standards and limits are derived from files compiled in the NOCC Support Subsystem. Spacecraft-dependent parameters, such as data rate, subcarrier frequency, alarm limits, and abort limits, are established via these messages. After the proper configuration standards and limits have been established, test commands are transmitted through the system to ensure that the system can accept spacecraft commands via GCF, temporarily store the commands, and confirm radiation. During this test the transmitter output is radiated into a dummy load. After the Network Operations Control Team (NOCT) has established that the system is operating properly, the station operator switches the transmitter to space radiation, and the NOCT transfers command data control to the flight project's MOC for loading of actual spacecraft command sequences to be radiated to the spacecraft during the track period.

At the time for radiation of each command element, the subsystem advances to the active mode (see Fig. 3 for description of the various modes) and command data are transferred from the CPA to the CMA for radiation via the Receiver-Exciter, Transmitter, Microwave, and Antenna Subsystems.

C. Command Data Handling

The DCD Subsystem design allows mission operations to prepare large files of spacecraft commands in advance and then to forward several files to the DSCC link at the beginning of a spacecraft track. The design also provides real-time system status monitoring and control. For protection of data integrity, every message block to or from the CPA contains a block checksum, in addition to the GCF error detection provisions.

1. Command files. Each file may consist of up to 256 GCF data blocks. The content of each data block is a file element. The first block in a file contains the *header element* and each subsequent block contains a *command element*. Each command element may consist of up to 800 bits of spacecraft command data. Up to 8 files for a given mission can be stored by the CPA. Thus, the available storage is over 1.6 million command bits.

The header element contains file identification information, file processing instructions, and a file checksum. The file processing instructions include optional file radiation open and close window times, and an optional file bit 1 radiation time. File open and close window times specify the time interval during which a command file may be radiated (i.e., a mission sequence may demand that specific commands not be sent before or after a certain time). The bit 1 radiation time allows the project to specify the exact time at which the file is to begin radiation to the spacecraft. The file checksum is created at the time of file generation and is passed intact to the CPA. It adds reliability to ensure that no data were dropped or altered in the transfer of the file from one facility to another. (This is in addition to the previously mentioned block checksums.)

The command elements each contain command bits, file identification, element number, element size, and an optional "delay time" (interval from start of previous element). If delay time is not specified, the element will start radiating immediately after the end of the previous element.

2. Receiving and storing command data at a DSCC. Normally, the files of commands to be radiated to the spacecraft will be sent from the MOC to the specified DSCC link at the beginning of a spacecraft track period. However, files may be sent to the DSCC link at any time during the spacecraft track period. The first step in receiving and storing command data at a DSCC is the process of opening a file area on the CPA disk. The MOC accomplishes this by sending a header element, which serves as a *file-open* directive. After the CPA acknowledges receipt of the header element, the MOC sends the remainder of the file (up to 255 command elements) and follows it with a *file-close* directive. The CPA acknowledges the file-close instruction and indicates whether the file loading was successful or unsuccessful. If the file loading was unsuccessful, the acknowledge message contains the reason for the failure and from what point in the file the command elements are to be retransmitted. When the file is successfully closed, the MOC may proceed to send additional files until the eight-file directory in the CPA is full.

3. Queuing the command data for radiation. After the files are stored at the CPA, the MOC then sends a *file-attach* directive for each of up to five file names to be placed in the radiation queue. The Mission Control Team determines in which order the files are to be attached. The order in which the file-attach directives are received at the CPA determines the sequence in which the files will be radiated; that is, first attached, first to radiate to the spacecraft.

4. Command radiation to the spacecraft. The first command element in the top (prime) file in the queue begins radiation to

the spacecraft immediately after attachment or as soon as all optional file instructions (such as bit 1 radiation time) are satisfied. Upon completion of radiation of the first command element, the second command element begins radiation either immediately or when the optional delay time has been satisfied. The process continues until all command elements in the file have been radiated. After the first file completes radiation, the second file in the queue automatically becomes the prime file and the command radiation process is repeated. After the second file completes radiation, the third file becomes prime, etc. This process is repeated until all files in the queue are exhausted. The MOC can attach new files to the queue whenever space is available.

Confirmations of prime-file command-element radiations are reported in *event* messages to the MOC and NOCC once per minute, or after five elements have been radiated, whichever occurs first. If a command element is aborted, an event message is sent immediately.

Status messages are sent to the MOC and NOCC once per minute and whenever an alarm occurs.

5. Additional data processing. The foregoing descriptions of the DSCC functions of storing the command files, attaching the files to the queue, and radiating the commands to the spacecraft assume nominal (standard) operation. Additional data processing functions are provided for non-nominal operations and failure recovery. Control of these functions is normally exercised remotely from the MOC. However, emergency control is also available at the SPC.

a. File erase. A file can be deleted from storage at the CPA by means of a *file erase* directive, if the file is not attached to the radiation queue.

b. Clearing the queue. As previously stated, the order of file radiation to the spacecraft is dependent on the order of files in the queue. To rearrange the order, a *clear-queue* directive must be sent, followed by file-attach directives in the desired order.

c. Suspend radiation. If the Mission Control Team desires to stop command radiation, a *suspend* message can be sent to the CPA. This message suspends command radiation to the spacecraft upon completion of the current element. When the prime file is suspended in this manner, the DCD remains in the Idle 2 mode.

d. Resume command radiation. To restart radiation of a suspended file (either suspended intentionally or from an abort), messages can be sent to *resume* radiation at any specified unconfirmed element in the file. The suspend and

resume-at directives can be used for skipping elements of the prime file, if desired.

e. Command abort. As each command bit is radiated to the spacecraft, numerous checks are made to ensure validity of the command data. If a failure is detected during the radiation, the command element is automatically aborted immediately, the prime file is suspended, and radiation is terminated until a mode update directive and a resume-at directive are received.

In addition to the automatic abort function, there is provision for the MOC to send an *abort-and-suspend* directive to terminate command radiation immediately without waiting for completion of an element.

f. Close-window time override. If a close-window time is specified in a file header element, and the Mission Operations Team later decides to extend the permissible time for radiation of the file, an *override* message can be sent (after the file becomes prime), which instructs the CPA to ignore the close-window time.

D. Data Records

All message blocks received by the CPA and all blocks sent from the CPA are logged at the DSCC on the Original Data Record (ODR). Message blocks from the DSCC are also recorded at the GCF central communications terminal (CCT).

The DSCC original data records and the CCT recording provide information for fault isolation in case problems occur in the Command System operation.

III. Throughput Command Functions for Earth-Orbiter Missions

The Mark IV-85 Network provides support for several low Earth Orbiters and geosynchronous orbiters that were not included in the original networks consolidation programs. Former GSTDN data processing and communication equipment has been retained in the 26-m antenna control centers for such missions (Ref. 4). Spacecraft commanding is handled by the Spacecraft Command Encoder (SCE) with real-time, "throughput command" protocol.

The command-modulated subcarrier output from the SCE is usually routed to the 26-m antenna exciter, but can be sent to the 34-m antenna exciter for emergency backup.

Command data are communicated via NASCOM to the SCE from the flight project's MOC for immediate radiation to the spacecraft. The data are formatted in message blocks containing up to 4592 bits each. The SCE can buffer up to 5 blocks before starting radiation of a block sequence.

Upon receipt of each throughput command data block, the SCE checks the block for correctness and, if the block is acceptable, returns a "command echo block" to the MOC. If a block is not acceptable to the SCE, it is discarded, and the MOC must try again.

Monitoring of command system status and alarms in the 26-m antenna control center is done by a local operator who reports by voice to the Network Operations Control Team.

IV. Subsystems Configurations for Mark IV-85 System

Modifications and reconfiguration of subsystems for the DSN Command System Mark IV-85 are summarized below.

A. Antenna Mechanical Subsystem

At Canberra and Madrid all antennas are located near the SPC. At Goldstone, the 64-m antenna is located near the SPC. The Goldstone 34-m S-band uplink antenna and the Goldstone 26-m former GSTDN antenna remain at their original locations, and are connected to the SPC via the GCF intersite analog communications subsystem. In addition to their SPC cross-support connections, all of the 26-m antenna stations retain their own control, processing, and NASCOM communications equipment for support of Earth-orbiter missions.

B. Antenna Microwave Subsystem

For the 64-m antenna at each complex, the Antenna Microwave Subsystem uplink frequency range is 2090 to 2120 MHz to provide command coverage in the upper end of the Earth-orbiter S-band and all of the deep space S-band allocation. The Microwave Subsystem of the 34-m S-band antenna will handle uplinks over the range of Earth-orbiter and deep space frequency allocations (2025–2120 MHz). The 26-m Antenna Microwave Subsystem also covers the 2025- to 2120-MHz range, for routine support of Earth orbiters and for post-launch initial acquisition of deep space mission spacecraft.

The 64-m Antenna Microwave Subsystem provides selection of linear, right-circular, or left-circular polarization of the S-band uplink. The 34-m and 26-m antennas are provided selection of right-circular or left-circular polarization.

C. Transmitter Subsystem

The 64-m antenna has a high-power and low-power transmitter. The high-power transmitter provides up to 400 kW at frequencies of 2110 to 2120 MHz and up to 300 kW at 2090 MHz. A 100-kW Klystron tube is also available as a

spare. The low-power transmitter provides up to 20 kW in the 2110- to 2120-MHz range.

The 34-m and 26-m antennas have tunable transmitters for the 2025- to 2120-MHz frequencies. Tuning is in 20-MHz steps. Maximum operating power is 20 kW on the 34-m antenna and 10 kW on the 26-m antenna.

D. Receiver-Exciter Subsystem

Functions of the Receiver-Exciter Subsystem include sending on/off messages to the DCD, receiving the command-modulated subcarrier from the DCD, phase-modulating that baseband signal on the uplink carrier, and returning a baseband verification signal to the DCD.

The Block 4 S-band exciter for the 64-m antenna covers a frequency range equal to that of the Antenna Microwave Subsystem. Minor modifications of the verification detector circuitry were made to provide an acceptable interface to the new CMA. The Block 3 exciter for the 34-m stations was upgraded to cover the full range of Earth-orbiter and deep space uplink frequencies. The GSTDN S-band exciter is retained for the 26-m antenna.

E. DSCC Command Subsystem

In the Mark IVA Network configuration the Command Subsystem in the SPC at each complex is implemented as shown in Fig. 1. The new Command Switch Assembly permits any of the exciters to be connected to any CMA under control of the Complex Monitor and Control console. New CMAs were implemented to accommodate the Mark IVA mission support requirements. The CPAs use existing Modcomp II-25 computers with core memory increased to maximum capacity. CPA software was upgraded to satisfy new mission support requirements, to modify the CMA interface functions, and to provide required functions for interfacing with the new DSCC Monitor and Control Subsystem.

F. DSCC Monitor and Control Subsystem

New equipment was implemented for the DSCC Monitor and Control Subsystem (DMC) at each complex in the Mark IVA Network configuration. Assignment of command equipment (antenna, transmitter, exciter, and command modulator-processor combinations) to a given "link," for each scheduled spacecraft pass or for a scheduled test, is accom-

plished by the DMC along with telemetry and tracking equipment assignments. Prepass countdown is controlled by inputs at the Link Monitor and Control console.

The DMC receives antenna pointing and uplink frequency predictions and relays them to the appropriate subsystems. The DMC sends link status information to the CPA, and the CPA sends command system status information to the DMC for link console displays.

G. GCF Subsystems

In the Mark IVA Network configuration, the GCF Digital Communication (GDC) Subsystem replaces the Mark III GCF High-Speed Data and GCF Wideband Data Subsystems. Command data blocks are communicated at a line rate of 56 kb/s, between the Central Communications Terminal at JPL and the Area Routing Assembly at each DSCC.

At the Goldstone DSCC the GCF Intersite Analog Communications Subsystem communicates the CMA signal from the SPC to the DSS 12 and DSS 16 exciters.

H. NOCC Command Subsystem

The NOCC Command Subsystem Real-Time Monitor software was upgraded to accommodate new destination codes, spacecraft identifiers, standards and limits tables, and test command tables. The NOCC Support Subsystem provides capability for generating test command files and configuration standards and limits tables.

V. Mark IV-88 X-Band Uplink

The Mark IVA Network configuration includes a 34-m, high-efficiency (HEF), downlink-only antenna at Goldstone and at Canberra. Another HEF antenna is to be completed at Madrid in 1986.

A task is in progress to provide deep space X-band uplink (7145-7235 MHz) capability on the 34-m HEF antennas at Canberra and Madrid, for support of Galileo and Magellan mission experiments. Spacecraft command capability on the X-band uplink is scheduled for completion in 1988. Implementation of X-band uplink command capability on the Goldstone 34-m HEF antenna is anticipated at a later date.

References

1. Yeater, M. L., Herman, D. T., and Luers, E. G., "Networks Consolidation Program," *TDA Progress Report 42-69*, pp. 10-13, Jet Propulsion Laboratory, Pasadena, Calif., June 15, 1982.
2. Thorman, H. C., "DSN Command System Mark IV-85," *TDA Progress Report 42-70*, pp. 8-15, Jet Propulsion Laboratory, Pasadena, Calif., Aug. 15, 1982.
3. Thorman, H. C., "DSN Command System Mark III-78," *DSN Progress Report 42-49*, pp. 11-18, Jet Propulsion Laboratory, Pasadena, Calif., Feb. 15, 1979.
4. Gordon, D. D., "Mark IVA DSN 26-Meter Subnet," *TDA Progress Report 42-79*, pp. 152-164, Jet Propulsion Laboratory, Pasadena, Calif., Nov. 15, 1984.

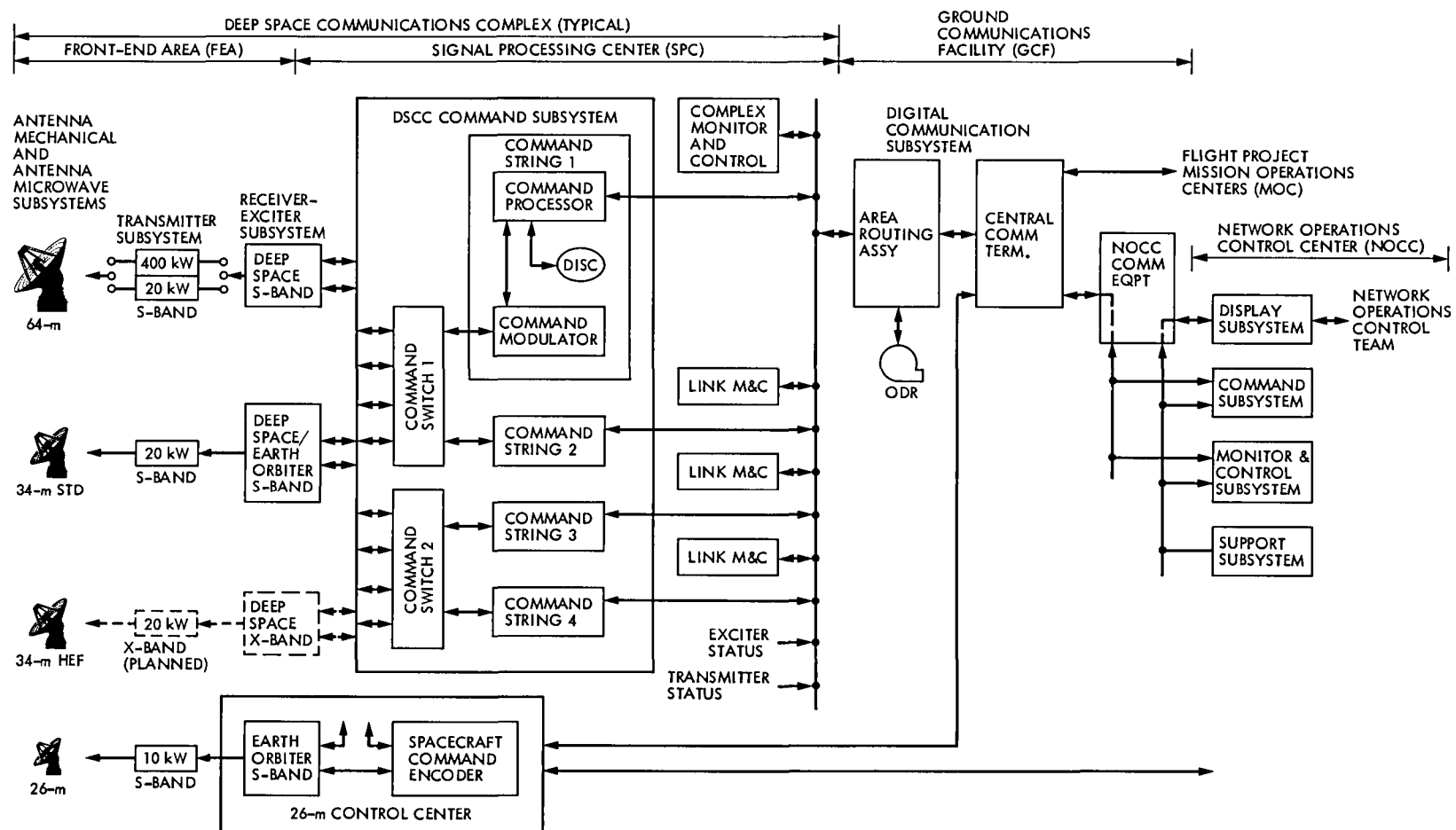


Fig. 1. DSN Command System Mark IV-85 block diagram

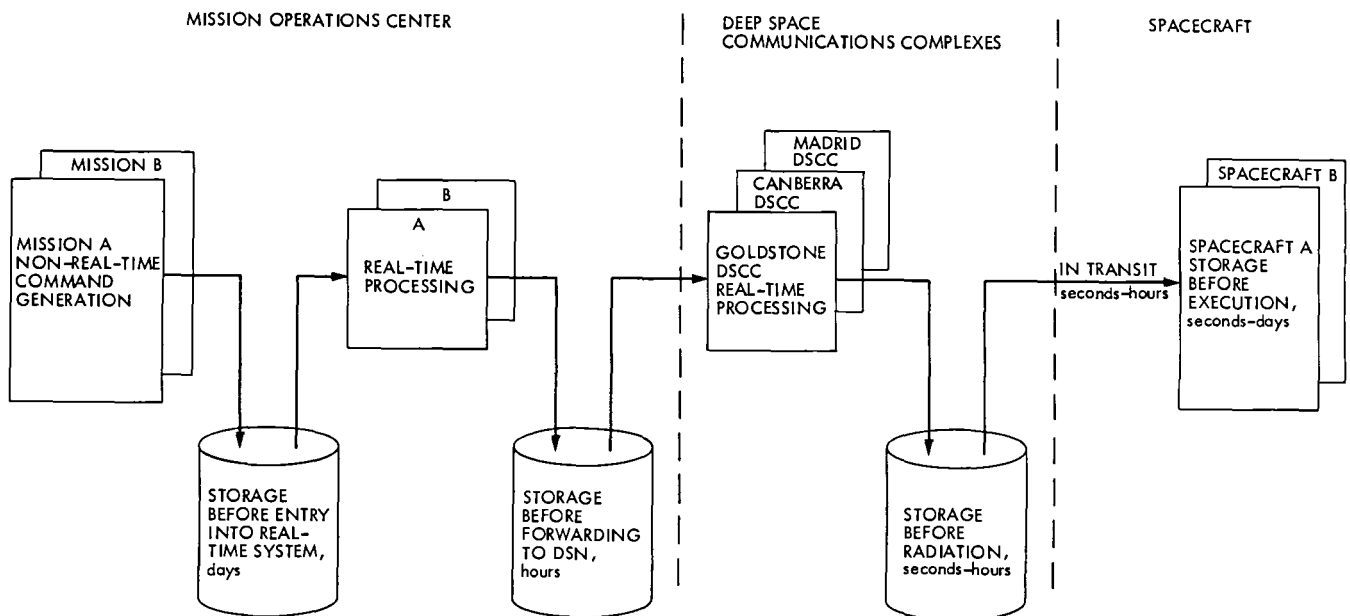
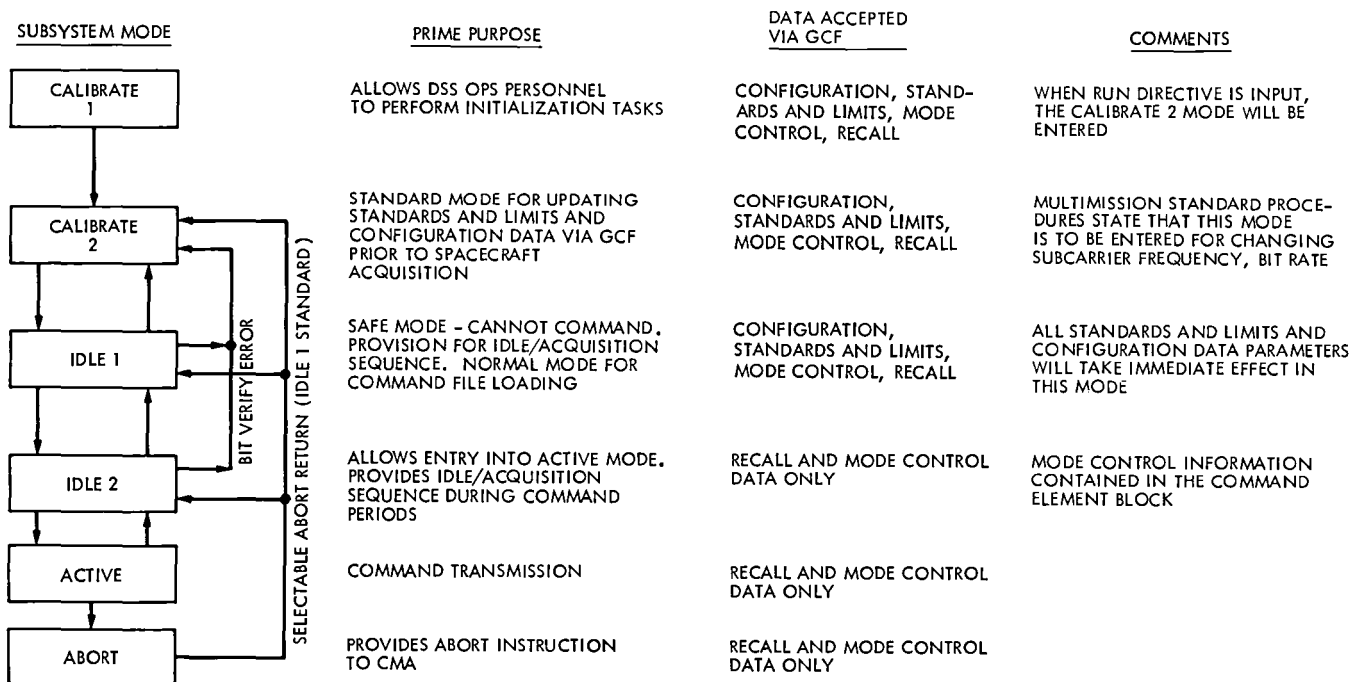


Fig. 2. End-to-end command data flow with typical storage times



- NOTES: 1. COMMAND DATA MESSAGES ARE ACCEPTED IN ALL MODES
 2. ALARM MESSAGES/ALARM DATA ARE TRANSMITTED TO THE MOC IN ALL MODES EXCEPT ABORT

Fig. 3. DSCC Command Subsystem modes

Deep Space Network Radio Science System for Voyager Uranus and Galileo Missions

T. K. Peng

Telecommunications Systems Section

F. F. Donovan

TDA Engineering Office

This article presents an overview of major new requirements, challenges and conceptual designs for the DSN Radio Science System in the 1985 to 1988 period. The Voyager Uranus encounter is being supported with larger combined aperture, higher sample rate, and a centrally controlled network. The Galileo mission will be provided with a high resolution S-Band Faraday rotation detection capability and a high-stability Doppler system with X-Band uplink for gravitational wave search.

I. Introduction

The Deep Space Network (DSN) Radio Science System is a collection of equipment, software, and procedures that enables the DSN to function as an instrument supporting spacecraft radio science experiments. The System has been used by past and present missions to receive and record spacecraft carrier signals in occultation and other propagation experiments. The recorded signals have been analyzed to produce scientific results characterizing planet atmosphere, ionosphere, ring structure, gravity field, solar wind, etc. From 1987, the System will further provide two new capabilities to support the Galileo mission: a Faraday rotation detection capability for mapping the Jovian ionosphere and a very stable two-way Doppler capability for gravitational wave search.

The purpose of this article is to present an overview of major requirements, challenges, and conceptual designs for the DSN radio science system as planned for the 1985 to 1988 period. In this period, the Voyager Uranus and Galileo mis-

sions require enhancement of the System beyond its existing capability. The enhanced capability is expected to meet the needs of all other missions as well. In 1989, the Voyager mission will encounter planet Neptune, requiring additional aperture to receive even weaker signals.

Two types of data are usually used by the radio scientists. One type is acquired by the open-loop receivers and recorded as broad-band data. The science results mentioned before are mainly derived from this type of data. The other type is the traditional radiometric data containing Doppler and range information. The radiometric data are acquired by the closed-loop receivers and are produced regularly by the DSN Tracking System. Description of the DSN Tracking System can be found in other articles of the *TDA Progress Report*. This article will address the open-loop data system only.

Section II describes the system configuration which is presently being implemented in the network to support

Voyager Uranus occultation experiments. This configuration contains equipment with improved performance, able to be centrally controlled, and capable of simultaneously receiving and recording the same spacecraft signal at multiple antennas.

Section III describes the configuration which will be implemented in the network to support the Galileo Faraday rotation experiment in 1988. This configuration contains new phase calibration and real-time verification capabilities.

Section IV describes the configuration planned for the Galileo gravitational wave experiment. This configuration strives to achieve the highest degree of phase stability ever attempted by a tracking station. It will contain the first DSN X-band transmitter and a set of highly stable receiving and calibrating equipment implemented on the new 34-m High Efficiency antenna.

II. Configuration for Voyager Uranus Occultation Experiments

A. The Challenge

The Voyager radio science occultation experiments at Uranus encounter will attempt to characterize the atmosphere of the planet and the structure of its rings. The objective of DSN support is similar to that at the Saturn encounter: recording spacecraft carrier signals during occultations by the rings, the planet and its atmosphere. The Uranus encounter experiments, however, present new challenges to the DSN. First, the signal from the Uranus distance will be weaker. Second, by the time of Uranus encounter, the DSN will have a completely different operational network, the Mark IVA Network, with which the radio science system equipment must interface. Third, some harmonic noises and record gaps that degraded data return at Saturn encounter must be eliminated to make the experiments successful.

B. Implementation at Canberra Complex

Because Uranus is visible mainly at encounter from the southern hemisphere, the DSN is implementing the configuration given in Fig. 1 at the Canberra Deep Space Communication Complex (DSCC) in Australia. This complex is able to cover the entire Uranus occultation experiment. Three antennas will be receiving signals: the 64-m Deep Space Station (DSS) 43, the 34-m DSS 42, and the 64-m radio telescope at the Australian Parkes Observatory. The first two antennas will receive both X-band and S-band signals while the third antenna will receive only the X-band signal, due to cost consideration. The combined aperture provides an increase in gain-noise ratio (G/T) of approximately 3 dB in X-band reception and 1 dB in S-band reception relative to the performance of a

single DSS 43, which was the only station available for radio science at the Voyager Saturn encounter.

As shown in Fig. 1, the system involves equipment in four different geometrical areas: the antennas at Canberra, the antenna at Parkes, the Signal Processing Center (SPC) at Canberra, and the Network Operations Control Center (NOCC) at JPL.

1. **The antennas at Canberra.** DSS 43 and DSS 42 will each have X-Band and S-Band maser amplifiers with approximately 20 K noise temperature, and identical downconverters with 300 MHz intermediate frequency (IF) outputs. Two channels from each antenna are transmitted to the SPC for further down-conversion and processing.

2. **The Signal Processing Center.** The four signals from the Canberra antennas are converted to video frequencies and filtered to 25 kHz bandwidth each. These signals are then sampled in the DSCC Spectrum Processing Subsystem (DSP) at a rate of 50 kps (kilo samples per second) per channel, 8 bits quantized, and are recorded on magnetic tapes at a total rate of 200 kps. These tapes are called the Original Data Record (ODR) which will be shipped after the encounter to the investigators for analysis.

The Spectrum Processing Subsystem (DSP) is the action center of the radio science system. Under the supervision of the DSCC Monitor and Control Subsystem (DMC), the DSP configures itself and tunes the frequencies of the receivers at DSS 43 and DSS 42 according to control messages and frequency predictions received from the NOCC. It also records the system temperature (T_{op}) and the received carrier signal level (P_c) measured by the Precision Power Monitor (PPM).

The sampled signals that are ready to be written on a magnetic tape will also be converted back to analog signals and transmitted to the Spectral Signal Indicator (SSI), a digital spectrum analyzer having a resolution bandwidth as narrow as a fraction of a Hertz. The SSI will display the signal spectrum locally and will also send digital spectral data to the DSP which relays the data to NOCC for display to the mission analysts.

3. **The Network Operations Control Center.** At the NOCC, the spectral data will be displayed by the NOCC Radio Science-VLBI Subsystem (NRV). The display will be observable in the Mission Support Area where Voyager radio science analysts will be able to monitor the performance of data acquisition at the complex and suggest changes in receiver tuning in case the observed frequency of the received signal changes unexpectedly.

The NOCC also contains the Network Support Subsystem (NSS) which generates frequency and pointing angle predictions and the mission sequence of events. This information is transmitted to the SPC to configure the equipment, point the antenna, and tune the receiver frequencies in a timely manner.

4. Performance improvement. There will be significant improvement of system performance compared with the performance at the Voyager Saturn encounter. The spurious noise level of the receiver has been reduced from -40 dBc (dB relative to the carrier) to lower than -50 dBc by redesigning the local oscillator multiplier chain. The sampling aperture jitter has been reduced from over 100 nsec to less than 5 nsec by hardware modification. More visibly, the new Spectrum Processing Subsystem (DSP) will be equipped with computer compatible magnetic tape drives with error detection capability that promises to reduce data recording errors from approximately 1% in the previous system to a thousandth of 1%. The Subsystem also uses an improved computer, a Modcomp Classic replacing the Modcomp II, to control sampling and recording at higher speed and with better reliability.

5. Parkes array. The Parkes 64-m antenna will be equipped with an X-Band maser amplifier with an approximately 20 K system temperature, an RF to IF converter, and a Mark III Occultation Data Assembly (ODA) equipped with an IF to video converter. The received carrier signal is down-converted and recorded on tape as an Original Data Record.

The Original Data Records containing carrier signal information received at DSS 43, DSS 42 and the Parkes antenna will be shipped to the laboratories of the investigators where the three streams of data will be synchronized, combined and analyzed.

6. Wideband backup. Since the occultation experiments are a one-time event lasting only 400 minutes, a wideband backup system is also implemented at the DSS 43 and DSS 42 antennas. The backup system receives the X-Band and S-Band signals at both antennas at a total bandwidth of 8 MHz and records the signals on tape. These backup tapes will be shipped to JPL to be filtered, reformatted and recorded in standard radio science format.

C. Baseline Radio Science Configuration at Goldstone and Madrid Complexes

A baseline radio science system still exists at both the Goldstone and Madrid complexes which will not be involved in Voyager Uranus occultation experiments. The baseline system includes data acquisition from the 64-m DSN antenna only, receiving 4 channels of signals coherently and recording

at a total data rate up to 200 kbps, 8 bits per sample. Various channel bandwidths from 100 Hz to 100 kHz can be selected for operation under the constraint of the total data rate. The 4 channels have often been used to receive X-band and S-band signals with right and left circular polarizations (RCP/LCP) simultaneously. The Canberra complex can be easily restored to this baseline configuration after the Voyager Uranus encounter. The capabilities to measure system temperature, carrier signal power and the signal spectrum are also available in the baseline system.

III. Configuration for Galileo Faraday Rotation Experiment

A. The Challenge

Besides regular occultation experiments similar to those conducted by Voyager, the Galileo mission will conduct two additional radio science experiments: a Faraday rotation experiment and a gravitational wave search. The Faraday rotation experiment will measure the rotation of a linearly polarized S-Band carrier signal when it propagates through the charged particle and magnetic fields of the Jovian environment. The objective is to characterize the spacial and temporal distribution of the magnetic and charged particle fields. The resolution required by the investigation to characterize the distribution is 5 deg or better, observed over time periods ranging from 1 min to 10 hours. Simultaneous reception of an X-band RCP coherent signal will permit separation of the charged particle effect from the magnetic field effect.

In addition, the DSN is required to show the presence of the linearly polarized signal in real time to verify the proper functioning of the data acquisition system.

B. Planned Implementation

To be consistent with the total error budget for the experiment the DSN is planning to design the data acquisition system for a 2.3-deg accuracy and to calibrate the earth ionospheric effect to 1.0 deg. This section will only describe the data acquisition system. The DSN plans to calibrate the earth ionosphere using signals from the NAVSTAR Global Positioning System (GPS) satellites. Description of the GPS system is beyond the scope of this article.

1. Data flow. The S-band data flow through the system is shown in Fig. 2. The X-band acquisition data flow uses the standard radio science technique, and will not be discussed further. The linearly polarized S-band signal received by the 64-m antenna will first be separated in the microwave Ortho Mode Junction (OMJ) into RCP and LCP components. Through two independent but identically configured channels, the

RCP and LCP components will be amplified in the maser amplifiers, down-converted to 300 MHz IF, and transmitted from the antenna to the control room in the SPC. There, both signals will be down-converted to narrow band video frequencies and will be digitized and recorded in the Spectrum Processing Subsystem (DSP). The recorded data will contain information that allows the investigators to measure the relative phase of the RCP and the LCP components of the carrier. The time history of this measurement indicates the received polarization angle vs time. Subtraction of the spacecraft orientation yields the needed results: the change of Faraday rotation angle through time.

There will be a major design change in the tuning of the receiver frequency compared with the Voyager configuration. The receiver frequencies will be tuned at the second local oscillator inside the control room, approximately at 300 MHz. It will no longer be tuned at the first local oscillator in the antenna at microwave frequencies. This change permits a fixed local oscillator with a higher frequency stability to be used at the RF-to-IF converter, improving the effective stability of the overall receiving system. This improved stability will be necessary for supporting the gravitational wave search to be discussed later.

2. Real-time verification. The rate and residual (difference between observed and predicted angles) of the polarization angles will be measured in real time by digitally processing the RCP and LCP signals in the Spectrum Processing Subsystem. The measured angle rate will approximate the spin rate of the Galileo spacecraft.

The measured rate and residuals of the polarization angle will be displayed at the complex, the NOCC, and the Mission Support Area. They will also be recorded on the Original Data Record for use by the investigators.

3. Phase calibration. The recorded data cannot avoid containing errors introduced by the receiving system when the two signals propagate through identical but separate receiver channels. To keep the error below 2.3 deg over 10 hr, it is necessary to calibrate the variation of phase difference between the two channels.

Since the LCP and RCP signals have the same frequency when separated and since the local oscillators that down-convert the two signals have the same source frequency, the differential phase between the two channels is expected to be small and stable. Indeed a recent test conducted at the 64-m antenna at Madrid has demonstrated that, when the antenna was stationary, the phase difference between the RCP and the

LCP channels from the RF to recording remained within 1×10^{-15} in terms of fractional frequency stability relative to S-band. This is equivalent to 1 deg for every 20 min. Another test conducted in the laboratory at JPL has demonstrated the phase difference between the two channels in the control room, from 300 MHz IF to video frequency output, to remain within 1 deg over 4 hr. These tests indicated that at least the control room equipment is stable over long hours within a small fraction of the total error budget. To maintain precise knowledge of the phase errors of the system over time, it is only necessary to calibrate the front end portion of the system, including the microwave amplifiers, down-converters and the long cables from the antenna to the control room.

The phase calibration scheme planned for this experiment will calibrate the angle of polarization of the received signal and the phase variation of the RCP and LCP channels through time. As indicated in Fig. 2, a stabilized S-band calibration signal which is generated by the Phase Calibration Generator (PCG) assembly will be injected into a linearly polarized microwave coupler. This coupler will be located where the RCP and the LCP components of the downlink signal are not yet separated, so that both RCP and LCP channels will receive the same calibration signal. The PCG generates high stability calibration signals by bringing a frequency reference from the hydrogen maser to the antenna, using a phase stabilized cable.

The hydrogen maser is the source of all frequencies and times used at the complex, making coherent all parts of the radio science system at the complex. A phase comparator will be used to extract the calibration tones imbedded in the signals transmitted from the antenna to the control room and to keep track of the phase changes through time. These detected changes are then sent to the Spectrum Processing Subsystem for processing, formatting and recording. As presently conceived, the phase comparator will be implemented with existing VLBI equipment in the complex: a Digital Tone Extractor preceded by an IF to Video converter.

This calibration is expected to reduce the polarization angle measurement error contributed by the front-end portion and the long transmission cables to less than 1.8 deg. By keeping the error from IF to recording within 1 deg, the total error can be maintained within the 2.3-deg allowance assigned to the DSN. This error budget serves as a starting point for system design. A detailed system design is under way, including a more precise definition of achievable system error and the contribution of major assemblies. The errors will finally be measured before the system is delivered to the network in early 1987.

IV. Galileo Gravitational Wave Experiment

A. The Challenge

The Galileo spacecraft is the first spacecraft to carry a transponder with an X-Band receiving capability to receive X-Band uplink signals and return X-Band and S-Band signals coherently. Since an X-Band signal experiences much less phase noise than an S-Band signal when propagating through charged particles, a two-way Doppler system with an X-Band uplink can detect a much smaller phase perturbation than can the same system with an S-Band uplink. The Galileo mission plans to take advantage of the X-Band uplink capability and the very long round-trip light time to search for gravitational waves (G Waves, for short). Detection of the G Waves requires the Doppler system to be stable to a few parts 10^{-15} or better in terms of fractional frequency stability ($\Delta F/F$), averaged over approximately 1000 sec. After examining technical feasibilities and costs, it was decided to implement X-Band uplink capabilities at the new 34-m High-Efficiency (HE) antennas, and to design its equipment so that the fractional frequency stability of the total ground system, including uplink and downlink, could be better than 5×10^{-15} . It will be the first time the DSN implements an X-band uplink capability, and the first time such a high level of phase stability is attempted.

B. Planned Implementation

1. The configuration. The planned configuration to support this experiment is depicted in Fig. 3. It includes an X-Band exciter and an X-Band transmitter in the uplink, with a Digitally Controlled Oscillator (DCO) controlling the uplink frequency. In the downlink it includes X-band and S-band low-noise amplifiers, open-loop receivers, and the Spectrum Processing Subsystem (DSP) that controls and calibrates the downlink system. The DSP also digitizes, processes, and records the data. The system also includes the Phase Calibration Generator (PCG) that delivers local oscillator frequencies and X-Band phase calibration signals to the antenna, with stability approaching that of the Hydrogen maser standard. The S-band signal is received for media calibration only. Since the S-band channel is expected to be stable enough for media calibration, no phase calibration is planned for the S-band channel.

Both uplink and downlink data are needed by the investigators to determine the Doppler frequency. The uplink data will contain frequencies commanded by the uplink DCO. The downlink data will include signals received in X-Band and S-Band, the local oscillator frequency of the receiver, and the phase calibration data for the X-band receiver channel.

2. Error budget. A detailed performance analysis was conducted in 1984 to see if the 5×10^{-15} stability goal for the ground station is achievable. The potentials of every element in the system were examined according to the actual measurements of prototype equipment under advanced development, experience on similar hardware, computer simulation, and theoretical calculations. The result of the design analysis showed that with careful design and testing on each component, the 5×10^{-15} overall stability goal is indeed achievable. The error contributed by each element of the system is estimated in Table 1 in terms of fractional frequency standard deviation (square root of Allan variance of $\Delta F/F$ relative to X-band and averaged over 1000 sec). The basis for each estimate is also indicated in Table 1.

When implemented, the stability of the ground system will be measured in the following ways. The stability of the hydrogen maser frequency standard and the stability of the up- and downlinks combined, excluding the hydrogen maser and the antenna, will be measured separately. The stability of the station, including the hydrogen maser and the up- and downlinks but excluding the antenna, will then be estimated from the results of the two measurements. These measurements do not require a spacecraft; a test translator will be used instead to convert uplink frequencies to downlink frequencies. The contribution of the antenna structure to the instability of the station can only be estimated by conducting a Doppler test with the spacecraft when the spacecraft and the media are quiet.

3. Further work. A detailed system design was developed in 1985 in which the error budgets reported here were confirmed and methods of testing for the system and the contributing subsystems were defined. The prototype equipment is being built. It will undergo a ground system test in May 1986 at DSS 13. The station will be used in a flight demonstration with the Galileo spacecraft in August 1986. The results will be reported in the future.

Table 1. Error budget for Galileo gravitational wave search: 34-m HEF antenna contribution with X-band uplink and X-band downlink

Square root of Allan variance of $\Delta F/F$ relative to 8.4 GHz
averaged over 1000 sec, $\times 10^{-15}$

1. Hydrogen maser		1.0 ^a
2. Uplink		2.8
Exciter and transmitter (with phase feedback) microwave	2.7 ^b 0.5 ^c	
3. Downlink		3.0
Microwave	0.5 ^c	
Phase calibration	2.2 ^d	
IF-video conversion	2.0 ^d	
Digitization	0.1 ^d	
4. Antenna structure (uplink and downlink, 10 mph wind)		1.4 ^e
Total Root Sum Squared (RSS)		4.5

^aFrom measurement of existing units
^bFrom measurement of advanced development units
^cAnalytical result
^dAnalysis of performance of similar or prototype units
^eComputer simulation

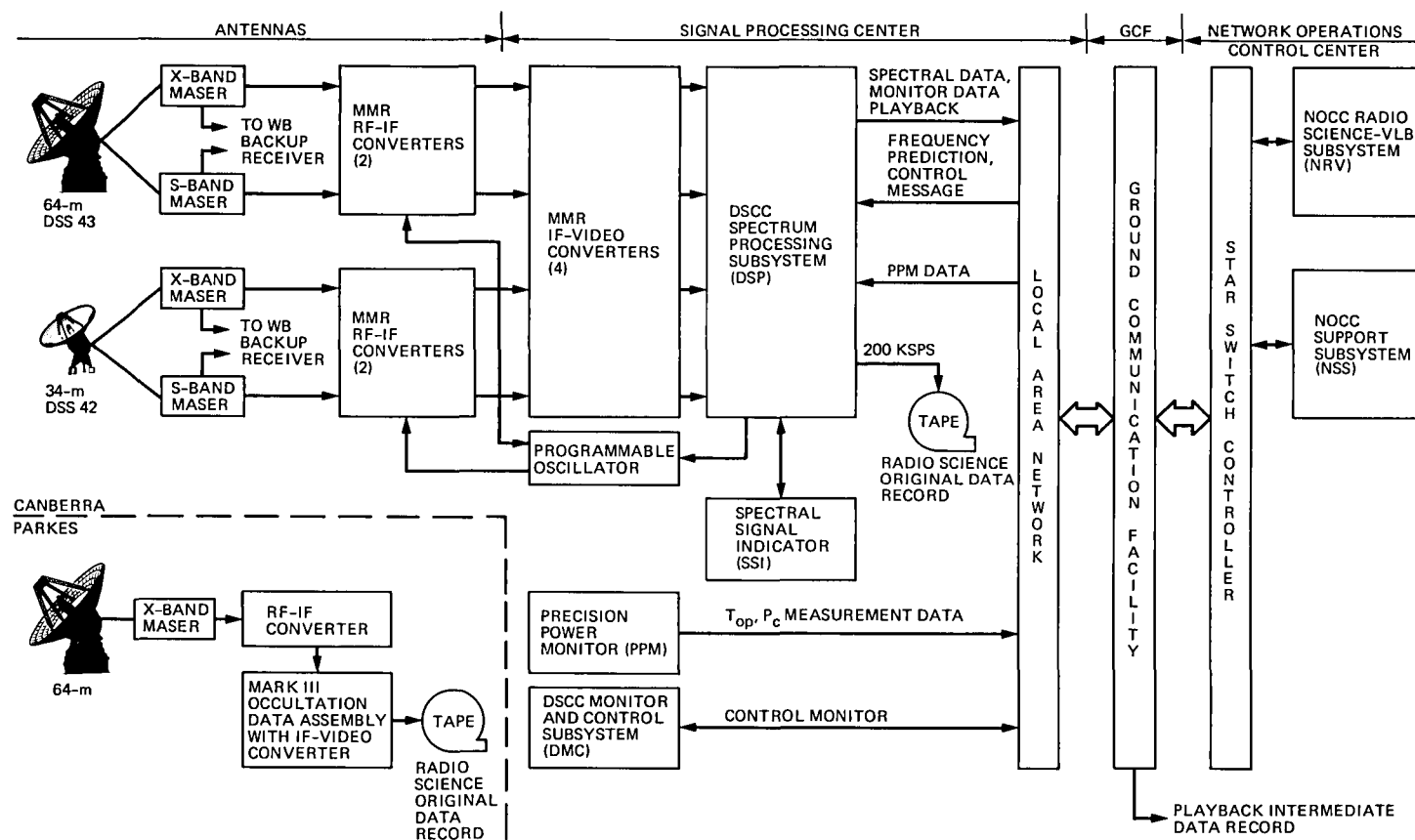


Fig. 1. DSN radio science data flow for the Voyager Uranus occultation experiments, Canberra DSCC

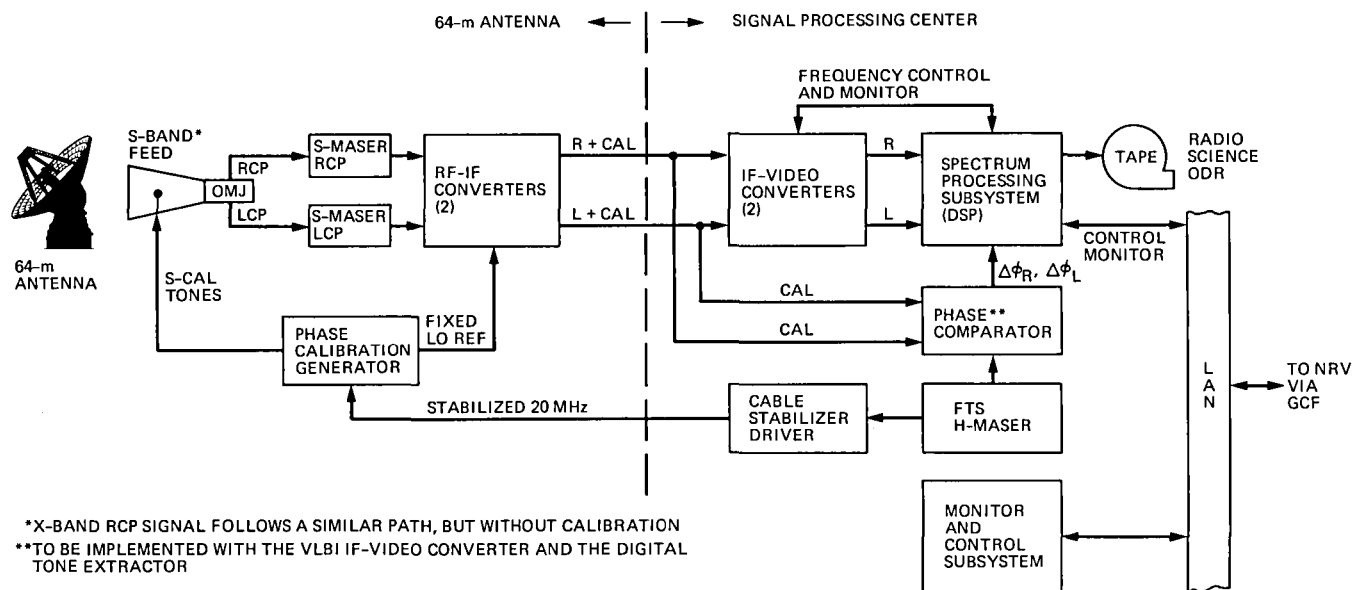


Fig. 2. DSN radio science data flow for the Galileo Faraday rotation experiment

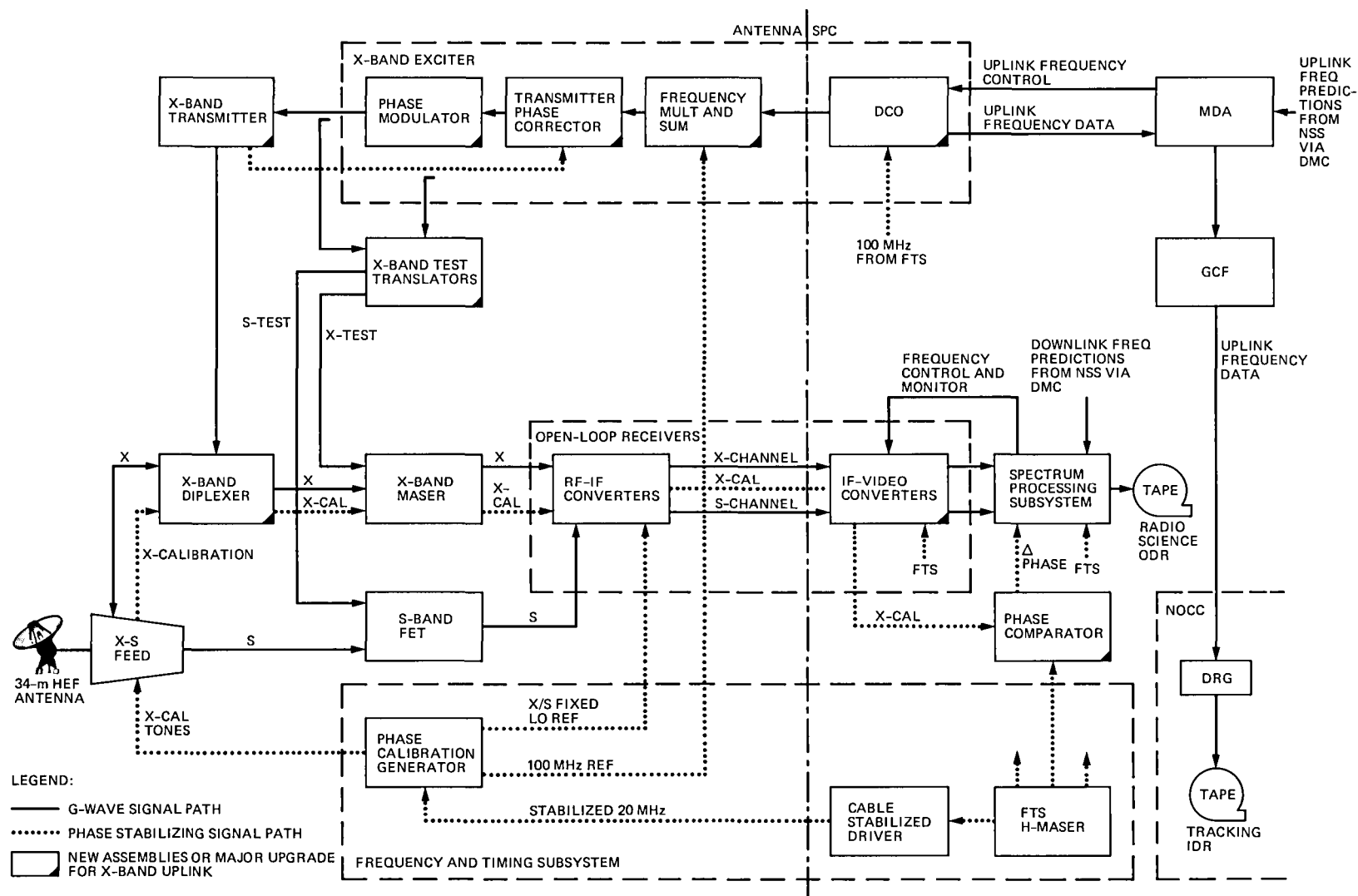


Fig. 3. Stabilized X-band signal path for the G wave experiment on the 34-m HEF antenna

The Search for Reference Sources for Δ VLBI Navigation of the Galileo Spacecraft

J. S. Ulvestad and R. P. Linfield

Tracking Systems and Applications Section

A comprehensive search has been made in order to identify celestial radio sources that can be used as references for navigation of the Galileo spacecraft by means of Δ VLBI observations. The astronomical literature has been searched for potential navigation sources, and several VLBI experiments have been performed to determine the suitability of those sources for navigation. This article reports on the results of such work performed since mid-1983. We present a summary of the source properties required, the procedures used to identify candidate sources, and the results of the observations of these sources. The lists of sources presented are not meant to be taken directly and used for Δ VLBI navigation, but they do provide a means of identifying the radio sources that could be used at various positions along the Galileo trajectory. Since the reference sources nearest the critical points of Jupiter encounter and probe release are rather weak, it would be extremely beneficial to use a pair of 70-m antennas for the Δ VLBI measurements.

I. Introduction

The Galileo spacecraft is scheduled to be launched in May 1986 on a mission to explore Jupiter and its satellites. On the way to Jupiter, it will fly past the asteroid Amphitrite. In July 1988, an atmospheric probe will be released from the main spacecraft bus. This passive probe will follow a path that diverges slightly from that of the orbiter. Both the probe and the orbiter are scheduled to arrive at Jupiter in December 1988. While the orbiter will make a tour of the Jovian system that is scheduled to last for approximately two years after the planetary encounter, the probe will enter the atmosphere and survive for about an hour.

Current plans call for Δ VLBI (VLBI = Very Long Baseline Interferometry) navigation to be used to help determine the

spacecraft trajectory precisely. The Δ VLBI observables are sensitive to position in the plane of the sky rather than to radial distance or velocity. As such, they can be complementary to the more traditional Doppler and ranging data. The increased accuracy afforded by including the Δ VLBI data will help conserve fuel during the tour of the Jovian system and will be especially useful in reconstructing the trajectory of the atmospheric probe. The more accurate trajectory reconstruction will allow a more detailed specification of the properties of Jupiter's atmosphere.

The basic principle of Δ VLBI navigation is to use two widely separated Deep Space Network (DSN) stations to find the angular separation between a spacecraft and a natural radio source, usually a quasar. The two stations are used as an inter-

ferometer and can acquire observables (phase and phase-delay rate) that depend on the geometry of the baseline connecting the stations, the quasar and spacecraft positions, the station clocks, and the Earth's atmosphere. Observed phase is used to reconstruct signal path delay, which in turn is a measure of source angular position. Observations from two baselines are needed to determine both components of angular position. By making sequential VLBI observations of the spacecraft and a quasar, the effects of a number of imperfectly known quantities can be reduced by differencing the observables. Since the quasar position has been determined previously in an inertial frame of radio sources, the JPL VLBI catalogue (Ref. 1), the angular position of the spacecraft is tied to an inertial frame. An important point to recognize is that the accuracy of the Δ VLBI results depends nonlinearly on the angular separation between the spacecraft and the natural radio source. Larger separations imply less complete cancellation of some errors and a less precise determination of the spacecraft position.

II. Searching for Suitable Δ VLBI Reference Sources

A. Identification of Candidate Sources

Jupiter's sidereal period of revolution is nearly 12 yr. Therefore, both Jupiter and the Galileo spacecraft will traverse a large portion of the ecliptic plane during the approximately 4-yr lifetime of the mission. Since the most accurate Δ VLBI navigation requires radio sources as close as possible to the spacecraft, a net of reference sources located along the ecliptic plane is needed.

A set of criteria for suitable reference source candidates is based on the properties of the Δ VLBI navigation system. The system in use is called the Block I system. It involves the recording and real-time transmission of VLBI data in a 250-kHz observing channel. This bandwidth, the maximum achievable coherent integration time (about 10 min), and the properties of the DSN 70-m antennas (to be upgraded from 64 m) can be combined to estimate the minimum correlated flux density for a usable VLBI navigation source; detailed error analysis has been performed in JPL Engineering Memorandum 335-26.¹ If corrections for propagation errors caused by charged particles in the ionosphere are to be made, observations at both S and X bands (2.3 and 8.4 GHz, respectively) are needed. This requires the reference source's correlated flux density to be at least 0.25 Jy ($1 \text{ Jy} = 10^{-26} \text{ W} \cdot \text{m}^{-2} \cdot \text{Hz}^{-1}$) in each band for a pair of 70-m antennas. For the

combination of a 70-m and a 34-m antenna, the required correlated flux density would be close to 0.5 Jy.

Counts of sources as a function of total flux density at different frequencies have been made by astrophysicists studying the distribution and evolution of radio sources in the universe (e.g., Ref. 2). In the strip of sky within 10° of the ecliptic plane, there should be a source with a total flux density of at least 0.25 Jy at 5 GHz about every 0.7° in ecliptic longitude. (Most radio astronomy surveys and source counts have been made at 1.4 or 5 GHz, not at the 2.3- and 8.4-GHz frequencies used by the DSN.) However, most natural radio sources are heavily resolved by interferometers with intercontinental separations. The fringe spacing (resolution element) of an interferometer with a 10,000-km baseline is about 0.7 milli-arcseconds (3.6 nanoradians) at X band. Only sources having more than 0.25 Jy in structure that is unresolved by such an interferometer are suitable as Block I Δ VLBI navigation references. Since very few extragalactic radio sources have more than half their total flux density in such compact structure, and most have considerably less, the density of reference sources is much lower than indicated by the total flux densities alone.

Typical extragalactic radio sources have "steep" spectra in which the flux density decreases with increasing frequency. However, some sources have relatively "flat" or "inverted" spectra, with the total flux density remaining fairly constant or even increasing with increasing frequency in the 1- to 10-GHz spectral range. It has long been known that such sources have a far higher probability of being very compact than do the steep spectrum sources, so these sources are the best candidates for Δ VLBI navigation. However, the most compact sources are also the most variable at X band (S band fluxes remain relatively constant).

The selection of candidate Δ VLBI reference sources proceeded based on the knowledge of system and source characteristics outlined above. Surveys of the northern and southern skies complete to flux densities of 0.5–0.6 Jy at 2.7 or 5 GHz were made in the 1960s and early 1970s (e.g., Refs. 3 and 4). Objects that appeared in these surveys were potential candidates for use as Block I Δ VLBI navigation sources. The astronomical literature was searched in order to find any available information on the radio structure and spectrum of the sources within 20° of the Galileo trajectory. Many were found to have most of their flux in components resolved on scales of arcseconds to arcminutes. Of the remaining sources, some had little structural information available, while some were known to have more than 0.25 Jy in components less than about an arcsecond in size. These sources were chosen as potential Δ VLBI navigation sources deserving further investigation.

¹ Thomas, J.B., "An Error Analysis for Galileo Angular Position Measurements with the Block I Δ DOR System," JPL Engineering Memorandum 335-26, 1981 (JPL internal document).

Preference was given to sources with flat radio spectra, as they are most likely to contain very compact components.

B. VLBI Observations of Candidate Radio Sources

Some of the candidate sources were already part of the JPL VLBI catalogue, and others had been observed prior to mid-1983. Thus, accurate positions and typical correlated flux densities were known. The other candidate sources were observed in several short baseline Mark II VLBI experiments, using the 40-m antenna at Caltech's Owens Valley Radio Observatory (OVRO) and the 26-m DSS 13 in the Goldstone complex as the two observing stations. Data were eventually obtained on all the good candidate sources along the Galileo trajectory. Typically, the available data on a given source include two or three observations of about 10-min duration at different hour angles on a single day. Since OVRO's S/X receiver is uncooled, its system temperatures were about 6 times the system temperature of 25 K for DSS 13. The Mark II system has a usable bandwidth of 1.8 MHz, so the OVRO-DSS 13 baseline was about a factor of two less sensitive than a baseline with two 70-m DSN antennas and the Block I VLBI system.

Data from the observations were processed on the Caltech/JPL Block 0 VLBI correlator. The main information extracted from post-correlation software was correlated flux densities at S and X bands and improved positions for the detected sources. The OVRO-DSS 13 baseline is approximately 250 km in length, yielding a fringe spacing of about 30 milliarcseconds at X band. Thus, presence of a correlated flux density greater than 0.25 Jy at both S and X bands on this baseline is a necessary but not a sufficient condition for a source to be deemed suitable for Δ VLBI navigation. Instead, those radio sources with at least 0.25 Jy in correlated flux on the 250-km baseline need to be observed on an intercontinental baseline to see if they have enough correlated flux on a 10,000-km baseline. As expected, the limiting factor for most sources is their weakness at X band. The total flux density at that frequency is less than at S band for the typical steep radio spectra, and the smaller fringe spacings at X band usually resolve a larger fraction of the total flux than at S band.

III. Observational Results

Results from the search for suitable Δ VLBI sources are presented in Tables 1 through 3. The sources in these tables are arranged in order of increasing right ascension, with the zero point shifted to be near the beginning of the Galileo trajectory. Table 1 lists sources currently in the JPL VLBI catalogue that might be usable reference sources for Galileo navigation. Included in the table are the source names, their positions, the typical correlated flux densities at S and X bands

on intercontinental baselines, and the minimum angular distance between each source and the spacecraft trajectory. It should be noted that some of these sources may not be suitable Δ VLBI references. Most have variable flux densities that may fall below the flux density threshold at which consistent detection can be expected, and some have structure that can cause them to have insufficient correlated flux densities when observed with some projected baselines.

Table 2 lists sources observed on the OVRO-DSS 13 baseline. In addition to the columns used in Table 1, the epoch of the short baseline observations is given here. The correlated flux densities listed are those found on the baseline within California and are larger than the correlated flux densities that would be found on intercontinental baselines. Table 2 is divided into two parts. First, we list those sources that were detected at both bands; then we list the sources that were undetected in one or both observing bands. The latter radio sources definitely will not have sufficient flux on intercontinental baselines to be used for navigation. Sources in the top half of the table cannot be ruled out on the basis of the short baseline observations alone, but further information is required to determine whether they can be used as navigation references. Separations from the Galileo trajectory are listed only for sources that were detected in at least one of the two observing bands. Typical position errors in this table are on the order of 5 arcseconds, compared to the milliarcsecond positional accuracy for most of the sources listed in Table 1.

Table 3 lists the sources that were selected from previous short baseline observations or from the astronomical literature and were observed in a long baseline experiment between DSS 13 and DSS 63 (the 64-m antenna in Spain) in November 1983. Several of these sources are part of the JPL VLBI catalogue and are also listed in Table 1. The correlated flux densities listed in Table 3 are those that were found on the nearly east-west intercontinental baseline. Values on the baseline between California and Australia could be higher or lower, depending on the structures of the individual sources. Positions listed in Table 3 have a typical accuracy of several tenths of an arcsecond.

A shortage of suitable Δ VLBI sources still exists near some critical parts of the Galileo trajectory. Figure 1 displays the Galileo trajectory from 1986 through 1991. The hatched regions are those within 10° of a radio source that has a high probability of being a usable navigation reference. Figure 2 is a blow-up of the section of the trajectory including probe release and Jupiter encounter, with 10° -radius circles plotted for the reference sources that can be used with a reasonable expectation of success. The radio source GC 0406+12 (not plotted) is the candidate reference source for Δ VLBI nearest the positions of probe release and Jupiter encounter, but it

often has a correlated flux density below 0.2 Jy at X band. We have concentrated our greatest efforts on finding reference sources in this region, but the results are not encouraging. Another region of potential importance is near the position of Jupiter in late 1989 and early 1990. This area is in a part of the ecliptic which intersects the galactic plane. Since regions within 10 deg of the galactic plane generally have not been surveyed for radio sources, few potential navigation sources have been identified in this area. It is a region that would be very important if the Galileo launch were delayed by about 18 months, as it would then be the location of probe release and initial Jupiter encounter.

It must be re-emphasized that navigation sources should not be selected from these tables without consultation with the VLBI Systems Group. The natural radio sources have variable flux densities; new information about the sources is being acquired by a variety of means; and positions of the sources are frequently updated and refined.

IV. Continuing Investigations

Two approaches are being taken currently in an effort to find more Δ VLBI navigation sources for Galileo. These approaches utilize radio source surveys which have been and are being made by astronomers not connected with JPL. A few of the sources identified in these surveys have some potential as navigation reference sources, so we are attempting to investigate them further. Neither of the ongoing investigations is very likely to yield any sources that would be better than those already known. However, the effort is continuing because of the high value of even a single usable navigation source if it is located in the right place.

The first of the continuing investigations utilizes a sensitive sky survey being performed by the radio astronomy group of the Massachusetts Institute of Technology (MIT) using the 91-m telescope of the National Radio Astronomy Observatory (NRAO), located in Green Bank, West Virginia. This survey will be complete to a limiting total flux density of about 0.1 Jy at 5 GHz. The MIT-Green Bank survey includes many sources that were not previously known because they are weaker than the 0.5–0.6 Jy completeness limits of previous surveys. Conceivably, one or more of these sources could have enough compact flux to be suitable navigation reference sources. The survey also includes some sources that have increased their flux densities in the last 10–20 yr, and now have somewhat more than 0.5 Jy at 5 GHz.

The portion of the sky survey between -0.5° and $+19.5^\circ$ declination has been completed by the MIT group (Ref. 5). This includes the region south of the ecliptic near the posi-

tion where Galileo encounters Jupiter. The survey has been used by JPL to select many of the sources that were investigated on the OVRO-DSS 13 baseline in August 1985. It is encouraging that the two sources nearest the critical encounter and probe release position, 0341+158 and 0342+147, were both detected at S and X bands in each of three scans. Observations of these sources have been made recently (in September 1985) on intercontinental baselines; the data from that experiment have not yet been analyzed. Intercontinental-baseline observations of several of the other sources listed in Table 2 are tentatively planned for the future.

The second ongoing investigation involves a recent low-frequency survey for scintillating sources in some regions of the galactic plane. This survey was made by a non-JPL group using the Ooty radio telescope in India (Ref. 6). Sources that were found to scintillate by the Ooty group are those that contain components less than an arcsecond in size. It is possible that one or several of these sources could be used for VLBI navigation in the region where the ecliptic intersects the galactic plane. The Indian group has already observed some of the sources with sub-arcsecond resolution at NRAO's Very Large Array (VLA) in New Mexico. We have collaborated with them on a proposal to observe the remaining sources with the VLA. The proposed observations would provide enough knowledge about the radio sources to judge whether any have enough potential as Δ VLBI navigation sources to be investigated on intercontinental baselines.

V. Summary and Speculations for the Future

An extensive search for potential Δ VLBI navigation sources for the Galileo spacecraft has been performed. This search has involved both investigation of the astronomical literature and new interferometric observations of a number of natural radio sources. The investigation of many radio sources in the ecliptic has also provided information that could be used in the navigation of other planetary exploration spacecraft in the future. Unfortunately, the distribution of strong, ultra-compact radio sources is such that there is apparently a lack of strong navigation sources near some critical parts of the Galileo trajectory. It is unlikely that any more suitable sources will be found in these critical regions. Since it is desirable to have reference sources near the spacecraft trajectory in order to provide the best navigation accuracy, it may be advantageous to use some sources whose correlated flux densities are too low to be detected consistently with the combination of a 34-m and a 70-m antenna. Therefore, it will be necessary to use two 70-m antennas if Δ VLBI observations utilizing these weak sources are attempted.

Improved navigation of future missions by the use of reference sources within a few degrees of the spacecraft would

require increased sensitivity of the Δ VLBI observations. Such an improvement in sensitivity could be achieved either with larger receiving antennas or by using a wider bandwidth VLBI system. The Mark III system currently used in astronomy has a maximum bandwidth of 56 MHz, more than 200 times that currently employed in the Block I system. This bandwidth is too high for a real-time VLBI system with satellite transmis-

sion of data. However, it could be useful for non-real-time work in such tasks as reconstructing trajectories of spacecraft and probes after the fact. A real-time system with an intermediate bandwidth of 5 MHz would provide nearly 5 times the sensitivity of the Block I system. This would allow Δ VLBI to be done with two 70-m antennas for sources having correlated flux densities above 0.05 Jy.

Acknowledgment

We thank D. D. Morabito for helping to reduce much of the data from the experiments reported in this article.

References

1. Fanelow, J. L., Sovers, O. J., Thomas, J. B., Purcell, G. H., Cohen, E. J., Rogstad, D. H., Skjerve, L. J., and Spitzmesser, D. J., "Radio Interferometric Determination of Source Positions Utilizing Deep Space Network Antennas-1971 to 1980," *Astronomical Journal*, Vol. 89, pp. 987-998, 1984.
2. Condon, J. J., "Cosmological Evolution of Radio Sources Found at 1.4 GHz," *Astrophysical Journal*, Vol. 284, pp. 44-53, 1984.
3. Pauliny-Toth, I. I. K., Kellermann, K. I., Davis, M. M., Fomalont, E. B., and Shaffer, D. B., "The NRAO 5-GHz Radio Source Survey. II. The 140-ft 'Strong,' 'Intermediate,' and 'Deep' Source Surveys," *Astronomical Journal*, Vol. 77, pp. 265-284, 1972.
4. Shimmins, A. J., Bolton, J. G., and Wall, J. V., "The Parkes 2700 MHz Survey (Tenth Part). Supplementary Catalogue for the Declination Zone $+4^\circ$ to $+25^\circ$," *Australian Journal of Physics, Astrophysical Supplement* 34, pp. 63-83, 1975.
5. Bennett, C. L., "The MIT-Green Bank 5 GHz Radio Survey," Ph.D. Thesis, Massachusetts Institute of Technology, pp. 1-222, 1984.
6. Rao, A. P., and Ananthakrishnan, S., "Interstellar Scattering in the Inner Parts of the Galaxy," *Nature*, Vol. 312, pp. 707-711, 1984.

Table 1. Potential Galileo Δ VLBI sources in the JPL VLBI catalogue

IAU name	Other name	Position (1950.0)		Correlated flux, Jy		D_{\min} , deg
		Right ascension, 00 ^h 00 ^m 00. ^s 0000	Declination, 00° 00' 00."000	S band	X band	
2155-152	OX-192	21 55 23.2414	-15 15 30.070	0.55	0.49	16.8
2216-038	P 2216-03	22 16 16.3814	-03 50 40.606	0.74	1.78	11.2
2223-052	3C 446	22 23 11.0774	-05 12.17.778	0.78	1.15	9.1
2243-123	OY-172.6	22 43 39.7925	-12 22 40.273	1.24	0.79	5.4
2320-035	P 2320-035	23 20 57.5248	-03 33 33.613	0.52	0.29	1.8
2345-167	P 2345-16	23 45 27.6822	-16 47 52.585	1.8	0.42	12.5
0019+058	P 0019+058	00 19 58.0233	05 51 26.473	0.43	0.41	4.7
0048-097	P 0048-09	00 48 09.9825	-09 45 24.237	0.83	0.73	12.7
0106+013	P 0106+01	01 06 04.5175	01 19 01.161	2.51	0.76	4.3
0119+041	GC 0119+04	01 19 21.3925	04 06 44.012	0.74	0.55	2.5
0202+149	P 0202+14	02 02 07.3961	14 59 50.961	1.00	1.33	3.6
0234+285	CTD 20	02 34 55.5896	28 35 11.426	1.48	1.97	13.7
0235+164	GC 0235+16	02 35 52.6301	16 24 04.033	1.65	1.82	2.1
0239+108	OD 166	02 39 47.0897	10 48 16.295	0.35	0.40	3.7
0333+321	NRAO 140	03 33 22.4049	32 08 36.674	0.60	0.40	13.3
0336-019	CTA 26	03 36 58.9525	-01 56 16.878	1.4	1.0	19.9
0406+121	GC 0406+12	04 06 35.4765	12 09 49.322	0.4	0.2	7.6
0420-014	P 0420-01	04 20 43.5393	-01 27 28.691	1.5	1.5	21.6
0528+134	P 0528+134	05 28 06.7590	13 29 42.295	0.86	0.74	9.4
0552+398	DA 193	05 52 01.4076	39 48 21.949	0.6	1.0	16.5
0735+178	P 0735+17	07 35 14.1262	17 49 09.254	0.50	0.69	4.1
0738+313	OI 363	07 38 00.1785	31 19 02.054	1.40	0.81	9.5
0742+103	DW 0742+10	07 42 48.4643	10 18 32.648	0.5	0.4	11.2
0745+241	B2 0745+24	07 45 35.7253	24 07 55.494	0.81	0.40	2.7
0748+126	P 0748+126	07 48 05.0601	12 38 45.468	0.75	0.30	8.6
0827+243	B2 0827+24	08 27 54.3987	24 21 07.646	0.8	0.26	4.4
0851+202	OJ 287	08 51 57.2503	20 17 58.402	1.32	2.00	1.9
1004+141	GC 1004+14	10 04 59.7838	14 11 10.893	0.27	0.30	1.6

Table 1 (contd)

IAU name	Other name	Position (1950.0)		Correlated flux, Jy		D _{min} , deg
		Right ascension, 00 ^h 00 ^m 00. ^s 0000	Declination, 00° 00' 00."000	S band	X band	
1038+064	OL 064.5	10 38 40.8845	06 25 58.514	0.58	0.42	3.0
1040+121	3C 245	10 40 06.0002	12 19 14.953	0.24	0.38	2.8
1055+018	P 1055+01	10 55 55.3130	01 50 03.518	1.00	0.88	5.8

Table 2. Short baseline source observations

IAU name	Other name	Position (1950.0)		Correlated flux, Jy		D _{min} , deg	Epoch
		Right ascension, 00 ^h 00 ^m 00. ^s 0	Declination, 00° 00' 00''	S band	X band		
A. Sources Detected at Both Frequencies:							
0259+121	P 0259+12	02 59 46.4	12 07 11	0.59	0.29	3.9	1985.6
0341+158	...	03 41 33.7	15 50 19	0.46	0.27	2.8	1985.6
0342+147	...	03 42 18.0	14 44 26	0.30	0.32	3.9	1985.6
0411+054	4C+05.14	04 11 58.3	05 27 14	0.6	0.25	14.4	1985.6
0425+048	P 0425+04	04 25 08.7	04 50 30	0.66	0.65	15.6	1985.6
0536+145	...	05 36 51.5	14 32 14	0.38	0.55	8.5	1985.6
0544+273	...	05 44 26.0	27 20 43	0.51	0.47	4.3	1984.2
0554+242	...	05 54 03.0	24 13 15	1.43	0.97	1.4	1984.2
0556+238	...	05 56 28.0	23 53 25	0.45	0.61	0.9	1984.2
0600+177	...	06 00 16.0	17 43 00	0.59	0.56	5.5	1984.2
0610+260	3C 154	06 10 43.8	26 05 30	0.56	0.3	7.1	1984.2
0629+104	...	06 29 29.4	10 24 13	1.6	0.3	12.6	1985.6
0629+160	...	06 29 50.3	16 02 25	1.2	0.6	7.0	1984.2
0657+172	...	06 57 07.7	17 13 37	0.95	1.4	5.8	1984.2
1011+250	...	10 11 06.1	25 04 06	0.53	1.05	12.2	1984.2
B. Sources Not Detected at One or Both Frequencies:							
0320+053	4C+05.14	03 20 41.4	05 23 37	1.12	<0.24	...	1985.6
0332+078	GC 0332+07	03 32 12.4	07 50 16	0.49	<0.25	...	1984.2

Table 2 (contd)

IAU name	Other name	Position (1950.0)		Correlated flux, Jy		D _{min} , deg	Epoch
		Right ascension, 00 ^h 00 ^m 00. ^s 0	Declination, 00° 00' 00''	S band	X band		
0333+128	4C+12.15	<0.25	<0.24	...	1985.6
0348+049	...	03 48 12.8	04 56 56	0.63	<0.25	...	1984.2
0408+070	P 0408+07	<0.21	<0.24	...	1985.6
0411+141	P 0411+14	<0.21	<0.24	...	1985.6
0417+177	P 0417+17	<0.21	<0.24	...	1985.6
0441+106	P 0441+10	04 41 26.8	10 37 17	0.65	<0.28	...	1984.2
0459+135	P 0459+13	04 59 43.8	13 33 56	0.41	<0.24	...	1985.6
0510+311	<0.25	<0.26	...	1984.2
0514+109	...	05 14 00.2	10 54 42	0.43	<0.26	...	1984.2
0520+244	<0.21	<0.24	...	1985.6
0523+327	<0.25	<0.26	...	1984.2
0531+194	P 0531+19	05 31 47.3	19 25 25	0.5	<0.26	...	1984.2
0538+286	<0.25	<0.26	...	1984.2
0539+290	<0.25	<0.26	...	1984.2
0548+165	...	05 48 24.9	16 35 49	1.10	<0.25	...	1984.2
0552+125	...	05 52 45.3	12 32 03	0.7	<0.25	...	1984.2
0557+191	...	05 57 03.0	19 09 00	0.32	<0.27	...	1984.2
0559+193	<0.25	<0.26	...	1984.2
0600+219	...	06 00 51.1	21 59 41	0.61	<0.26	...	1984.2
0606+163	<0.25	<0.26	...	1984.2
0607+174	<0.25	<0.26	...	1984.2
0611+131	...	06 11 16.0	13 09 00	0.34	<0.25	...	1984.2
0618+145	3C 158	<0.25	<0.26	...	1984.2
0618+197	<0.25	<0.26	...	1984.2
0622+179	<0.25	<0.26	...	1984.2
0623+264	P 0623+26	<0.25	<0.26	...	1984.2
0624+176	<0.25	<0.26	...	1984.2
0626+168	<0.25	<0.26	...	1984.2

Table 2 (contd)

IAU name	Other name	Position (1950.0)		Correlated flux, Jy		D _{min} , deg	Epoch
		Right ascension, 00 ^h 00 ^m 00. ^s 0	Declination, 00° 00' 00''	S band	X band		
0631+142	...	06 31 55.0	14 16 00	0.32	<0.24	...	1984.2
0640+089	...	06 40 42.4	08 57 00	0.34	<0.23	...	1984.2
0645+147	<0.25	<0.26	...	1984.2
0648+153	<0.25	<0.26	...	1984.2
0710+118	P 0710+11	<0.25	<0.26	...	1984.2
0711+146	<0.25	<0.26	...	1984.2
0721+161	<0.25	<0.26	...	1984.2
0725+147	3C 181	<0.25	<0.26	...	1984.2
0727+153	<0.25	<0.26	...	1984.2
0801+303	<0.25	<0.26	...	1984.2
0928+008	...	09 28 18.1	00 48 12	0.35	<0.26	...	1984.2
1042+071	P 1042+071	10 42 19.7	07 11 39	0.34	<0.31	...	1984.2

Table 3. Long baseline observations, 1983.9

IAU name	Other name	Position (1950.0)		Correlated flux, Jy		D _{min} , deg
		Right ascension, 00 ^h 00 ^m 00. ^s 00	Declination, 00° 00' 00.''0	S band	X band	
2223-114	P 2223-114	22 23 04.52	-11 28 56.7	0.40	0.43	9.1
2233-148	P 2233-140	22 33 53.99	-14 48 56.1	0.15	<0.16	8.8
2325-150	P 2325-150	23 25 11.62	-15 04 26.8	0.45	0.26	8.9
2351-006	...	23 51 35.39	-00 36 25.2	0.34	<0.11	1.5
2354-117	P 2354-11	23 54 57.22	-11 42 21.0	1.00	0.23	9.1
2355-106	P 2355-106	23 55 36.96	-10 36 50.4	0.54	0.49	8.3
0003-066	NRAO 5	00 03 40.30	-06 40 17.0	0.54	0.37	5.4
0047-051	...	00 47 49.03	-05 08 39.4	0.15	0.26	8.5
0048-097	P 0048-09	00 48 09.98	-09 45 24.2	0.8	0.7	12.7
0234+285	CTD 20	02 34 55.59	28 35 11.4	1.40	1.97	13.7
0237+040	GC 0237+04	02 37 14.43	04 03 30.1	0.27	0.52	9.9

Table 3 (contd)

IAU name	Other name	Position (1950.0)		Correlated flux, Jy		D _{min} , deg
		Right ascension, 00 ^k 00 ^h 00. ^s 00	Declination, 00° 00' 00."0	S band	X band	
0423+051	P 0423+051	04 23 57.26	05 11 36.3	0.52	0.25	15.2
0430+052	3C 120	04 30 31.64	05 14 58.3	0.1	0.4	15.5
0446+112	P 0446+11	04 46 21.24	11 16 17.0	0.31	0.5	10.6
0454+066	P 0454+06	04 54 26.42	06 40 28.2	0.14	0.42	15.4
0456+060	P 0456+06	04 56 08.17	06 03 32.5	0.14	0.11	16.1
0459+060	GC 0459+06	04 59 34.80	06 04 50.9	0.42	0.31	16.2
0502+049	P 0502+049	05 02 43.83	04 55 39.1	0.30	0.50	17.4
0507+179	P 0507+17	05 07 07.51	17 56 58.2	0.26	0.75	4.7
0509+152	P 0509+152	05 09 49.47	15 13 51.4	0.80	0.22	7.3
0620+389	OH 335	06 20 51.56	38 58 26.8	0.47	0.24	15.6
0650+371	GC 0650+37	06 50 35.31	37 09 26.7	0.56	0.3	14.1
0711+356	OI 318	07 11 05.62	35 39 52.2	0.72	0.1	13.0
0722+145	P 0722+145	07 22 26.99	14 31 12.1	0.45	0.35	7.8
0729+259	GC 0729+25	07 29 32.87	25 55 06.9	0.21	0.26	3.9
0733+300	GC 0733+30	07 33 04.67	30 01 04.2	0.34	0.32	8.0
0738+313	OI 363	07 38 00.18	31 19 02.1	1.4	0.7	9.5
0738+272	B2 0738+27	07 38 20.94	27 13 48.7	0.15	<0.1	5.5
0742+318	B2 0742+31	07 42 30.78	31 50 16.3	0.2	0.3	10.1
0742+103	DW 0742+10	07 42 48.46	10 18 32.6	2.4	0.3	11.2
0743+259	GC 0743+25	07 43 23.09	25 56 25.0	0.48	0.36	4.5
0748+333	GC 0748+33	07 48 41.09	33 21 03.7	0.32	<0.09	11.9
0754+100	P 0754+100	07 54 22.61	10 04 39.5	0.87	0.6	10.9
0759+183	GC 0759+18	07 59 55.32	18 18 15.4	0.30	0.21	2.6
0802+212	GC 0802+21	08 02 42.63	21 15 28.6	0.5	<0.10	0.7
0820+225	P 0820+22	08 20 28.54	22 32 45.2	0.30	0.28	2.4
0834+250	GC 0834+25	08 34 42.33	25 04 54.5	0.31	<0.18	5.5
0839+180	GC 0839+18	08 39 14.11	18 46 27.5	0.23	<0.13	0.6
0952+179	AO 0952+17	09 52 11.83	17 57 44.9	0.15	0.36	4.0

Table 3 (contd)

IAU name	Other name	Position (1950.0)		Correlated flux, Jy		D _{min} , deg
		Right ascension, 00 ^k 00 ^h 00. ^s 00	Declination, 00° 00' 00."0	S band	X band	
0953+254	OK 290	09 52 59.77	25 29 34.0	0.37	0.2	11.3
1004+141	GC 1004+14	10 04 59.78	14 11 10.9	0.27	0.28	1.6
1013+208	GC 1013+20	10 13 59.44	20 52 47.4	0.33	0.35	8.6
1022+194	GC 1022+19	10 22 01.49	19 27 35.2	0.31	0.26	7.9
1042+071	P 1042+071	10 42 19.48	07 11 26.2	0.20	0.22	2.0

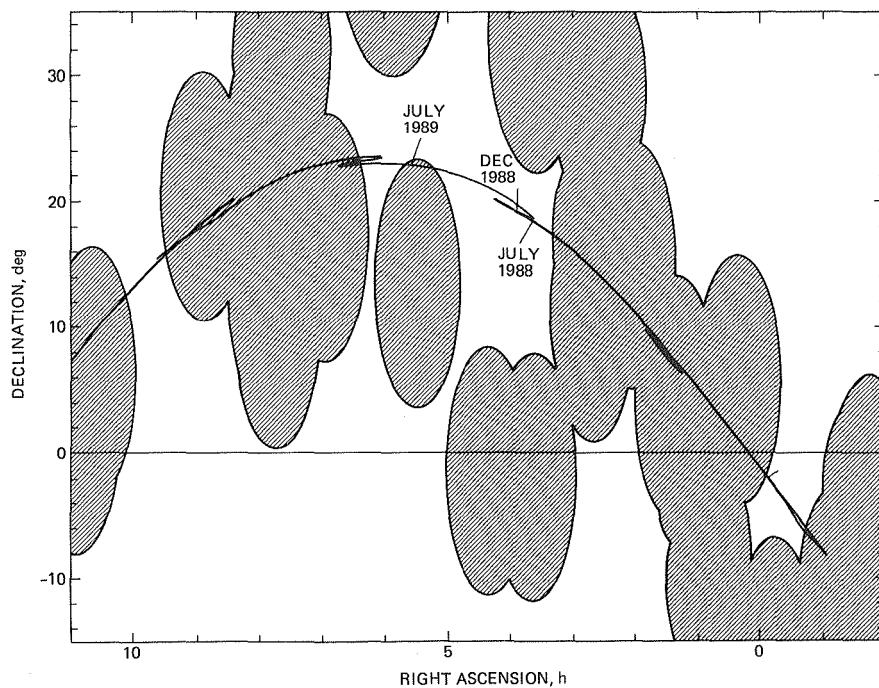


Fig. 1. Plot of the Galileo trajectory from 1986 through 1991. Hatched regions are within 10° of a potential Δ VLBI reference source that is likely to be usable in the Block I navigation system.

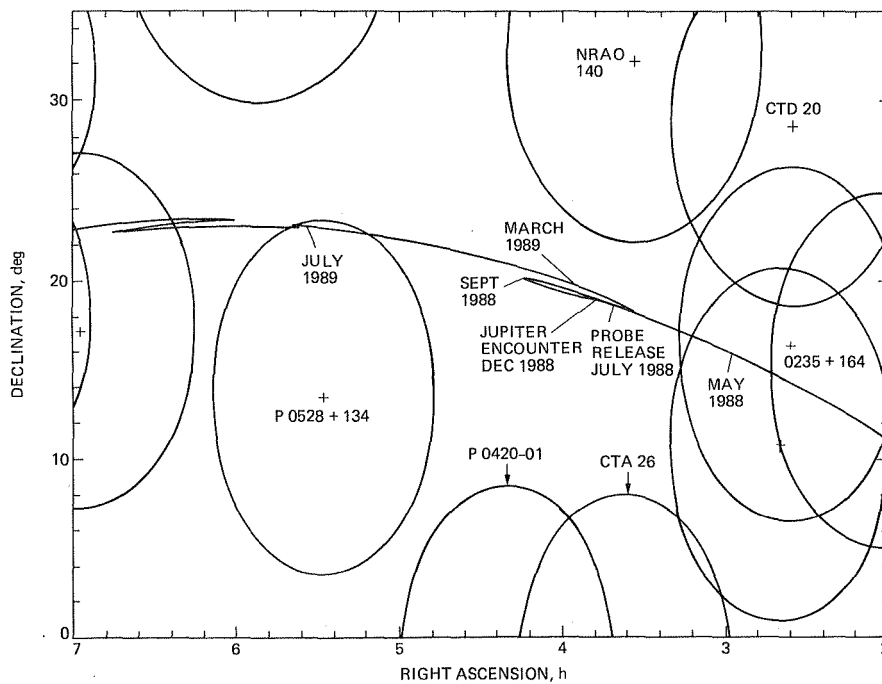


Fig. 2. Plot of the Galileo trajectory in 1988 and 1989, with several important points marked. The sources likely to be usable for Δ VLBI navigation are shown with 10° -radius circles centered on each radio source position. Note the lack of sources in the region where probe release and Jupiter encounter will occur.

Gain, Phase, and Frequency Stability of DSS-42 and DSS-43 for Voyager Uranus Encounter

A. G. Cha

Radio Frequency and Microwave Subsystems Section

R. Levy

Ground Antennas and Facilities Engineering Section

In the present article, we derive theoretically rigorous definitions of such parameters as RF signal path length, phase delay, and phase/frequency stability in a Cassegrainian antenna applicable to a narrow bandwidth channel, as well as algorithms for evaluating these parameters. This work was performed in support of the Voyager spacecraft encounter with Uranus in January 1986. The information was needed to provide Voyager/Uranus radio science researchers with a rational basis for deciding the best strategy to operate the three antennas involved during the crucial 5-hour occultation period of the encounter. Such recommendations are made at the end of the article.

I. Introduction

The vast majority of Cassegrainian antenna articles are written about communications applications. The articles address well-defined communications characteristics of the antenna such as gain, sidelobe level, cross-polarization level, system gain over noise temperature ratio (G/T), and carrier over interference (C/I) ratio. The list above can be characterized as pertaining to the amplitude of the complex radiation pattern of the antenna. In recent years, the phase characteristics of the antenna radiation pattern have become extremely important for much scientific research in radio astronomy, geology, and planetary sciences. These phase characteristics

include group delay time, phase delay, and Doppler shift (due to internal motion of antenna parts) in the antenna.

For large Cassegrainian antennas used in deep space communications and scientific research, normal operational practices based on communications considerations alone are often not sensible for scientific research where phase information is vital. In such applications, a careful balance must be maintained between the often conflicting communications requirements (gain) and antenna phase/frequency stability requirements dictated by scientific applications. An excellent example can be found in the NASA/JPL Deep Space

Network, where ground station antennas support both communications and scientific data acquisitions from outer space. For communications data acquisition, the subreflector is normally refocused to correct for gain loss due to gravity induced surface distortions, and the antenna is periodically con-scanned to peak up the gain. For VLBI and radio science applications, these gain-maximizing maneuvers are often deactivated to maintain better phase/frequency stability, but at the expense of sustaining some gain losses.

Given the importance of antenna phase characteristics in numerous scientific research projects, it is surprising that only scant information on phase-related characteristics can be found in parabolic and Cassegrainian reflector antenna literature. The paper by Cha, Rusch, and Otoshi appears to be the first rigorous analysis of RF signal group delay time through a reflector antenna (Ref. 1). In that paper, a GTD subreflector diffraction analysis and a physical optics main reflector diffraction analysis were made on a Cassegrainian antenna to determine the signal group delay on a theoretically rigorous basis. In the present article, we further derive theoretically rigorous definitions of such parameters as RF signal path length, phase delay, and phase/frequency stability in a Cassegrainian antenna applicable to a narrow bandwidth channel, as well as algorithms for evaluating these parameters. This work was performed in support of the Voyager spacecraft encounter with Uranus in January 1986. The information was needed to provide Voyager/Uranus radio science researchers with a rational basis for deciding the best strategy to operate the three antennas involved during the crucial 5-hour occultation period of the encounter. Such recommendations are made at the end of the article.

II. Mathematical Formulation of RF Signal Path Length, Phase Delay, and Doppler Shift in a Cassegrainian Antenna

The basis used to derive RF signal path length in a Cassegrainian antenna is ray optics and scalar diffraction theory. More elaborate diffraction theory can be used, but it has been shown that the simple approach described below yields an excellent approximation to a full two-reflector vector diffraction analysis insofar as delay characteristics in a large Cassegrainian antenna are concerned (Ref. 1). In Ref. 1, a rigorous two-reflector vector diffraction analysis was performed to determine RF signal group delay in a Cassegrainian antenna. The results were compared to results of a simpler analysis based on ray optics and aperture theory and were found to be nearly the same.

The procedure used to derive mathematical formulae for phase delay and Doppler shift is as follows. The well-known Kirchhoff scalar diffraction equation (variously known as

Huygen's principle or aperture field integration method), is used to express the far field of a planar source of electromagnetic (EM) radiation. The amplitude and phase of the planar source are in turn determined from the feed horn radiation pattern using ray optics. The aperture field integration problem geometry is shown in Fig. 1. The source of radiation is the tangential components of the EM field (from Ref. 2, p. 161).

$$\begin{aligned} \bar{E}(R, \theta, \phi) = & \frac{-jk}{4\pi R} \exp[-jk(R - R_o)] \hat{R} \\ & \times \int \{ \hat{n} \times \bar{E}(\bar{R}') - \eta_o \hat{R} \times [\hat{n} \times \bar{H}(\bar{R}')] \} \\ & \cdot \exp(jk\bar{R}' \cdot \hat{R}) dS' \end{aligned} \quad (1)$$

where

$$\begin{aligned} \eta_o &= \text{free space impedance} \\ k &= \text{free space wave number} \\ \hat{R} &= \text{unit radial vector} \\ \hat{n} &= \text{unit normal vector to the aperture} \end{aligned}$$

In Eq. (1), the primed coordinate variables are the source coordinates and the unprimed coordinates are the field (observer) coordinates, all with an origin at point 0. The origin is selected away from the aperture center because a stationary origin relative to the ground is required. The aperture center, on the other hand, is a point that moves with the antenna pointing motion. Without loss of generality, assuming the E field is \hat{y} polarized, the observer is in a direction normal to the aperture plane and ray optics is valid,

$$\hat{R} = \hat{n} = \hat{z} \quad (2)$$

$$\bar{E}(\bar{R}') = E_y(\bar{R}') \hat{y} \quad (3)$$

$$\bar{H}(\bar{R}') = -\frac{E_y(\bar{R}')}{Z_o} \hat{x} \quad (4)$$

Using Eqs. (2), (3), (4), Eq. (1) becomes

$$\bar{E}(R, 0, 0) = \frac{jk}{2\pi R} \exp[-jk(R - R_o)] \int E_y(\bar{R}') dS' \hat{y} \quad (5)$$

Dropping the vector notation in Eq. (5), and including the exp($j\omega t$) time dependence hitherto suppressed,

$$E(R) = \frac{jk}{2\pi R} \exp[j\omega t - jk(R - R_o)] \int E_y(\bar{R}') dS' \quad (6)$$

Eq. (6) is used to precisely define such quantities as RF signal path length, phase delay, and Doppler shift in a Cassegrainian antenna in a manner that allows these quantities to be separated from other path length, phase delay, and Doppler in the overall signal propagation path.

With reference to Fig. 2, the path length is defined in the ray optics sense to start at the feedhorn phase center and end in the aperture plane. In Fig. 2, a typical ray pathlength is shown as $L_1 + L_2 + L_3$. The aperture plane is defined as the plane at a constant distance R_0 from a stationary rotational axis (hour-angle axis for HA-dec antennas, azimuth axis for az-el antennas) in which the EM field has zero phase gradient (i.e., only quadratic phase error is present). Note that the paraboloid main reflector focal plane cannot generally be used as the aperture plane in our present formulation when the feedhorn or subreflector is not in a focused position. Our path length definition requires a number of rays to be used, an aperture plane to be found by searching (for a zero phase gradient plane), and ray path lengths to be averaged. The antenna beam peak, and not the main reflector axis, is assumed to be pointing at the spacecraft. This definition of antenna signal path length makes sense in that it neatly separates the antenna path length from other path lengths and phase delays in the signal propagation path, as will be shown.

Using ray optics, Eq. (6) can be written as

$$E(R) = \frac{\exp(j\omega t - jkR + jkR_0)}{R} \times \int |E(r', \phi')| \exp[-jk(L_1 + L_2 + L_3)] dS' \quad (7)$$

Equation (7) shows explicitly that the aperture field is derivable from ray optics and the phase of the aperture field is determined by the path lengths of rays originating from the feedhorn phase center. The constant factor $jk/2\pi$ has been omitted in Eq. (7) because it has no bearing on discussions in this article. We now define

$$L_s = L_1 + L_2 + L_3 \\ = \text{total pathlength of individual ray} \quad (8)$$

$$E_0 \exp(-jk\bar{L}_s) = \int E(r', \phi') \exp[-jk(L_1 + L_2 + L_3)] dS' \\ = \text{illumination weighted average phase delay} \quad (9)$$

where E_0 and \bar{L}_s are real, positive numbers.

The quantity \bar{L}_s in Eq. (9) is the average ray path length in the Cassegrainian antenna and is synonymous to RF signal path length in the antenna in this article. The phase and Doppler shift are then

$$\Delta\Phi = \text{phase change in antenna} \\ = k\Delta\bar{L}_s \quad (10)$$

$$\Delta f = \text{Doppler shift due to } \frac{d\bar{L}_s}{dt} \\ = (-)f \frac{d\bar{L}_s}{c} \quad (11)$$

where

f = frequency
 c = light velocity

The definition in Eq. (11) is justified as follows. Substituting Eq. (9) in Eq. (7),

$$E(R) = \frac{E_0}{R} \exp[j(\omega t - kR + kR_0 - k\bar{L}_s)] \\ = \frac{E_0}{R} \cdot \exp(j\Phi) \quad (12)$$

where

$\Phi = \Phi(t)$ = phase as function of time

The instantaneous angular frequency is

$$\frac{d\Phi}{dt} = \omega - k \frac{dR}{dt} - k \frac{d\bar{L}_s}{dt} \\ = \omega - kc \frac{dR}{c} - kc \frac{d\bar{L}_s}{c} \\ = \omega - w \frac{dR}{c} - w \frac{d\bar{L}_s}{c} \quad (13)$$

where $w ([dR/dt]/c)$ is the Doppler due to spacecraft motion and $w ([d\bar{L}_s/dt]/c)$ is the Doppler due to internal motion in the antenna. To summarize:

$$\text{Phase change in antenna} = k \Delta \bar{L}_s \quad (14)$$

$$\text{Doppler shift} = (-) f \frac{d\bar{L}_s}{c} \quad (15)$$

where $\Delta \bar{L}_s$ is the averaged path length change in the Cassegrainian antenna due to subreflector movement or surface deformation under varying gravity load conditions.

III. Phase Delay Change and Doppler Shift Due to Subreflector Motion Along z Axis

It is possible and useful to derive signal phase and frequency change caused by subreflector motion in terms of axial movement Δz and velocity $V_z = dz/dt$. As shown in Fig. 2, it is clear that a subreflector motion of Δz causes the overall path-length to change by $2\Delta z$ approximately (Δz each in L_1 and L_2). Thus,

$$\Delta \bar{L}_s \cong 2\Delta z \quad (16)$$

The factor of 2 is exactly correct for the ray (speaking in ray optics terms) on axis. When all ray path lengths are averaged, the theoretical computation by R. Levy¹ and experimental measurement of group delay time by Ootshi and Young (Ref. 3) suggest that the average path length change is more accurately given by

$$\Delta \bar{L}_s = 1.8 \Delta z \quad (17)$$

It then follows that the phase delay change is

$$\Delta \text{PHASE} = 1.8k \Delta z \quad (18)$$

At first look, it would appear reasonable to use the axial (z-axis) velocity of the subreflector to arrive at a first-order estimate of the signal Doppler shift in antenna, $f(V_z/c)$. Comparing with Eq. (15), it becomes apparent that a better estimate may be $1.8f(V_z/c)$. The factor of 1.8 comes in from the folded optical path length $L_1 + L_2 + L_3$, as explained above. Substituting $\Delta \bar{L}_s = 1.8 \Delta z$ in Eq. (15), we obtain the Doppler shift as $1.8f(V_z/c)$. To summarize in terms of z displacement and speed of subreflector (for $V_z/c \ll 1$):

$$\text{Phase delay change} = 1.8k \Delta z \quad (18)$$

$$\text{Doppler shift} = (-) 1.8f(V_z/c) \quad (19)$$

It is hoped that someone who is familiar with the special theory of relativity can verify these. The relative merits of formulae for Eqs. (14) and (15) versus Eqs. (18) and (19) are as follows:

- (1) Equations (14) and (15) are more accurate.
- (2) Equations (18) and (19) are very simple to apply. The only relevant subreflector parameters are Δz and V_z . To use Eqs. (14) and (15), a detailed table of subreflector x, y, z position versus time is needed. The time dependence is non-trivially determined by computer programs in most large ground station antennas.

Insofar as Eqs. (18) and (19) are approximate formulae, some remarks and cautions are required. First, note that the z-axis subreflector motion is approximately parallel to the optical propagation path, while the x- and y-axis motions are approximately perpendicular to it. Therefore, the z-axis subreflector motion must be the dominant factor in phase change and Doppler determination. If one is faced with a situation where x- and y-axis displacements and velocities are an order or two of magnitude larger than z-axis motion, it is less clear when Eqs. (18) and (19) cease to be accurate approximations. The answer can probably come only from a large number of case studies. For the present, it is advised that Eqs. (14) and (15) be used when in doubt. In the meantime, Eqs. (18) and (19) do serve many useful purposes in providing quick estimates in cases where x- and y-axis motions are not orders of magnitude larger than z-axis motions.

IV. Numerical Results for Voyager Uranus Encounter

Three antennas are used in the Voyager closest encounter with Uranus, DSS-42 and DSS-43 in the NASA/JPL Deep Space Network, and the Australian Parkes antenna. During the 5-hour occultation period, the antennas are at $(-23^\circ (337^\circ))$ declination and sweep through the sky from approximately $335^\circ (-25^\circ)$ to $360^\circ (0^\circ)$, then to 50° in antenna (or local) hour-angle. The spacecraft location in antenna angular coordinates and the spacecraft occultation time from 0 to 5 hours in time are shown in Fig. 3. Note that every 15° in antenna hour-angle change corresponds to 1 hour in time. The chart in Fig. 3 is used to convert antenna angular coordinates from declination and hour angles to elevation and azimuth angles. As is well known, large ground-station antenna gain is dependent on the elevation angle because of gravity. During the 5-hour occultation period, the range of elevation angle is seen to be between 45° and 78° . The two antennas studied, DSS-42 and DSS-43, have diameters of 34 m and 64 m, respectively. The 34-m antenna has a HA-dec mount, while the 64-m antenna has an az-el mount. In the normal operation of the antennas, the subreflector is automatically refocused to

¹R. Levy, "X-Band Uplink D-Level Review on Antenna Mechanical Subsystem" (internal document), oral presentation at the Jet Propulsion Laboratory, Pasadena, Calif., July 1985.

partially compensate for gain degradation induced by gravity as the elevation angle changes. This is especially important for the 34-m antenna, as the data will show. In addition, the entire antenna is periodically con-scanned to maintain pointing accuracy.

As stated previously, the radio science project scientists are highly concerned that the instruments used should not introduce either significant amplitude or phase distortions to signals returned from the spacecraft. It is desired that the antenna gain should be high as well as stay fairly constant over the range of elevation angles. For phase/frequency stability, it is believed that even a few degrees of phase change and/or a 0.01-Hz frequency shift introduced by the instrument could lead to loss of valuable scientific information (instrument sensitivity is such that a few degrees of phase change can be detected). Based on these considerations, the preliminary plan for tracking the spacecraft during occultation is as follows:

- (1) The antennas will not be con-scanned but will be "blind-pointed" using pointing tables built into the control computer.
- (2) The DSS-43 subreflector will be fixed instead of auto-focused.
- (3) The DSS-42 subreflector will be auto-focused.

The reason for the different focusing techniques of DSS-42 and DSS-43 is that it is suspected that DSS-42 would sustain severe gain loss if it were not auto-focused.

The study reported herein was initiated in October 1985 to substantiate decisions (2) and (3) above and to determine the best position for fixing the DSS-43 subreflector. The results of our investigation are summarized in Tables 1 through 4 and cover the following cases:

- Case I: DSS-43, subreflector fixed at position for 42° elevation.
- Case II: DSS-43, subreflector fixed at position for 67° elevation.
- Case III: DSS-42, subreflector auto-focused.
- Case IV: DSS-42, subreflector fixed at position for 67° elevation.

The independent variable for the tables is mission time, tabulated in the first column. The tables are intended to show how the antenna gain, phase, and Doppler shift vary within

the 5-hour occultation period. The gain variation is computed from a theoretical structural deformation model, including the RMS surface error loss and defocusing loss in cases where the subreflector is not auto-focused. For Cases I, II, and IV, the phase and frequency changes are computed from Eqs. (14) and (15), again using the theoretical structural deformation model. For these cases, the subreflector is fixed, and the antenna phase/frequency instability is caused by the continuous smooth (small-scale) reflector surface deformation under varying gravity load conditions, resulting in excellent antenna phase/frequency stability. For Case III, the antenna phase/frequency changes are computed from Eqs. (18) and (19). In this case, the subreflector is auto-focused and the phase/frequency stability is determined largely by subreflector motion rather than the main reflector structural deformation. Although it is preferable to use the exact Eqs. (14) and (15), it is difficult to determine a detailed subreflector position versus time table (i.e., x , y , z versus T), due to the complexity of the subreflector-motion controlling computer program. Since a quick but only approximate answer was needed, Eqs. (18) and (19) were chosen for use in this case. For DSS-43 (64-m antenna), it is clear from Tables 1 and 2 that the subreflector should be fixed at the position corresponding to a 67° elevation angle, by virtue of higher absolute gain and much smaller gain variation over the range of elevation angles of concern. For DSS-42 (34-m antenna), a comparison of Tables 3 and 4 substantiates the decision to auto-focus the subreflector, in view of the large gain loss and gain variation seen in Case IV. The phase/frequency stability of Case III is much worse, as expected, due to subreflector focusing movement. The Doppler shift reflects the way the subreflector is designed and/or programmed to move — the focusing motion comes in short spurts of constant-velocity motion of 0.0023 in./sec along the z axis and lasts about 10 seconds or so. This leads to a ± 0.0029 -Hz phase stability prediction at X-band based on Eq. (19).

The following background information should be a helpful supplement to the tables:

- (1) The case with DSS-43 subreflector auto-focused was not included. For this case, X-band $\Delta f = 0.03$ Hz; X-band $\Delta \text{phase} = 22^\circ$ over a 2-second period sporadically. The phase and frequency changes are computed from Eqs. (18) and (19). In this case, the subreflector is programmed to move only when the position error (relative to focused position for maximum gain) in either x , y , or z axis is at least 0.0488 in. The subreflector z -axis velocity is 0.024 in./sec, leading to the rather significant 0.03-Hz Doppler shift.
- (2) All X-band Δphase and Δf numbers can be multiplied by (f_s/f_x) to obtain S-band numbers.

- (3) The tables are for $\Delta T = 20$ min. For cases where the subreflector is auto-focused, it is predicted that the frequency and phase changes take place sporadically in short periods of a few seconds in the 20-minute time-span. If needed, it appears possible that a subreflector position versus time history, i.e., (x, y, z) versus T for $\Delta T =$ a few seconds, may be obtained through a combination of operator console actions and the use of chart recorders at each antenna.
- (4) The possibility of focusing the subreflector in x - and y -axes and fixing the subreflector z -axis position during occultation has been suggested. This appears a viable alternative, especially for DSS-42. Using this option, the gain loss with elevation-angle characteristics is believed to be only a couple of hundredths of a dB worse than full three-axis focusing, while the frequency stability is believed to be a couple of orders of magnitude better than the full three-axis focusing case.

V. Conclusions and Recommendations

For the Voyager Uranus encounter, the original plan (in late October 85) was to fix the DSS-43 subreflector at position of 42° elevation angle while auto-focusing the DSS-42 subreflector during occultation. The rationale has been explained above. The investigation described herein has substantiated the soundness of the different approaches to operating the two antennas. In addition, the optimal elevation angle for the DSS-43 subreflector has been determined. The results of the investigation support the following approach:

- (1) A fixed DSS-43 subreflector position of 67° elevation angle.
- (2) Auto-focusing the DSS-42 subreflector in x - and y -axes only.

In addition, rigorous formulations and exact definitions have been presented of parameters such as path length, phase delay, and Doppler shift in the antenna that do not appear to exist in a consistent and exact manner.

References

1. Cha, A. G., Rusch, W. V. T., and Otoshi, T., "Microwave Delay Characteristics of Cassegrainian Antennas," *IEEE Trans. on Antennas and Propagation*, Vol. AP-26, No. 6, pp. 860-865, Nov. 1978.
2. Silver, S., editor, *Microwave Antenna Theory and Design*, McGraw Hill, 1949.
3. Otoshi, T., and Young, L., "An Experimental Investigation of the Changes of VLBI Time Delays Due to Antenna Structural Deformations," *TDA Progress Report 42-68*, pp. 8-16, Jet Propulsion Laboratory, Pasadena, Calif., April 15, 1982.



Table 1. DSS-43 (64 m) X-band subreflector fixed at position for 42° elevation, declination = 337° (-23°)

Mission Times, hr-min	Antenna Hour Angle, deg	Antenna Elevation Angle, deg	Subreflector Position, in.			Relative Gain, dB ^{1,2}	Δ Phase, deg	Cumulative Δ Phase, deg	Δ Freq, μ Hz (Hz $\times 10^{-6}$)
			x	y	z				
0 - 0	335	65				-0.35	0.0	0.0	--
0 - 20	340	69				-0.47	0.3	0.3	-0.85
0 - 40	345	72				-0.60	0.5	0.8	-0.78
1 - 0	350	75				-0.72	0.3	1.1	-0.64
1 - 20	355	77				-0.81	0.3	1.4	-0.35
1 - 40	0	78	No x motion in normal antenna operation, y, z normally refocused, fixed for occultation:			-0.85	0.0	1.4	0.0
2 - 0	5	77				-0.81	-0.3	1.1	+0.35
2 - 20	10	75				-0.72	-0.3	0.8	+0.64
2 - 40	15	72				-0.60	-0.5	0.3	+0.78
3 - 0	20	69		y = +0.18		-0.47	-0.3	0.0	+0.85
3 - 20	25	65		z = -0.04		-0.35	-0.5	-0.5	+0.85
3 - 40	30	61				-0.24	-0.3	-0.8	+0.78
4 - 0	35	57				-0.15	-0.3	-1.1	+0.74
4 - 20	40	53				-0.08	-0.3	-1.4	+0.67
4 - 40	45	49				-0.03	-0.3	-1.7	+0.59
5 - 0	50	45				0.0	--	--	--
5 - 20	55	41				--	--	--	--

Notes:

1. Gain reference: 0 dB is at rigging angle of 45° elevation; subreflector is focused.
2. Relative gain loss includes surface deformation and defocusing effects due to gravity. However, pointing loss is not included.

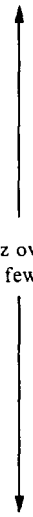
Table 2. DSS-43 (64 m) X-band subreflector fixed at position for 67° elevation, declination = 337° (-23°)

Mission Times, hr-min	Antenna Hour Angle, deg	Antenna Elevation Angle, deg	Subreflector Position, in.			Relative Gain, dB ^{1,2}	Δ Phase, deg	Cumulative Δ Phase, deg	Δ Freq, μ Hz (Hz $\times 10^{-6}$)
			x	y	z				
0 - 0	335	65				-0.04	0.0	0.0	--
0 - 20	340	69				-0.06	0.3	0.3	-0.85
0 - 40	345	72				-0.10	0.5	0.8	-0.78
1 - 0	350	75				-0.13	0.3	1.1	-0.64
1 - 20	355	77				-0.17	0.3	1.4	-0.35
1 - 40	0	78				-0.18	0.0	1.4	0.0
2 - 0	5	77				-0.17	-0.3	1.1	+0.35
2 - 20	10	75				-0.13	-0.3	0.8	+0.64
2 - 40	15	72				-0.10	-0.5	0.3	+0.78
3 - 0	20	69				-0.06	-0.3	0.0	+0.85
3 - 20	25	65		y = -1.53		-0.04	-0.5	-0.5	+0.85
3 - 40	30	61		z = +0.25		-0.05	-0.3	-0.8	+0.78
4 - 0	35	57				-0.08	-0.3	-1.1	+0.74
4 - 20	40	53				-0.12	-0.3	-1.4	+0.67
4 - 40	45	49				-0.19	-0.3	-1.7	+0.59
5 - 0	50	45				--	--	--	--
5 - 20	55	41				--	--	--	--

Notes:

1. Gain reference: 0 dB is at rigging angle of 45° elevation; subreflector is focused.
2. Relative gain loss includes surface deformation and defocusing effects due to gravity. However, pointing loss is not included.


Table 3. DSS-42 (34 m) X-band subreflector auto-focused, declination = 337° (-23°)

Mission Times, hr-min	Antenna Hour Angle, deg	Subreflector Position, in.			Δ Gain, dB	Δ Phase deg	Cumulative Δ Phase deg	Δ Freq. μ Hz (Hz $\times 10^{-6}$)
		x	y	z				
0 - 0	335	1.013	0.894	0.055	-0.17	0.0	0.0	 ± 2900 Hz over duration of a few seconds
0 - 20	340	0.820	0.912	0.060	-0.17	2.3	2.3	
0 - 40	345	0.621	0.927	0.064	-0.16	1.8	4.1	
1 - 0	350	0.416	0.437	0.067	-0.16	1.4	5.5	
1 - 20	355	0.209	0.944	0.068	-0.16	0.5	6.0	
1 - 40	0	0.000	0.946	0.069	-0.16	0.5	6.5	
2 - 0	5	-0.209	0.944	0.068	-0.16	-0.5	6.0	
2 - 20	10	-0.416	0.937	0.067	-0.16	-0.5	5.5	
2 - 40	15	-0.621	0.927	0.064	-0.16	-1.4	4.1	
3 - 0	20	-0.820	0.912	0.060	-0.17	-1.8	2.3	
3 - 20	25	-1.013	0.896	0.055	-0.17	-2.3	0.0	
3 - 40	30	-1.199	0.872	0.049	-0.17	-2.8	-2.8	
4 - 0	35	-1.375	0.846	0.042	-0.18	-3.2	-6.0	
4 - 20	40	-1.541	0.816	0.034	-0.18	-3.7	-9.7	
4 - 40	45	-1.695	0.784	0.025	-0.19	-4.1	-13.8	
5 - 0	50	-1.837	0.748	0.016	--	-4.1	-17.9	
5 - 20	55	-1.964	0.710	0.006	--	-4.6	-22.5	
5 - 40	60	-2.077	0.670	-0.005	--	-4.6	-27.1	

Notes:

1. Gain reference: 0.dB is at rigging angle of 40° elevation; subreflector is focused.
2. Relative gain loss includes surface deformation and defocusing effects due to gravity. However, pointing loss is not included.
3. Receding subreflector (going away from feed/main reflector) leads to positive Δ phase and negative Δ frequency.

Table 4. DSS-42 (34 m) X-band subreflector fixed at 67° elevation, declination = 337° (-23°)

Mission Times, hr-min	Antenna Hour Angle, deg	Subreflector Position, in.			Δ Gain, dB	Δ Phase, deg	Cumulative Δ Phase, deg	Δ Freq. μ Hz (Hz $\times 10^{-6}$)
		x	y	z				
0 - 0	335		 $x = 0.82$ in. $y = 0.91$ in. $z = 0.06$ in. for el = 67° (HA = 340°)		-0.45	0.0	0.0	-1.9
0 - 20	340				-0.36	0.8	0.8	-1.6
0 - 40	345				-0.27	0.5	1.3	-1.2
1 - 0	350				-0.21	0.5	1.8	-0.8
1 - 20	355				-0.17	0.3	2.1	-0.4
1 - 40	0				-0.17	0.	2.1	0.0
2 - 0	5				-0.17	-0.3	1.8	+0.4
2 - 20	10				-0.21	-0.5	1.3	+0.8
2 - 40	15				-0.27	-0.5	0.8	+1.2
3 - 0	20				-0.36	-0.8	0.0	+1.6
3 - 20	25				-0.45	-1.0	-1.0	+1.9
3 - 40	30				-0.57	-1.0	-2.0	+2.3
4 - 0	35				-0.70	-1.3	-3.3	+2.7
4 - 20	40				-0.84	-1.3	-4.6	+3.3
4 - 40	45				-0.99	--	--	--
5 - 0	50				--	--	--	--
5 - 20	55				--	--	--	--
5 - 40	60				--	--	--	--

Notes:

1. Gain reference: 0 dB is at rigging angle of 40° elevation; subreflector is focused.
2. Relative gain loss includes surface deformation and defocusing effects due to gravity. However, pointing loss is not included.

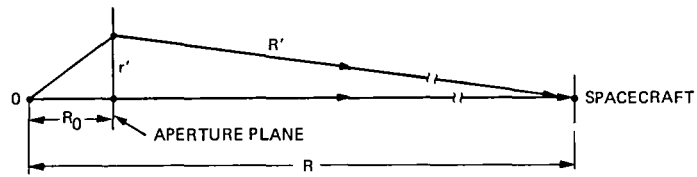


Fig. 1. Coordinate systems in aperture field integral

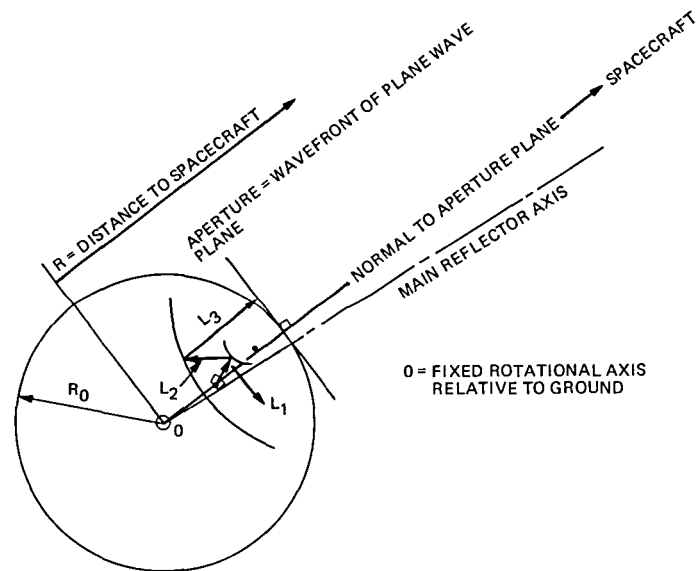


Fig. 2. Defining aperture plane and ray path length

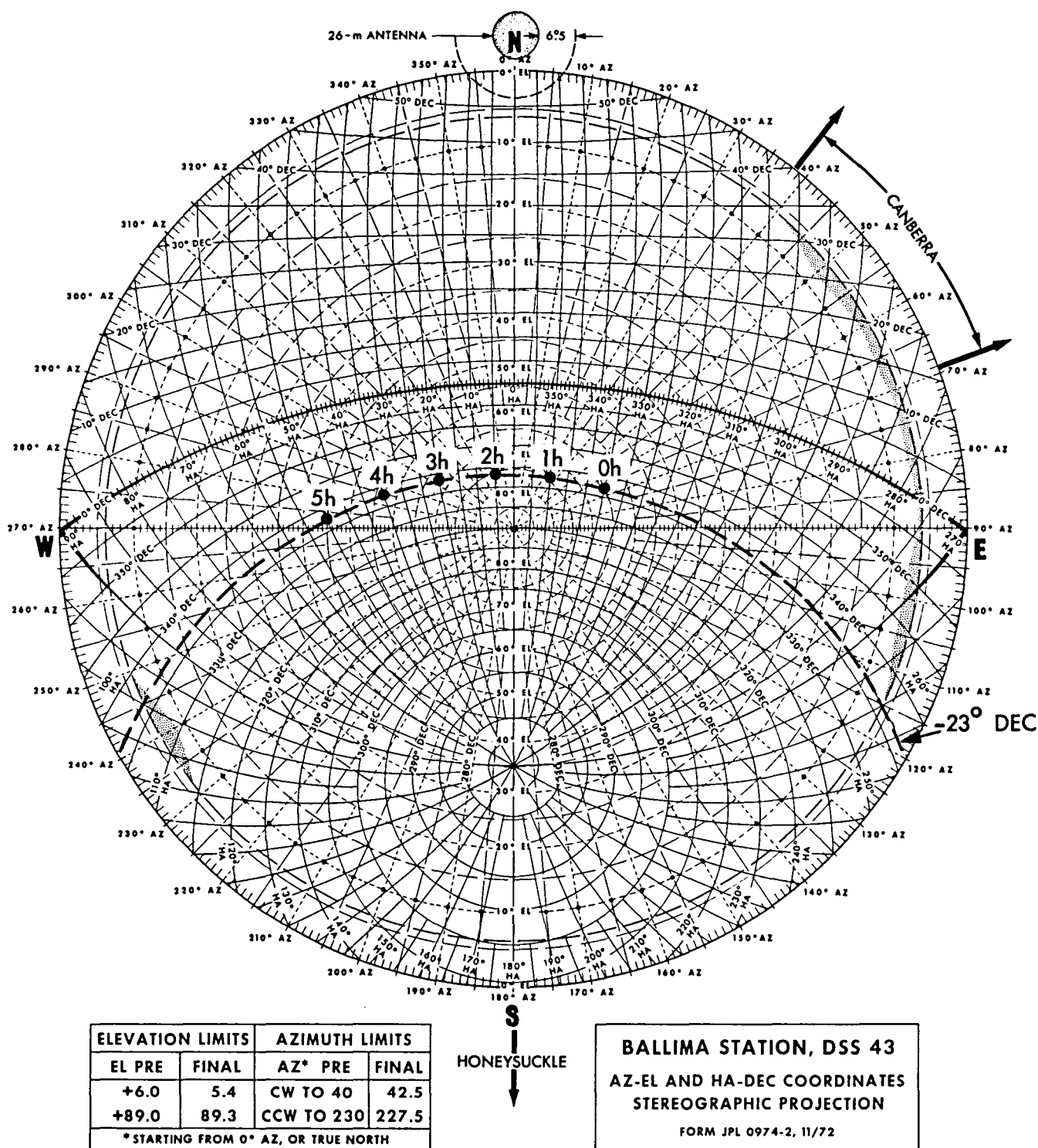


Fig. 3. DSS-42 and -43 Az-El and HA-Dec coordinates for Voyager Uranus Encounter

ICE Encounter Operations

N. Fanelli

TDA Mission Support and DSN Operations

D. Morris

DSN Control Center and Operations Section

This article documents the operations encompassing the International Cometary Explorer's (ICE) encounter with the Comet Giacobini-Zinner on September 11, 1985. The ICE mission presented new challenges for the Deep Space Network (DSN) 64 meter subnetwork. Because of poor telemetry link margin predicted for Giacobini-Zinner (GZ) encounter, supplemental support by the Japanese Institute for Space and Astronautical Sciences 64-meter antenna at Usuda, Japan and the 305-meter Arecibo Radio Observatory in Puerto Rico was required. To improve the 64 meter subnetwork telemetry performance the following were also implemented: (1) Real time antenna array of 64 meter and 34 meter at a single complex and the required performance testing. (2) Non-real time antenna array of two complexes was implemented as a backup in the event of ground or spacecraft failure. Other articles following this one provide details.

I. Introduction

The International Sun Earth Explorer (ISEE-3) was launched in 1978. ISEE-3 spent the next five years in Earth orbit where its prime task was to measure the solar wind. During this period the 26 meter antenna operated by the Ground Spaceflight Tracking and Data Network (GSTDN) was used for ISEE-3 support. In December 1983, using a Lunar swingby, the ISEE-3 spacecraft was sent on a new mission to intercept the comet Giacobini-Zinner (GZ) on 11 September 1985. The ISEE-3 spacecraft was renamed for the new mission, International Cometary Explorer (ICE). The ICE deep space mission placed the spacecraft at a greater distance from its previous Earth orbit mission. In January 1984, the ICE spacecraft went out of range of the 26-meter antenna and required support from the Deep Space Network (DSN) 64-meter

antenna for the remainder of the mission. The ICE mission achieved its prime goal on 11 September 1985 when it became the first spacecraft to encounter a comet; in this case the comet was Giacobini-Zinner.

II. Spacecraft Systems

The ICE spacecraft is a 16-sided cylinder which is 1.61 meters tall and 1.74 meters wide. There are two bands of solar arrays above and below an equipment platform where most of its payload of scientific instruments is mounted (Fig. 1). The solar array provides for all of the power requirements of the spacecraft. If an undervoltage condition occurs, the spacecraft will shutdown automatically. The array currently provides approximately 160 Watts to the spacecraft. The load of using

both transponders is 138 Watts. Power management within the spacecraft is an important item to monitor. To ration electric power aboard the spacecraft, all of the heaters in the propulsion system were to be shut off during the comet encounter.

The propulsion system is arranged in two independent and redundant systems consisting of 12 jet thrusters and 8 fuel tanks. This system is used for all despin, spin-up, trajectory corrections, and attitude control maneuvers. The spacecraft rotates around the central axis of the cylinder at a rate of approximately 20 revolutions per minute. The spin axis is maintained in an orientation perpendicular to the plane of the Earth's orbit around the sun. The spacecraft orientation sensor system consists of two fine sun sensors and a panoramic attitude scanner.

The ICE telecommunications links are two identical and independent systems. The two transponders operate on separate S-band frequencies and can operate simultaneously. This fact was utilized by the DSN to design a system to effectively combine the two signals which allowed the ICE project to meet one of its goals of providing a high bit rate of information throughout the encounter (Ref. 1). Two separate transmitters with an output power of 5 Watts each radiate through a medium gain antenna with 7 dB gain over an effective beamwidth of 12°. The polarization of the two transmitted signals are right hand and left hand circularly polarized.

The spacecraft carries 13 scientific investigations or experiments (Table 1). A few of these investigations utilize appendages to measure conditions around the spacecraft without spacecraft interference. Magnetic fields are measured by two search coils located at the end of two 3-meter-long booms that extend in opposite directions out from the cylinder. Also, four long wires which are 91 meters tip-to-tip extend radially from the cylinder and are used to map radio waves along with two other antenna that are located along the spin axis both on top and below the spacecraft. The experiments aboard the spacecraft have directly affected the strategy for targeting the spacecraft on its comet intercept.

A. Mission Goals and Objectives

ICE was targeted to pass on the anti-sunward side of Comet Giacobini-Zinner, that is, directly through the tail. The lack of a camera and other remote sensing devices gave the ICE Project scientists no choice. The next decision was where in the tail to go, and they picked a target that was 10,000 km down the tail from the nucleus, a value compatible with avoiding a comet wake region and still having a 99 percent or greater probability of intersection (Ref. 2).

The expected science return falls into three areas:

- (1) The physics of the cometary bow shock: to evaluate the location, strength, structure, and related particle acceleration and to determine the extent of the foreshock.
- (2) The physics of the interaction between the interplanetary magnetic field and the cometary plasma and an evaluation of the ionization phenomena and turbulence characteristics.
- (3) The physics of the comet tail.

All of these goals produce a requirement of monitoring the spacecraft for a complete solar rotation (27 days) prior to the comet encounter at the encounter bit rate to ascertain what phenomena are caused by the comet environment and what is normal for that area of the solar system. The Giotto spacecraft was to also measure solar wind during the ICE comet encounter.

III. Comet Giacobini-Zinner

A. Where It Is

The orbit of Comet Giacobini-Zinner takes it around the Sun about once every 6.6 years. It is named for two astronomers who discovered it independently of each other 13 years apart. Giacobini of the Nice Observatory in France initially found it December 20, 1900 and Zinner found it October 23, 1913 at Remeis Observatory in Bamberg, Germany. Apparitions or observations of the comet have been made since then and good orbit was known. For a comet intercept mission, a precise orbit would have to be updated from these previous sightings. To facilitate this, D. Yeomans of JPL and J. Brandt of GSFC collected comet data and documented it in *The Giacobini-Zinner Handbook* (Ref. 2).

B. How Did ICE Get to the Comet?

A key point in planning a spacecraft voyage to a celestial body is that one must have adequate knowledge of its orbit several years in advance of the proposed encounter to plan and develop the mission. In the case of ICE, Comet Giacobini-Zinner had been observed since 1900 and its orbit was predictable. The ICE spacecraft though was already in space and would need to be retargeted. It did not have enough propellant aboard to get to Comet Giacobini-Zinner without an assist. A novel solution to this dilemma was proposed by R. Farquhar, the ICE Flight Director (Ref. 3).

Farquhar proposed a complex set of orbital maneuvers to get there. The onboard hydrazine propulsion system was used starting in mid-June 1982 to move the spacecraft back toward Earth from its orbit at the Earth-Sun libration point.

In mid-October 1982, the spacecraft had intersected the Moon's orbit and was thrown outward and behind the Earth, passing across the Earth's geomagnetic tail. Figure 2 shows the orbit of the spacecraft during these maneuvers. The most crucial of these maneuvers occurred on December 22, 1983 when the trajectory carried the spacecraft toward the Moon. The spacecraft passed behind the Moon and spent more than 30 minutes in its shadow during its passage within 120 km of its surface (Ref. 4). It was renamed the International Cometary Explorer; its previous name was the International Sun Earth Explorer-3. Lunar gravity altered the spacecraft's trajectory and accelerated it toward Comet Giacobini-Zinner. Figure 3 illustrates this critical Lunar flyby which increased its velocity from approximately 4800 km/h to 8000 km/h.

The flyby accomplished two important criteria for a successful comet intercept. The first was that the spacecraft achieved the required orbital energy to leave the Earth-Moon system and the second was a close targeting for a comet that no one had seen since 1978. Figure 4 illustrates the ICE trajectory relative to a fixed Sun-Earth line and shows the relative positions of the spacecraft, Comet Giacobini-Zinner and Halley, the Sun and Earth referenced to calendar dates. The looping motion of the spacecraft is due to its elliptical motion around the sun. When it is further from the Sun than the Earth (G-Z encounter = 1.03 AU), the Earth orbits around the Sun at a velocity that is faster than the spacecraft and the Earth seems to catch up to it. The comet intercept by ICE was timed to occur only 6 days after the 1985 perihelion of September 5. The plane of the comet's orbit is tilted by 31.9° with respect to the ecliptic plane; although at perihelion it is only slightly above it. This means the comet's tail should be at its brightest and greatest length which is estimated to be 500,000 km from a photo during the 1959 apparition for its encounter with ICE.

Ultimately, a major trajectory maneuver was executed on June 5, 1985 after JPL (Yeomans) had updated the comet ephemeris from over two months of reliable worldwide observations. Two trim maneuvers were also made on July 9 and September 6 to correct for any burn errors. The final trim retargeted the spacecraft to a point 7815 km from the comet's nucleus, but kept the original intercept time of 11:04 UTC on September 11, directly above the Arecibo Radio Observatory only 70 million kilometers from Earth.

IV. Data Acquisition for Encounter

A. Telecommunication Needs

From the previous discussion of the spacecraft systems, mission goals and the Comet Giacobini-Zinner intercept point, the technical requirements were determined for what was

needed to support the ICE encounter. These requirements were as follows:

- The ability to receive the 2217.5 MHz downlink frequency at DSS-14 and DSS-63 (Ref. 5).

- The ability to symbol synchronize biphas-modulated carrier frequencies (Ref. 6).

- The ability to format decoded telemetry data into an agreed upon DSN-GSFC interface data block (Ref. 7).

- The ability to combine the two spacecraft downlink channels (Ref. 1).

- The ability to array together the telemetry output of the 34-meter and 64-meter antenna at each DSN complex.

- Deliver a tunable S-band 400 kW klystron for commanding (Ref. 8).

- The ability to uplink at 2090.66 MHz without interfering with the newly acquired ability to simultaneously receive the 2217.5 MHz downlink frequency (Ref. 9).

- To implement the Usuda, Japan 64-meter antenna to fill the gap caused by the Canberra complex poor spacecraft look angle (Ref. 10).

- To implement an R & D non-real time decoding system as an insurance policy to guarantee data acquisition (Ref. 11).

- To determine the orbit of ICE from its geotail mission through its comet intercept (Ref. 4).

- To integrate the Arecibo support with ICE operations (Ref. 12).

All of these requirements featured implementations that were accomplished along with the Mark IV upgrade.

B. Worldwide Coverage

The DSN's plan for supporting the ICE encounter required array support throughout the 36 hours prior to and after the comet intercept. In Madrid, both DSS-61 and DSS-63 were arrayed. In Goldstone, DSS-15, DSS-12, and DSS-14 were arrayed, and in Canberra, DSS-42 and DSS-43 were arrayed. Even with this all-out support, the DSN would be strained at the distance of the encounter to maintain the slim link margin. Accordingly, that was why the Usuda, Japan and the Arecibo Radio Observatory support was requested (Refs. 10, 11, 12, and 13).

The Usuda 64-meter site would be used to gather valuable pre-encounter and post-encounter telemetry between the

Goldstone array period and the Madrid support. This configuration was first checked out in mid-May, and in a pre-encounter test in late May, they successfully supported the 1024 bit rate at an Earth-spacecraft distance comparable to the encounter time frame. In fact, conditions would only get better because the peak elevation angle would increase almost 30 degrees.

The maneuvering of the spacecraft back in 1983 had the Arecibo Radio Observatory in mind the whole time. The intercept of the comet was planned to occur within the very short view period that this observatory could listen to the ICE spacecraft. This insurance policy was not taken out by NASA until early in 1985. The implementation by GSFC was complete in August; and the first test pass occurred August 19.

V. Encounter Operations

A. Test and Training

To ensure successful operations throughout the worldwide coverage for the ICE encounter, many configuration tests were run at all sites. DSN array testing began in early June at the Goldstone complex. These tests provided analysis for an encounter configuration to optimize the link margin performance. Findings are documented in this issue (Ref. 13) but some meaningful work bears mentioning in the next few paragraphs.

There were a number of significant problems and solutions that were brought to light and engineered under the auspices of these tests. The most crucial of these problems was the testing of the hardware to be used for encounter arraying operations. The device that was used throughout testing and training was what will be referred to in this article as a "resistive combiner" (Ref. 1). Five combiners were built for the DSN, specifically for ICE dual telemetry combining and intra-complex arraying. They were multi-input port (two, three, or four), single or triple output port devices which allowed operational flexibility to ICE operations and testing (Fig. 5). Access to the combiners was designed to be easy and efficient via patchcord in the baseband patch panel. Baseband receiver telemetry phase detector output would be patched directly into an input port and the output of the combiner would be patched directly to a telemetry string consisting of a Subcarrier Demodulator Assembly (SDA), Symbol Synchronizer Assembly (SSA), and a Telemetry Processor Assembly (TPA). The combiner needed external monitoring to validate its performance. An individual telemetry string provided two assessments of proper performance — the SSA measured

signal-to-noise ratios and the sequential decoder provided a symbol error rate statistic. Thus, when array testing was underway, all available telemetry strings were used to measure configuration setup conditions and long term performance. Soon, DSN station operations were adept at using this equipment for ICE arraying and frequency combining. In addition, a nagging problem was found early with both Voyager 2 and ICE array testing at Goldstone and a prepass calibration procedure was developed to effectively handle a receiver phase detector imbalance which could occur from routine adjustments to the equipment. Ultimately, Goldstone testing provided an operable system that consistently performed to expectations with little maintenance and was easily configured for array support.

The array testing at Madrid did not begin until mid-August. A problem with baseband combining within the 64-meter antenna was found which threatened the encounter support there. The problem was a consistently low output of approximately 0.5 dB in SNR from each of the receivers when receiver baseband was used for the decoding process instead of a 10 MHz intermediate frequency (IF) receiver telemetry output. This had not occurred at either Goldstone or Canberra during their testing. Station engineering proposed and tested a configuration where this 10 MHz IF was used instead of receiver baseband. Intensive crew training was the next important step in using this configuration for encounter support.

Understandably, a conservative configuration was planned for the encounter support. The array configuration was the prime data sent to the project. A backup telemetry string was used to decode the frequency combined signals within the 64-meter antenna at each complex. As an added insurance policy a research and development "soft symbol" recording was made on site for non-real time decoding purposes (Ref. 11). These configurations provided excellent results.

B. Operations

The ICE Comet Giacobini-Zinner encounter provided real-time science highlights to the ICE Principal Investigators at Goddard Space Flight Center. Telemetry was sent via high speed data line from three tracking complexes simultaneously. The Madrid, Spain DSN complex sent arrayed data from their 34-meter and 64-meter antennas, while the Goldstone DSN complex sent data from an array of both of their 34-meter antennas with their 64-meter antenna. The Arecibo Radio Observatory also sent data to GSFC during the overlap of Madrid and Goldstone (Fig. 6). The multiple data streams allowed the scientists to choose the best data stream to insure that this historic first comet intercept would not be missed.

Array performance at all complexes was better than predicted. ICE Project scientists reported a direct intercept of the Comet Giacobinni-Zinner. Ground antenna telemetry performance was at an all time high. No detectable spacecraft degradation was observed after the comet encounter.

ICE encounter operations were performed in a very professional and flawless manner by the many participants and supporting facilities. The encounter support was deemed outstanding by the ICE Project Manager, JPL and NASA management.

References

1. Marina, M. M., "Resistive Combiners for ICE," *TDA Progress Report* (in preparation), Jet Propulsion Laboratory, Pasadena, Calif.
2. Yeomans, D. K. and Brandt, J. C., *The Comet Giacobini-Zinner Handbook*. Pasadena: NASA, JPL 400-254, 3/85.
3. Farquhar, R. J., Muhonen, D., Church, L., "Trajectories and Orbital Maneuvers for the ISEE-3/ICE Comet Mission," *Journal of the Astronautical Sciences*, Vol. 33, No. 3, July-Sept 1985, pp. 235-254.
4. Efron, L., D. K. Yeomans, and A. F. Schanzle, "ISEE-3/ICE Navigation Analysis," *Journal of the Astronautical Sciences*, Vol. 33, No. 3, July-Sept 1985, pp. 301-323.
5. Petty, S. M., Trowbridge, D. L., "Block 5 Traveling Wave Maser," *TDA Progress Report* (in preparation), Jet Propulsion Laboratory, Pasadena, Calif.
6. Burt, R., "MKIV-A DSCC Telemetry System Description," *TDA Progress Report 42-68*, Jet Propulsion Laboratory, Pasadena, Calif., April 15, 1982, pp. 130-138.
7. "Interface Control Document Between the JPL and the GSFC for GSFC Missions Using the DSN," Greenbelt, MD, MDOD-1ICD/0182 Rev. 1, July 1984.
8. Goldfinger, A., M. A. Gregg, and R. Hartop, "A New High-Power Klystron for the DSN," *TDA Progress Report 42-69*, Jet Propulsion Laboratory, Pasadena, Calif., June 15, 1982, pp. 157-173.
9. Galvez, J., H. Marlin, and P. Stanton, "ISEE-3 Microwave Filter Requirements," *TDA Progress Report 42-76*, Jet Propulsion Laboratory, Pasadena, Calif., Feb. 15, 1984, pp. 114-119.
10. Goodwin, J. P., "Usada Deep Space Center Support for ICE," *TDA Progress Report 42-84*, Jet Propulsion Laboratory, Pasadena, Calif., Feb. 15, 1986.
11. Hurd, W. J., "Intercontinental Antenna Arraying by Symbol Stream Combining at Giacobini-Zinner Encounter," *TDA Progress Report 42-84*, Jet Propulsion Laboratory, Pasadena, Calif., Feb. 15, 1986.
12. Gordon, D. D., and M. J. Ward, "Arecibo Observatory Support of the U.S. International Cometary Explorer Mission Encounter at Comet Giacobini-Zinner," *TDA Progress Report 42-84*, Jet Propulsion Laboratory, Pasadena, Calif., Feb. 15, 1986.
13. Layland, J. W., "ICE Telemetry Performance," *TDA Progress Report 42-84*, Jet Propulsion Laboratory, Pasadena, Calif., Feb. 15, 1986.

Table 1. ICE investigations

Title	Principal Investigator	Affiliation	Experiment Status
Solar Wind Plasma*	Bame	Los Alamos National Lab	Electrons only (Ion Portion Failed)
Plasma Composition*	Ogilvie	GSFC	Operational
Magnetometer*	Smith	JPL	Operational
Plasma Waves*	Scarf	TRW Systems	Operational
Energetic Protons*	Hynds	Imperial College, London	Operational
Radio Waves*	Steinberg	Paris Observatory, Meudon	Operational
X-Rays, Low Energy Electrons	Anderson	UCB	X-Rays and E > 200 keV (Low Energy Electron Portion Failed)
Low Energy Cosmic Rays	Hovestadt	MPI	Partial Failure (Ulezeq)
Medium Energy Cosmic Rays	von Rosenvinge	GSFC	Operational
High Energy Cosmic Rays	Stone	CIT	Partial Failure (Isotope Portion)
High Energy Cosmic Rays	Heckman	UCB/LBL	Partial Failure (Drift Chamber)
Cosmic Ray Electrons	Meyer	University of Chicago	Operational
Gamma Ray Bursts	Teegarden	GSFC	Partial Failure (PHA Memory)

*Significant experiments during a comet tail encounter.

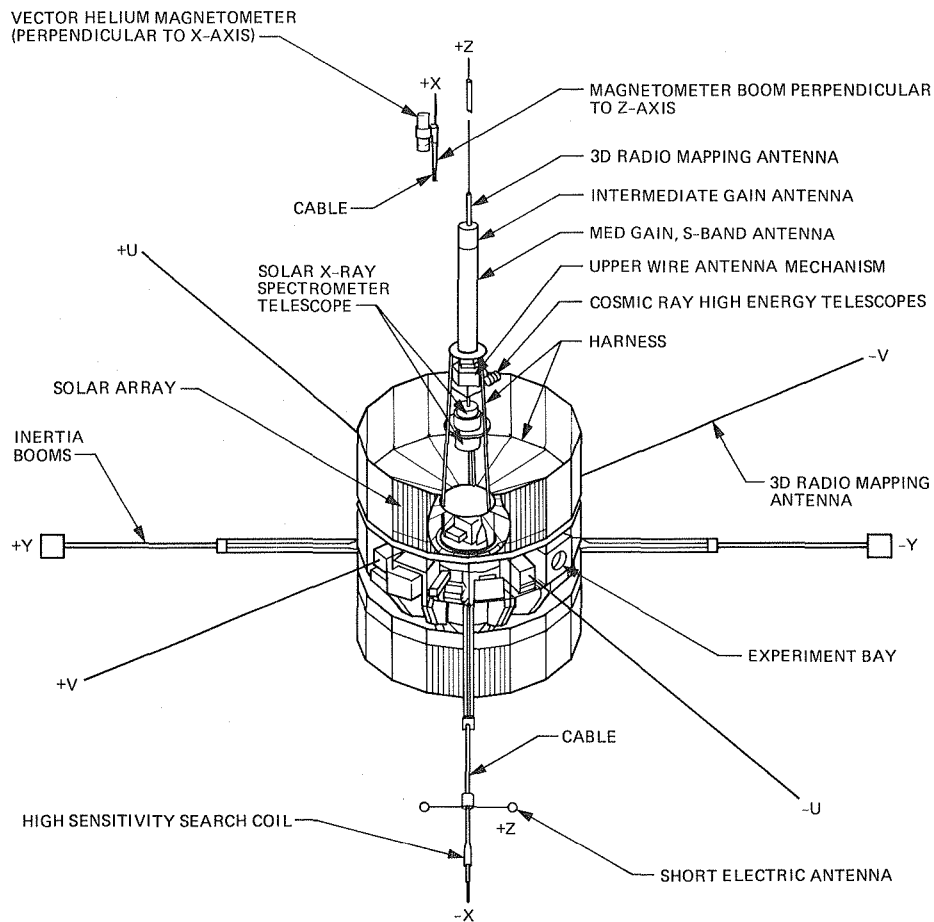


Fig. 1. ICE spacecraft

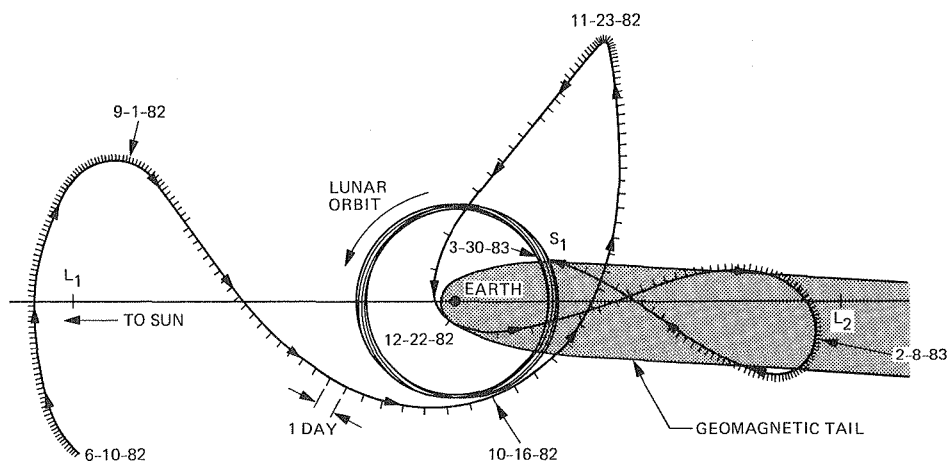


Fig. 2. Geomagnetic tail trajectory

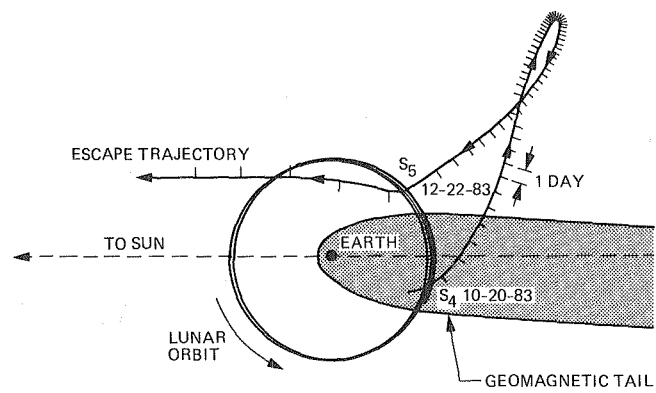


Fig. 3. Lunar flyby trajectory

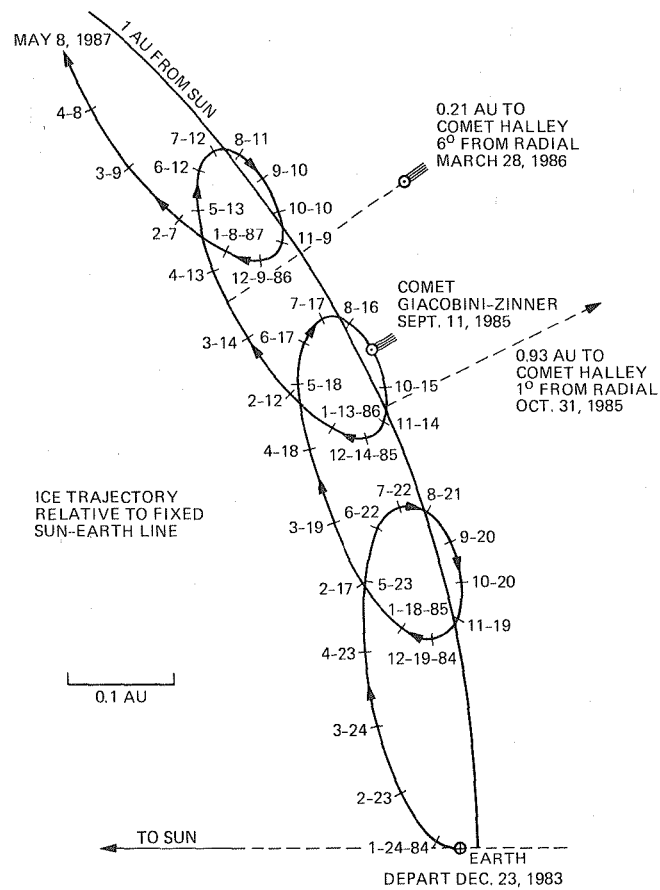


Fig. 4. ICE trajectory relative to fixed sun-earth line

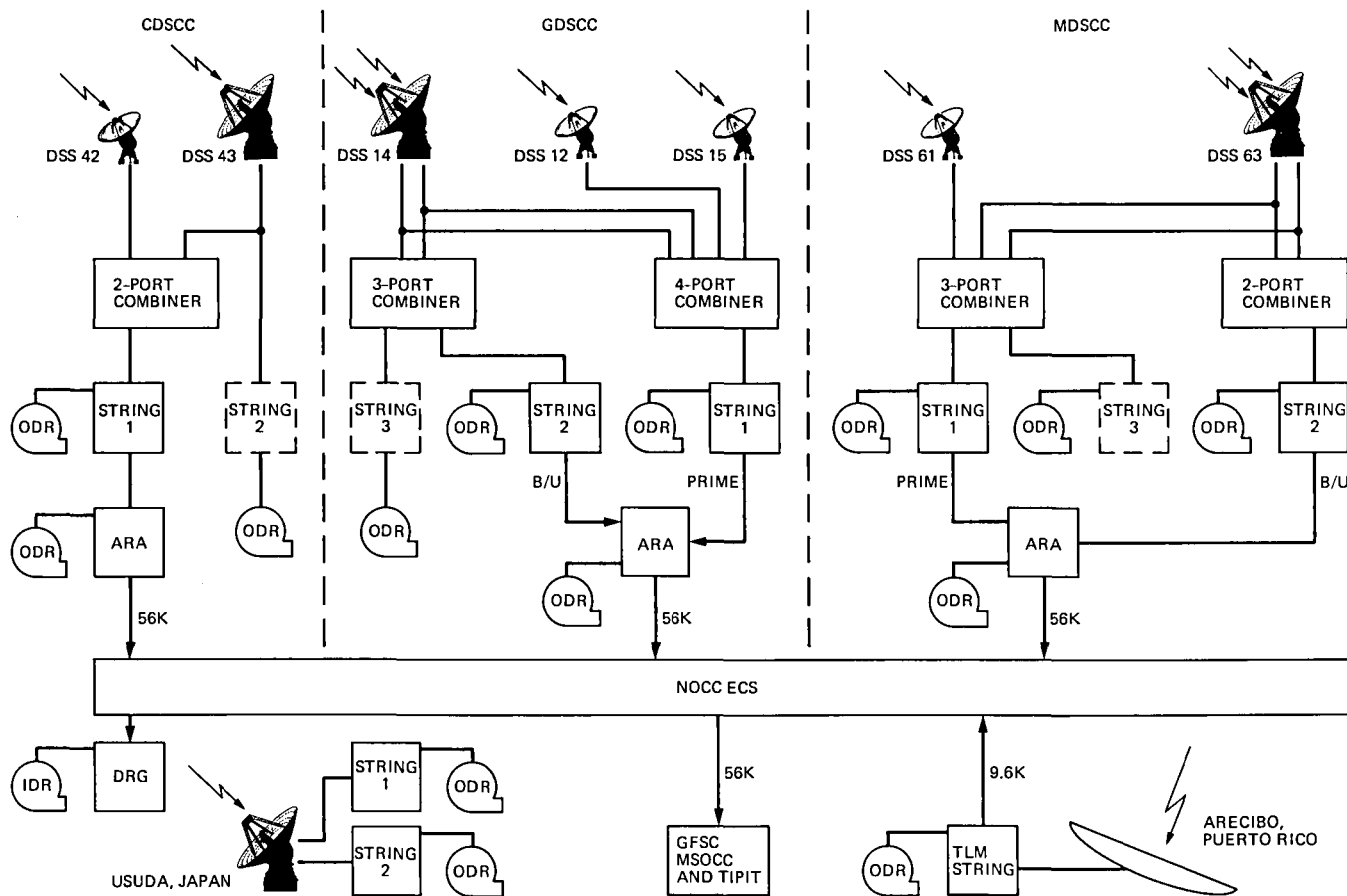


Fig. 5. ICE Encounter support configuration

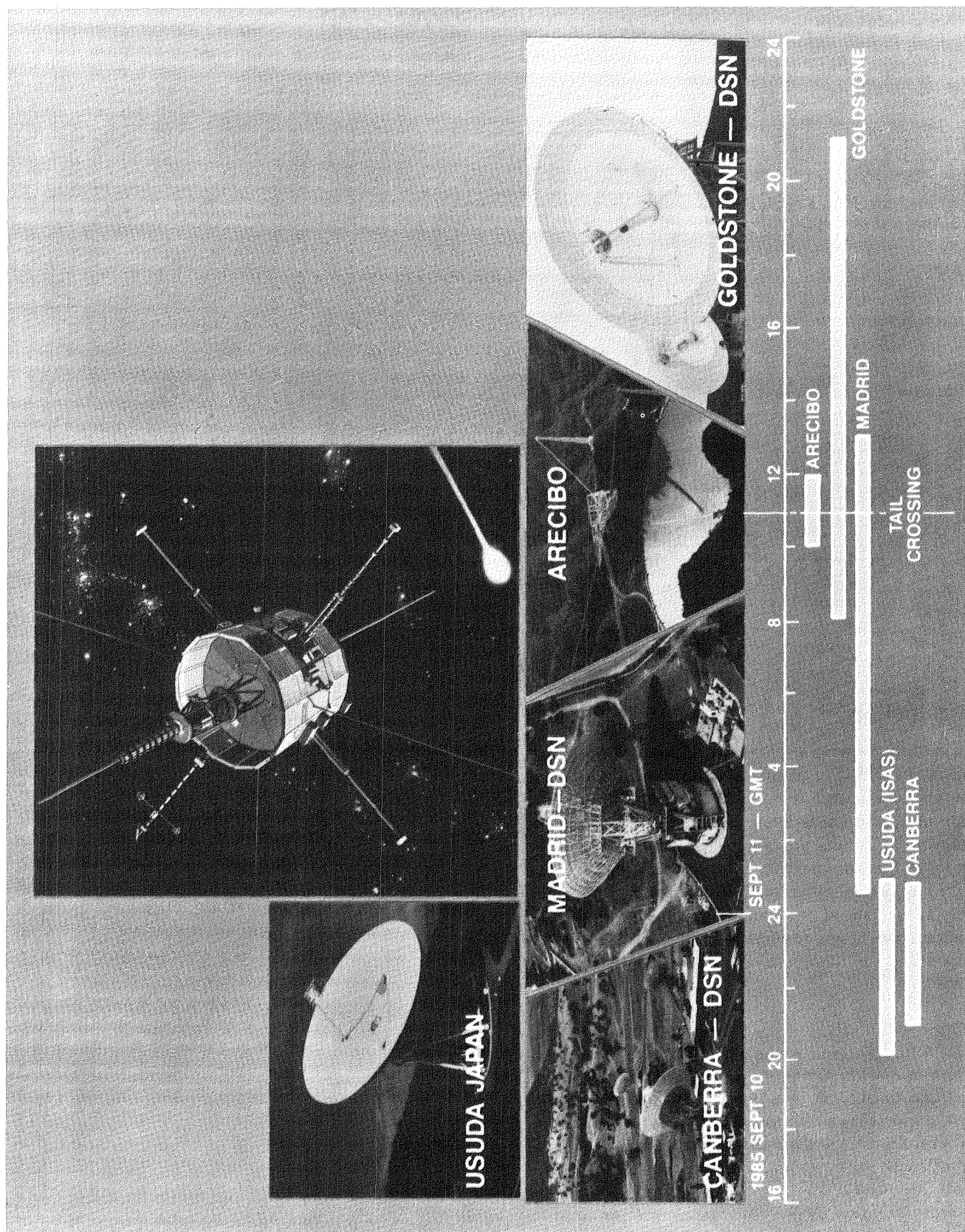


Fig. 6. Encounter support timeline

Usuda Deep Space Center Support for ICE

J. P. Goodwin

TDA Mission Support and DSN Operations

This article summarizes the planning, implementation and operations that took place to enable the Usuda, Japan, Deep Space Center to support the International Cometary Explorer (ICE) mission. The results show that even on very short notification our two countries can provide mutual support to help ensure mission success. The data recovery at the Usuda Deep Space Center contributed significantly to providing the required continuity of the experiment data stream at the encounter of the Comet Giacobini-Zinner.

I. Introduction

An agreement between the National Aeronautics and Space Administration (NASA) and the Japanese Institute of Space and Astronautical Science (ISAS) for the instrumentation and operation of ISAS's Usuda Deep Space Center in support of the International Cometary Explorer (ICE) mission was signed in early 1985. This agreement made the Jet Propulsion Laboratory (JPL) responsible for implementing, maintaining, and operating all equipment temporarily installed in the Usuda configuration which was required for support of ICE. ISAS was responsible for the operation and maintenance of the Usuda facility.

ISAS is a Japanese government institute which was established in 1981 by reorganizing the Institute of Space and Astronautical Science of the University of Tokyo. One of the tasks ISAS was chartered to do was research and development of interplanetary probes and the tracking of those probes. In support of this element of their charter, they built the 64-m antenna at Usuda, Japan.

The Japanese space program is divided into two general classifications. ISAS is the central institute in organizing

scientific space research while the National Space Development Agency (NASDA) is in charge of development of application programs.

The ISAS Deep Space Center at Usuda, Japan, consists of a new 64-m antenna which uses wheel and track drives with an elevation over azimuth configuration. The antenna has a shared main and sub-reflector with a beam waveguide feed system. The Usuda antenna is located about 160 km northwest of Tokyo in a mountainous region at an elevation of 1074 m. The approximate longitude is 138°E and a latitude of 36°N.

The location of the Usuda antenna made it a candidate for improving data recovery return from the longitude. The southern hemisphere DSN complex at Canberra, Australia, had a very low elevation ground station to spacecraft look-angle compared to Usuda in approximately the same longitude.

II. Task Goals

The primary goal of the Usuda support for the ICE task was to provide telemetry data at an acceptable signal-to-noise ratio (SNR) to supplement the DSN Australian complex dur-

ing Giacobini-Zinner encounter (see Refs. 1 and 3). A non-realtime telemetry interface would be sufficient. Other secondary goals were: to provide a demonstration of symbol stream recording which would be used with another site's recordings for non-realtime symbol stream combining (see Ref. 2); to gain experience with beam waveguides; and, finally, to demonstrate the advantages of international cooperative work.

III. Planning

The first step in planning the ICE support from the Usuda Deep Space Center was a feasibility study by a group from JPL under the direction of the Office of Telecommunications and Data Acquisition. This group found that the Usuda antenna and drive system, the receiver, and general facility were compatible with project requirements. The Usuda front-end amplifier, which was a cooled paramp, would not be adequate for the expected Giacobini-Zinner encounter signal level; therefore, a different front end would be required. Table 1 indicates the parameters of the Usuda installation. Figure 1 shows the Usuda block diagram. The telemetry processing that the Usuda site used did not deliver a product compatible with the DSN so either changes at JPL or different telemetry processors at Usuda would be needed.

At this point an implementation team was formed to determine the equipment required, its source, and an implementation and test schedule. The low-noise amplifier (LNA) selected was an ultra-low-noise MASER developed by the Radio Frequency and Microwave Subsystems Section with the advanced Systems Program Resources; the MASER had many years of reliable service including a lengthy installation period at DSS 14. This MASER, with its long performance history, made an excellent baseline measurement device to compare the conventional waveguide installation at DSS 14 with the beam waveguide installation used at Usuda. This comparison would be a valuable experience for future DSN antenna feed designs. It was decided that the most cost effective implementation would be to use DSN telemetry processing equipment at Usuda. The telemetry equipment selected consisted of two strings of the DSN Mark III configuration, which were available after DSS 12 was taken down for implementation into Mark IV-A. Timing equipment to supply Mark III reference pulses and time code was assembled from Mark III surplus equipment and some items from CTA 21 spares. A high level block diagram of the Usuda site modified for ICE support is shown in Fig. 2.

IV. Implementation

For implementation of the equipment, personnel were provided by the DSN Operations and Engineering Support

Section, who were responsible for the implementation of the Telemetry Strings, their testing, and for the overall System Performance Test (SPT). The Radio Frequency and Microwave Subsystems Section provided a person for installation and test of the LNA. DSN Operations and Engineering Support personnel also assisted in the installation and test of the LNA in order to help train them for the maintenance and operation of the LNA during the operational phase of the task. The personnel left for Japan on March 29, 1985. Equipment was shipped from JPL on March 13, 1985 with JPL responsible for U.S. export license, customs clearance, and transportation to Tokyo, Japan. ISAS was responsible for customs clearance in Tokyo and transportation to Usuda. The shipment arrived at Usuda on April 1, 1985. Equipment was uncrated, inspected, and inventoried. The only physical damage to the equipment was to a door hinge on one of the magnetic tape units, which was repaired on site.

The LNA was installed on the second floor of the antenna equipment building. Figure 3 is a drawing of the antenna structure. This room rotates in azimuth but is stationary in elevation. Negotiations between JPL and ISAS gave responsibility to ISAS to produce a listen-only feed horn assembly to interface the JPL-supplied LNA to the beam waveguide system, and to provide adequate space, power, and air conditioning for the JPL-supplied equipment. The LNA was mounted on its side to allow for the installation of the horn with the shortest possible waveguide transition. The beam waveguide is a feed method where the propagation does not depend on the boundary conditions of the walls. A system of mirrors is used to move the focal point to a convenient location. Figure 4 indicates an example of this technique. A tube encloses the mirror/focusing system just to ensure nothing penetrates the beam. The listen-only system noise temperature measured after the implementation was approximately 15.5 K with the antenna at zenith.

The telemetry processors were installed in the control room. Power had to be adapted by ISAS from 200 Vac, 60 Hz, to 117 Vac, 60 Hz. A series of transformers were used for this purpose. The control room was air conditioned and had a computer floor, but the floor was primarily solid with removable panels only along a few cable run areas. Since the removable panels did not coincide with the allocated layout of JPL equipment installation, small stands (25 cm X 61 cm X 71 cm) were built by ISAS to set the racks on. This allowed for cable entry through the bottom of the rack and for cold air flow entry into the racks.

The implementation process proceeded according to plan. Some small technical problems occurred but nothing which wouldn't be encountered at any other site. LNA cooldown,

system noise temperature measurements, star tracks, and SPTs were all completed on schedule.

Measurements of system noise temperatures at 2295 MHz is summarized in Table 2. The Usuda antenna aperture efficiency is $79\% \pm 1\%$ (1.05 dB higher than DSS 14). For low-noise communications at 30-deg elevation, the Usuda system sensitivity (antenna gain divided by system temperature or G/T) in dB is 1.58 dB better than DSS 14 in the comparable low-noise configuration. For ICE tracking at 2270 MHz the Usuda G/T was 2.2 dB more than DSS 14 because DSS 14 was configured to operate in the diplexed mode. The data clearly show that the Usuda beam waveguide system does not degrade the overall system noise temperature.

V. Operations

The negotiations between JPL and ISAS developed a schedule for ICE support by Usuda for the following three periods of time:

May 15 – June 29, 1985
September 8 – September 12, 1985
October 28 – November 6, 1985

The first tracking period helped alleviate a heavy workload at the Australian complex. The second period covered the Giacobini-Zinner encounter, and the third period covered the first Halley radial by ICE.

ISAS had a Halley Comet project with two spacecraft. One of the spacecraft, which was called MST5 prior to its successful injection and now called Sakigake, was already on its way to measure the environment prior to the Halley Encounter. The second spacecraft was successfully injected between the first and second periods of ICE support at Usuda. The second spacecraft, known as Planet A prior to successful injection and now called Suisei, will encounter Halley's Comet. The view periods for Sakigake, Suisei, and ICE unfortunately had quite a bit of overlap so scheduling became a tough problem. Complicating the problem was the single crew staffing at Usuda. The end result was that the majority of the scheduled passes for ICE was from 4-1/2 to 5 h long. During the first support period these blocks of time were starting near the horizon and terminated with an antenna elevation of about 49 deg.

Antenna pointing was accomplished using predicts generated by ISAS from state vectors supplied by JPL. The Navigations Systems Section supplied the state vectors periodically during the time Usuda was tracking ICE. The state vectors were generated at JPL and sent by Telex to ISAS in Tokyo, where the computer that generated the predicts was located.

As the operational date of May 15, the start of the first support period, approached the LNA warmed up. There was evidence that the refrigerator had massive contamination of the engine circuit. During the first support period there were several warmups by the LNA. The drive unit displacer was changed. Leaks were repaired. The compressor was replaced. None of the attempted fixes seemed to cure the problem. Although the LNA made it through the other two support periods without any loss of support to scheduled tracking passes, the problem persisted. It took a great deal of coordination between JPL personnel at the site and the Radio Frequency and Microwave Subsystems Section personnel to keep the LNA going as well as it did.

Table 3 indicates the performance during the first support period. On DOY 143 the Earth-spacecraft distance was approximately equal to what it would be at Giacobini-Zinner encounter. On this day the spacecraft was switched from its normal data rate of 512 bps coded to the encounter rate of 1024 bps coded. The objective was to demonstrate the network data recovery capability in the encounter environment. The Usuda performance on that day was very encouraging; the telemetry decoding string locked up near the horizon with a symbol SNR of -0.1 dB and it peaked at the end of the track support at $+1.25$ dB with an antenna elevation of 40 deg.

During the first support period for Usuda there were the three LNA refrigerator problems referred to earlier. On the days the LNA was not available, the ISAS-cooled paramp was used, and the symbol SNR was approximately 3 dB lower than when the DSN LNA was used. This still gave acceptable data at 512 bps coded but would not have been an adequate configuration for the Giacobini-Zinner encounter at 1024 bps coded. The second telemetry string at Usuda was for redundancy in case of a failure on the prime string. When both strings were operational, which turned out to be the case on all passes except the next to last pass of the third support period, the second telemetry string was used for making symbol stream recordings.

The tapes from both the telemetry decoding string and the tape from the symbol stream recording were retained at Usuda until approximately a 10-day quantity had accumulated and then were shipped back to JPL in a single shipment. At JPL an Original Data Record (ODR) to Intermediate Data Record (IDR) conversion was made by the Network Data Processing Area (NDPA) and the IDR data was electrically transmitted to the project.

For the second support period of the Giacobini-Zinner encounter, the scheduled track times for ICE were at better elevation angles; the tracks were scheduled from 1900Z to 0100Z daily which corresponded to elevation 57 deg at the

beginning of the scheduled support increased to 77 deg and by end of the pass was 40 deg. The ground station support during the encounter period was without incident and the symbol SNRs were higher than on the test day, DOY 143, due to the better elevation angles. Table 4 indicates the performance on a pass basis. The tapes for this period were sent to JPL on a daily basis. During practice sessions several modes of tape delivery were tried but the only one which got us tapes within 24–30 h of end of pass was an express handling service called DHL. The decoded telemetry tapes were expedited to NDPA for transmission to the project. The symbol stream recordings were delivered to the Communications Research Section for processing (see Ref. 2).

The third support period, for the first Halley radial the times scheduled for the ICE support, gave better antenna elevation angles than the first period and the symbol SNR for the 512 bps coded averaged 3.6 dB to 6.0 dB during a pass. Results are indicated in Table 5. The only abnormal event was that both telemetry strings were not available on October 31 so no symbol stream recording was made. The problem was in a Symbol Synchronizer Assembly (SSA), which was repaired after the pass and both strings were available again for the next

pass, which was the last one. Tapes for the third support period were consolidated into one batch shipment for return to JPL.

After the November 1 pass the JPL equipment was disconnected and prepared for shipment. The Japanese customs broker/exporter picked up the equipment on November 10 and by December 9, 1985 the equipment had cleared customs in Los Angeles and was returned to JPL.

VI. Summary

The objectives of the task were all met. The Usuda Deep Space Center supported as negotiated, and the data supplied sufficiently enhanced the data recovery from that longitude. A demonstration of non-realtime symbol stream combining was accomplished by combining recordings from Usuda and Goldstone. The beam waveguide feed system was analyzed and considered to have many advantages over conventional waveguide systems. The experience with the Usuda beam waveguide will be useful in the decision-making process for future DSN designs. The practicality of our two countries sharing the use of scientific facilities was shown to be mutually advantageous and very cooperative.

Acknowledgments

As in any task there are many people to thank and no one wants to forget anyone, but I will still attempt to acknowledge some outstanding efforts. In the planning, there were R. Clauss of the TDA Technology Development Section and R. Bolan of the DSN Operations and Engineering Support Section. In the implementation, S. Petty, D. Neff, M. Britcliffe, and all of the Radio Frequency and Microwave Subsystems Section were responsible for the installation test and repair of the LNA. The people who kept the JPL site equipment working and did a great job interfacing with the Usuda site personnel were C. Hoynes and R. Spear of DSN Operations and Engineering Support Section and N. Williams of Goldstone Operations. In Japan two people without whose assistance we would never have met our commitments were Dr. T. Nishimura and Dr. T. Takano of ISAS.

References

1. Layland, J.W., "ICE Telemetry Performance," *TDA Progress Report 42-84*, this Issue.
2. Hurd, W.J., "Symbol Stream Combining for ICE," *TDA Progress Report 42-84*, this Issue.
3. Fanelli, N.A., and Morris, D.G., "ICE Encounter Operations," *TDA Progress Report 42-84*, this Issue.

Table 1. Usuda system characteristics

Characteristics	For ICE Mission	For Planet-A Mission
Antenna type	Cassegrain antenna fed by 4-ref. beam-waveguide	Cassegrain antenna fed by 5-ref. beam-waveguide
Antenna mount	Azimuth-elevation mount with wheel and track	
Antenna drive	DC motor anti-backrush drive	
Tracking mode	Manual and program	Manual, program and monopulse
Angular travel and maximum drive speed	AZ: $\pm 270^\circ$ (Rf. T.N.), 0.5 deg/s EL: 5° to 92° , 0.5 deg/s	
Pointing accuracy	0.01° rms for S-band use	
Angle readout resolution	0.001° rms	
Frequency range	Receive: 2.2 to 2.3 GHz	Transmit: 2.11 to 2.12 GHz Receive: 2.29 to 2.30 GHz
Antenna gain at feed horn throat	62.0 dB at 2.25 GHz	61.2 dB at 2.1 GHz 62.0 dB at 2.3 GHz
Antenna noise temperature with feed loss	19 K (EL $\geq 20^\circ$) [Feed loss ≤ -0.08 dB]	30 K (EL $\geq 20^\circ$) [Feed loss ≤ -0.25 dB]
Wide-angle radiation pattern	Equivalent to CCIR Rec. 465-1	Equivalent to CCIR Rec. 465-1
Beam-alignment between RHCP and LHCP	$\pm 2\%$ of beamwidth	$\pm 3.5\%$ of beamwidth
Axial ratio	---	No more than 2 dB
VSWR	No more than 1.1 at feed horn	No more than 1.3
Isolation between transmit and receive	---	No less than 100 dB
Power handling capacity	---	40 kW (CW) nominal

Table 2. Usuda 64-m antenna noise comparison (low-noise configurations at 2295 MHz)

Element	DSS 14		Usuda	
	Zenith	30° EL	Zenith	30° EL
Maser	2.5 K	2.5 K	2.5 K	2.5 K
Feed components*	4.4 K	4.4 K	3.9 K	3.9 K
Antenna (spillover)	4.5 K	6.7 K	4.0 K	4.9 K
Sky (cosmic + atmos)	4.6 K	6.5 K	4.6 K	6.5 K
Totals	16.0 K	20.1 K	15.0 K	17.8 K

*Feed components at DSS 14 include: calibration coupler, switch, transmit filter, orothomode junction, polarizer, rotary-joints, feed-horn and 2 reflex feed reflectors.
Feed components at Usuda include: calibration coupler, switch, orothomode junction, polarizer, mode generator, feedhorn, and 4 beam waveguide reflectors.

Table 3. Usuda ICE performance May 15–June 30, 1985

DOY 1985	Length of pass, <i>h</i>	Bit rate, bps/coded	Peak symbol SNR, dB	Comments	DOY 1985	Length of pass, <i>h</i>	Bit rate, bps/coded	Peak symbol SNR, dB	Comments
134	4 1/2	512	1.1	Maser red	155	4 1/2	512	4.2	Maser green
				Used paramp	156	4 1/2	512	4.2	
135	4 1/2	512	4.3	Maser green	157	4 1/2	512	4.2	
136	4 1/2	512	4.3		158	4 1/2	512	4.1	
137	8	512	4.3		160	4 1/2	512	4.1	
138	8	512	4.3		161	4 1/2	512	4.1	
139	4 1/2	512	4.3		162	4 1/2	512	4.0	
140	4 1/2	512	4.3		163	4 1/2	512	4.0	
141	4 1/2	512	4.3		164	4 1/2	512	4.0	
142	4 1/2	512	4.3		165	4 1/2	512	4.0	
143	4 1/2	1024	1.25		167	4 1/2	512	4.0	
144	4 1/2	512	4.3		168	4 1/2	512	4.0	
146	4 1/2	512	4.2		169	4 1/2	512	4.0	
147	4 1/2	512	1.3	Maser red	170	4 1/2	512	4.0	
				Used paramp	171	4 1/2	512		Missed pass
148	4 1/2	512	1.3	Maser red					ISAS predict
				Used paramp					computer
149	4 1/2	512	1.3	Maser red					problem
				Used paramp	172	4 1/2	512	4.0	
150	4 1/2	512	1.3	Maser red	174	4 1/2	512	1.0	Maser red
				Used paramp					Used paramp
151	4 1/2	512	1.3	Maser red	175	4 1/2	512	4.0	
				Used paramp	176	4 1/2	512	4.0	
153	4 1/2	512	1.3	Maser red	177	4 1/2	512	4.0	
				Used paramp	178	4 1/2	512	4.0	
154	4 1/2	512	1.3	Maser red	179	4 1/2	512	4.0	Last pass
				Used paramp					this period

Table 4. Usuda ICE performance for Giacobini–Zinner encounter support

DOY 1985	Pass	UTC	Bit rate, bps/coded	Symbol SNR, dB	Elevation, deg	Comments
251	794	1900-0100Z	1024	1.8 – 2.0–1.6	57–77–40	
252	795	1900-0100Z	1024	1.7 – 2.0–1.6	57–77–40	Decoding string had varying SNR
253	796	1900-0100Z	1024	1.9 – 2.1–1.4	57–77–40	Heavy rain storm towards end of track
254	797	1900-0100Z	1024	1.8 – 2.15–1.6	57–77–40	RCVR momentarily dropped lock 0040Z; cause unknown
255	798	1900-0100Z	512	4.8 – 5.0–4.5	57–77–40	

Table 5. Usuda ICE performance for Halley first radial support

DOY 1985	Length of pass, h	Bit rate, bps/coded	Peak symbol SNR, dB	Comments
300	4	512	6.0	
301	4	512	6.0	
302	4	512	5.8	Heavy rain
303	4	512	5.8	Fog and rain
304	4	512	5.8	SSA failure No symbol stream recording Drizzling
305	4	512	6.0	

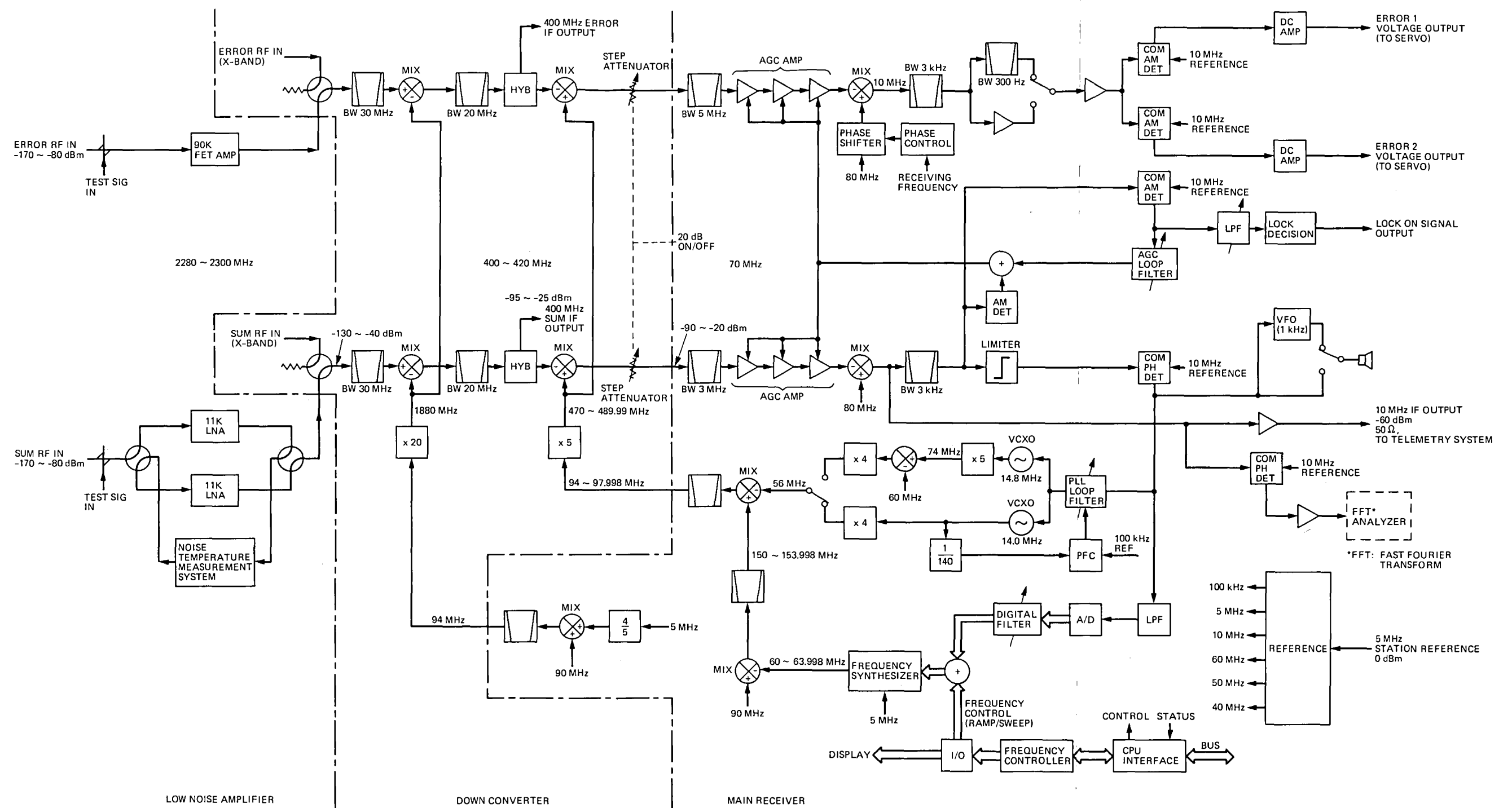


Fig. 1. Usuda block diagram

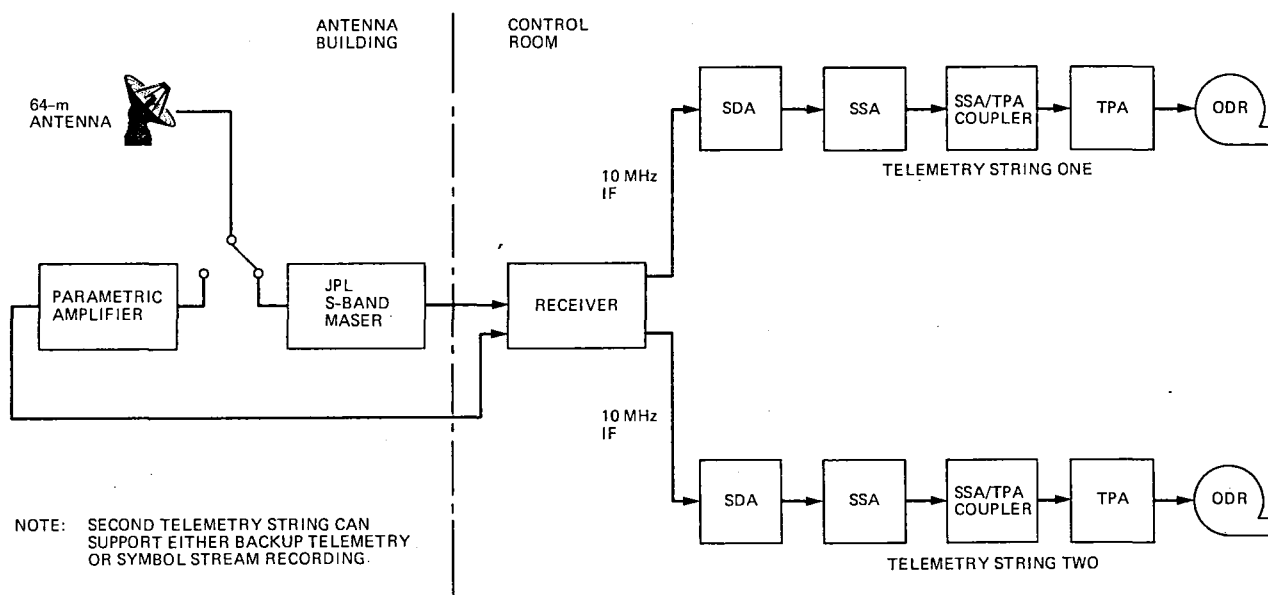
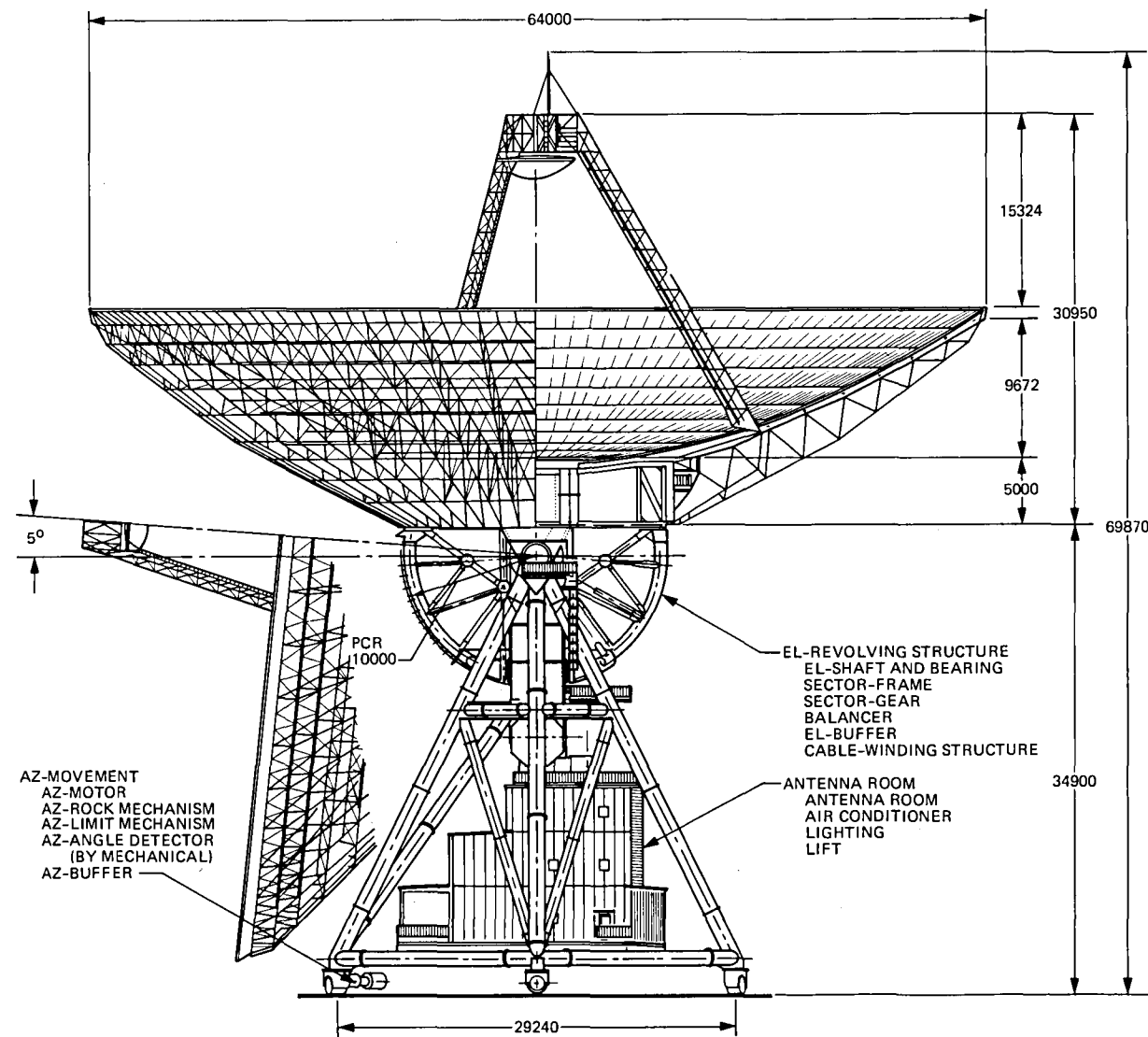


Fig. 2. Usuda Deep Space Center ICE configuration



DIMENSIONS IN MILLIMETERS

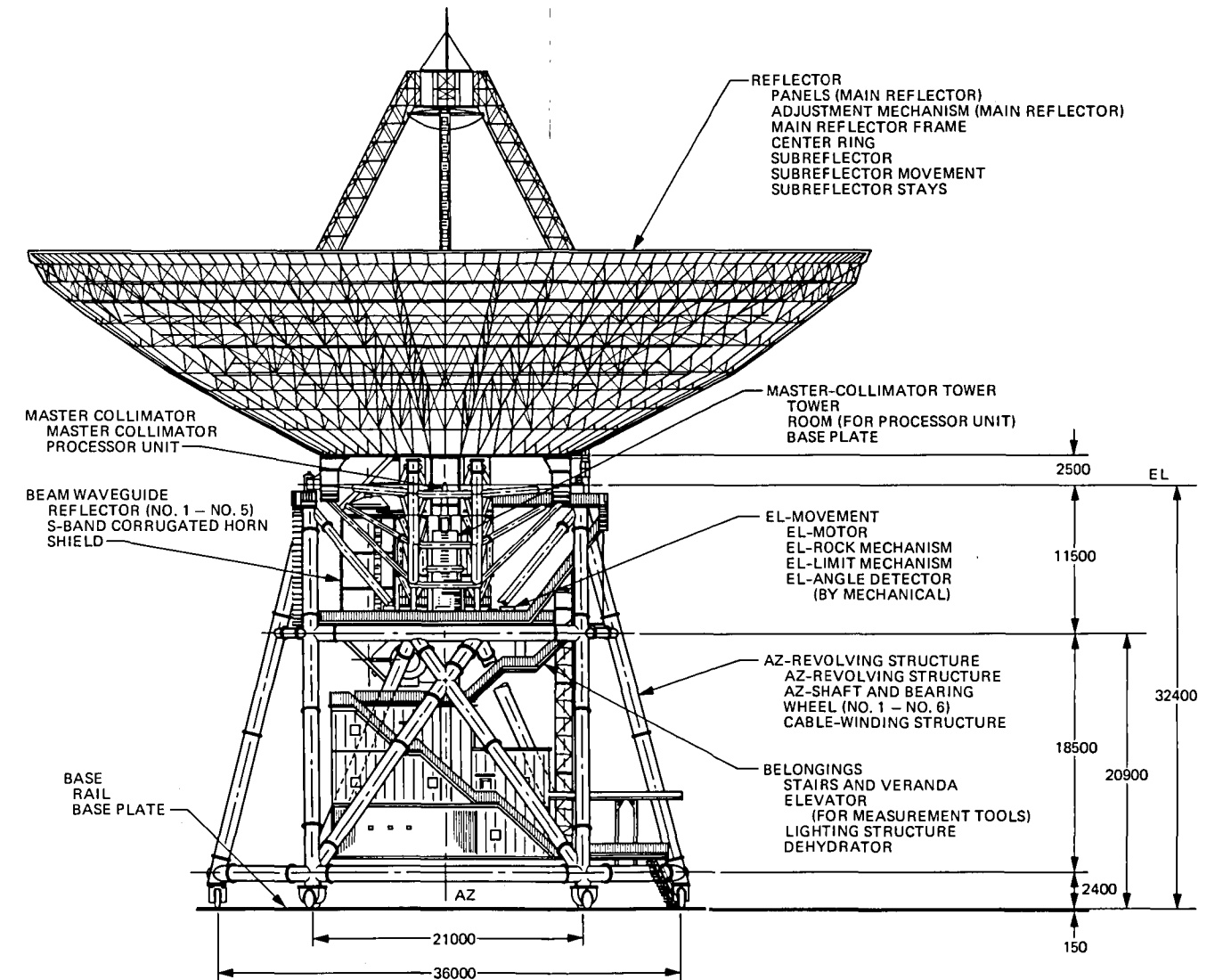


Fig. 3. Usuda 64-m antenna

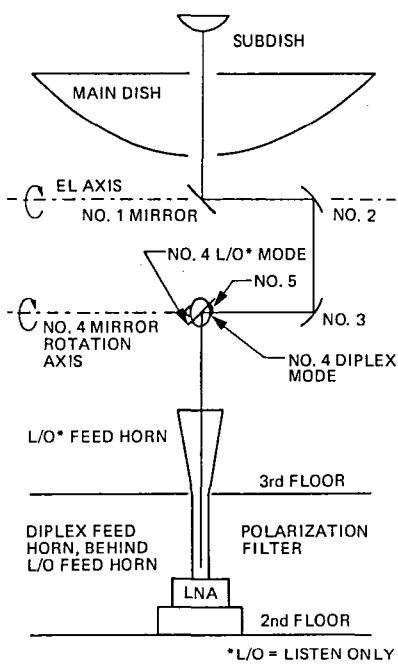


Fig. 4(a). Beam feed configuration

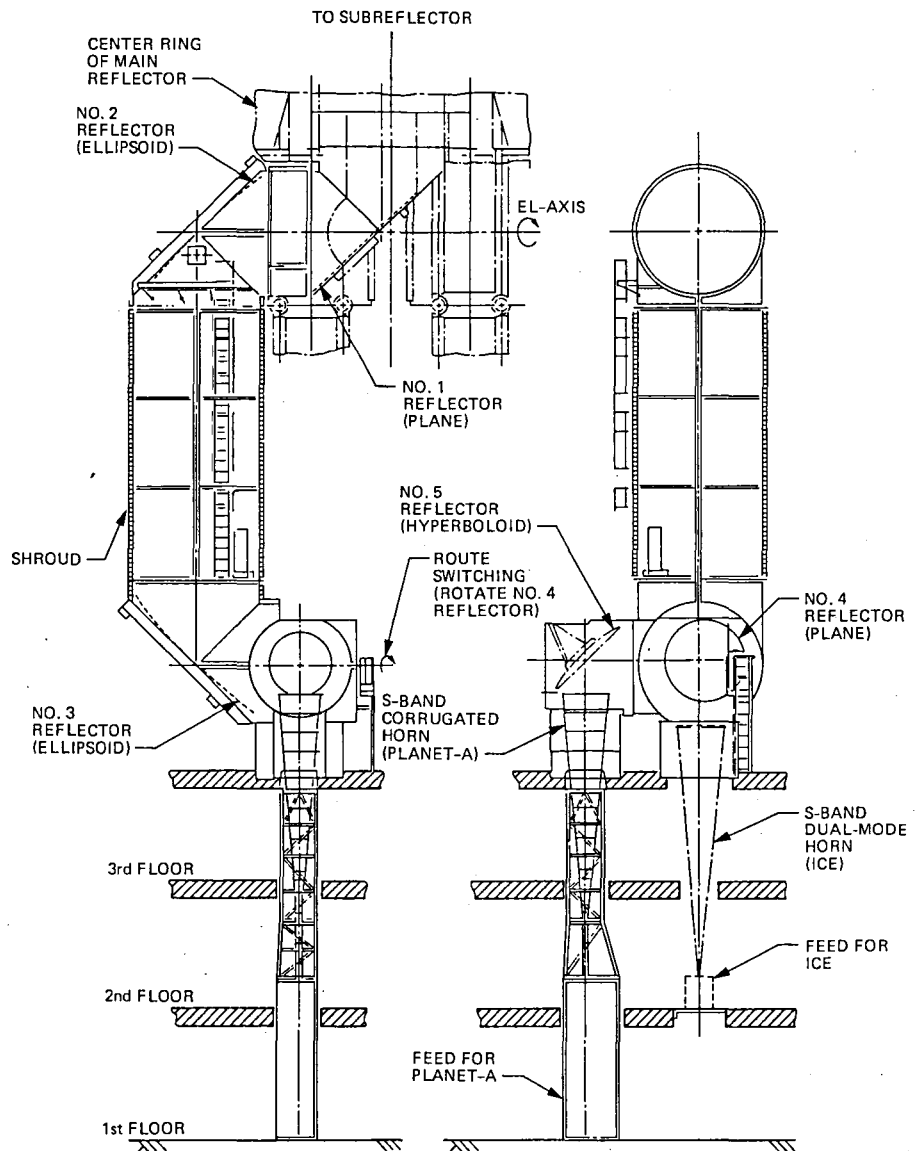


Fig. 4(b). Feed system of Usuda 64-m antennas

Arecibo Observatory Support of the U.S. International Cometary Explorer Mission Encounter at Comet Giacobini-Zinner

D. D. Gordon

TDA Engineering Office

M.T. Ward

Flight Mission Support Office
Goddard Space Flight Center

The Arecibo Observatory in Puerto Rico participated in the support of the U.S. International Cometary Explorer (ICE) mission when the ICE spacecraft passed through the tail of comet Giacobini-Zinner on September 11, 1985. The Arecibo Observatory is a research facility of the National Astronomy and Ionosphere Center (NAIC) operated by Cornell University under contract to the National Science Foundation (NSF). Coverage of the encounter involved the use of the observatory's 305-m (1000-ft) radio reflector antenna and RF and data system equipment fabricated or modified specifically for support of the ICE mission. The successful implementation, testing, and operation of this temporary receive, record, and data relay capability resulted from a cooperative effort by personnel at the Arecibo Observatory, the Goddard Space Flight Center, and the Jet Propulsion Laboratory.

I. Introduction

The Arecibo Observatory in Puerto Rico provided support to the U.S. International Cometary Explorer (ICE) mission when the ICE spacecraft passed through the tail of the comet Giacobini-Zinner (G-Z) on September 11, 1985. The Arecibo Observatory is a research facility of the National Astronomy and Ionosphere Center (NAIC) operated by Cornell University under contract to the National Science Foundation (NSF). The support involved the use of the observatory's spherical radio reflector antenna (Fig. 1) having a diameter of 305 m (1000 ft) and the installation of telemetry receiving and recording equipment designed to handle the ICE spacecraft

telemetry signal. The Arecibo facility does not normally receive modulated signals, and the frequency of the ICE spacecraft signal is slightly below the observatory's S-band receive capability. Observations of the comet at Kitt Peak Observatory in April 1984 made it possible to target the ICE spacecraft for the encounter coverage by the Arecibo Observatory.

The ICE spacecraft, formerly designated the International Sub-Earth Explorer-3 (ISEE-3) consistent with the objectives of its earlier mission, was launched on August 12, 1978. For that mission the NASA Ground Spaceflight Tracking and Data

Network (GSTDN), managed and operated by Goddard Space Flight Center (GSFC), provided telecommunication and data acquisition support for the spacecraft. After the spacecraft was diverted from its earlier orbit and placed on an intercept path with the comet Giacobini-Zinner (Ref. 1), it soon traveled out of range of GSTDN stations and support responsibility was transferred to the NASA Deep Space Network (DSN) operated by the Jet Propulsion Laboratory (JPL).

Early DSN link margin calculations, which took into consideration the 70 million-kilometer communication distance and the desired 1024-bps telemetry data rate, indicated that a signal-to-noise ratio margin of 1.0 ± 0.5 dB would be experienced at encounter. However, it was recognized that there was a potential for signal strength degradation and, therefore, a loss in science data return due to the effects of cometary dust. Use of the Arecibo facility to enhance the capability for data recovery at encounter was deemed to be advisable in order to increase the confidence in achieving a successful ICE mission.

Goddard Space Flight Center had responsibility for implementation and testing of the modified telemetry receiving and recording system. GSFC also provided personnel to assist the observatory staff in the operation of the NASA-supplied equipment.

II. ICE Mission Support Requirement

The Arecibo Observatory was requested to provide coverage for approximately 2 h each day for the 8-day period bracketing the ICE spacecraft encounter at the comet. This support required the installation of RF and data system equipment to provide a receive and record capability compatible with the ICE spacecraft transponder A telemetry signal, and activation of a real-time data quality circuit between the observatory and GSFC.

The ICE spacecraft transponder A downlink characteristics are as follows:

- (1) Transponder A, link 2, 2270.4 MHz
- (2) Convolutionally coded PCM
- (3) 1024-bps telemetry rate
- (4) Split phase modulation code
- (5) PM modulation
- (6) 1.08 modulation index

III. System Implementation

Studies at JPL and GSFC indicated that the most expedient and cost effective approach to implementing a temporary

receive, record, and data relay capability at the Arecibo facility included: (1) fabricate a circularly polarized antenna feed and cryogenically cooled low-noise amplifiers (LNAs) to accommodate the 2270.4-MHz downlink signal from the ICE spacecraft transponder A; (2) make use of existing RF and data processing hardware borrowed from GSFC; and (3) arrange through NASCOM for the lease of a data quality circuit for transfer of data from the Arecibo Observatory to GSFC.

A. Functional Description

The implemented operational configuration is represented in Fig. 2. The functions depicted in Fig. 2 are as follows:

- (1) LNAs receive and amplify ICE spacecraft signal at 2270.4 MHz.
- (2) Down convert (D/C) the 2270.4-MHz signal to 260 MHz.
- (3) Up convert (U/C) the 260-MHz signal to 670 MHz.
- (4) Input the 420-MHz signal to the multi-function receivers (MFRs, R_x).
- (5) MFR video output to bit synchronizers.
- (6) Hard decision output of bit synchronizers to frame synchronizers.
- (7) Soft decision output of frame synchronizers to sequential decoders.
- (8) Output of decoders to tape recorders and communication data formatters (CDFs).
- (9) Output of the CDFs through a modem to the NASCOM line.

B. NSF/NAIC Fabricated Equipment

NAIC designed the circularly polarized antenna feed and low-noise amplifier (LNA) to be compatible with the ICE telemetry signal at 2270.4 MHz. These items were fabricated at NAIC's engineering laboratory at Cornell University and shipped to the observatory in May and June 1985 for installation in the carriage house suspended over the antenna (Fig. 3). NAIC also provided down converters at the output of the LNA for conversion of the received signal to a 260-MHz intermediate frequency.

The LNA was designed with two channels to accommodate reception and amplification of both left-circular polarized and right-circular polarized signals. This allowed some redundancy, as one channel could substitute for the other in the event of a failure. The right-circularly polarized channel was the prime supporting channel, as that is the polarization of the ICE downlink signal. There was no on-line operational redundancy

in the remaining components of the LNA; however, spare parts had been procured and were on hand for replacement of components considered to be candidates for failure.

NAIC development of these devices was funded by NASA specifically for support of the ICE mission, but are to be retained at the observatory for use by NAIC in future scientific applications.

C. NASA/GSFC-Supplied Equipment

GSFC provided the additional RF and telemetry data processing equipment required to complete the ICE spacecraft compatible link at the Arecibo Observatory. In order to increase the probability of successful data capture, redundant equipment was installed for all operational functions:

- (1) Multi-function receivers: 2
- (2) Analog tape recorders: 2
- (3) Up converters: 2
- (4) Bit synchronizers: 2
- (5) Frame synchronizers: 2
- (6) Sequential decoders: 2
- (7) Time code generators: 2
- (8) Communication data formatters: 2
- (9) Signal generator: 1
- (10) Cables for the above equipment

All of the above equipment was assembled and tested at GSFC prior to shipment. It was delivered to the observatory pre-assembled in equipment racks for installation and integration at the observatory. This equipment was provided on loan from GSFC specifically for support of the ICE mission and was returned to GSFC following the comet encounter.

D. Communications Link

After the implementation task was underway, approval and funding became available for a communications circuit to provide the real-time transfer of telemetry data from the Arecibo Observatory to the Multi-Satellite Operations Control Center (MSOCC) and the Telemetry Processing Facility (TPF) at GSFC. NASCOM procured a commercial link for this purpose. The link was composed of several segments, principally a satellite link to an Earth station in Puerto Rico and microwave links from there to the observatory. The operational employment of this circuit routed data through JPL's Network Operations Control Center, which maintained overall operations control of communications circuits in support of the ICE mission.

IV. Test and Training

The test and training for the Arecibo support (NASA/GSFC document¹) was composed of two basic parts: (1) a series of engineering tests, and (2) a series of operations tests, with the latter including operations training.

Initial testing began with the completion of the equipment link implementation at GSFC prior to its shipment to the observatory. A series of tests were conducted at GSFC to verify the functional integrity of the link and its interface with the MSOCC and TPF facilities. The results of these tests were satisfactory except for a timing interface problem between the link and the TPF. This problem was discovered early in the testing and survived through several tests until isolated in the Communications Data Formatter firmware. Upon its discovery the problem was promptly corrected, and the system was declared ready for shipment to the observatory.

Prior to shipment of the GSFC equipment to Arecibo, NAIC personnel installed the feed and LNA in the carriage house suspended over the antenna and performed preliminary tests of these units. After arrival of the GSFC equipment, an engineering test of the entire link was possible for the first time.

A. Engineering Tests

The engineering test series at Arecibo tested the link's capability to process ICE telemetry signals. During the first tests, simulated and pre-recorded signals were injected into the system. After successful conclusion of these tests, the link successfully tracked the ICE spacecraft, and the recorded data was shipped to the GSFC for verification by the TPF. At this point the link was declared operational and operations tests began, although the communications circuit remained to be tested since it was not yet available from the vendor.

B. Operations Tests

The operations tests consisted of a series of simulations to exercise equipment and procedures under conditions simulating those of the encounter support. These tests were conducted using both live spacecraft and recorded data sources with the participation of Arecibo, JPL, and GSFC. The tests concluded with an Operational Readiness Test conducted on September 6 after the communications circuit was available.

¹"Space Tracking and Data Network ICE Network Test Plan," STDN No. 403/ICE, NASA/GSFC document, June 1985.

V. Operations

Encounter operations support at the observatory (Refs. 2 and 3) began on September 8, 1985, and continued through September 14, three days following the transit through the comet tail on September 11. The daily support consisted of an approximately 2-h period, the maximum coverage time available at the observatory during which telemetry data was received, transmitted to the MSOCC and TPF at GSFC, and recorded on station for possible playback. Operations at the observatory were supported by a team of NAIC personnel and GSFC personnel who operated the GSFC equipment. The overall opera-

tions control, integrating the Arecibo support operations with that of the DSN complexes at Madrid and Goldstone, was carried out by the JPL Network Operations Control Center.

The Arecibo Observatory performance profile is represented in Fig. 4. The telemetry equipment performed very well during the encounter, achieving solid lock with good data delivered at 72 deg of elevation. The effective threshold corresponds to an AGC reading of -154 dBm. At higher elevations, and for at least one-half hour of the time of comet tail crossing, the SNR was about 3.5 dB above this threshold value.

References

1. Farquhar, R., Muhonen, D., and Church, L. C., "Trajectories and Orbital Maneuvers for the ISEE-3/ICE Comet Mission," *Journal of Astronautical Sciences*, Vol. 33, No. 3, pp. 235-254, July-Sept. 1985.
2. Fanelli, N. A., and Morris, D. G., "ICE Encounter Operations," *TDA Progress Report 42-84*, this issue.
3. Layland, J. W., "ICE Telemetry Performance," *TDA Progress Report 42-84*, this issue.

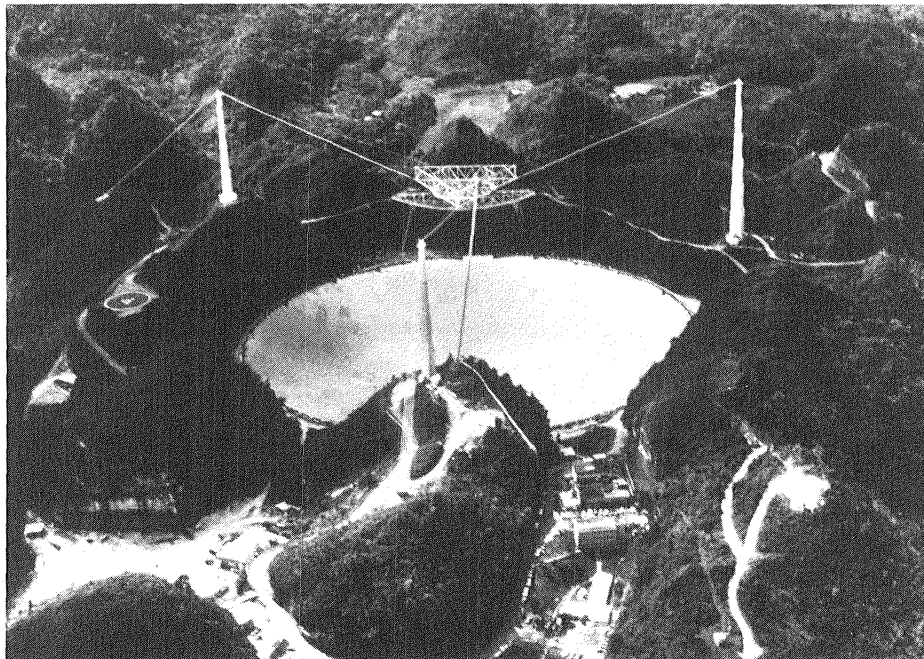


Fig. 1. Arecibo Observatory 305-m (1000-ft) diam radio reflector antenna

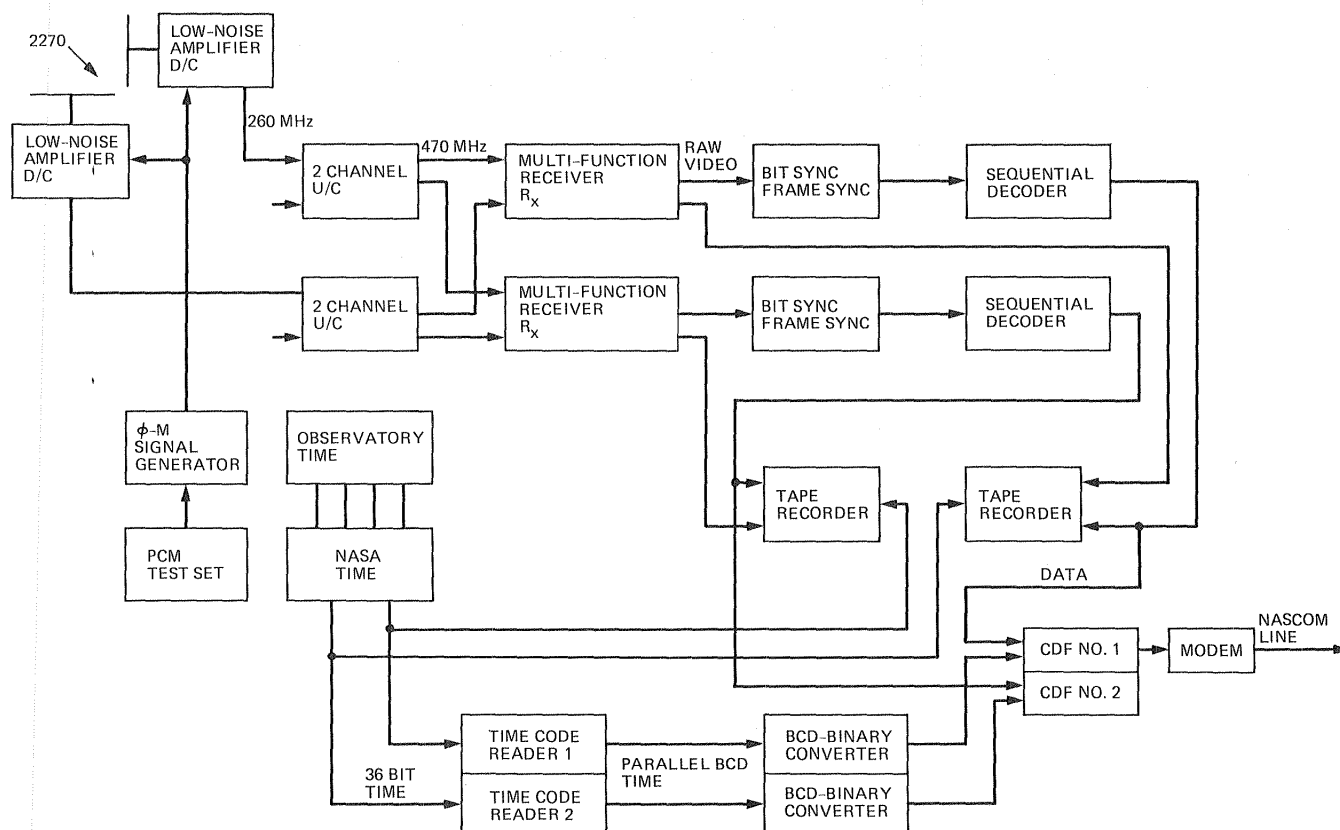


Fig. 2. ICE Arecibo support capability functional block diagram

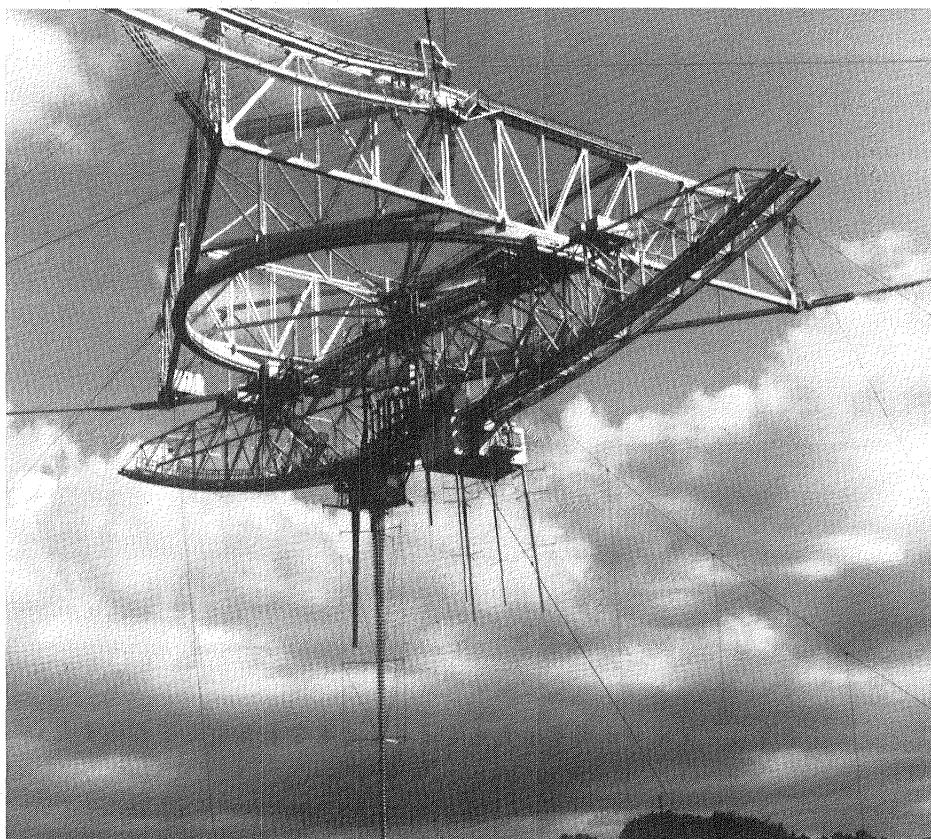


Fig. 3. Close-up view of the structure suspended above the reflector antenna supporting two carriage houses and the antenna feeds

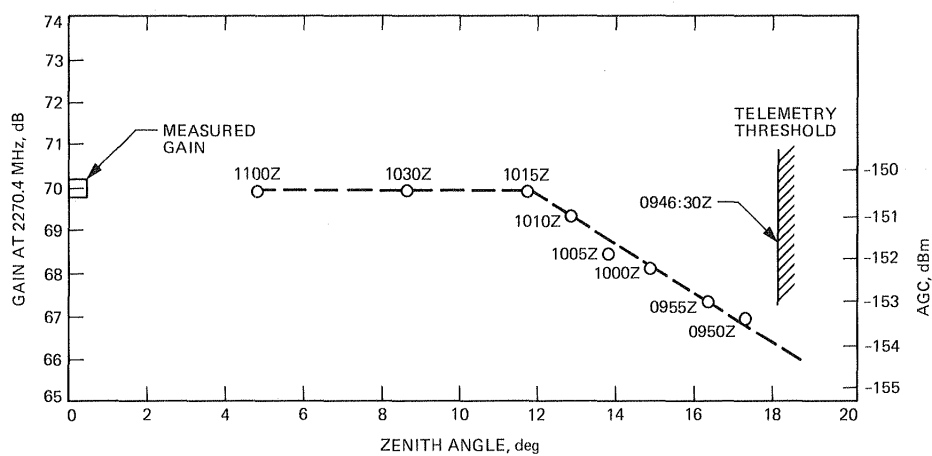


Fig. 4. Arecibo Observatory performance at ICE mission encounter on September 11, 1985 (DOY 254)

ICE Telemetry Performance

J. W. Layland
TDA Planning

Acquiring telemetry data from the International Cometary Explorer (ICE) at its encounter with the comet Giacobini-Zinner on September 11, 1985 proved to be among the more difficult challenges the DSN has met in recent years. The ICE spacecraft began its life as an earth-orbiting monitor of the Solar Wind. At the comet, ICE was nearly 50 times as distant as in its initial role, with its signal strength diminished nearly 2500 times. Collecting enough of that weak signal to provide meaningful scientific data about the comet required unique new telemetry capabilities and special handling by the DSN. This article describes the development and validation of the DSN telemetry capability for ICE from its early planning stages through the successful comet encounter.

I. Introduction

When it was launched in 1978, the ISEE-3 (International Sun-Earth Explorer) was a mild-mannered observer of the Solar wind on its way to the Earth. In late 1983, some time after the close of the ISEE primary mission, and after much debate and complicated orbital maneuvering, the ISEE-3 spacecraft had a new name, the International Cometary Explorer (ICE), and was on its way to an encounter with comet Giacobini-Zinner (Refs. 1, 2). As ISEE-3, the spacecraft orbited the Earth with the Sun at a distance of 0.01 Astronomical Units (AU), or 1 percent of the distance from the Earth to the Sun. At the encounter with Giacobini-Zinner on Sept. 11, 1985, the ICE would be at a distance of 0.47 AU, or nearly 50 times as far away as the spacecraft had been during its primary mission. That increase in distance effected a corresponding decrease in received signal strength by almost 2500 times, and posed a significant challenge for the DSN to provide the support needed by the ICE.

The ISEE-3 spacecraft was supported by the 26-m antennas of the Ground Spaceflight Tracking and Data Network

(GSTDN), in an environment characterized by high link margins and corresponding wide tolerances for link parameters. Those tolerances had to be tightened and much of the margin consumed in order to provide the desired data return from the comet encounter. The spacecraft has two separate transmitters on different frequencies in the 2 GHz band which were used interchangeably for telemetry and radio metrics when it was supported by the GSTDN. For the comet mission, both transmitters were used for telemetry, and the DSN 64-m antennas at Goldstone and Madrid were given new low-noise Maser amplifiers which enabled them to simultaneously receive the two downlinks from ICE and combine the signals to achieve a doubling of the rate at which comet data could be acquired. The Maser amplifiers for the lower of the two ICE frequencies were not available until early 1985 for validating the comet encounter performance predictions.

II. Preliminary Planning and Analysis

Planning and performance analysis for the ICE mission had started by early 1981. A flight to Halley's comet was consid-

ered for a time, but dropped because the distance at that encounter would have been too great, and because an ISEE encounter with Giacobini-Zinner could be done better and be done first. Preparations for the comet mission included careful measurements by the Goldstone DSS of the received power in the two downlinks of ISEE-3. The channel A signal (2270 MHz), which fell within the tuning range of the standard DSN equipment was measured on November 30, 1981,¹ and then measurements of the relative power in the two ISEE-3 downlinks followed in early 1983. These measurements were used to calibrate and refine the telemetry link design control tables for the anticipated comet encounter.

Performance of the DSN's telemetry receiving systems for the ICE was estimated from the standard references,² which had been based upon analysis done in support of Helios and the Pioneers several years ago. In the meantime, the DSN's sequential decoders had been replaced with faster ones, the DSN's receivers were capable of a narrower bandwidth operation, and the ISEE's signal characteristics were different than the earlier spacecraft so that the overall telemetry receiving system performance could be expected to be modestly improved over that predicted from the reference. The link analysis showed that reception from ICE at Giacobini-Zinner encounter at the desired 1024 bps data rate would be feasible by combining the two downlinks received by the DSN 64-m antennas. But margins would be slim, about 1 dB or so,³ and a few assumptions were still awaiting verification. Arraying with the adjacent 34-m antennas was examined as a possible enhancement and considered as not being too difficult since the new arraying capability under development to support Voyager at Uranus and Neptune would be available.

The ISEE spacecraft rotates at about 19 rpm and has a four-lobed antenna pattern which sweeps past the earth once each rotation. The impact of this rotation on the telecom link was assessed from the pre-launch antenna pattern measurements, which suggested that peak to peak level variations of the 2217 MHz signal were limited to only 0.2 dB, but that the 2270 MHz signal would exhibit about 2.2 dB peak to peak variations. For the purpose of link planning, the expected signal level was ascribed to be at the minimum for the antenna pattern. It was recognized, however, that measurements of the

signal level would typically show the average, about 1 dB higher than these predicts. Link performance testing and the assessment of expected performance based upon this testing were carried out with respect to the average observed Symbol SNR. The bookkeeping to compare actual against predicted levels included this 1 dB.

One assumption made in the early link analysis which later became a concern was that the effect of the comet environment upon the telemetry link could be neglected. The models of the dust tail for the comet kept open the possibility that the spacecraft itself could be damaged early in the encounter. Severe telemetry link degradation could be one of the results. As insurance against that potential, Cornell University's Arecibo Observatory in Puerto Rico was instrumented to receive ICE telemetry, and the Symbol-Stream combining capability was devised to combine the ICE signals as received simultaneously at two distinct DSN sites. The time of the ICE crossing of the comet tail was scheduled to fall within the simultaneous field of view of the Arecibo Observatory and the DSN sites at Goldstone and Madrid. These developments are described elsewhere in this issue (Ref. 3, 4).

III. Decoder Analysis and Single-Channel Tests

Surprises which were encountered in testing the DSN receiving/decoding configuration for ICE led to an extensive analysis and testing activity throughout 1984. The analysis work, already reported (Ref. 5), extended the older analysis of the DSN's sequential decoding performance to faithfully represent the current configurations of DSN and ICE spacecraft. This detailed analysis agreed well with the extrapolation that had been done using the older reference material. But analysis alone is not enough — the system itself must perform as well. The extensive self-monitoring capability of the DSN sequential decoders was used in conjunction with the Madrid 64-m station and the ICE spacecraft to characterize the DSN decoder behavior. The accumulated result of these tests was agreement with the analysis to within the experimental uncertainty.

Performance tests during 1984 were limited to channel A (2270 MHz) by the extant DSN equipment. Full configuration tests had to await the installation of the new Maser amplifiers (Ref. 6), and the signal combining equipment (Ref. 7). Telemetry performance parameters which were monitored included those which characterize both the input and output of the sequential decoder. The AGC-estimate of received carrier power, the observed symbol SNR and symbol error rate, the decoder deletion rate, and the decoder computation count were all monitored by the DSN Telemetry Processor and communicated to the Network Operations Control Center where

¹D. J. Bell and R. D. Shaffer, "Final Results from ISEE-3 Carrier Power Measurements," IOM 3392-82-86 (internal report), Jet Propulsion Laboratory, Pasadena, Calif., May 21, 1982.

²*Deep Space Network/Flight Project Interface Design Handbook, Vol. 1: Existing DSN Capabilities* (Document 810-5, Rev. D; internal report), Module TLM-40, DSN Telemetry System Data Decoding pp. 1-19, Jet Propulsion Laboratory, Pasadena, Calif., 1984.

³D. J. Bell, "ISEE-3 Telemetry Downlink — 1984-1990," IOM 3392-83-100 (internal report), Jet Propulsion Laboratory, Pasadena, Calif., May 31, 1983.

they were recorded for final analysis. New plotting display software was needed and was developed by the DSN Performance Analysis Group to present this data for effective understanding.

Most of the performance data were gathered during routine spacecraft support passes within which ranging operations occurred. With ranging active, the spacecraft configuration is such that the single channel signal level would drop by 2 dB to near its threshold region. Changes in the spacecraft-earth distance during the period of testing allowed the SNR region around threshold to be probed without resorting to artificial means of manipulating the signal.

Figure 1 shows the accumulated effect of the 1984 testing. Not all data points are included here, to avoid an unreadable clutter. Those from late in the year which are not shown are consistent with those shown. The background lines of this figure are from the analysis (Ref. 5), and correspond to expected decoder deletion rate for the DSN decoder using receiver bandwidths of 3 Hz or 10 Hz. Experimental data points are calibrated into this background via the observed symbol SNR at the input to the decoder. Data points are indicated by large crosses, with arm lengths representing two-sigma uncertainty in the observation. The numbers which label each data point are the Day-of-Year (DOY) in 1984 on which they were acquired. Where a Tee mark is used in place of a cross, it means simply that there were no deletions observed in that interval, and the top of the Tee indicates the top of the two-sigma uncertainty range. The bottom of that range is zero. The inferred threshold of acceptable performance is indicated by the vertical hashed bar at 0.5 dB of Symbol SNR at the input to the decoder.

Figure 2 is one example of the raw data plots which entered into the analysis. This data corresponds to 1984-DOY-185, with a spacecraft pass from about 0330 to 1230 GMT. Data were acquired on this date using the 3-Hz receiver bandwidth only. The period of lowered SNR is the ranging interval, which appears to have two distinct segments. For 0640-0650, the symbol error rate (SER) was 8.8 percent, representing a symbol SNR of -0.3 dB, and giving a deletion rate of 1.7 percent. For 0650-0720, the SER was 8.2 percent for an SSNR of -0.1 dB, which gave a deletion rate of 0.25 percent. Here, as in other tests, the SER, an output of the decoder itself, is used as the calibrator because of the smaller statistical scatter on that observable. The main part of the non-ranging interval of 7 hours showed no deletions, giving two-sigma confidence that the deletion rate is below 0.8×10^{-4} , at the SSNR of 1.0 to 2.0 dB. These three points all appear on Fig. 1 tagged with #185.

The sequential decoder's workload, the number of computational steps needed to decode a block, is a sensitive measure not only of the SNR of the symbol stream which the decoder receives, but also of the alignment and proper operation of the receiving and data detection equipment. Plotting the computation count against the observed SER eliminated confusion from short-term variations in signal level and provided a tool for assessing correctness of gain settings, combiner ratios, etc. in the upstream equipment. Figure 3 is a plot of decoder computation count per frame (DCF) vs symbol error rate (SER) for a pass which represented good performance on the 2270 MHz channel. Deletions occur whenever the computations needed to decode a given block exceed the number available before work must be started on the next block. Deletion of individual random blocks has become likely whenever the average computation per bit exceeds about 5 (or log DCF about 3.3), which occurs around the SER of 7.5 percent, or Symbol SNR of 0.2 dB, somewhat below the declared threshold level.

It was later learned that the DCF vs SER graph for the 2217 MHz channel would be in agreement with Fig. 3, despite the presumed difference in antenna patterns. This and other factors led to the examination of the antenna rotation patterns in the observed data, and to the surprise discovery that both the 2217 and 2270 MHz channels showed strong variations in signal level with the rotation angle of ICE (Ref. 8).

Twice during 1984, on DOY 148 and 157, attempts were made to retune one of the Maser amplifiers on the Madrid 64-m antenna to receive the lower frequency ICE signal to validate telemetry performance with it. When calibrated onto a chart like Fig. 1, using the SSNR at the decoder input, the performance of this channel was consistent with Fig. 1 data. However, in absolute signal level terms when compared against predicts, the link performance was significantly below that expected. At the time, that difference was ascribed to a side-effect of tuning the Maser beyond its normal range.

IV. ICE Encounter Support Configuration

Near its encounter, the ICE was provided nearly continuous coverage. The two 64-m antennas at Spain and Goldstone each listened to both of the two ICE downlink signals with separate low-noise Maser amplifiers and narrowband phase-locked receivers. A coherently detected baseband from each of the two channels was fed to a resistive combiner at each site. A resistive combiner was chosen for use here because it was simple to build, install, and test, and was adequate for the purpose with the small bandwidth of the ICE signal (Ref. 7). The nearby 34-m antennas, one at Madrid and two at Goldstone, also listened to the 2270 MHz signal from ICE and provided

another detected baseband to the resistive combiner at that site. Two combiners were operated at each site during the encounter, the prime unit combining all available signals, and a second as backup combining only the two strong signals from the 64-m antenna.

As noted earlier, the ICE was scheduled to be within the narrow field of view of the Arecibo Observatory during the crossing of the comet tail. To enable it to support ICE at that time, Arecibo was provided with new receiving equipment for the ICE 2270 MHz downlink and telemetry equipment from the GSTDN (Ref. 3). Actual spacecraft support was provided for only a few days around encounter, preceded by periods of installation and testing.

The DSN 64-m antenna in Australia was not configured to receive both ICE downlinks because of the limited visibility from its southern latitude due to the northern declination of the ICE spacecraft at encounter. However, it was provided with a two-port resistive combiner to allow both the 64-m and the 34-m STD to combine for support of the lower data rates.

Additional support to ICE over the Asian longitude was provided by the new 64-m deep space station at Usuda Japan which was built by the Japanese Institute for Space and Astronautic Sciences for support of their Planet-A mission to Halley's comet (Ref. 9). This support was arranged in exchange for DSN support to Planet-A, and was enabled by the installation of equipment from the DSN. This equipment included DSN telemetry data acquisition computers, and a very low noise Maser amplifier from the DSN Advanced Systems area. Even though only the 2270 MHz downlink was received, the high aperture efficiency of the new antenna coupled with a low noise listen-only configuration to give the Usuda station almost the same overall performance as the two channels into the DSN 64-m antenna.

V. Combined Channel Testing

Testing for the planned encounter support configuration began early in 1985, as soon as the new equipment had been installed at the Goldstone Complex. Early tests were hampered by problems with initial operation of the newly-designed wide bandwidth low noise Maser amplifier for the 2217 MHz channel. Comparison tests between the two channels repeatedly showed the received SNR of the 2217 MHz channel to be below that of the 2270 MHz channel, contrary to expectation, but observed drifts in Maser performance were identified as the probable cause. It was only after the new Maser had successfully emerged from its break-in period that it became clear that the early tests in Spain had correctly indicated the

lower performance in the 2217 MHz channel. An extensive search for probable cause uncovered only corrections on the order of a few tenths of a dB for the DSN antenna gain. Incorporating all identified adjustments, the 2217 MHz channel SNR was about 1 dB below the expected level.

As encounter approached, the only leads which had not been fully explored pertained to the spacecraft configuration or antenna attitude during the tests in 1983. These tests had shown the 2217 MHz channel power level to be about 1 dB stronger, compared to the 2270 MHz channel, than had been expected on the basis of pre-launch analysis. Hence, the appearance of weakness in the performance of the 2217 MHz channel could be eliminated if the 1983 tests were ignored. This lead was not followed because it did not appear that the knowledge gained thereby could have improved the link performance at encounter.

During the summer, several hundred hours of link performance statistics were accumulated and plotted from telemetry monitor data. Except for periods when a recognized degradation occurred, the 2270-MHz channel performance statistics were consistent with the predicted level and the 2217-MHz channel consistently showed the 1 dB lower performance than predicted. Meanwhile the combined performance was consistently about 0.5 dB below predicts and showed less than 0.2 dB degradation as compared to the sum of individual channels.

Figure 4 illustrates these points with data from a successful test on 1985 DOY 185 (July 4). Points to indicate the predicted levels have been added by hand, and the approximate residuals for the 2217-MHz channel and for combined data are indicated by the double-headed arrows. Figure 5 shows the test at 1024 bps on DOY 207 where again there was about a 0.5 dB residual between the predicted and observed performance for the combined data. This was reasonably consistent through the two months prior to encounter at the Goldstone 64-m system.

Most of the performance data for the combined performance were acquired at 512 bps, in part because the spacecraft was further away from June through August than it would be at encounter, and in part because the Network was not yet fully ready to support the planned encounter rate of 1024 bps. Operation at the 1024 bps data rate began 1985 DOY 226, and showed performance which was consistent with the 512 bps performance data after correcting for the 3 dB change in data rate. In addition, early 1984 comparisons of predicted (minimum) vs observed (average) SSNR for the 2270 MHz channel at the higher data rates showed positive residuals of 0.8 to 1.0 dB, consistent with the difference between minimum and average SSNR for the rotating spacecraft. As noted before, equipment to handle the 2217 MHz channel signal was not available at that time.

VI. Expected Encounter Performance

Figure 6 is a sketch of the performance profile for the ICE encounter day. Each of the individual sites which would be supporting the encounter is shown. The indicated link margin for the specific time of encounter was low enough that the added 0.5 dB from arraying with the 34-m antennas was believed to be important to ensuring overall success. In the figuring of the contribution of the 34-m antennas, differences in antenna effective areas, system temperatures, and the loss due to the time delay of the DSS-12 signal were included. Because of the geometry, this time delay was no problem for the several hours around encounter, but reduced the DSS-12 contribution to only 0.1 dB by end of pass.

Variations in observed performance are indicative of a tolerance which should be placed upon that expected for encounter. There is a short-term scatter in SER of about 0.2–0.3 dB, which could be an antenna pointing (conscan) artifact. There appears to be a gradual within-the-day downward drift in performance at both Goldstone and Madrid which accumulates to 0.2–0.4 dB by end of pass – i.e., in daylight hours. There is a day-to-day scatter of 0.3–0.4 dB. And there is at Goldstone one telemetry string (TPA-3) which continued to underperform the others with baseband (array) inputs. The performance profile for encounter was set to approximate the lower end of the day-to-day variations. The probable tolerance about this profile was +0.7/–0.2 dB. Performance of the Goldstone 64-m antenna prior to encounter tended to be near the upper end of this range, while that at Madrid was at the lower end.

Arecibo performance is discussed in Ref. 3. The received signal was nominally above telemetry threshold for all elevation angles of 75 deg or higher, and the received carrier level was about 3 dB higher at 80 deg than at 75. This implied that the telemetry margin at Arecibo would be on the order of 3 dB for the comet tail crossing which occurred at an elevation of about 85 deg. The Arecibo performance profile as sketched is mildly conservative, and was in fact exceeded by about one dB.

Usuda performance with one receive channel was comparable to, or slightly in excess of, that of the Goldstone 64-m antenna with the two channels combined (Ref. 9). The contributors to this were a higher antenna efficiency (62.4 dBi gain), and lower system temperature (14.5 K) in a listen-only configuration. These factors combined to make the Usuda effective performance about 2.7 dB stronger than that of the Goldstone 64-m single channel duplex configuration, or comparable to that of the Goldstone two-channel.

VII. Summary: ICE Encounter

The passage of ICE through the tail of comet Giacobini-Zinner took place on 1985 Sept. 11, at approximately 1104 GMT. All three supporting sites, Madrid, Arecibo, and Goldstone, reported good performance and successfully acquired spacecraft data during the tail crossing. Figure 7 shows the observed performance of the two DSN sites for this time interval. Madrid essentially performed at the expected level, while Goldstone's performance exceeded it. Arecibo operated above threshold for almost 2.5 hours on the encounter pass, far longer than on any other day. Such problems as did occur were minor and did not affect more than one site at a time. There is no sign of the anticipated degradation due to comet dust or other factors in the vicinity of the comet. All supporting sites acquired ICE data at the desired 1024 bps data rate.

In summary, the International Sun Earth Explorer-3 was retargeted for an encounter with comet Giacobini-Zinner with the expectation that scientific data about the constituents of the comet's tail could be acquired at a data rate of 1024 bps. Link margins were very slim, even though the DSN was being outfitted to receive and combine both downlinks from the spacecraft. Several times prior to the encounter, problems arose which threatened the viability of the expected support. But in the final analysis, the expectations were fulfilled, and much new data (described by the scientists as very exciting) were acquired about the comet.

Acknowledgment

Successful support to the International Cometary Explorer is the product of the labors of many devoted people. Some of these are the authors of the many companion articles referenced in this article. Other key JPL contributors include W. L. Martin, T. O. Patterson, and S. S. Kent, plus the many unnamed workers of the DSN Operations Organization and Performance Analysis Groups who provided extra attention and effort when it was needed.

References

1. Farquhar, R. J., Muhonen, D., and Church, L. C., "Trajectories and Orbital Maneuvers for the ISEE-3/ICE Comet Mission," *Journal of the Astronautical Sciences*, Vol 33, No. 3, July-Sept. 1985.
2. Fanelli, N. A., and Morris, D. G., ICE Encounter Operations, *TDA Progress Report 42-84*, Jet Propulsion Laboratory, Pasadena, Calif., 1986.
3. Gordon, D. D., and Ward, M. T., Arecibo Observatory Support of the International Cometary Explorer Mission Encounter at Comet Giacobini-Zinner, *TDA Progress Report 42-84*, Jet Propulsion Laboratory, Pasadena, Calif., 1986.
4. Hurd, W. J., Pollara, F., Russell, M. D., Siev, B., and Winter, P. U., Intercontinental Antenna Arraying by Symbol Stream Combining at Giacobini-Zinner Encounter, *TDA Progress Report 42-84*, Jet Propulsion Laboratory, Pasadena, Calif., 1986.
5. Divsalar, D. D., A Sequential Decoding Performance Analysis for International Comet Explorer, *TDA Progress Report 42-82*, Jet Propulsion Laboratory, Pasadena, Calif., pp. 82-91, Aug. 15, 1985.
6. Petty, S. M., and Trowbridge, D. L., Block 5 Traveling Wave Maser, *TDA Progress Report* (in preparation), Jet Propulsion Laboratory, Pasadena, Calif.
7. Marina, M. M., Resistive Combiners for ICE, *TDA Progress Report* (in preparation), Jet Propulsion Laboratory, Pasadena, Calif.
8. Nadeau, T., Periodic Variation in SNR of Signals Received from the ICE Spacecraft, *TDA Progress Report 42-84*, Jet Propulsion Laboratory, Pasadena, Calif., 1986.
9. Goodwin, J. P., Usuda Deep Space Center Support to ICE, *TDA Progress Report 42-84*, Jet Propulsion Laboratory, Pasadena, Calif., 1986.

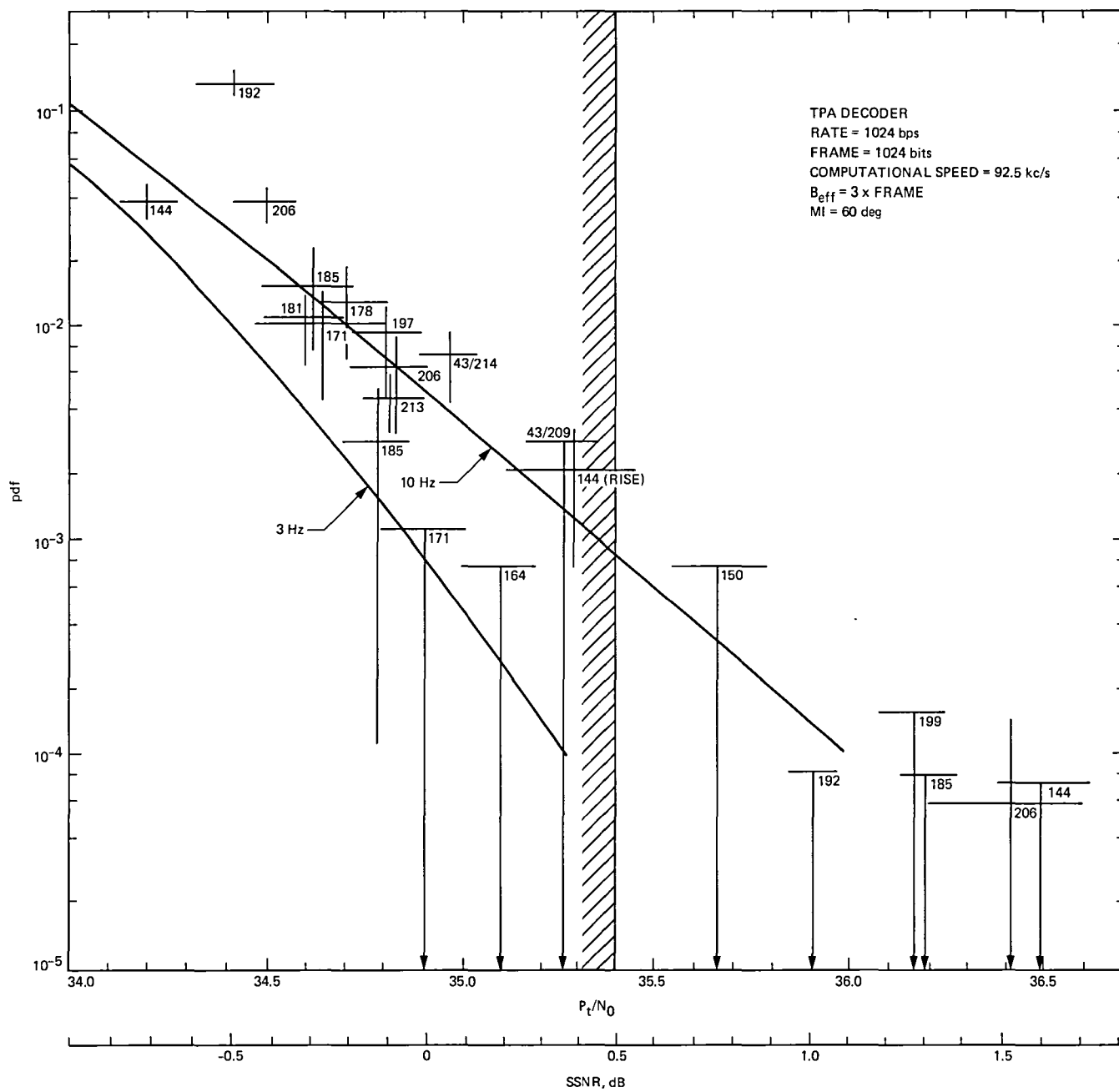


Fig. 1. Test summary and performance curves for single channel tests

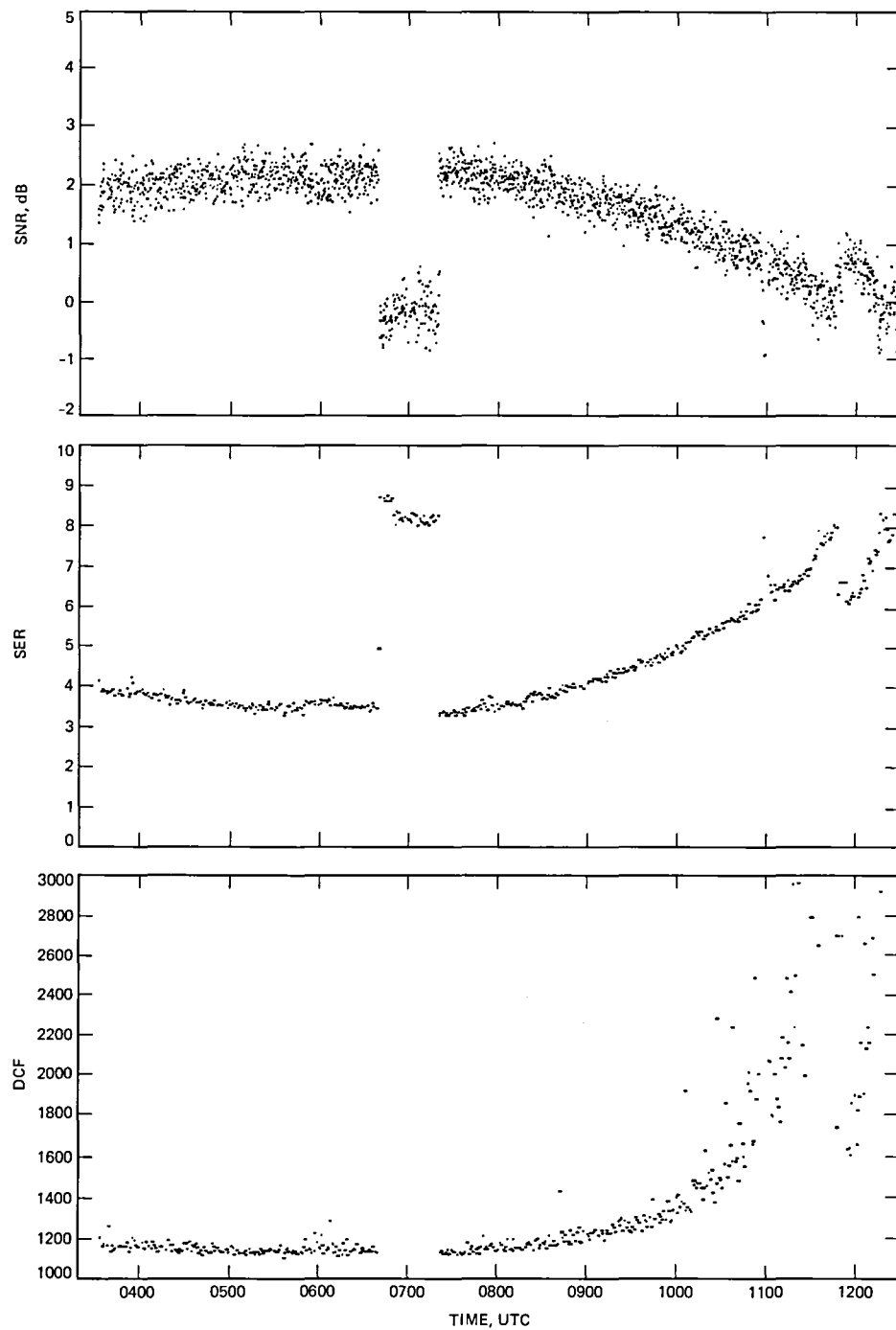


Fig. 2. Performance of Madrid 64-meter system for 1984 DOY 1985

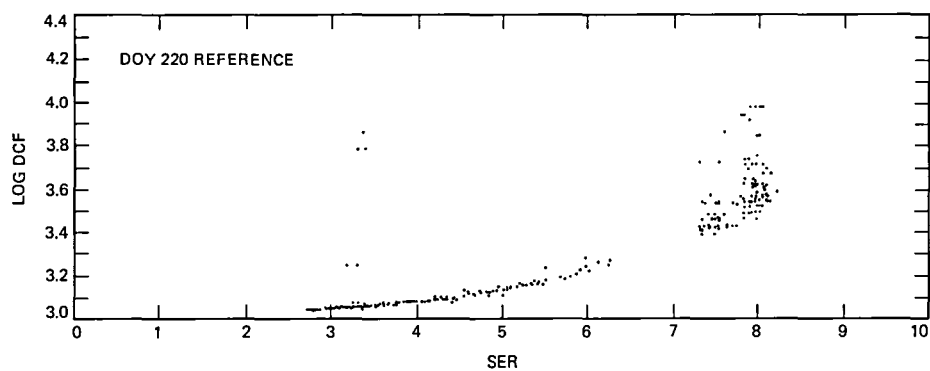


Fig. 3. Decoder computations vs symbol error rate

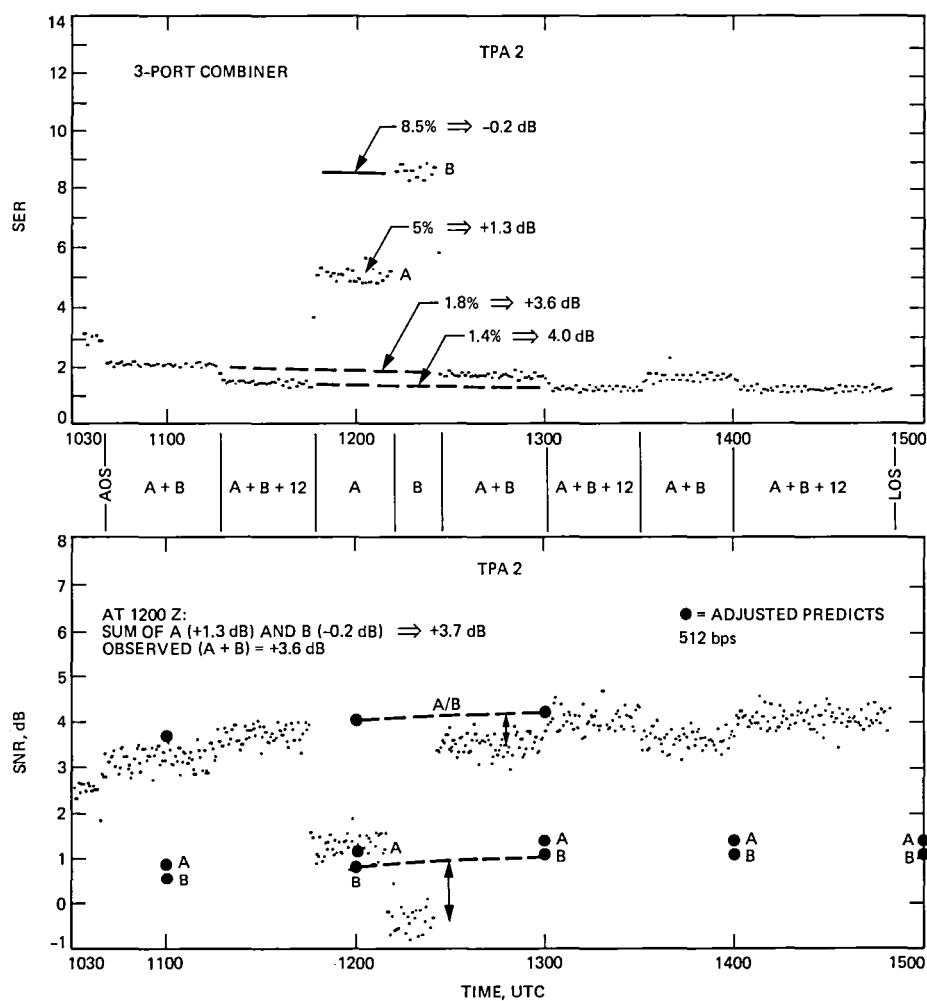


Fig. 4. Performance of Goldstone at 512 bps on 1985 DOY 185

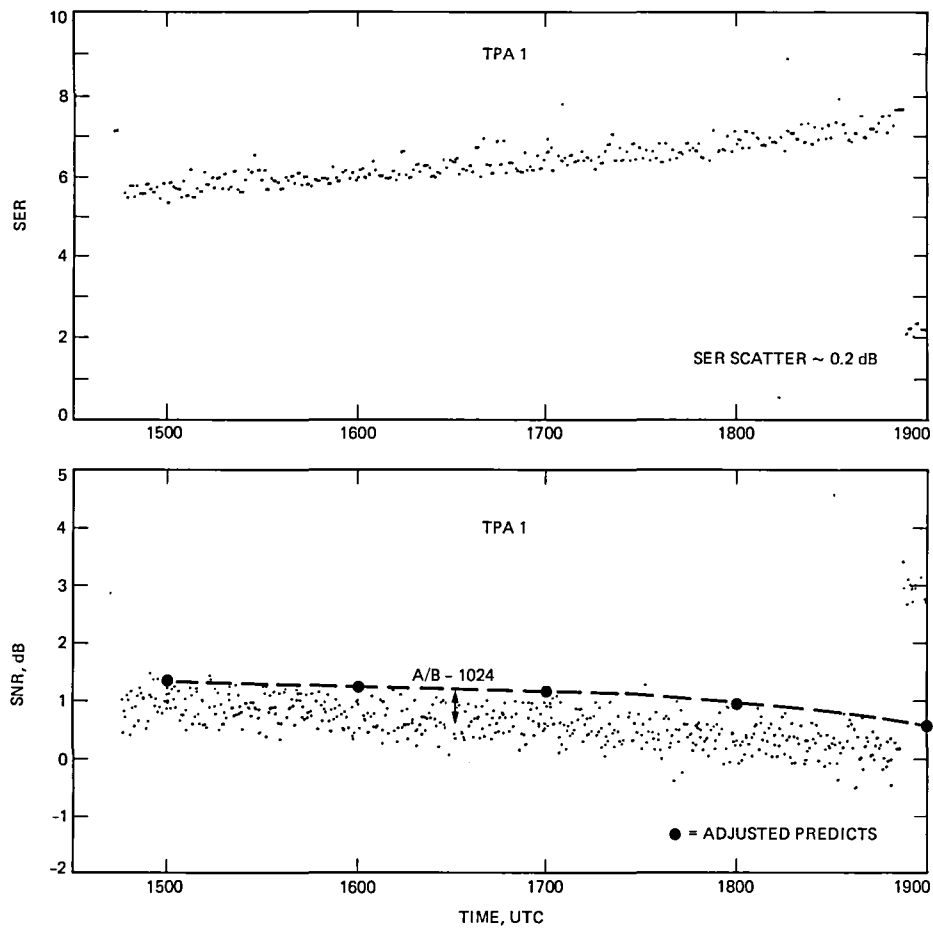


Fig. 5. Performance of Goldstone at 1024 bps on 1985 DOY 207

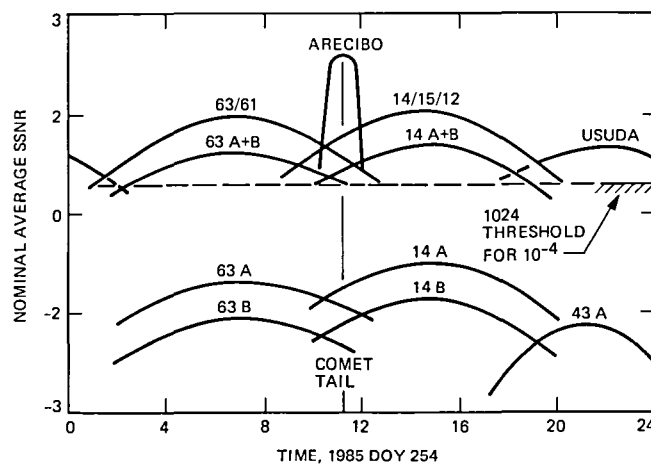


Fig. 6. Expected Encounter-day link performance for ICE

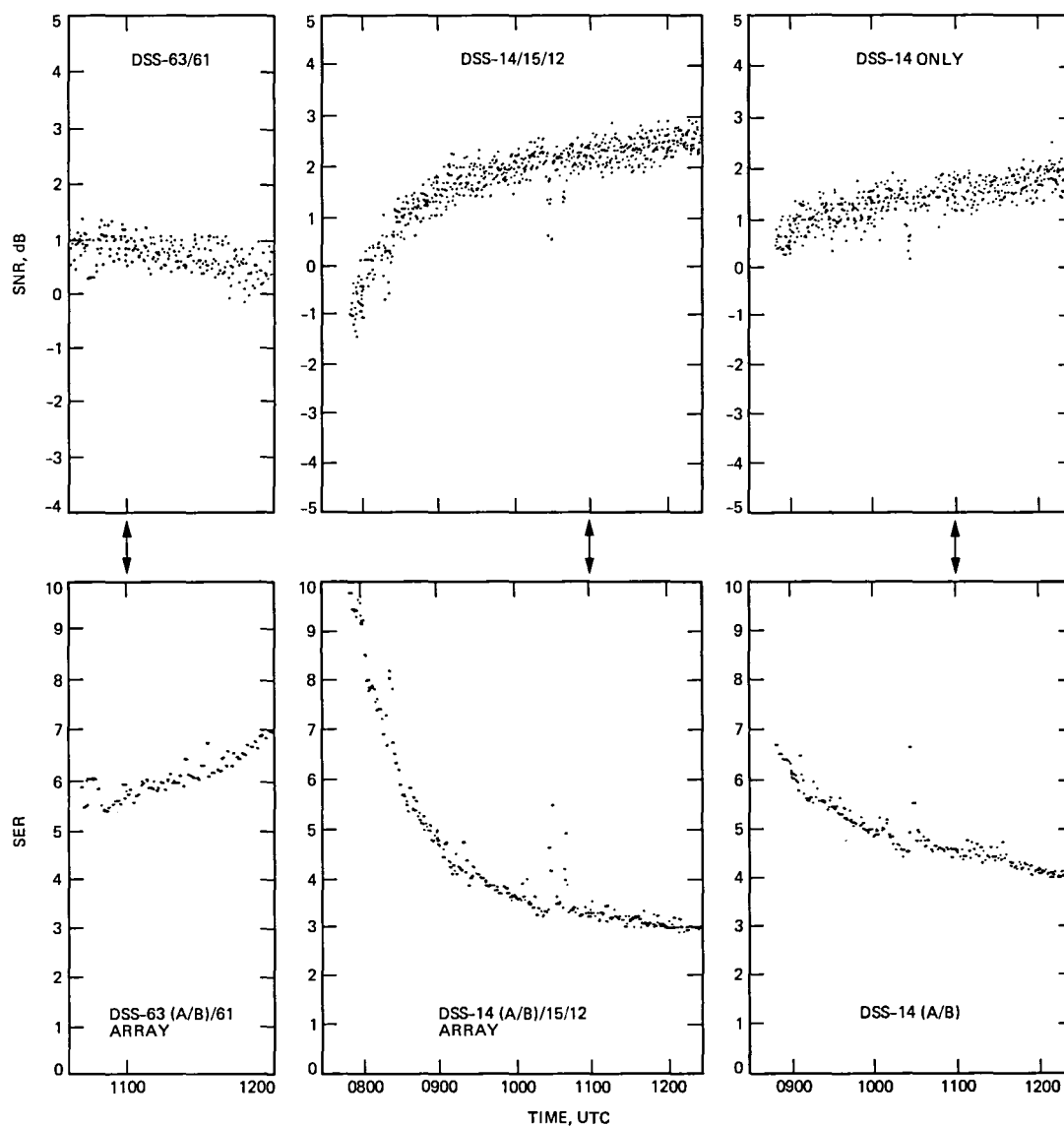


Fig. 7. Observed ICE link performance at Encounter. Comet tail crossing = 1104 Z on DOY 254

Periodic Variations in the Signal-to-Noise Ratios of Signals Received From the ICE Spacecraft

T. Nadeau

Communications Systems Research Section

Data from the ICE probe to comet Giacobini-Zinner are analyzed to determine the effects of spacecraft rotation upon the signal-to-noise ratio (SNR) for the two channels of data. In addition, long-term variations from sources other than rotation are considered. Results include a pronounced SNR variation over a period of three seconds (one rotation) and a lesser effect over a two-minute period (possibly due to the receiving antenna conscan).

I. Introduction

The use of a former Earth satellite to probe the tail of the comet Giacobini-Zinner has recently been accomplished. The probe, known as International Cometary Explorer (ICE), transmits data from two 4-lobed antennas mounted on a boom emanating from the top of the spacecraft. Figure 1 shows the positions of the probe relative to the Earth and the probe's two antennas. The rotation of the probe causes a rotating doughnut-shaped antenna pattern, with a small skew angle, to be observed from the Earth station(s).

The spacecraft transmits identical data symbols on two S-band carriers: channel A at 2270 MHz and channel B at 2217 MHz. This article examines the received symbol signal-to-noise ratios (SNRs) for channels A and B in order to determine the periodic components of the SNR time variations.

II. Description of Data

The experiment was based on data received from ICE at DSS-14 from 1125 Z to 1203 Z on 1985 DOY 148. The

detected symbol streams quantized to 8 bits at the output of the symbol synchronizer assemblies (SSAs) were recorded simultaneously for channels A and B on the Telemetry Processing Assembly (TPA) computers using software developed for symbol stream combining (Ref. 1). Initial processing was to estimate the symbol SNRs as a function of time for the two channels using the moment method (Refs. 2, 3). This processing also produced sample absolute moments and sample second moments for the two channels. These data were produced by summing over 57 data symbols, received from the probe at a rate of 1024 symbols per second (symp/s). This pre-sum interval is short enough that the actual SNR is almost constant within it, yet long enough to make subsequent processing tractable.

III. Short-Term Variation

The rate of rotation of the spacecraft is known to be about 19.65 rpm, or 0.3275 Hz, and each channel's antenna consists of four approximately equally spaced lobes. Therefore, peaks and troughs in the received SNR occur at about 1.31 Hz or four times the rotational rate.

The first step in the data analysis was to accurately determine the frequency of the dominant periodic component. This was done by calculating the energy at closely spaced frequencies near 1.31 Hz, for a data record 83 seconds in length. The final estimate of the true dominant frequency, averaged over the first (absolute) and second moment streams of the A and B channels, was 1.3108 Hz. Thus, 0.3277 Hz or one-fourth of the dominant frequency was the actual rotational frequency. Note that this result assumes that the symbol rate was exactly 1024 symb/s.

The next step was to determine the Fourier coefficients of each data stream at harmonics of the fundamental, 0.3277 Hz. Reconstruction of the time functions of the four statistics from these harmonics resulted in smoothed estimates of the periodic time variations. Then smoothed estimates of the symbol SNR were determined at each time step of the reconstructed A and B channels using the unbiased moment method (Refs. 2, 3).

The relative magnitudes of the first 20 Fourier coefficients of the A- and B-channel second moment data determined which of the coefficients were statistically significant. Using the average SNR estimates and the mean square levels of the input data, the statistics were calculated for the Fourier coefficients at frequencies with no non-random energy. In the second moment data, the means and standard deviations of the amplitude of Fourier coefficients with noise only were 1.21 and 0.48 for channel A, and 0.86 and 0.34 for channel B. The decision to use the fourth and eighth harmonics of the 0.3277 Hz fundamental was based on the data in Table 1. Harmonics four and eight are greater than the mean plus three standard deviations, and are clearly significant. Some others were of borderline significance, but were not used.

The resultant A- and B-channel SNRs, reconstructed using the fourth and eighth harmonics, are illustrated in Fig. 2. The A-channel SNR was on the average 1.5-dB stronger than the B-channel SNR. The variations ranged over approximately 1.4 dB peak-to-peak for the A-channel and 2.0 dB for the B-channel. This effect was obviously due to the combined probe rotation effect and the 4-lobed antenna pattern. The

short-term variations of the A and B channels were nearly in phase.

IV. Long-Term Variation

A 24-minute span of data (472 spacecraft rotations) was used to determine if other, long-term, variations in SNR existed. The observation of the symbol error rate (SER) by J. W. Layland had shown a variation with a principal period of about two minutes. The mean SNR of each rotation was found for channels A and B; Fourier analysis of this 472-point data stream yielded a strong variation with a period of 132 s (frequency 0.00758 Hz). This variation is shown in Fig. 3.

Table 2 lists the Fourier coefficients for the first 20 harmonics of the 0.00758 long-term fundamental frequency. The first harmonic is in general one order of magnitude larger than any other harmonic; statistical analysis of these coefficients was not necessary since the first harmonic so clearly dominated all other harmonics listed.

The A-channel mean SNR varied over a range of about 0.3 dB peak-to-peak while the B-channel mean SNR varied over a range of about 0.6 dB. The reconstruction using the first harmonic of 0.00758 Hz was sufficiently accurate to represent the long-term variation in SNR. The variations of the two channels were in phase. The 132-s period is consistent with the conscan period of the ground-based antenna system of approximately 128 seconds.

V. Conclusions

There are significant short-term and long-term variations in the SNR of signals received from the ICE spacecraft. The dominant short-term effects are at 1.31 Hz and 2.62 Hz, the fourth and eighth harmonics of the spacecraft rotation rate. The dominant long-term effect is at 0.00758 Hz, which is approximately the receiving antenna conscan rate. The short-term variations of period 3.05 seconds are much greater than the long-term effect. Short-term variations are 1.4 dB peak-to-peak for the A channel and 2.0 dB for the B channel, whereas long-term variations are 0.3 dB for the A channel and 0.6 dB for the B channel.

References

1. Hurd, W. J., Reder, L. J., and Russell, M. D., "Symbol Stream Combiner: Description and Demonstration Plans," *TDA Progress Report 42-78*, Jet Propulsion Laboratory, Pasadena, CA, Aug. 15, 1984, pp. 115-121.
2. Vo, Q., "Signal-to-Noise Ratio and Combiner Weight Estimation for Symbol Stream Combining," *TDA Progress Report 42-76*, Jet Propulsion Laboratory, Pasadena, CA, February 15, 1984, pp. 86-98.
3. Layland, J.W., "On S/N Estimation," *Space Program Summary 37-48*, Volume III, Jet Propulsion Laboratory, Pasadena, CA, Dec. 31, 1967, pp. 209-212.

**Table 1. Fourier coefficients of short-term variation of ICE SNR, $f_1 = 0.3277$ Hz
(1125 Z, DOY 148)**

Channel	Harmonic = n	A_n	B_n	Magnitude
A, Sum of Absolutes	0	20.423	0.000	20.423
	1	-0.020	0.041	0.045
	2	0.009	-0.064	0.065
	3	0.080	-0.028	0.085
	4	-0.037	-0.357	0.359
	5	0.060	-0.034	0.069
	6	0.075	-0.007	0.075
	7	0.035	-0.004	0.036
	8	-0.153	0.067	0.167
B, Sum of Absolutes	0	14.959	0.000	14.959
	1	0.023	0.065	0.068
	2	0.083	-0.071	0.109
	3	0.023	-0.058	0.063
	4	-0.268	-0.489	0.558
	5	0.066	0.026	0.071
	6	0.044	0.006	0.044
	7	0.004	0.015	0.015
	8	-0.080	0.028	0.084
A, Sum of Squares	0	545.348	0.000	545.348
	1	-0.929	1.089	1.431
	2	1.001	-2.813	2.986
	3	4.201	-0.924	4.302
	4	-1.580	-15.649	15.729
	5	2.908	-2.095	3.584
	6	2.596	-0.603	2.665
	7	2.236	-1.104	2.494
	8	-6.899	2.229	7.250
B, Sum of Squares	0	308.269	0.000	308.269
	1	0.389	1.886	1.925
	2	2.872	-2.692	3.936
	3	0.474	-2.151	2.203
	4	-9.818	-16.780	19.441
	5	1.990	1.068	2.259
	6	1.182	0.197	1.198
	7	0.420	0.380	0.566
	8	-2.975	1.141	3.186

**Table 2. Fourier coefficients of long-term variation of ICE SNR, $f_1 = 0.007576$ Hz
(1125 Z to 1149 Z, DOY 148)**

Channel	Harmonic = n	A_n	B_n	Magnitude
A	0	1.3800	0.0000	1.3800
	1	-0.0094	-0.0183	0.0205
	2	-0.0019	0.0004	0.0020
	3	-0.0001	0.0006	0.0006
	4	0.0044	-0.0034	0.0056
	5	-0.0033	0.0020	0.0038
	6	-0.0006	-0.0007	0.0009
	7	0.0019	0.0043	0.0048
	8	0.0007	-0.0030	0.0031
	9	-0.0025	-0.0018	0.0031
	10	0.0002	0.0006	0.0006
	11	0.0020	0.0000	0.0020
	12	0.0009	0.0010	0.0013
	13	-0.0007	0.0037	0.0038
	14	0.0006	-0.0016	0.0017
	15	-0.0037	-0.0011	0.0038
	16	-0.0027	0.0027	0.0038
	17	0.0022	-0.0021	0.0030
	18	-0.0021	0.0015	0.0026
	19	-0.0005	0.0008	0.0010
	20	-0.0025	0.0029	0.0038
B	0	0.9500	0.0000	0.9500
	1	-0.0182	-0.0301	0.0352
	2	-0.0004	0.0020	0.0021
	3	0.0005	-0.0020	0.0021
	4	-0.0013	0.0023	0.0026
	5	0.0021	0.0010	0.0023
	6	0.0000	-0.0009	0.0009
	7	0.0048	-0.0019	0.0052
	8	-0.0010	-0.0007	0.0012
	9	0.0015	0.0002	0.0015
	10	-0.0027	-0.0020	0.0034
	11	-0.0029	-0.0020	0.0035
	12	0.0033	0.0006	0.0033
	13	0.0032	-0.0012	0.0034
	14	0.0012	0.0010	0.0015
	15	0.0013	0.0006	0.0015
	16	-0.0009	0.0022	0.0024
	17	-0.0001	0.0009	0.0010
	18	-0.0004	-0.0014	0.0014
	19	-0.0022	-0.0002	0.0022
	20	0.0002	-0.0028	0.0028

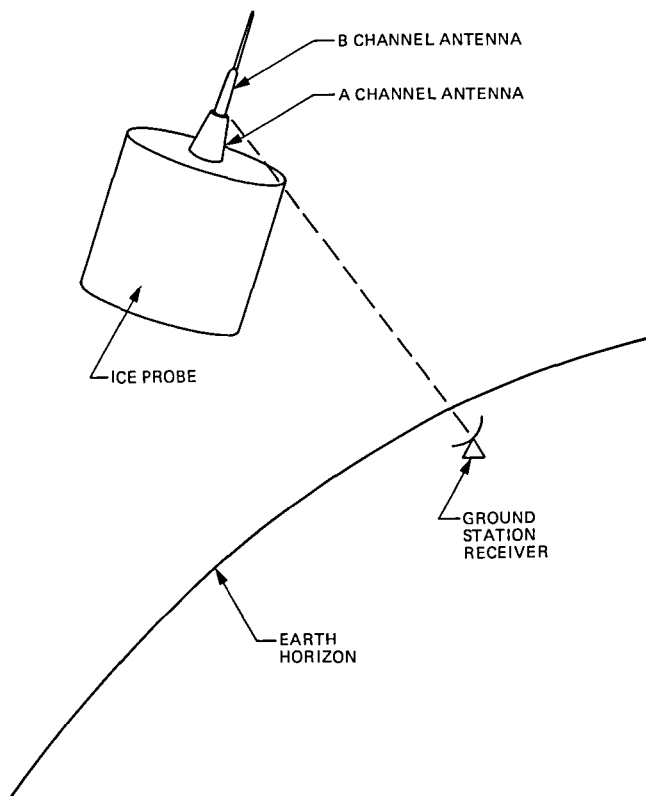


Fig. 1. ICE spacecraft orientation

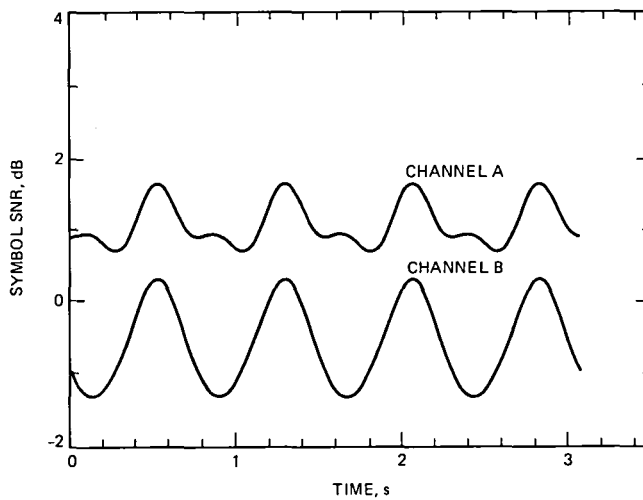


Fig. 2. SNRs for channels A and B vs time (1125 Z, DOY 148)

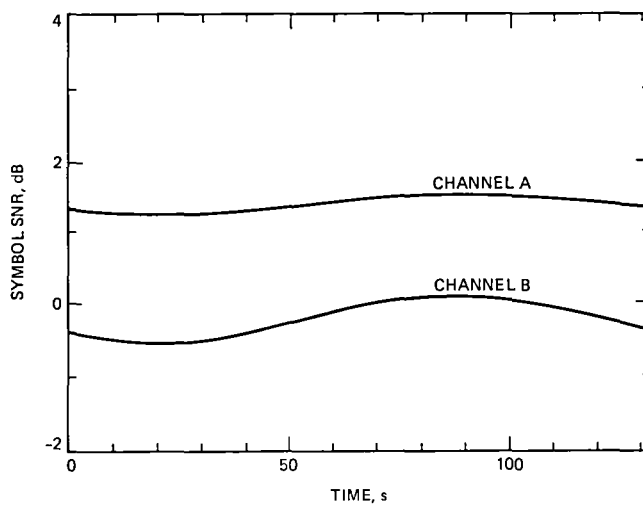


Fig. 3. SNRs for channels A and B vs time (1125 Z to 1149 Z, DOY 148)

Intercontinental Antenna Arraying by Symbol Stream Combining at ICE Giacobini-Zinner Encounter

W. J. Hurd, F. Pollara, M. D. Russell, and B. Siev
Communications Systems Research Section

P. U. Winter
DSN Data Systems Section

Deep space tracking stations on different continents were arrayed during the encounter of the International Cometary Explorer (ICE) spacecraft with the comet Giacobini-Zinner during September 9 through 12, 1985. This is the first time that telemetry signals received on different continents have been combined to enhance signal-to-noise ratio. The arraying was done in non-real time using the method of symbol stream combining. The improvement in signal-to-noise ratio was typically 2 dB over the stronger of the two stations in each array.

I. Introduction

Symbol stream combining is a promising method of antenna arraying to enhance telemetry performance. Its main advantage over baseband combining is that much less data need to be transmitted from the stations to the combiner location. For example, for the Giacobini-Zinner data rate of 2048 symbols/s, the data rate for symbol stream combining is 16 kilobits per second (kb/s), whereas the data rate for baseband combining is approximately 90 Mb/s, or 6 MHz analog bandwidth. The savings are 3 to 4 orders of magnitude either in ground communications link capacity, for a real-time system, or in data storage capacity, for a non-real-time system (Ref. 1).

The theoretical performance of symbol stream and baseband combining is the same, except for minor differences in synchronization losses and in data transmission losses in a real-time baseband combiner with an analog ground link. On

balance, there is a slight advantage for symbol stream combining of $0.2 \text{ dB} \pm 0.2 \text{ dB}$ (Ref. 1).

The International Cometary Explorer (ICE) spacecraft encounter with the comet Giacobini-Zinner presented an ideal opportunity to demonstrate symbol stream combining, and, at the same time, to provide enhanced reliability to the mission. As ICE passed through the comet tail, on September 11, 1985, the spacecraft was visible from the DSN complexes at Goldstone, California, and Madrid, Spain, as well as from the Arecibo Radio/Radar Observatory in Puerto Rico. Neither Goldstone nor Madrid has sufficient antenna aperture to reliably receive the signal at 1024 bits per second (b/s) (2048 symbols/s), in the event of signal loss due to the comet tail. Thus, Arecibo acted as a real-time backup capability, and symbol stream combining between Goldstone and Madrid provided a non-real-time backup capability with sufficient antenna aper-

ture to provide reliable signal reception in the event of the above-mentioned degradations.

Symbol stream combining was also performed between Usuda, Japan, and Goldstone, between Canberra, Australia, and Usuda, and between Canberra and Goldstone. An additional benefit to the combining system is that it recorded the telemetry symbols prior to decoding, thus providing redundancy in case of failure of the real-time decoders.

II. System Description

Figure 1 shows the overall block diagram of the non-real-time symbol stream combining system. Data are recorded in real time to magnetic tape at the Deep Space Network (DSN) stations and Usuda. The tapes are then brought to JPL where the symbols from station pairs are combined on a VAX 750 computer.

The combining software produces a tape of combined data in the same format as the original tapes. Statistics for both input tapes and the output tape are also produced by the combining software. These statistics include input and output symbol signal-to-noise ratios (SNRs), signal levels and dc offsets and data stream alignment points. The combined output symbol stream is then decoded in a VAX 750 computer, and an output tape of decoded data is produced in the same standard format as for data decoded at DSN stations.

A. Station Configurations

All data received for the non-real-time combining process, except for Australia, were produced using the 64-m antennas in a stand-alone mode and a Telemetry Processing Assembly (TPA) Modcomp Computer at each station. The ICE spacecraft transmits data from two antennas mounted on top of the spacecraft. Identical data symbols are transmitted on two S-band carriers: channel A at 2270 MHz and channel B at 2217 MHz. Except for day of year (DOY) 255, the spacecraft data rate was 1024 b/s. On DOY 255 the data rate was 512 b/s.

From both Spain and Goldstone, data from channels A and B were received on one 64-m antenna, and combined using resistor networks. Data received from Usuda were channel A only. Data received from Australia were channel A only, with one 64-m antenna and one 34-m antenna arrayed. Figure 2 shows the configuration of the Madrid and Goldstone stations and the resistor combining network.

B. Recording

Soft symbols quantized to 8 bits were recorded at Usuda using a MARK III telemetry string and at Goldstone, Spain, and Australia using MARK IV telemetry strings. The MARK III

and MARK IV TPA software were modified to accommodate the soft symbol recording requirements. These modifications included changes to the TPA/SSA coupler commands so that the coupler would pass the full 16-bit quantized symbol from the Symbol Synchronizer Assemblies (SSAs) to the TPAs. The modified software strips off the high order 8 bits, which are merely the extended sign of the symbol value, packs the low order 8 bits into 16-bit words, and stores these words into buffers in the standard Original Data Record (ODR) format shown in Figure TLM-3-13-2 of the 820-13 document. These buffers are written to the magnetic tape. One tape record comprises five of these buffers, for a total of 2850 symbols per record. Tape handling, which included the ping-ponging between the two TPA tape drives and the operator prompts to the Local Monitor and Control (LMC), is performed in the standard TPA fashion. The soft symbol recording software is invoked from the LMC with the same commands that invoke the standard TPA software.

C. Combining

The combiner program was written in VAX/VMS FORTRAN and can take inputs from tape, disk or a combination of tape and disk. The program performs three functions: alignment, SNR and weight estimation, and combining.

The data are stored on tape in ODR format. The two incoming streams of records must be shifted relative to one another because the different geographical locations of the stations result in different arrival times of the same symbols at different stations. Data which are recorded when two stations were receiving spacecraft data simultaneously are combined by the program.

The alignment is done in two steps. First, a rough alignment is performed using the time tags in the headers of the ODR record. The time tags indicate the ground received time of the last bit in a block of data and are accurate to 1 ms. Once the tapes from each station have been aligned using the time tags, the difference between two adjacent time tags on the same tape is used to compute the symbol alignment positions within a data block. The data are then separated from the header portion of the record and placed in a separate array for the second step, fine alignment. The symbols from the two tapes are cross correlated for the 2850 lags closest to zero delay, as predicted from the above alignment. These values are used to compute a correlation threshold. The point at which the greatest correlation value occurs is the symbol alignment point, provided that this peak value exceeds the threshold.

SNRs and weights are computed for each data stream, for every record. The algorithm to compute SNR and symbol stream weights uses sums of absolutes and sums of squares and

is described in Ref. 2. The 2850 symbols used to estimate SNRs and combined weights are sufficient to result in a loss due to weighting errors of less than 0.02 dB. SNR variations caused by rotation of the spacecraft transmitting antenna are described in Ref. 3.

In the combining step the data symbols and weights are used to produce a single output data stream. To combine the two streams, two aligned symbols are each multiplied by their weights and added together to produce the combined output symbol. This process is repeated for each symbol to produce a combined output stream. The combined data are placed back into the data portions of the first tape's record. This record is then written out to tape, ready for decoding. The SNR of the combined symbols is estimated using the same algorithm as for the input symbols, and the combining efficiency is calculated. This efficiency (in dB) is the sum of the input SNRs, less the SNR of the combined symbols.

D. Decoding

Decoding is performed by a software decoder written in "C" language on a VAX 750 computer. This sequential decoder is based on the Fano algorithm and uses soft quantized input symbols, as described in Ref. 4.

The decoder also performs the task of frame synchronization, by correlating the channel symbols with a known "tail pattern." For the ICE code, the total frame size is 1024 bits (2048 channel symbols), where 984 bits are information and 40 are tail. The particular tail pattern used is (at the encoder input):

{0,0,0,1,0,0,1,0,1,1,1,1,1,0,0,1,0,0,0,0,0,1,1,
0,0,1,1,1,1,1,0,1,1,1,1,1,0}

Since the code rate is 1/2 and the constraint length K is 24, there are 80 channel symbols due to the tail, of which

$$80 - 2(K-1) = 34$$

form a fixed pattern, independent of the data. Synchronization is based on these 34 fixed symbols:

{-1,1,1,1,1,1,1,-1,1,-1,1,1,1,-1,-1,1,1,-1,-1,1,
1,-1,1,-1,-1,-1,-1,-1,-1,-1,-1,-1,-1,-1,-1,-1}

and is continuously checked and reacquired if necessary.

The decoder has two kinds of output: one is the actual decoded data and the other is statistics on the probability of frame deletion, average number of computations per frame, and information on which frames were deleted.

E. Output Tape

The output decoded data are written to a tape in DSN-Goddard Space Flight Center (GSFC) format.

III. Results

All data received simultaneously from station pairs were combined successfully and decoded. Figure 3 shows the DOY and times of data received. Encounter day was September 11, 1985, DOY 254. For days 252, 253, 254, and 255, data were received from Goldstone and Usuda. Data were received from Spain and Australia for DOY 254. Overlap times were approximately 1.5 hours for Goldstone and Usuda, 5 hours for Goldstone and Spain, 4 hours for Goldstone and Australia, and 4 hours for Usuda and Australia.

Figures 4 through 7 were produced from data generated by the combiner program. They show the SNR of the two input symbol streams, the SNR of the combined symbols and the efficiency of the combining process, as functions of time.

Figures 4(a), (b), (c), and (d) show the Usuda-Goldstone results for the four days. All data were at a bit rate of 1024 b/s except for DOY 255. At the 1024-b/s data rate, the symbol SNR for Usuda is typically 2 dB, increasing slightly with time as the antenna elevation angle increases. Performance of the telemetry string used at Goldstone for symbol recording was somewhat weaker than that used for real-time data. The SNR from the Goldstone 64-m antenna decreases from approximately 0.2 dB to -0.7 dB as the elevation angle decreases. The combining efficiency is approximately -0.3 dB. A short signal outage is apparent at Usuda on DOY 253. The results at 512 b/s, DOY 255, are similar but with 3 dB higher SNRs.

Figure 5 shows the Goldstone-Spain results for DOY 254. The symbol SNR increases at Goldstone and decreases at Spain as the elevation angles change. The combined SNR is typically 3.7 dB, and the efficiency is -0.1 dB. There were several short intervals of lower SNR at Spain and one such interval at Goldstone.

Figure 6 shows the Goldstone-Australia results for DOY 254. Results are similar to the above, with more change in SNR due to antenna elevation. The combined SNR is typically 2.7 dB, and the efficiency is -0.3 dB.

Figure 7 shows the Usuda-Australia results for DOY 254. Because Usuda and Canberra are close to each other longitudinally, the symbol SNRs increase and decrease together. The combined SNR is typically 3.7 dB, and the efficiency is -0.3 dB.

A. Combiner Efficiency

The combining efficiencies varied from -0.1 to -0.3 dB. There is some small loss in the combining process, due to imperfect weighting of the data from the different stations and due to quantization, but these losses are believed to be less than 0.1 dB. There is some error both in defining and in measuring the symbol SNRs, because the signals are time-varying and the measurement assumes constant SNR. Another possible cause of inefficiency is the time-varying nature of the signal strengths, and the differences in this time-varying nature for the different stations. These differences are due to reception of channel A only at some stations and channels A and B at other stations, and due to ground antenna conscan. Examples of these variations are given by Nadeau (Ref. 3). Exact characterization of the effects of these variations on combiner efficiency is outside the scope of the present work.

B. Decoding Results

The software decoder and synchronization system was used successfully to decode a number of combined data tapes.

Due to the high SNR, no frame deletions occurred in decoding the combined symbols, nor did frame synchronization errors occur. This confirmed that the data had been properly combined, formatted, and correctly interfaced with the decoder. Except for Usuda, the uncombined symbol streams did not have high enough SNRs for this error-free decoding. This dramatically illustrates the usefulness of symbol stream combining.

IV. Summary

This work establishes the feasibility and the utility of intercontinental antenna arraying by symbol stream combining. Data were taken at four tracking complexes in California, Japan, Spain, and Australia. Data were successfully combined on all four antenna pairs where there was mutual visibility of the spacecraft. Most important, all data were successfully decoded, demonstrating the reliability and applicability of the system.

References

1. Hurd, W. J., Reder, L. J., and Russell, M. D., "Symbol-Stream Combiner: Description and Demonstration Plans," *TDA Progress Report 42-78*, Jet Propulsion Laboratory, Pasadena, Calif., pp. 115-121, Aug. 15, 1984.
2. Vo, Q., "Signal-to-Noise Ratio and Combiner Weight Estimation for Symbol Stream Combining," *TDA Progress Report 42-76*, Jet Propulsion Laboratory, Pasadena, Calif., pp. 86-98, Feb. 15, 1984.
3. Nadeau, T., "Periodic Variations in SNR of Signals Received from ICE Spacecraft," *TDA Progress Report 42-84*, this issue.
4. Pollara, F., "A Software Simulation Study of a Sequential Decoder Using the Fano Algorithm," *TDA Progress Report 42-81*, Jet Propulsion Laboratory, Pasadena, Calif., pp. 40-46, May 15, 1985.

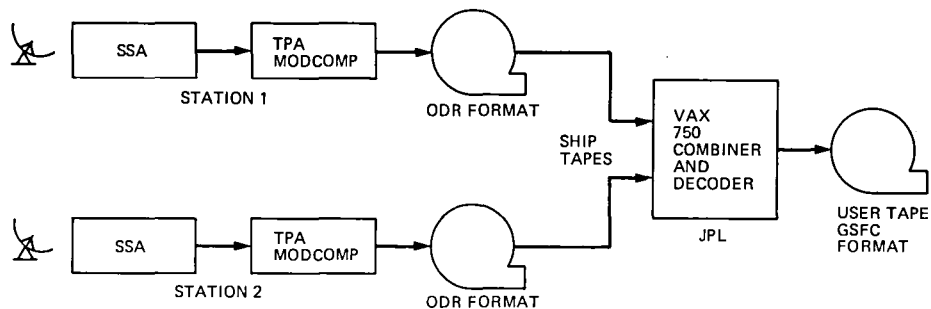


Fig. 1. Non-real-time symbol stream combiner block diagram

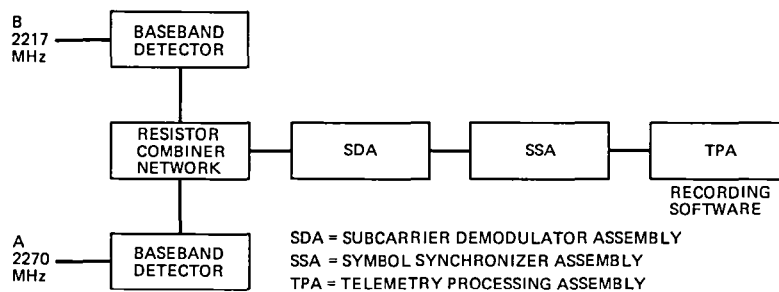


Fig. 2. Symbol stream recording hardware block diagram

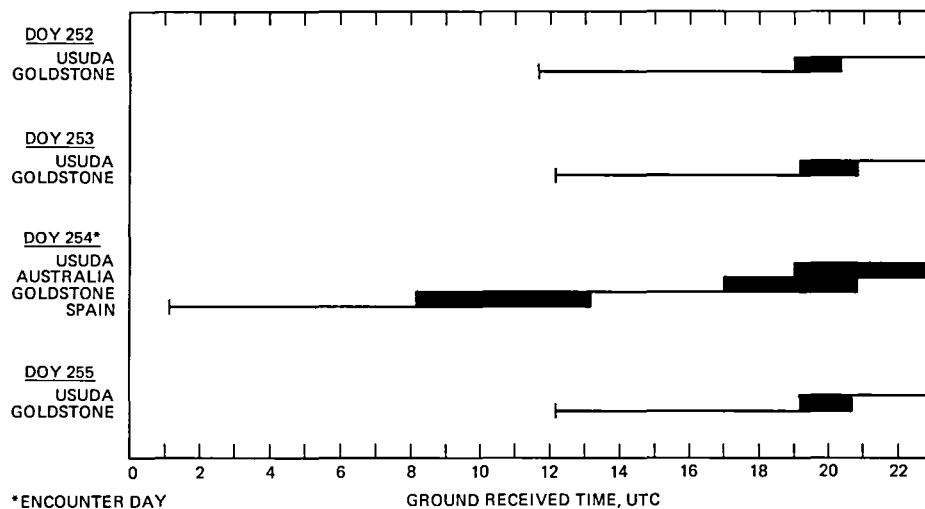


Fig. 3. Tracking coverage

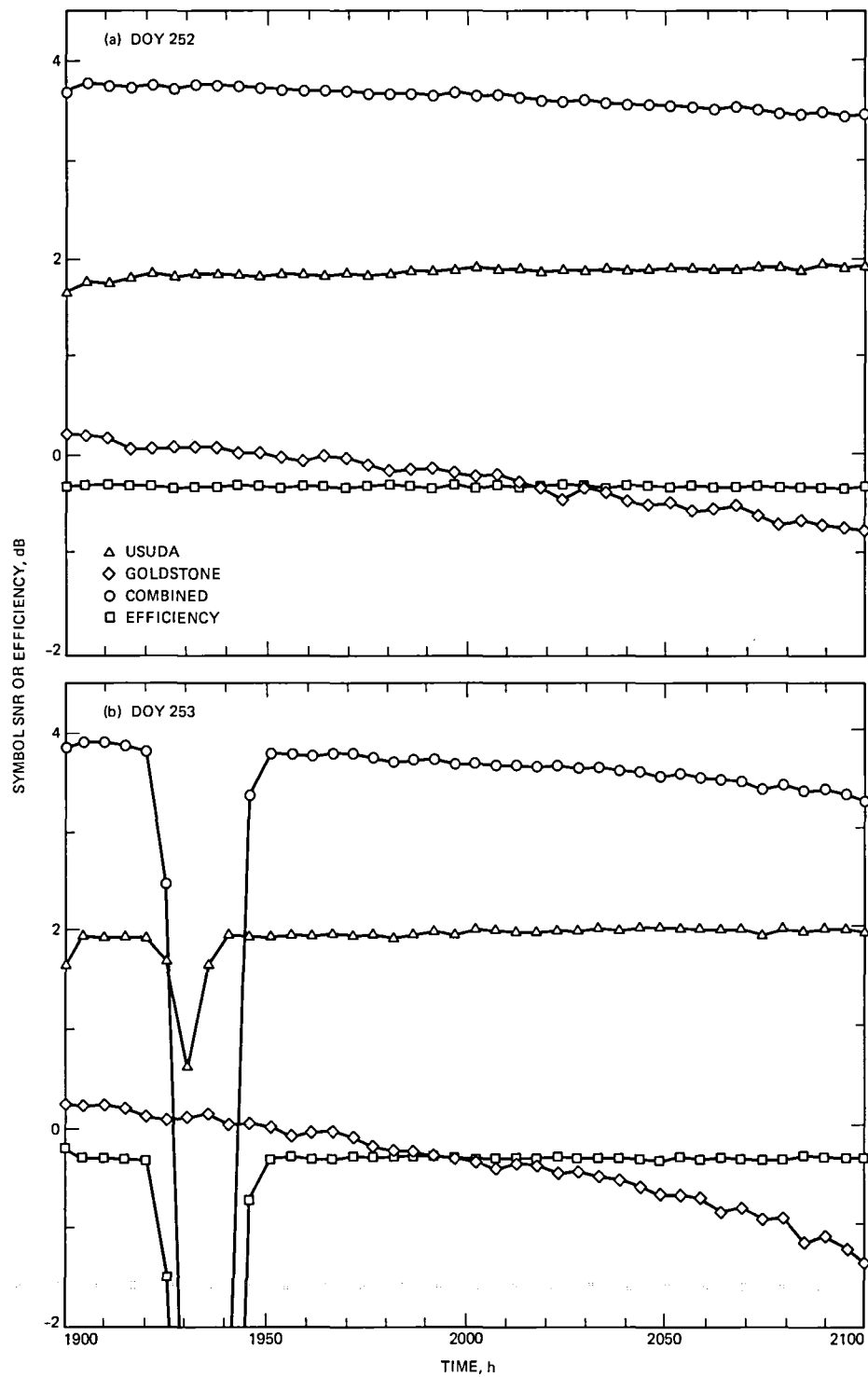


Fig. 4. Combining results for Usuda and Goldstone

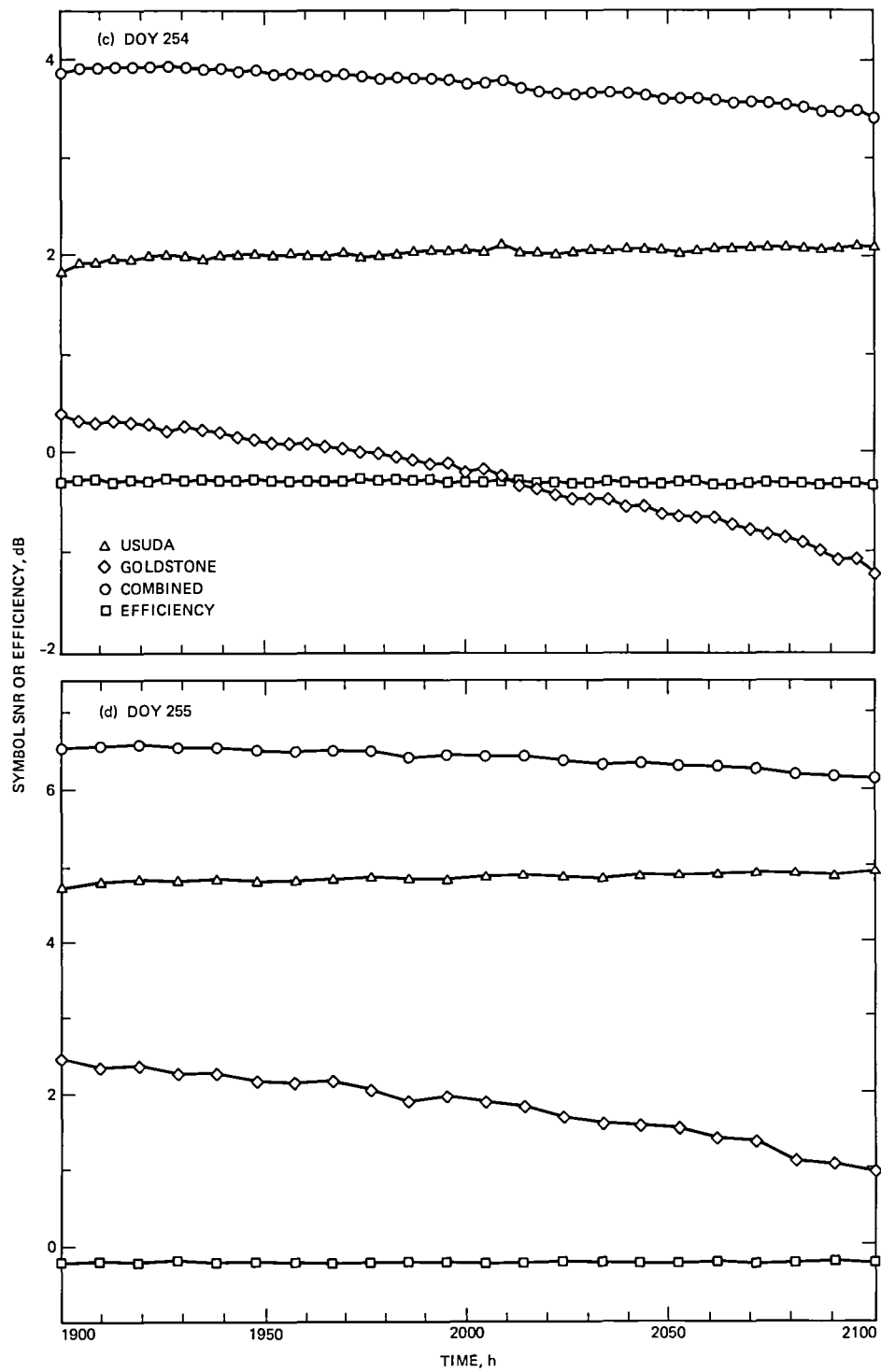


Fig. 4 (contd)

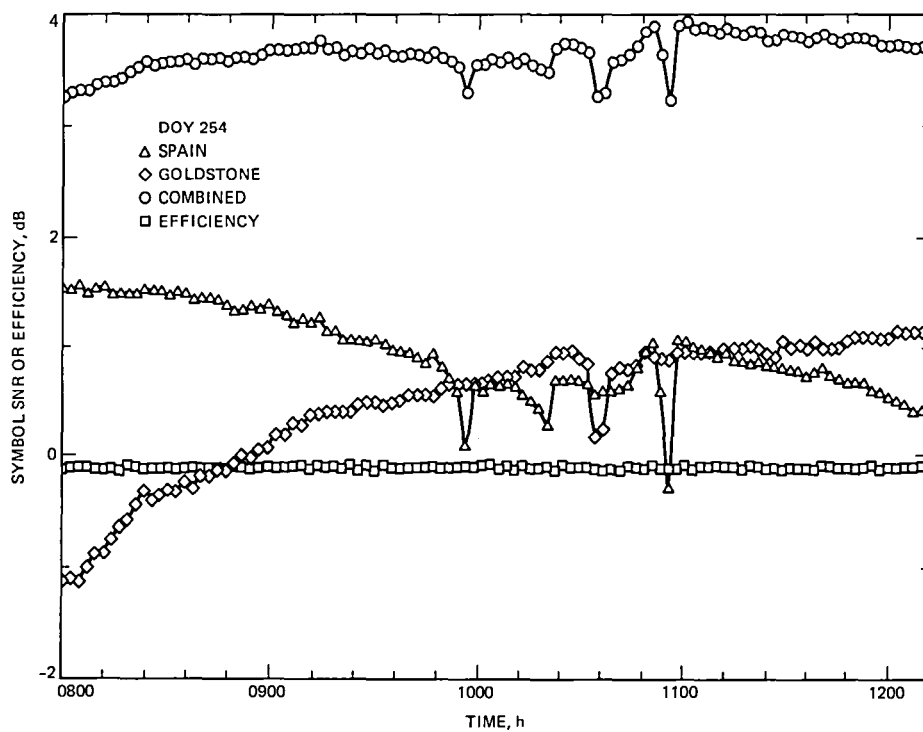


Fig. 5. Combining results for Goldstone and Spain

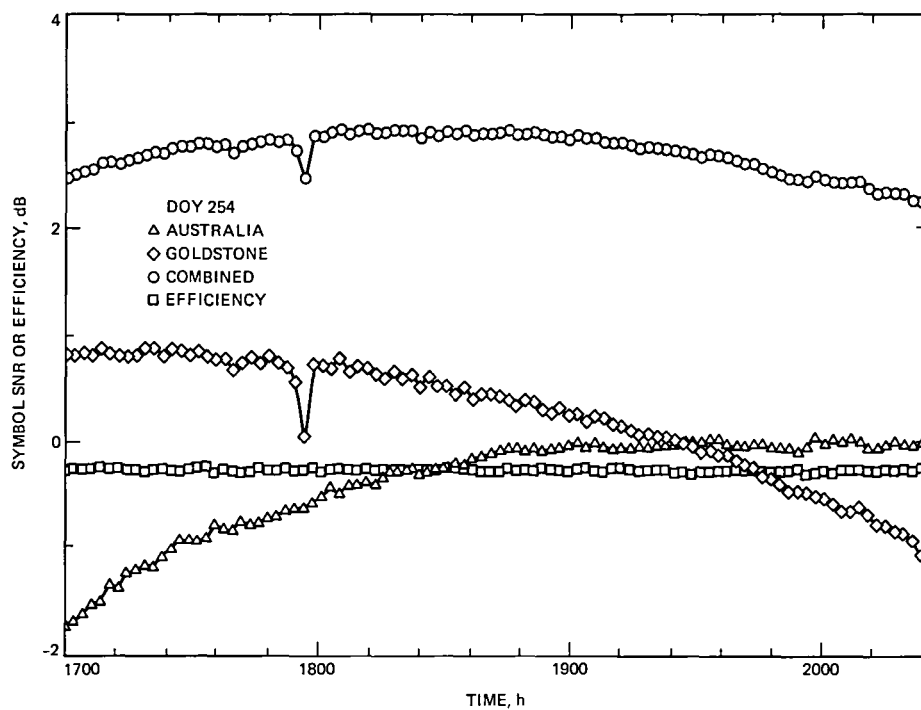


Fig.6. Combining results for Goldstone and Australia

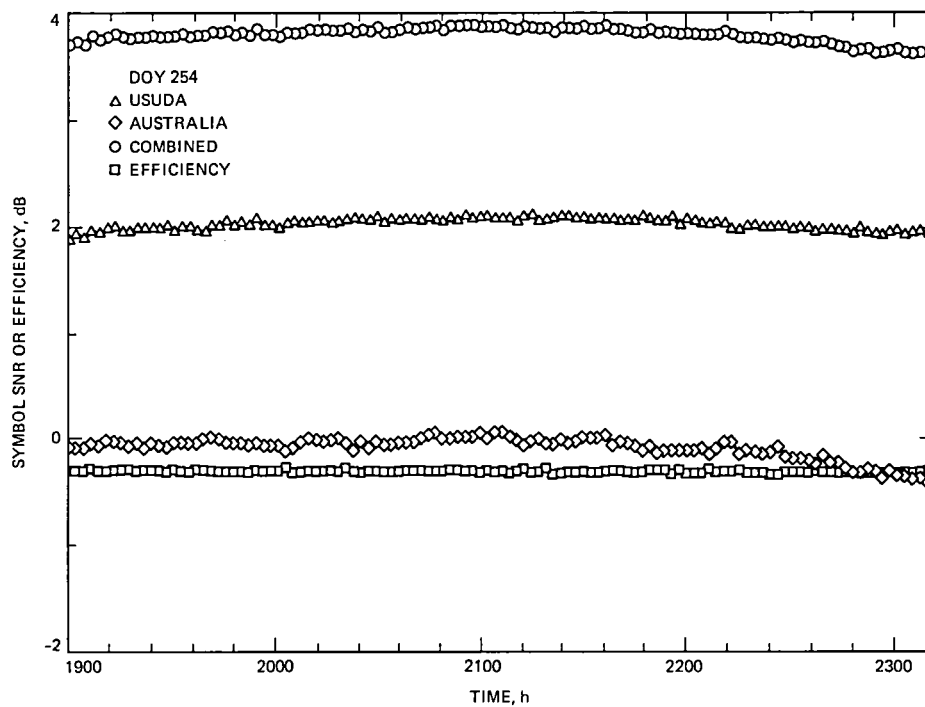


Fig. 7. Combining results for Usuda and Australia

Time and Space Integrating Acousto-Optic Folded Spectrum Processing for SETI

K. Wagner¹ and D. Psaltis

California Institute of Technology

Time and space integrating folded spectrum techniques utilizing acousto-optic devices (AOD) as 1-D input transducers are investigated for a potential application as wideband, high resolution, large processing gain spectrum analyzers in the search for extra-terrestrial intelligence (SETI) program. The space integrating Fourier transform performed by a lens channels the coarse spectral components diffracted from an AOD onto an array of time integrating narrowband fine resolution spectrum analyzers. The pulsing action of a laser diode samples the interferometrically detected output, aliasing the fine resolution components to baseband, as required for the subsequent CCD processing. The raster scan mechanism incorporated into the readout of the CCD detector array is used to unfold the 2-D transform, reproducing the desired high resolution Fourier transform of the input signal.

I. Introduction

The Search for Extra-Terrestrial Intelligence (SETI) is an ambitious program to examine 773 of the nearest solar type stars as well as the entire celestial sphere for any evidence of intelligent microwave activity, either beamed at us or leaked from a civilization's internal communications (Ref. 1). The interstellar distances are so large and the resulting $1/R^2$ attenuation is so great that the receiver sensitivity to a signal buried in cosmic background noise must be as large as possible. Without a priori knowledge as to the transmitted signal structure, ideal matched filters cannot be constructed; however, a good assumption is that a transmitted beacon would

have a narrow band highly coherent structure in a sea of broadband white noise. Thus a narrow bandpass filter, with resolution as small as 1–100 Hz, could achieve enough processing gain to detect the presence of an intelligent CW signal. Since the preferred frequency for interstellar microwave communication could conceivably lie anywhere from 0.1 to 10 or 100 GHz, then from 10^8 to 10^{11} frequency measurements must be made for each resolvable spot on the celestial sphere observed by the radio telescope. If these measurements were performed sequentially with a swept local oscillator tuned bandpass filter, then as much as a million years of observation time could be required. A much more practical approach would be to build a wideband, high resolution spectrum analyzer with a million or more parallel channels of band pass filters, thereby cutting down observation time to on the order of a year. Currently two approaches are being pursued,

¹Graduate student in Electrical Engineering.

a digital multi-channel spectrum analyzer (MCSA) (Ref. 1) with a tree configuration of DFT and FFT subunits, and an analog acousto-optic folded spectrum processor as reported in this article.

The advanced state of the art of wideband acousto-optic (AO) Bragg cells make them ideal candidates for entering 1-D data into an optical signal processing system, and the Fourier transforming property of a lens makes the implementation of real-time spectrum analyzers with 1000 resolvable frequencies routine. In this article we explore some possible approaches to performing narrow band time integrating (TI) spectrum analysis on each of the 10^3 channels of a space integrating (SI) AO spectrum analyzer, thereby obtaining a high resolution folded spectrum through time and space integration (TSI).

II. Folded Spectrum Processing

The concept of the Folded Spectrum was introduced by Thomas (Ref. 2), who showed that the 2-D Fourier transform of a raster scanned signal was an orthogonally raster scanned version of the long 1-D spectrum of the original signal. This is schematically illustrated in Fig. 1. The folded spectrum is ideal for an optical signal processing system since it utilizes the two available spatial coordinates to perform a high resolution spectrum analysis that would be impossible in a 1-D system due to the limitations in space bandwidth product of 1-D devices. This processing operation can be performed in real time by raster scanning a very long input signal $s(t)$ onto a 2-D spatial light modulator (SLM), and using the 2-D space integrating Fourier transform operation performed by a spherical lens. After the complete 2-D raster is formed, coherent light is passed through the SLM and the resulting amplitude distribution $f(x,n)$ is Fourier transformed by the lens. The power spectrum $|F(u_c, v_f)|^2$ is detected by a 2-D charge coupled device (CCD) detector array at the back focal plane. The orthogonally oriented raster readout of the CCD turns the 2-D power spectrum back into a high resolution 1-D power spectrum $|S(f)|^2$, at a rate of up to 60 such transformations each second. However, the availability of highly mature CCD devices with up to 2000×2000 pixels can not be fully utilized because of the lower resolution and dynamic range of currently available 2-D SLMs. Thus an architecture for performing the high resolution folded spectrum operation without the need for 2-D SLMs is highly desirable.

Turpin (Ref. 3) and Kellman (Ref. 4) have suggested such an approach utilizing acousto-optic devices (AODs) in an interferometric time integrating configuration. In this approach a 2-D array of local oscillators with coarse and fine frequen-

cies in x and y is produced by orthogonal AODs to which fast and slow chirps are applied respectively. When a frequency component of the input signal matches that of a particular local oscillator, a baseband heterodyne component is generated, and a time integrated peak is created at that location, proportional in amplitude to the amplitude of the corresponding Fourier component. Since this approach involves interferometric detection, a bias term will be generated due to the local oscillator reference and a signal dependent bias will occur uniformly throughout the detector array. These components can be separated by placing the desired heterodyne term on a spatial carrier. However in a white noise environment, as envisioned for the SETI search with a weak narrow band CW peak, the signal dependent bias term will produce a large bias because all its frequency components are incoherently detected at each CCD pixel, thereby using up the available CCD dynamic range. Thus the 2-D time integrating technique for folded spectrum processing suffers in a multi-signal environment from a large signal dependent bias term, and places too large a requirement on CCD dynamic range.

A hybrid approach that utilizes the 1-D space integrating Fourier transformation property of a lens in one dimension followed by an interferometric time integrating fine resolution spectral analysis can combine the best features of the 2-D SI and 2-D TI approaches to folded spectrum processing. This approach utilizes a standard space integrating acousto-optic spectrum analyzer (Fig. 3) to perform the coarse spectral analysis without introducing a signal dependent bias term. The number of resolvable coarse frequency bins is limited by the time bandwidth product of the AOD and the input apodization to approximately $T_a B = 1000$. The doppler frequency shift associated with acousto-optic Bragg diffraction produces a linear spatial dependence of the temporal frequency at the output spectrum that must be converted to baseband at all positions for further time integrating processing on a CCD. Bader (Refs. 5, 6) proposed a way to do this with a spatially distributed local oscillator (DLO) reference wave which is produced with an auxiliary AOD that has a repetitive wideband signal applied to its transducer. Interferometric detection of the signal and reference Fourier spectra produces narrow band baseband signal components at each output location. These narrow band signals can be used to produce a time integrating fine frequency analysis in the orthogonal direction on a 2-D CCD through the use of the chirp transform algorithm by premultiplying each narrow band signal with a slow chirp and then convolving with a matched chirp using another AOD. This type of system has a less severe signal dependent bias build up problem because only signals within a single coarse frequency bin contribute any bias to that bin. In this article we will present an alternative approach to time and space integrating folded spectrum processing.

This method, which utilizes pulsed laser diodes, was originally proposed by Psaltis (Refs. 7, 8) and is illustrated schematically in Fig. 2. A very long wideband signal is to be optically processed utilizing an acousto-optic device as the input transducer. However, since the limited time-bandwidth product of the AOD will not allow the entire signal to be entered into the AOD simultaneously, we will successively slide overlapping portions of the long signal into the AOD and freeze the acoustic motion by pulsing the illuminating laser diode with a very narrow pulse. For each laser diode pulse we have a 1-D spatial representation of part of the input signal as an optically coherent wavefront, and on successive pulses we will transduce successive portions of the input signal into the optical system. Thus we have transformed the long signal into a 2-D raster of space (x), and time or pulse number (n). The transformation performed by the AOD illuminated with a repetitively pulsed laser diode is given by

$$f(x, n) = \sum_{n=0}^{N-1} s(t - x/v) \text{rect}(x/A) \delta(t - nT) \quad (1)$$

In this expression v is the acoustic velocity of the traveling wave AOD, A is the AOD width, and T is the laser diode pulse repetition interval. If $A > vT$, the raster is oversampled, which means that successive raster lines are overlapping. We perform the desired long 1-D Fourier transform on the input signal $s(t)$, with a 2-D transform on its oversampled 2-D raster representation $f(x, n)$. Because of the separability of the multidimensional Fourier kernel, a 2-D transform can be performed as N 1-D transforms along one axis, followed by N 1-D transforms along the orthogonal axis. This cascaded system can be implemented by performing a spatial Fourier transform with a lens for each of the N laser diode pulses, producing an intermediate data set $F_x(u, n)$, which is also a space-time raster. This is followed by an array of time integrating Fourier transform modules that utilize the second spatial dimension (v) to perform the desired accumulation of partial products. After a succession of N laser diode pulses the full folded spectrum is produced in a 2-D format on a CCD detector array. The 2-D spectrum can be very simply unfolded back into the desired long 1-D spectrum by utilizing the raster readout mechanism incorporated in the CCD itself. The resulting system utilizes the mature component technologies of acousto-optics, charge coupled devices and laser diodes to produce a valuable real-time signal processing module for high resolution spectral analysis.

III. Space Integrating Spectrum Analyzer With a Pulsed Laser Diode

The operation of a space integrating (SI) acousto-optic spectrum analyzer is explained with reference to Fig. 3. A

collimated coherent optical plane wave of wavelength λ is incident upon the AOD at the Bragg angle,

$$\Theta_B = -\sin^{-1} \lambda/2 \Lambda_0 \sim -\lambda f_0/2v,$$

in order to maximize the optical power coupled into the first order diffracted beam. In this expression f_0 is the transducer center frequency, $\Lambda_0 = v/f_0$ is the midband acoustic wavelength, and v is the acoustic velocity. A band-limited signal is mixed to the AOD center frequency f_0 , producing an octave bandwidth signal $s(t)$, that is amplified and applied to the piezoelectric transducer, thereby launching an acoustic wave replica of $s(t)$ into the photo-elastic medium. The acoustic wave creates a traveling wave volume index perturbation through the photo-elastic effect, which Bragg diffracts some of the incident light into the first order diffracted optical replica of a single sideband version of the portion of the signal $s(t)$ that is currently within the AOD aperture A . In the frequency domain this can be viewed as each Fourier component $S(f)$ of the signal $s(t)$ within the AOD bandwidth $B = 2f_0/3$, producing a diffracted plane wave of aperture A propagating at an angle $\theta_d \sim \lambda f/2v$ with respect to the optic axis, doppler shifted by the frequency f due to the acoustic wave motion. This diffracted field propagates through a distance F and is incident on a Fourier Transforming lens of focal length F , so that at a distance F behind the lens the spatial Fourier transform of the signal within the AOD is formed. At the back focal plane the field observed is

$$\begin{aligned} F(x', t) &= \int_A s(t - x/v) e^{-j2\pi x x'/\lambda F} dx e^{j\omega t} \\ &= \int_A \left[\int_B S(f) e^{j2\pi f(t - x/v)} df \right] \\ &\quad \times e^{-j2\pi x x'/\lambda F} dx e^{j\omega t} \\ &= \int S(f) e^{j2\pi f t} \\ &\quad \times A \text{sinc}[A(x'/\lambda F - f/v)] df e^{j\omega t} \\ &= [\nu S(x'v/\lambda F) e^{j2\pi \nu x' t/\lambda F} e^{j\omega t}] \\ &\quad * A \text{sinc}(Ax'/\lambda F) \end{aligned} \quad (2)$$

In this expression x is the spatial coordinate along the axis of acoustic propagation, x' is the spatial coordinate at the Fourier plane, and $\omega = 2\pi c/\lambda$ is the optical radian frequency. The symbol $*$ represents the convolution operation. We have

neglected effects of input apodization, acoustic attenuation, anisotropic diffraction and band limitation, as well as other higher order effects. The exact doppler temporal phase history of each Fourier component is reproduced at the back focal plane, but the spatial representation of the spectrum is blurred by the Fourier transform of the finite aperture function of width A thereby limiting the effective frequency resolution to $\delta f = 1/T_a = v/A$, where T_a is the acoustic transit time across the aperture. This shows that the number of independent analog samples stored within the AOD at any particular instant, which is given by the time bandwidth product $T_a B$, also gives the effective number of independent frequencies that can be determined in the spatial Fourier transform plane. The actual frequency resolution is limited by the AOD finite aperture sinc convolved with the transforms of the optical and acoustic apodization functions, in order to produce an overall blur spot $Q(x'/\lambda F)$ which yields somewhat worse frequency resolution than $1/T_a$. Normal operation of an acousto-optic spectrum analyzer involves the square law detection process on a 1-D array of integrating photosensors, which incoherently accumulate charge for a time T' in order to improve the signal to noise ratio.

$$\begin{aligned} F(x') &= \int_0^{T'} |F(x', t)|^2 dt \\ &= \int_0^{T'} |S(x'v/\lambda F) * Q(x'/\lambda F)|^2 dt \end{aligned} \quad (3)$$

The output of this type of spectrum analyzer is a power spectrum of the signal $s(t)$ with a resolution limited by the blur spot $Q(u)$, with a normalized spatial frequency variable $u = x'/\lambda F$. For a single sinusoid of frequency f' input to the spectrum analyzer, $s(t) = 2a \cos(2\pi f' t)$, with a single sided temporal Fourier spectrum given by $S(f) = a \delta(f - f')$, the time integrated output of the spectrum analyzer is given by

$$F(u) = T' |a|^2 Q^2(u - f'/v) \quad (4)$$

A heterodyne detection technique can be employed by the addition of a simple plane wave reference beam. The instantaneous output of such an interferometric spectrum analyzer has a linear spatial dependence of the doppler induced temporal frequency that is given by

$$\begin{aligned} F(u, t) &= |[S(uv) e^{j2\pi vut} e^{j\omega t}] * Q(u) + r e^{j\omega t}|^2 \\ &= |S(uv) * Q(u)|^2 + |r|^2 \\ &\quad + 2r [S(uv) \cos(2\pi vut + \Omega(uv))] * Q(u) \end{aligned} \quad (5)$$

where the amplitude and phase of the complex spectrum $S(f) = |S(f)|e^{j\Omega(f)}$ are reproduced as temporal modulations of each resolved frequency bin which is spatially blurred due to the apodization. For the case of the single sinusoidal input tone at a frequency f' , with amplitude $|a|$ and phase Ω , the heterodyne detected instantaneous output is

$$\begin{aligned} F(u, t) &= |a Q(u - f'/v) e^{j2\pi f' t} \times e^{j\omega t} + r e^{j\omega t}|^2 \\ &= |a|^2 Q^2(u - f'/v) + |r|^2 \\ &\quad + 2|a|r Q(u - f'/v) \cos(2\pi f' t + \Omega) \end{aligned} \quad (6)$$

The temporal modulation on the last term thus reproduces the input sinusoid in both amplitude and phase, and could be used as the input to a fine resolution time integrating processor if we first heterodyne it to baseband. A repetitively pulsed light source is a simple and effective means of accomplishing this as long as the pulse width τ is less than the inverse of the bandwidth of $s(t)$, and much greater than the optical period of oscillation. When these conditions are satisfied we can consider the laser diode pulsed modulation to be approximated by a series of delta functions separated by a time T .

$$\begin{aligned} p(t) &= \sum_n \text{rect}\left[\frac{t - nT}{\tau}\right] \\ &= \sum_n \delta(t - nT) \end{aligned} \quad (7)$$

This series of delta functions will act as sampling impulses on the interferometrically detected temporal modulation present at the output plane. It is convenient to consider the input temporal frequency to be broken up into a coarse and fine part by choosing the closest harmonic of the laser diode pulse repetition frequency as the coarse term and the offset from this frequency as the band-limited fine resolution component. Thus we substitute $f' = k/T + \delta$ into Eq. (6), where $k = \text{mod}_{1/T} f'$ is an integer and $\delta = \text{res}_{1/T} f' < 1/T$. For the case of repetitively pulsed laser illumination the heterodyne output of the AO spectrum analyzer for a single applied sinusoidal tone, is given by

$$\begin{aligned} F(u, t) &= [|a|^2 Q^2(u - (k/T + \delta)/v) \\ &\quad + |r|^2 + 2|a|r Q(u - (k/T + \delta)/v) \\ &\quad \times \cos(2\pi(k/T + \delta)t + \Omega)] p(t) \end{aligned} \quad (8)$$

The fine frequency component δ will not move the blur spot $Q(u)$ by a significant amount and can be dropped from within $Q(u)$. The coarse frequency component k/T will be sampled by the laser diode pulses at times $t = nT$ resulting in an argument within the cosine function of $2\pi nk$, with n and k both integers, so that this term can be dropped leaving only the fine frequency modulation. Thus for the n th laser diode pulse at time $t = nT$ the sampled output can be approximated as

$$F(u, nT) = |a|^2 Q^2(u - k/Tv) + |r|^2 + 2|a|r Q(u - k/Tv) \cos(2\pi\delta nT + \Omega) \quad (9)$$

Thus for a single sinusoidal input the interferometric output of the space integrating spectrum analyzer illuminated with a series of delta functions can be seen to consist of a signal dependent bias term located at the position corresponding to the coarse frequency component, a uniform reference bias term and a sampled interferometrically detected spot located at the coarse frequency locus and oscillating in time at the fine frequency δ , with phase Ω . This effect of the sampling pulse train is usually referred to as aliasing and is considered undesirable. It indicates that the sampling rate is too low for the given signal bandwidth, and it results in different parts of the signal spectrum folding over on top of each other thereby producing invalid signal components. However in this case, the coarse frequency channeling of the SI spectrum analyzer effectively separates in space the various frequency components that could alias with each other. It is important to make sure that the sampling rate is fast enough to avoid aliasing of the band-limited signals within each coarse frequency blur spot $Q(u)$. Since the bandwidth of the signal information within each blur spot is increased over $1/T_a$ due to the apodization effects, we will assume that an appropriate bandwidth would be $2/T_a$. To adequately sample these band-limited signal components the Nyquist criterion indicates that we should sample at least twice as fast as the highest frequency signal component present; thus the minimum sampling rate should be $1/T > 4/T_a$. This indicates that the laser diode should be pulsed at least 4 times as an acoustic signal transits across the laser beam aperture illuminating the AOD in order to produce the appropriately oversampled space-time raster.

IV. Time Integrating DFT Based Fine Resolution Processor

A narrow band fine resolution spectrum analysis operation requires the coherent accumulation of data samples for a period at least as long as the inverse spectral resolution. For this reason an SI AO spectrum analyzer is limited in resolution to the inverse aperture time of the AOD. In order to obtain a higher resolution spectrum analysis with AODs a time integrating (TI) approach must be utilized. Coherent

accumulations can be carried out on an integrating charge coupled device (CCD) detector array as long as the thermally generated detector dark current and optical bias contributions do not saturate the desired signal components. With typical CCD device defect densities, thermal generation rates and signal well capacities, it should be possible to integrate for a full second, obtaining 1 Hz resolution capabilities, and with cooled detectors it would be possible to integrate even longer. For the SETI program these resolution capabilities should be more than sufficient since spectral coherence of better than 1 Hz would be very difficult to obtain after propagating through the interstellar medium and being doppler shifted by both transmitter and receiver motions.

The required operation that needs to be performed on the output of each coarse frequency bin of the interferometric SI spectrum analyzer with a pulsed LD reported in the previous section is a narrow band discrete Fourier transform (DFT). The DFT is the discrete version of the Fourier transform as is appropriate for sampled data streams such as that produced by the interferometric spectrum analyzer illuminated by a pulsed laser diode. If we examine the third term in Eq. (9) we can see that for each input sinusoid we have a sampled fine frequency temporal oscillation $s(n)$ that we want to perform a DFT on. The DFT is defined for such a sampled input signal $s(n)$ as

$$S(m) = \sum_n^N s(n) e^{-j2\pi nm/N} \quad (10)$$

This operation is a vector matrix multiplication, where the sampled input signal $s(n)$ is the input vector, the DFT kernel is the matrix, and $S(m)$ is the output vector. A possible time integrating interferometric optical implementation using a pulsed laser diode is shown schematically in Fig. 4. The light from a repetitively pulsed laser diode is split into two by a beam splitter. One arm illuminates an acousto-optic modulator that has a narrowband signal $s(t)$ applied to its transducer sampled by the narrow pulse of the laser diode producing a temporal modulation $s(nT)$. In the other arm, a reference AOD with aperture T , equal to the LD pulse repetition interval, is schlieren imaged onto the output CCD array where it is interferometrically combined with the spatially uniform signal beam producing a sinusoidal spatial fringe pattern. With each laser diode pulse a new column of the DFT matrix is applied to the reference AOD transducer, and propagates across the aperture to align with the CCD at which time its motion is frozen by the LD pulse, thereby imaging that column onto the CCD. Thus the reference signal is analogous to a raster scanned version of the DFT matrix, except that along the columns a continuous representation is used which is later

sampled by the spatially discrete CCD pixel structure. Since the successive columns of the DFT matrix represent sinusoids of successively higher frequencies the reference waveform is a stepped frequency chirp, with the constraint that each new frequency phase resets to zero phase each T . The reference signal starts at frequency f and frequency steps by Δf each time T which is analytically represented as

$$r(t) = \sum_{n=0}^{N-1} \text{rect} \left[\frac{t-nT}{T} \right] \times \cos [2\pi(f+n\Delta f)(t-NT)] \quad (11)$$

This signal propagates in the y direction at a velocity v , and aligns with the AOD and CCD apertures at the times of the laser diode pulses as given in Eq. (7). The spatial modulation diffracted by the AOD on the n th pulse is given by

$$\begin{aligned} r(y, n) &= r(t - y/v) \text{rect} [y/vT] \delta(t - nT) \\ &= \text{rect} [y/VT] e^{j2\pi(f+n\Delta f)y/v} \end{aligned} \quad (12)$$

which is seen to be a finite aperture plane wave with an angular spatial frequency that is stepped linearly with the pulse number n . The interferometrically detected intensity pattern on the n th LD pulse is found by combining weighted signal and reference beams. The signal beam propagates at an angle θ with respect to the starting frequency of the reference, resulting in a spatial carrier of spatial frequency $\alpha = \sin\theta/\lambda$.

$$\begin{aligned} I(y, n) &= |Gs(nT) e^{j2\pi(\alpha+f/v)y} + b r(y, n)|^2 \\ &= |G|^2 + |b|^2 + 2Gb s(nT) \\ &\quad \times \cos [2\pi(n\Delta fy/v + \alpha y)] \end{aligned} \quad (13)$$

By time integrating over N successive LD pulses we obtain a discrete summation of the interferometrically detected charge distributions due to each pulse.

$$\begin{aligned} I(y) &= N(|G|^2 + |b|^2) \\ &\quad + 2Gb \sum_{n=0}^{N-1} s(nT) \cos [2\pi(n\Delta fy/v + \alpha y)] \end{aligned} \quad (14)$$

This can be recognized as the discrete cosine transform of the sequence $s(nT)$, with an analysis bandwidth of Δf , on a spatial carrier of frequency $\gamma = \alpha + (N-1)\Delta f/2v$. The carrier allows a bandpass filter operation to remove the bias terms,

and the full complex DFT can be reconstructed by measuring the phase angle of the carrier for each resolvable frequency component. The CCD is composed of an array of pixels that must have sufficient resolution to adequately sample the spatial fringe structure under the DFT transform. For a pixel size Δy , the number of pixels per cycle of the fringe structure is $1/\gamma\Delta y$, and should be adjusted to 4 to 8 pixels per cycle. The total number of CCD pixels required is the product of the DFT space bandwidth product with the number of pixels per frequency resolution element, which must be at least one cycle. Thus $M = N\Delta fT/\gamma\Delta y > 4N\Delta fT$.

V. TSI Folded Spectrum Based on TI DFT

The characteristics of the TI DFT processor described in the previous section are complementary to those of the SI AO spectrum analyzer. The TI DFT processor is a narrow band processor with analysis bandwidth $\Delta f < 1/2T$, and high resolution of $1/NT$. The SI AO spectrum analyzer is a broadband processor with bandwidth B , and resolution $\sim 2/T_a$, which may also be limited by the CCD pixel size which has a frequency width of $v\Delta x/\lambda F$. Since the TI DFT processor is a 1-D system, we can spatially multiplex an array of such processors in the orthogonal dimension by using a 2-D CCD detector array. Since each of the TI DFT processors in the array needs to perform the same narrow band spectrum analysis operation, and each signal is brought down to baseband by the pulsed laser diode, then they all can use the same reference AOD. One way that we can configure a 2-D acousto-optic folded spectrum processor is as an additive Mach-Zehnder interferometer with an SI AO spectrum analyzer to perform coarse frequency analysis in the x dimension in one arm of the interferometer, and a spatially multiplexed array of TI DFT processors in the other arm in order to perform fine frequency analysis in the y dimension on each coarse frequency bin. The fine frequency analysis bandwidth Δf should be equal to the coarse frequency resolution per pixel in order to produce a full folded spectrum without any gaps.

The description and analysis of the TSI AO folded spectrum processor is made with reference to Fig. 5, which schematically illustrates the Mach-Zehnder architecture in the upper half, and shows cross sections of the fine and coarse arms in the bottom half of the figure. The timing of the system is controlled by a 10 MHz stable crystal oscillator that is digitally divided by 100 to produce a stable 100 kHz pulse train used as the laser diode trigger. The laser diode is biased just below threshold and pulsed with a 50 nsec pulse every 10 μ sec. The anamorphic Gaussian beam profile of the laser diode is collimated by the spherical lens and oriented with the long axis along the x direction in order to optimally illuminate the entire SI AOD aperture. For the initial single tone experiments reported in this article the beam splitter

reflects only about 10% of the light to the SI arm of the interferometer, because the processing gain associated with the spatial integration performed by the Fourier lens collects enough light to make this arm brighter at the output plane, so the optical efficiency can be increased by directing more light to the TI arm. For an actual SETI signal environment of broadband noise, the beam ratio can best be balanced through the use of a 50% beam splitter. In the SI arm a cylindrical lens with power in y focuses the light to a narrow slit positioned to coincide with the center of the diffracting acoustic beam, and incident on the AOD at the Bragg angle. The AODs used in this experiment are slow shear mode TeO_2 devices with an aperture $T_a = 70 \mu\text{sec}$ and a bandwidth $B = 40 \text{ MHz}$. The signal $s(t)$ applied to the transducer of AOD1 produces a diffracted component which is Fourier transformed in x by the following spherical lens, which simultaneously recollimates in y . Thus each frequency component of $s(t)$ produces a uniform slit of light at the output plane, and the position of this slit varies linearly with the input coarse frequency. In the TI arm of the interferometer a cylindrical lens with power in x is used to focus the light down to a narrow slit along y which is incident on AOD2 at the Bragg angle. Only a $10 \mu\text{sec}$ portion of the AOD needs to be uniformly illuminated with the narrow dimension of the LD elliptical beam profile. The reference signal is generated by incrementing a 10 bit digital counter with each LD pulse, and driving a 10 bit digital-to-analog converter in order to make a 1024 level staircase lasting 10.24 msec. This signal is then applied to a phase resettable voltage controlled oscillator whose phase is reset each LD pulse producing the waveform $r(t)$ of Eq. (11), which is amplified and applied to AOD2. The diffracted signal from AOD2 is Fourier transformed by the spherical lens which recollimates in the x dimension and allows a bandpass filter to be placed in the transform plane. The filtered light is retransformed in y by the following cylinder, producing an image of the signal in AOD2 with the appropriate scale so that one $10 \mu\text{sec}$ sinusoid fills the entire CCD aperture H in the y dimension, and is uniformly spread out in the x dimension. The final beam splitter recombines the two beams at an adjustable angle, and the CCD time integrates the interferometric product between the two waves for a single video frame time of 16.7 msec. The CCD vertical synchronization signal is used to reset the 10 bit digital counter and begin another folded spectrum calculation by time integrating the next 1024 laser diode pulses.

The operation of the processor can be described analytically by combining the results of the previous two sections. The optical field incident on the CCD during the n th pulse is the sum of the reference wave acting as a linear spatial frequency modulation in the y dimension, with the spatially Fourier transformed signal within the aperture of AOD1. The

photogenerated charge profile detected by the CCD on each LD pulse is the modulus squared of the field incident during that pulse. Thus the time integrated interferometrically generated charge distribution recorded on the CCD after a full frame of processing is given by

$$\begin{aligned}
 I(u,y) &= \sum_{n=0}^{N-1} \left| b e^{j2\pi(f+n\Delta f)y/v} \right. \\
 &\quad \left. + G e^{j2\pi(\alpha+f/v)y} \times \int_A f(x,n) e^{-j2\pi ux} dx \right|^2 \\
 &= N |b|^2 + N \left| G \int_A f(x,n) \times e^{-j2\pi ux} dx \right|^2 \\
 &\quad + 2bG \sum_{n=0}^{N-1} \left[\int_A f(x,n) e^{-j2\pi ux} dx \right] \\
 &\quad \times \cos [2\pi (n\Delta f y/v + \alpha y)] \quad (15)
 \end{aligned}$$

The phase reset reference wave starts at frequency f and steps through N discrete frequencies separated by Δf , and the angle of incidence in the y direction Θ can be adjusted to make the resulting fringe structure at a desired spatial frequency $\gamma = \alpha + (N - 1) \Delta f / 2v$. The output pattern consists of a uniform bias term due to the reference beam, a signal dependent bias term with no variation in the y dimension, and the last term which is recognized as the 2-D Fourier transform of $f(x,n)$, which is the desired folded spectrum of the long 1-D signal $s(t)$. The folded spectrum term is riding on a spatial carrier of spatial frequency γ in the y dimension so that it can be demodulated from the bias terms by an appropriate electronic bandpass filter. For the case of a single sinusoidal signal of frequency $f' = k/T + \delta$, amplitude $|a|$, and phase Ω , the output becomes

$$\begin{aligned}
 I(u,y) &= \sum_{n=0}^{N-1} |b e^{j2\pi(f+n\Delta f)y/v} \\
 &\quad + G e^{j2\pi(\alpha+f/v)y} \times a Q(u - k/Tv) e^{j2\pi\delta nT}|^2 \\
 &= N |b|^2 + N G^2 |a|^2 Q^2(u - k/Tv) \\
 &\quad + 2 G |a| |b| Q(u - k/Tv) \\
 &\quad \times N \text{sinc} [NT(\delta - \Delta f y/H)] \\
 &\quad \times \cos (2\pi\gamma y + \Omega) \quad (16)
 \end{aligned}$$

This pattern is the single tone impulse response of the system and is shown schematically in Fig. 6. It consists of a uniform bias term, a signal dependent bias ridge at the coarse frequency location $u = k/Tv$, and the folded spectrum impulse of amplitude $|a|$ riding on top of the ridge at fine frequency position $y = \delta H/\Delta f$. The impulse is on a spatial carrier of frequency γ in the y dimension, with phase angle Ω which will vary on successive frames according to its super fine frequency $\Delta = \text{res}_{2/NT}\delta$; thus processing of successive frames can achieve even finer resolution. The resolution of Eq. (16) is given by the width of the sinc function and is limited by the integration time to $1/NT$; however, the CCD spatial frequency response will apodize the DFT and decrease the achievable resolution. The fine frequency analysis bandwidth is seen to be Δf as y is allowed to vary over the CCD height H .

Experimental results from this processor are shown in Fig. 7 for a fine frequency analysis bandwidth $\Delta f = 4$ kHz. The processor was operated with a coarse frequency resolution per pixel of 80 kHz, but due to limitations of the electronics, the fine frequency analysis bandwidth was limited to 10 kHz and the data presented in Fig. 7 is therefore only a portion of a full folded spectrum. Cross sections along the bias ridge are shown in Fig. 7 (a-d) with different fine frequency inputs. The bias pedestal drops away near the edge of the output trace indicating the region of processor analysis $H = vT$. At a fine frequency difference of 120 Hz the constructive peak is quite large and well away from the edge. At a frequency of 240 Hz the destructive peak has moved over by about its width indicating that a resolution of 120 Hz or better has been achieved. At a frequency of 600 Hz the peak has moved over much farther but seems to be broadening. At 2100 Hz it is clear that the peak is broadening and decreasing in size. This appears to be due to the analog nature of the reference waveform generation introducing statistical frequency variations that produce larger phase uncertainties at higher frequencies. This problem can be alleviated through the use of a digital buffer memory and digital to analog converter in order to produce the reference waveform. However, this digital buffer would need to contain 1024 lines of 1024 words each that must be read out at a 100 MHz rate, which is currently unavailable to us. For this reason an alternative architecture with a much simpler reference function was built for comparison purposes.

VI. Time Integrating Chirp Transform on TDI CCD

A common method of performing spectral analysis with analog convolvers is the chirp transform algorithm. This algorithm results from the observation that the Fourier kernel

can be decomposed into a convolution and two products through the use of the following identity:

$$-2nm = (n-m)^2 - n^2 - m^2 \quad (17)$$

This expression can be substituted into Eq. (10), which defines the desired DFT, and rearranged to yield the chirp transform expression.

$$\begin{aligned} S(m) &= \sum_{n=0}^{N-1} s(n) \exp(-j2\pi nm/N) \\ &= \exp(-j\pi m^2/N) \sum_{n=0}^{N-1} [s(n) \\ &\quad \times \exp(-j\pi n^2/N)] \exp(j\pi (n-m)^2/N) \quad (18) \end{aligned}$$

An examination of this representation indicates that we can accomplish a DFT by first pre-multiplying the input signal with a chirp, convolving the resulting product with a matched chirp, and finally post-multiplying the convolver output with a matched chirp in the Fourier domain. Often only the power spectrum is required in which case we can neglect the final post-multiplication by the quadratic phase factor, since its magnitude is unity everywhere.

There are a large number of methods for performing convolutions with time integrating optical techniques utilizing acousto-optics and charge coupled devices. The features which must be incorporated in a convolver are an array of multiplications, a shift operation and an integration. An architecture we have used with great success for chirp correlations (Ref. 10) requires a temporally modulated input, a fixed chirp reference mask, and a CCD operated in the time delay and integrate (TDI) mode, where the detector time integrates in a sliding coordinate frame. The CCD readout circuitry is modified so that it operates in a continuously scrolling fashion referred to as TDI or shift and add. In this manner the CCD accumulates photogenerated charge at each pixel site for one or more laser pulses, the charge is then transferred vertically (y) by one pixel of width Δy , and each pixel accumulates more charge, adding it to that previously detected. By the time a pixel has fully traversed the array of height Y , it has accumulated photogenerated charge from each position in space at successively delayed times. If a temporally modulated sampled signal $f(nT)$ is uniformly incident on the chirp mask

$$c(y) = \cos(by^2) \text{rect}(y/Y)$$

and then imaged on the TDI CCD the resulting signal that scrolls off the edge of the detector is given by the convolution of the temporal signal with the spatially sampled image of the mask.

$$\begin{aligned}
 I(mT) &= \sum_n f(nT) c(m\Delta y) * \delta(m - n) \\
 &= \sum_n f(nT) c((m - n) \Delta y) \quad (19)
 \end{aligned}$$

The index m enumerates the output samples obtained at the edge of the CCD at successive times mT . We can use this convolver to configure a time integrating interferometric chirp transform power spectrum analyzer by introducing a quadratically phase modulated reference beam, and interfering this with a baseband phase modulated signal beam in order to perform an interferometric chirp pre-multiplication of the input signal as the detected intensity

$$f(nT) = s(nT) \cos(b(nT)^2 V^2)$$

where $V = \Delta y/T$ is the TDI CCD shifting velocity. The resulting time integrated power spectrum output would be obtained by demodulating the interferometric product term from the bias terms and squaring the chirp transform electronically. The analysis bandwidth of this type of TDI chirp transform spectrum analyzer is limited by the sampled mask resolution to half the CCD shift rate for each sideband of the reference chirp. A two sided chirp reference can cover an analysis bandwidth equal to the CCD shift rate. A feature of this type of chirp transform is that the spectral amplitude decreases linearly away from the center frequency as does the spectral resolution, due to a decrease in the matching chirp overlap.

The chirp transform spectrum analyzer can be readily incorporated in the TSI folded spectrum processor by including a quadratically phase modulated reference beam, and a chirp reference mask imaged onto a TDI CCD. The resulting system architecture is shown schematically in Fig. 8 and can be seen to be just a modification of the previous optical system. The analytical description of the TSI folded spectrum system with the TDI chirp transform fine resolution processors results in the same signal and bias terms as in the previous system shown in Fig. 6. However the TDI approach has the advantageous feature that it averages coherent optical artifacts and CCD pixel noise along the shifting column thereby minimizing the system fixed pattern noise. The system output is given by

$$\begin{aligned}
 F(u, m) &= \sum_{n=0}^{N-1} \left| \int_A f(x, n) e^{-j2\pi u x} dx \right. \\
 &\quad \left. + r \exp[-jb(nT)^2 V^2] \right|^2 \\
 &\quad \times \cos(b(m\Delta y)^2) \text{rect}[m\Delta y/Y] * \delta(m - n) \\
 &= \sum_{n=0}^{N-1} \left[\int_A f(x, n) e^{-j2\pi u x} dx \right] \\
 &\quad \times 2r \cos[b(n\Delta y)^2] \cos(b((m - n) \Delta y)^2) \\
 &\quad \times \text{rect}[(m - n) \Delta y/Y] + \text{bias terms} \quad (20)
 \end{aligned}$$

We can see that the quadratically phase modulated reference beam results in an interferometric premultiplication of each sampled baseband coarse frequency bin with a temporal chirp. The combination of the chirp mask and the TDI CCD results in a chirp convolution for each coarse frequency channel, and the resulting folded spectrum raster scans out of the CCD as it scrolls. Experimental results from this processor are shown in Figs. 9 and 10. Figure 9 (a-d) shows cross sections through the coarse frequency ridge of the impulse response of Fig. 6 for several input fine frequencies, and the decrease of peak height with increasing frequency is apparent. Figure 10 shows the 2-D Folded Spectrum output displayed on a video monitor for a variety of input frequencies, where the coarse ridge is seen to move with 10 MHz frequency change, and 3 kHz moves the fringes in the fine dimension along the ridge. The spatial and temporal chirp references used in these experiments were two sided with 9 fringes per side giving a compression of 36, and resulting in a spectrum analysis with 36 independently resolvable frequencies. The sideband structure is highly visible due to the hard clipping of the mask, both the spectral resolution and the linearity are better than 100 Hz, and the performance closely matches the expected theoretical behavior.

VII. Demodulation of Signal From Bias Terms

A crucial requirement for the successful operation of a TSI signal processing system is the ability to demodulate the signal from the bias terms. There are two main approaches to signal demodulation which are shown in Fig. 11, spatial carrier demodulation and CCD based demodulation. In carrier demodulation the interferometric signal term is placed on a spatial carrier by the adjustment of the reference beam incidence angle, while the bias terms remain at baseband. When these signals are output from the CCD, a bandpass filter can sepa-

rate the different components, and allow measurement of spectral amplitude and phase. The filtered output can be electronically squared and low passed in order to obtain a power spectrum, or rectification followed by a low pass can be used for measuring spectral amplitude components. The CCD raster readout mechanism can be used to change a spatial carrier in the horizontal direction into a fast temporal carrier that can be simply bandpassed by an active filter. A spatial carrier in the vertical dimension requires a more complicated set of video delay lines and a tapped filter in order to implement the desired bandpass operation. The spatial carrier can be placed in the coarse or fine frequency directions, but will cut down the available CCD space bandwidth product in whichever dimension it is used. In order to avoid losing detector resolution, another possible approach is to have two synchronously operating CCD detectors, one to detect the interferometric signal and bias terms, and the other with just the signal term in order to detect the signal dependent bias. The two detectors must be precisely aligned and subtracted pixel by pixel in order to remove the signal dependent bias; the reference beam bias term should be uniform across the array and can be subtracted with a level shifter. An experimental bias subtraction technique we are investigating requires a special purpose CCD with a fill and spill structure abutted to the transfer register in order to bleed off an appropriate amount of charge to leave the signal term and a small amount of bias, rather than have the bias use up the available CCD dynamic range.

VIII. AO Folded Spectrum Processor Performance

A summary of the performance parameters for the TSI folded spectrum processor described in this article are given in Table 1, for the Caltech prototype, and for the potential of a fully engineered state of the art brassboard. The processor analysis bandwidth is determined by the AOD bandwidth, the CCD width and Fourier lens focal length, and by the laser diode pulse width at an acceptable level of illumination and temporal coherence. The Caltech prototype was limited by the CCD width, which can easily be modified. The minimum laser diode pulse width is determined by the multimode transient operation for the first 1 nsec which results in incoherent operation inappropriate for this processor (Ref. 11); however, light limitations will also dictate a minimum pulse width determined by peak output power. The number of coarse frequency bins is determined primarily by the number of CCD pixels, but another limitation is due to the AOD time bandwidth product and apodization uniformity. The availability of the Tektronix 2000 X 2000 CCD is very encouraging for the development of optical processors requiring high resolution 2-D detectors. The coarse frequency resolution is limited by the AOD transit time and apodization, but also

determined by the FT lens focal length and pixel width. The number of fine frequency resolution bins is determined by the space bandwidth of the reference functions and the number of CCD pixels available. If a spatial carrier is included in the fine frequency dimension, then the number of fine resolution bins is further limited, and a maximum spatial carrier frequency of 4-6 pixels per cycle indicates that a maximum of 500 fine frequency bins could be predicted. The fine resolution is fundamentally limited by the CCD integration time during which the LD is being pulsed, and the prototype processor has closely approached this limit. Actually a greater difficulty is encountered in attempting to achieve a fine frequency analysis bandwidth equal to the coarse frequency resolution, which requires high bandwidth electronic reference generation currently not obtainable with our prototype circuitry. The TDI chirp transform approach is limited in analysis bandwidth by the mask resolution and by the obtainable CCD shift rate, which is currently limited to 15 kHz for video compatible devices, but could be increased with special CCD circuitry. The total number of independent spectral measurements made in our initial experiments was only 15,000 but a potential for on the order of 10^6 clearly exists. The dynamic range is currently quite small due to coherence limitations and light starvation, but this will be greatly improved in the next generation processor. The most important performance parameter for the SETI search is the sensitivity to a signal buried in noise, and the processing gain limitations of the analog technique used to perform the spectral analysis. The large AOD dynamic range allows very weak signals to be effectively transduced into the optical processor, but a huge CCD dynamic range is not required to achieve the desired processing gain, since the spatial integration achieves much of it.

Since sensitivity and processing gain are so important to the SETI application we will include a simple analysis of the processor limitations based on the model presented in Fig. 12. For a weak narrowband CW input buried in white noise with power σ_n^2 we will have a system input

$$s(t) = a e^{j\omega t} + n(t) \quad (21)$$

The amplifier and AOD have a large linear region and a saturation regime that will introduce third order intermodulation products that will degrade system performance. An ideal gain G is included due to an optical power increase which will not increase the relative power in the intermodulation terms. The processor consists of an SI coarse frequency channelizer which acts as 10^3 bandpass filters (BPF), cascaded onto an array of 10^3 TI spectrum analyzers, resulting in the synthesis of 10^6 narrow band filters. The detected spectral amplitudes are corrupted by the inclusion of signal dependent noise, and the detector noise term with variance σ_d^2 . The processing gain

is defined as the ratio of input signal to noise ratio (SNR) to output SNR, and ideally it would be given by

$$PG = \frac{SNR_{out}}{SNR_{in}} = \frac{a^2/\beta^2 \sigma_n^2}{a^2/\sigma_n^2} = 1/\beta^2 \sim 10^6 \quad (22)$$

where β^2 is the BPF width divided by the entire bandwidth, which is equivalently the inverse of the number of channels. After the demodulation operation, which will remove the bias terms, including the bias shot noise contribution in σ_d^2 , the expected value of the power spectrum component at the frequency of the input tone will be

$$\langle S_\omega^2 \rangle = a^2 G^2 + \beta^2 G^2 \sigma_n^2 + \sigma_d^2 \quad (23)$$

The input sensitivity is determined by the minimum detectable signal at the desired false alarm probability, which for SETI is on the order of $10^{-10} \sim e^{-20}$, in order to keep the total number of false alarms manageable. By cross scanning the sky and comparing positions and frequencies of spectral components exceeding the given threshold, the false alarm probability can easily be squared. Thus the minimum detectable signal resulting in a false alarm probability of e^{-10} would be 10 standard deviations above the noise.

$$a_{min}^2 G^2 > 10 [\beta^2 G^2 \sigma_n^2 + \sigma_d^2] \quad (24)$$

To minimize effect of the detector noise limitations we increase the gain G to the point that the signal dependent noise and the detector noise are comparable. In this case minimum input SNR that can result in a signal exceeding the threshold is given by

$$\begin{aligned} SNR_{min} &= a_{min}^2 / \sigma_n^2 \\ &= 10 [\beta^2 + \sigma_d^2 / G^2 \sigma_n^2] \sim 20\beta^2 \end{aligned} \quad (25)$$

Thus the resulting input sensitivity is degraded by 13 dB from the initial -60 dB, but only 3 dB of the degradation are an artifact of the analog optical processor. This estimate for the actual input sensitivity of -47 dB will be further degraded by the intermodulation product terms due to the amplifier and AOD nonlinearities, by the shot noise due to the bias, and probably most importantly by light starvation limiting the gain G .

IX. Conclusion

In this article we have presented preliminary experimental results from time and space integrating folded spectrum processors that may have potential application in the SETI program. The sampling action of the repetitively pulsed laser diode eliminates the need for a distributed local oscillator reference wave by aliasing all of the fine frequency components to baseband at the output of the coarse frequency channelizing space integrating spectrum analyzer as is required for the following CCD based narrow band time integrating spectrum analyzers. Two methods of time integrating fine frequency analysis were presented, the time integrating DFT, and the time delay and integrate chirp transform. The TI DFT has the attractive possibility for incoherent addition of spectra in order to improve SNR, but requires a very complex and accurate reference waveform. The TDI chirp transform helps average out coherent noise and detector noise, and has a simple reference function, but does not allow simple complex spectral demodulation, and is bandwidth limited by the available CCD shift rate. The possible advantage of this technique over alternative digital approaches is a decrease in system cost and complexity, along with the elimination of the high speed analog to digital converter required for digital processing. For a possible future spaceborne SETI search the optical processor has decreased size, weight and power requirements over that of a digital approach.

Acknowledgments

This work was performed under grants from the AFOSR and NASA and an ARO graduate research fellowship at Caltech. We thank Sam Gulkis and the entire SETI science working group for introducing us to SETI and partially motivating this work. We also thank Mike Haney for his collaboration on TSI optical processing.

References

1. Drake, F., Wolfe, J. H., and Seeger, C. L., Eds., "SETI Science Working Group Report," NASA Tech. Paper 2244, Washington, D.C., Oct. 1983.
2. Thomas, C. E., "Optical Spectrum Analysis of Large Space Bandwidth Signals," *Applied Optics*, vol. 5, pp. 1782-1790, 1966.
3. Turpin, T. M., "Spectrum Analysis Using Optical Processing," *Proc. IEEE*, vol. 69, pp. 79-92, Jan. 1981.
4. Kellman, P., "Time Integrating Optical Signal Processing," Ph.D. dissertation, Stanford Univ., Stanford Ca., 1979.
5. Bader, T. R., "Coherent Optical Hybrid Techniques For Spectrum Analysis," *Proc. SPIE*, vol. 185, pp. 140-146, 1979.
6. Bader, T. R., "Acousto-Optic Spectrum Analysis: A High Performance Hybrid Technique," *Applied Optics*, vol. 18, pp. 1668-1672, 1979.
7. Psaltis, D., and Casasent, D., "Time and Space Integrating Spectrum Analyzer," *Applied Optics*, vol. 18, pp. 3203-3204, 1979.
8. Psaltis, D., "Two Dimensional Optical Processing Using One-Dimensional Input Devices," *Proc. IEEE*, vol. 72, pp. 962-974, 1984.
9. Van der Lugt, A., "Interferometric Spectrum Analyzer," *Applied Optics*, vol. 20, pp. 2770-2779, 1981.
10. Psaltis, D., and Wagner, K., "Real-Time Optical SAR Processor," *Optical Eng.*, vol. 21, pp. 822-828, 1982.
11. Haney, M., and Psaltis, D., "Measurement of the Temporal Coherence Properties of Pulsed Laser Diodes," *Applied Optics*, vol. 24, pp. 1926-1932, 1985.

Table 1. AO processor performance

Parameter	Caltech Prototype	Potential
B = Bandwidth	30 MHz	1 GHz
n_c = Course Bins	384	2000
f_c = Course Resolution	80 kHz	$B/1000$
n_f = Fine Bins	36 (actual) $491/a_{\text{carrier}}$ (potential)	$2000/a_{\text{carrier}}$
f_f = Fine Resolution	120 Hz (actual) 1 kHz (potential)	$f_c/1000$
N = Spectral Resolution	15,000	10^6
DR = Dynamic Range	50 levels	1000 levels
Sensitivity	-40 dB	-60 dB

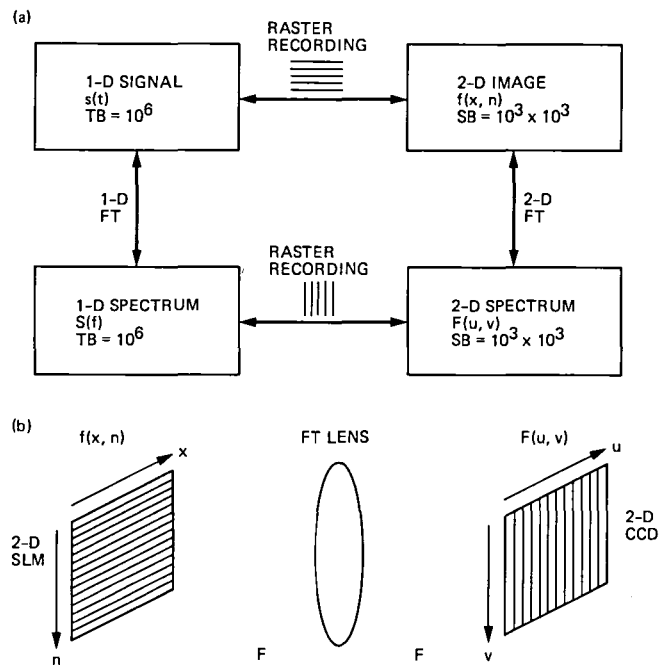


Fig. 1. Two-dimensional space integrating folded spectrum processing: (a) the relationship between a long 1-D signal, its high resolution spectrum, the folded spectrum, and the signal's raster representation; (b) a space integrating folded spectrum processor.

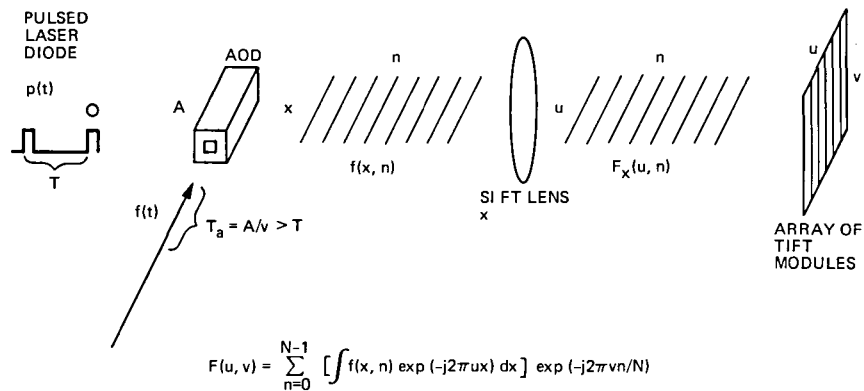


Fig. 2. Time and space integrating folded spectrum processor showing the conversion to a space-time raster, spatial Fourier transformation cascaded onto an array of temporal Fourier transforms.

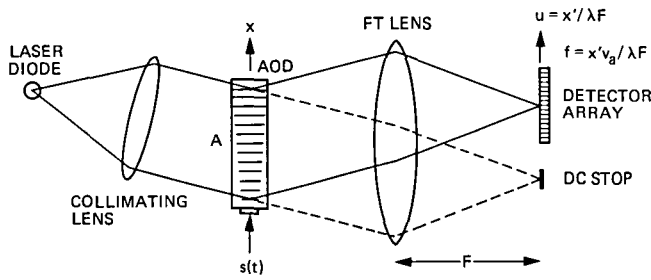


Fig. 3. The space integrating acousto-optic spectrum analyzer

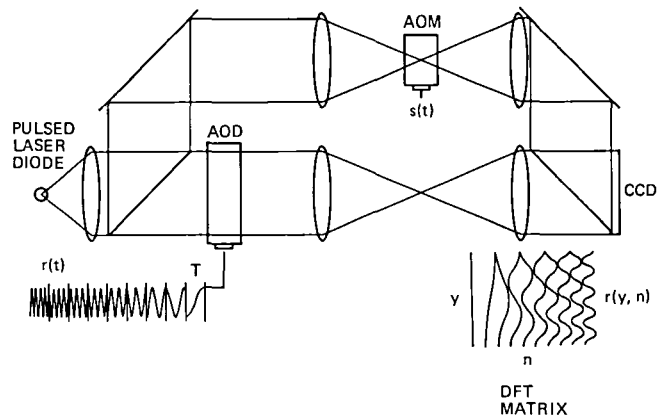


Fig. 4. Interferometric time integrating DFT narrow band spectrum analyzer with phase locked stepped frequency reference

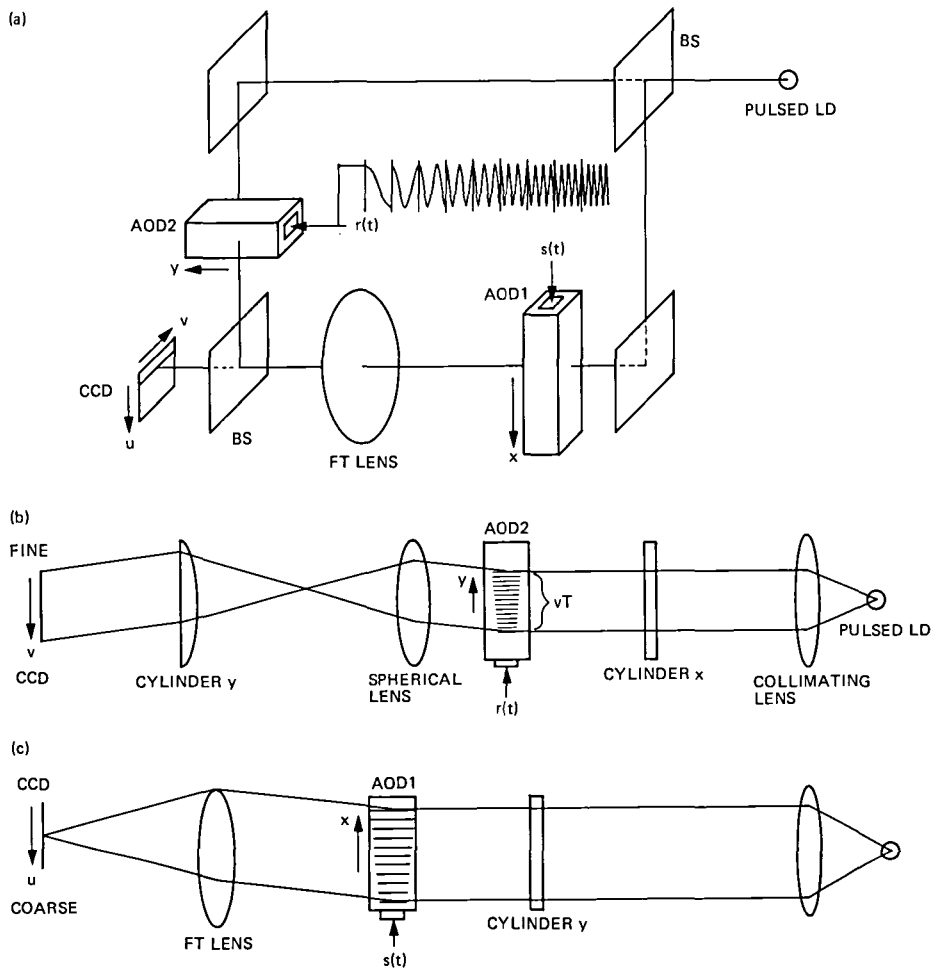


Fig. 5. The Mach-Zehnder interferometer architecture: (a) for performing the TSI folded spectrum; (b) cross section through TI fine resolution spectrum analyzer arm; (c) cross section through SI coarse resolution spectrum analyzer arm

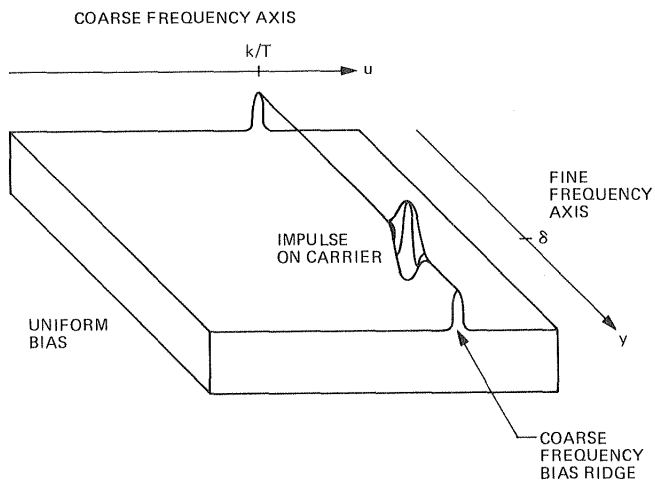


Fig. 6. Impulse response for TSI folded spectrum processor for a single tone input at frequency $f' = k/T + \delta$, showing uniform bias, signal dependent bias, and impulse riding on carrier

(a) $\delta f = 120$ Hz

(b) $\delta f = 240$ Hz

(c) $\delta f = 600$ Hz

(d) $\delta f = 2100$ Hz

Fig. 7. Experimental results for the TSI folded spectrum processor of Fig. 5, showing cross sections through the coarse frequency ridge for various fine frequencies

$$F(u, v) = \sum_{n=0}^{N-1} \left| \int f(x, n) \exp(-j2\pi ux) dx + r \exp[-jb(nT)^2 V^2] \right|^2 \cos(by^2) * \delta(nT - y/V)$$

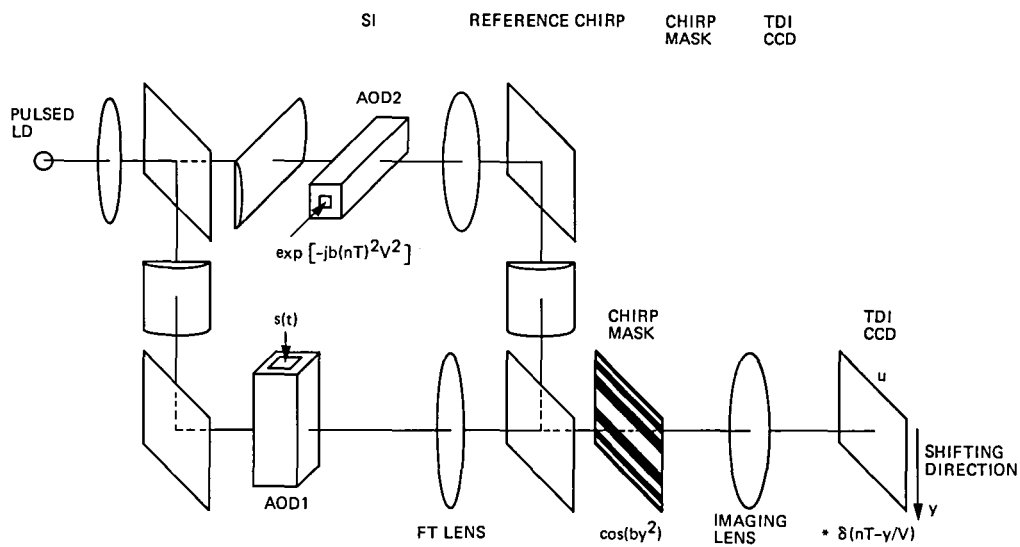


Fig. 8. Architecture for performing TSI folded spectrum using a TDI CCD to perform a fine resolution chirp transform

(a) $\delta f = -100$ Hz

(b) $\delta f = -1000$ Hz

(c) $\delta f = -2000$ Hz

(d) $\delta f = -3000$ Hz

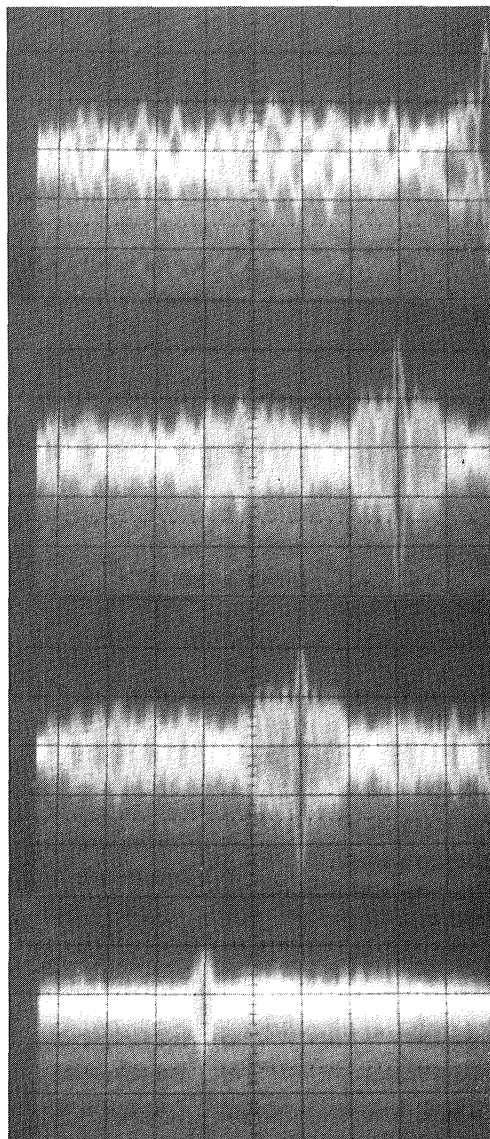
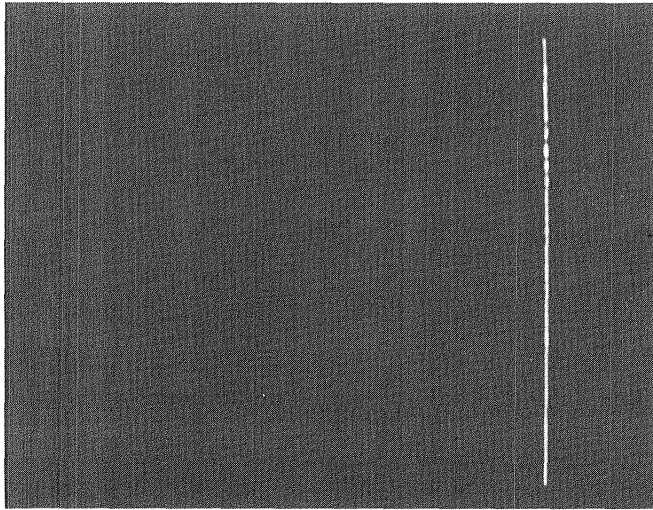
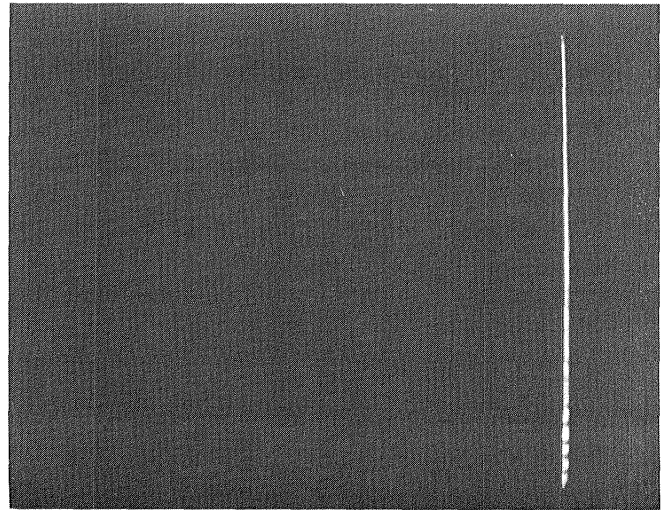


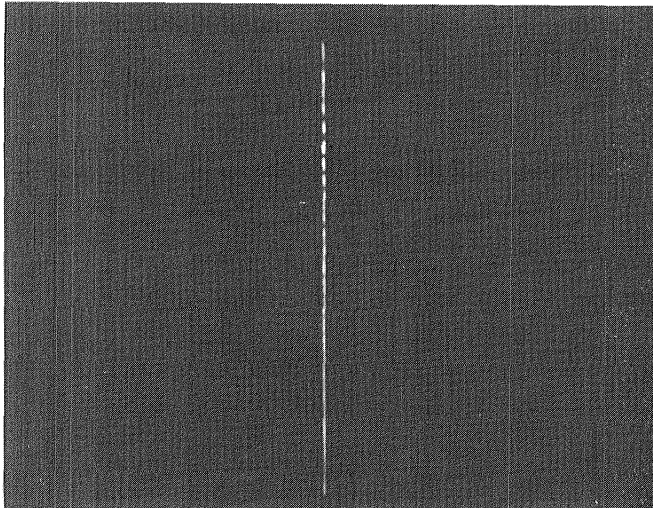
Fig. 9. Cross sections through coarse frequency ridge for the folded spectrum processor of Fig. 8 for various fine frequencies



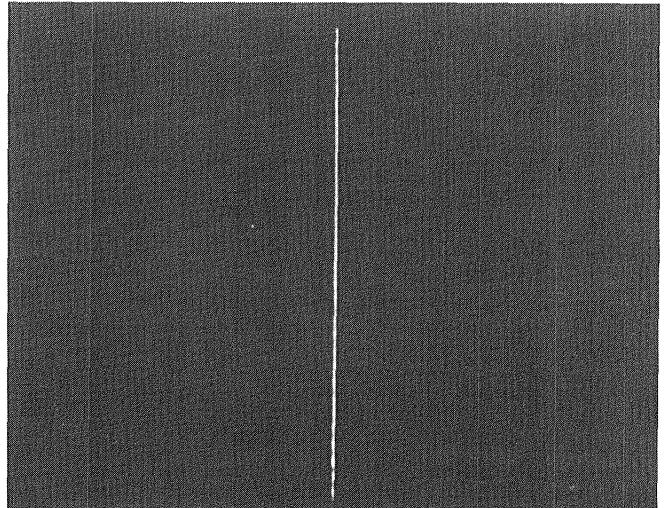
(a) 60.000 MHz



(b) 60.003 MHz



(c) 50.000 MHz



(d) 50.003 MHz

Fig. 10. Impulse response of TSI folded spectrum processor displayed in a two-dimensional format on a video monitor

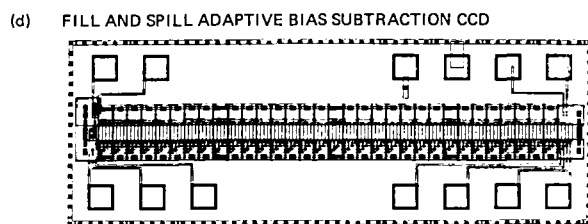
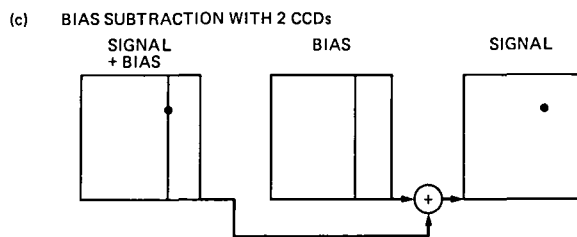
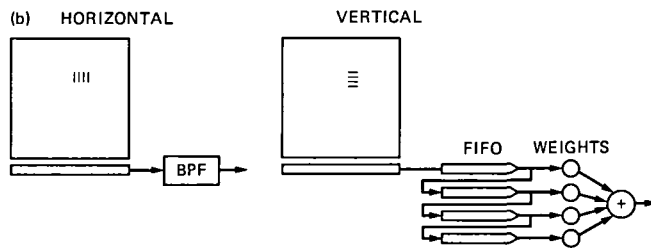
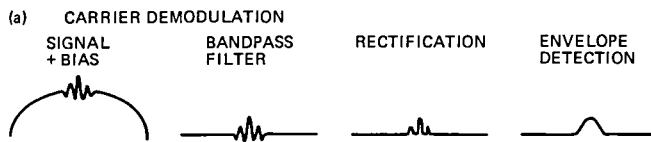


Fig. 11. Demodulation schemes required to separate signal from bias terms

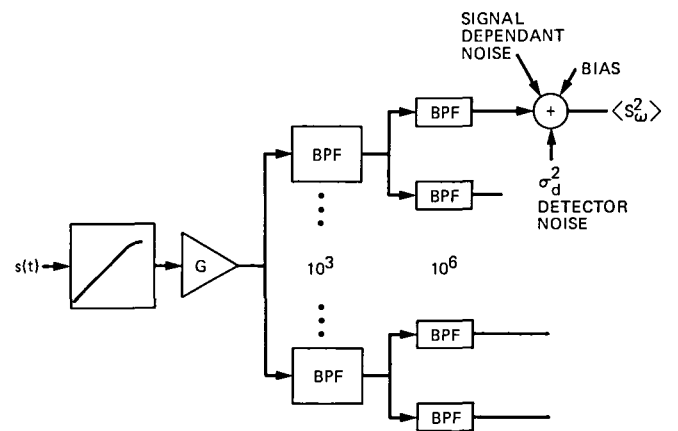


Fig. 12. Model used for sensitivity and processing gain analysis

Viterbi Algorithm on a Hypercube: Concurrent Formulation

F. Pollara

Communications Systems Research Section

The similarity between the Fast Fourier Transform and the Viterbi algorithm is exploited to develop a Concurrent Viterbi Algorithm suitable for a multiprocessor system interconnected as a hypercube. The proposed algorithm can efficiently decode large constraint length convolutional codes, using different degrees of parallelism, and is attractive for VLSI implementation.

I. Introduction

Concurrent computers have the potential to obtain large increases in computational power. This is true if one can find a concurrent decomposition of a given algorithm.

We consider the Viterbi Algorithm for decoding $(m, 1/n_0)$ convolutional codes, where m is the memory (constraint length = $m + 1$) and $1/n_0$ is the code rate, and we describe an efficient decomposition of this problem, the Concurrent Viterbi Algorithm (CVA), which is suitable for multiprocessor systems with a Hypercube architecture.

There are two key requirements in the problem decomposition:

- (1) Divide the problem in equal parts, in order to share equally the execution time available in each processor.
- (2) Minimize the communication between the parts, so that each processor needs to share information only with its neighbors.

Fox (Ref. 1) has shown that the Hypercube is a natural topology for the binary Fast Fourier Transform (FFT), and high efficiency can be obtained with this structure. We will

show that there is a simple correspondence between the connectivity of the FFT algorithm and the trellis diagram of the Viterbi Algorithm. Therefore, efficient methods for implementing the Viterbi Algorithm on a Hypercube computer can be developed.

II. Hypercube Computer Structure

In general, it is desirable for an interconnection structure to have a low number of links per node (low degree of a node), and a small internode distance. This distance d_{xy} between any two nodes x and y is defined as the minimum number of links required to send a message from x to y . The diameter D of a network with N nodes is defined as $D = \max \{d_{xy} | 0 \leq x, y \leq N\}$.

A Boolean n -cube computer, or just Hypercube (Ref. 2), is a network of $N = 2^n$ processors placed at the vertices of an n -cube, and connected by its edges. Such a structure is attractive because both the degree of a node and the diameter, which are equal to n , grow only linearly with the dimensionality of the cube.

In a multiprocessor network there is always a trade-off between the degree of a node and the diameter, the extreme

case being the completely connected network which has $N - 1$ links per node and $D = 1$. In general a low degree of a node implies a large diameter.

The Hypercube structure seems a reasonable compromise for practical multiprocessor systems, except for the disadvantage of offering limited input/output capability. This negative aspect, which is less important for computationally intensive (vs. I/O intensive) algorithms, is furthermore mitigated by the small diameter of the network, and the simplicity of efficient broadcasting methods.

Two processors x and y will be called neighbors if their binary labels differ only in one position, i.e.,

$$x = [x_{n-1}, x_{n-2}, \dots, x_k, \dots, x_0]$$

$$= \sum_{k=0}^{n-1} 2^k x_k$$

where $x_k \in \{0, 1\}$, $y = [x_{n-1}, x_{n-2}, \dots, x_k, \dots, x_0]$, and \bar{x}_k is the complement of x_k . In this context, the distance d_{xy} between two processors is just the Hamming distance of their binary labels, and neighbors have $d_{xy} = 1$. In the Hypercube, the number of nodes at distance d from a given node (node $[0, 0, \dots, 0]$ can be considered without loss of generality) is $N_d = \binom{n}{d}$, so that the average distance is

$$\bar{d} = \frac{1}{N-1} \sum_{d=1}^n d \binom{n}{d}$$

$$= \frac{n}{2} \frac{N}{N-1} \approx \frac{n}{2}$$

III. Equivalence of Networks

We now define two basic network structures: the m -stage Viterbi algorithm trellis (de Bruijn graph), shown in Fig. 1 for $M = 2^m = 8$ states, and the FFT decimation-in-time graph of Fig. 2.

Let $x = [x_{m-1}, \dots, x_0]$ be the binary index of a state or node of the graphs, and $u = [u_0, \dots, u_k, \dots, u_{m-1}]$, $u_k \in \{0, 1\}$, be a sequence of input bits which define one of the two possible paths out of each node, where k represents the stage.

First, consider the elementary transformation $\sigma(x, u_k)$ which describes the state transitions at stage k , and is defined as

$$\sigma(x, u_k) = \sigma([x_{m-1}, \dots, x_0], u_k)$$

$$\stackrel{\Delta}{=} [u_k, x_{m-1}, \dots, x_1] \quad (1)$$

This is a cyclic right shift of x , with x_0 replaced by u_k . Then the transformation $\sigma(\cdot, \cdot)$ completely describes the transitions of the graph in Fig. 1, and the m -stage transformation from a state x at stage 0 to state y at stage m is defined as

$$y = \sigma^{(m)}(x, u)$$

$$\stackrel{\Delta}{=} \sigma(\sigma(\dots \sigma(\sigma(x, u_0), u_1) \dots), u_{m-1}) \quad (2)$$

The elementary transformation needed to describe Fig. 2 is given by

$$\omega(x, u_k) \stackrel{\Delta}{=} [x_{m-1}, \dots, x_{k+1}, u_k, x_{k-1}, \dots, x_0] \quad (3)$$

which replaces x_k by u_k . The complete m -stage graph of Fig. 2 is then described by the transformation $\omega^{(m)}(x, u)$,

$$y = \omega^{(m)}(x, u)$$

$$\stackrel{\Delta}{=} \omega(\omega(\dots \omega(\omega(x, u_0), u_1) \dots), u_{m-1})$$

$$= [u_{m-1}, \dots, u_0] \quad (4)$$

Now, it is easy to verify that, at the m th stage,

$$\sigma^{(m)}(x, u) = \omega^{(m)}(x, u)$$

Therefore, the two networks lead from a given state x to the same state y , after m stages.

The equivalence of the two networks can be further expressed, at any stage, by defining the cyclic right shift operator

$$\rho^{(k)}(x) = [x_{k-1}, x_k, \dots, x_{m-1}, x_0, \dots, x_{k-2}]$$

where $\rho^{(m)}(x) = \rho^{(0)}(x) = x$, and verifying that,

$$\sigma^{(k)}(x, u) = \rho^{(k)}(\omega^{(k)}(x, u)) \quad (5)$$

This result shows that, if we relabel each node x of the graph in Fig. 1 with the label $\hat{x} = \rho^{(k)}(x)$ at stage k , the two networks are functionally and topologically equivalent; that is, they are just two different ways of drawing the same network. A given path generated by an input sequence u visits the same nodes in Fig. 1 and Fig. 2, if we relabel each node x in Fig. 1 by $\rho^{(k)}(x)$.

Having established this formalism on networks, we can now apply the above results to the study of algorithm structures, in particular to the Viterbi algorithm and its relationship with the radix-2 FFT.

IV. Concurrent Viterbi Algorithm

Consider a multiprocessor system with N processors located at the vertices of an n -cube and linked only by the edges of the cube (see an example for $n = 3$ in Fig. 3[a]). Note that the nodes are labeled by an n -bit binary number, so that the i th bit is the coordinate of a node along the i th dimension.

If in Fig. 2 we collapse the horizontal dimension, we obtain a graph which is exactly identical to that of Fig. 3, i.e., with the same connections between nodes. This observation, as explained in Refs. 1 and 3, suggests a natural way to implement the FFT on a Hypercube computer.

The implementation of the FFT on the Hypercube can be stated more formally if we define the Hypercube (m -cube) network by the transformation,

$$\gamma[x_{m-1}, \dots, x_k, \dots, x_0] = [x_{m-1}, \dots, x_k, \dots, x_0] \quad (6)$$

where \bar{x}_k is the complement of x_k , and observe that the transformation in Eq. (3) can always be obtained by Eq. (6), since $u_k \in \{0, 1\}$ and $u_k \equiv x_k$ requires no communication (self-loop).

To perform the first stage of Fig. 2, let the nodes of Fig. 3 communicate along the first dimension, and so on for each stage and dimension. In this way, the links provided by the n -cube are just those necessary to perform the FFT. This implementation on the n -cube is possible since the FFT requires communication only between neighboring nodes of the cube.

At first, the network of Fig. 1 might seem to require communication between distant nodes on the cube. But this problem can be easily overcome if we relabel the nodes as discussed in Sec. III. Specifically, at stage k , processor x will represent state $\rho^{(k)}(x)$ of the Viterbi trellis. Processor transitions are described by the graph of Fig. 2, while state transitions are given by Fig. 1, as desired. Therefore a Viterbi decoder can be efficiently implemented on the Hypercube, exactly as for the FFT. The similarity between the FFT and Viterbi trellis was previously pointed out by Forney (Ref. 3), but apparently not exploited in any practical way.

Each processor, at stage k , receives the accumulated metric and survivor of its neighbor along dimension k of the cube,

and performs the usual comparison and update. In a practical Viterbi decoder for a $(m, 1/n_0)$ code, the number of stages required to obtain a performance very close to optimum is approximately $5m$. Notice that, when the stage k is a multiple of m , the state and processor labels are identical, since $\rho^{(m)}(x) = x$, so that we may easily select the decoded bit belonging to the most likely survivor. However, in order to minimize internode communications, it may be more advantageous to increase slightly the number of stages and read the decoded bit at node zero, which simplifies I/O operations (see Sec. V).

V. Message Broadcasting

Performing the CVA requires that blocks of data be loaded in every processor: This operation is called broadcasting. In the Hypercube (Ref. 2), data from the host processor is directly exchanged only through node zero (the origin of the cube). Therefore, an efficient concurrent method is required to broadcast a message from node zero to all other nodes. Since the diameter of an n -cube is n , a lower bound on the broadcasting time is n time units (where the unit is the time to send a message to a neighbor).

Assume that message A is in node zero, at time zero. In each subsequent time slot k , send messages in parallel from each node $x = [x_{m-1}, \dots, x_{k+1}, 0, x_{k-1}, \dots, x_0]$ to each node $\gamma(x)$, the neighbors along dimension k . After n time units, message A has propagated to all nodes.

Even though this method does not minimize the number of communications (with the advantage of a very simple indexing), it optimizes the total broadcasting time to n time units. The result is clearly optimum, since it achieves the lower bound.

VI. Decoders for Large Constraint Length

Existing Hypercube computers have up to 128 nodes ($n = 7$), and will soon be extended to 1,024 nodes ($n = 10$). Yet, in order to decode powerful convolutional codes with $m > 10$, one needs to obtain algorithms which assign more than one state per processor. This need is dictated not only by the practical limitations on the physical size of the computer, but also by the goal of achieving high computational efficiency.

The efficiency η of a parallel computer is defined as,

$$\eta = \frac{N_o t_o}{N_o t_o + N_t t_t} = \frac{\text{sequential algorithm time}}{N \times (\text{parallel algorithm time})}$$

and the speed-up σ is given by $\sigma = \eta N$, where N is the number of processors, N_o is the number of parallel operations (butterflies), t_o is the time required by each operation, N_t is the number of parallel data transfers, and t_t is the communication time.

When the number of states M of the decoder is larger than the available number of processors N , states can be grouped in sets of $S = 2^s$ states per processor, where $M = SN$. To see how this is possible for $S = 2$ in the proposed CVA implementation, consider Fig. 2 and group each pair of nodes into one processor $P_{[i/2]}$, for all nodes $i, i = 0, \dots, 7$, where $[j]$ is the largest integer less than or equal to j . Similarly, with two processors $P_{[i/4]}$, $i = 0, \dots, 7$, we obtain the case $S = 4$. The extreme cases, $S = M$ and $S = 1$ represent the completely sequential and completely parallel decoder, respectively. Intermediate cases represent different degrees of parallelism or a different *granularity* of the algorithm, which is defined as the amount of computation between successive data transfers. In general, the efficiency increases with the granularity.

During m stages of the CVA, the number of parallel data transfers is,

$$N_t = S(m - s) = \frac{M}{N}n \quad (7)$$

since only $m - s$ stages of Fig. 2 need to communicate with neighbors (s stages do only internal computations). The number of parallel operations (butterflies) N_o is given by:

$$N_o = \frac{S}{2}m = \frac{M}{2N}m \quad (8)$$

As an example, N_t and N_o are plotted in Fig. 4 for $M = 64$. From Eqs. (7) and (8) we have that the efficiency η decreases as S decreases from N to 1, and, for $N = M$, η is equal to the

ratio $t_o/(t_o + 2t_t)$, which depends on the hardware implementation.

The CVA with $S > 1$ is useful because it allows the implementation of complex decoders, avoiding the pin-limitation constraint problem encountered in existing VLSI decoders. This problem is due to the particular partitioning of the traditional decoder into a branch metric computation block and a path memory storage block. This partition requires a rapidly increasing number of pins in the VLSI chips. The proposed CVA has instead a number of connections per node increasing only linearly with the dimensionality of the cube, and is therefore more suitable for VLSI implementation.

Furthermore, the CVA has been extended to high rate $(m, k_o/n_o)$ codes with $k_o > 1$, where k_o is the number of input bits in the encoder. This extension is possible only for a limited range of m, k_o and S , the number of states per processor. An example for $(3, 2/n_o)$ codes is given in Fig. 5, where $S = 2$.

Given a rate $1/n_o$ code it is known how to generate all the punctured codes of rate k_o/n_o , $k_o > 1$. Since these codes involve only pairwise comparisons at each stage, it is certainly possible to decode them with the CVA. It must be noted however that punctured codes require more stages, and this is equivalent to linking nodes of the Hypercube which are not neighbors, by using multiple stages.

VII. Conclusion

The proposed CVA decoder has been implemented and successfully tested on a 64-node Hypercube computer for $(m, 1/n_o)$ codes, with $m = 2, \dots, 14$. Present results confirm the usefulness of the CVA for large constraint length codes.

Acknowledgment

The author wishes to thank R. J. McEliece and C. L. Seitz of Caltech for providing access to the Hypercube and E. Majani for some of the programs.

References

1. Fox, G. C., and Otto, S. W., "Algorithms for Concurrent Processors," *Physics Today*, Vol. 37, No. 5, pp. 50-59, May 1984.
2. Seitz, C. L., "The Cosmic Cube," *Communications of the ACM*, Vol. 28, No. 1, pp. 23-33, January 1985.
3. Pease, M. C., "An Adaptation of the Fast Fourier Transform for Parallel Processing," *Journal of the ACM*, Vol. 15, No. 2, pp. 252-264, April 1968.
4. Forney, G. D., "The Viterbi Algorithm," *Proc. IEEE*, Vol. 61, No. 3, pp. 268-278, March 1973.

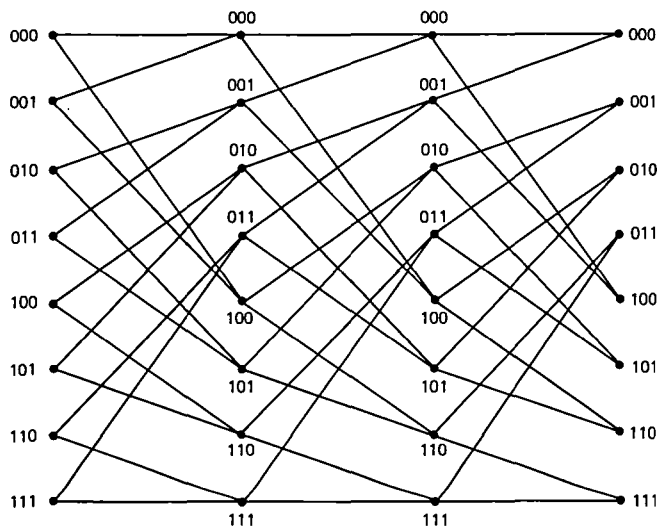


Fig. 1. The m -stage Viterbi algorithm trellis ($m = 3$)

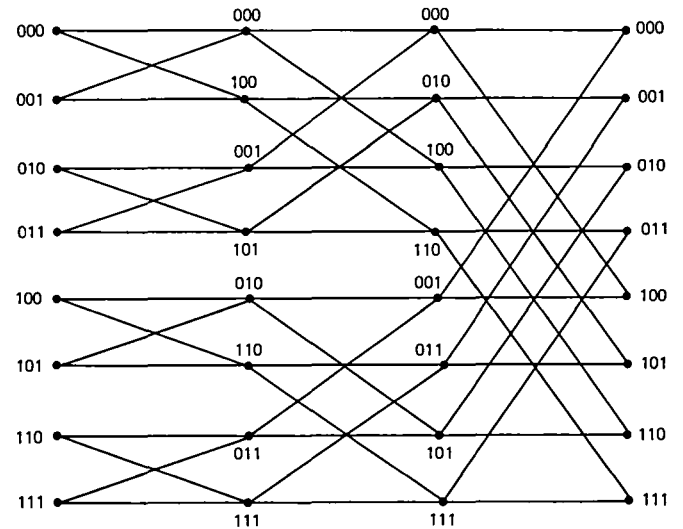


Fig. 2. The FFT decimation-in-time graph ($m = 3$)

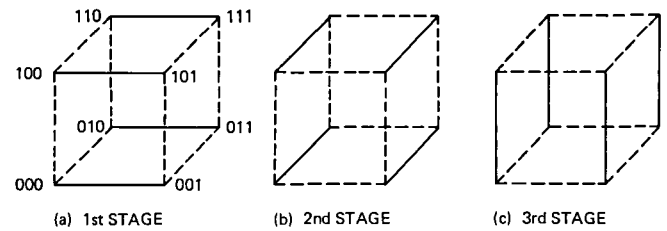


Fig. 3. The 3-cube graph

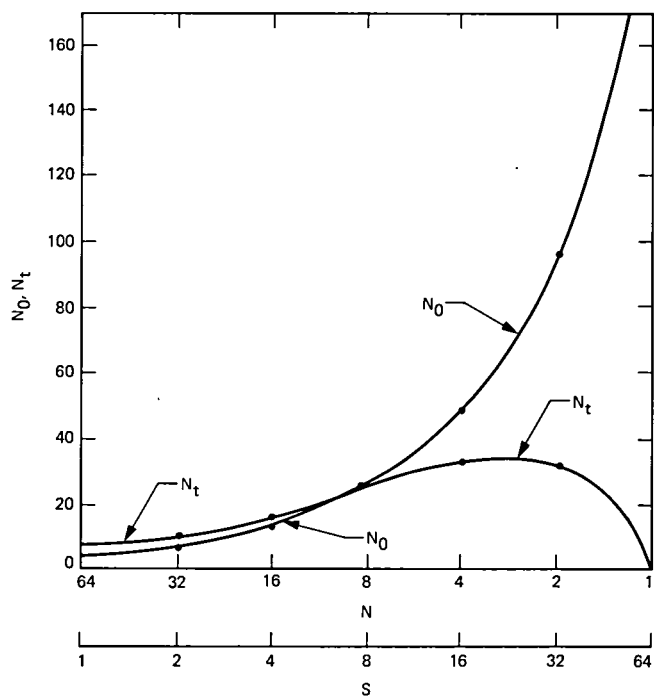


Fig. 4. N_0 and N_t vs S and N

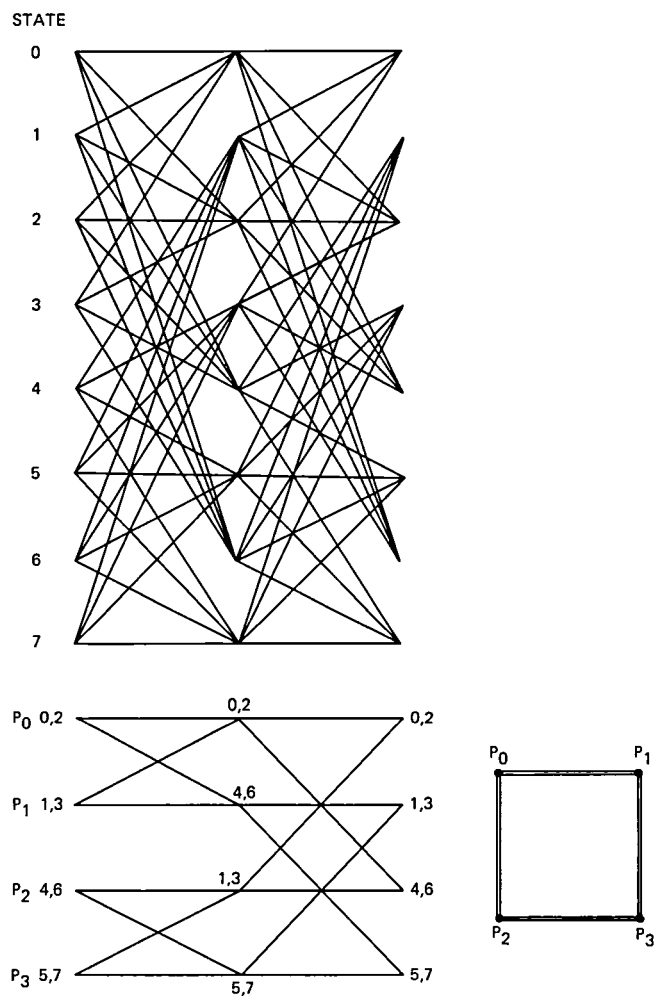


Fig. 5. Decoder for $(3, 2/n_0)$ code, with $S = 2$

Author Index,¹ 1985

The Telecommunications and Data Acquisition Progress Report

42-81, January–March, May 15, 1985
 42-82, April–June, August 15, 1985
 42-83, July–September, November 15, 1985
 42-84, October–December, February 15, 1986

Aguirre, S.

- 42-84 Acquisition Times of Carrier Tracking Sampled Data Phase-Locked Loops, pp. 88-93.

Berge, G. L.

- 42-81 Relating the Planetary Ephemerides and the Radio Reference Frame, pp. 1-8.

See Niell, A. E.

Berner, J. B.

- 42-83 Error and Erasure Probabilities for Galileo Uplink Code, pp. 165-179.

J. B. Berner, R. J. McEliece, and E. C. Posner

Borutzki, S. E.

- 42-81 Maintenance of Time and Frequency in the DSN Using the Global Positioning System, pp. 94-108.

See Clements, P. A.

Brockman, M. H.

- 42-84 Performance Characteristics for an Array of Two Receiving Systems With Equal Apertures and Enhanced Radio Frequency Carrier Margin Improvement, pp. 112-126.

- 42-84 Performance Characteristics for an Array of Two Receiving Systems With Unequal Predetection Signal-to-Noise Ratios and Enhanced Radio Frequency Carrier Margin Improvement, pp. 101-111.

Brokl, S. S.

- 42-83 Controller and Interface Module for the High-Speed Data Acquisition System Correlator/Accumulator, pp. 113-124.

- 42-83 A General Monitor and Control Interface to the VAX UNIBUS by Way of the DR11-C I/O Port, pp. 125-133.

Brown, D. W.

- 42-82 Planning for VLA/DSN Arrayed Support to the Voyager at Neptune, pp. 125-135.

See Layland, J. W.

Campbell, J. K.

- 42-81 Relating the Planetary Ephemerides and the Radio Reference Frame, pp. 1-8.

See Niell, A. E.

Cha, A. G.

- 42-84 Physical Optics Analysis of a Four-Reflector Antenna: Part 1, pp. 94-100

- 42-84 Gain, Phase, and Frequency Stability of DSS-42 and DSS-43 for Voyager Uranus Encounter, pp. 164-175.

A. G. Cha and R. Levy

Chan, F. P.

- 42-81 High-Speed Digital Baseband Mixer, pp. 63-80.

F. P. Chan, M. P. Quirk, and R. F. Jurgens

¹In the case of joint authorship, the reader is referred to the citation under the first author where all authors of the article are listed.

Chang, J. J.

- 42-81 Techniques for Computing the DFT Using the Residue Fermat Number Systems and VLSI, pp. 18-30.

See Truong, T. K.

Chatburn, C. C.

- 42-81 Network Information Management Subsystem, pp. 109-115.

Chian, C. T.

- 42-82 Load-Deflection Tests and Computer Analyses of a High-Precision Adhesive-Bonded Antenna Reflector Panel, pp. 68-81.

C. T. Chian and R. Levy

- 42-82 Seismic Analysis of the Large 70-Meter Antenna, Part 1: Earthquake Response Spectra Versus Full Transient Analysis, pp. 31-42.

See Kiedron, K.

- 42-83 Seismic Analysis of the Large 70-Meter Antenna, Part II: General Dynamic Response and a Seismic Safety Check, pp. 12-25.

See Kiedron, K.

Ching, L.

- 42-82 SETI Radio Spectrum Surveillance System, pp. 173-184.

See Crow, B.

Clements, P. A.

- 42-81 Maintenance of Time and Frequency in the DSN Using the Global Positioning System, pp. 94-108.

P. A. Clements, A. Kirk, and S. E. Borutzki

Crow, B.

- 42-82 SETI Radio Spectrum Surveillance System, pp. 173-184.

B. Crow, A. Lokshin, M. Marina, and L. Ching

Crowe, R. A.

- 42-82 The GCF Mark IV Implementation and Beyond, pp. 163-172.

Cucchissi, J. J.

- 42-82 A New 70-Meter Antenna Quadripod With Reduced RF Blockage, pp. 24-30.

Daher, K;

- 42-84 Preliminary Results Toward Injection Locking of an Incoherent Laser Array, pp. 26-34.

Davidson, J. M.

- 42-82 Mobile VLBI and GPS Measurement of Vertical Crustal Motion, pp. 185-198.

See Kroger, P. M.

Deutsch, L. J.

- 42-81 An Integrated UNIX-Based CAD System for the Design and Testing of Custom VLSI Chips, pp. 51-62.

- 42-83 A Laser Plotting System for VLSI Chip Layouts, pp. 81-91.

See Harding, J. A.

- 42-83 A VLSI Single Chip 8-Bit Finite Field Multiplier, pp. 45-50.

See Hsu, I. S.

- 42-83 A VLSI Single Chip (255, 223) Reed-Solomon Encoder, pp. 51-56.

See Hsu, I. S.

- 42-84 A Single Chip VLSI Reed-Solomon Decoder, pp. 73-81.

See Shao, H. M.

Divsalar, D.

- 42-82 A Sequential Decoding Performance Analysis for International Comet Explorer, pp. 82-91.

Donivan, F. F.

- 42-84 Deep Space Network Radio Science System for Voyager Uranus and Galileo Missions, pp. 143-151.

See Peng, T. K.

Esposito, P. B.

- 42-81 Relating the Planetary Ephemerides and the Radio Reference Frame, pp. 1-8.

See Niell, A. E.

Falin, B. W.

- 42-82 DSN Frequency and Timing System, Mark IV-85, pp. 113-119.

Fanelli, N. A.

- 42-82 JPL Emergency Support of TDRSS and Compatible Satellites, pp. 120-124.

- 42-84 ICE Encounter Operations, pp. 176-185.

N. Fanelli and D. Morris

Faulkner, J.

- 42-82 A VLBI Survey at 2.29 GHz, pp. 1-10.

See Morabito, D. D.

Galindo-Israel, V.

- 42-84 Low-Loss Off-Axis Feeds for Symmetric Dual-Reflector Antennas, pp. 35-59.

See Veruttipong, V.

Gardner, E. C.

- 42-82 Mobile VLBI and GPS Measurement of Vertical Crustal Motion, pp. 185-198.

See Kroger, P. M.

Goodwin, J. P.

- 42-84 Usuda Deep Space Center Support for ICE, pp. 186-196.

Gordon, D. D.

- 42-84 Arecibo Observatory Support of the U.S. International Cometary Explorer Mission Encounter at Comet Giacobini-Zinner, pp. 197-202.

D. D. Gordon and M. T. Ward

Grimm, M. J.

- 42-83 A Wide-Band, High-Resolution Spectrum Analyzer, pp. 180-190.

See Quirk, M. P.

Harding, J. A.

- 42-83 A Laser Plotting System for VLSI Chip Layouts, pp. 81-91.

J. A. Harding and L. J. Deutsch

Hays, D. A.

- 42-81 Photodetection With Cooled Avalanche Photodiodes: Theory and Preliminary Experimental Results, pp. 9-17.

See Robinson, D. L.

Hoppe, D.

- 42-82 An Experimental TE_{12} - TE_{11} Circular Waveguide Mode Converter, pp. 43-56.

- 42-82 Propagation and Radiation Characteristics of a Multimode Corrugated Waveguide Feedhorn, pp. 57-67.

Hsu, I. S.

- 42-81 Techniques for Computing the DFT Using the Residue Fermat Number Systems and VLSI, pp. 18-30.

See Truong, T. K.

- 42-82 The VLBI Design of Error-Trellis Syndrome Decoding for Convolution Codes, pp. 92-107.

See Reed, I. S.

- 42-83 A VLSI Single Chip (255, 223) Reed-Solomon Encoder, pp. 51-56.

I. S. Hsu, L. J. Deutsch, T. K. Truong, and I. S. Reed

- 42-83 A VLSI Single Chip 8-Bit Finite Field Multiplier, pp. 45-50.

I. S. Hsu, L. J. Deutsch, T. K. Truong, and H. M. Shao

- 42-84 A Single Chip VLSI Reed-Solomon Decoder, pp. 73-81.

See Shao, H. M.

Hurd, W. J.

- 42-83 A Class of Optimum Digital Phase Locked Loops for the DSN Advanced Receiver, pp. 63-80.

See Kumar, R.

- 42-83 Carrier Tracking by Smoothing Filter Can Improve Symbol SNR, pp. 57-62.

See Pomalaza-Raez, C. A.

- 42-84 Intercontinental Antenna Arraying by Symbol Stream Combining at ICE Giacobini-Zinner Encounter, pp. 220-228.

W. J. Hurd, F. Pollara, M. D. Russell, B. Sieve and P. U. Winter

Imbriale, W.

- 42-84 Low-Loss Off-Axis Feeds for Symmetric Dual-Reflector Antennas, pp. 35-59.

See Veruttipong, V.

Jauncey, D. L.

- 42-82 A VLBI Survey at 2.29 GHz, pp. 1-10.

See Morabito, D. D.

Jensen, J. M.

- 42-82 The VLBI Design of Error-Trellis Syndrome Decoding for Convolution Codes, pp. 92-107.

See Reed, I. S.

Jurgens, R. F.

- 42-81 High-Speed Digital Baseband Mixer, pp. 63-80.

See Chan, F. P.

Katow, M. S.

- 42-83 Coupled Translations of the 64-Meter Antenna Subreflector Supports, pp. 1-11.

Kiedron, K.

- 42-82 Seismic Analysis of the Large 70-Meter Antenna, Part I: Earthquake Response Spectra Versus Full Transient Analysis, pp. 31-42.

K. Kiedron and C. T. Chian

- 42-83 Seismic Analysis of the Large 70-Meter Antenna, Part II: General Dynamic Response and a Seismic Safety Check, pp. 12-25.

K. Kiedron and C. T. Chian

Kirk, A.

- 42-81 Maintenance of Time and Frequency in the DSN Using the Global Positioning System, pp. 94-108.

See Clements, P. A.

Kroger, P. M.

- 42-82 Mobile VLBI and GPS Measurement of Vertical Crustal Motion, pp. 185-198.

P. M. Kroger, J. M. Davidson, and E. C. Gardner

Kumar, R.

- 42-83 A Class of Optimum Digital Phase Locked Loops for the DSN Advanced Receiver, pp. 63-80.

R. Kumar and W. J. Hurd

Lanyi, G. E.

- 42-84 The Effect of the Dynamic Wet Troposphere on VLBI Measurements, pp. 1-17.

See Treuhaft, R. N.

Lawton, W.

- 42-83 A Signal Detection Strategy for the SETI All Sky Survey, pp. 191-208.

See Solomon, J.

Layland, J. W.

- 42-82 Planning for VLA/DSN Arrayed Support to the Voyager at Neptune, pp. 125-135.

J. W. Layland and D. W. Brown

- 42-82 A VLA Experiment — Planning for Voyager at Neptune, pp. 136-142.

J. W. Layland, P. J. Napier, and A. R. Thompson

- 42-84 ICE Telemetry Performance, pp. 203-213.

Lee, P. J.

- 42-81 Bit Error Rate of Coherent M -ary PSK, pp. 31-37.

- 42-82 High-Rate Convolution Code Construction With the Minimum Required SNR Criterion, pp. 108-112.

Levy, R.

- 42-82 Load-Deflection Tests and Computer Analyses of a High-Precision Adhesive-Bonded Antenna Reflector Panel, pp. 68-81.

See Chian, C. T.

- 42-84 Gain, Phase, and Frequency Stability of DSS-42 and DSS-43 for Voyager Uranus Encounter, pp. 164-175.

See Cha, A. G.

- 42-84 New Reflective Symmetry Design Capability in the JPL-IDEAS Structure Optimization Program, pp. 18-25.

See Strain, D.

Linfield, R. P.

- 42-84 The Search for Reference Sources for Δ VLBI Navigation of the Galileo Spacecraft, pp. 152-163.

See Ulvestad, J. S.

Loftsson, J.

- 42-82 Periodic Binary Sequences With Very Good Auto-correlation Properties, pp. 143-158.

See Tyler, S.

- 42-82 A Binary Sequence of Period 60 With Better Auto-correlation Properties Than the Barker Sequence of Period 13, pp. 159-162.

See Watkins, J.

Lokshin, A.

- 42-82 SETI Radio Spectrum Surveillance System, pp. 173-184.

See Crow, B.

Ma, C.

- 42-83 Comparison of GSFC and JPL VLBI Modeling Software Benchmark, pp. 101-112.

See Sovers, O. J.

Marina, M.

- 42-82 SETI Radio Spectrum Surveillance System, pp. 173-184.

See Crow, B.

McClure, D.

- 42-81 Repair of the DSS-14 Pedestal Concrete, pp. 136-148.

McEliece, R. J.

- 42-81 Symbol Stream Combining in a Convolutionally Coded System, pp. 47-50.

R. J. McEliece, F. Pollara, and L. Swanson

- 42-83 Error and Erasure Probabilities for Galileo Uplink Code, pp. 165-179.

See Berner, J. B.

- 42-83 The Number of Stable Points of an Infinite-Range Spin Glass Memory, pp. 209-215.

R. J. McEliece and E. C. Posner

- 42-84 On the Decoder Error Probability for Reed-Solomon Codes, pp. 66-72.

R. J. McEliece and L. Swanson

- 42-84 A Note on the Wideband Gaussian Broadcast Channel, pp. 60-65.

R. J. McEliece, E. C. Posner, and L. Swanson

McGinness, H.

- 42-81 A Description of the 64-Meter Antenna Elevation Drive Gears and Their Strange Wear, pp. 116-135.

Mileant, A.

- 42-81 Digital Filters and Digital Phase-Locked Loops, pp. 81-92.

See Simon, M.

Morabito, D. D.

- 42-82 A VLBI Survey at 2.29 GHz, pp. 1-10.

D. D. Morabito, R. A. Preston, J. G. Williams, J. Faulkner, D. L. Jauncey, and G. D. Nicolson

Morris, D.

- 42-84 ICE Encounter Operations, pp. 176-185.

See Fanelli, N.

Muhleman, D. O.

- 42-81 Relating the Planetary Ephemerides and the Radio Reference Frame, pp. 1-8.
See Niell, A. E.

Nadeau, T.

- 42-84 Periodic Variations in the Signal-to-Noise Ratios of Signals Received from the ICE Spacecraft, pp. 214-219.

Napier, P. J.

- 42-82 A VLA Experiment — Planning for Voyager at Neptune, pp. 136-142.
See Layland, J. W.

Newhall, X X

- 42-81 Relating the Planetary Ephemerides and the Radio Reference Frame, pp. 1-8.
See Niell, A. E.

Nicolson, G. D.

- 42-82 A VLBI Survey at 2.29 GHz, pp. 1-10.
See Morabito, D. D

Niell, A. E.

- 42-81 Relating the Planetary Ephemerides and the Radio Reference Frame, pp. 1-8.
A. E. Niell, X X Newhall, R. A. Preston, G. L. Berge, D. O. Muhleman, D. J. Rudy, J. K. Campbell, P. B. Esposito and E. M. Standish

Olsen, E. T.

- 42-83 A Signal Detection Strategy for the SETI All Sky Survey, pp. 191-208.
See Solomon, J.

Pei, D. Y.

- 42-81 Techniques for Computing the DFT Using the Residue Fermat Number Systems and VLSI, pp. 18-30.
See Truong, T. K.

Peng, T. K.

- 42-84 Deep Space Network Radio Science System for Voyager Uranus and Galileo Missions, pp. 143-151.
T. K. Peng and F. F. Donivan

Pitt, III, G. H.

- 42-83 Decoding Convolutionally Encoded Images, pp. 34-38.
G. H. Pitt, III, and L. Swanson
42-83 Erasure Information for a Reed-Solomon Decoder, pp. 39-44.
G. H. Pitt, III, and L. Swanson

Pollara, F.

- 42-81 A Software Simulation Study of a Sequential Decoder Using the Fano Algorithm, pp. 40-46.
42-81 Symbol Stream Combining in a Convolutionally Coded System, pp. 47-50.
See McEliece, R. J.
42-84 Viterbi Algorithm on a Hypercube: Concurrent Formulation, pp. 249-255.
42-84 Effects of Quantization on Symbol Stream Combining in a Convolutionally Coded System, pp. 82-87.
F. Pollara and L. Swanson
42-84 Intercontinental Antenna Arraying by Symbol Steam Combining at ICE Giacobini-Zinner Encounter, pp. 220-228.
See Hurd, W. J.

Pomalaza-Raez, C. A.

- 42-83 Carrier Tracking by Smoothing Filter Can Improve Symbol SNR, pp. 57-62.
C. A. Pomalaza-Raez and W. J. Hurd

Posner, E. C.

- 42-83 Error and Erasure Probabilities for Galileo Uplink Code, pp. 165-179.
See Berner, J. B.

- 42-83 The Number of Stable Points of an Infinite-Range Spin Glass Memory, pp. 209-215.
See McEliece, R. J.
- 42-84 A Note on the Wideband Gaussian Broadcast Channel, pp. 60-65.
See McEliece, R. J.
- Preston, R. A.**
- 42-81 Relating the Planetary Ephemerides and the Radio Reference Frame, pp. 1-8.
See Niell, A. E.
- 42-82 A VLBI Survey at 2.29 GHz, pp. 1-10.
See Morabito, D. D.
- Psaltis, D.**
- 42-84 Time and Space Integrating Acoustic-Optic Folded Spectrum Processing for SETI, pp. 229-248.
See Wagner, K.
- Quach, C. T.**
- 42-81 Determining Availability Characteristics of DSN Data Systems Using Discrepancy Report Data, pp. 149-161.
See Ruskin, A. M.
- Quirk, M. P.**
- 42-81 High-Speed Digital Baseband Mixer, pp. 63-80.
See Chan, F. P.
- 42-83 A Wide-Band, High-Resolution Spectrum Analyzer, pp. 180-190.
M. P. Quirk, H. S. Wilck, and M. J. Grimm
- 42-83 A signal Detection Strategy for the SETI All Sky Survey, pp. 191-208.
See Solomon, J.
- Reed, I. S.**
- 42-81 Techniques for Computing the DFT Using the Residue Fermat Number Systems and VLSI, pp. 18-30.
See Truong, T. K.
- 42-82 The VLBI Design of Error-Trellis Syndrome Decoding for Convolution Codes, pp. 92-107.
I. S. Reed, J. M. Jensen, T. K. Truong, and I. S. Hsu
- 42-83 A VLSI Single Chip (255, 223) Reed-Solomon Encoder, pp. 51-56.
See Hsu, I. S.
- 42-84 A Single Chip VLSI Reed-Solomon Decoder, pp. 73-81.
See Shao, H. M.
- Robinson, D. L.**
- 42-81 Photodetection With Cooled Avalanche Photodiodes: Theory and Preliminary Experimental Results, pp. 9-17.
D. L. Robinson and D. A. Hays
- Rodemich, E. R.**
- 42-82 Improved Mapping of Radio Sources From VLBI Data by Least-Squares Fit, pp. 199-210.
- Ross, D. L.**
- 42-83 Mark IV-A DSCC Telemetry System Description, pp. 92-100.
- Rudy, D. J.**
- 42-81 Relating the Planetary Ephemerides and the Radio Reference Frame, pp. 1-8.
See Niell, A. E.
- Ruskin, A. M.**
- 42-81 Determining Availability Characteristics of DSN Data Systems Using Discrepancy Report Data, pp. 149-161.
A. M. Ruskin and C. T. Quach
- Russell, M. D.**
- 42-84 Intercontinental Antenna Arraying by Symbol Stream Combining at ICE Giacobini-Zinner Encounter, pp. 220-228.
See Hurd, W. J.

Scheid, J. A.

- 42-82 Comparison of the Calibration of Ionospheric Delay in VLBI Data by the Methods of Dual Frequency and Faraday Rotation, pp. 11-23.

Shao, H. M.

- 42-83 A VLSI Single Chip 8-Bit Finite Field Multiplier, pp. 45-50.

See Hsu, I. S.

- 42-84 A Single Chip VLSI Reed-Solomon Decoder, pp. 73-81.

H. M. Shao, T. K. Truong, I. S. Hsu, L. J. Deutsch, and I. S. Reed

Siev, B.

- 42-84 Intercontinental Antenna Arraying by Symbol Stream Combining at ICE Giacobini-Zinner Encounter, pp. 220-228.

See Hurd, W. J.

Simon, M.

- 42-81 Digital Filters and Digital Phase-Locked Loops, pp. 81-92.

M. Simon and A. Mileant

Slobin, S. D.

- 42-84 A Conceptual 34-Meter Antenna Feed Configuration for Joint DSN/SETI Use From 1 to 10 GHz, pp. 127-134.

Solomon, J.

- 42-83 A Signal Detection Strategy for the SETI All Sky Survey, pp. 191-208.

J. Solomon, W. Lawton, M. P. Quirk, and E. T. Olsen

Sovers, O. J.

- 42-83 Comparison of GSFC and JPL VLBI Modeling Software Benchmark, pp. 101-112.

O. J. Sovers and C. Ma

Standish, E. M.

- 42-81 Relating the Planetary Ephemerides and the Radio Reference Frame, pp. 1-8.

See Niell, A. E.

Stephenson, S. N.

- 42-83 Mark IVA Project Training Evaluation, pp. 134-164.

Strain, D.

- 42-84 New Reflective Symmetry Design Capability in the JPL-IDEAS Structure Optimization Program, pp. 18-25.

D. Strain and R. Levy

Swanson, L.

- 42-81 Synchronizing Heavily Encoded Data in Bad Weather, pp. 38-39.

- 42-81 Symbol Stream Combining in a Convolutionally Coded System, pp. 47-50.

See McEliece, R. J.

- 42-83 Decoding Convolutionally Encoded Images, pp. 34-38.

See Pitt, III, G. H.

- 42-83 Erasure Information for a Reed-Solomon Decoder, pp. 39-44.

See Pitt, III, G. H.

- 42-84 A Note on the Wideband Gaussian Broadcast Channel, pp. 60-65.

See McEliece, R. J.

- 42-84 On the Decoder Error Probability for Reed-Solomon Codes, pp. 66-72.

See McEliece, R. J.

- 42-84 Effects of Quantization on Symbol Stream Combining in a Convolutionally Coded System, pp. 82-87.

See Pollara, F.

Thompson, A. R.

- 42-82 A VLA Experiment — Planning for Voyager at Neptune, pp. 136-142.

See Layland, J. W.

Thorman, H. C.

- 42-84 DSN Command System Mark IV-85, pp. 135-142.

Treuhart, R. F.

- 42-84 The Effect of the Dynamic Wet Troposphere on VLBI Measurements, pp. 1-17.

R. N. Treuhart and G. E. Lanyi

Truong, T. K.

- 42-81 Techniques for Computing the DFT Using the Residue Fermat Number Systems and VLSI, pp. 18-30.

T. K. Truong, J. J. Chang, I. S. Hsu, D. Y. Pei, and I. S. Reed

- 42-82 The VLBI Design of Error-Trellis Syndrome Decoding for Convolution Codes, pp. 92-107.

See Reed, I. S.

- 42-83 A VLSI Single Chip 8-Bit Finite Field Multiplier, pp. 45-50.

See Hsu, I. S.

- 42-83 A VLSI Single Chip (255, 223) Reed-Solomon Encoder, pp. 51-56.

See Hsu, I. S.

- 42-84 A Single Chip VLSI Reed-Solomon Decoder, pp. 73-81.

See Shao, H. M.

Tyler, S.

- 42-82 Periodic Binary Sequences With Very Good Auto-correlation Properties, pp. 143-158.

S. Tyler and J. Loftsson

- 42-82 A Binary Sequence of Period 60 with Better Auto-correlation Properties Than the Barker Sequence of Period 13, pp. 159-162.

See Watkins, J.

Ulvestad, J. S.

- 42-84 The Search for Reference Sources for Δ VLBI Navigation of the Galileo Spacecraft, pp. 152-163.

J. S. Ulvestad and R. P. Linfield

Veruttipong, T.

- 42-84 Low-Loss Off-Axis Feeds for Symmetric Dual-Reflector Antennas, pp. 35-59.

T. Veruttipong, V. Galindo-Israel, and W. Imbriale

Vo, Q. D.

- 42-83 In Search of a 2-dB Coding Gain, pp. 26-33.

See Yuen, J. H.

Wagner, K.

- 42-84 Time and Space Integrating Acoustic-Optic Folded Spectrum Processing for SETI, pp. 229-248.

K. Wagner and D. Psaltis

Ward, M. T.

- 42-84 Arecibo Observatory Support of the U.S. International Cometary Explorer Mission Encounter at Comet Giacobini-Zinner, pp. 197-202.

See Gordon, D. D.

Watkins, J.

- 42-82 A Binary Sequence of Period 60 With Better Auto-correlation Properties Than the Barker Sequence of Period 13, pp. 159-162.

J. Watkins, J. Loftsson, and S. Tyler

Wilck, H. S.

42-83 A Wide-Band, High-Resolution Spectrum Analyzer, pp. 180-190.

See Quirk, M. P.

Winter, P. U.

42-84 Intercontinental Antenna Arraying by Symbol Stream Combining at ICE Giacobini-Zinner Encounter, pp. 220-228.

See Hurd, W. J.

Williams, J. G.

42-82 A VLBI Survey at 2.29 GHz, pp. 1-10.

See Morabito, D. D.

Yuen, J. H.

42-83 In Search of a 2-dB Coding Gain, pp. 26-33.

J. H. Yuen and Q. D. Vo

End of Document